

# TECHNISCHE UNIVERSITÄT MÜNCHEN

Fakultät für Chemie

WACKER-Lehrstuhl für Makromolekulare Chemie

---

## **Tailoring Polypropylene: Behind the Scenes of Group IV Metallocene Catalysis**

---

**Martin Rolf Machat**

Vollständiger Abdruck der von der Fakultät für Chemie der Technischen Universität München zur Erlangung des akademischen Grades eines

### **Doktors der Naturwissenschaften**

genehmigten Dissertation.

Vorsitzender:

Prof. Dr. Kai-Olaf Hinrichsen

Prüfer der Dissertation

1. Prof. Dr. Dr. h. c. Bernhard Rieger
2. apl. Prof. Dr. Wolfgang Eisenreich
3. Prof. Dr. Timo Repo (schriftliche Beurteilung)  
Prof. Dr. Klaus Köhler (mündliche Prüfung)

Die Dissertation wurde am 05.03.2018 bei der Technischen Universität München eingereicht und durch die Fakultät für Chemie am 02.05.2018 angenommen.



*„Probleme kann man niemals mit derselben Denkweise lösen, durch die sie entstanden sind.“*

- Albert Einstein -

Die vorliegende Arbeit wurde in der Zeit von Dezember 2014 bis Dezember 2017 am WACKER-Lehrstuhl für Makromolekulare Chemie, Technische Universität München, unter Betreuung von Herrn *Prof. Dr. Dr. h.c. Bernhard Rieger* angefertigt.

## Acknowledgement

Mein Dank gilt Herrn Prof. Dr. Dr. h.c. Rieger für die Möglichkeit meine Doktorarbeit an seinem Lehrstuhl anfertigen zu dürfen. Ich möchte mich für das entgegengebrachte Vertrauen bedanken, die hervorragenden Arbeitsbedingungen und die vielen Freiräume, die Sie uns gewähren, sowie die zahlreichen intensiven und aufschlussreichen Diskussionen über die letzten drei Jahre.

Ein besonderer Dank gilt Carsten und Sergei, die bei fachlichen und technischen Problemen immer ein offenes Ohr haben und bei den kleineren und größeren Problemen im Laboralltag stets eine Lösung parat haben. Des Weiteren möchte ich Frau Bauer und Katia für die gute Organisation rund um dem Lehrstuhl danken.

Alex, Philipp und Christian aus dem SC XRD Labor gilt mein großer Dank, die in unzähligen Messungen versucht haben auch das letzte Prozent für all meine Projekte herauszuholen. Natürlich möchte ich hier auch allen Beteiligten unseres Projektes mit der Universität Augsburg für die erfolgreiche Zusammenarbeit danken. Außerdem gilt mein Dank Herrn Dr. Drees für die zahlreichen DFT Berechnungen, Frau Dr. Häßner für die durchgeführten ESR-Messungen und Ulli für ihre Elementaranalysen. Natürlich bin ich auch all meinen Studenten (Werner, Lara, Ruben und Theresa) und unseren Auszubildenden dankbar, die die letzten Jahre wichtige Arbeit für mich geleistet haben.

Bei Dominik Lanzinger möchte ich mich für den regen fachlichen Austausch über die letzten Jahre bedanken. Durch seine fachliche Vorarbeit und seine Kompetenz auf dem Gebiet der Polymerisationskatalyse war er für mich stets ein wichtiger und hilfsbereiter Ansprechpartner.

Des Weiteren danke ich allen Mitarbeitern des Lehrstuhls für das angenehme Arbeitsklima, die Hilfsbereitschaft und Unterstützung bei der Benutzung von Geräten sowie bei fachlichen Fragen und Problemen. Besonders bedanken möchte ich mich bei meinen früheren Kollegen aus dem Si-Institut (Matze, Sven und Basti Kraus) und der jüngeren Generation aus dem CRC (Basti, Markus, Fabi, Tobi, Michi, Marc, Tom und Andi, sowie Marina, Christina, Rike, Arzu und Theresa). Natürlich muss ich hier Daniel und Philipp noch besonders hervorheben: Vielen Dank für die gemeinsame Studien- und Promotionszeit, die zahlreichen Diskussionen und Hilfestellungen, das Korrekturlesen, die zahlreichen unterhaltsamen Abende, Nächte und Urlaube und die gute Freundschaft mit euch beiden.

## *Acknowledgements*

---

Mein größter Dank gilt meiner Familie; meinen Großeltern, meiner Mutter Inge, meinem Vater Ewald und meinem Bruder Fabian. Ihr habt mich immer unterstützt, während meines Studiums und meiner Promotionszeit, sowohl moralisch als auch finanziell, und dafür bin ich euch sehr dankbar. Auch meiner Cousine Sibylle und natürlich meinem Onkel Rolf gilt ein besonderer Dank, für das Korrekturlesen und für die stets hilfreichen Ratschläge in der Chemie und darüber hinaus. Und zuallerletzt: Mein größter Dank auch an dich, liebe Chrissi, dass du während meinem Studium und meiner Promotion immer für mich da warst, mir wenn nötig den Rücken freigehalten hast, mich immer unterstützt hast und für mich stets der perfekte Gegenpol zu meinem wissenschaftlichen Alltag warst. Danke, dass du stets an meiner Seite bist.

**Table of Contents**

<b>1. Introduction</b>	<b>1</b>
<b>2. Polypropylene Catalysis</b>	<b>4</b>
2.1 <i>Historic Milestones in the Coordinative Polymerization of Propylene – Where does the journey lead to?</i>	4
2.2 <i>General Aspects of Metallocenes</i>	6
2.3 <i>Precatalyst Activation</i>	8
2.3.1 <i>Methylaluminoxane</i>	8
2.3.2 <i>Borane and Borate Reagents</i>	9
2.4 <i>Chain Propagation</i>	10
2.5 <i>Regioselectivity in the Migratory Insertion Pathway</i>	11
2.6 <i>Stereoselectivity in the Migratory Insertion Pathway</i>	12
2.6.1 <i>Chain End Control and Enantiomorphic Site Control</i>	13
2.6.2 <i>Chain End Epimerization</i>	14
2.6.3 <i>Chain Migration</i>	15
2.6.4 <i>Which mechanism determines the final tacticity?</i>	16
2.7 <i>Chain Release</i>	17
2.7.1 <i><math>\beta</math>-Hydride Transfer</i>	18
2.7.2 <i><math>\beta</math>-Methyl Transfer</i>	20
2.7.3 <i>Further Chain Transfer Reactions</i>	21
2.7.4 <i>Detection and Assignment of Chain Transfer Reactions</i>	21
2.8 <i>The Crucial Role of the Group IV Metal Center</i>	22
2.8.1 <i>Titanium</i>	23
2.8.2 <i>Zirconium vs. Hafnium</i>	23
<b>3. Aim of this Work</b>	<b>26</b>
<b>4. Striving for Perfection: High Molecular Weight, High-Melting <i>i</i>PP</b>	<b>30</b>
<b>5. Titanocenes in Olefin Polymerization: Sustainable Catalyst System or an Extinct Species?</b>	<b>41</b>

<b>6. Behind the Scenes of Group IV Metallocene Catalysis: Examination of the Metal–Carbon Bond</b>	<b>53</b>
<b>7. High-Melting, Elastic Polypropylene</b>	<b>69</b>
<b>8. Excursus: New Microstructures in Olefin-Based Polymers</b>	<b>86</b>
8.1 <i>Ethylene – Propylene Copolymerization Using State of the Art <sup>i</sup>PP-Catalysts</i>	86
8.2 <i><sup>a</sup>PP – <sup>i</sup>PP Copolymers via Chain Shuttling</i>	92
<b>9. Summary and Outlook</b>	<b>98</b>
<b>10. Zusammenfassung und Ausblick</b>	<b>104</b>
<b>11. Bibliography</b>	<b>111</b>
<b>12. Appendix</b>	<b>116</b>
12.1 <i>Supporting Information – Chapter 4: Striving for Perfection: High Molecular Weight, High-Melting <sup>i</sup>PP</i>	116
12.2 <i>Supporting Information – Chapter 5: Titanocenes in Olefin Polymerization: Sustainable Catalyst System or an Extinct Species?</i>	135
12.3 <i>Supporting Information – Chapter 6: Behind the Scenes of Group IV Metallocene Catalysis: Examination of the Metal–Carbon Bond</i>	160
12.4 <i>Supporting Information – Chapter 7: High-Melting, Elastic Polypropylene</i>	247
12.5 <i>Experimental Information – Chapter 8: Excursus: New Microstructures in Olefin-Based Polymers</i>	291
12.6 <i>Licences for Copyrighted Content</i>	294

List of Abbreviations

$^a$ PP	atactic polypropylene
eq.	equivalent
Bu	butyl
Cp	cyclopentadienyl and derivatives
Cp*	pentamethylcyclopentadienyl
CGC	constrained geometry complex
cga	coordination gap aperture
CSA	chain shuttling agent
DFT	density functional theory
DSC	differential scanning calorimetry
EBFI-complex	ethylene-bridged fluorenyl-indenyl complex
$^e$ PP	elastic polypropylene
Et	ethyl
$^i$ PP	isotactic polypropylene
GPC	gel permeation chromatography
HDPE	high density polyethylene
HT	high temperature
$M_n$	number average molecular weight
$M_w$	mass average molecular weight
MAO	methylaluminoxane
Me	methyl
NMR	nuclear magnetic resonance
Ph	phenyl
<i>rac</i>	racemic
SC XRD	single crystal X-ray diffraction analysis
$^s$ PP	syndiotactic polypropylene
$^t$ Bu	<i>tert</i> -butyl
TCB	1,2,4-trichlorobenzene
TMA	trimethylaluminum
TIBA	triisobutylaluminum
TPE	thermoplastic elastomer
ZN	<i>Ziegler-Natta</i>

## Publication List

- Machat, M. R.; Lanzinger, D.; Drees, M.; Altmann, P. J.; Herdtweck, E.; Rieger, B., High-Melting, Elastic Polypropylene: A One-Pot, One-Catalyst Strategy toward Propylene-Based Thermoplastic Elastomers, *Macromolecules* **2018**, *51*, 914-929.
- Machat, M. R.; Jandl, C.; Rieger, B., Titanocenes in Olefin Polymerization: Sustainable Catalyst System or an Extinct Species? *Organometallics* **2017**, *36*, 1408-1418.
- Machat, M. R.; Lanzinger, D.; Pöthig, A.; Rieger, B., Ultrarigid Indenyl-based Hafnocene Complexes for the Highly Isoselective Polymerization of Propene: Tunable Polymerization Performance Adopting Various Sterically Demanding 4-Aryl Substituents, *Organometallics* **2017**, *36*, 399-408. (ACS Editors' Choice)
- Schöbel, A.; Winkenstette, M.; Anselment, T. M. J.; Machat, M. R.; Rieger, B., Copolymerization of Alkenes and Polar Monomers by Early and Late Transition Metal Catalysts, *Reference Module in Materials Science and Materials Engineering*, Elsevier, **2016**.
- Adams, F.; Machat, M. R.; Altenbuchner, P. T.; Ehrmaier J.; Pöthig, A.; Karsili, T. N. V.; Rieger, B.; Toolbox of Nonmetallocene Lanthanides: Multifunctional Catalysts in Group-Transfer Polymerization, *Inorganic Chemistry* **2017**, *56*, 9754–9764.
- Shcherbina, M. A.; Meshchankina, M. Y.; Odarchenko, Y. I.; Machat, M. R.; Rieger, B.; Chvalun, S. N., From elastomers to thermoplasts – Precise control of isotactic propylene structure and properties and the role of different structural elements in its mechanical behavior, *Polymer* **2017**, *133*, 213-222.

### ***Currently in the publication process:***

- Machat, M. R.; Fischer, A.; Schmitz, D.; Vöst, M.; Drees, M.; Jandl, C.; Pöthig, A.; Casati, N. P. M.; Scherer, W.; Rieger, B., Behind the Scenes of Group IV Metallocene Catalysis: Examination of the Metal–Carbon Bond, *Journal of the American Chemical Society*.

## 1. Introduction

Picturing necessary changes for a sustainable future, two main aspects usually come into our mind: First, we think of a “green” energy supply completely deriving from renewable resources, and second, we consider a severe reduction of the overall energy consumption by the development of new, smart, and more efficient processes. While the ongoing, and mostly still upcoming, changes from finite fossils to renewable resources mean a huge effort for society, economy and politics, the development of more efficient processes has already constituted a routine task for every researcher and process developer for decades. The pursuit of higher efficiency has always been an economically driven phenomenon, which does not just hold for the chemical industry, but for the whole industrial sector itself. Regarding the chemical industry, the symbol of sustainable and efficient processes is catalysis. Catalysis reduces energy costs, catalysis determines the “right” reaction path to the desired product, catalysis even facilitates reactions, which otherwise would have never worked in the first place.

The first description of catalysis was reported by *Berzelius* in the year 1835. The definition of a catalytic process as we still define it in the 21<sup>st</sup> century, was given by *Wilhelm Ostwald*:<sup>1</sup>

*"Ein Katalysator ist jeder Stoff, der, ohne im Endprodukt einer chemischen Reaktion zu erscheinen, ihre Geschwindigkeit verändert."*

*(Wilhelm Ostwald, 1901)*

Nowadays, the essential characteristics that define a so called catalyst constitute key knowledge for every new generation of chemists: A catalyst increases the rate of a chemical reaction regarding both directions, it does not change the equilibrium position and it is regenerated at the end of each catalytic conversion. There is no doubt, that the way of live as we know it today, would not exist without the opportunities enabled by catalysis. In this context, the Haber-Bosch process is certainly to be considered the most crucial, since a world with more than seven billion people would have never existed without it. But the production of plastics also necessitates the help of catalysis. The vast development of synthetic polymer production over the last century, which is often described as the “age of plastics”, was essentially facilitated by catalysis. And the polymer class that certainly benefited the most from the application of catalytic processes in the production of plastics are polyolefins. Visualized in Figure 1, the three polymer types which nowadays comprise the largest production volumes are all based on an olefin feedstock.

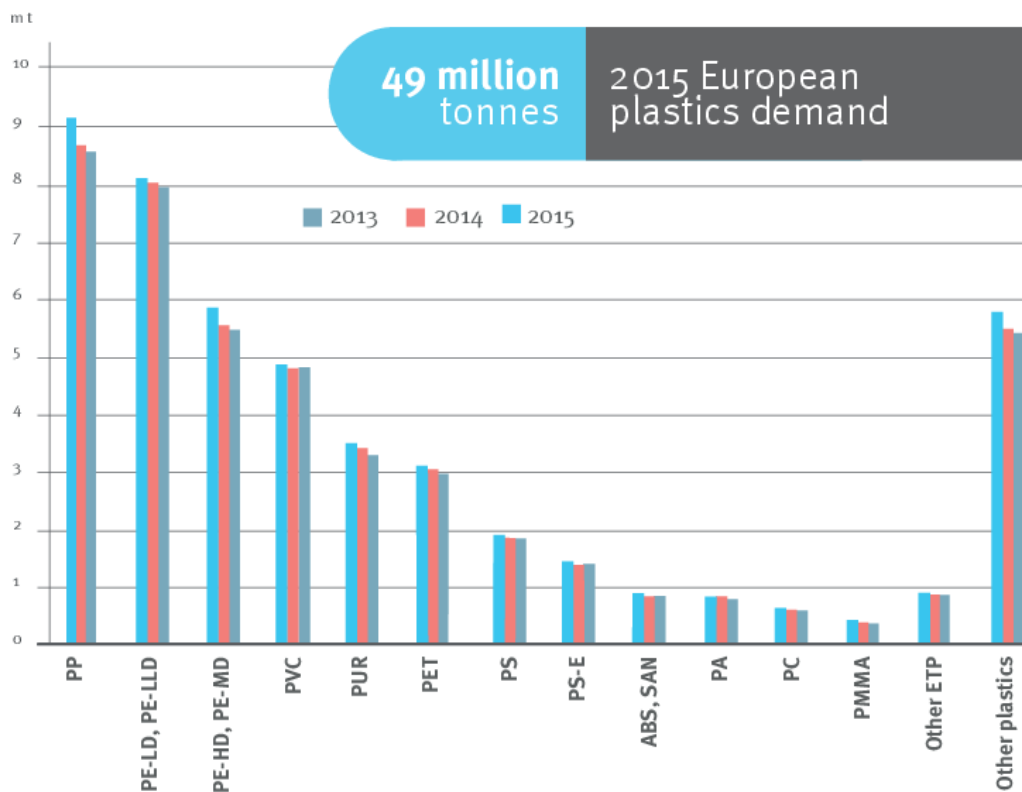


Figure 1. European demand of plastic materials divided by different polymer classes.<sup>2</sup>

Less than seven decades after the genesis of metal-catalyzed olefin polymerization in 1955,<sup>3</sup> this catalytic process has grown into an economic sector with tremendous industrial relevance and an uncountable number of applications, which we all take for granted in our everyday lives. Due to the extraordinary efficiency of this catalytic process - that even eclipses the one of enzymes<sup>4</sup> - polyolefins are very well available and moreover, the diverse properties of these polymer materials can be tailored to each desired field of application (Figure 2), thereby provoking a massive industrial demand of olefin-based polymers. In this context, polypropylene is certainly the most versatile polyolefin material comprising thermoplastic, elastomeric, elastic or even viscoelastic properties. The integration of a prochiral monomer into the polymerization process with an accurate control over the established stereocenters is herein considered crucial to tailor the desired mechanical properties of the final product.<sup>5-6</sup> Consequently, polypropylene can generally be found in simple applications like packaging or cladding but also in more challenging ones like construction, automotive or electronic devices.<sup>7</sup>

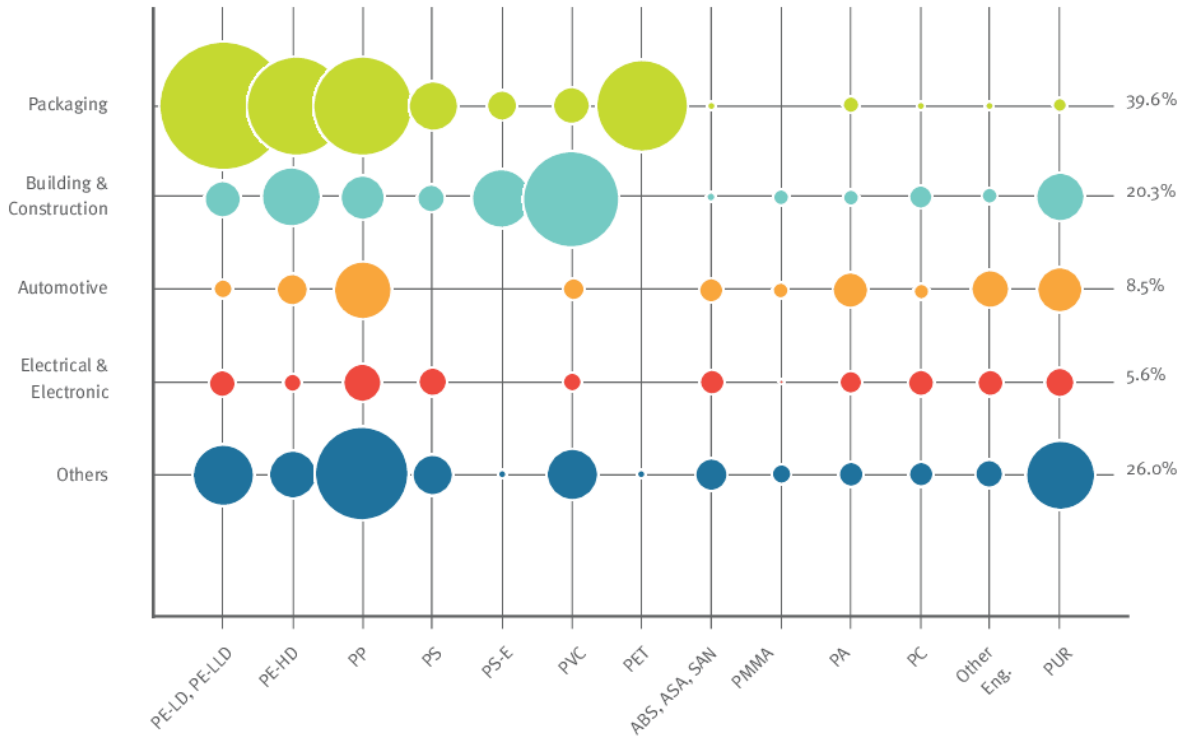


Figure 2. Markets of plastic by segment and polymer type in 2013.<sup>7</sup>

Although the coordinative polymerization catalysis has obviously passed the industrial threshold decades ago, and tailored structures of various polyolefin materials are nowadays accessible, the potential of this catalytic process and of the respective polymer materials are far from having been completely exhausted. The detailed elucidation of mechanisms and processes herein represents a major task for the development of a more profound understanding, which is indispensable for prospective improvements and the realization of new strategies for a more sustainable future.

## 2. Polypropylene Catalysis

### 2.1 Historic Milestones in the Coordinative Polymerization of Propylene – Where does the journey lead to?

The groundbreaking discovery of *Karl Ziegler* in 1955, when he polymerized ethylene with a mixture of  $\text{TiCl}_4$  and  $\text{AlEt}_3$ , represents the genesis of a unique story of success regarding the tremendous field of coordinative polymerization catalysis (Figure 3).<sup>3</sup> This catalyst mixture, which facilitated the synthesis of high density polyethylene at low monomer pressure and polymerization temperature, was applied by *Guilio Natta* for the first synthesis of polypropylene just one year later.<sup>8</sup> Down to the present day, the application of  $\text{TiCl}_4$  in combination with aluminum alkyls, immobilized on a chiral  $\text{MgCl}_2$  surface, depicts the state of the art heterogeneous multi-site catalyst system for the efficient and large-scale production of isotactic polypropylene.<sup>9</sup>

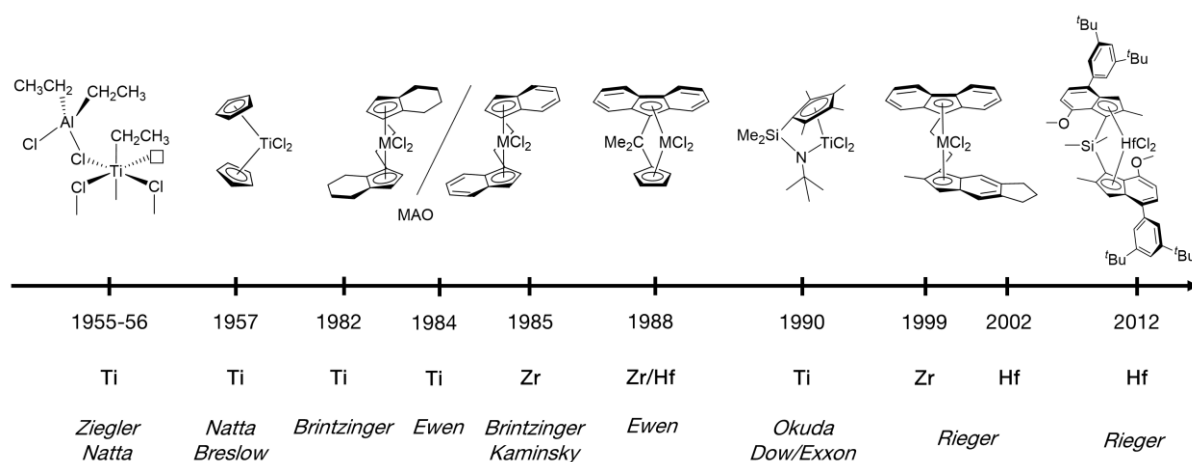


**Figure 3. Timeline of some essential developments in the coordinative polymerization of propylene.**

*Natta* and *Breslow* applied the first homogenous, metallocene based polymerization catalyst in 1957. The catalytically active species was herein build up by the combination of a plain titanocene ( $\text{Cp}_2\text{TiCl}_2$ ) with aluminum alkyls.<sup>10-11</sup> While the initial catalyst mixture revealed generally low catalytic activities, the discovery of methylaluminoxane as an alternative activation reagent substantially changed the role of metallocene catalysis in the polymerization of olefins. In this context, the controlled partial hydrolysis of trimethylaluminum by *Kaminsky* and *Sinn* in 1980 provoked a substantial increase of the catalytic activity, if applied as cocatalyst in combination with metallocene complexes.<sup>12</sup> With the introduction of varying symmetries in the complex framework, an essential impact on the

polymer microstructure was achieved. First approaches were realized by *Brintzinger et al.* in 1982 synthesizing *ansa*-titanocene derivatives with bridged tetrahydroindenyl ligands.<sup>13</sup> The application of these *ansa*-bisindenyl metallocene structures in combination with MAO finally enabled the controlled synthesis of isotactic polypropylene using a C<sub>2</sub>-symmetric metallocene framework. The replacement of titanium by zirconium herein further accelerated the catalytic activity.<sup>14-15</sup> The fundamental relation between the stereoselective polymerization behavior and the symmetry of the applied metallocene structure was disclosed by *John Ewen* in 1984.<sup>16</sup> Consequently, beside the directed synthesis of isotactic and atactic polypropylene, syndiotactic polymers became likewise feasible.<sup>17</sup> Starting in the late 1980s, a countless number of new metallocenes with plenty substitutional variations facilitated the catalysis of polypropylene comprising almost any degree of stereoregularity. Notable highlights are the application of unbridged zirconocenes in the polymerization of propylene possessing an oscillating stereocontrol mechanism and the synthesis of ethylene bridged fluorenyl-indenyl (EBFI) *ansa*-metallocenes revealing a variable stereoselectivity in the polymerization of propylene.<sup>18-20</sup> Beside the application of a classic metallocene motive, the implementation of half-sandwich complexes like the constrained geometry systems for the homogenous copolymerization of  $\alpha$ -olefins developed quite successfully, even in terms of industrial utilization.<sup>21-22</sup> Regarding recent advances applying a highly substituted, rigid, C<sub>2</sub>-symmetric *ansa*-bisindenyl metallocene framework by *Rieger et al.*, the synthesis of almost perfect, high molecular weight, isotactic polypropylene became accessible, comprising the highest observed melting transitions for <sup>1</sup>PP (>170 °C, *ex reactor*) to this day.<sup>23-24</sup>

Keeping all these achievements over the last six decades in mind, the following question necessarily rises at some point: Regarding such a vastly investigated, and sometimes even considered mature research area, where is still room for further improvement and prospective development? Therefore, I would like to highlight just a few significant perspectives: First of all, a more profound knowledge about various processes simultaneously taking place in the complex polymerization setup is still indispensable for further smart catalyst and process development. And although various degrees of different stereoregularities are nowadays accessible, an appropriate combination of the desired stereoregularity together with the desired molecular weight for optimized polymer properties still represents a major challenge especially under industrially relevant conditions. Thinking of tailored stereoregularities, the production of elastic polypropylene certainly displays one of the huge advantages using homogenous metallocene complexes compared to heterogeneous *Ziegler-Natta* (ZN) systems. However, these propylene-based thermoplastic elastomers still possess an insufficient

temperature stability due to the generally low melting transitions. Switching the focus toward a catalytic perspective, the last six decades (Figure 3) have exhibited a quite balanced distribution of different group IV metal centers regarding different fields of specialized applications. While titanium has proven its capability in the area of heterogeneous ZN-catalysis, zirconium is usually applied in highly active metallocene/MAO catalysts and hafnium is generally the metal center of choice, if high molecular weights are indispensable in the final polymer product. In this context, the fundamental intrinsic differences of each metal center, which provoke certain peculiarities in the polymerization of olefins, necessitate an individual choice for each particular application. However, the actual origin for these differences in the catalytic conversion of olefins still represents a “black box” to this day. Although significant differences in the strength of the M–C bond are proposed, a conclusive scientific proof for the observable catalytic differences of varied group IV metal centers is still missing. Inspired by all the fundamental questions, the present work will shed light on some of these essential but still unresolved issues in the field of homogenous coordinative polymerization catalysis.

## 2.2 General Aspects of Metallocenes

Metallocenes, suitable for the coordinative polymerization of olefins, are generally built up by two cyclopentadienyl anions ( $\eta^5$ -coordinated), two halogen substituents ( $\sigma$ -coordinated) and a group IV metal center ( $M^{+IV}$ ) in a pseudo-tetrahedral coordination sphere. While the cyclopentadienyl anions are attached to the metal center during the whole polymerization process, the halogen substituents are replaced by an alkyl group and a free coordination site. Common examples for cyclopentadienyl substituents are plain cyclopentadienyls, methylated ones and indenyl or fluorenyl derivatives.<sup>5</sup> In order to introduce a stereogenic information into the metallocene complexes, both cyclopentadienyl substituents are often linked by different sort of bridges therein generating *ansa*-metallocene structures. Classic building blocks are  $-(CH_2)_2-$ ,  $-C(CH_3)_2-$ , or  $-Si(CH_3)_2-$ .<sup>25</sup> Figure 4 illustrates a schematic representation of important geometric parameters in an *ansa*-metallocene framework. One of the most common parameters to evaluate the structural properties of *ansa*-metallocenes is the so called bite angle, which classifies the bridged structures according to their more or less opened character. In close relation is the coordination gap aperture (cga), describing the angle of the metallocene structure that touches the inner van der Waal surface of the surrounding ligand

framework. Therefore, the latter is a more accurate indication of the actual spatial situation of the coordination sphere.<sup>26-27</sup> In addition, the parameter D is sometimes used indicating the exposure of the metal center to the surrounded chemical environment.<sup>28</sup>

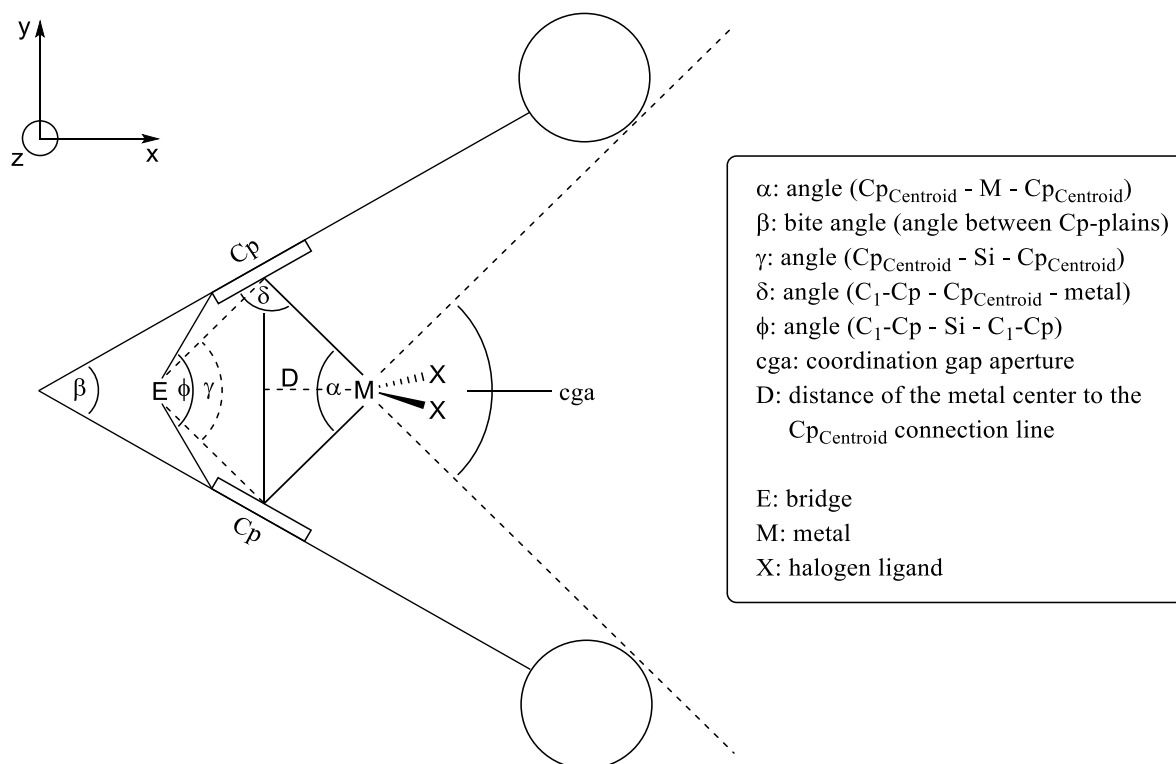


Figure 4. Important structural and geometric parameters of a schematic *ansa*-metallocene.

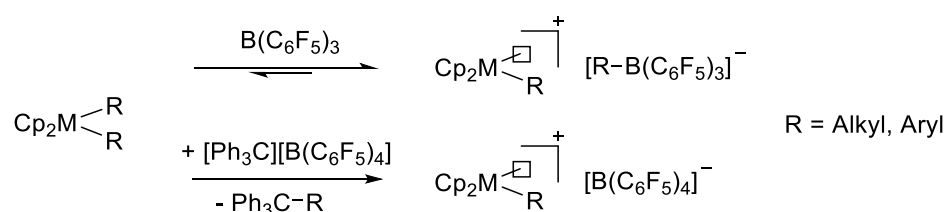
Precatalytic metallocene structures for the purpose of olefin polymerization catalysts are usually classified by their symmetry differentiating between  $C_1$ -,  $C_2$ -,  $C_S$ - and  $C_{2v}$ -symmetric complexes. In this connection, a close correlation between complex symmetry and a stereoselective polymerization catalysis was distinguished, if a prochiral monomer like propylene is polymerized.<sup>16</sup> For  $C_2$ - and  $C_S$ -symmetric metallocenes both coordination sites are isotropic and therefore described as single-site catalysts. If both coordination sites are anisotropic, like for the quite prominent class of  $C_1$ -symmetric ethylene bridged fluorenyl-indenyl (EBFI) metallocenes, a dual-site nature is ascribed. Synthesis of group IV metallocenes is generally conducted by salt metathesis of the lithiated ligand structure with metal halogen salt derivatives. In contrast to the synthesis of  $C_1$ -,  $C_S$ - or  $C_{2v}$ -symmetric complexes, for the synthesis of  $C_2$ -symmetric group IV metallocenes, the general formation, and usually also the separation of racemic and meso-structures needs to be considered. After salt metathesis, the synthesized metallocene is generally of a bis-halogenated fashion and referred as precatalytic. By the application of a cocatalyst, the precatalytic species is transferred into a catalytically active one.



application of this cocatalyst in combination with hafnocenes is considered far more problematic. Free TMA was attributed a crucial role in this regard, since the predominant formation of “dormant” metallocene-TMA adducts is suggest by DFT calculations if hafnium complexes are applied (see also Chapter 2.8.2).<sup>32, 35</sup>

### 2.3.2 Borane and Borate Reagents

While the activation with MAO combines both functionalities of alkylation and lewis acidity in just one reagent, the activation with boranes or borates is usually a two-step procedure. In the first step, the precatalytic bis-halogenated metallocene needs to be alkylated with lithium alkyls or grignard reagents. Even more common is the *in situ* alkylation with an excess of aluminum alkyl. In the second step, free coordination sites are generated by the addition of different boranes or borates (Scheme 2).<sup>36-38</sup>

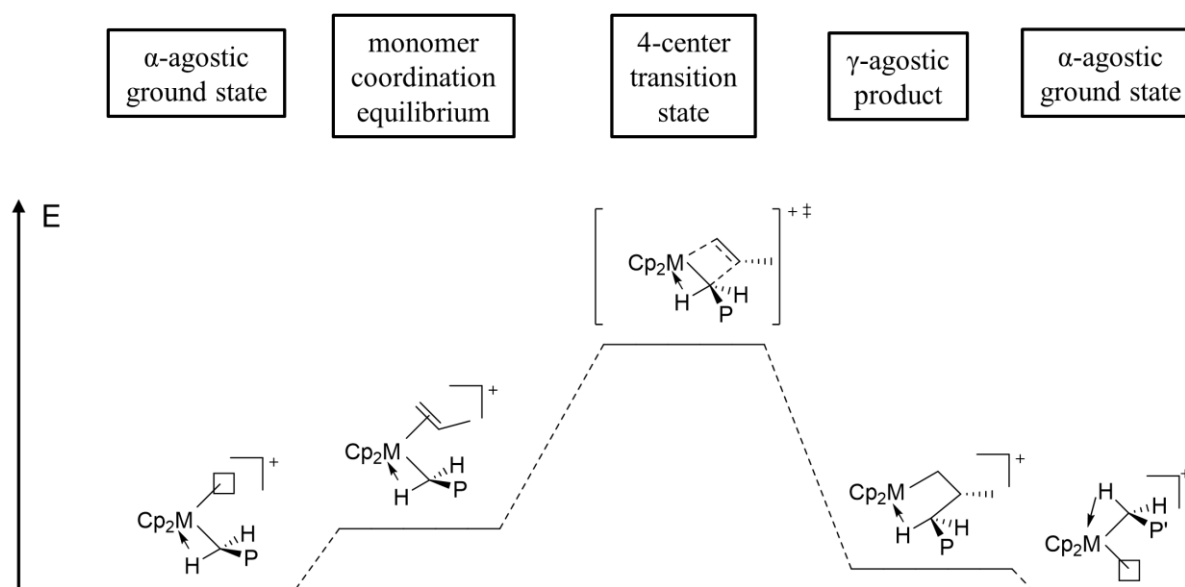


**Scheme 2. Metallocene activation with a borane B(C<sub>6</sub>F<sub>5</sub>)<sub>3</sub> or borate salt [Ph<sub>3</sub>C][ B(C<sub>6</sub>F<sub>5</sub>)<sub>4</sub>] (M: Ti, Zr, Hf).**

By the formation of monoalkylated, cationic complexes, an alkyl substituent is transferred to the plain borane or to the trityl cation. For the first example, under conditions generally referred as catalytically active, the cationic complex is coordinated moderately by the alkyl–borane adduct, while for the second example, the borate anion is only slackly attached to the correspondent, positive charged metal center resulting in significantly higher polymerization activities. Since the activation with the trityl borate salt leads to the formation of a stable side product, the whole process is considered to proceed quantitatively. On the contrary, the activation process with the plain borane occurs in a dynamic equilibrium of catalytically active and inactive species.<sup>37, 39-40</sup> Between 1.0 to 5.0 eq. of borane or borate are generally applied with respect to the metallocene complex. However, this activation procedure necessitates the use of additional scavenger (usually aluminum alkyls). These circumstances can also impact the respective catalytic performances by possible side reactions between cocatalyst and the scavenging agent resulting in the formation of multinuclear complexes.<sup>41</sup>

## 2.4 Chain Propagation

One of the first proposed mechanisms for the coordinative polymerization of olefins was presented by *Cossée* and *Arlman* in the early 1960s.<sup>42-45</sup> This mechanism already included the three essential steps which are still considered crucial today: First of all, monomer coordination at the metal center takes place. Subsequently, the  $\pi$ -intermediate is converted into a four-membered cyclic transition state. Finally, *via* migratory insertion, the monomer unit is incorporated into the polymer chain again regenerating a free coordination site.

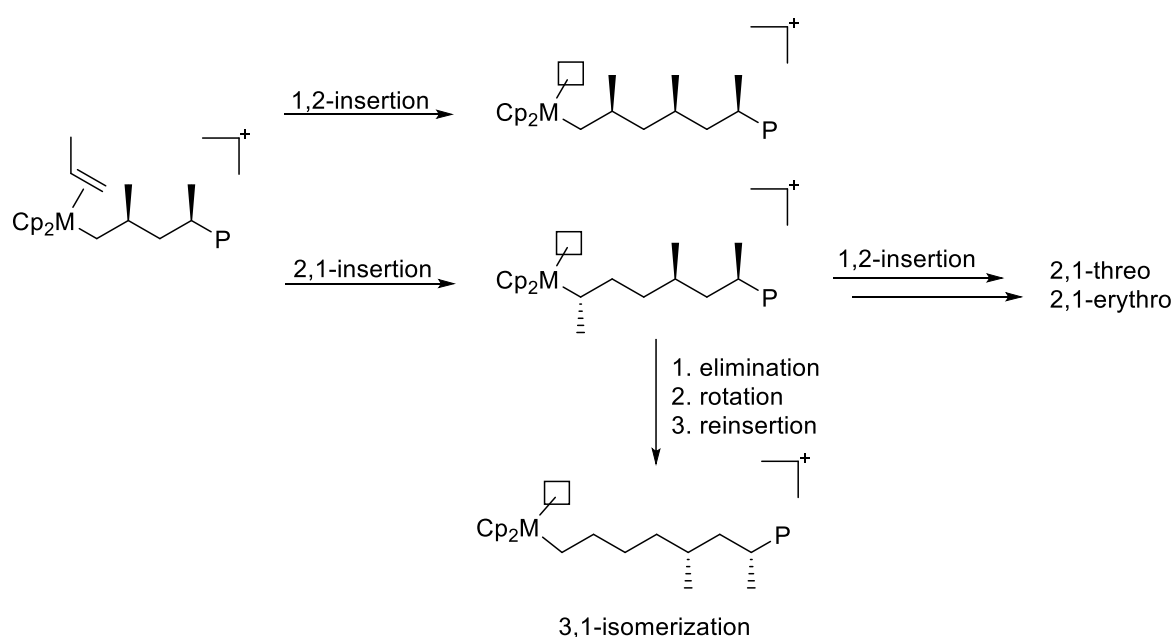


**Scheme 3.** Chain propagation described by the *Green-Rooney* mechanism and complemented by basic kinetic considerations (M: Ti, Zr, Hf; P: polymeryl; anion is omitted for clarity).

By the additional consideration of stabilizing agostic interaction the modified *Green-Rooney* mechanism was developed, which still represents the most accepted chain propagation mechanism (Scheme 3).<sup>46-47</sup> DFT-calculations on the chain propagation mechanism generally ascribe the rate determining step to the 4-center transition state. Stabilization *via* agostic interactions is also verified. However, beside  $\alpha$ - and  $\gamma$ -agostic interactions, also  $\beta$ -agostic stabilization is proposed.<sup>48-51</sup> Nevertheless, a total generalization of particular energy barriers is hardly feasible, since additional impact of the ligand structure, the anion-binding capacity or solvent effects severely complicate the situation.<sup>52</sup>

## 2.5 Regioselectivity in the Migratory Insertion Pathway

Regarding the regioselectivity of metallocene catalysts in the polymerization of propylene, the 1,2-insertion pathway (primary insertion) is generally favored, although the dependency on the respective ligand structure (electronic and steric effects) and the applied polymerization conditions should not be underestimated.<sup>5, 49</sup> Consequently, a 2,1-insertion (secondary insertion) is usually considered as misinsertion or regioirregular insertion, going along with an opposite enantiofacial selectivity (Chapter 2.6) compared to the regioregular insertion pathway (Scheme 4).<sup>53</sup>



**Scheme 4. Regio-insertion products in the coordinative polymerization of propylene with metallocene catalysts (M: Ti, Zr, Hf; P: polymeryl; anion is omitted for clarity).**

If a regioirregular insertion occurs, the rate constant of the subsequent insertion step is significantly lowered thereby promoting chain release and epimerization reactions.<sup>54</sup> Dependent on the stereoselectivity of the subsequent insertion step 2,1-threo or 2,1-erythro regiodefects are observed.<sup>55</sup> In addition, epimerization provokes the formation of a 3,1-isomerization product, which is favored at low monomer concentrations (unimolecular process) and at higher polymerization temperatures (accelerates the elimination/rotation-pathway).<sup>56-57</sup> Since all insertion products caused by the secondary insertion pathway disrupt the otherwise ordered polymer structure, a distinct impact on the respective melting transitions must be considered.<sup>24</sup>

## 2.6 Stereoselectivity in the Migratory Insertion Pathway

In the polymerization of propylene, a prochiral monomer unit is inserted into the polymer chain at every migratory insertion step. Consequently, a new stereogenic center is built up for every incorporated monomer unit. In this context, a precise control over the stereoregularities is key for a tailored synthesis of the desired polymer properties. The stereoregularity of polypropylene is generally characterized by its tacticity, which describes the relative stereoconfiguration of neighboring methyl residues within a polymer chain. If two neighbored stereogenic centers comprise the same stereoinformation, a *meso*-dyad is present, otherwise, it is listed as *racemic* dyad. If we extend the scope to the neighboring stereocenter on the other site of the polymer chain we talk about triads. Considering several consecutive dyads, we can distinguish between pentades, heptades or even nonades. Since the neighboring stereocenters around a methyl group (or methine or methylene group) cause an unequal chemical environment, a varying shift in the  $^{13}\text{C}$   $\{^1\text{H}\}$  NMR spectrum is observed. If we consider the two neighboring stereocenters of one particular methyl group within the polymer chain, pentads are resolved in the  $^{13}\text{C}$   $\{^1\text{H}\}$  NMR spectrum (Figure 5). The degree of isotacticity is herein determined by the mole fraction of the isotactic pentad (*mmmm*) to the sum of all steric pentads.<sup>58-59</sup>

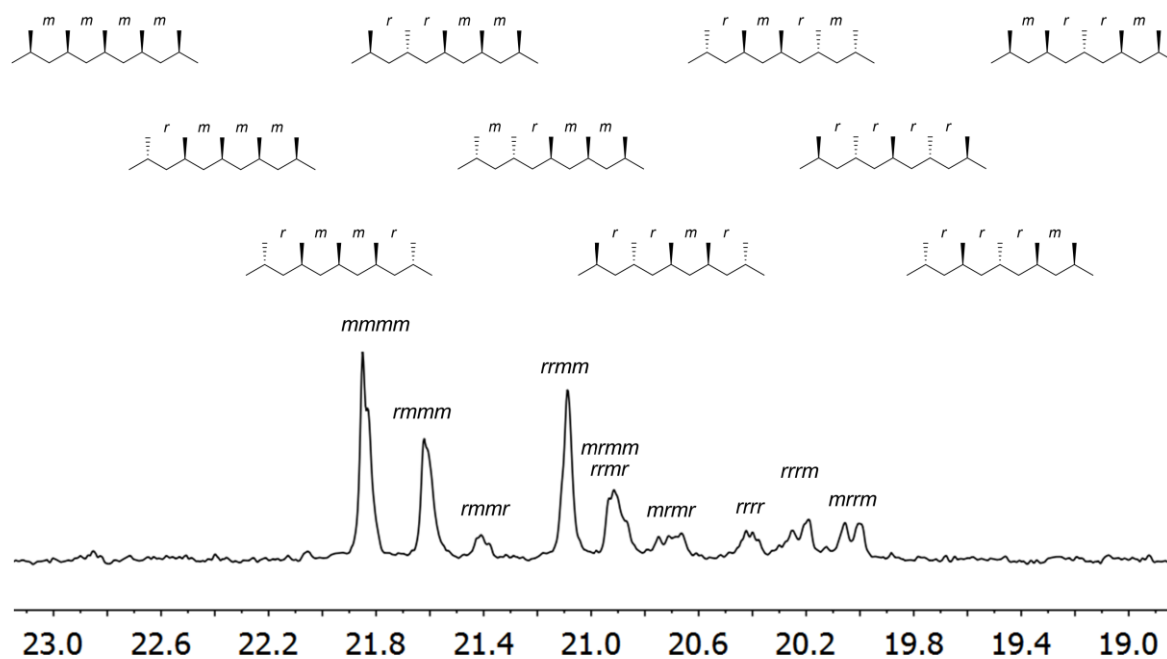


Figure 5. Exemplary pentad assignment of polypropylene (21 % *mmmm*) in the  $^{13}\text{C}$   $\{^1\text{H}\}$  NMR (300 MHz) spectrum ( $\text{C}_6\text{D}_5\text{Br}$ , 140 °C). All chemical shifts are internally referenced to the methyl signal of the isotactic pentad (*mmmm*) at 21.85 ppm.

Facilitated by *Ewen's* symmetry rules, different stereoregularities in polypropylene can be linked to the symmetry of the applied metallocene catalyst.<sup>16</sup> These correlations still serve as a rule of thumb for the synthesis of atactic, isotactic or syndiotactic polypropylene (Table 1).

**Table 1. Selected examples for the correlation of complex symmetry and the respective tacticity in the polypropylene microstructure.**

C <sub>1</sub>	C <sub>2</sub> ( <i>rac</i> )	C <sub>s</sub> ( <i>meso</i> )	C <sub>2v</sub>	C <sub>s</sub>
hemiisotactic	isotactic	atactic		syndiotactic

To understand the mechanism which lays the foundation for *Ewen's* symmetry rules, a detailed investigation of the preferred monomer coordination together with the preferred conformation of the growing polymer chain is necessary. Since propylene is a prochiral monomer, it can coordinate with two different enantiofaces (*re*-face or *si*-face according to the Cahn-Ingold-Prelog nomenclature). According to the enantiofacial selectivity of the catalyst the tacticity of the polymer is determined. In general, every metallocene catalyst has two main mechanisms, which determine the enantiofacial selectivity. While the chain end control mechanism is independent of the applied complex structure, the mechanism of enantiomeric site control determines the stereoregularities according to the present symmetry in the ligand framework.

### 2.6.1 Chain End Control and Enantiomeric Site Control

In the case of the chain end control mechanism, the configuration of the last inserted monomer defines the enantiofacial selectivity for the subsequent propylene unit. In this context, the preferred conformation of the growing polymer is essentially determined by the configuration of the last inserted monomer. Regarding this process, the complex framework does not trigger a specific conformation dependent on the present complex symmetry. Furthermore, the methyl group of the new, incoming monomer preferably coordinates *anti* to the growing polymer chain. According to this mechanism, isotactic polypropylene is

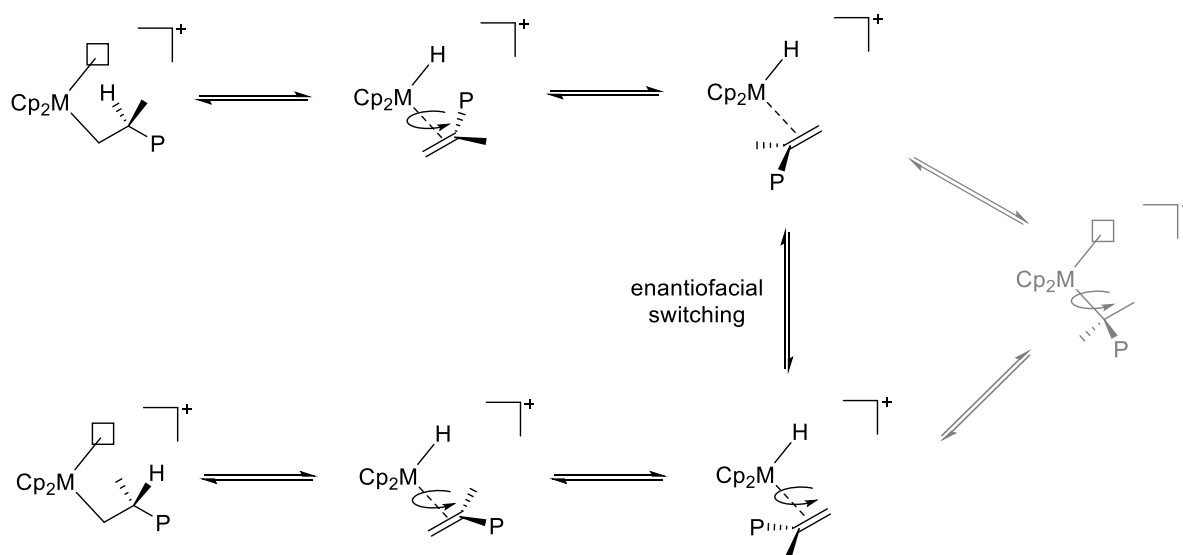
generated using achiral complexes (e.g.  $\text{Cp}_2\text{MCl}_2$ ) at temperatures distinctly lower than 0 °C. Isotactic polypropylene produced with a chain end control mechanism usually comprises a 1:1 ratio of the *mrrm* and *mmmr* pentad in the  $^{13}\text{C} \{^1\text{H}\}$  NMR spectrum.<sup>5, 60</sup>

If a metallocene catalyst is applied which introduces a chiral chemical environment, an enantiomorphic site control mechanism occurs. In principle, this mechanism proceeds analog to the chain end control mechanism. However, the preferred conformation of the growing polymer chain is no longer determined by the configuration of the last inserted monomer, but by the chiral environment of the complex structure. Monomer coordination still prefers an *anti*-orientation to the growing polymer chain and is not directly influenced by the surrounding ligand structure. This statement was verified by the examination of the first monomer insertion step applying alkyl residues of varying steric demand, which mimic the growing polymer chain. The results underlined the crucial interaction of the growing polymer chain with the chiral environment triggering a selective *anti*-coordination of the incoming monomer. At the same time, a negligible direct interaction of the coordinating monomer with the surrounded ligand structure was observed.<sup>61-64</sup> Regarding the enantiomorphic site control mechanism, stereoerror formation can basically proceed *via* two different pathways: If a propylene unit coordinates *anti* to the metal center at a state of disfavored polymer chain orientation the formation of a stereoerror occurs.<sup>53</sup> At a state of preferable chain orientation to the less crowded site, but with a *syn*-selective monomer coordination with respect to the growing polymer chain an analog result is suggested.<sup>48, 63</sup> In the case of a stereoselective misinsertion, there is no direct impact on the enantiofacial discrimination of the subsequent incorporated monomer unit. Consequently, for polypropylenes produced with an enantiomorphic site control mechanism, a 1:1 ratio of the *mmrr* and *mrrm* pentad is generally detectable in the  $^{13}\text{C} \{^1\text{H}\}$  NMR spectrum.<sup>60</sup>

### 2.6.2 Chain End Epimerization

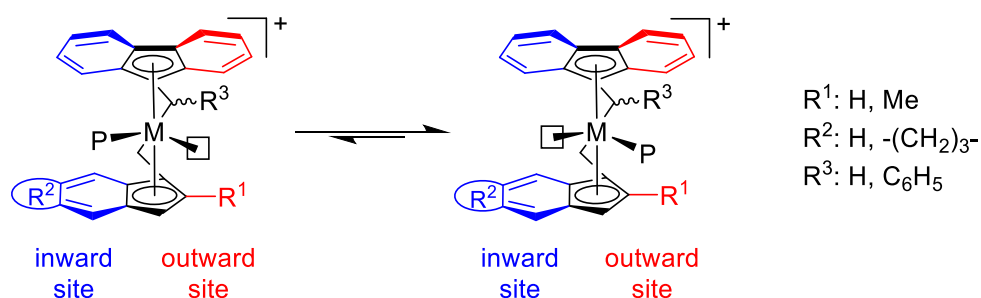
The cascade reaction of chain end epimerization represents a post-insertion mechanism leading to randomization of the last stereocenter in a growing polymer chain. Epimerization especially occurs at high polymerization temperatures and low monomer concentrations and has a particular impact in the catalysis of highly stereoregular polypropylenes. The epimerization process was first proposed by *Busico et al.* describing a cascade reaction of  $\beta$ -hydride elimination and several consecutive rotation and reinsertion steps (Scheme 5). The

enantiofacial switching, which is a molecular process of insertion, rotation and elimination, is considered more likely than a complete dissociation and recoordination with the other enantioface of the  $\pi$ -coordinated polymer chain.<sup>65-68</sup> Beside the depicted epimerization pathway, an epimerization *via* a metallocene allyl dihydrogen intermediate was also suggested in literature.<sup>69</sup> However, the results of additional studies with deuterium labeled propylene supported the initial pathway depicted in Scheme 5.<sup>70</sup>



**Scheme 5.** The chain end epimerization mechanism proposed by *Busico et al.* as a cascade process of elimination, rotation and reinsertion steps (M: Ti, Zr, Hf; P: polymeryl; anion is omitted for clarity).

### 2.6.3 Chain Migration



**Scheme 6.** Ground states before propylene coordination at the inward and outward site using dual-site EBFI-type metallocenes (M: Ti, Zr, Hf; P: polymeryl; anion is omitted for clarity).

If the chemical environment of both coordination sites are considered unequal, these metallocene complexes are usually referred as dual-site systems. For these systems, switching of the polymeryl chain from the sterically crowded (inward site) to the less crowded site

(outward site) occurs in the absence of a coordinating monomer unit (Scheme 6). This switch is also known as chain back skip mechanism or unimolecular site epimerization.<sup>19, 71-72</sup> Beside the absence of  $\pi$ -coordinating monomer, the binding strength of the counterion is crucial for the rate of this unimolecular site epimerization. Accordingly, weakly coordinating outer sphere ion pairs accelerate chain migration from the inward to the outward site.<sup>35, 52, 73</sup> In accordance with this proposed mechanism, a strong dependency of the stereoregularities of the produced polypropylenes on the applied monomer concentration is observed. Consequently, higher stereoselectivities are usually obtained if lower monomer concentrations are adjusted.<sup>19, 72, 74-76</sup>

#### 2.6.4 Which mechanism determines the final tacticity?

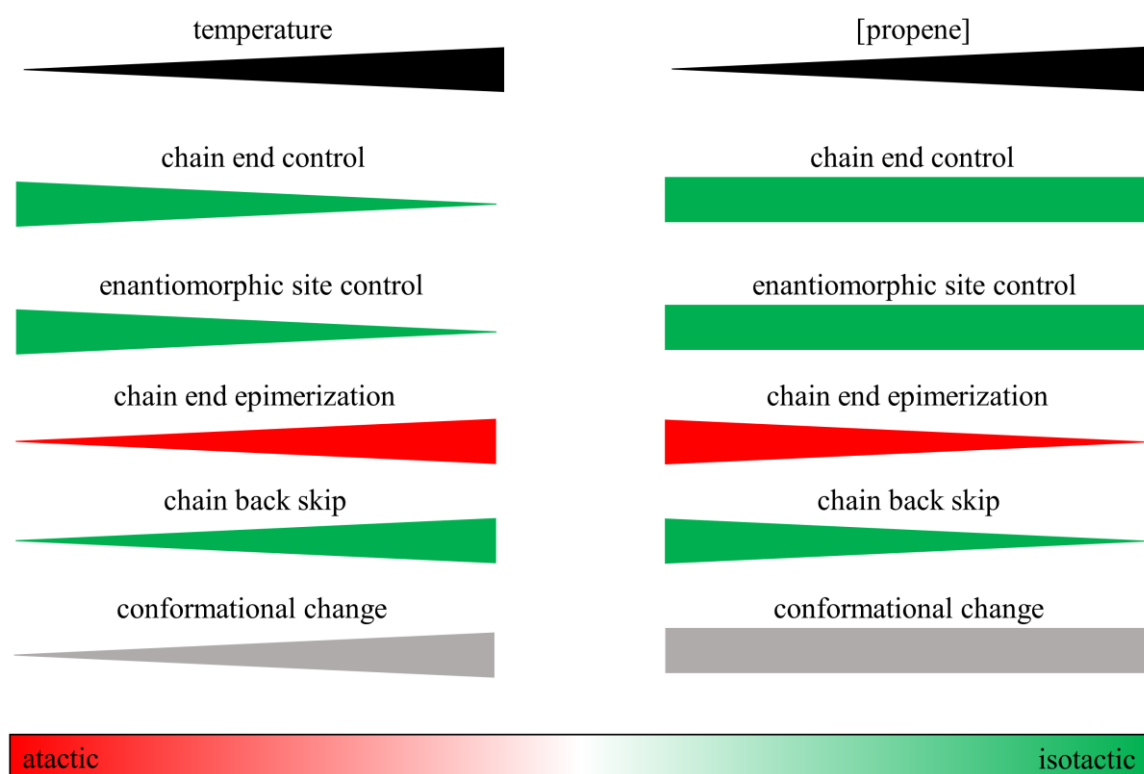


**Figure 6. Mechanisms potentially impacting the stereoselective behavior of non- or isospecific *ansa*-metallocenes in the polymerization of propylene.**

Chapter 2.6 has disclosed several mechanisms all impacting the final stereoregularities of the produced polypropylenes using *ansa*-metallocene complexes (Figure 6). In this connection, the mechanism of chain end and enantiomorph site control are basically valid regarding every metallocene catalyst. Both mechanisms loose selectivity, if higher polymerization

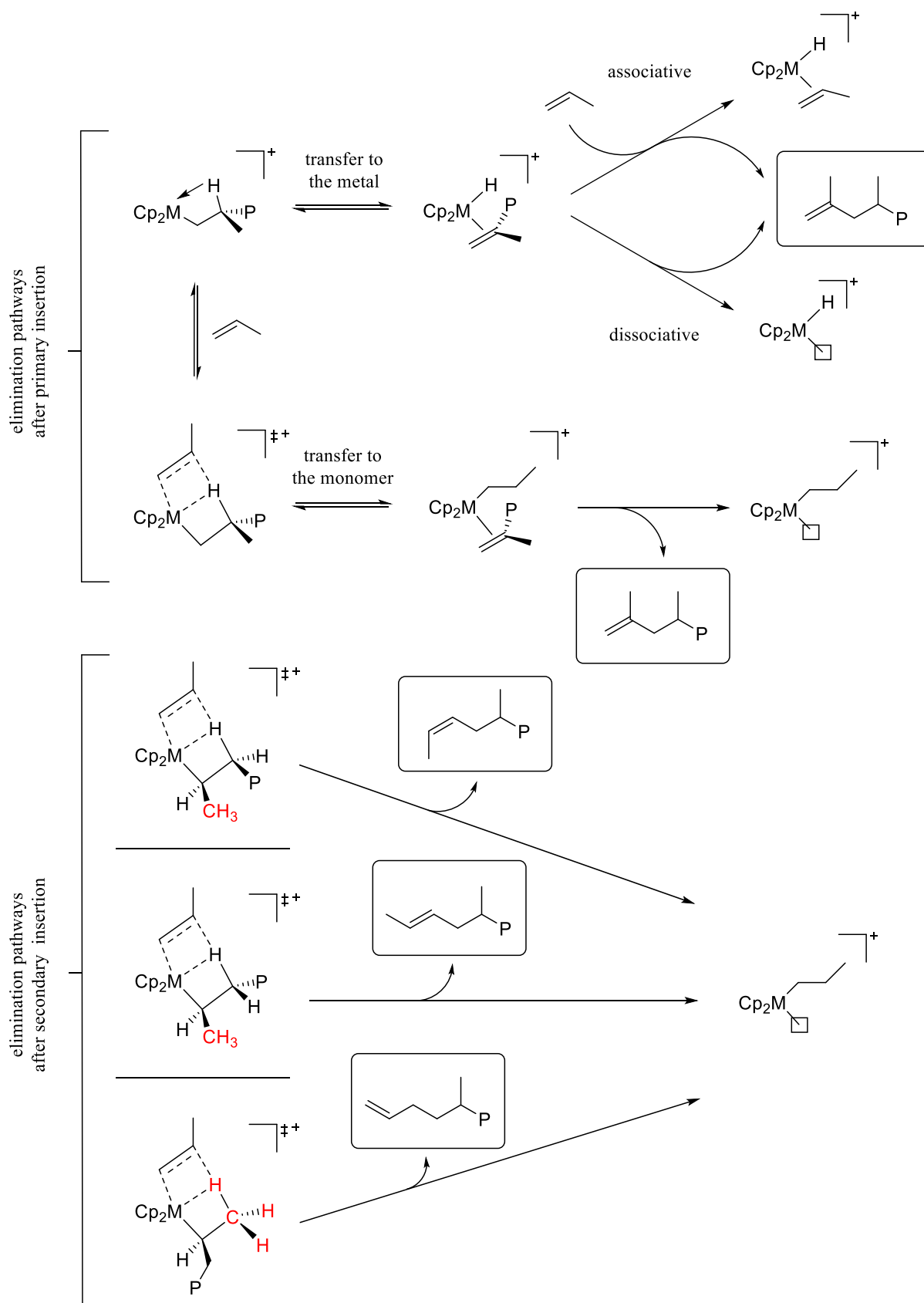
temperatures are applied. The post-insertion chain end epimerization mechanism also takes place regarding any metallocene based polymerization catalysis. The random epimerization process is particularly pronounced in the case of highly stereoregulative polymerization catalysis, and is favored at high polymerization temperatures and low monomer concentrations. On the contrary, unimolecular site epimerization enhances isotacticities at high temperatures and low propylene concentrations if dual-site metallocenes are applied. Additionally, in the case of bipartite bridges using EBI or EBFI-metallocenes, a severe impact of different chelate ring conformations on the stereoselectivity has been reported.<sup>71, 76-77</sup> In summary, we need to conclude, that the interpretation of the stereoselective performance of new as well as known catalysts under different polymerization conditions always represents a major challenge. Over the past decades, examples has been found, in which the origination of the observed stereoselectivities has been, at first glance, assigned to the wrong mechanism.<sup>68</sup> Therefore, thorough investigation of different polymerization conditions is necessary to elucidate the key factors that determine the stereoselectivity of a particular catalyst system. As concluding remark, it may be worth mentioning that not all impact factors depicted in Figure 6 are valid for all types of *ansa*-metallocenes, but should at least be kept in mind regarding a well-grounded interpretation.

## 2.7 Chain Release

Facilitated by a fundamental metalorganic side reaction, one active catalyst species can, at least theoretically, produce an infinite amount of polymer chains, thus essentially contributing to the unique efficiency in the coordinative polymerization catalysis of olefins. Caused by an elimination process, a produced polymer chain is set free from the catalytically active metallocene keeping its catalytic capability intact for the production a new polymer sequence. Although a substantial amount of polymer chains can be produced by one single catalyst unit, this process also prevents a potential living character in the coordinative polymerization of olefins using metallocene catalysts. In addition, the chain release reactions limit the average molecular weight of the produced polyolefin, since the rate ratio of chain propagation and chain release defines the resulting chain length.<sup>53</sup> Furthermore, a molar mass distribution ( $\bar{D} = M_w/M_n$ ) between 1.5 to 2.0 is usually obtained.<sup>26</sup>

### 2.7.1 $\beta$ -Hydride Transfer

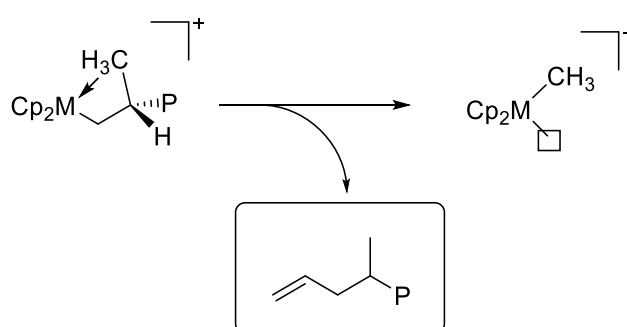
The most common chain release mechanism is based on a  $\beta$ -hydride elimination pathway transferring the hydride either to the metal center or to a coordinated monomer unit (Scheme 7).<sup>78</sup> If a transfer to the metal center occurs, the  $\beta$ -hydride elimination process proceeds *via* a  $\beta$ -agostic ground state and the  $\pi$ -bound polymer chain is released by an associative or dissociative displacement. Whereas a dissociative displacement is considered unlikely from an energetic point of view and may only occur at high polymerization temperatures, an associative displacement displays the generally more favored pathway.<sup>79</sup> In addition, reinsertion of the  $\pi$ -bound polymer chain after a  $\beta$ -hydride elimination process always needs to be considered representing an essential sub-process in the chain-end epimerization pathway.<sup>67, 79</sup> However, a bimolecular hydride transfer to the monomer is suggested by several DFT-calculations to be energetically favored toward the unimolecular transfer to the metal center.<sup>78</sup> In this context, transition states including a hydride metal interaction (Scheme 7) and transition states without any interaction of the  $\beta$ -hydride with the metal center are proposed.<sup>79-81</sup> Since the elimination process of hydride transfer to the metal center is unimolecular and the hydride transfer to a coordinated monomer unit is a bimolecular mechanism (just as the propagation mechanism), the dependency of the average molecular weight on the monomer concentration can elucidate the actual proceeding type of chain release mechanism. Apart from that, the tendency toward chain release is particularly high, if a 2,1-regioirregular insertion occurred. In this case, the energy barrier for the next insertion step is significantly higher, thus promoting the chain transfer processes.<sup>79</sup> After a secondary insertion,  $\beta$ -hydride transfer to the monomer can take place in three different ways (Scheme 7). If a  $\beta$ -methylene hydride is transferred, *cis*- or *trans*-2-butenyl end groups are detectable, dependent on the stereoregularity of the last inserted monomer unit. For the hydride transfer from the methyl-group, 3-butenyl chain ends can be monitored.<sup>82</sup>



Scheme 7.  $\beta$ -hydride elimination pathways and products after 1,2- and 2,1-regioinsertion in the polymerization of propylene (M: Ti, Zr, Hf; P: polymeryl; anion is omitted for clarity).

2.7.2  $\beta$ -Methyl Transfer

For the occurrence of chain release *via* a  $\beta$ -methyl elimination pathway, a primary insertion of the last inserted monomer unit is required (Scheme 8). Analogous to the  $\beta$ -hydride elimination process, transfer to the metal center or a monomer unit seems likely.<sup>83</sup> However, DFT calculations ruled out a bimolecular mechanism including a direct methyl transfer to the coordinated monomer, since the energy barriers are considerably higher. Nevertheless, experimental data do not contradict with a displacement that occurs in an associative or dissociative fashion.<sup>5, 54, 84-85</sup>



**Scheme 8.** Unimolecular  $\beta$ -methyl elimination pathway in the polymerization of propylene (M: Ti, Zr, Hf; P: polymeryl; anion is omitted for clarity).

In general, the  $\beta$ -hydrogen should be favored toward the  $\beta$ -methyl transfer due to the notable activation energy differences between C–H and C–C bond cleavage.<sup>86</sup> However, a particularly high selectivity toward  $\beta$ -methyl elimination is observed if sterically demanding ligand structures or hafnium as central metal (see 2.8.2) are applied. While steric repulsion of the polymeryl and methyl group with the ligand framework is assumed for a unimolecular process of  $\beta$ -hydride elimination, less steric repulsion is provoked in the correspondent  $\beta$ -methyl elimination process (Figure 8).<sup>87-89</sup> In addition,  $\gamma$ -agostic interactions are reported accompanying the  $\beta$ -methyl elimination process, which, in principle, comprises the reverse reaction pathway of chain propagation.<sup>90</sup>

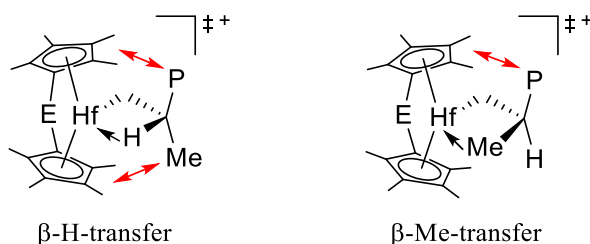


**Figure 7.** Transition state of unimolecular  $\beta$ -hydride and  $\beta$ -methyl elimination in the polymerization of propylene (M: Ti, Zr, Hf; P: polymeryl; E: bridge; anion is omitted for clarity).

### 2.7.3 Further Chain Transfer Reactions

Beside the chain transfer *via* an elimination pathway also a chain transfer to an aluminum center can occur. In this context, the steric encumbrance of the alkyl substituents attached to the aluminum center and the amount of aluminum reagent in the reaction mixture are crucial. Therefore, chain transfer to aluminum must be considered for the application of MAO with large excess, especially if it comprises significant amounts of TMA. After hydrolyzing the produced aluminum polymer chain adducts, saturated chain ends are obtained. In this case, a significant decrease of the overall molecular weights is usually observed. If an alternative alkylation reagent like the sterically more demanding triisobutylaluminum (TIBA) is applied, transfer to aluminum is distinctly reduced.<sup>5, 91</sup>

In order to decrease, or adjust the respective molecular weights in a coordinative polymerization setup at a definite temperature and monomer concentration, molecular hydrogen is added to the monomer feed and is able to set free saturated polymer chains. Hydrogen herein represents a common additive in the industrial production of polyolefins.<sup>5</sup>

### 2.7.4 Detection and Assignment of Chain Transfer Reactions

The most common analytic tool to determine the type of chain release reactions being present in a particular polymerization setup is the investigation of the olefinic end group composition *via* <sup>1</sup>H NMR spectroscopy of the produced polypropylenes. Especially for the application of metallocenes, activated with sterically demanding aluminum alkyls (TIBA) and borate salts, olefinic end group analysis comprises a comprehensive picture of all relevant chain transfer pathways. Figure 8 provides the assignment of typical olefinic endgroups to the corresponding signals in the <sup>1</sup>H NMR spectrum in the case of regioregular polypropylene. Vinylidene end groups (Figure 8, orange) and allylic chain ends (Figure 8, green) are detected, caused by  $\beta$ -hydride and  $\beta$ -methyl elimination. In addition, the signals of two different internal endgroups are present, deriving from allylic C–H bond activation (Figure 8, blue) and epimerized vinylidene chain ends (Figure 8, red). While the former end group (blue) does not indicate an actual chain transfer, the latter (red) is the result of a cascade reaction comprising several elimination, rotation and reinsertion steps, before the polymer chain is released.<sup>69, 87, 92</sup>

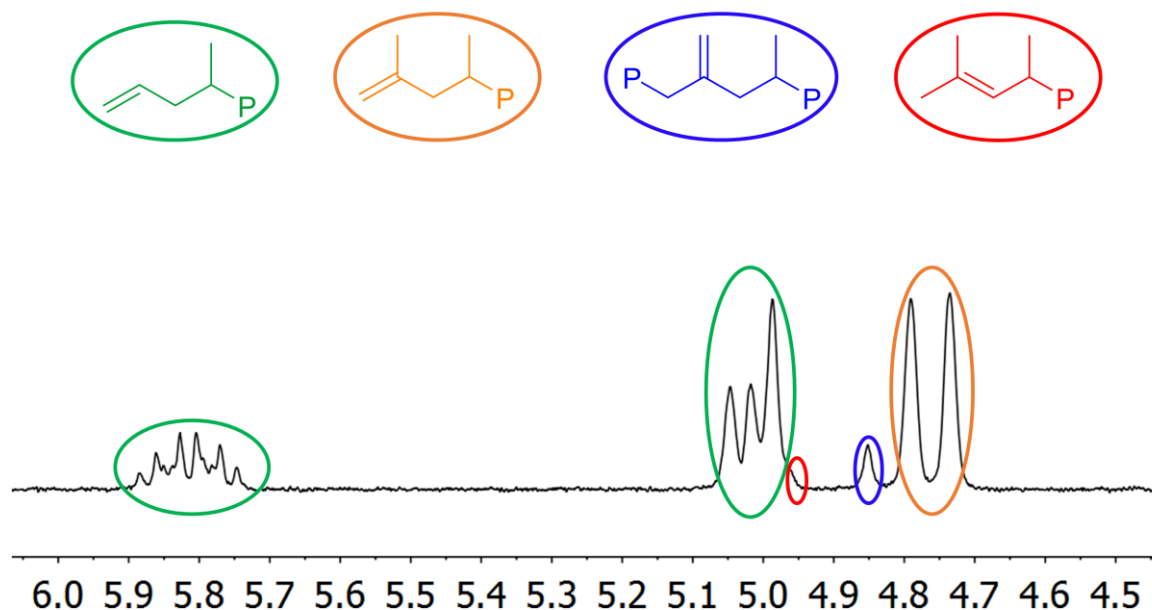


Figure 8. Exemplary olefinic end group assignment of regioselective polypropylene via  $^1\text{H}$  NMR spectroscopy ( $\text{C}_6\text{D}_5\text{Br}$ ,  $140\text{ }^\circ\text{C}$ ).

## 2.8 The Crucial Role of the Group IV Metal Center

With regard to the tremendous research on novel coordinative polymerization catalysts over the last seven decades, the vast majority of these catalysts includes the application of different group IV metal centers. While titanium is the most abundant element, being present in the earth's crust in greater quantities than carbon, nitrogen, or chlorine, zirconium is more than 30-fold less common, and hafnium can only be obtained as a byproduct in the refinement of zirconium.<sup>93</sup> Considering the location of the group IV metals in the periodic table of elements, the nuclear characteristics of titanium and zirconium seem quite expectable. In this context, the relation of zirconium and hafnium appears particularly interesting. Due to the phenomena of lanthanide contraction, the higher homolog Hf possesses a slightly smaller ion radius than Zr under isoelectronic conditions (Shannon (effective ionic radii, CN: IV):  $\text{Hf}^{+IV}$ :  $0.58\text{ \AA}$ ,  $\text{Zr}^{+IV}$ :  $0.59\text{ \AA}$ ,  $\text{Ti}^{+IV}$ :  $0.42\text{ \AA}$ ).<sup>94-95</sup> However, after the initial discoveries of Ziegler and Natta<sup>3, 8</sup> the focus was placed on titanocene complexes. First reports on the application of the higher homologs (Zr, Hf) appeared in the 1980s.<sup>12, 14, 96</sup> Since then, each group IV metal has proven its catalytic capability regarding different areas of specialized applications. Accordingly, the following sections will highlight major differences applying titanium, zirconium and hafnium in the homogeneous polymerization of olefins.

### 2.8.1 Titanium

Although the single-site catalysis using metallocene complexes in combination with a co-catalyst originated from the utilization of titanium, the replacement by higher homologs led to the almost complete disappearance of titanocenes in the polymerization of olefins over the last three decades.<sup>5, 10-11</sup> Only a few examples have been presented in literature where titanocene complexes can compete with isostructural hafnocene and zirconocene analogs in terms of catalytic activity, which is why titanium-based systems are predominantly stated to be far less productive or almost inactive.<sup>97-100</sup> It is generally accepted, that the low productivities derive from side reactions that deactivate the active titanocene catalyst *via* reduction of the  $Ti^{+IV}$  center. This deactivation process is reported to be especially accelerated in the presence of higher monomer concentrations and elevated temperatures.<sup>38, 100-103</sup> A fundamental investigation on activation and deactivation pathways in 2005 by *Bryliakov et al.* illustrated the unsuitability of  $C_2$ -symmetric *ansa*-titanocene complexes in the polymerization of olefins and may be retrospectively considered as death sentence for titanium-based metallocene catalysts in olefin polymerization catalysis. Detailed investigation *via* UV/VIS,  $^1H$  NMR and EPR spectroscopy underlined the fast transformation of catalytically active  $Ti^{+IV}$ - to a catalytically inactive  $Ti^{+III}$ -species under conditions typically applied in the polymerization of olefins.<sup>101</sup> In contrast to these observations, the application of titanium in homogenous post/non-metallocene systems, such as constrained geometry complexes (CGC), for the production of polyolefins developed quite successfully over the last two and a half decades.<sup>22</sup> In addition, titanium has already proven its capability in heterogeneous *Ziegler-Natta* systems for the industrial production of high density polyethylene (HDPE) and especially isotactic polypropylene.<sup>9</sup> However, the stabilization of the  $Ti^{+IV}$  centers under classic polymerization conditions must be considered decisive for the future application of titanium based metallocene catalysts in the polymerization of olefins.<sup>104</sup>

### 2.8.2 Zirconium vs. Hafnium

In general, the chemical properties of zirconium and hafnium are expected to be very similar, because the atom and ion radii and the electronegativities are almost identical.<sup>93</sup> In this connection, the so called lanthanide contraction is responsible that the radius of the higher homolog is reduced by weakened shielding of the 4f orbitals causing enhanced contraction of

the corresponding valence orbitals. In addition, relativistic effects condense the inner s- and p-orbitals and lead to a radial expansion of the 5d orbitals. Thus, the lanthanide contraction and the relativistic effects both determine the final size and shape of the hafnium atom.<sup>105</sup> But in contrast to these assumptions, when zirconium and hafnium are applied in metallocenes for the coordinative polymerization of propylene, severe differences are observed.

In the 1980s, MAO as co-catalyst facilitated the transformation of bis-halogenated metallocenes into catalytically active complexes comprising dramatically higher catalytic activities. Especially the combination of zirconocenes and MAO boosted the productivities, whereas analogously activated hafnocenes were usually found to be far less active.<sup>17, 106-108</sup> At first glance, this was attributed to a stronger  $\sigma$ -M-C bond, provoking a larger energy barrier during chain propagation, and therefore slowing down the catalytic reaction.<sup>105, 109</sup> In addition, experimental investigation of the M-C bond enthalpies *via* titration calorimetry using isostructural Cp\*<sub>2</sub>MMe<sub>2</sub> complexes indeed supported a stronger bond in the case of hafnium (Hf-C: 306 kJ/mol, Zr-C: 284 kJ/mol, Ti-C: 281 kJ/mol).<sup>110-112</sup> However, further studies on the activation process of hafnocenes with MAO disclosed a more decisive role of TMA. By the formation of a stable dinuclear methyl-bridged resting state formerly active hafnocene catalyst became inactive in the presence of TMA.<sup>35</sup> Comparing these binuclear complexes of zirconium and hafnium, the latter was calculated to be 3 kcal/mol more stable.<sup>32</sup> If the traditional MAO activation was replaced by the two-step activation mechanism with TIBA/[Ph<sub>3</sub>C][B(C<sub>6</sub>F<sub>5</sub>)<sub>4</sub>], comparable catalytic activities of hafnocenes and zirconocenes were observed.<sup>20, 23, 92</sup> Consequently, it is not an intrinsic property of hafnium which causes lower catalytic activities but an inefficient activation strategy, if cationic hafnocene structures are exposed to free TMA.<sup>20, 32</sup>

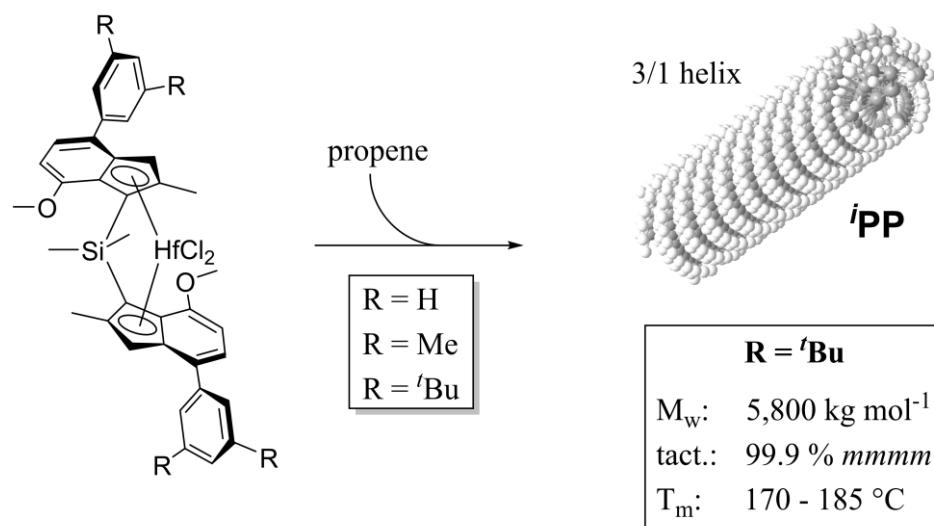
The differences between zirconocene and hafnocene catalysts become particularly important with respect to the molecular weights of the polypropylenes. Higher molar masses for the polymers of the hafnocene compared to the zirconocene analog were herein observed for several classes of metallocene catalysts regarding a C<sub>1</sub>-, C<sub>2</sub>- and C<sub>s</sub>-symmetric *ansa*-metallocene framework.<sup>20, 23, 105</sup> Based on these observations, the capability of hafnium to produce significantly higher molecular weights became known as the “hafnium-effect”. The stronger M-C bond using hafnium catalysts is herein considered crucial for more than three decades.<sup>20, 49, 105, 109</sup> Since the rate ratio of propagation and chain release determines the average chain length of the produced polypropylene, differences regarding the chain release mechanisms need to be considered. In this context, comparative quantum chemical studies

revealed significantly higher activation energies for the  $\beta$ -hydride transfer of hafnocene compared to zirconocene complexes.<sup>49</sup> Additional theoretical investigations also suggest a bimolecular  $\beta$ -hydride elimination pathway proceeding on a coordinated monomer unit without direct hafnium–hydride interaction.<sup>81</sup> However, investigation of the olefinic end group composition of polypropylenes produced with isostructural zirconocene and hafnocene complexes revealed a significantly higher selectivity toward allylic chain ends deriving from  $\beta$ -methyl elimination, if hafnocenes were applied in the polymerization setup.<sup>92</sup>

In general, differences between zirconocene and hafnocene catalysts are less established regarding their stereo- and regioselective polymerization behavior. Beside the limited amount of publications addressing isostructural hafnocene as well as zirconocene complexes under identical conditions, especially the accuracy of ancient NMR data hinders reliable comparative conclusions. However, theoretical investigations using a plain  $\text{Cp}_2\text{MCl}_2$  metallocene suggest an improved regioselectivity if hafnium as metal center is applied.<sup>49</sup> In addition, recent contributions of *Rieger et al.* indicate predominantly higher regio- and stereoselectivities going along with higher melting transitions for the hafnocene species of an ultra-rigid  $\text{C}_2$ -symmetric *ansa*-metallocene framework.<sup>23-24, 113</sup>

### 3. Aim of this Work

Over the last four decades, a plethora of different metallocene complexes have been synthesized and evaluated in the polymerization of olefins in order to tune and develop the corresponding polymer characteristics. Doubtless, numerous advances have been made, although catalyst design and development has, at least in many occasions, been based on a simple trial and error principle. However, for a precise development of the next generation of polymerization catalysts, a detailed understanding of all relevant reaction pathways simultaneously taking place in the highly complex polymerization setup is indispensable, as is a profound knowledge of accurate structure-property relationships between the molecular shape of the catalyst and the final polymer product.



**Scheme 9. Application of 2,4,7-substituted bisindenyl hafnocene complexes with varied 4-aryl substituents for the highly isoselective polymerization of propylene.**<sup>23-24</sup>

Heterogeneous, state of the art ZN-catalysts, which still account for the vast majority of industrially produced <sup>i</sup>PP, synthesize polypropylenes with a broad molecular weight distribution, isotacticities between 90 % to 98 % isotactic pentad (*mmmm*) and melting transitions at about 160 °C.<sup>9</sup> In contrast, with the development of ultra-rigid, C<sub>2</sub>-symmetric, bisindenyl *ansa*-metallocenes by the group of *Rieger et al.* in 2012, ultra-high molecular weight polypropylenes of narrow polydispersity and tacticities up to 99.9 % *mmmm* became feasible (Scheme 9, R = <sup>t</sup>Bu).<sup>23, 113</sup> Due to the almost perfect stereo- and regiocontrol mechanism, high-melting, isotactic polypropylene was generated comprising the highest melting transitions of isotactic polypropylene to date.<sup>23-24</sup> Inspired by the extraordinarily precise catalytic performance of this particular complex structure, the essential structural

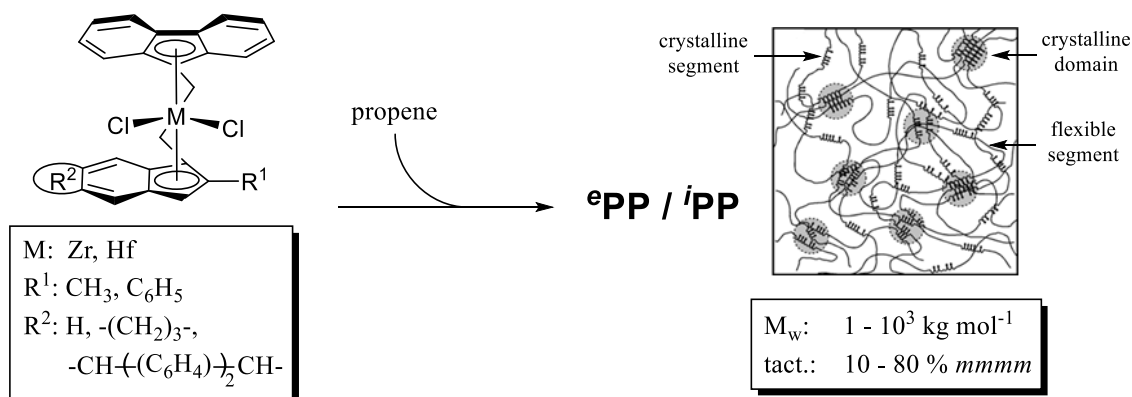
components which contribute to these exceptional polymer properties are elucidated as part of this thesis. Therefore, the synthesis and catalytic evaluation of hafnium-based metallocenes, which possess 4-aryl substituents of varied steric demand, were targeted (Scheme 9).

With the application of hafnium in the catalytic conversion of propene, a new dimension of high molecular weight polypropylenes became accessible. This not just holds for the application of  $C_2$ -symmetric 2,4,7-substituted bisindenyl hafnocene complexes (Scheme 9), but also for other  $C_1$ - and  $C_s$ -symmetric hafnocene derivatives.<sup>20, 23, 105</sup> Although the intrinsic potential of hafnium to catalyze significantly higher molecular weights merely displays a general observation that still lacks a fundamental scientific explanation, utilization of this “hafnium-effect” today represents a well-established method of boosting the respective molecular weights in polyolefin catalysis. However, the catalytic performance of different group IV metallocenes differs not only with respect to the molecular weights of the produced polymers, the metal center also determines the catalytic activity and several other characteristics in the final polymer product (Chapter 2.8). For several decades, metallocenes of different group IV metals have been applied in the polymerization of propylene, and each metal center has proven its capability regarding different specialized fields of application, but the actual origin which is accountable for all the observable differences is unknown to this day. Nevertheless, a fundamental impact of different M–C bond characteristics is usually considered, since the  $\sigma$ -M–C binding unit is involved in the vast majority of catalytically relevant sub-processes.<sup>105, 112</sup> Therefore, the synthesis and examination of isostructural, alkylated group IV metallocenes, which constitute the state of the art catalysts for stereo- and regiodeflect free *i*PP (Scheme 9), constitutes the central project of this thesis. Accordingly, the synthesis route to the  $C_2$ -symmetric, rigid hafnocene complexes needed to be adapted in order to synthesize the isostructural titanium and zirconium analogs. In addition, alkylation strategies needed to be developed to convert the halogenated complexes into alkylated ones for further profound analysis of the M–C  $\sigma$ -bond. Beside the catalytic evaluation, the kinetic examination of the M–C bond characteristics by a monitored conversion of this binding unit represents an essential aspect of this work. Furthermore, the fundamental electronic properties of the M–C  $\sigma$ -bond should, for the first time, be disclosed experimentally *via* high resolution single-crystal X-ray diffraction analysis (SC XRD) of the alkylated, isostructural titanocene, zirconocene and hafnocene complexes. Thereby, the verification of different M–C bond strengths was targeted. Facilitated by the multidimensional approach of this study, the elucidation of fundamental electronic and chemical differences of isostructural group IV metallocenes should, in the end, reform the fundamental understanding of basic group IV

metallocene chemistry, and the catalytic peculiarities of each group IV metal center in the polymerization of olefins.

In contrast to zirconium and hafnium, the application of titanium in metallocene-based polyolefin catalysis generally leads to the formation of unstable catalysts (Chapter 2.8.1).<sup>101</sup> However, the complex structures presented above (Scheme 9) have proven their capability in the successful prevention of undesired processes such as chain release or epimerization reactions. Inspired by the precise catalytic performance of this exceptional complex framework, the application of titanium in combination with these structural motives is evaluated in more detail. Therefore, various activation methods were examined and polymerization conditions were screened in order to evaluate the suitability of titanium in a modern and precise state of the art metallocene framework for the coordinative polymerization of propylene.

With the development of extraordinarily precise *i*PP-catalysts, based on an ultra-rigid C<sub>2</sub>-symmetric *ansa*-metallocene structure, boundaries were pushed significantly regarding the formation of high-melting, high molecular weight, perfectly stereo- and regioselective polypropylene. However, the advantage of metallocene catalysis is not just the higher precision in the polymerization process, but also the extreme flexibility of the stereocontrol mechanism in the catalytic conversion of propylene. One of the most prominent examples for the formation of elastic polypropylene, a polymer class which is not accessible by classic heterogeneous ZN-catalysts, is the application of C<sub>1</sub>-symmetric, ethylene-bridged fluorenyl-indenyl *ansa*-metallocenes for the production of polypropylenes with 10 % to 80 % isotactic pentad (Scheme 10).<sup>19, 75, 114</sup>



**Scheme 10.** Application of C<sub>1</sub>-symmetric ethylene-bridged fluorenyl-indenyl (EBFI) *ansa*-metallocenes for the polymerization of propylene with variable stereoselectivity.

Especially the formation of high molecular weight, elastic polypropylene using hafnium-based EBFI-type *ansa*-metallocene complexes led to a new class of elastic polypropylene materials with excellent mechanical properties.<sup>20</sup> But apart from the outstanding elastic characteristics, these polymers always exhibited insufficient temperature stability due to low melting transitions.<sup>19, 115</sup> Therefore, a detailed examination of the intricate interplay of various mechanisms which collectively define the stereoregularity of the produced polypropylenes using EBFI-catalysts became an additional project of this thesis. In this context, a comparative in-depth analysis of the catalytic behavior of several new, as well as literature-known, EBFI-type metallocenes in the polymerization of propylene was targeted. Accordingly, the impact of essential setup parameters such as the polymerization temperature and the monomer concentration should be investigated. The detailed examination should gain a more profound understanding of the key aspects that trigger the formation of elastic polypropylene. In the end, this approach should contribute to a more directed synthesis of new and defined polypropylene microstructures, with particular focus on elastic polypropylenes comprising high-melting characteristics. In addition, alternative strategies which facilitate the formation of new microstructures in polyolefin materials for potential application as thermoplastic elastomers (TPE) should be developed and evaluated as a part of this thesis.

#### 4. Striving for Perfection: High Molecular Weight, High-Melting *i*PP

- Title:** “Ultrarigid Indenyl-based Hafnocene Complexes for the Highly Isoselective Polymerization of Propene: Tunable Polymerization Performance Adopting Various Sterically Demanding 4-Aryl Substituents”
- Status:** Full Paper, Published online December 17<sup>th</sup>, 2016
- Journal:** Organometallics, 2017, Volume 36, 399 – 408
- Publisher:** American Chemical Society
- DOI:** 10.1021/acs.organomet.6b00814
- Authors:** Martin R. Machat, Dominik Lanzinger, Alexander Pöthig, Bernhard Rieger<sup>a</sup>

**Content:** In 2012, our research group published a paper on the state of the art homogenous metallocene catalyst for ultra-high molecular weight polypropylene with almost perfect stereo- and regioregularity.<sup>23</sup> This strictly isotactic polymer, possessing the highest known melting transition for untreated *i*PP (*ex reactor*), is not just the result of striving for perfection, but also provides the potential to gain novel insight into further intelligent catalyst development. The focus of this study was directed towards the crucial substitution pattern being decisive for the rigid complex framework and the outstanding precision in the polymerization catalysis. Therefore, two new hafnocene complexes were synthesized, fully characterized, including single crystal X-ray diffraction analysis, and applied in a broad range of polymerization conditions, to compare them with the above mentioned benchmark system. This contribution not only addresses the unique polymer properties, but also provides unadulterated insight into the catalytic performance, with special focus on activity as a pure function of rate of chain growth. The key to perfect *i*PP catalysis is herein attributed to the successful prevention of chain release and chain end epimerization reactions in combination with an extremely accurate enantiomeric site control mechanism.

---

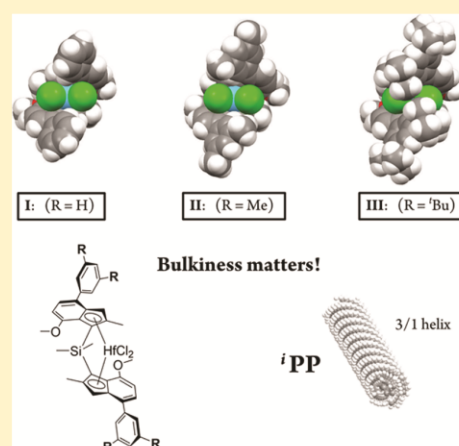
<sup>a</sup> M. Machat planned and executed all experiments and wrote the manuscript. D. Lanzinger developed the synthesis of some organic precursors and contributed with fruitful mental input. A. Pöthig conducted all SC XRD-measurements and managed the processing of the respective data. All work was performed under the supervision of B. Rieger.



# Ultrarigid Indenyl-based Hafnocene Complexes for the Highly Isoselective Polymerization of Propene: Tunable Polymerization Performance Adopting Various Sterically Demanding 4-Aryl Substituents

Martin R. Machat,<sup>†</sup> Dominik Lanzinger,<sup>‡</sup> Alexander Pöthig,<sup>§</sup> and Bernhard Rieger<sup>\*,†</sup><sup>†</sup>Wacker-Lehrstuhl für Makromolekulare Chemie, Technische Universität München, Lichtenbergstraße 4, 85748 Garching bei München, Germany<sup>‡</sup>Advanced Materials & Systems Research, BASF SE, GCP/PM-B001, 67056 Ludwigshafen am Rhein, Germany<sup>§</sup>Catalysis Research Center, Technische Universität München, Ernst-Otto-Fischer Straße 1, 85748 Garching bei München, Germany**S** Supporting Information

**ABSTRACT:** Two novel silyl-bridged  $C_2$ -symmetric (2-methyl-4-aryl-7-methoxy) substituted bisindenyl based *ansa*-hafnocene complexes of varied steric demand (I, 4-phenyl; II, 4-[(3',5'-methyl)-phenyl]) were synthesized and examined in the coordinative polymerization of propene. Both complexes enable a comparative study with the state of the art homogeneous metallocene catalyst (III, 4-[(3',5'-*tert*-butyl)-phenyl]) for high melting ultrahigh molecular weight isotactic polypropylene. All three activated complexes exhibit extremely concise stereoregularity along with high molecular weights and high melting transitions at low to moderate polymerization temperatures. Increased sterical encumbrance of the 4-aryl substituent prevents the process of chain release reactions more effectively, especially due to enhanced reduction of  $\beta$ -methyl elimination. Accordingly, end group analysis disclosed the highest selectivity toward allylic chain ends as a result of  $\beta$ -methyl elimination with the less sterically encumbered complex I. Examination of the catalytic activity of I–III disclosed considerable impact of the varied 4-aryl substituents on the maximum productivity with respect to the applied polymerization conditions considering the combined influence of activation, monomer diffusion rate, catalyst deactivation, and rate of chain growth.

**■ INTRODUCTION**

In 1985 the first indenyl based *ansa*-zirconocene-methylaluminumoxane (MAO) catalytic system for the narrow molecular weight distributed isospecific polymerization of propene was discovered by the combined work of Kaminsky and Brintzinger.<sup>1–3</sup> Since then vast interest aroused to optimize the polymerization performance of metallocene complexes in the single-site catalysis to polypropylene (PP).<sup>4</sup> Ewen's symmetry rules describing the relationship between complex symmetry and polymer microstructure were crucial for further development of complex design with respect to the desired PP properties.<sup>5</sup> The synthesis of polypropylenes with variable microstructures, which were not accessible using heterogenic Ziegler–Natta systems,<sup>6,7</sup> evoked huge scientific effort concerning polypropylene with tailored tacticities particularly comprising elastic behavior.<sup>8–11</sup> In 1994 Spaleck and co-workers reported the catalysis to highly isotactic polypropylene using –SiMe<sub>2</sub>– bridged (2-methyl-4-phenyl) substituted *rac*-bisindenyl zirconocene complexes (SBI type) which revealed

exceptional potential in the precise single-site catalysis of high molecular weight *i*PP.<sup>12–16</sup> The remarkable high molecular weights obtained with these systems activated with MAO are attributed to the effective shielding of the ligand preventing exchange reactions with AlMe<sub>3</sub> setting free the polymer chain.<sup>17</sup> Further strategies toward highly isoselective PP catalysis were developed using  $C_1$ -symmetric *ansa*-cyclopentadienyl(*cp*)-fluorenyl coordinated zirconocene complexes, titanium salen complexes and bis(phenolate) ether complexes (Zr, Hf) respectively.<sup>18–23</sup> While initially low activities were observed applying hafnocene complexes for the polymerization of olefins alternative activation reagents to MAO enabled the utilization of hafnocene complexes as highly productive metallocene catalysts.<sup>24–27</sup> In 2012 further adjustment of the primary Spaleck-type ligand structure by Schöbel et al. lead to ultrarigid metallocene complexes producing polypropylenes with ex-

Received: October 26, 2016

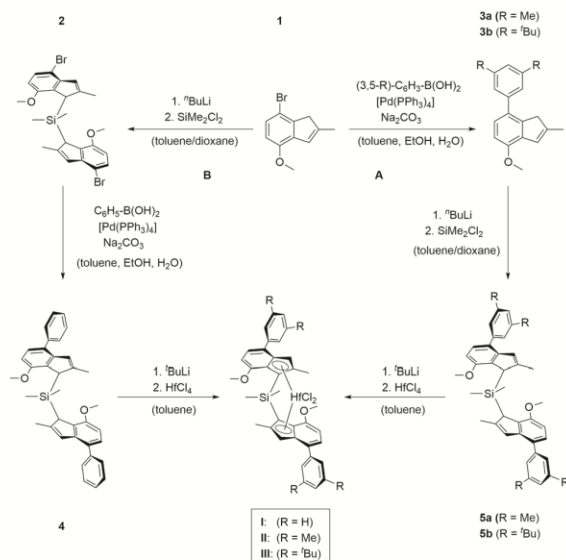
Published: December 17, 2016

remely high molecular weights and extraordinary precision with respect to the stereo- and regioselective polymerization behavior.<sup>28</sup> To date the resulting polymer exhibits the highest melting transition for untreated iPP (*ex reactor*) and was further investigated regarding the exceptional thermal characteristics of the almost perfect iPP polymer.<sup>29</sup> Just recently, the high potential in terms of catalytic activity of SBI-type metallocene complexes was reported as a result of weak electrophilic attraction of the metal center toward the respective counterion.<sup>30,31</sup> Calculations on related zirconocene complexes supported the additional effect of 3',5'-substitution on the 4-phenyl substituent with respect to the stereo- and regioselectivity.<sup>16,32</sup> In order to gain deeper insight into the outstanding catalyst performance of these ultrarigid 2,4,7-substituted bisindenyl hafnocene complexes the focus is drawn to different 4-aryl substituents possessing a varied 3',5'-substitution pattern of decreased steric encumbrance.

## RESULTS AND DISCUSSION

**Syntheses.** Varied ligand structures with different 4-aryl substituents were obtained starting with the literature known indene derivative **1** followed by a Suzuki cross-coupling reaction in order to implement different aryl groups in position 4 of the indenyl fragment.<sup>28,33</sup> Whereas **3a** and **b** react with  $\text{SiMe}_2\text{Cl}_2$  in a regioselective manner after the deprotonation with  ${}^t\text{BuLi}$ , a mixture of regioisomers regarding position 1 and 3 of the indenyl fragment was obtained with the phenyl substituted fragment. Therefore, the alternative reaction pathway **B** (Scheme 1) for the synthesis of ligand **4** was

**Scheme 1. Synthesis Route to 2,4,7-Substituted Hafnocene Complexes with Varied 4-Aryl Substituents**



developed. The lithiated substrate **1** turned out to react with  $\text{SiMe}_2\text{Cl}_2$  regioselective at position 1 of the indenyl fragment followed by a subsequent introduction of the phenyl groups. Deprotonation of ligands **4**, **5a-b** with  ${}^t\text{BuLi}$  in toluene and the successive addition of  $\text{HfCl}_4$  led to a mixture of the corresponding *racemic* and *meso* complex. Separation was conducted with different pentane/toluene mixtures at adjusted

temperatures isolating the desired *rac*-hafnocene complexes **I–III**.

Single crystals suitable for X-ray diffraction analysis were obtained of **I** and **II** by diffusion of pentane into a saturated complex solution in toluene or benzene. Crystals of complex **I** possess an additional incorporation of 1.0 eq. of benzene. The crystal structure of complex **III** is already literature known (CCDC: 841806).<sup>28</sup> ORTEP style representations of **I** and **II** are given in Figure 1, important bond lengths and angles of all three complexes are depicted in Table 1.

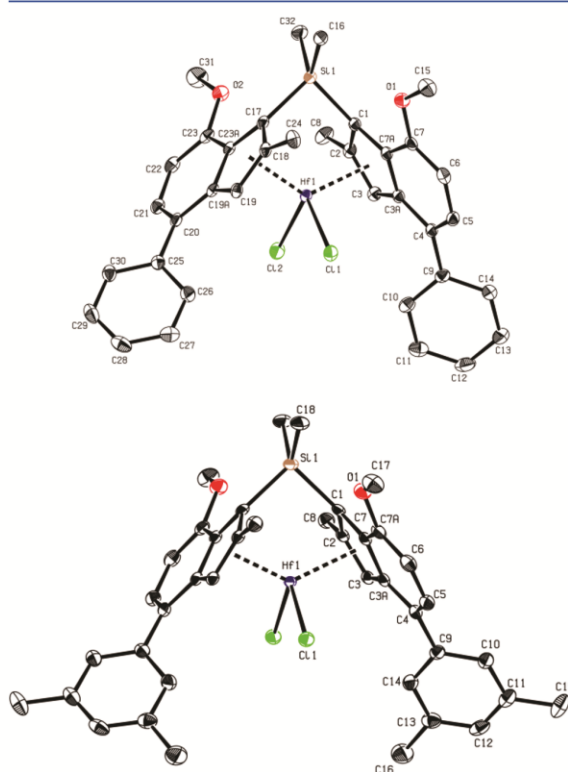


**Figure 1.** ORTEP style representation of **I** (top) and **II** (bottom) with ellipsoids drawn at 50% probability level. Hydrogen atoms are omitted for clarity.

In the solid state, the largest dihedral angle is observed for complex **II** possessing the largest bite angle. The shortest bond length between the central metal and the cp-center as well as the lowest D-value indicating that the metal center is less exposed to the surrounded environment, were measured in the solid state of complex **III**. Unfortunately, a consistent trend of

**Table 1. Characteristic Angles and Distances of the Solid State Structures (I–III)**

	bite angle <sup>a</sup> (deg)	dihedral angle <sup>a</sup> (deg)	Hf–C <sub>p</sub> centroid (Å)	D <sup>a</sup> (Å)
<b>I</b>	58.9	41.1/45.2	2.224 ± 2	0.949 ± 4
<b>II</b>	59.6	48.6	2.231	0.949
<b>III</b> <sup>28</sup>	57.8	42.6	2.218	0.926

<sup>a</sup>According to refs 34 and 35. Complex **I** differs from accurate C<sub>2</sub> symmetry.

bond lengths and angles with respect to an increased steric demand of the 4-aryl substituents is not observed in the solid state. The incorporation of solvent molecules in the case of I as well as lattice effects leading to enhanced compression especially for the <sup>t</sup>Bu-substituted complex during crystal packaging disables the opportunity to draw further conclusion regarding the chemical behavior in solution. Nevertheless, the impact of increased sterically encumbered 4-aryl substituents on the coordination gap aperture<sup>36</sup> is conveniently illustrated by the solid state structures (Figure 2).

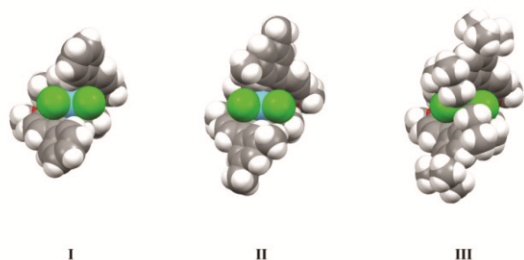


Figure 2. Space filling representation of I–III illustrating the effect of different 4-aryl substituents on the coordination gap aperture (cga).

Evaluation of geometric characteristics of the complex structures is presented based on the graphic illustration of Figure 3. All three complexes carry a methoxy substituent in

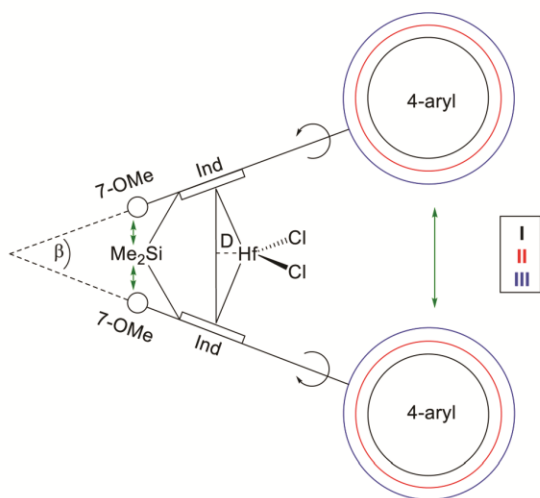


Figure 3. Graphic illustration of I–III pointing out the steric interactions leading to the rigid complex framework.

position 7 of the indenyl fragment, which is known to cause stereorrigidity in the complex structure by repulsive interaction with the  $-\text{SiMe}_2-$  bridge. As a consequence the bite angle is lowered.<sup>28,37</sup> In addition, two opposing interactions determining the conformation of the 4-aryl substituents related to the indenyl fragment are essential for the structure of these complexes. This phenomena, being partially described by the dihedral angle, is a result of reaching the energetic minimum in a coplanar structure by maximized delocalization, interfering with the reduction of steric interactions by rotation of the 4-aryl substituent. On a molecular level including rotational, vibra-

tional and motional processes the steric interaction of the 3',5'-substituents of both indenyl fragments tends to widen the bite angle in connection with increased steric encumbrance. This suggestion is supported by the space filling representations of Figure 2 and the schematic representation of Figure 3. The result of combined compressing and widening forces (green arrows, Figure 3) is expected to preserve the rigid complex framework in a broad temperature range.

**Productivity.** All three complexes were tested regarding their catalytic behavior in the polymerization of propene under identical conditions (Table 2). The activated complexes I–III are capable of producing high molecular weight and highly isotactic polypropylenes possessing high productivities. To gain detailed information on the particular catalytic activities Figure 4 visualizes essential factors determining the overall productivity.

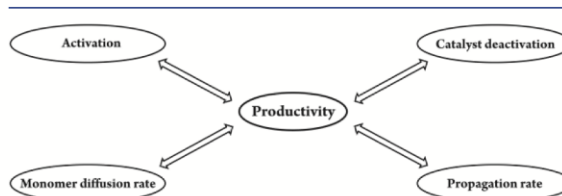


Figure 4. Main influencing factors affecting the productivity in the coordinative polymerization of olefins.

Activation of all three complexes proceeds in two steps starting with an alkylation of the bishalogenated complex using 200 eq. of triisobutylaluminum (TIBA) at 60 °C for 1 h. The cationic, catalytically active species is generated *in situ* by the addition of 5 eq. of  $[\text{Ph}_3\text{C}][\text{B}(\text{C}_6\text{F}_5)_4]$ . Monitoring the reaction of I–III with 200 eq. of TIBA at 60 °C via UV VIS spectroscopy indicates a fast substitution reaction due to a shift of the absorbance maxima to lower wavelength (see Supporting Information). Although the substitution reaction is much slower for complex III compared to I and II a distinct shift of the absorbance maxima is observed after 1 h. The reaction of  $[\text{Ph}_3\text{C}][\text{B}(\text{C}_6\text{F}_5)_4]$  with alkylated metallocenes is stated to proceed quite rapid leading to the assumption that the overall activation process should be comparable for all three complexes.<sup>24,25,38,39</sup>

The polymers from complexes I–III produced at temperatures up to 30–50 °C almost exclusively precipitate during the polymerization therefore limiting the productivity since accessibility of further monomer units to the catalytically activated complexes is significantly reduced. In addition, during precipitation of the polymer also active catalyst may be removed from the solution. At higher polymerization temperatures the polymer remains in solution enabling higher yields in the batch process as the produced polymer is acting as additional viscous solvent during the polymerization reaction. Hence, the averaged chain length as well as the stereo- and regioregularity of the polymer are crucial for the viscosity of the reaction mixture in addition to the total amount of produced polymer. In general, enhanced viscosity reduces the productivity since diffusion of monomer to the metal center is rather limited. Due to the direct relation of viscosity and polymer formation the diffusion rate is particularly lowered at longer reaction times. Thus, the amount of catalyst is adjusted generating comparable reaction mixtures keeping limitation by

Table 2. Conditions and Results for the Polymerization of Propene with Complexes I–III in Toluene<sup>a</sup>

entry	complex	<i>n</i> <sup>b</sup>	<i>p</i> <sup>c</sup>	<i>T</i> <sub>p</sub> <sup>d</sup>	<i>T</i> <sub>m</sub> <sup>e</sup>	<i>m</i> <i>m</i> <i>m</i> <i>m</i> <i>m</i> <sup>f</sup>	<i>M</i> <sub>w</sub> <sup>g</sup>	<i>D</i> <sup>h</sup>	<i>P</i> <sup>i</sup>
1	I	2	3	0	165	>99	1600	2.0	4000
2	I	1	4	30	162	>99	1400	1.6	16000
3	I	1	4	50 <sup>j</sup>	161	98	680	1.8	33000
4	I	2	4	70 <sup>j</sup>	149	88	200	2.2	40000
5	I	5	4	90 <sup>j</sup>	128	80	29	2.4	9500
6	I	5	4	110 <sup>j</sup>	108	67	6	2.1	3600
7	II	2	3	0	164	>99	2200	1.5	3200
8	II	2	4	30	163	>99	1500	1.5	15000
9	II	2	4	50	162	>99	710	1.7	16000
10	II	2	4	70 <sup>j</sup>	154	93	200	1.7	47000
11	II	5	4	90 <sup>j</sup>	143	89	31	2.1	11000
12	II	5	4	110 <sup>j</sup>	122	76	6	1.7	7500
13	III	2	3	0	171 <sup>l</sup>	99.9 <sup>l</sup>	5800 <sup>l</sup>	1.2 <sup>l</sup>	1000
14	III	2	4	30	170 <sup>l</sup>	99.5 <sup>l</sup>	1700 <sup>l</sup>	1.5 <sup>l</sup>	13000
15	III	2	4	50	165 <sup>l</sup>	99.3 <sup>l</sup>	1100 <sup>l</sup>	1.6 <sup>l</sup>	14000
16	III	2	4	70 <sup>l</sup>	160 <sup>l</sup>	98.4 <sup>l</sup>	410 <sup>l</sup>	1.5 <sup>l</sup>	46000
17	III	5	4	90 <sup>k</sup>	152	94	97	2.4	50000
18	III	5	4	110 <sup>j</sup>	128	84	12	2.1	21000
19	I	2	3	50 <sup>j</sup>	155	93	290	2.3	30000
20	II	2	3	50	156	97	380	1.9	19000

<sup>a</sup>*t*<sub>p</sub> = 30 min; *V*<sub>toluene</sub> = 300 mL; scavenger (TIBA) = 2.2 mmol. <sup>b</sup>In micromoles. <sup>c</sup>*p* = *p*<sub>Ar</sub> + *p*<sub>propene</sub> in bar; *p*<sub>Ar</sub> = 1.3 bar. <sup>d</sup>*T*<sub>p</sub> in °C ± 2 °C. <sup>e</sup>In °C. <sup>f</sup>Determined via <sup>13</sup>C NMR spectroscopy assuming the enantiomorphic site model. <sup>g</sup>In kg·mol<sup>-1</sup>. <sup>h</sup>*D* = *M*<sub>w</sub>/*M*<sub>n</sub>. <sup>i</sup>In kg<sub>pp</sub>·[mol<sub>M</sub>·(mol/L)·h]<sup>-1</sup> ± 5 °C. <sup>k</sup>±8 °C. <sup>l</sup>According to ref 28.

mass-transport to a minimum or at least comparable for all three catalyst systems.

Olefin polymerization basically proceeds via  $\pi$ -coordination of an olefin unit followed by the migratory insertion via four-center transition state. Variation of the ligand structure of complexes I–III may affect the monomer association/dissociation equilibrium but since the rate-determining step is generally assigned to the process of olefin insertion, the focus is directed to the influence of varied ligand structure on the rate of chain propagation ( $\nu$ ).<sup>40–42</sup> The latter takes place first order with respect to the amount of added catalyst (cat) and monomer (C<sub>3</sub>H<sub>6</sub>), the rate constant of monomer insertion (*k*<sub>p</sub>) and the fraction of catalytically active complex ( $\chi$ ) (eq 1).<sup>43</sup>

$$\nu = k_p \cdot \chi \cdot [\text{cat}] \cdot [\text{C}_3\text{H}_6] \quad (1)$$

To compare the catalytic activity of complexes I–III as a preferably unadulterated function of the chain propagation rate, the productivities are normalized to catalyst and monomer concentration (the latter determined by the equation of Busico<sup>44</sup>). A crucial point for the catalytically active fraction ( $\chi$ ) is the initial complex activation procedure being already discussed in a previous section, but also catalyst deactivation due to decomposition at high temperatures becomes progressively important thereby irreversibly lowering  $\chi$ . This process is indicated by a significant drop of activity over the polymerization time excluding a prevalent impact of mass-transport limitation due to enhanced viscosity. The possible formation of resting states during the polymerization is an important as well as hardly predictable issue. Beside the interaction with aluminum alkyls being always present in the reaction mixture the role of the counterion is also essential in this connection. Whereas the applied [B(C<sub>6</sub>F<sub>5</sub>)<sub>4</sub>]<sup>-</sup> anion possesses a low coordination strength to the catalytically active cationic complex in the case of [MeB(C<sub>6</sub>F<sub>5</sub>)<sub>3</sub>]<sup>-</sup> the tight cation–anion interaction results in an equilibrium of active and dormant species.<sup>45</sup> The impact of varied ligand structure on the

complex cation–anion interaction potentially affecting the coordination strength, the anion mobility, the monomer assisted dissociative displacement or the prevalent formation of solvated/outer-sphere ion pairs may depict a substantial reason for the different catalytic behavior of complexes I–III.<sup>45,46</sup> These interactions may directly affect the rate constant (*k*<sub>p</sub>), itself representing a very complex aggregate accounting all factors of influence related to chain propagation. Most essentially, the influence of varied steric demand of the 4-aryl substituents in complexes I–III on the chain propagation step should be expressed by this constant. However, experimental determination of *k*<sub>p</sub> appears to be rather difficult and is only feasible monitoring the molecular weight with respect to the reaction time. Since the reaction time to build up one polymer chain is usually well below one second only few examples of quantitative kinetic investigation are known using quenched flow techniques.<sup>43,47–49</sup> Consequentially, a more qualitative evaluation of the impact of varied ligand structure on the catalytic activity is in the scope of this work. The temperature dependent productivities of complexes I–III adjusted to the present complex and monomer concentration are depicted in Figure 5.

It is illustrated, that the maximum productivity of all three complexes I–III is shifted with respect to the applied polymerization temperature and the absolute value of the maximized productivity increases. Complex I comprising the smallest steric demand at the 4-aryl substituent, reveals its highest productivity at about 60–65 °C (~40 000 kg<sub>pp</sub>·[mol<sub>M</sub>·(mol/L)·h]<sup>-1</sup>). The maximum productivity is displaced up to about 70 °C (~45 000 kg<sub>pp</sub>·[mol<sub>M</sub>·(mol/L)·h]<sup>-1</sup>) for complex II and to 80–85 °C (~50 000 kg<sub>pp</sub>·[mol<sub>M</sub>·(mol/L)·h]<sup>-1</sup>) for the <sup>t</sup>Bu-substituted complex III, respectively. At low polymerization temperatures the less sterically demanding complex I exhibits the highest productivities leading to the assumption that chain propagation is rather limited in the case of bulkier substituted systems. Interaction of the skipping polymer chain

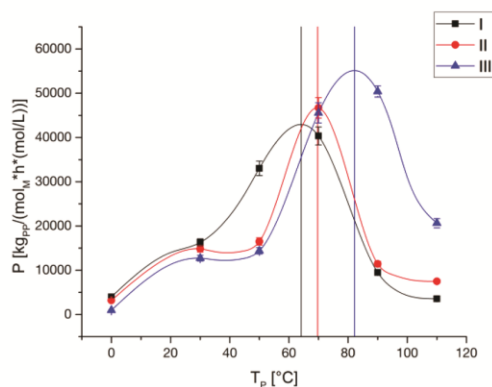


**Figure 5.** Spline representation of the productivity for complexes I–III in the polymerization of propene (see Table 2 for details). Error bars are depicted according to possible deviations during the preparation process.

due to the migratory insertion mechanism with the 4-aryl substituents may exhibit a crucial role considering low rotation rates. Switching to polymerization temperatures of 30 °C results in a productivity increase of all three complexes I–III. Further temperature increase to 50 °C rises the productivity of I distinctly, whereas the more sterically encumbered complexes II–III need polymerization temperatures of  $T_p \geq 70$  °C to become highly active. Higher steric demand from I to III in the complex framework seems to limit the catalytic activity at low to moderate temperatures. The temperature shifted progressive increase of the productivity of I vs II and III may be at least partially ascribed to different solubility of the produced polymer. Without going into detail on the polymer properties at this point, a more precise stereoselective behavior as well as higher molecular weights are obtained with a bulkier 4-aryl substituent. As a result, polypropylene produced at 50 °C with I is partly soluble, whereas that of II and especially III still precipitates thereby removing active catalyst at an early stage of the polymerization process. Consequently, II and III display high catalytic activities not until predominant solubility of the produced polymer is provided. Regarding high polymerization temperatures ( $T_p \geq 70$  °C) enhanced sterical encumbrance in the complex structure accounts for higher catalytic activities. Considering the volume uptake of propene during the adopted polymerization time this observation seems to be a reason for different thermal stability of the catalytically activated complexes (Figure 6, 7).

At 70 °C the productivity, representing the averaged catalytic performance over the polymerization time, is in a comparable range for all three activated complexes I–III. Nevertheless, the volume uptake of propene indicates a distinct different catalytic behavior. Although complex I and II show very high initial activities (Figure 6, 70 °C, large slope of the curves), the sterically most encumbered complex III reveals the highest activities at longer polymerization times resulting in a similar overall volume uptake of all three catalytic systems. At 90 °C the initial activities are almost identical for all three complexes, but III is the only complex which is active during the whole polymerization time. By contrast, the catalytically active species of complex I is completely deactivated after about 4 min and II after about 10 min.

**Polymer properties.** The molecular weights are determined by the rate ratio of propagation and chain release. All

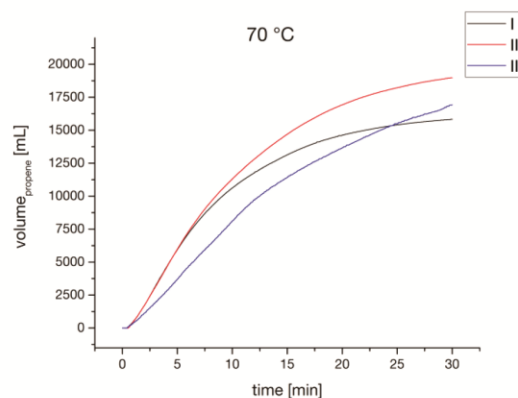


**Figure 6.** Consumption of propene with respect to the polymerization time at 70 °C (entries 4, 10, and 16) standardized on 2.0  $\mu$ mol of I–III.

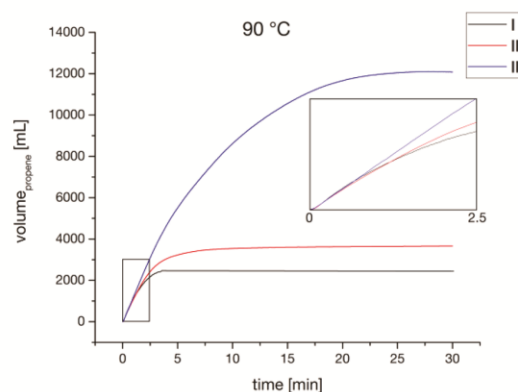


**Figure 7.** Consumption of propene with respect to the polymerization time at 90 °C (entries 5, 11, and 17) standardized on 2.0  $\mu$ mol of I–III.

three complexes I–III produce polymers with ultrahigh molecular weights particularly at low polymerization temperatures. Switching to higher temperatures and lower monomer concentrations endothermal elimination processes become more favored (Figure 8).

An increased steric demand of the 4-aryl substituent results in higher molecular weights of the produced polymers suggesting progressive prevention of elimination reactions. This effect is especially pronounced for III at lower polymerization temperatures although the lowest propagation rates of all complexes are observed under these conditions.

Crucial for the molecular weight of the polymer chains are the chain release reactions. Investigation of the olefinic end group composition facilitates the determination of chain release reactions using the catalytically activated complexes I–III. Due to low concentration of olefinic end groups in high molecular weight polymer samples the end group composition can only be identified in polymer samples produced at higher polymerization temperatures and lower monomer concentrations via  $^1\text{H}$  NMR spectroscopy (Figure 9). In the case of complex I and II  $\beta$ -methyl elimination is observed as most favored chain release reaction pathway leading to the formation of allylic end groups (Figure 9, green). Vinylidene end groups as a result of  $\beta$ -hydride elimination can be detected as second preferred chain

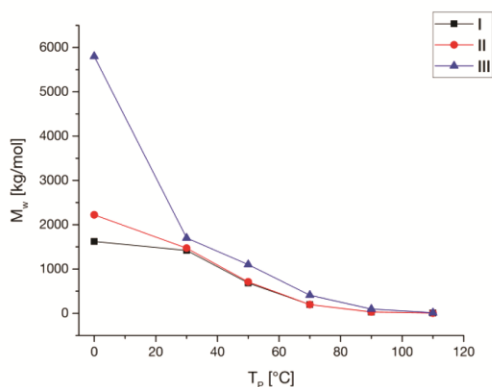


**Figure 8.** Weight-average molecular weight ( $M_w$ ) of polypropylene dependent on the polymerization temperatures with I–III (see Table 2 for details).

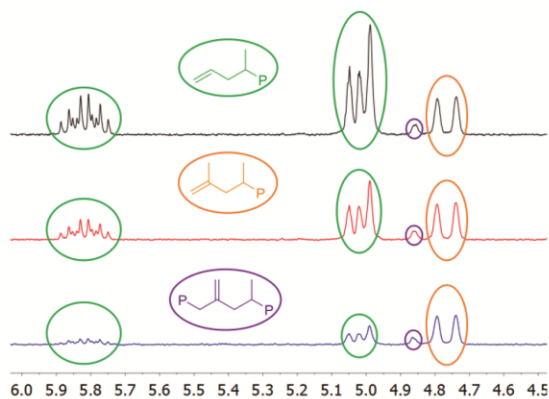


**Figure 9.** Determination of olefinic end group composition via  $^1\text{H}$  NMR spectroscopy (at 140 °C,  $\text{C}_6\text{D}_6\text{Br}$ ) of polypropylene (entries 5, 11, and 17;  $T_p = 90$  °C) with I (black), II (red), and III (blue).

release reaction (Figure 9, orange). Regarding complex III the probability toward vinylidene end groups is higher compared to allylic end groups. Internal end groups as a result of allylic C–H bond activation are also monitored for all three complexes (Figure 9, purple).<sup>50,51</sup> The impact of the polymerization temperature on the selectivity of  $\beta$ -hydride and  $\beta$ -methyl elimination is depicted in Figure 10 considering the polymerization results at 110 °C.

At 90 °C as well as 110 °C the catalytically active species of complex I bearing the lowest steric demand at the 4-aryl substituent possesses the highest selectivity toward allylic chain ends. This fact contradicts with previous studies revealing much higher selectivities toward  $\beta$ -methyl transfer in the case of the bulkier substituted  $\text{Cp}^*\text{ZrHfCl}_2/\text{MAO}$  system (M: Zr, Hf) compared to the unsubstituted  $\text{Cp}_2\text{HfCl}_2/\text{MAO}$  system (M: Zr, Hf).<sup>52–55</sup> Rising the polymerization temperature favors the pathway of  $\beta$ -methyl elimination in all three cases. Varying the temperature from 90 to 110 °C particularly affects the end group selectivity of complex III resulting in the predominant formation of allylic chain ends at 110 °C in contrast to the observed end group composition at 90 °C.

In accordance to Figure 8 the average molecular weight decreases with elevated temperatures since all chain release reactions more preferentially occur. The results of Figure 10

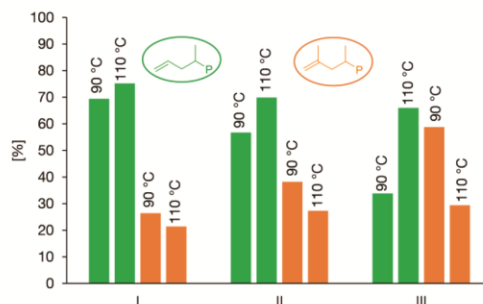


**Figure 10.** Determination of allylic and vinylidene chain ends of polypropylene produced at 90 and 110 °C (entries 5, 6, 11, 12, 17, and 18).

suggest that especially  $\beta$ -methyl elimination is accelerated rising the temperature. This is in line with a higher estimated activation barrier for the process of  $\beta$ -methyl compared to  $\beta$ -hydride elimination considering the notable energy difference for C–C vs C–H bond cleavage.<sup>56</sup> An increased steric demand of the 4-aryl substituents prevents both elimination pathways, whereupon the process of  $\beta$ -methyl elimination is obviously reduced more distinctly.

For PP produced by complex III very low amounts of regiodefects are reported.<sup>28</sup> The results of I and II confirm the concise regioselectivity for these type of complexes since neither 2,1-erythro nor 3,1-isomerization regio defects are detected using standard  $^{13}\text{C}$  NMR spectroscopy (s. Experimental). The remarkable selectivities especially at elevated polymerization temperatures may be attributed to the high rigidity in all three catalytic systems. The rigidity preserves the accurate molecular structure being indispensable for a precise regio control mechanism in conditions usually stimulating potentially undesired rotational, vibrational and motional processes.

All three complexes exhibit almost perfect stereoselective behavior in the polymerization of propene at low temperatures following the mechanism of enantiomorphic site control.<sup>57–60</sup> Switching to higher polymerization temperatures as well as lower monomer concentrations isolated stereoregions become detectable. The tacticity is determined by the ratio of the *mmmm*-pentad to the sum of all pentads (Figure 11).

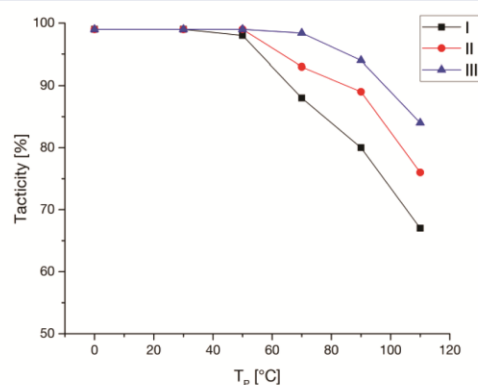


**Figure 11.** Tacticities (% *mmmm*) of the polymers produced with complexes I–III determined via  $^{13}\text{C}$  NMR spectroscopy (see Table 2 for details).

Assignment of the isotacticity (% *mmmm*) via  $^{13}\text{C}$  NMR spectroscopy indicates at least 99% *mmmm* regarding polymerization temperatures up to 30 °C for I and II with respect to the signal-to-noise ratio, although no other pentads are observable. All tacticities of polymers produced with complex III (except entry 17 + 18) were determined with an accuracy of  $\pm 0.1\%$ .<sup>28</sup> Investigation of the pentad distribution at polymerization temperatures above 50 °C reveals the presence of additional pentads (*mmmr*, *mmrr*, *mrrm*) attributed to isolated stereo errors.

Taking into consideration that the polymerizations between 70–110 °C were performed at isobar pressure, lower monomer concentrations at higher temperatures evoke predominant impact on the stereo control mechanism beside the general loss of selectivity caused by rising the temperature itself. Particularly stereoerror formation via chain end epimerization<sup>61</sup> is favored at low monomer concentration and is attributed to be the main reason turning down the isotacticity employing complex I–III under these conditions.<sup>44,62–65</sup> This assumption is supported by polymers produced with I and II at 50 °C and 3 bar, possessing significantly lower tacticities (I: 93% *mmmm*, II: 97% *mmmm*) than the ones produced at 4 bar. Consequently, complex III comprising the highest steric demand at the 4-aryl substituent is able to preserve the formation of isotactic sequences at elevated temperatures best, whereas I produces polymers with the lowest amount of *mmmm*-pentads. These results indicate that an increased steric demand more sufficiently prevents the cascade process of chain end epimerization comparing complex I–III. Disregarding the predominant stereoerror formation via chain end epimerization in the presence of low monomer concentration, we believe, that the enantiofacial selectivity of our systems is still accurate at elevated temperatures due to the high rigidity of the complexes. One example demonstrating the precise catalytic control at higher temperatures is the polymerization with III at 70 °C increasing the monomer concentration from 0.88 M (Entry 16) to 1.53 M. The result is a highly isoselective polymer with an *mmmm*-pentad distribution of 99.0%.<sup>28</sup>

The melting behavior of the polymers is mainly influenced by the tacticity of the polypropylenes. In the case of short chain lengths the average molecular weight possesses a more distinguished impact on the melting transition.<sup>66</sup> The melting transition of all generated polymers is depicted in Figure 12.

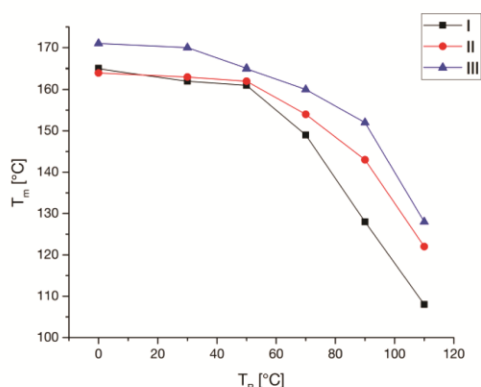


**Figure 12.** Melting transition of polypropylene samples produced at different polymerization temperatures with I–III (see Table 2 for details).

High melting temperatures above 160 °C are observed for polymerization temperatures up to 50 °C in all cases. An overall decrease of the melting transitions is noticed for the polymers of complexes I–III applying higher polymerization temperatures, at which the effect is less pronounced with increased steric demand of the ligand. The results are in line with the determined tacticities (Figure 11) as well as molecular weights (Figure 8).

Regarding industrial application, the focus is directed to highly productive catalyst systems, most substantially, comprising long-term stability. A precise stereo- and regio control mechanism in combination with high molecular weight polymer chains are indispensable to ensure the quality of the produced high performance polyolefins. Considering the production process, elevated temperatures are always preferred to improve heat transmission (larger  $\Delta T$ ) as well as the processability, since better solubility of the produced polymer is assured. In this context, the most promising results are obtained with the catalytic system III revealing the highest selectivities and productivities combined with the most distinctive temperature stability. The high rigidity in the complex framework, provided by the combined steric effects of the 7-OMe and the sterically encumbered 4-[(3',5'-*tert*-butyl)-phenyl] substituents, is suggested to be key for this essential contribution. The introduced rigidity-concept as a result of the unique substitution pattern displays a new, alternative approach for further catalyst design and development.

## CONCLUSION

In this report two novel  $C_2$ -symmetric indenyl based *ansa*-hafnocene complexes with 4-aryl substituents of varied steric demand (I–II) were synthesized enabling a comparative study with the literature known complex (III). The latter is stated as benchmark for the catalysis of high melting ultrahigh molecular weight *i*PP comprising extraordinary precise stereo- and regioselectivity. Complete characterization including X-ray diffraction analysis was conducted for both new complexes illustrating the crucial impact of the 4-aryl substituent on the coordination gap aperture. The activated complexes I–III were examined regarding their polymerization behavior applying identical conditions. The varied steric demand of the 4-aryl substituent revealed considerable impact on the maximum productivity with respect to the polymerization temperature. Therefore, the direct relationship between complex structure and catalytic activity is extensively discussed with respect to the combined impact of activation, monomer diffusion rate, catalyst deactivation and rate of chain growth. The highest temperatures to reach the maximized productivity in combination with the largest overall catalytic activity were necessary for the most sterically encumbered complex III. GPC analysis determined remarkable high molecular weights for the polymers of all three complexes at low polymerization temperatures. A decrease of the average molecular weight is observed applying higher polymerization temperatures as well as lower monomer concentrations. Increased steric encumbrance of the ligand leads to higher molecular weights due to enhanced prevention of chain release reactions. Olefinic end group analysis discloses increased selectivity toward allylic vs vinylidene end groups regarding elevated polymerization temperatures, since  $\beta$ -methyl elimination is rather accelerated. Furthermore, the process of the  $\beta$ -methyl elimination is particularly prevented in the case of increased steric demand at the 4-aryl substituent. At low to moderate polymerization temperatures going along with higher

monomer concentrations the catalytic performance in terms of stereoregularity is very concise for all three complexes I–III. Consequentially, the *mmmm*-pentad is exclusively detected using  $^{13}\text{C}$  NMR spectroscopy. The formation of isolated stereoregularities, predominant a result of chain end epimerization, rather occurs at lower monomer concentrations. The sterically most encumbered complex III is capable of still preserving the highest isotacticities impeding the cascade reaction of chain end epimerization better than I and II. Accurate regioselectivities for all polymers produced with I–III were detected in a broad temperature range. High rigidity in the complex framework is key for a precise stereo and regio control up to elevated temperatures. DSC analysis provides a high melting behavior for the polymer of all three complexes dependent on the varied polymerization conditions in analogy to the determined tacticities and molecular weights.

## EXPERIMENTAL SECTION

**General.** All reactions containing air- and moisture-sensitive compounds were performed under argon atmosphere using standard Schlenk or glovebox techniques. All chemicals, unless otherwise stated, were purchased from Aldrich, Acros, or VWR and used as received. Dry toluene and *n*-pentane were obtained from an MBraun MB-SPS-800 solvent purification system. Deuterated dichloromethane was refluxed over  $\text{CaH}_2$  and distilled prior to use. Propene (99.5% by Westfalen AG) was purified by passage through two columns filled with BASF catalyst (R3-11) and molecular sieves 3–4 Å. Elemental analysis was conducted with a EURO EA (HEKA tech) instrument equipped with a CHNS combustion analyzer.

$^1\text{H}$  and  $^{13}\text{C}$  NMR measurements were recorded on a Bruker ARX-300, AV-500C, AV400, or AV500 spectrometer at ambient temperature. Chemical shifts  $\delta$  are reported in ppm relative to tetramethylsilane and calibrated to the residual  $^1\text{H}$  or  $^{13}\text{C}$  signal of the deuterated solvent. Polymer spectra were measured with an ARX-300 spectrometer at 140 °C in bromobenzene- $d_5$  with 50–60 mg/mL.

Gel permeation chromatography (GPC) was performed with a PL-GPC 220 instrument equipped with 2X Olexis 300 mm  $\times$  7.5 mm columns and triple detection via differential refractive index detector, PL-BV 400 HT viscometer, and light scattering (Precision Detectors model 2040; 15°, 90°). Measurements were performed at 160 °C using 1,2,4-trichlorobenzene (TCB; 30 mg BHT/L) with a constant flow rate of 1 mL/min and a calibration set with narrow MWD polystyrene (PS) and polyethylene (PE) standards. Samples were prepared dissolving 0.9–1.1 mg of polymer in 1.0 mL of stabilized TCB for 10–15 min at 160 °C immediately before each measurement.

Differential scanning calorimetry (DSC) analysis was conducted on a DSC Q2000 instrument. Polymer (3–8 mg) was sealed into a DSC aluminum pan and heated from 20 to 200 °C at 10 °C/min. After holding the temperature for 2 min, the sample was cooled down to 20 °C at 10 °C/min and heated up again in the same manner. The reported values are those determined in the second heating cycle.

**Synthesis.** All compounds that are not listed below were synthesized according to literature procedures.<sup>28,67,68</sup>

**Bis(4-bromo-7-methoxy-2-methylindenyl)dimethyl Silane, 2.** 4-Bromo-7-methoxy-2-methylindene (10.3 g, 43.1 mmol, 2.00 equiv) was diluted in 200 mL of dry toluene/dioxane (1/1) in a pressurizable Schlenk flask. At –10 °C, 17.2 mL (43.1 mmol, 2.00 equiv) of  $^t\text{BuLi}$ , 2.5 M in hexane, was added dropwise to the solution. After stirring at room temperature for 2 h, 2.62 mL (21.5 mmol, 1.00 equiv) of dichlorodimethylsilane was added at –10 °C. After stirring at 60 °C for additional 24 h, the reaction mixture was poured into 50 mL of water. Diethyl ether (150 mL) was added, phases were separated, and the organic layer was washed with water (150 mL) and brine (150 mL). The organic phase was dried with  $\text{Na}_2\text{SO}_4$ , the solvent is evaporated, and the crude product was recrystallized in a DCM/MeOH mixture leading to 8.25 g (72%) of colorless needles (2). Anal. Calcd for  $\text{C}_{24}\text{H}_{26}\text{Br}_2\text{O}_2\text{Si}$ : C, 53.95; H, 4.90. Found: C, 53.99; H, 4.78.  $^1\text{H}$  NMR (500 MHz,  $\text{CDCl}_3$ , 298 K):  $\delta$  (ppm) = 7.28 (d,  $^3J = 8.5$  Hz,

2H, H–Ar), 6.60 (m, 2H, –CH=), 6.53 (d,  $^3J = 8.5$  Hz, 2H, H–Ar), 4.24 (s, 2H, –CH–Si), 3.85 (s, 6H, –OCH<sub>3</sub>), 2.24 (d,  $^3J = 1.4$  Hz, 6H, –CH<sub>3</sub>), –0.44 (s, 6H, Si–CH<sub>3</sub>).  $^{13}\text{C}$  NMR (126 MHz,  $\text{CDCl}_3$ , 298 K):  $\delta$  (ppm) = 153.51, 150.19, 145.96, 134.30, 129.05, 125.54, 106.65, 105.62, 54.99, 48.18, 17.70, –3.71.

**7-(3',5'-Dimethylphenyl)-4-methoxy-2-methylindene, 3a.** All solvents were degassed prior to use. A solution of 4.63 g (30.8 mmol, 1.10 equiv) of (3,5-dimethylphenyl)boronic acid in ethanol (40 mL) and a solution of 3.88 g (3.36 mmol, 0.12 equiv)  $\text{Pd}(\text{PPh}_3)_4$  in toluene (200 mL) were added to 6.70 g (28.0 mmol, 1.00 equiv) of 4-bromo-7-methoxy-2-methylindene. After the subsequent addition of 56.0 mL (56.0 mmol, 2.00 equiv) of 1 M NaOH solution, the mixture was refluxed for 3 days. Water (250 mL) and toluene (250 mL) were added, phases were separated, and the aqueous phase was extracted two times with toluene (2  $\times$  100 mL). The combined organic layers were dried over  $\text{Na}_2\text{SO}_4$  and the solvent was removed *in vacuo*. Compound 3a was isolated via column chromatography (toluene,  $R_f = 0.75$ ) as a white solid (6.10 g, 82%). Anal. Calcd for  $\text{C}_{19}\text{H}_{20}\text{O}$ : C, 86.32; H, 7.63. Found: C, 86.69; H, 7.60.  $^1\text{H}$  NMR (300 MHz,  $\text{CDCl}_3$ , 298 K):  $\delta$  (ppm) = 7.11 (s, 2H, H–Ar'), 7.07 (d,  $^3J = 8.3$  Hz, 1H, H–Ar), 6.97 (s, 1H, H–Ar'), 6.84 (d,  $^3J = 8.3$  Hz, 1H, H–Ar), 6.64 (s, 1H, –CH=), 3.88 (s, 3H, –OCH<sub>3</sub>), 3.39 (s, 2H, –CH<sub>2</sub>–), 2.35 (s, 6H, CH<sub>3</sub>–Ar'), 2.13 (s, 3H, –CH<sub>3</sub>).  $^{13}\text{C}$  NMR (75 MHz,  $\text{CDCl}_3$ , 298 K):  $\delta$  (ppm) = 152.05, 145.28, 143.04, 141.52, 138.40, 134.95, 131.42, 128.72, 126.66, 125.76, 123.46, 109.66, 55.97, 43.96, 21.68, 16.93.

**Bis[4-phenyl-7-methoxy-2-methylindenyl]dimethyl Silane, 4.** All solvents were degassed prior to use. A solution of 6.10 g (50.0 mmol, 4.00 equiv) of phenylboronic acid in ethanol (70 mL) as well as a solution of 3.46 g (2.99 mmol, 0.24 equiv) of  $\text{Pd}(\text{PPh}_3)_4$  in toluene (400 mL) were added to 6.66 g (12.5 mmol, 1.00 equiv) of bis(4-bromo-7-methoxy-2-methylindenyl)dimethyl silane (2). After the subsequent addition of 50.0 mL (50.0 mmol, 4.00 equiv) of 1 M NaOH solution, the mixture was refluxed for 3 days. Water (200 mL) and toluene (200 mL) were added, phases were separated, and the aqueous phase was extracted two times with toluene (2  $\times$  100 mL). The combined organic layers were dried over  $\text{Na}_2\text{SO}_4$  and the solvent was removed *in vacuo*. A 1:1 mixture of *rac*-/*meso*-isomers (4) was obtained via column chromatography (pentane/EtOAc 20/1,  $R_f = 0.36$ ). Recrystallization in DCM/MeOH led to the desired product as colorless needles (5.20 g, 79%). Anal. Calcd for  $\text{C}_{36}\text{H}_{36}\text{O}_2\text{Si} \times 1/3 \text{CH}_2\text{Cl}_2$ : C, 78.34; H, 6.63. Found: C, 78.26; H, 6.60 (presence of additional  $\text{CH}_2\text{Cl}_2$  was confirmed via NMR spectroscopy).  $^1\text{H}$  NMR (300 MHz,  $\text{CDCl}_3$ , 298 K):  $\delta$  (ppm) = 7.54 (m, 4H, H–Ar'), 7.45 (m, 4H, H–Ar'), 7.33 (m, 2H, H–Ar'), 7.24 (dd,  $^3J = 8.2$ , 1.7 Hz, 2H, H–Ar), 6.74 (m, 4H, H–Ar, –CH=), 4.23, 4.06 (s, 2H, –CH–Si), 3.92, 3.85 (s, 6H, –OCH<sub>3</sub>), 2.30, 2.17 (s, 6H, –CH<sub>3</sub>), –0.20, –0.22, –0.34 (s, 6H, Si–CH<sub>3</sub>).  $^{13}\text{C}$  NMR (75 MHz,  $\text{CDCl}_3$ , 298 K):  $\delta$  (ppm) = 153.70, 153.66, 149.82, 149.63, 144.35, 144.26, 141.42, 133.48, 128.97, 128.95, 128.43, 127.75, 127.68, 126.78, 126.77, 126.34, 125.19, 125.08, 105.41, 105.35, 54.78, 54.67, 47.06, 46.62, 17.81, 17.72, –2.65, –3.83, –3.85.

**Bis[4-(3',5'-dimethylphenyl)-7-methoxy-2-methylindenyl]dimethyl Silane, 5a.** Compound 3a (5.97 g, 22.6 mmol, 2.00 equiv) was diluted in 100 mL of dry toluene/dioxane (1/1) in a pressurizable Schlenk flask. At –10 °C, 6.42 mL (22.6 mmol, 2.00 equiv) of  $^t\text{BuLi}$ , 2.4 M in hexane, was added dropwise to the solution. After stirring at room temperature for 2 h, 1.38 mL (11.3 mmol, 1.00 equiv) of dichlorodimethylsilane was added at –10 °C. After stirring at 60 °C for additional 24 h, the reaction mixture was poured into 25 mL of water. Diethyl ether (100 mL) was added, phases were separated, and the organic layer was washed with water (70 mL) and brine (70 mL). The organic phase was dried with  $\text{Na}_2\text{SO}_4$ , the solvent was evaporated, and the crude product was recrystallized in a DCM/MeOH mixture leading to 3.11 g (47%) of a 1:1 *rac*-/*meso*-isomer mixture as white solid. Anal. Calcd for  $\text{C}_{40}\text{H}_{44}\text{O}_2\text{Si}$ : C, 82.14; H, 7.58. Found: C, 81.79; H, 7.53.  $^1\text{H}$  NMR (300 MHz,  $\text{CDCl}_3$ , 298 K):  $\delta$  (ppm) = 7.19, 7.18 (d,  $^3J = 8.3$  Hz, 2H, H–Ar), 7.12, 7.10 (s, 4H, H–Ar'), 6.96 (s, 2H, H–Ar'), 6.71 (m, 4H, H–Ar, –CH=), 4.22, 4.02 (s, 2H, –CH–Si), 3.90, 3.84 (s, 6H, –OCH<sub>3</sub>), 2.39, 2.36 (s, 12H, CH<sub>3</sub>–Ar'), 2.28, 2.15 (s, 6H, –CH<sub>3</sub>), –0.23, –0.25, –0.39 (s, 6H, Si–CH<sub>3</sub>).  $^{13}\text{C}$  NMR (75

MHz, CDCl<sub>3</sub> 298 K):  $\delta$  (ppm) = 153.62, 153.59, 149.57, 149.39, 144.38, 144.29, 141.43, 137.87, 137.86, 133.51, 133.43, 128.05, 127.99, 127.92, 126.87, 126.85, 126.78, 126.74, 125.34, 125.20, 105.35, 105.28, 54.78, 54.65, 47.12, 46.61, 21.60, 17.81, 17.74, -2.57, -3.76, -3.79.

*rac*-Dimethylsilanediybis(4-phenyl-7-methoxy-2-methylindenyl)-hafnium Dichloride, I. Compound 4 (750 mg, 1.42 mmol, 1.00 equiv) was dissolved in 50 mL of dry toluene and cooled down to -78 °C, and 1.67 mL (2.84 mmol, 2.00 equiv) of 1.7 M <sup>t</sup>BuLi solution in pentane was added dropwise. After maintaining the temperature for 1 h, the reaction mixture was stirred for additional 3 h at room temperature. The yellow suspension was cooled down to 0 °C and subsequently transferred via cannula to a suspension of 454 mg (1.42 mmol, 1.00 equiv) of HfCl<sub>4</sub> in 25 mL of dry toluene at -78 °C. The reaction mixture was allowed to thaw overnight resulting in an orange suspension. The suspension was filtered, and the residue was extracted with dry toluene (2 × 100 mL). The extract was concentrated to 10 mL and cooled down to -20 °C overnight. Pure *rac*-isomer (110 mg, 10%) was obtained as an orange crystalline solid after removal of the overlaying solution. Anal. Calcd for C<sub>36</sub>H<sub>34</sub>Cl<sub>2</sub>HfO<sub>2</sub>Si: C, 55.71; H, 4.42. Found: C, 55.52; H, 4.32. <sup>1</sup>H NMR (400 MHz, C<sub>2</sub>D<sub>2</sub>Cl<sub>2</sub>, 298 K):  $\delta$  (ppm) = 7.60 (m, 4H, H-Ar'), 7.41 (m, 4H, H-Ar', H-Ar), 7.31 (m, 4H, H-Ar'), 6.86 (s, 2H, -CH=), 6.43 (d, <sup>3</sup>J = 7.8 Hz, 2H, H-Ar), 3.92 (s, 6H, -OCH<sub>3</sub>), 2.24 (s, 6H, -CH<sub>3</sub>), 1.21 (s, 6H, Si-CH<sub>3</sub>). <sup>13</sup>C NMR (100 MHz, C<sub>2</sub>D<sub>2</sub>Cl<sub>2</sub>, 298 K):  $\delta$  (ppm) = 156.11, 140.40, 133.16, 132.93, 130.63, 129.07, 129.01, 128.26, 127.60, 121.71, 120.33, 103.26, 85.70, 17.67, 6.17.

*rac*-Dimethylsilanediybis[4-(3',5'-dimethylphenyl)-7-methoxy-2-methylindenyl]hafnium Dichloride, II. Compound 5a (1.33 g, 2.27 mmol, 1.00 equiv) was dissolved in 70 mL of dry toluene and cooled down to -78 °C, and 2.68 mL (4.55 mmol, 2.00 equiv) of 1.7 M <sup>t</sup>BuLi solution in pentane was added dropwise. After maintaining the temperature for 1 h, the reaction mixture was stirred for additional 3 h at room temperature. The yellow suspension was cooled down to 0 °C and subsequently transferred via cannula to a suspension of 727 mg (2.27 mmol, 1.00 equiv) of HfCl<sub>4</sub> in 40 mL of dry toluene at -78 °C. The reaction mixture was allowed to thaw overnight resulting in a dark yellow suspension. After filtration, the solvent of the filtrate was distilled off, and the residue was washed with dry pentane (2 × 100 mL) and a 1:2 toluene/pentane-mixture (240 mL). After recrystallization in a toluene/pentane mixture, 360 mg (19%) of yellow powder was obtained containing the pure *rac*-isomer. Anal. Calcd for C<sub>40</sub>H<sub>42</sub>Cl<sub>2</sub>HfO<sub>2</sub>Si: C, 57.73; H, 5.09. Found: C, 57.69; H, 4.95. <sup>1</sup>H NMR (400 MHz, CD<sub>2</sub>Cl<sub>2</sub>, 298 K):  $\delta$  (ppm) = 7.26 (d, <sup>3</sup>J = 7.8 Hz, 2H, H-Ar), 7.24 (s, 4H, H-Ar'), 6.96 (s, 2H, -CH=), 6.87 (s, 2H, H-Ar'), 6.40 (d, <sup>3</sup>J = 7.8 Hz, 2H, H-Ar), 3.91 (s, 6H, -OCH<sub>3</sub>), 2.31 (s, 12H, CH<sub>3</sub>-Ar'), 2.25 (s, 6H, -CH<sub>3</sub>), 1.20 (s, 6H, Si-CH<sub>3</sub>). <sup>13</sup>C NMR (100 MHz, CD<sub>2</sub>Cl<sub>2</sub>, 298 K):  $\delta$  (ppm) = 155.96, 140.10, 138.58, 133.07, 132.83, 130.93, 129.20, 127.85, 126.81, 122.12, 120.29, 103.20, 85.45, 21.62, 17.66, 6.16.

**Polymerization.** All polymerization reactions were performed in a 1.1 L Büchi steel autoclave equipped with a paddle agitator, temperature sensor, and heating/cooling jacket attached to a cryo-/thermostat unit (Thermo Scientific HAAKE DynaMax). Ar-pressure for all manipulations was set at 1.3 bar. Prior to polymerization, the autoclave was equipped with 300 mL of dry toluene and 2.0 mL of 1.1 M TIBA solution in toluene and heated up to 90 °C. After maintaining the temperature for 15 min, the scrubbing solution was released. For the polymerization, the autoclave was charged with 280 mL of dry toluene and 2.0 mL of 1.1 M TIBA solution in toluene. The metallocene complex (1.0 equiv) was dissolved in 10 mL of toluene and preactivated with 200 equiv of TIBA at 60 °C for 1 h. After the desired temperature was adjusted, the activated metallocene solution was transferred into the autoclave and was pressurized with propene. When the system was equilibrated and stable, the polymerization was started adding 5.0 equiv of [Ph<sub>3</sub>C][B(C<sub>6</sub>F<sub>5</sub>)<sub>4</sub>] dissolved in 10 mL of toluene to the autoclave via a pressure buret (*p*<sub>pol</sub> + 1.0 bar). The propene consumption was monitored using a gas flow meter (Bronkhorst F-111C-HA-33P). Temperature, pressure, time, and total propene consumption were recorded as well. The polymerization reaction was quenched with 2.0 mL of methanol, and the reaction

mixture was poured into 1.0 L of acidified methanol. Precipitated polymer was removed from the autoclave, and all combined polymer was washed exhaustively and dried at 70 °C *in vacuo* overnight.

## ■ ASSOCIATED CONTENT

### Supporting Information

The Supporting Information is available free of charge on the ACS Publications website at DOI: 10.1021/acs.organomet.6b00814.

<sup>1</sup>H NMR and <sup>13</sup>C NMR spectra of the new key compounds I and II, UV VIS spectra, <sup>1</sup>H NMR spectra for end group analysis, <sup>13</sup>C NMR spectra for tacticity determination, charts providing propene consumption during the polymerization time, SC-XRD data (PDF) Crystallographic information for compounds I and II (CIF)

## ■ AUTHOR INFORMATION

### Corresponding Author

\*E-mail: rieger@tum.de. Tel: +49-89-289-13570. Fax: +49-89-289-13562.

### ORCID

Bernhard Rieger: 0000-0002-0023-884X

### Notes

The authors declare no competing financial interest.

## ■ ACKNOWLEDGMENTS

The authors thank Philipp Pahl and Daniel Wendel for proofreading the manuscript and valuable discussions. The second author D. L. substantially contributed to this work during his time as a co-worker of the Wacker-Lehrstuhl für Makromolekulare Chemie.

## ■ REFERENCES

- (1) Kaminsky, W.; Külper, K.; Brintzinger, H. H.; Wild, F. R. W. P. *Angew. Chem., Int. Ed. Engl.* **1985**, *24*, 507–508.
- (2) Kaminsky, W. *Macromolecules* **2012**, *45*, 3289–3297.
- (3) Wild, F. R. W. P.; Zsolnai, L.; Huttner, G.; Brintzinger, H. H. J. *Organomet. Chem.* **1982**, *232*, 233–247.
- (4) Resconi, L.; Cavallo, L.; Fait, A.; Piemontesi, F. *Chem. Rev.* **2000**, *100*, 1253–1345.
- (5) Ewen, J. A. J. *Am. Chem. Soc.* **1984**, *106*, 6355–6364.
- (6) Ziegler, K.; Holzkamp, E.; Breil, H.; Martin, H. *Angew. Chem.* **1955**, *67*, 541–547.
- (7) Natta, G. *Angew. Chem.* **1956**, *68*, 393–403.
- (8) Coates, G. W.; Waymouth, R. M. *Science* **1995**, *267*, 217–219.
- (9) Mallin, D. T.; Rausch, M. D.; Lin, Y. G.; Dong, S.; Chien, J. C. W. *J. Am. Chem. Soc.* **1990**, *112*, 2030–2031.
- (10) Dietrich, U.; Hackmann, M.; Rieger, B.; Klinga, M.; Leskelä, M. *J. Am. Chem. Soc.* **1999**, *121*, 4348–4355.
- (11) Cobzaru, C.; Hild, S.; Boger, A.; Troll, C.; Rieger, B. *Coord. Chem. Rev.* **2006**, *250*, 189–211.
- (12) Spaleck, W.; Antberg, M.; Rohrmann, J.; Winter, A.; Bachmann, B.; Kiprof, P.; Behm, J.; Herrmann, W. A. *Angew. Chem., Int. Ed. Engl.* **1992**, *31*, 1347–1350.
- (13) Spaleck, W.; Kueber, F.; Winter, A.; Rohrmann, J.; Bachmann, B.; Antberg, M.; Dolle, V.; Paulus, E. F. *Organometallics* **1994**, *13*, 954–963.
- (14) Ewen, J. A.; Zambelli, A.; Longo, P.; Sullivan, J. M. *Macromol. Rapid Commun.* **1998**, *19*, 71–73.
- (15) Stehling, U.; Diebold, J.; Kirsten, R.; Roell, W.; Brintzinger, H. H.; Juengling, S.; Muelhaupt, R.; Langhauser, F. *Organometallics* **1994**, *13*, 964–970.

- (16) Kuklin, M. S.; Virkkunen, V.; Castro, P. M.; Izmer, V. V.; Kononovich, D. S.; Voskoboynikov, A. Z.; Linnolahti, M. *J. Mol. Catal. A: Chem.* **2016**, *412*, 39–46.
- (17) Panchenko, V. N.; Babushkin, D. E.; Brintzinger, H. H. *Macromol. Rapid Commun.* **2015**, *36*, 249–253.
- (18) Press, K.; Cohen, A.; Goldberg, I.; Venditto, V.; Mazzeo, M.; Kol, M. *Angew. Chem., Int. Ed.* **2011**, *50*, 3529–3532.
- (19) Razavi, A.; Thewalt, U. *Coord. Chem. Rev.* **2006**, *250*, 155–169.
- (20) Kirillov, E.; Marquet, N.; Razavi, A.; Belia, V.; Hampel, F.; Roisnel, T.; Gladysz, J. A.; Carpentier, J.-F. *Organometallics* **2010**, *29*, 5073–5082.
- (21) Kirillov, E.; Marquet, N.; Bader, M.; Razavi, A.; Belia, V.; Hampel, F.; Roisnel, T.; Gladysz, J. A.; Carpentier, J.-F. *Organometallics* **2011**, *30*, 263–272.
- (22) Bader, M.; Marquet, N.; Kirillov, E.; Roisnel, T.; Razavi, A.; Lhost, O.; Carpentier, J.-F. *Organometallics* **2012**, *31*, 8375–8387.
- (23) Kiesewetter, E. T.; Randoll, S.; Radlauer, M.; Waymouth, R. M. *J. Am. Chem. Soc.* **2010**, *132*, 5566–5567.
- (24) Bochmann, M. *Organometallics* **2010**, *29*, 4711–4740.
- (25) Chen, E. Y.-X.; Marks, T. J. *Chem. Rev.* **2000**, *100*, 1391–1434.
- (26) Bryliakov, K. P.; Talsi, E. P.; Voskoboynikov, A. Z.; Lancaster, S. J.; Bochmann, M. *Organometallics* **2008**, *27*, 6333–6342.
- (27) Alt, H. G.; Köppl, A. *Chem. Rev.* **2000**, *100*, 1205–1222.
- (28) Schöbel, A.; Herdtweck, E.; Parkinson, M.; Rieger, B. *Chem. - Eur. J.* **2012**, *18*, 4129–4129.
- (29) Tranchida, D.; Mileva, D.; Resconi, L.; Rieger, B.; Schöbel, A. *Macromol. Chem. Phys.* **2015**, *216*, 2171–2178.
- (30) Theurkauff, G.; Bader, M.; Marquet, N.; Bondon, A.; Roisnel, T.; Guegan, J.-P.; Amar, A.; Boucekkine, A.; Carpentier, J.-F.; Kirillov, E. *Organometallics* **2016**, *35*, 258–276.
- (31) Song, F.; Cannon, R. D.; Lancaster, S. J.; Bochmann, M. *J. Mol. Catal. A: Chem.* **2004**, *218*, 21–28.
- (32) Kuklin, M. S.; Virkkunen, V.; Castro, P. M.; Resconi, L.; Linnolahti, M. *Eur. J. Inorg. Chem.* **2015**, *2015*, 4420–4428.
- (33) Izmer, V. V.; Lebedev, A. Y.; Nikulin, M. V.; Ryabov, A. N.; Asachenko, A. F.; Lygin, A. V.; Sorokin, D. A.; Voskoboynikov, A. Z. *Organometallics* **2006**, *25*, 1217–1229.
- (34) Shaltout, R. M.; Corey, J. Y.; Rath, N. P. *J. Organomet. Chem.* **1995**, *503*, 205–212.
- (35) Moehring, P. C.; Coville, N. J. *Coord. Chem. Rev.* **2006**, *250*, 18–35.
- (36) Brintzinger, H. H.; Fischer, D.; Mühlhaupt, R.; Rieger, B.; Waymouth, R. M. *Angew. Chem., Int. Ed. Engl.* **1995**, *34*, 1143–1170.
- (37) Schulte, J.; Sell, T.; Thorn, M. G.; Winter, A.; Dimeska, A. International Patent WO2009054831A1, 2009.
- (38) Bochmann, M.; Lancaster, S. J. *Angew. Chem., Int. Ed. Engl.* **1994**, *33*, 1634–1637.
- (39) Zhou, J.; Lancaster, S. J.; Walker, D. A.; Beck, S.; Thornton-Pett, M.; Bochmann, M. *J. Am. Chem. Soc.* **2001**, *123*, 223–237.
- (40) Laine, A.; Linnolahti, M.; Pakkanen, T. A.; Severn, J. R.; Kokko, E.; Pakkanen, A. *Organometallics* **2010**, *29*, 1541–1550.
- (41) Laine, A.; Linnolahti, M.; Pakkanen, T. A.; Severn, J. R.; Kokko, E.; Pakkanen, A. *Organometallics* **2011**, *30*, 1350–1358.
- (42) Ehm, C.; Budzelaar, P. H. M.; Busico, V. *J. Organomet. Chem.* **2015**, *775*, 39–49.
- (43) Cipullo, R.; Melone, P.; Yu, Y.; Iannone, D.; Busico, V. *Dalton Transactions* **2015**, *44*, 12304–12311.
- (44) Busico, V.; Brita, D.; Caporaso, L.; Cipullo, R.; Vacatello, M. *Macromolecules* **1997**, *30*, 3971–3977.
- (45) Bochmann, M. *J. Organomet. Chem.* **2004**, *689*, 3982–3998.
- (46) Song, F.; Lancaster, S. J.; Cannon, R. D.; Schormann, M.; Humphrey, S. M.; Zuccaccia, C.; Macchioni, A.; Bochmann, M. *Organometallics* **2005**, *24*, 1315–1328.
- (47) Ciancaleoni, G.; Fraldi, N.; Budzelaar, P. H. M.; Busico, V.; Cipullo, R.; Macchioni, A. *J. Am. Chem. Soc.* **2010**, *132*, 13651–13653.
- (48) Ehm, C.; Cipullo, R.; Budzelaar, P. H. M.; Busico, V. *Dalton Transactions* **2016**, *45*, 6847–6855.
- (49) Song, F.; Cannon, R. D.; Bochmann, M. *J. Am. Chem. Soc.* **2003**, *125*, 7641–7653.
- (50) Resconi, L.; Camurati, I.; Sudmeijer, O. *Top. Catal.* **1999**, *7*, 145–163.
- (51) Resconi, L. *J. Mol. Catal. A: Chem.* **1999**, *146*, 167–178.
- (52) Resconi, L.; Piemontesi, F.; Franciscono, G.; Abis, L.; Fiorani, T. *J. Am. Chem. Soc.* **1992**, *114*, 1025–1032.
- (53) Yang, P.; Baird, M. C. *Organometallics* **2005**, *24*, 6005–6012.
- (54) Yang, P.; Baird, M. C. *Organometallics* **2005**, *24*, 6013–6018.
- (55) Suzuki, Y.; Yasumoto, T.; Mashima, K.; Okuda, J. *J. Am. Chem. Soc.* **2006**, *128*, 13017–13025.
- (56) Sini, G.; Macgregor, S. A.; Eisenstein, O.; Teuben, J. H. *Organometallics* **1994**, *13*, 1049–1051.
- (57) Castonguay, L. A.; Rappe, A. K. *J. Am. Chem. Soc.* **1992**, *114*, 5832–5842.
- (58) Longo, P.; Grassi, A.; Pellicchia, C.; Zambelli, A. *Macromolecules* **1987**, *20*, 1015–1018.
- (59) Dahlmann, M.; Erker, G.; Nissinen, M.; Fröhlich, R. *J. Am. Chem. Soc.* **1999**, *121*, 2820–2828.
- (60) Resconi, L.; Fait, A.; Piemontesi, F.; Colonnese, M.; Rychlicki, H.; Zeigler, R. *Macromolecules* **1995**, *28*, 6667–6676.
- (61) Busico, V.; Cipullo, R. *J. Am. Chem. Soc.* **1994**, *116*, 9329–9330.
- (62) Leclerc, M. K.; Brintzinger, H. H. *J. Am. Chem. Soc.* **1995**, *117*, 1651–1652.
- (63) Leclerc, M. K.; Brintzinger, H. H. *J. Am. Chem. Soc.* **1996**, *118*, 9024–9032.
- (64) Busico, V.; Caporaso, L.; Cipullo, R.; Landriani, L.; Angelini, G.; Margonelli, A.; Segre, A. L. *J. Am. Chem. Soc.* **1996**, *118*, 2105–2106.
- (65) Busico, V.; Cipullo, R.; Caporaso, L.; Angelini, G.; Segre, A. L. *J. Mol. Catal. A: Chem.* **1998**, *128*, 53–64.
- (66) Busico, V.; Cipullo, R. *Prog. Polym. Sci.* **2001**, *26*, 443–533.
- (67) Chien, J. C. W.; Tsai, W. M.; Rausch, M. D. *J. Am. Chem. Soc.* **1991**, *113*, 8570–8571.
- (68) Schmid, M.; Eberhardt, R.; Klinga, M.; Leskelä, M.; Rieger, B. *Organometallics* **2001**, *20*, 2321–2330.

## 5. Titanocenes in Olefin Polymerization: Sustainable Catalyst System or an Extinct Species?

**Title:** “Titanocenes in Olefin Polymerization: Sustainable Catalyst System or an Extinct Species?”

**Status:** Full Paper, Published online March 28<sup>th</sup>, 2017

**Journal:** Organometallics, 2017, Volume 36, 1408 – 1418

**Publisher:** American Chemical Society

**DOI:** 10.1021/acs.organomet.7b00112

**Authors:** Martin R. Machat, Christian Jandl, Bernhard Rieger<sup>b</sup>

**Content:** While the application of titanium in the conversion of olefins turned out to be an unconfined success regarding classic heterogeneous Ziegler-Natta and post/non-metallocene catalysis, pure metallocene catalysts are almost exclusively dominated by the higher homologs. The poor stability of the catalytically active titanium derivatives displays an insurmountable hurdle to this day. This study focuses on the utilization of recent advances in ligand design and complex activation to build up a stable class of catalytically active titanocene systems. Therefore, two novel titanocene complexes were synthesized, fully characterized and examined in the coordinative polymerization of propylene in a broad range of polymerization conditions using various activation strategies. Combination of the most capable complex framework with the most effective activation mechanism represents, to the best of our knowledge, the most stable and productive titanium based metallocene catalyst for the polymerization of propylene to date. A precise catalysis, leading to almost stereo- and regiodeflect free isotactic polypropylene with melting transitions exceeding 170 °C (*ex reactor*) underlines the remarkable potential of these titanium based metallocene catalysts.

---

<sup>b</sup> M. Machat planned and executed all experiments and wrote the manuscript. C. Jandl conducted all SC XRD-measurements and managed the processing of the respective data. All work was performed under the supervision of B. Rieger.

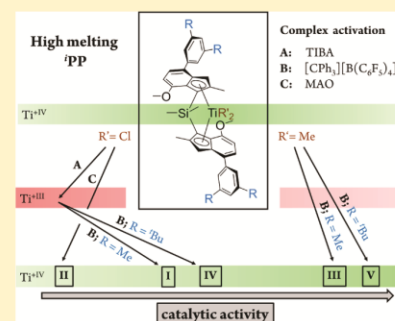
## Titanocenes in Olefin Polymerization: Sustainable Catalyst System or an Extinct Species?

Martin R. Machat,<sup>†</sup> Christian Jandl,<sup>‡</sup> and Bernhard Rieger<sup>\*,†</sup><sup>†</sup>Wacker-Lehrstuhl für Makromolekulare Chemie, Catalysis Research Center, Technische Universität München, Lichtenbergstraße 4, 85748 Garching bei München, Germany<sup>‡</sup>Catalysis Research Center, Technische Universität München, Ernst-Otto-Fischer Straße 1, 85748 Garching bei München, Germany

## Supporting Information

**ABSTRACT:** Two novel silyl-bridged  $C_2$ -symmetric 2-methyl-4-aryl-7-methoxy-substituted bis-indenyl-based titanocene complexes with varied steric demand (**a**, 4-(3',5'-dimethyl)phenyl; **b**, 4-(3',5'-di-*tert*-butyl)phenyl) were synthesized, characterized, and examined in the coordination polymerization of propene. Both adapted ligand structures have proven their capability as precise catalysts in the formation of stereodeflect- and regiodeflect-free isotactic polypropylene. Several activation pathways to the catalytically active, cationic complexes were analyzed in terms of catalytic activity and stability, taking into account the influence of polymerization temperature, monomer concentration, polymerization time, and type of applied scavenger. The overall lowest activities were observed using the methylaluminoxane (MAO) activated catalyst. The two-step activation mechanism of in situ alkylation with an excess of triisobutylaluminum (TIBA) and subsequent addition of  $[\text{Ph}_3\text{C}][\text{B}(\text{C}_6\text{F}_5)_4]$  resulted in moderate productivities of the respective catalyst systems. However, the highest catalytic activities were observed when

eliminating the in situ alkylation step by application of bis-methylated titanocenes in combination with  $[\text{Ph}_3\text{C}][\text{B}(\text{C}_6\text{F}_5)_4]$ . The latter activation mechanism in combination with the sterically more encumbered ligand framework **b** results in the most productive titanium-based metallocene catalyst for the polymerization of propene to date, at least with respect to reasonable reaction times. The determined molecular weights of the produced polymers were significantly affected by the ligand structures **a** and **b** but were only negligibly influenced by the applied activation method. End-group analysis via  $^1\text{H}$  NMR spectroscopy disclosed a chain release mechanism dominated by  $\beta$ -hydride elimination. In accordance with the observed accurate stereo- and regiocontrol mechanism, extraordinarily high melting transitions of up to 170 °C (ex reactor) underline the remarkable potential of these titanium-based catalyst systems in the polymerization of propene.



## INTRODUCTION

The majority of catalytic processes addressing the coordinated conversion of olefins are based on the group IV metals titanium, zirconium, and hafnium. While the first is the most abundant, being present in the earth's crust in greater quantities than carbon, nitrogen, or chlorine, zirconium is more than 30-fold less common, and hafnium can only be obtained as a byproduct in the refinement of zirconium.<sup>1</sup> Regarding the well-established heterogeneous Ziegler–Natta catalysis, which comprises a binary combination of  $\text{TiCl}_4$  and  $\text{AlR}_3$  ( $\text{R}$  = alkyl, aryl, hydride) supported on  $\text{MgCl}_2$ , the application of titanium became an unrivaled success, enabling the large-scale production of isotactic polypropylene (iPP) and high-density polyethylene (HDPE).<sup>2–4</sup> Single-site catalysis using metallocene complexes in combination with an activation reagent also originated with the utilization of titanium, but accelerated replacement with higher homologues led to the almost complete disappearance of titanocenes in the polymerization of olefins over the last three decades.<sup>5–8</sup> Very few examples are known where titanocene complexes can compete with isostructural hafnocene and zirconocene analogues in terms

of catalytic activity, which is why titanium-based systems are predominantly stated to be far less productive or almost inactive.<sup>9–12</sup> It is generally accepted that the low productivities derive from side reactions that deactivate the active titanocene catalyst via reduction of the  $\text{Ti}^{4+}$  center. This deactivation process is reported to be especially accelerated in the presence of higher monomer concentrations and elevated temperatures.<sup>12–16</sup> A fundamental investigation on activation and deactivation processes in 2005 by Bryliakov et al. illustrated the unsuitability of  $C_2$ -symmetric *ansa*-titanocene complexes in the polymerization of olefins and was the death sentence for titanium-based metallocenes in polymerization catalysis.<sup>14</sup> In contrast, the application of titanium in post-/nonmetallocene systems, such as constrained geometry complexes (CGC), for the production of polyolefins has been developed quite successfully over the last two and a half decades.<sup>17</sup> In recent years, our group reported on the synthesis and catalytic evaluation of highly substituted (2-methyl-4-aryl-7-methoxy)-

Received: February 13, 2017

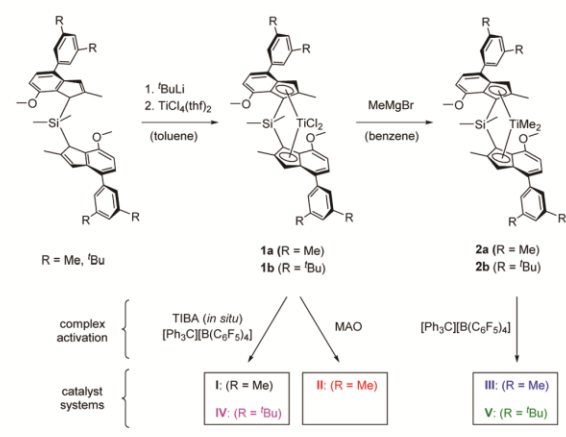
Published: March 28, 2017

indenyl-based, silyl-bridged  $C_2$ -symmetric metallocene complexes (M = Zr, Hf) for the polymerization of high-molecular-weight 'PP with almost perfect regio- and stereocontrol.<sup>18–20</sup> This precise catalytic performance, which is predetermined by the rigid ligand structure as a result of opposing intramolecular forces within the entire complex framework, indicates the successful prevention of undesired processes such as chain release and epimerization reactions.<sup>20</sup> In this report, the potential of this strictly regulative complex structure is evaluated using isostructural titanocene complexes in the polymerization of propene by applying various activation methods. In addition to the catalytic activity, the polymer properties are a matter of investigation.

## RESULTS AND DISCUSSION

**Syntheses.** Ligand structures with varied 4-aryl substituents were synthesized according to established literature procedures.<sup>18,20</sup> The complexation to **1** is carried out in a two-step reaction starting with *in situ* lithiation using <sup>t</sup>BuLi followed by a salt metathesis reaction, in which  $TiCl_4(thf)_2$  is added. Separation of the racemic and meso isomers is conducted by repeated recrystallization in a dichloromethane/*n*-hexane mixture. The bis-methylated complexes **2** are obtained by adding 2.0 equiv of MeMgBr to the bis-chlorinated titanocenes **1** in benzene. Different activation strategies were applied in order to generate the catalytically active titanocene species I–V. *In situ* alkylation of **1** with 200 equiv of TIBA for 1 h at room temperature followed by the subsequent addition of 5.0 equiv of  $[Ph_3C][B(C_6F_5)_4]$  leads to I and IV. Conversion of **1a** with 2000 equiv of MAO generates II. Catalysts III and V are formed by the combination of the methylated complexes **2** and 5.0 equiv of  $[Ph_3C][B(C_6F_5)_4]$  (Scheme 1).

**Scheme 1. Synthesis and Activation of Rigid 2,4,7-Substituted Titanocene Complexes with Varied 4-Aryl Substituents**



Single crystals suitable for X-ray diffraction analysis were obtained of all four complexes (**1** and **2**) by diffusion of pentane into a saturated complex solution in toluene. ORTEP-style representations of all complexes (CCDC 1531610–1531613) are provided in the Supporting Information. Important bond lengths and angles are depicted in Table 1. In the solid state, the bulkier substituted 4-(3',5'-*tert*-butyl)-phenyl complexes **1b** and **2b** exhibit shorter bond lengths to the Cp substituents and lower *D* values, indicating less exposure

**Table 1. Characteristic Angles and Distances of the Solid-State Structures of **1** and **2****

	bite angle (deg) <sup>a</sup>	Ti–Cp <sub>Centroid</sub> (Å)	Ti–Cl/Me	<i>D</i> <sup>a</sup>
<b>1a</b>	58.4	2.157/2.159	2.334/2.309	0.873
<b>1b</b>	56.5	2.133	2.320	0.846
<b>2a</b>	56.7	2.161	2.152	0.863
<b>2b</b>	55.0	2.144	2.151	0.844

<sup>a</sup>According to refs 21 and 22, the molecular structure of **1a** does not possess an exact  $C_2$  symmetry in the triclinic crystalline solid state.

of the metal center to the surrounding environment. To our surprise, the bite angles of the less bulky analogues **1a** and **2a** exceed those of **1b** and **2b**, although on a molecular level steric repulsion of the 4-(3',5'-*R*)-phenyl substituents would suggest enlarged spread due to increased steric interaction. The unexpected result may derive from lattice effects leading to enhanced compression of the <sup>t</sup>Bu-substituted complex during crystal packing. Exchange of chloride with methyl substituents lowers the bite angle, since the electron density in the cavity is reduced. In addition, the distance of the metal center to the Cp planes and the *D* value increase as a result of methylation of the bis-chlorinated complexes. While the effect of the substitution pattern on the Ti–Me bond length is found to be negligible, a significant influence of the 4-(3',5'-*R*)-phenyl substituents on the coordination gap aperture (cga) is depicted by the solid-state structures (Figure 1). However, for a detailed investigation on the effect of the varied ligand framework on the catalytic cycle, calculations regarding gas-phase optimization of the solid-state structures and substituent changes addressing the actual transition state are of high relevance to evolve strategies for further catalyst development.

**Complex Activation.** Different activation strategies were conducted to convert titanocene complexes **1** and **2** to the catalytically active species. The approved method for related zirconocene and hafnocene complexes is a two-step procedure including the *in situ* alkylation of the bis-halogenated titanocenes using 200 equiv of TIBA (60 °C, 1 h) and the addition of  $[Ph_3C][B(C_6F_5)_4]$  in order to start the polymerization reaction.<sup>18,20</sup> The described alkylation process was applied to the titanocenes **1** and monitored via UV/vis spectroscopy. It was found that shorter reaction times and lower temperatures are sufficient to alkylate both titanocenes, which is indicated by a distinct shift of the absorbance maxima to lower wavelengths (Supporting Information). Since TIBA can also act as a reducing agent due to the presence of traces of  $HAL(^tBu)_2$ , the reduction of  $Ti^{4+}$  needs to be taken into consideration under the applied reaction conditions. Bryliakov et al. reported that the addition of only 10 equiv of TIBA to the complex *rac*- $C_2H_4(1-Ind)_2TiCl_2$  led to an immediate and complete reduction from  $Ti^{4+}$  to  $Ti^{3+}$ , thereby causing full deactivation of the potential catalytic activity.<sup>14</sup> <sup>1</sup>H NMR spectroscopy of **1a** after the addition of 100 equiv TIBA in  $C_6D_6$  indeed indicated conversion from diamagnetic  $Ti^{4+}$  to paramagnetic  $Ti^{3+}$  complexes since all complex signals immediately vanished. To verify the susceptibility of complexes **1** toward undesired reductive processes, several reaction conditions were screened and analyzed via EPR spectroscopy, assuring no interfering signals of the excess component. Evaluation of the *in situ* alkylation was performed with **1a** using varying amounts of TIBA (Figure 2).

After addition of TIBA to **1a**, the two partially overlapping EPR signals become detectable with  $g = 1.971$  ( $a_H = 6.6$  G) and

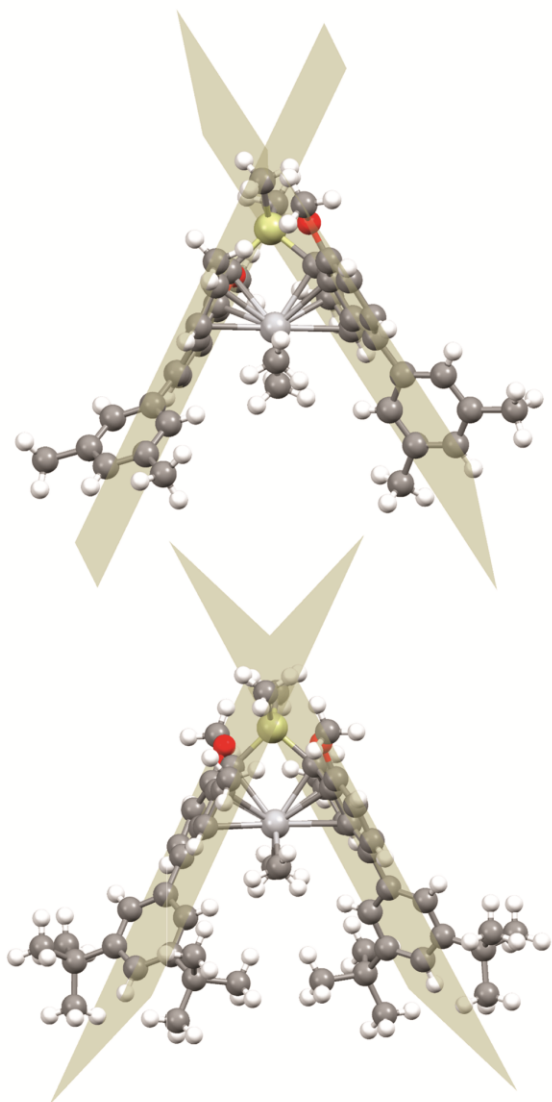


**Figure 1.** Molecular representations of **2a** (top) and **2b** (bottom) in the solid state. The effect of the adopted 4-aryl substituents on the coordination gap aperture is visualized by additional illustration of the Cp planes.

$g = 1.974$  ( $a_{\text{H}} = 14.3$  G,  $a_{\text{Al}} = 1.7$  G). The first sharper signal dominates at TIBA concentrations up to 200 equiv, whereas the latter signal progressively increases as the TIBA concentration rises further. Broadening of the latter signal derives from additional coupling with an Al nucleus ( $^{27}\text{Al}$ ,  $I = 5/2$ ) as indicated by the hyperfine structure. In accordance with assigned zirconocene/TIBA species described in previously reported EPR studies, the sharper signal at  $g = 1.971$  may be assigned to a reduced complex of type **1a**- $\text{Ti}^{3+}\text{-}^i\text{Bu}$  and the signal at  $g = 1.974$  to a binuclear complex of type **1a**- $\text{Ti}^{3+}(\mu\text{-Cl})(^i\text{Bu})\text{Al}(^i\text{Bu})_2$ .<sup>23</sup> Increased amounts of TIBA shift the equilibrium toward the formation of the binuclear complex ( $g = 1.974$ ). The same trend is observed for increased reaction times (Figure 3). Similar results regarding the reaction with

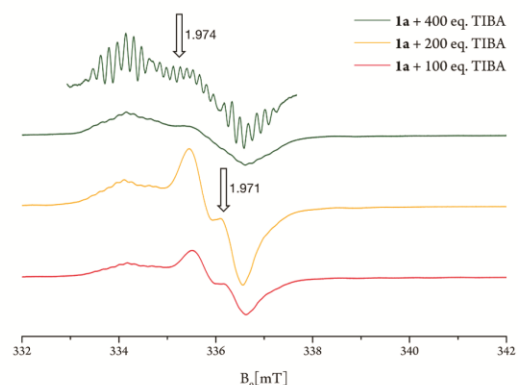


**Figure 2.** EPR spectra of **1a** in toluene ( $1 \times 10^{-4}$  M) with different amounts of TIBA 30 min after onset at 15 °C. The hyperfine structure of **1a** with 400 equiv of TIBA is depicted at the top.

TIBA are obtained with the related titanocene complex **1b** (Supporting Information).

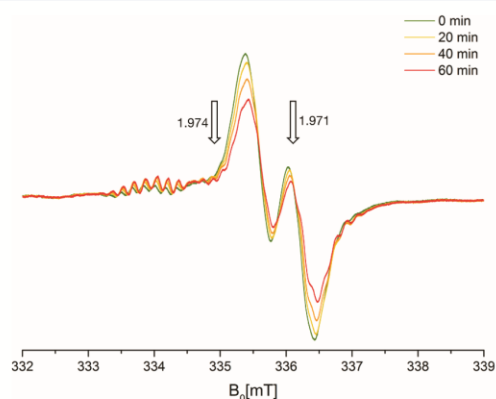


**Figure 3.** Time-dependent EPR spectra of **1a** in toluene ( $1 \times 10^{-4}$  M) with 200 equiv of TIBA at 15 °C.

In accordance with results in the literature<sup>14,23</sup> concerning the exposure of other metallocene complexes to TIBA, our sterically encumbered titanocenes **1** undergo complete conversion from  $\text{Ti}^{4+}$  to  $\text{Ti}^{3+}$  using the commonly applied conditions for the in situ alkylation (200 equiv of TIBA, 1 h). Although these results were not promising for the generation of a catalytically active  $\text{Ti}^{4+}$  complex, the reaction of both in situ alkylated titanocenes **1** with  $[\text{Ph}_3\text{C}][\text{B}(\text{C}_6\text{F}_5)_4]$  was monitored via EPR spectroscopy (Figure 4). The addition of 5.0 equiv of  $[\text{Ph}_3\text{C}][\text{B}(\text{C}_6\text{F}_5)_4]$  leads to the immediate formation of an additional signal at  $g = 1.994$  ( $a_{\text{p}} = 2.9$  G,  $a_{\text{m}} = 1.1$  G,  $a_{\text{o}} = 2.6$  G), which indicates the formation of trityl radicals.<sup>24</sup> In contrast to the common activation mechanism generating the cationic  $\text{M}^{4+}$  complex in combination with the noncoordinating  $\text{B}(\text{C}_6\text{F}_5)_4^-$  anion by formation of the  $^i\text{Bu-CPh}_3$  side product, the present trityl radicals suggest another reaction pathway. Since the original  $\text{Ti}^{3+}$  complex (mono- or bimetallic after the in situ alkylation with 200 equiv of TIBA) does not possess an alkyl substituent for the trityl cation to generate the conventional side product, we believe that single-electron transfer from titanium to the trityl cation takes place to build up the catalytically active  $\text{Ti}^{4+}$  complex releasing the detectable

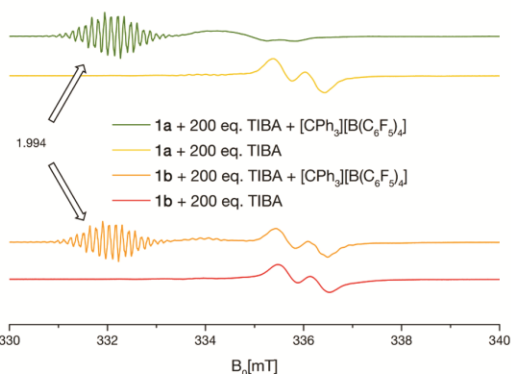


**Figure 4.** EPR spectra of **1a,b** in toluene ( $1 \times 10^{-4}$  M, in situ alkylated with 200 equiv of TIBA for 1 h) at 15 °C before and after addition of 5.0 equiv of  $[\text{Ph}_3\text{C}][\text{B}(\text{C}_6\text{F}_5)_4]$ . Spectra were recorded after the in situ alkylation was complete and 10 min after addition of the trityl borate salt.

trityl radicals as a side product. This postulated process is not only confirmed by the detection of trityl radicals via EPR spectroscopy but also by the unexpected catalytic activity observed when using the described activation method. In addition, especially for the activation of **1a**, a significant reduction in the  $\text{Ti}^{3+}$  EPR signals is observed after the addition of  $[\text{Ph}_3\text{C}][\text{B}(\text{C}_6\text{F}_5)_4]$ , which indicates oxidation of the respective metal center.

As well as the approved two-step activation process for isostructural zirconocene and hafnocene complexes, the conventional activation procedure with MAO is evaluated at this juncture. MMAO-12 (2000 equiv; equivalents referenced to Al content) is used in combination with the bis-chlorinated complex **1a** for the in situ generation of the catalytically active species **II**. Hereby, MAO combines the required functions of alkylation reagent, Lewis acid, and scavenging agent for possible catalyst poisoning impurities.

To facilitate unadulterated insight into the catalytic potential of these titanocene complexes in the catalytic conversion of olefins, the process of in situ alkylation was removed from the activation procedure using the alkylated complexes **2**. Conversion to the catalytically active systems **III** and **V** was conducted by the addition of 5.0 equiv of  $[\text{Ph}_3\text{C}][\text{B}(\text{C}_6\text{F}_5)_4]$  in the presence of different scavenging aluminum alkyls.

**Catalytic Performance.** All five catalyst systems **I–V** were examined in the solution polymerization of propene under identical conditions (Table 2 and Table S1 in the Supporting Information). Figure 5 depicts the productivities at different polymerization temperatures adjusted to the applied monomer concentration (1.88 M). The productivity decreases as the polymerization temperature increases, irrespective of the applied activation method. This observation is quite typical with respect to the temperature-dependent catalytic activity of titanocenes in the polymerization of olefins.<sup>12,14</sup> All conducted polymerizations were performed under conditions ensuring only negligible effect of mass transport limitation on the catalytic activity as a result of increased viscosity.<sup>20</sup> Consequently, the overall decrease in productivity caused by increased temperature must be derived from deactivation processes that lower the concentration of the catalytically active species. Most likely, reduction of the  $\text{Ti}^{4+}$  centers is involved in this regard.

**Table 2.** Conditions and Results for the Polymerization of Propene with **I–V** in Toluene<sup>a</sup>

entry	catalyst	$n^b$	$T_p^c$	$T_m^d$	$mmmm^e$	$M_n^f$	$\mathcal{D}^g$	$P^h$
1	I	2	-10	167		150	1.6	340
2	I	2	0	167		110	1.9	300
3	I	2	15	166		84	2.7	120
4	I	2	30	164		62	2.7	100
5	I	5	50	162	$\geq 99$	49	1.7	80
6	II	2	-10	165		160	1.5	120
7	II	2	0	165		120	1.7	74
8	II	2	15	164		98	1.5	48
9	II	2	30	162	$\geq 99$	82	1.6	42
10	II	2	50	160	98	45	1.8	16
11	III	2	-10	168		160	1.6	1400
12	III	2	0	166		130	1.7	1300
13	III	2	15	166		93	1.7	740
14	III	2	30	164		64	1.7	430
15	III	2	50	162	$\geq 99$	35	1.7	64
16	IV	2	-10	170		200	2.2	300
17	IV	2	0	169		190	1.8	270
18	IV	2	15	168		140	2.0	160
19	IV	2	30	166		130	1.7	160
20	IV	5	50	165	$\geq 99$	56	2.0	150
21	V	2	-10	170		190	2.0	3700
22	V	2	0	169		170	2.2	2200
23	V	2	15	169		150	1.7	1800
24	V	2	30	166		120	1.6	1100
25	V	2	50	165	$\geq 99$	60	1.5	330

<sup>a</sup>Selected examples (all polymerization experiments are given in Table S1 in the Supporting Information). Conditions: [propene], 1.88 M (estimated using Busico's equation),<sup>25</sup>  $t_p$ , 30 min;  $V_{\text{toluene}}$ , 300 mL; scavenger (TIBA), 2.2 mmol. <sup>b</sup>In  $\mu\text{mol}$ . <sup>c</sup> $T_p$  in °C  $\pm 1$  °C. <sup>d</sup>In °C. <sup>e</sup>Determined via  $^{13}\text{C}\{^1\text{H}\}$  NMR spectroscopy assuming the enantiomorphic site model. <sup>f</sup>In  $\text{kg mol}^{-1}$ . <sup>g</sup> $\mathcal{D} = M_w/M_n$ . <sup>h</sup> $P$  in  $\text{kg}_{\text{PP}}/[\text{mol}_M (\text{mol/L}) \text{h}]^{-1}$ .

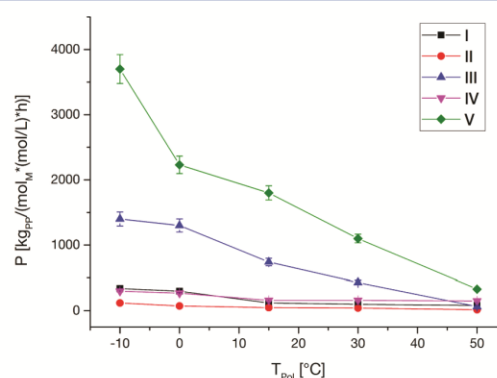


**Figure 5.** Productivity of **I–V** in the polymerization of propene at a constant monomer concentration and different polymerization temperatures (Table 2). Error bars are depicted according to possible deviations in the preparation process.

The lowest productivities at all applied polymerization temperatures are observed for the MAO-activated catalyst **II**. Higher values are obtained by adapting the two-step activation mechanism of in situ alkylation with TIBA and subsequent addition of  $[\text{Ph}_3\text{C}][\text{B}(\text{C}_6\text{F}_5)_4]$  to generate the catalytically active, cationic complexes **I** and **IV**. The most significant improvement in the catalytic activities is achieved using the

alkylated complexes **2** in combination with the cationizing agent  $[\text{Ph}_3\text{C}][\text{B}(\text{C}_6\text{F}_5)_4]$  (**III** and **V**). The largest productivities under all applied conditions are observed with the most sterically encumbered catalyst, **V**. To the best of our knowledge, the latter example represents the most productive titanocene system for the polymerization of propene to date, at least with respect to reasonable reaction times in the range of minutes to hours. At  $-10\text{ }^\circ\text{C}$ , the productivity of catalyst **V** ( $3700\text{ kg}_{\text{PP}}[\text{mol}_{\text{M}}(\text{mol}/\text{L})\text{h}]^{-1}$ ) even exceeds that of commonly activated ( $200\text{ equiv TIBA}/[\text{Ph}_3\text{C}][\text{B}(\text{C}_6\text{F}_5)_4]$ ) isostructural Zr ( $3400\text{ kg}_{\text{PP}}[\text{mol}_{\text{M}}(\text{mol}/\text{L})\text{h}]^{-1}$ ) and Hf ( $880\text{ kg}_{\text{PP}}[\text{mol}_{\text{M}}(\text{mol}/\text{L})\text{h}]^{-1}$ ) analogues. Furthermore, the results demonstrate that the generally applied in situ alkylation with TIBA or MAO is not sufficient when using these titanocenes in the polymerization of olefins. UV/vis experiments (Supporting Information) on the reaction with TIBA suggest that the desired substitution of both chlorides proceeds quite rapidly but is accompanied by the undesired reduction of the  $\text{Ti}^{4+}$  metal center. Although the activation with  $[\text{Ph}_3\text{C}][\text{B}(\text{C}_6\text{F}_5)_4]$  is in any case capable of generating a catalytically active species, most presumably by oxidation of the initially reduced complex, this activation pathway reveals only low to moderate productivities. The application of MAO is even less efficient. The in situ alkylation process with MAO may be sterically hindered by repulsion of the oligomeric MAO structure by the rigid complex framework of the highly substituted *ansa*-bis-indenyl ligand in this regard, but the interaction with trimethylaluminum (TMA) also needs to be considered. Reference experiments using catalyst **III** with TMA as scavenging agent reveal only negligible productivities even at low polymerization temperatures (Table S1, entry S25, in the Supporting Information). The tendency to form binuclear complexes is an important consideration regarding the catalytic activity of metallocenes in the presence of aluminum alkyls. It is suggested in our present studies that the equilibrium of the cationic complex and TMA is significantly shifted to the binuclear species, thereby forming a poorly active/inactive resting state potentially comparable to that observed with hafnocenes.<sup>26–31</sup> Consequently, activation using commercially available MAO, which always contains substantial amounts of TMA, results in low productivities. Furthermore, the application of modified MAO (e.g., MMAO-12) is known to cause increased reduction of the metal center.<sup>23</sup> Improvement of our MAO-activated titanocene catalysts may be feasible by trapping free TMA via addition of sterically demanding phenols.<sup>27,32</sup> Nevertheless, we believe that the exceptional catalytic potential offered by our prealkylated titanocene complexes is a considerable alternative regarding the straightforward alkylation reaction with  $\text{MeMgBr}$ , although MAO activation still dominates processes of industrial relevance.

The effect on the productivity of **III** using different TIBA (scavenger) concentrations at different polymerization temperatures with identical monomer concentrations is depicted in Figure 6. The generally applied amount of scavenging agent is indicated by triangles, and the results using smaller amounts of TIBA are depicted by circles (50%) and squares (25%). This illustrates that at  $0\text{ }^\circ\text{C}$  higher productivities are observed using larger amounts of scavenger. Increasing the polymerization temperature to  $30\text{ }^\circ\text{C}$  leads to negligible effect of the different TIBA concentrations, while at  $50\text{ }^\circ\text{C}$ , lower scavenger concentrations account for higher catalytic activities. These results are in line with the assumption that the catalytically active titanocene complex is progressively prone to reduction at

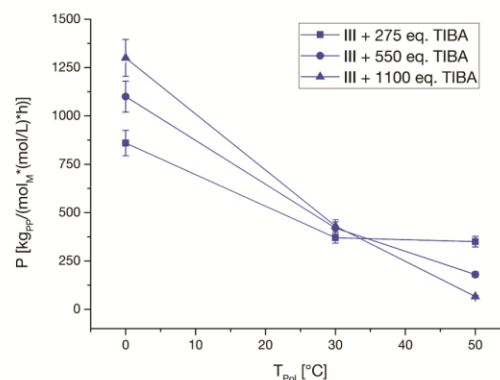


**Figure 6.** Productivities of **III** at a constant monomer concentration with different amounts of scavenger/TIBA (Table S1, entries S22–S24 and S29–S34, in the Supporting Information). Error bars are depicted according to possible deviations in the preparation process.

higher temperatures. While the desired scavenging effect is observed with an increased amount of TIBA at low temperatures, higher amounts of potential reducing agent lead to lower catalytic activities at elevated temperatures. Regarding the observed role of TMA, as well as different amounts of TIBA at different polymerization temperatures, the application of the right scavenging agent in combination with the appropriate amount under each adjusted condition is essential. Since TMA leads to very low catalytic activities due to a presumed strong interaction with the cationic complex, and TIBA reveals limited suitability due to its reduction potential, the ideal scavenger for this type of titanocene catalyst remains a matter for further investigation. Affordable costs combined with low or, most preferably, no interaction with the catalytically active cationic species, thus preserving long-term stability of the latter in the reaction medium, are the ultimate targets in this context.

Although Figure 5 shows exceptional productivities for catalysts **III** and **V** at low polymerization temperatures, the significant decrease in the observed catalytic activities at elevated temperatures raises the general question of the overall catalyst stability. Therefore, the time-dependent catalytic behavior became a matter for investigation. Figure 7 provides

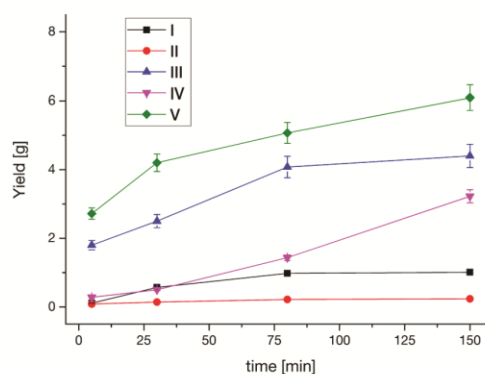


**Figure 7.** Total yields on application of **I–V** at  $0\text{ }^\circ\text{C}$  under identical conditions with different reaction times (Table S1, entries S2–S5, S13–S16, S21, S22, S26, S27, S36–S39, and S47–S50, in the Supporting Information). Error bars are depicted according to possible deviations in the preparation process.

the yields of polypropylene for different reaction times from 5 to 150 min at 0 °C under otherwise identical conditions. In accordance with the observed productivities at different temperatures, the highest yields for each polymerization time are observed for the activation of the methylated complexes **2** with  $[\text{Ph}_3\text{C}][\text{B}(\text{C}_6\text{F}_5)_4]$ , thereby avoiding the in situ alkylation step. Regarding catalytic systems **III** and **V**, increased steric encumbrance always accounts for higher yields, leading to the most promising results with **V**. Nevertheless, for both catalyst systems, the relationship between the yield and the polymerization time deviates considerably from theoretical linear behavior, which is a generally observed phenomenon of metallocene catalysts in the polymerization of olefins.<sup>7,13</sup> This may be due to polymer precipitation removing active catalyst from the solution, which additionally leads to enhanced mass transport limitation arising as a result of increased viscosity of the reaction mixture. Further explanations are the possible formation of resting states as well as catalyst deactivation. However, the extrapolated productivities at 5 min of catalysts **III** (5800 kg<sub>PP</sub> [mol<sub>M</sub> (mol/L) h]<sup>-1</sup>) and **V** (8500 kg<sub>PP</sub> [mol<sub>M</sub> (mol/L) h]<sup>-1</sup>) underline the high potential of these titanocene complexes in the polymerization of propene. Overall low yields in combination with a poor long-term stability of the catalyst systems were observed with **I** and **II**, which underlines the unsuitable application of MAO. Quite unexpected results were obtained using the more sterically demanding complex **1b** in combination with the two-step activation mechanism to **IV**, since this catalyst revealed even higher yields at longer polymerization times than the theoretical yields that followed a linear correlation. This may derive from a slower activation of the <sup>t</sup>Bu-alkylated complex with  $[\text{Ph}_3\text{C}][\text{B}(\text{C}_6\text{F}_5)_4]$  to the catalytically active cationic complex in comparison to the activation of catalysts **III** and **V**, necessitating longer reaction times in this case to increase the concentration of active catalyst. In addition, the catalytically active species of the sterically more encumbered <sup>t</sup>Bu-substituted complex is stable at higher temperatures and exhibits an increased long-term stability; thus, this exceeds the catalytic performance of **IV** in comparison to **I** and **III** at longer reaction times.

Figure 8 displays the effect of different monomer concentrations on the catalytic activity using the identically activated catalysts **I** and **IV** at 50 °C. Regarding theoretical

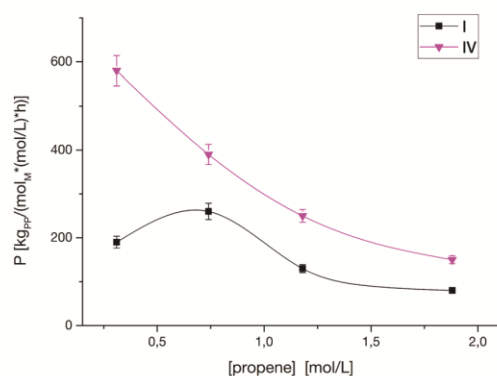


**Figure 8.** Productivities of **I** and **IV** at 50 °C using different monomer concentrations under otherwise identical conditions (Table S1, entries S8–S11 and S42–S45, in the Supporting Information). Error bars are depicted according to possible deviations in the preparation process.

relations in the process of chain propagation, the propagation rate has a first-order dependence on the mole fraction of the catalytically active catalyst as well as the monomer concentration.<sup>20,35</sup> In contrast, higher monomer concentrations are known to accelerate reductive catalyst deactivation.<sup>14</sup> The sterically more encumbered catalyst system **IV** reveals consistent behavior in the applied concentration range and shows higher productivities at lower monomer concentrations. The trend for catalyst **I** is comparable at high to moderate monomer concentrations, but a significant decrease in the productivity is observed when switching to the lowest applied concentration. It becomes obvious that the catalytic performance of both systems is generally dominated by the process of reductive catalyst deactivation in the presence of substantial monomer concentrations. If the propene concentration is severely reduced below a certain limit, its effect on the propagation rate determines the productivity. This particular concentration seems to be higher for catalyst **I**, whereas that for **IV** is assumed to be in the range of even lower monomer concentrations than the applied range. Taking into account the productivities of these ligand structures in related hafnocene systems, decreased steric encumbrance of the complex framework is responsible for higher catalytic activities at the applied temperature of 50 °C, which is due to a faster propagation rate.<sup>20</sup> In contrast, an increased stability of the catalytically active species was observed where there was higher steric demand at the 4-aryl substituent for the respective titanocenes. Consequently, with respect to identical monomer concentrations, smaller amounts of catalytically active catalyst with a theoretically higher catalytic reaction rate are assumed for **I**, whereas the application of catalyst **IV** provides higher concentrations of catalytically active catalyst in combination with a theoretically lower rate constant. Since extremely low monomer concentrations were used, we may enter a range in which diffusion limitations dominate the observable productivities (Figure 8, I: [propene] < 0.75 M). This range may be shifted to higher monomer concentrations for catalyst **I** due to a lower concentration of catalytically active complex leading to a significantly lower collision rate in comparison to that with **IV** under identical conditions.

Although catalysts **III** and **V** reveal remarkable catalytic performances especially at low polymerization temperatures, the susceptibility toward reduction in the presence of scavengers such as TIBA and increased monomer concentrations still remain the major drawbacks of titanocenes in the polymerization of olefins. The crucial effect of temperature and polymerization time reveal critical issues in this regard. However, investigation of the applied two-step activation by in situ alkylation with TIBA and the addition of  $[\text{Ph}_3\text{C}][\text{B}(\text{C}_6\text{F}_5)_4]$  to **I** and **IV** disclosed the opportunity to convert the reduced  $\text{Ti}^{3+}$  complex to the catalytically active cationic  $\text{Ti}^{4+}$  complex by addition of  $[\text{Ph}_3\text{C}][\text{B}(\text{C}_6\text{F}_5)_4]$ . These findings offer the opportunity to apply  $[\text{Ph}_3\text{C}][\text{B}(\text{C}_6\text{F}_5)_4]$  as a regeneration agent for reduced titanocenes in the polymerization of olefins in order to reactivate the deactivated catalyst. Therefore, the effect of increased amounts of  $[\text{Ph}_3\text{C}][\text{B}(\text{C}_6\text{F}_5)_4]$  (20 equiv) was tested as an alternative to the generally applied 5 equiv, and also a pulsed addition ( $3 \times 5$  equiv) in steps of 10 min with a total reaction time of 30 min was evaluated using **III** in the polymerization of propene at 0 °C under otherwise identical conditions. However, there appeared to be no benefit from the additional  $[\text{Ph}_3\text{C}][\text{B}(\text{C}_6\text{F}_5)_4]$  on the overall productivity in either case. Although possible side reactions of TIBA and

$[\text{Ph}_3\text{C}][\text{B}(\text{C}_6\text{F}_5)_4]$  are known to accelerate the formation of poorly active catalyst species, these results raise the fundamental question of catalyst deactivation using titanocenes in the polymerization of olefins.<sup>34</sup> It seems that the main deactivation pathway/product significantly differs from that featuring the in situ alkylation of the bis-halogenated titanocene with TIBA. The possible formation of dormant species by interaction with the aluminum alkyl or other titanocene complexes ( $\text{Ti}^{3+}$  and/or  $\text{Ti}^{4+}$ ) should not be neglected at this juncture. Increased deactivation of the catalytically active catalyst in the presence of higher monomer concentrations is one of the most crucial aspects in this regard. Elucidation of the deactivation pathways and products remains essential in determining the suitability of titanocene complexes in the polymerization of olefins.

**Polymer Properties.** The average molecular weights of all polymers produced with catalysts I–V, which are given in Table 2, were determined via GPC analysis; this indicated a uniform molecular weight distribution for all of the applied catalysts and conditions. A general decrease in the molecular weights is observed as the temperature is increased, which is a common observation in the homogeneous polymerization of olefins (Figure 9).<sup>7</sup> In addition, the average chain lengths are

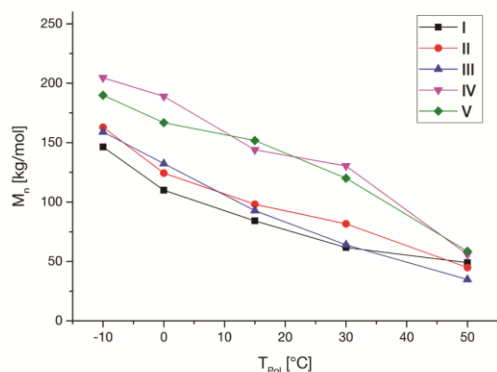


**Figure 9.** Average molecular weights of polypropylene produced with I–V at a constant monomer concentration and different polymerization temperatures (Table 2).

obviously more dependent on differences in the ligand structures than on the applied activation mechanisms. Similar trends are observed for catalysts I–III and IV and V, in which the latter catalyze polymers with longer average chain lengths at all applied temperatures. These observations are all in line with those of related hafnocene complexes, although the molecular weights are roughly 1 order of magnitude lower with the Ti-based catalyst systems.<sup>20</sup>

Since the average molecular weight is defined by the rate ratio of chain propagation and chain release reactions, the olefinic end-group composition is disclosed for low-molecular-weight polypropylene samples using catalysts I and IV (Figure 10). Both complexes exhibit an extraordinarily high selectivity toward vinylidene chain ends (Figure 10, orange), indicating chain release via  $\beta$ -hydride elimination. For both complexes, allylic chain ends (Figure 10, lime green) resulting from  $\beta$ -methyl elimination are detectable. Using the sterically more encumbered catalyst IV, small amounts of internal end groups (Figure 10, dark purple) are found caused by isomerization reactions.<sup>35,36</sup> Although small differences in the end-group

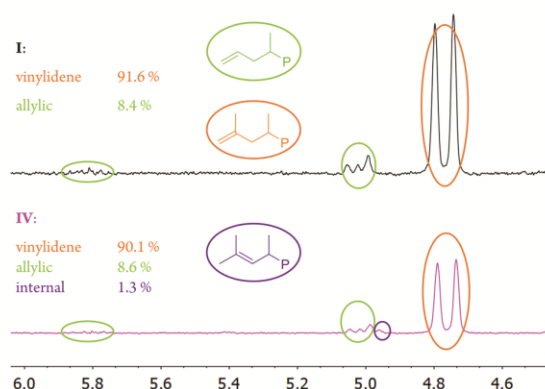


**Figure 10.** Determination of olefinic end-group composition via  $^1\text{H}$  NMR spectroscopy (300 MHz, 140 °C,  $\text{C}_6\text{D}_6\text{Br}$ ) of polypropylene (Table S1, entries S8 and S42, in the Supporting Information) produced with I and IV.

selectivity of both complexes are observable, the dominating reaction pathway determining the molecular weights is considered to be the process of  $\beta$ -hydride elimination. This is in contrast to the results of isostructural hafnocene complexes revealing a much higher selectivity toward allylic chain ends. In addition, accelerated chain release via  $\beta$ -methyl elimination was observed in the case of higher polymerization temperatures as well as decreased steric demand of the 4-aryl substituent for the respective hafnocenes.<sup>20</sup>

In addition to the effect of the polymerization temperature, the monomer concentration has a substantial influence on the average molecular weights (Table S1, entries S8–S11 and S42–S45, in the Supporting Information). The polypropylenes produced with I and IV at 50 °C and different monomer concentrations depict a consistent decline in the average chain lengths as the monomer concentration decreases.<sup>18,20</sup> In analogy to the results of the temperature-dependent behavior (Figure 9), increased steric demand of the 4-aryl substituent leads to higher molecular weights under all applied conditions.

In previous studies on isostructural hafnocene complexes, the rigid ligand framework appeared to be crucial for precise regio- and stereoselective behavior over a broad temperature range.<sup>20</sup> The stereoselectivity of all five titanocene-based catalyst systems I–V is determined to be very accurate from 0 to 50 °C at a constant monomer concentration following the mechanism of enantiomorphic site control (Table 2).<sup>37–40</sup> Tacticity determination is carried out by calculating the ratio of *mmmm*-pentad to the sum of all the pentads. Consequently, the *mmmm*-pentad is exclusively detected using standard  $^{13}\text{C}\{^1\text{H}\}$  NMR spectroscopy (see the Experimental Section) and indicates at least 99% *mmmm*. The only exception was found to be the MAO-activated complex II, which produced polypropylene that slightly differed from perfect isotacticity at 50 °C. Additionally, the impact of the monomer concentration on the stereoselectivity of the produced polypropylenes was a matter for investigation with catalysts I and IV (Figure 11). Although a significant decrease in the overall tacticity is observed in both cases at lower monomer concentrations, the sterically more encumbered complex better preserves the formation of isotactic sequences. Since the polymerization results indicate that the enantiofacial selectivity is still accurate for both complex frameworks at 50 °C at sufficient monomer concentrations, the loss in selectivity originates in stereoerror

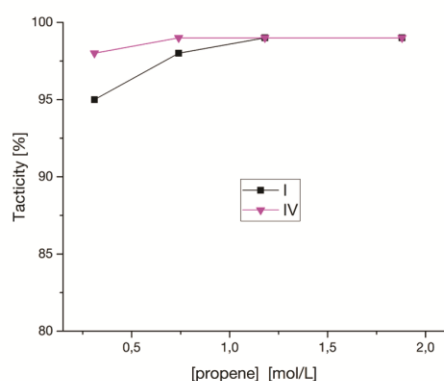


**Figure 11.** Tacticities (% *mmmm*) of polypropylenes produced with I and IV at 50 °C and different monomer concentrations determined with  $^{13}\text{C}\{^1\text{H}\}$  NMR spectroscopy (300 MHz, 140 °C,  $\text{C}_6\text{D}_6\text{Br}$ ; Table S1, entries S8–S11 and S42–S45, in the Supporting Information).

formation via chain-end epimerization. This cascade reaction is known to be particularly favored in the presence of low monomer concentrations.<sup>41–45</sup> Similar to the results for isostructural hafnocene complexes, the process of chain-end epimerization is more successfully prevented in the case of increased steric demand of the 4-aryl substituent.<sup>20</sup>

The applied rigid ligand framework has been shown to polymerize propylene with extraordinarily low amounts of regiodeflects.<sup>18,20</sup> The results on potential regioerror formation using isostructural titanocenes are in line with reported values. No 2,1-erythro or 3,1-isomerization regiodeflects are detected with any of the investigated catalysts I–V under all applied conditions using standard  $^{13}\text{C}$  NMR spectroscopy (see the Experimental Section).

The melting points of the produced polymers are predominantly determined by the stereo- and regioselectivity of the respective polypropylenes. Regarding very short average chain lengths, the molecular weight has a significant effect on the melting transitions as well.<sup>46</sup> All polypropylenes produced with I–V at 0–50 °C at constant monomer concentration (Figure 12) show high melting transitions above 160 °C. However, the lowest values are observed with the MAO-activated complex II. Since similar molecular weights and accurate regioselectivities were found for the polymers of the

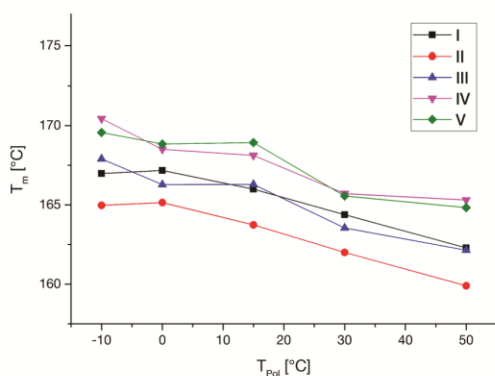


**Figure 12.** Melting transitions of polypropylene samples produced with I–V at a constant monomer concentration and different polymerization temperatures (Table 2).

applied titanocene catalysts, the lower melting points are correlated to differences in the stereoselectivities. This assumption is in line with the determined tacticities, since the generated MAO anion coordinated to the catalytically active cationic complex apparently causes a reduction in the stereoselectivity in comparison to the  $\text{B}(\text{C}_6\text{F}_5)_4^-$  anion.<sup>47</sup> No significant effect of the applied activation method was observed on comparison of the classic two-step activation of I and the activation of 2 with  $[\text{Ph}_3\text{C}][\text{B}(\text{C}_6\text{F}_5)_4]$ . Nevertheless, the two different ligand frameworks explicitly determine the melting points of the respective polypropylenes. Similar results are found regarding the effect of the 4-aryl substituents on the melting transitions of the polymers at different monomer concentrations. A comparative study of I and IV at 50 °C and different monomer concentrations revealed that the polypropylenes produced with the increased sterically encumbered ligand framework had higher melting points in all cases (Table S1, entries S8–S11 and S42–S45, in the Supporting Information). When low polymerization temperatures are applied, the latter complex demonstrates its capability to synthesize polypropylene with extraordinarily high melting transitions, which are among the highest reported values for untreated PP to date.<sup>18</sup>

## CONCLUSION

On the basis of an ultrarigid, highly regulative, silyl-bridged  $\text{C}_2$ -symmetric 2-methyl-4-aryl-7-methoxy-substituted bis-indenyl *ansa*-metallocene framework, the suitability of titanium in the polymerization of propene has been the subject of this report. The catalytic potentials using different activation mechanisms and the respective polymer properties were investigated with two novel titanocene complexes with different steric demands of the 4-aryl substituent (a, 4-(3',5'-dimethyl)phenyl; b, 4-(3',5'-di-*tert*-butyl)phenyl). Bis-chlorinated as well as bis-methylated titanocene complexes with both ligand frameworks were completely characterized, including by X-ray diffraction analysis. In the polymerization of propene, extremely low productivities were observed when conventional M-MAO was applied for the in situ activation of the bis-chlorinated complexes. Reference experiments underlined the unsuitability of TMA in combination with these titanium-based complexes. Alternatively, the established two-step activation mechanism for related zirconocene and hafnocene complexes was investigated. The in situ alkylation with excess TIBA (200 equiv) was monitored via EPR spectroscopy and showed complete reduction from  $\text{Ti}^{4+}$  to  $\text{Ti}^{3+}$  as well as the desired exchange of the chloride substituents. The subsequent addition of  $[\text{Ph}_3\text{C}][\text{B}(\text{C}_6\text{F}_5)_4]$  to the reduced titanocenes resulted in the immediate formation of trityl radicals. Since reduction of the trityl cation was observed, the consequential reoxidation from  $\text{Ti}^{3+}$  to  $\text{Ti}^{4+}$  is postulated. The catalytic capability of this activation method in combination with our titanocene complexes corroborates our estimated mechanism, since  $\text{Ti}^{3+}$  complexes are generally stated to be catalytically inactive in the polymerization of olefins. Nevertheless, the most promising results in terms of catalytic activity were observed when the in situ alkylation step was eliminated on application of bis-methylated titanocene complexes. Activation was conducted using  $[\text{Ph}_3\text{C}][\text{B}(\text{C}_6\text{F}_5)_4]$  in the presence of scavenging aluminum alkyls. The latter activation method in combination with the sterically more encumbered complex framework (catalyst V) resulted in the most productive titanocene catalyst system for the polymerization of propene to date, at least with

respect to reasonable reaction times. All catalyst systems were extensively screened in terms of productivity, considering the effect of polymerization temperature, monomer concentration, and reaction time. In all cases the most promising results were obtained with the bis-alkylated titanocenes in combination with  $[\text{Ph}_3\text{C}][\text{B}(\text{C}_6\text{F}_5)_4]$ . Moderate productivities were observed with the two-step activation mechanism of the bis-chlorinated titanocenes with TIBA/ $[\text{Ph}_3\text{C}][\text{B}(\text{C}_6\text{F}_5)_4]$  and the lowest values were those with MAO. In addition, application of the sterically more encumbered complex framework accounts for higher catalytic activities, which is most presumably due to the increased long-term stability of the catalyst system. Investigation of the most promising activation mechanism in combination with different scavenging agents and amounts demonstrated the intricacy of finding a scavenger that demonstrated low or most preferably no interaction with the catalytically active species. Determination of the molecular weights disclosed a negligible effect of the applied activation method on the resulting average chain length. However, the steric demand of the 4-aryl substituent in the ligand structures of the respective titanocenes has a significant effect. Although catalyst **V** is capable of producing high-molecular-weight polypropylenes (up to  $M_n \approx 200$  kg/mol), the values are roughly about 1 order of magnitude lower in comparison to those produced using isostructural hafnocenes. Olefinic end-group analysis via  $^1\text{H}$  NMR spectroscopy displayed an extraordinarily high selectivity toward chain release via  $\beta$ -H elimination (>90%), which was almost independent of the ligand framework of the applied titanocenes. Precise regio- and stereoselective behavior was observed for all the applied catalyst systems. With respect to low monomer concentrations, the overall tacticity is reduced due to accelerated stereoregulation formation via chain-end epimerization. Under these conditions, the more sterically encumbered ligand framework better preserves the exclusive formation of *mmmm*-pentads. In line with the accurate stereo- and regioselective behavior, high melting transitions ( $T_m > 160$  °C) of the polypropylenes are obtained with all of the applied catalysts. However, significant differences are observed using different ligand structures. At low polymerization temperatures, catalyst **V** is capable of synthesizing polypropylene with melting transitions of up to 170 °C, which are among the highest reported values for untreated  $^1\text{P}$  (ex reactor) to date.

In addition to the remarkable polymer properties, the present study demonstrates a convenient activation pathway for titanocenes to form highly active catalyst systems. Although the desired inhibition of deactivation processes was not fulfilled, especially considering elevated polymerization temperatures, this report claims significant advances regarding the application of titanocenes in the polymerization of olefins. Concerning the outstanding melting behavior, even regarding short average chain lengths, in combination with unsaturated end-group functionalization, these polymers unify essential properties with respect to their possible application as attractive macromonomers.

## ■ EXPERIMENTAL SECTION

**General Considerations.** All reactions involving air- and moisture-sensitive compounds were performed under an argon atmosphere using standard Schlenk or glovebox techniques. All chemicals, unless otherwise stated, were purchased from Aldrich, Acros, or VWR and used as received. Dry toluene, dichloromethane, *n*-pentane, and *n*-hexane were obtained from an MBraun MB-SPS-800

solvent purification system. Deuterated dichloromethane was refluxed over  $\text{CaH}_2$  and distilled prior to use. Propene (99.5% by Westfalen AG) was purified by passage through two columns filled with BASF catalyst (R3-11) and molecular sieves 3–4 Å. Elemental analysis was conducted with a EURO EA (HEKA tech) instrument equipped with a CHNS combustion analyzer.

NMR ( $^1\text{H}$  and  $^{13}\text{C}$   $\{^1\text{H}\}$ ) measurements were recorded on a Bruker AV400 spectrometer at ambient temperature. Chemical shifts  $\delta$  were reported in ppm relative to tetramethylsilane and calibrated to the residual  $^1\text{H}$  or  $^{13}\text{C}$  signal of the deuterated solvent. Polymer spectra were measured with an ARX-300 spectrometer at 140 °C in 50–60 mg/mL bromobenzene- $d_5$ .

EPR spectra were recorded using a JEOL JES-RE 2X spectrometer at X-band frequency at 15 °C. The spectra were measured at a microwave frequency of approximately 9.26 GHz with a microwave power of 5 mW, a modulation amplitude of 0.4 (0.04) mT, a sweep time of 4 min, a sweep width of 10–15 mT, a time constant of 0.1 s, and a modulation frequency of 100 kHz. The microwave frequency was measured with an Advantest R5372 microwave frequency counter. The temperature was monitored with a JEOL ES DVT2 temperature controller equipped with a calibrated thermocouple. The values of *g* and *A* were determined by using  $\text{Mn}^{2+}$  (nuclear spin  $I = 5/2$ ) embedded in MgO as a standard (the fourth low field line has *g* = 1.981).

Gel permeation chromatography (GPC) was performed with a PL-GPC 220 instrument equipped with 2× Olexis 300 × 7.5 mm columns and triple detection via a differential refractive index detector, a PL-BV 400 HT viscometer, and light scattering (Precision Detectors Model 2040; 15, 90°). Measurements were performed at 160 °C using 1,2,4-trichlorobenzene (TCB; 30 mg BHT/L) with a constant flow rate of 1 mL/min and a calibration set with narrow-MWD polystyrene (PS) and polyethylene (PE) standards. Samples were prepared by dissolving 0.9–1.1 mg of the polymer in 1.0 mL of stabilized TCB for 10–15 min at 160 °C immediately before each measurement.

Differential scanning calorimetry (DSC) was conducted on a DSC Q2000 instrument. Between 3 and 8 mg of the polymer was sealed into a DSC aluminum pan and heated from 20 to 200 °C at a rate of 10 °C/min. After the temperature was held for 2 min, the sample was cooled to 20 °C at a rate of 10 °C/min and heated again in the same manner. The reported values are those determined during the second heating cycle.

**Synthesis.** All compounds that are not listed below were synthesized according to literature procedures.<sup>18,20</sup> All syntheses/handling of titanocene compounds were performed with exclusion of light.

*rac*-Dimethylsilanediybis[4-(3',5'-dimethylphenyl)-7-methoxy-2-methylindenyl]titanium Dichloride (**1a**). A 1.00 g portion (1.71 mmol, 1.00 equiv) of bis[4-(3',5'-dimethylphenyl)-7-methoxy-2-methylindenyl]dimethylsilane was dissolved in 60 mL of dry toluene and cooled to –78 °C, and 2.02 mL (3.42 mmol, 2.00 equiv) of 1.7 M  $^t\text{BuLi}$  solution in pentane was added dropwise. After the temperature was maintained for 1 h, the reaction mixture was stirred for an additional 3 h at room temperature. The yellow suspension was cooled to –78 °C, and 571 mg (1.71 mmol, 1.00 equiv) of  $\text{TiCl}_4(\text{thf})_2$  was added. The reaction mixture was allowed to thaw overnight, resulting in a dark green-brown suspension (*rac/meso*  $\approx$  5/1). After filtration, the solvent of the filtrate was distilled off and the residue was washed with dry pentane (2 × 40 mL). The residue was dissolved in 30 mL of dry dichloromethane followed by the addition of 30 mL of dry *n*-hexane. The mixture was concentrated to 10 mL at 0 °C in vacuo, and 400 mg (33%) of a dark brownish green powder containing the pure *rac* isomer was obtained after filtration. Anal. Calcd for  $\text{C}_{40}\text{H}_{44}\text{Cl}_2\text{O}_2\text{SiTi}$ : C, 68.48; H, 6.03. Found: C, 68.40; H, 6.03.  $^1\text{H}$  NMR (500 MHz,  $\text{CD}_2\text{Cl}_2$ , 298 K):  $\delta$  (ppm) 7.42 (d,  $^3J = 7.8$  Hz, 2H, H-Ar), 7.32 (s, 4H, H-Ar'), 7.18 (s, 2H, –CH=), 6.96 (s, 2H, H-Ar'), 6.43 (d,  $^3J = 7.8$  Hz, 2H, H-Ar), 3.88 (s, 6H, –OCH<sub>3</sub>), 2.31 (s, 12H, Ar'-CH<sub>3</sub>), 2.00 (s, 6H, –CH<sub>3</sub>), 1.23 (s, 6H, Si-CH<sub>3</sub>).  $^{13}\text{C}$   $\{^1\text{H}\}$  NMR (126 MHz,  $\text{CD}_2\text{Cl}_2$ ):  $\delta$  (ppm) 156.3, 139.8, 138.5, 137.3, 133.9, 131.6, 130.0, 129.2, 127.0, 123.8, 104.6, 83.5, 21.6, 19.0, 5.8.

*rac*-Dimethylsilanediylbis[4-(3',5'-di-*tert*-butylphenyl)-7-methoxy-2-methylindenyl]titanium Dichloride (**1b**). A 2.00 g portion (2.66 mmol, 1.00 equiv) of bis[4-(3',5'-di-*tert*-butylphenyl)-7-methoxy-2-methylindenyl]dimethylsilane was dissolved in 120 mL of dry toluene and cooled to  $-78\text{ }^{\circ}\text{C}$ , and 3.12 mL (5.31 mmol, 2.00 equiv) of a 1.7 M  $\text{tBuLi}$  solution in pentane was added dropwise. After the temperature was maintained for 1 h, the reaction mixture was stirred for an additional 3 h at room temperature. The yellow suspension was cooled to  $-78\text{ }^{\circ}\text{C}$ , and 887 mg (2.66 mmol, 1.00 equiv) of  $\text{TiCl}_4(\text{thf})_2$  was added. The reaction mixture was allowed to thaw overnight, resulting in a dark green-brown suspension (*rac/meso*  $\approx 2/1$ ). After filtration, the solvent of the filtrate was distilled off and the residue was washed with dry pentane (80 mL). The residue was dissolved in 35 mL of dry dichloromethane followed by the addition of 35 mL of dry *n*-hexane. The mixture was concentrated to about 15–20 mL at  $0\text{ }^{\circ}\text{C}$  in vacuo, and the residual solution was filtered off. This recrystallization procedure was repeated four times, resulting in 390 mg (17%) of dark brownish green powder containing the pure *rac* isomer. Anal. Calcd for  $\text{C}_{52}\text{H}_{66}\text{Cl}_2\text{O}_2\text{SiTi}$ : C, 71.79; H, 7.65. Found: C, 72.08; H, 7.73.  $^1\text{H}$  NMR (400 MHz,  $\text{CD}_2\text{Cl}_2$ , 298 K):  $\delta$  (ppm) 7.59 (d,  $^4J = 1.8\text{ Hz}$ , 4H, H-Ar'), 7.49 (d,  $^3J = 7.8\text{ Hz}$ , 2H, H-Ar), 7.37 (t,  $^4J = 1.8\text{ Hz}$ , 2H, H-Ar'), 7.19 (s, 2H,  $-\text{CH}=\text{}$ ), 6.46 (d,  $^3J = 7.8\text{ Hz}$ , 2H, H-Ar), 3.89 (s, 6H,  $-\text{OCH}_3$ ), 2.02 (s, 6H,  $-\text{CH}_3$ ), 1.31 (s, 36H, 'Bu-Ar'), 1.24 (s, 6H, Si- $\text{CH}_3$ ).  $^{13}\text{C}\{^1\text{H}\}$  NMR (100 MHz,  $\text{CD}_2\text{Cl}_2$ , 298 K):  $\delta$  (ppm) 156.4, 151.7, 139.1, 138.9, 137.4, 134.0, 132.2, 130.2, 124.1, 124.0, 121.3, 104.7, 83.7, 35.6, 31.9, 19.0, 5.9.

*rac*-Dimethylsilanediylbis[4-(3',5'-dimethylphenyl)-7-methoxy-2-methylindenyl]dimethyltitanium (**2a**). A 100 mg portion (143  $\mu\text{mol}$ , 1.00 equiv) of **1a** was dissolved in 20 mL of dry benzene, and 97.4  $\mu\text{L}$  (292  $\mu\text{mol}$ , 2.05 equiv) of 3.0 M MeMgBr solution in diethyl ether was added. After the dark red reaction mixture was stirred for 15 min, the filtrate was isolated, and the solvent was removed in vacuo. After recrystallization in a dry toluene/*n*-pentane mixture, 72.0 mg (76%) of dark red crystalline solid **2a** was isolated. Anal. Calcd for  $\text{C}_{42}\text{H}_{48}\text{O}_2\text{SiTi}$ : C, 76.34; H, 7.32. Found: C, 76.41; H, 7.24.  $^1\text{H}$  NMR (400 MHz,  $\text{CD}_2\text{Cl}_2$ , 298 K):  $\delta$  (ppm) 7.43 (s, 2H,  $-\text{CH}=\text{}$ ), 7.31 (d,  $^3J = 7.8\text{ Hz}$ , 2H, H-Ar), 7.29 (s, 4H, H-Ar'), 6.97 (s, 2H, H-Ar'), 6.33 (d,  $^3J = 7.8\text{ Hz}$ , 2H, H-Ar), 3.78 (s, 6H,  $-\text{OCH}_3$ ), 2.33 (s, 12H, Ar'- $\text{CH}_3$ ), 1.76 (s, 6H,  $-\text{CH}_3$ ), 0.93 (s, 6H, Si- $\text{CH}_3$ ),  $-0.83$  (s, 6H, Ti- $\text{CH}_3$ ).  $^{13}\text{C}\{^1\text{H}\}$  NMR (100 MHz,  $\text{CD}_2\text{Cl}_2$ ):  $\delta$  (ppm) 156.6, 141.3, 138.5, 135.1, 133.9, 131.1, 128.9, 127.0, 126.9, 124.0, 122.0, 102.0, 81.9, 50.6, 21.7, 17.7, 5.8.

*rac*-Dimethylsilanediylbis[4-(3',5'-di-*tert*-butylphenyl)-7-methoxy-2-methylindenyl]dimethyltitanium (**2b**). A 150 mg portion (172  $\mu\text{mol}$ , 1.00 equiv) of **1b** was dissolved in 10 mL of dry toluene, and 126  $\mu\text{L}$  (379  $\mu\text{mol}$ , 2.20 equiv) of 3.0 M MeMgBr solution in diethyl ether was added. After the dark red reaction mixture was stirred for 30 min, the filtrate was isolated, and the solvent was removed in vacuo. After recrystallization in a dry toluene/*n*-pentane mixture at  $6\text{ }^{\circ}\text{C}$ , 60.0 mg (42%) of dark red crystalline solid **2b** was isolated. Anal. Calcd for  $\text{C}_{54}\text{H}_{72}\text{O}_2\text{SiTi}$ : C, 78.23; H, 8.75. Found: C, 76.77; H, 8.78 (elemental analysis suggested traces of inorganic salts ( $\leq 2\text{ wt } \%$ ) that appeared to be irremovable by repeated recrystallization).  $^1\text{H}$  NMR (400 MHz,  $\text{CD}_2\text{Cl}_2$ , 298 K):  $\delta$  (ppm) 7.53 (d,  $^4J = 1.8\text{ Hz}$ , 4H, H-Ar'), 7.39 (m, 6H, H-Ar, H-Ar',  $-\text{CH}=\text{}$ ), 6.37 (d,  $^3J = 7.8\text{ Hz}$ , 2H, H-Ar), 3.79 (s, 6H,  $-\text{OCH}_3$ ), 1.77 (s, 6H,  $-\text{CH}_3$ ), 1.30 (s, 36H, 'Bu-Ar'), 0.93 (s, 6H, Si- $\text{CH}_3$ ),  $-0.61$  (s, 6H, Ti- $\text{CH}_3$ ).  $^{13}\text{C}\{^1\text{H}\}$  NMR (100 MHz,  $\text{CD}_2\text{Cl}_2$ ):  $\delta$  (ppm) 156.7, 151.5, 140.5, 135.1, 134.3, 131.5, 127.4, 124.4, 123.6, 122.2, 121.3, 102.1, 81.7, 50.2, 35.5, 31.9, 17.8, 5.9.

**Polymerization.** All polymerization reactions were performed in a 1.1 L Büchi steel autoclave equipped with a paddle agitator, a temperature sensor, and a heating/cooling jacket attached to a cryo-/thermostat unit (Thermo Scientific HAAKE DynaMax). The Ar pressure for all manipulations was set at 1.3 bar. Prior to polymerization, the autoclave was equipped with 300 mL of dry toluene and 2.0 mL of 1.1 M TIBA solution in toluene and heated to  $90\text{ }^{\circ}\text{C}$ . After the temperature was maintained for 15 min, the scrubbing solution was released. For the polymerization, the autoclave was charged with 280 mL of dry toluene and the desired amount of 1.1 M TIBA solution in toluene (or MMAO-12 (7 wt % Al in toluene) in the

case of **II**) was added. The metallocene complex (1.0 equiv of **1** or **2**) was dissolved in 10 mL of toluene and, for catalysts **I** and **IV**, the bischlorinated complexes **I** were preactivated with 200 equiv of TIBA at room temperature for 1 h. After adjustment to the desired temperature, the metallocene solution was transferred into the autoclave and the autoclave was pressurized with propene. When the system was equilibrated and stable, the polymerization was started by adding 5.0 equiv of  $[\text{Ph}_3\text{C}][\text{B}(\text{C}_6\text{F}_5)_4]$  dissolved in 10 mL of toluene to the autoclave via a pressure buret ( $p_{\text{pol}} + 1.0\text{ bar}$ ). In the case of **II**, the polymerization was started by adding the complex solution via the pressure buret to the pressurized toluene/MAO solution. The propene consumption was monitored using a gas flow meter (Bronkhorst F-111C-HA-33P). Temperature, pressure, time, and total propene consumption were also recorded. The polymerization reaction was quenched with 2.0 mL of methanol, and the reaction mixture was poured into 1.0 L of acidified methanol. The precipitated polymer was removed from the autoclave, and all combined polymer was washed exhaustively and dried at  $70\text{ }^{\circ}\text{C}$  in vacuo overnight.

## ■ ASSOCIATED CONTENT

### Supporting Information

The Supporting Information is available free of charge on the ACS Publications website at DOI: 10.1021/acs.organomet.7b00112.

Polymerization conditions and results,  $^1\text{H}$  NMR and  $^{13}\text{C}$  NMR spectra of the new key compounds **1** and **2**, EPR spectra, UV/vis spectra,  $^{13}\text{C}$  NMR spectra for tacticity determination, and SC-XRD data (PDF)  
Crystallographic data (CIF)

## ■ AUTHOR INFORMATION

### Corresponding Author

\*B.R.: e-mail, rieger@tum.de; tel, +49-89-289-13570; fax, +49-89-289-13562.

### ORCID

Bernhard Rieger: 0000-0002-0023-884X

### Notes

The authors declare no competing financial interest.

## ■ ACKNOWLEDGMENTS

We are exceptionally grateful to WACKER Chemie AG for continued financial support. We extend a big thank you to Dr. Carmen Haeßner and Prof. Dr. Klaus Koehler for the conducted EPR measurements and processing of the data. We also thank Dr. Alexander Poethig as head of the SC-XRD laboratory of the Catalysis Research Center. The authors thank Philipp Pahl and Daniel Wendel for proofreading the manuscript and valuable discussions.

## ■ REFERENCES

- Holleman, A. F.; Wiberg, E.; Wiberg, N. *Lehrbuch der Anorganischen Chemie (Textbook of Inorganic Chemistry, Engl. Transl.)*, 102nd ed.; Walter de Gruyter: Berlin, 2007.
- Ziegler, K.; Holzkamp, E.; Breil, H.; Martin, H. *Angew. Chem.* **1955**, *67*, 541–547.
- Natta, G. *Angew. Chem.* **1956**, *68*, 393–403.
- Stalzer, M. M.; Delferro, M.; Marks, T. J. *Catal. Lett.* **2015**, *145*, 3–14.
- Breslow, D. S.; Newburg, N. R. *J. Am. Chem. Soc.* **1957**, *79*, 5072–5073.
- Natta, G.; Pino, P.; Mazzanti, G.; Giannini, U. *J. Am. Chem. Soc.* **1957**, *79*, 2975–2976.
- Resconi, L.; Cavallo, L.; Fait, A.; Piemontesi, F. *Chem. Rev.* **2000**, *100*, 1253–1345.

- (8) Brintzinger, H. H.; Fischer, D.; Mülhaupt, R.; Rieger, B.; Waymouth, R. M. *Angew. Chem., Int. Ed. Engl.* **1995**, *34*, 1143–1170.
- (9) Mallin, D. T.; Rausch, M. D.; Lin, Y. G.; Dong, S.; Chien, J. C. W. *J. Am. Chem. Soc.* **1990**, *112*, 2030–2031.
- (10) Llinas, G. H.; Dong, S. H.; Mallin, D. T.; Rausch, M. D.; Lin, Y. G.; Winter, H. H.; Chien, J. C. W. *Macromolecules* **1992**, *25*, 1242–1253.
- (11) Llinas, G. H.; Day, R. O.; Rausch, M. D.; Chien, J. C. W. *Organometallics* **1993**, *12*, 1283–1288.
- (12) Lee, M. H.; Han, Y.; Kim, D.-h.; Hwang, J.-W.; Do, Y. *Organometallics* **2003**, *22*, 2790–2796.
- (13) Bochmann, M. *Organometallics* **2010**, *29*, 4711–4740.
- (14) Bryliakov, K. P.; Babushkin, D. E.; Talsi, E. P.; Voskoboinikov, A. Z.; Gritz, H.; Schröder, L.; Damrau, H.-R. H.; Wieser, U.; Schaper, F.; Brintzinger, H. H. *Organometallics* **2005**, *24*, 894–904.
- (15) Miyake, S.; Okumura, Y.; Inazawa, S. *Macromolecules* **1995**, *28*, 3074–3079.
- (16) Bravakis, A. M.; Bailey, L. E.; Pigeon, M.; Collins, S. *Macromolecules* **1998**, *31*, 1000–1009.
- (17) Baier, M. C.; Zuideveld, M. A.; Mecking, S. *Angew. Chem., Int. Ed.* **2014**, *53*, 9722–9744.
- (18) Schöbel, A.; Herdtweck, E.; Parkinson, M.; Rieger, B. *Chem. - Eur. J.* **2012**, *18*, 4129–4129.
- (19) Tranchida, D.; Mileva, D.; Resconi, L.; Rieger, B.; Schöbel, A. *Macromol. Chem. Phys.* **2015**, *216*, 2171–2178.
- (20) Machat, M. R.; Lanzinger, D.; Pöthig, A.; Rieger, B. *Organometallics* **2017**, *36*, 399–408.
- (21) Shaltout, R. M.; Corey, J. Y.; Rath, N. P. *J. Organomet. Chem.* **1995**, *503*, 205–212.
- (22) Moehring, P. C.; Coville, N. J. *Coord. Chem. Rev.* **2006**, *250*, 18–35.
- (23) Lyakin, O. Y.; Bryliakov, K. P.; Panchenko, V. N.; Semikolenova, N. V.; Zakharov, V. A.; Talsi, E. P. *Macromol. Chem. Phys.* **2007**, *208*, 1168–1175.
- (24) Sharma, M.; Yameen, H. S.; Tumanskii, B.; Filimon, S.-A.; Tamm, M.; Eisen, M. S. *J. Am. Chem. Soc.* **2012**, *134*, 17234–17244.
- (25) Busico, V.; Brita, D.; Caporaso, L.; Cipullo, R.; Vacatello, M. *Macromolecules* **1997**, *30*, 3971–3977.
- (26) Bryliakov, K. P.; Talsi, E. P.; Bochmann, M. *Organometallics* **2004**, *23*, 149–152.
- (27) Busico, V.; Cipullo, R.; Pellicchia, R.; Talarico, G.; Razavi, A. *Macromolecules* **2009**, *42*, 1789–1791.
- (28) Bryliakov, K. P.; Talsi, E. P.; Voskoboinikov, A. Z.; Lancaster, S. J.; Bochmann, M. *Organometallics* **2008**, *27*, 6333–6342.
- (29) Ehm, C.; Cipullo, R.; Budzelaar, P. H. M.; Busico, V. *Dalton Transactions* **2016**, *45*, 6847–6855.
- (30) Theurkauff, G.; Bondon, A.; Dorcet, V.; Carpentier, J.-F.; Kirillov, E. *Angew. Chem., Int. Ed.* **2015**, *54*, 6343–6346.
- (31) Theurkauff, G.; Bader, M.; Marquet, N.; Bondon, A.; Roisnel, T.; Guegan, J.-P.; Amar, A.; Boucekkine, A.; Carpentier, J.-F.; Kirillov, E. *Organometallics* **2016**, *35*, 258–276.
- (32) Busico, V.; Cipullo, R.; Cuttillo, F.; Friederichs, N.; Ronca, S.; Wang, B. *J. Am. Chem. Soc.* **2003**, *125*, 12402–12403.
- (33) Cipullo, R.; Melone, P.; Yu, Y.; Iannone, D.; Busico, V. *Dalton Transactions* **2015**, *44*, 12304–12311.
- (34) Bochmann, M.; Sarsfield, M. J. *Organometallics* **1998**, *17*, 5908–5912.
- (35) Resconi, L.; Camurati, I.; Sudmeijer, O. *Top. Catal.* **1999**, *7*, 145–163.
- (36) Resconi, L. *J. Mol. Catal. A: Chem.* **1999**, *146*, 167–178.
- (37) Castonguay, L. A.; Rappe, A. K. *J. Am. Chem. Soc.* **1992**, *114*, 5832–5842.
- (38) Longo, P.; Grassi, A.; Pellicchia, C.; Zambelli, A. *Macromolecules* **1987**, *20*, 1015–1018.
- (39) Dahlmann, M.; Erker, G.; Nissinen, M.; Fröhlich, R. *J. Am. Chem. Soc.* **1999**, *121*, 2820–2828.
- (40) Resconi, L.; Fait, A.; Piemontesi, F.; Colonna, M.; Rychlicki, H.; Zeigler, R. *Macromolecules* **1995**, *28*, 6667–6676.
- (41) Busico, V.; Cipullo, R. *J. Am. Chem. Soc.* **1994**, *116*, 9329–9330.
- (42) Leclerc, M. K.; Brintzinger, H. H. *J. Am. Chem. Soc.* **1995**, *117*, 1651–1652.
- (43) Leclerc, M. K.; Brintzinger, H. H. *J. Am. Chem. Soc.* **1996**, *118*, 9024–9032.
- (44) Busico, V.; Caporaso, L.; Cipullo, R.; Landriani, L.; Angelini, G.; Margonelli, A.; Segre, A. L. *J. Am. Chem. Soc.* **1996**, *118*, 2105–2106.
- (45) Busico, V.; Cipullo, R.; Caporaso, L.; Angelini, G.; Segre, A. L. *J. Mol. Catal. A: Chem.* **1998**, *128*, 53–64.
- (46) Busico, V.; Cipullo, R. *Prog. Polym. Sci.* **2001**, *26*, 443–533.
- (47) Bochmann, M. *J. Organomet. Chem.* **2004**, *689*, 3982–3998.

## 6. Behind the Scenes of Group IV Metallocene Catalysis: Examination of the Metal–Carbon Bond

- Title:** “Behind the Scenes of Group IV Metallocene Catalysis: Examination of the Metal–Carbon Bond”
- Status:** Full Paper, ready for submission
- Journal:** Journal of American Chemical Society
- Publisher:** American Chemical Society
- DOI:** -
- Authors:** Martin R. Machat, Andreas Fischer, Dominik Schmitz, Marcel Vöst, Markus Drees, Christian Jandl, Alexander Pöthig, Nicola P. M. Casati, Wolfgang Scherer, and Bernhard Rieger<sup>c</sup>

**Content:** Over the last decades, each of the group IV metals (Ti, Zr, Hf) has proven its capability in the polymerization of olefins regarding different fields of specialized application. While titanium still dominates the industrial production of polypropylene using heterogeneous ZN-catalysts, zirconocenes, especially in combination with MAO, are generally stated to be the most active metallocene catalysts, and the application of hafnium can lead to extremely high molecular weights which are not accessible with the other homologs. In this context, the M–C  $\sigma$ -bond is considered decisive in numerous catalytic sub-processes, thereby determining the final polymer properties. Accordingly, the present contribution provides detailed analysis of the M–C (methyl) bond of three alkylated, isostructural group IV metallocenes. Therefore, this crucial unit in the coordinative polymerization catalysis was examined experimentally for the first time concerning its electronic properties *via* high resolution single crystal X-ray diffraction analysis and SC XRD under high pressure. In addition, the kinetic behavior of M–C  $\sigma$ -bond conversion was analyzed with all three group IV metals disclosing an essential impact of different enthalpic and entropic contributions to the respective activation barrier. The combined results suggest a covalent Ti–C bond comprising a high enthalpic contribution to the activation barrier, a highly ionic Hf–C bond which is also dominated by a high enthalpic impact and a moderately covalent Zr–C bond that reveals a significantly higher entropic contribution to the activation barrier. Inspired by this new perspective, we exemplarily correlated our findings to the catalytic abilities of all three isostructural metallocenes in order to provide a new and comprehensive perspective on the peculiarities of these metals in the vast field of group IV metallocene catalysis. As a result, deviations between zirconium- and hafnium-based catalysts concerning the catalytic activity and the stereoregularities became clearly explainable, as well as the “hafnium-effect” in the production of extraordinarily high molecular weight polypropylenes.

---

<sup>c</sup> M. Machat planned and executed all synthetic, polymerization and kinetic experiments and wrote most parts of the manuscript. A. Fischer calculated and processed all computational data concerning the electron density distributions. A. Fischer, C. Jandl and A. Pöthig conducted all SC XRD-measurements and managed the processing of the data. D. Schmitz and M. Vöst performed all high pressure SC XRD-measurements and managed the processing of the data. M. Drees conducted all DFT-calculations concerning the transition states of the kinetic measurements. W. Scherer wrote the passages about the electron density examination. All work was performed under the supervision of W. Scherer and B. Rieger.

## Behind the Scenes of Group IV Metallocene Catalysis: Examination of the Metal–Carbon Bond

Martin R. Machat<sup>†</sup>, Andreas Fischer<sup>†</sup>, Dominik Schmitz<sup>‡</sup>, Marcel Vöst<sup>‡</sup>, Markus Drees<sup>§</sup>, Christian Jandl<sup>§</sup>, Alexander Pöthig<sup>§</sup>, Nicola P. M. Casati<sup>⊥</sup>, Wolfgang Scherer<sup>\*†</sup>, and Bernhard Rieger<sup>\*†</sup>

<sup>†</sup>Wacker-Lehrstuhl für Makromolekulare Chemie, Catalysis Research Center, Technische Universität München, Lichtenbergstraße 4, 85748 Garching bei München, Germany

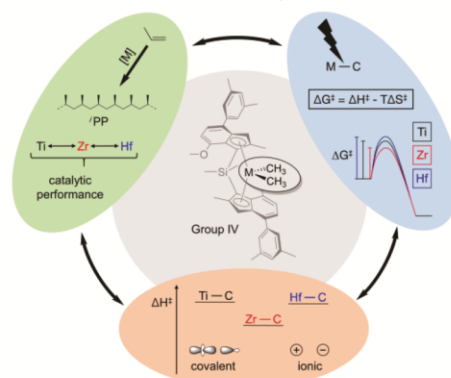
<sup>‡</sup>Lehrstuhl für Chemische Physik und Materialwissenschaften, Institut für Physik, Universität Augsburg, Universitätsstraße 1, 86159 Augsburg, Germany

<sup>⊥</sup>Paul Scherrer Institut, WLGA/229, 5232 Villigen PSI, Switzerland

<sup>§</sup>Catalysis Research Center, Technische Universität München, Ernst-Otto-Fischer Straße 1, 85748 Garching bei München, Germany

*Metallocene – zirconium – hafnium – group IV chemistry – bond strength – bond compressibility – electron density – electron localization – lanthanide contraction – ionic character – covalent character – enthalpy – entropy – polyolefin catalysis – propene polymerization – polypropylene – high melting transition – stereoselectivity*

**ABSTRACT:** This contribution provides the first detailed analysis of the nature of the *M*–C (methyl)  $\sigma$ -bond of three alkylated, isostructural Group IV (*M* = Ti, Zr, Hf) metallocenes, thereby elucidating individual peculiarities of each metal center in the catalytic conversion of olefins. Therefore, the subtle electronic differences of the individual *M*–C  $\sigma$ -bonds, which are considered crucial for several sub-processes in the coordinative polymerization of olefins, were examined by detailed experimental charge density and high-pressure diffraction studies. These studies provided measures of the increasing ionic character of the *M*–C bonds along the Group 4 elements (Ti–C < Zr–C < Hf–C). High pressure diffraction studies offered additional evidence that the Hf–C bond is more compressible than the Zr–C bond despite the larger force constant of the latter one. This puzzling result was explained by the different degree of electron localization in the valence shells of the respective transition metal atoms. All findings were then correlated to the kinetic characteristics of group IV *M*–C  $\sigma$ -bond conversion. The combined results confirmed the distinct ionic character of the Hf–C bond compared to the less ionic Zr–C bond, resulting in a significantly higher activation enthalpy of the higher homolog. However, the entropic contribution to the activation barrier turned out to be explicitly higher for a Zr–C bond conversion. The combined results of the kinetic and electronic analysis herein shed new light on the different catalytic behavior of group IV metallocenes with regard to the applied transition metal atom. Particular focus was directed to zirconium- and hafnium-based metallocenes to probe the generally accepted assumption that their differences in *M*–C bond strength are mainly responsible for their differing catalytic performance. In this context, deviations between zirconium- and hafnium-based catalysts concerning the catalytic activity and the stereoregularities became clearly explainable, just as the well-known “hafnium-effect” in the production of extraordinarily high molecular weight polypropylenes.



### INTRODUCTION

In 1957, first reports on titanocene complexes in olefin polymerization by Natta and Berslow<sup>1,2</sup> laid the foundation for more than half a century of extensive research on group IV metallocene chemistry in the homogenous polymerization catalysis of alkenes. While the focus was placed on titanocene complexes after the initial discoveries of Ziegler and Natta,<sup>3,4</sup> first reports on the application of higher hom-

ologs (Zr, Hf) appeared in the 1980s.<sup>5–8</sup> A breakthrough to highly active metallocene based polymerization catalysts was the implementation of methylaluminoxane (MAO) as cocatalyst in 1980,<sup>5</sup> still representing one of the most popular activation reagents especially concerning industrial application.<sup>9,10</sup> An alternative approach was achieved using boron based Lewis acids leading to well defined, catalytically active, cationic complexes with sterically encumbered weakly coordinating anions.<sup>11</sup> Nowadays, zirconocene complexes

are commonly stated to be the most active ones in the polymerization of propene, whereupon examples are known in which suitably activated hafnocenes exhibit comparably high activities.<sup>12–16</sup> This is contrary to previous reports assigning the lower activities of Hf to lower chain propagation rates as a result of a stronger metal–carbon bond.<sup>8, 17–18</sup> In contrast, the catalytic activity of titanocene complexes generally suffers by catalyst deactivation due to reductive processes.<sup>9, 19–20</sup> The exchange from Zr to Hf becomes particularly important regarding the molecular weights of the respective polymers. Significantly higher molar masses for the polymers of the hafnocene compared to the zirconocene analog are herein observed for  $C_{1-}$ ,  $C_2$ - and  $C_s$ -symmetric *ansa*-metallocene complexes and have established the so called “hafnium effect”.<sup>12, 14, 18, 21–22</sup> In this context, a stronger Hf–C vs. Zr–C bond serves as most plausible explanation for more than three decades.<sup>8, 12, 18, 23</sup> Focusing on chain release mechanisms, calculations indicate a distinctly higher activation barrier for  $\beta$ -hydride elimination using hafnium based metallocenes.<sup>23–24</sup> On the contrary, the selectivity towards  $\beta$ -methyl elimination is reported to be higher for hafnocene compared to zirconocene complexes.<sup>15, 25</sup> It becomes rather obvious, that the metal center has a severe impact on several processes in the coordinative polymerization of olefins, thereby essentially determining the overall catalytic behavior and the characteristics of the final polymer product.

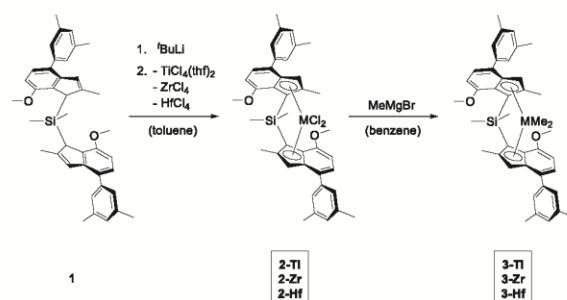
Taking into account the location of the group IV metals in the periodic table of elements, the nuclear characteristics of titanium and zirconium seem quite expectable. In this context, the relation of zirconium and hafnium appears particularly interesting (Shannon: effective ionic radii (CN: IV): Hf<sup>IV</sup>: 0.58 Å, Zr<sup>IV</sup>: 0.59 Å, Ti<sup>IV</sup>: 0.42 Å)<sup>26–27</sup>. The nuclear charge of the 3<sup>rd</sup> row transition metals is higher than that of 2<sup>nd</sup> row transition elements. The larger nuclear charge in combination with the larger quantum number of the valence orbitals causes the contraction of the 3<sup>rd</sup> row transition elements thus evoking atomic radii comparable to the 2<sup>nd</sup> row transition metals. Accordingly, the higher homolog Hf possesses a slightly smaller ionic radius than Zr due to the described phenomena of lanthanide contraction. This is basically witnessed in purely nonrelativistic calculations, but it is amplified in a relativistic description.<sup>18, 28</sup> In summary, identical electronic configurations and oxidation states in combination with comparable ionic radii suggest a very similar chemical behavior arousing the general question of distinct chemical differences regarding this unique pair (Zr vs. Hf) in the periodic table of elements.

Considering several relevant processes in the polymerization of propene, like chain propagation, chain release or epimerization reactions, the metal–carbon (alkyl/polymeryl)  $\sigma$ -bond possesses a fundamental role. In the late 1980s quantification of the metal–carbon bond strength of various metallocene complexes was carried out determining the bond enthalpies *via* titration calorimetric methods. Among others, the metal–methyl  $\sigma$ -bond enthalpies of (Cp\*)<sub>2</sub>MMe<sub>2</sub> complexes were determined indicating the largest bond enthalpy in the case of the Hf–C (306 (7) kJ/mol) compared to the Zr–C (284 (2) kJ/mol) and the Ti–C bond (281 (8) kJ/mol).<sup>29–32</sup> Although the presented approach represents a rare example in which the metal–carbon bond enthalpy of group IV metal alkyls was experimentally evaluated, the determined values only offer limited validity regarding the actual bond characteristics and the respective chemical

behavior of this crucial binding unit. As a result, the significant differences in metallocene chemistry applying different group IV metals are, to this day, far from being completely understood.

This contribution provides substantial insight into group IV metallocene chemistry comprising a multidisciplinary study of detailed metal–carbon bond investigation in correlation with the catalytic behavior in the polymerization of propene. The research is based on three  $C_2$ -symmetric, bis-methylated, isostructural complexes (Scheme 1) with varied group IV metal center. The applied metallocene framework represents the state of the art complex geometry for high molecular weight, highly isotactic polypropylene comprising exceptionally high melting transitions.<sup>14, 20, 33–34</sup> Explicit examination of the metal–carbon bond characteristics was conducted by high resolution X-ray diffraction (XRD) analysis and XRD-measurements under external pressure to gain insight into the electron density distribution of this crucial binding moiety. The electronic properties were herein disclosed by combined experimental and computational approaches. An additional study elucidated the chemical behavior by investigation of the kinetic metal–carbon bond stability. Thereby, enthalpic and entropic contributions to the activation barrier in the case of M–C bond conversion were determined. Finally, the fundamental findings of both approaches were correlated to the results of all three isostructural metallocene catalysts in the polymerization of propene, facilitating a new and comprehensive perspective on the field of metallocene catalysis.

## RESULTS AND DISCUSSION



**Scheme 1.** Synthesis route to the methylated metallocene complexes **3**.

**Synthesis and Characterization.** The synthesis of the ligand framework **1** as well as the hafnocene (**2-Hf**) and titanocene (**2-Ti** and **3-Ti**) complexes have been reported recently.<sup>20, 33</sup> The zirconocene analog (**2-Zr**) was synthesized accordingly. The conversion to the bis-methylated complexes **3** is conducted by treatment with a methyl grignard reagent under adjusted conditions. The ligand exchange from chloride to methyl takes place instantly in the case of **3-Ti**, whereupon an excess of MeMgBr reagent, several hours and elevated temperatures are necessary for **3-Zr** and especially **3-Hf** (Scheme 1).

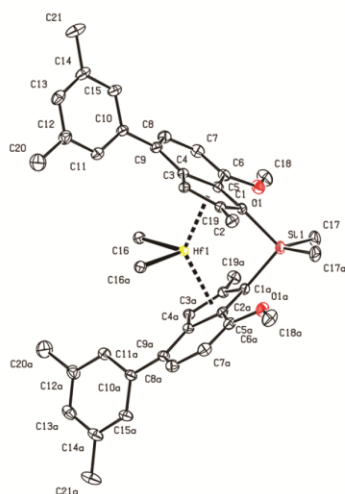


Figure 1. ORTEP style representation of 3-Hf with ellipsoids drawn at 50 % probability level. Hydrogen atoms are omitted for clarity.

Single crystals suitable for high resolution X-ray diffraction studies and subsequent electron density analysis were obtained by diffusion of pentane into a saturated solution of **3** in benzene at 7 °C. Figure 1 depicts the crystal structure of **3-Hf**. Crystal structures of **2-Zr**, **3-Ti** and **3-Zr** are provided in the Supporting Information (S31-S34). Important angles and bond lengths of the complexes **3** are presented in Table 1.

Table 1. Characteristic angles and distances of 3-Ti, 3-Zr and 3-Hf in the solid state.

	M–Me	M–C <sub>pcentr.</sub>	M–Si	D*
<b>3-Ti</b>	2.1527(3) Å	2.1586(3) Å	3.2483(4) Å	0.863 Å
<b>3-Zr</b>	2.2655(3) Å	2.2638(2) Å	3.3128(3) Å	0.967 Å
<b>3-Hf</b>	2.2443(5) Å	2.2484(3) Å	3.3109(4) Å	0.957 Å
	Bite angle*	Me–M–Me angle	C <sub>pcentr.</sub> –M–C <sub>pcentr.</sub> angle	
<b>3-Ti</b>	56.67(2)°	92.79(1)°	132.87(1)°	
<b>3-Zr</b>	59.21(2)°	97.24(1)°	129.45(1)°	
<b>3-Hf</b>	58.71(4)°	96.00(2)°	129.63(1)°	

\*According to ref.<sup>33,35-36</sup>

The bite angles of **3-M** (M = Ti, Zr, Hf) reflect the trends observed for the ionic radii. Accordingly, the titanocene complex **3-Ti** possesses the smallest angle, whereas the biggest one is observed for Zr. In line with these findings titanium reveals the shortest metal–carbon (methyl)  $\sigma$ -bond being considerably smaller than the one of the zirconium and hafnium analogs. Same trends are observed in the case of the M–C<sub>pcentr.</sub> distances and D. The closeness of the structural parameters of Group 4 complexes **3-Zr** and **3-Hf** appears to be a natural consequence of the lanthanoid contraction yielding a slightly lower ionic radius for Hf<sup>IV</sup> vs. Zr<sup>IV</sup> (see above). However, the trends observed for the Me–M–Me and Cp–M–Cp angles clearly have a different electronic origin and warrant a detailed inspection of the electron density distribution in the valence shell of the transition metals of **3-M**.

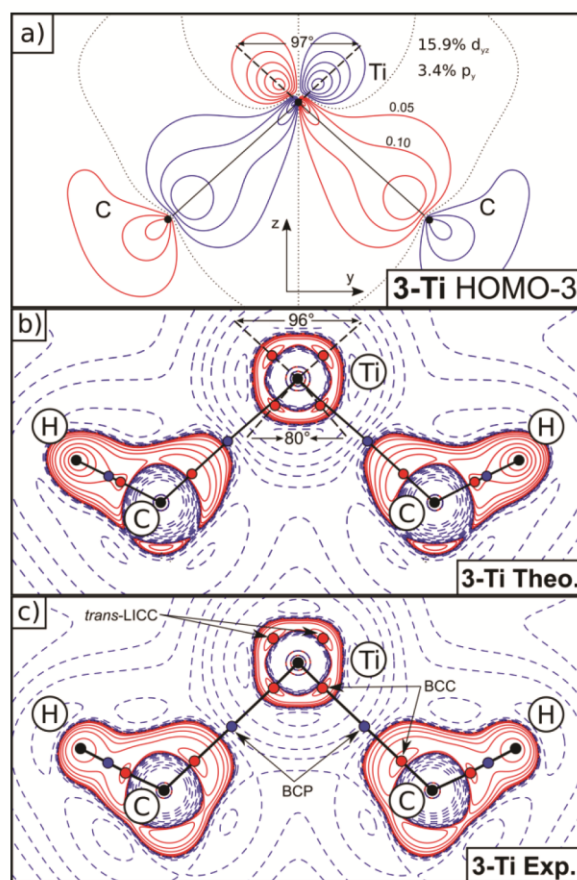


Figure 2. (a) Density contour map of the most important M–C(Me) bonding molecular orbital (HOMO-3) in the molecular plane of **3-Ti**. Contour levels are specified in atomic units and the percentage %p, and %d<sub>z</sub> character of the titanium atom refers to gross populations of symmetrized fragment (valence) orbitals (SFO). Note that the angle between the density-maxima of ligand-opposed p<sub>y</sub>-d<sub>z</sub> hybrid lobes and the enclosed metal is larger than 90°; (b,c) The topology of the negative Laplacian,  $L(r) = -\nabla^2\rho(r)$ , reveals ligand-induced charge concentrations in the valence shell of the titanium atom opposite to the methyl ligands (denoted *trans*-LICCs) and pronounced bonded charge concentrations (BCC) in the valence shell of the carbon atom reflecting their carbanionic character. Positive (red, solid) and negative (blue, dashed)  $L(r)$  contour lines were drawn at  $\pm 2.0 \times 10^{-4}$ ,  $\pm 4.0 \times 10^{-4}$ ,  $\pm 8.0 \times 10^{-4}$  e/Å<sup>3</sup> with  $n = \pm 2, \pm 1, 0$ .

**Electron Density Determination.** We first recall some peculiarities of the M–C bond in early d<sup>0</sup> transition metal alkyls. In general these are considered as highly polar. Indeed, a partitioning of the experimental electron density in the framework of the Quantum Theory of Atoms In Molecules (QTAIM)<sup>37</sup> supports the carbanionic nature of the methyl carbon atom  $Q(C) = -0.77$  [–0.32] (**3-Ti**),  $-1.19$  [–0.39] (**3-Zr**) and  $-1.22$  [–0.41] (**3-Hf**). Note, that we specify here and in the following values obtained from DFT in square brackets. Due to the pronounced M→C charge transfer also the methyl hydrogen atoms of **3-M** are characterized by hydridic (high-field shifts) of the corresponding protons in the <sup>1</sup>H NMR spectra ( $\delta_{\text{IH}} = -0.83$  ppm (**3-Ti**),  $-1.17$  ppm (**3-Zr**) and  $-1.35$  ppm (**3-Hf**).

Hence, these results suggest an increase of the ionic character of the  $M-C$  bond in the sequence **3-Ti** < **3-Zr** < **3-Hf**. This is also evident from the fine structure of the negative Laplacian of the electron density,  $L(\mathbf{r}) = -\nabla^2\rho(\mathbf{r})$ , in the molecular ( $C_rM_rC$ ) plane (Figure 2). The red solid/blue broken contour lines reveal regions in Figure 2b and c where the electron density is locally concentrated/depleted, respectively.<sup>38</sup> Apparently, each methyl carbon atom displays a bonded charge concentration (BCC) in its valence shell which is located on the  $M-C$  bond path and provides a measure of the lone pair character at the respective carbon atom.<sup>39-40</sup> The magnitude of these BCCs increases in the sequence **3-Ti** < **3-Zr** < **3-Hf** from  $L(\mathbf{r}) = 26.8 - 33.2 \text{ e}\text{\AA}^{-5}$  in line with the increasing carbanionic character of the respective methyl carbon atoms. However, the  $L(\mathbf{r})$  topology reveals also a significant residual covalent character of the  $M-C$  bonds despite their polar nature. Especially, in **3-Ti** the covalent nature of the  $M-C$  bonds is clearly signaled by the characteristic pattern of two opposing BCCs in the valence shell of metal and the methyl carbon atom (Figure 2b,c) which are connected by a bond path. The formation of pronounced ligand-induced charge concentrations (*trans*-LICCs) opposite to the  $M-C$  bonds provides another signature of covalent  $M-C$  bonding<sup>41</sup> and is a natural consequence of the overlap between the  $sp^x$  hybridized orbitals at the methyl carbon atoms and  $Ti(p_y, d_{z^2})$  hybrids (Figure 2a). The  $M-C$  covalency is also witnessed by the surprisingly small  $C-M-C$  angle of  $92.79^\circ$  in **3-Ti**. On contrast the  $Cp-Ti-Cp$  angles which are formed by the centroid of the  $Cp$ -rings and the metal are significantly larger ( $132.87^\circ$ ).

One might argue in the framework of the VSEPR concept that the acuteness of the  $C-M-C$  angle might be a direct consequence of the polarity of the  $M-C$  (methyl) bond which minimizes the repulsion between the  $M-C$  bonding domains and enhanced by the large steric request of the *ansa*-bridging  $\pi$ -ligands. However, this simplistic picture appears to be misleading. Indeed, isolobal replacement of the *ansa*-bridging  $\pi$ -ligands in **3-Ti** by chloro ligands leads to the Lewis acid  $Me_2TiCl_2$  **3'-Ti** which represents the perhaps simplest model system. Also in **3'-Ti** which is not affected by steric intra-ligand repulsion the smallest valence is again formed by the ligands displaying the stronger covalent bond:  $\angle C-Ti-C = 102.8^\circ$  and  $\angle Cl-Ti-Cl$  angle =  $117.3^\circ$ .<sup>42</sup> Hence, **3'-Ti** and **3-Ti** (and also **3-Zr** and **3-Hf**) are at variance with the prediction of the VSEPR model for  $d^0$ -complexes and should be classified as non-VSEPR compounds.<sup>43-44</sup> The acuteness of their  $Me-Ti-Me$  angles is therefore a natural consequence of the covalent character of their  $M-C$  bonds. Indeed, the presence of *trans*-LICCs is an integral part of covalent  $M-C$  bond formation in  $d^0$  metal complexes<sup>44</sup> and their repulsion in the metal's valence shell provides a physical explanation for the compression of the  $C-M-C$  angles (Table 1). In case of the 3d metal-complex **3-Ti** the repulsion between the pronounced *trans*-LICCs ( $L(\mathbf{r}) = 287 [300] \text{ e}\text{\AA}^{-5}$ ) is significantly larger than that between the rather subtle BCCs ( $L(\mathbf{r}) = 258 [235] \text{ e}\text{\AA}^{-5}$ ). As a consequence the angle between the *trans*-LICCs at the titanium atom of  $91.2 [96.0]^\circ$  is larger than that spanned by the BCCs and the metal of  $88.1 [80.3]^\circ$ . Hence, the smaller  $Me-Ti-Me$  angle in **3-Ti** vs  $Me_2TiCl_2$  is therefore a clear indication of the larger covalent  $M-C$  bonding character in case of the metallocene complex.

Also in case of the 4d and 5d metal complexes **3-Zr** and **3-Hf** somewhat larger  $Me-M-Me$  angles are observed relative to **3-Ti**. This can be taken as another evidence for the larger ionic character

of these  $M-C$  bonds and the increasing diffuse character of their valence shells. Accordingly, only subtle (**3-Zr**) or even vanishing (**3-Hf**) *trans*-LICCs are observed in the 4d and 5d metal complexes and the repulsion between these spurious *trans*-LICCs is small in the rather diffuse valence shells of zirconium and hafnium.

To summarize, the increasing ionic character of the  $M-C$  bond from **3-Ti** to **3-Hf** is clearly supported by the trends observed for the (i) atomic charges, (ii) the carbanionic character of the carbon atoms, and (iii) the hydridic  $^1H$  chemical shifts. However, the presence of (iv) bonded and ligand opposed charge concentrations (denoted BCC and *trans*-LICCs in Figure 2) in the valence shell of the metal atoms in **3-Ti** and **3-Zr** suggests that the  $M-C$  bonding scenario is best described by highly polar bonds with residual but decreasing covalent character in the sequence **3-Ti** > **3-Zr** > **3-Hf**.

This decrease of covalency in the  $M-C$  bonds has been probed in the next Section by experimental high pressure diffraction studies.

**High pressure diffraction studies.** In the following we have studied the pressure-induced structural changes in single crystals of **3-M**. In general it is assumed that “forces in crystals act through localized bonds” which in turn can be identified by the QTAIM methods via the presence of a bond path.<sup>45</sup> In case of highly symmetrical covalent compounds, hardness is defined by the bulk modulus  $B$  and controlled by the compressibility of their individual chemical bonds.<sup>46</sup> These case studies showed that the bond compressibility in turn increases with enhancement of the bond ionicity and lowering of the bond strength.<sup>46-47</sup> In case of molecular crystals, however, the scenario is more complex and the low bulk modulus is mainly reflecting the softness of van der Waals contacts at lower pressure.<sup>45</sup> It is therefore essential to compare the compressibility of chemical bonds in molecular crystals displaying virtually identical crystal packing forces. This is actually the case for **3-Zr** and **3-Hf** which are crystallographic isotypic (identical spacegroup & isostructural) and characterized by virtually identical lattice parameters. As a consequence of the lanthanide contraction also the corresponding metal to ligand bonds are very similar (Table 1). Indeed, the Hf-C bond length of  $2.2443(5) \text{ \AA}$  differs by less than 1% from the Zr-C bond distance of  $2.2655(3) \text{ \AA}$ .

As a consequence, we expect in case of the  $\sigma$ - $M-C$  bonded methyl groups in **3-Zr** and **3-Hf** an increasing bond compressibility with increasing ionic character of the respective  $M-C$  bonds – if we assume that the bond strength of Hf-C is not significantly larger than that of Zr-C.<sup>48</sup> In that case, the Hf-C bond should display the larger bond compressibility in comparison to the Zr-C bond due to its higher ionic character as determined in the experimental and theoretical charge density studies (see above). Indeed the experimental high-pressure studies (Figure 3) clearly reveal the larger bond compressibility of the Hf-C bond vs the Zr-C bond. However, the calculated force constants  $k$  of isolated  $\nu(M-C)$  stretching frequencies<sup>49</sup> increase down the row of the Group 4 complexes  $k/Nm^{-1} = 157$  (**3-Ti**),  $156$  (**3-Zr**) and  $176$  (**3-Hf**) with a subtle minimum in case of **3-Zr**. In general there is a cross correlation<sup>50</sup> between the increasing polarity of a chemical bond and the enhancement of its force constant  $f$ . However, the larger polarity of the Zr-C vs Ti-C bond is not reflected in the calculated force constants. We also need to explain why the stiffer Hf-C bond is more compressible compared to the softer Zr-C bond in the **3-M** complexes. One might argue empiri-

cally that the *bond iconicity rather than the bond strength* predominantly controls the compressibility of the *M–C* bond. However, we will search in the next step of our analysis for the microscopic control parameters of the *M–C* bond compressibilities in **3-M**.

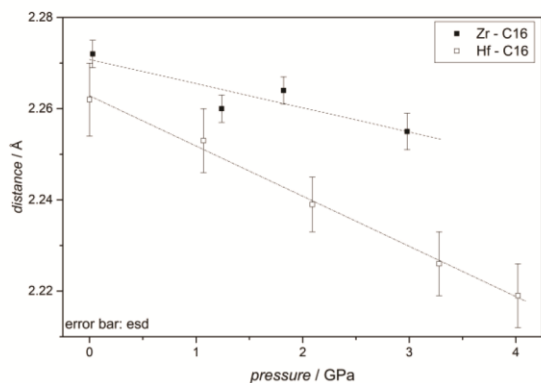


**Figure 3.** X-ray single-crystal diffraction studies of **3-Zr** and **3-Hf** at variable pressure (0–4.0 (1) GPa). The Hf–C bonds show a larger bond compressibility at increasing pressures due to the larger ionic character of the Hf–C vs. Zr–C bond.

A recent study by Contreras-García<sup>51</sup> used the electron localization function (ELF)<sup>52–53</sup> as method to decompose the bulk compressibility of solids into contributions from individual atomic basins. Their partitioning showed that *lone pair basins* are more compressible than *bonding basins*, while the atomic cores are rather incompressible and do not contribute to the bulk modulus. They also showed that it is only the outermost part of pressure active basins which is compressed as a consequence of the Pauli principle which prevents the mixing of the individual atomic basins. In the following we have used the ELF scalar field  $\eta(\mathbf{r})$  as a complement to the  $L(\mathbf{r})$  field to visualize electron localization domains and their compressibility behavior.<sup>54</sup>

Inspection of the  $\eta(\mathbf{r})$  and  $L(\mathbf{r})$  contour maps in the molecular  $\text{MC}_2$  plane (Figure 2 and 4), reveals that both scalar fields are homeomorphic in case of **3-Ti**. Hence, the pair of bonded charge concentrations on the Ti–C bond path in  $L(\mathbf{r})$  and the *trans*-LICC (Figure 2) which are an integral part of the *M–C* bond are reflected by the corresponding (3,–3) critical points in  $\eta(\mathbf{r})$  (Figure 4). Accordingly, the  $V(\text{Ti,C})$  localization domain represents a carbanionic lone pair while the maxima in the *M*-shell of titanium represent ligand-directed (LD) and ligand-opposed (LO) localization basins<sup>55</sup> which occur at somewhat larger radii than the corresponding BCC and *trans*-LICCs maxima in  $L(\mathbf{r})$ . This trend is obvious from the relative location of the  $L(\mathbf{r})$  and  $\eta(\mathbf{r})$  with respect to the zero-flux surface (for details, see S50–S53) and is a characteristic difference of both scalar fields.<sup>54</sup> Inspection of the  $\eta(\mathbf{r})$  maps of the **3-M** series shows that the magnitudes of the  $V(\text{Ti,C})$  domains is rather constant. Apparently, the localization degree of  $\eta(\mathbf{r}) > 0.92$  for the  $V(\text{Ti,C})$  maxima in **3-M** suggests that the carbanionic lone pair is highly localized.<sup>52</sup> The major difference in the  $\eta(\mathbf{r})$  topology along the *M–C* vector occurs, however, in the outermost core of the transition metals which are the *M*, *N* and *O* shell in **3-Ti**, **3-Zr** and **3-Hf**, respectively.<sup>56</sup> These maxima decrease continually in the series **3-Ti** ( $\eta(\mathbf{r})$

$= 0.86$ ) > **3-Zr** ( $\eta(\mathbf{r}) = 0.76$ ) > **3-Hf** ( $\eta(\mathbf{r}) = 0.53$ ). In the latter case (**3-Hf**) the degree of electron localization in the fifth shell is already low and close to the reference value in a region of electron gas-like behavior (Figure 4b).<sup>52</sup> Artificial shortening of the *M–C* bond (Figure 4c) shows that the outermost core domains and (to a lesser extent) the  $V(\text{Ti,C})$  domains are mainly affected and compressed by the imposed bond shortening. Furthermore, the compression of the outermost cores of the transition metal increases along the sequence series **3-Ti** < **3-Zr** < **3-Hf** in line with their decreasing degree of electron localization. Hence, the *M–C* bond compressibility is largest for **3-Hf** as a consequence of the low degree of electron localization in its outermost core. On contrast, **3-Ti** displays the least compressible *M–C* bond due to the high degree of electron localization at the ligand-directed maximum in its *M*-shell. Hence, Pauli-repulsion is severe between the LD maximum at titanium and the carbanionic lone pair  $V(\text{Ti,C})$  at carbon and hinders the compressibility of the Ti–C bond.

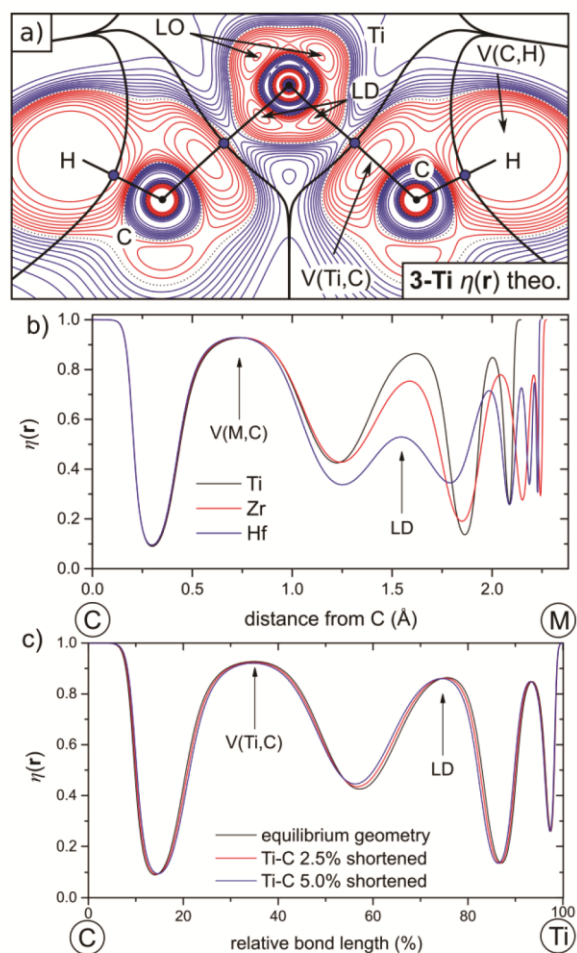


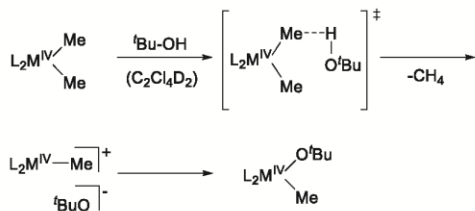
**Figure 4.** (a) ELF contour map in the  $\text{TiMe}_2$  plane of **3-Ti**. The dashed contour in  $\eta(\mathbf{r})$  has the value 0.50. Red/blue contours increase/decrease in steps of 0.05 away from the 0.5 contour line. The atomic boundaries, as determined by the zero-flux surface condition, and the BCPs are indicated by a black solid line and blue dots, respectively. The location of the  $V(\text{Ti,C})$  and  $V(\text{C,H})$  localization basins at carbon and the ligand-directed (LD) and ligand-opposed

(LO) localization basins in the  $M$ -shell of titanium are indicated by arrows. (b) ELF profile along the  $M$ –C bond path showing the decreasing degree of electron localization in the outermost core of the transition metal from 3-Ti to 3-Hf; (b) ELF profile along the Ti–C bond path of 3-Ti at the equilibrium geometry and in case of enforced bond shortening by 2.5 and 5% percent.

Inspection of the complementing  $L(r)$  maps (Figure 2 and S50-S53) reveals a similar picture: the domains of bonded charge concentrations (BCCs) in the valence shell of the metals  $M$  are diminishing in the series 3-Ti > 3-Zr > 3-Hf (and even disappear in the latter case) while the corresponding BCCs in the carbon's valence shell increase slightly in opposite order. Hence, Pauli repulsion between the two opposing BCCs along the Ti–C bond path is at a maximum in case of 3-Ti and significantly lower in case of 3-Zr. We therefore propose that the microscopic origin of the high compressibility of the Hf–C bond lies in its ionic characters which provides the lowest Pauli repulsion between the carbanionic BCCs at the methyl carbon atoms and the rather diffuse valence shell of charge concentration at the hafnium atom which is not even resolved in the  $L(r)$  maps.

Hence, the compressibility of a  $M$ –C bond depends not only on its (i) force constant but also on its (ii) ionicity, the (iii) magnitude of bonded charge concentration in the valence shell of the metal and carbon atom and (iv) the degree of electron localization in the carbanionic lone pair and in the outermost core of the metal atom which represents its effective valence shell.<sup>43</sup>

**Kinetic evaluation.** Electron density examination of the  $M$ –C bond disclosed different bond characteristics strongly dependent on the metal center. To clarify the relationship between the individual bond characteristics and the resulting chemical behavior, the crucial unit in the catalytic polymerization of olefins was examined kinetically. Therefore, the conversion of the  $M$ –C  $\sigma$ -bond was investigated in a model reaction with excess of <sup>1</sup>BuOH under pseudo first order conditions. The proposed transition state of Scheme 2 was supported by DFT-calculations (see Supporting Information, Chapter 23). Accordingly, the reaction with <sup>1</sup>BuOH was suggested to take place in a stepwise mechanism, since no hint for a concerted mechanism was observed. In this context, protonation of the methyl group occurs in the rate determining step, herein releasing methane during  $M$ –C bond cleavage. The subsequent step, which possesses no further energy barrier, involves the combination of both ions (<sup>1</sup>BuO<sup>−</sup> and the cationic complex fragment).



**Scheme 2.** Reaction of 3-Ti, 3-Zr and 3-Hf with 100 eq. <sup>1</sup>BuOH in C<sub>2</sub>Cl<sub>4</sub>D<sub>2</sub>.

Via <sup>1</sup>H NMR spectroscopy the  $M$ –(Me)<sub>2</sub> signal was detected following the concerted decay between 70 – 90 °C in steps of 5 °C for the reaction of 3-Ti, 3-Zr and 3-Hf (decay series and the logarithmic

plots are provided in the Supporting Information, Figure S13-S18). Side reactions of the complexes with the deuterated solvent as well as proton deuterium exchange reactions between <sup>1</sup>BuOH and the deuterated solvent were found to be negligible by reference experiments. The fastest reaction was observed for the zirconium complex, whereas the hafnium complex provoked the longest reaction times. These results were in line with our computational data (Supporting Information, Scheme S1), since the largest energy barrier was proposed for the hafnium analog.

Eyring plots based on the calculated rate constants ( $k$ ) at different temperatures exhibited a linear behavior (Supporting Information, Figure S19). Enthalpy ( $\Delta H^\ddagger$ ) and entropy ( $\Delta S^\ddagger$ ) of activation were determined *via* intercept and slope of the curves according to the linearized Eyring equation (1) for all three metal centers (Figure 5). Further required parameters are the Boltzmann constant  $k_B$ , the Planck constant  $h$  and the gas constant  $R$ .

$$\ln(k/T) = -\Delta H^\ddagger/R \cdot 1/T + \Delta S^\ddagger/R + \ln(k_B/h) \quad (1)$$

The titanocene complex exhibited the largest enthalpic contribution (93.3 (1.3) kJ/mol) to the activation barrier, while the entropy (−50.7 (3.7) J/(mol·K)) was rather subordinated. A similar trend was observed for the hafnocene complex possessing a high enthalpic impact (90.5 (0.7) kJ/mol) along with an entropic contribution of −67.9 (2.0) J/mol·K. In contrast, the zirconocene complex was rather entropically dominated (−112 (1.9) J/(mol·K)), whereupon the enthalpic input (+66.3 (0.7) kJ/mol) was the lowest of all three complexes.

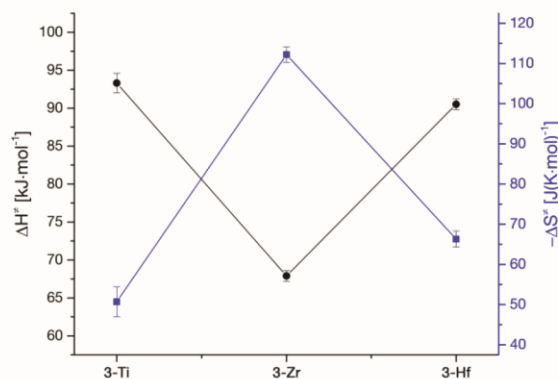


**Figure 5.** Enthalpic (black) and entropic (blue) contributions to the activation energy of  $M$ –C bond (Ti, Zr, Hf) conversion.

The results depicted in Figure 5 point out, that the required activation energy for the conversion of the  $M$ –C  $\sigma$ -bond is a combination of enthalpic and entropic contributions, which are heavily dependent on the chosen metal center. Regarding the overall activation barriers ( $\Delta G^\ddagger$ ), provided by the equation for the Gibbs free energy (2), 3-Hf possesses the highest activation energies at ambient conditions being about 11 kJ/mol higher compared to 3-Zr. The activation barriers for 3-Ti are determined in between the ones of 3-Hf and 3-Zr.

$$\Delta G^\ddagger = \Delta H^\ddagger - T \cdot \Delta S^\ddagger \quad (2)$$

In first approximation, the activation enthalpy may be connected to the  $M$ –C bond strength, or more precisely the bond enthalpy

D ( $M-C$ ), which needs to be compensated energetically in the transition state to disrupt the  $M-C$  bond. Accordingly, a continuous increase of the bond enthalpy is assumed going down the group IV elements ( $D(Hf_{IV}-C) > D(Zr_{IV}-C) > D(Ti_{IV}-C)$ ).<sup>57</sup> This ordering is in line with the general assumption, that the bond enthalpy of transition metal ligand interactions increase from 3d to 5d metals by a more sufficient orbital overlap and reduced d-d repulsion. It is also in accordance with experimental calorimetric determinations of the group IV  $M-C$  bond enthalpies  $D(M-C)$ .<sup>29-31</sup> Furthermore, the results of our charge density studies support the given ordering (*vide supra*) when considering the respective bond enthalpies by the Pauling equation (3) for polar covalent bonding. In this context, an accelerated ionic character of the  $M-C$  bond results in an increasing bond enthalpy.<sup>57</sup>

$$D_{M-C} = (D_{M-M} \cdot D_{C-C})^{0.5} + k|\chi_M - \chi_C| \quad (3)$$

In agreement with all these results for the  $M-C$  bond enthalpies, the kinetically determined activation enthalpy for the conversion of the  $Hf-C$  bond is significantly larger than the activation enthalpy that is necessary to convert the  $Zr-C$  bond. However, more puzzling is the obtained activation enthalpy for the conversion of the  $Ti-C$  bond, which cannot be exclusively explained by the corresponding bond enthalpy, since the kinetically determined enthalpic contribution to the activation barrier is significantly higher than expected. An additional impact may herein derive from the less polarized  $Ti-C$  bond, which amplifies the activation enthalpy in addition to the assumed impact of the corresponding bond enthalpy.

In accordance with Scheme 2 and the underlying DFT-calculations, the kinetically determined negative activation entropies for all metal centers confirm an associative reaction path. The entropy of activation is prevalently linked to vibrational, rotational and translational restrictions. The reaction with  $tBuOH$  was herein calculated to take place *via* protonation of the methyl group releasing methane after  $M-C$  bond cleavage in the rate determining step. In this context, the metal size possesses an essential role regarding vibrational, rotational and translational restrictions in the ground and transition state, mainly due to repulsive steric interactions. While the transition state for all complexes is considered to be a highly confined and constrained arrangement of both reactants with large restrictions in several degrees of freedom, the situation significantly differs in the ground state. Titanium possesses the smallest ionic radius, the smallest bond lengths around the metal center and the smallest bite angle, thereby provoking a larger content of vibrational, rotational and translational restrictions in the ground state. On the contrary, the restrictions are less explicit in the ground state for the hafnium and zirconium analog. Consequently, less energy is in turn required for the titanocene complex to get from a considerably restricted ground state to a highly restricted transition state. Accordingly, larger amounts of energy are necessary to transfer the hafnium and zirconium analog from the less restricted ground state to the highly restricted transition state. But the entropy of activation is not exclusively determined by the steric situation in the ground and transition state. We believe, that the electronic situation additionally influences the activation entropy. Regarding the examined reaction (Scheme 2), the  $M-C$  bond is cleaved in a heterolytic fashion. During this process charges must be separated completely. This process is certainly expressed by the enthalpic term, but vibrational modes can impact the dipol character of a bond as well. Additionally, the general electron distribution of the  $M-C$  bond reveals a crucial role.

In this context, the electron density determination of the  $M-C$  bond stated an increasing ionic character going down the group IV elements. Therefore, states of electron fluctuation, in which charge separation in the  $M-C$  bond is more distinct, are higher populated for hafnium and lower populated for zirconium and titanium. In the end, from an entropic point of view, decreasing amounts of energy are needed to separate charges in the process of  $M-C$  bond cleavage going down the group IV elements. Combining the electronic and steric contributions, both defining the term of activation entropy, the obtained differences (Figure 5) can be conveniently explained by the distinct impact of the ionic radius and the particular electronic situation of each  $M-C$  bond.

Pointed out by equation 2 the entropic content of the activation barrier is temperature dependent, whereupon the enthalpic one remains constant. Consequently, a different temperature dependent chemical behavior of  $M-C$  bond conversion is disclosed for **3-Ti**, **3-Zr** and **3-Hf**. A conversion of the  $Zr-(Me)_2$  groups is already feasible at lower temperatures, since the enthalpic barrier is low and the entropic one plays a more subordinated role. Due to a significantly higher enthalpic impact using **3-Ti** and **3-Hf**, the contribution to the overall activation energy is generally higher. When higher temperatures are adjusted, the entropic contribution to the activation barrier becomes particularly pronounced for **3-Zr**, whereas the one of **3-Hf** and **3-Ti** is considerably lower.

**Catalytic behavior.** The catalytic performance of **2-Hf**, focusing on varying ligand substitution patterns and its impact on the resulting polypropylene, was reported recently.<sup>33</sup> The synthesis and catalytic evaluation of **2-Ti** and **3-Ti**, including screening methods for proper catalyst activation, were also matter of recent publication.<sup>20</sup> In this contribution, the pure impact of the group IV metal center on the polymerization of propene is addressed in a comparative study using isostructural metallocenes of titanium, zirconium and hafnium (Table 2).

**2-Zr** and **2-Hf** were activated in two steps starting with an alkylation reaction of the bis-halogenated complexes using 200 eq. of triisobutylaluminum (TIBA) at 60 °C for one hour. Under the applied conditions the substitution reaction was monitored *via* UV VIS spectroscopy disclosing a shift of the absorbance maxima to lower wavelength (see supporting information, Figure S20-S21). The cationic, catalytically active species were generated *in situ* by the addition of 5 eq. of  $[Ph_3C][B(C_6F_5)_4]$ . The titanocene analog was found to be more suitably activated by elimination of the *in situ* alkylation step using the methylated titanocene complex (**3-Ti**) in combination with 5 eq. of  $[Ph_3C][B(C_6F_5)_4]$ .<sup>20</sup> The productivities of all three complexes are depicted in Figure 6.

Table 2. Condition and results for the polymerization of propene with complex 3-Ti, 2-Zr and 2-Hf in toluene.<sup>a</sup>

Entry	Complex	n <sup>b</sup>	p <sup>c</sup>	T <sub>p</sub> <sup>d</sup>	T <sub>m</sub> <sup>e</sup>	mmmm <sup>f</sup>	M <sub>w</sub> <sup>g</sup>	Đ <sup>h</sup>	P <sup>i</sup>
1 <sup>m</sup>	3-Ti	2	3	0	166	≥99	130	1.7	1300
2	3-Ti	2	4	30	165	≥99	44	1.9	420
3	3-Ti	2	4	50	159	≥99	30	2.7	200
4	3-Ti	5	4	70	149	74	11	8.7 <sup>k</sup>	50
5	3-Ti	5	4	90	126	37	10	9.6 <sup>k</sup>	60
6	3-Ti	5	4	110	-	-	-	-	0 <sup>j</sup>
7	2-Zr	1	3	0	166	≥99	990	1.8	14000
8	2-Zr	1	4	30	164	≥99	510	1.9	29000
9	2-Zr	1	4	50 <sup>j</sup>	162	≥99	240	2.2	36000
10	2-Zr	2	4	70	160	98	190	2.1	18000
11	2-Zr	5	4	90	151	96	29	1.9	2800
12	2-Zr	5	4	110	142	89	4.0	1.6	1100
13 <sup>m</sup>	2-Hf	2	3	0	164	≥99	1400	1.5	3200
14 <sup>m</sup>	2-Hf	2	4	30	163	≥99	970	1.5	15000
15 <sup>m</sup>	2-Hf	2	4	50	162	≥99	410	1.7	16000
16 <sup>m</sup>	2-Hf	2	4	70 <sup>j</sup>	154	93	120	1.7	47000
17 <sup>m</sup>	2-Hf	5	4	90 <sup>j</sup>	143	89	14	2.1	11000
18 <sup>m</sup>	2-Hf	5	4	110 <sup>j</sup>	122	76	3.5	1.7	7500

<sup>a</sup>t<sub>p</sub>: 30 min, V<sub>toluene</sub>: 300 mL, scavenger (TIBA): 2.2 mmol. <sup>b</sup>In micromoles. <sup>c</sup>p = p<sub>Ar</sub>+p<sub>propene</sub> in bar, p<sub>Ar</sub> = 1.3 bar. <sup>d</sup>T<sub>p</sub> in °C ± 2 °C. <sup>e</sup>T<sub>m</sub> in °C. <sup>f</sup>Determined via <sup>13</sup>C {<sup>1</sup>H} NMR spectroscopy assuming the enantiomorphic site model. <sup>g</sup>In kg mol<sup>-1</sup>. <sup>h</sup>Đ: M<sub>w</sub>/M<sub>n</sub>. <sup>i</sup>P in kg<sub>PP</sub>·[mol<sub>M</sub>·(mol/L)·h]<sup>-1</sup>. <sup>j</sup>T<sub>p</sub> in °C ± 5 °C. <sup>k</sup>Bimodal distribution. <sup>l</sup>No polymer was obtained. <sup>m</sup>According to Ref. <sup>33,20</sup>.

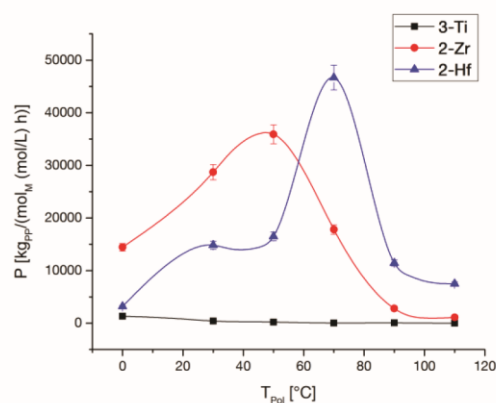


Figure 6. Spline representation of the productivities for complexes 3-Ti, 2-Zr and 2-Hf in the polymerization of propene (See Table 2 for details on reaction conditions).

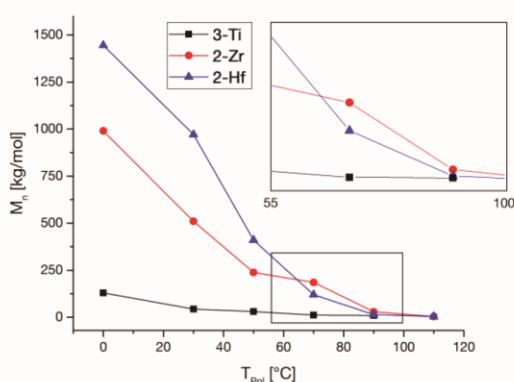
The activated zirconocene complex 2-Zr exhibited a remarkably high catalytic activity at low to moderate polymerization temperatures exceeding the ones of 2-Hf and 3-Ti. The largest productivity of 2-Zr was observed at temperatures of about 50 °C. The optimized polymerization conditions for the hafnocene complex in terms of catalytic activity were distinctly shifted to higher polymerization temperatures compared to 2-Zr. In this context, the hafnocene complex was by far the most productive one at temperatures exceeding ~60 °C. 3-Ti revealed an overall low catalytic activity compared to the other two metal centers. The highest productivities were observed at 0 °C, whereupon a continuous decrease was noticed with increasing polymerization temperature. This is in line with general

observations of titanocene complexes in the polymerization of olefins being rapidly deactivated at elevated temperatures, most likely by reduction of the metal center.<sup>19-20, 58-59</sup>

The first proposed mechanism for the catalytic polymerization of olefins by Cossee and Arlman,<sup>60-63</sup> complemented by consideration of stabilizing agostic interactions in the modified Green-Rooney mechanism<sup>64-65</sup> is nowadays commonly accepted.<sup>9</sup> After formation of the  $\pi$ -intermediate by olefin coordination to the cationic complex, the rate determining step proceeds *via* a four-center transition state. The described mechanism of chain propagation is also confirmed by several calculations regarding ordinary metallocene systems.<sup>23-24, 66-67</sup> In order to overcome the RDS barrier, the C=C bond of the monomer is prolonged, switching from  $\pi$ - to  $\sigma$ -donation, followed by the formation of new C–C and M–C single bonds and the disruption of the primary M–C  $\sigma$ -bond. In the process of M–C bond cleavage, the impact of different metal centers becomes particularly important. We have demonstrated that the influence of the M–C bond strength, a varying electronic situation in the  $\sigma$ -M–C bond and different sizes of the metal center are expressed in the individual chemical behavior of each unit by different enthalpic and entropic contributions to the activation barrier. Consequently, these differences also impact the catalytic behavior of the investigated group IV metallocenes regarding all processes involving M–C bond cleavage in the rate determining step.

2-Zr exhibited high catalytic activities at low to moderate polymerization temperatures in line with an overall lower enthalpic contribution to the RDS barrier. In contrary, 2-Hf needed higher temperatures to overcome the larger enthalpically driven energy barrier. High productivities were observed at elevated polymerization temperatures due to a generally lower entropic impact. At high polymerization temperatures the catalytic activity of 2-Zr suffers

from a high entropic contribution. Beside the increasing entropic factor for **2-Zr** applying high temperatures, **2-Hf** may also be considered more temperature stable than **2-Zr** making it better suitable for application at higher polymerization temperatures. The above mentioned side-reactions in the polymerization of propene with titanocene complexes severely limit a meaningful comparison to the Zr and Hf analog at this stage, since the essential reaction pathways for the deactivation of the  $Ti^{+IV}$ -species are not known.<sup>20</sup> The results of our kinetic investigation with **3-Ti** suggest a similar catalytic behavior to **3-Hf** at low polymerization temperatures (0 °C). Taking into consideration, that catalyst deactivation of **3-Ti** is distinctly accelerated upon rising the temperature, the intrinsic catalytic potential of titanocene complexes is, until now, far from being completely exhausted.



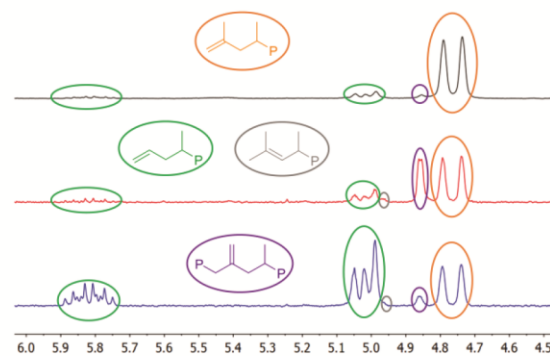
**Figure 7.** Molecular weight ( $M_n$ ) of polypropylene produced at different polymerization temperatures with complexes **3-Ti**, **2-Zr** and **2-Hf** (see Table 2 for details on reaction conditions).

Figure 7 illustrates a general decrease of the molecular weights with rising polymerization temperatures, since endothermal elimination pathways become more favored.<sup>66</sup> Decreasing monomer concentrations at elevated temperatures under isobar conditions herein additionally accelerate the reduction of the averaged chain lengths.<sup>68</sup> At low polymerization temperatures extraordinarily high molecular weights were obtained using catalyst **2-Hf** obviously exceeding those of **2-Zr**. If temperatures above 50 °C were applied, **2-Zr** was capable of producing longer polymer chains than **2-Hf**. The polypropylenes produced with **3-Ti** were significantly shorter compared to the ones of the Zr and Hf analogs under all applied conditions.

Essential for the length of an averaged polymer chain is the rate proportion of chain growth and chain release reactions. The most common chain release reactions under the applied conditions are known to be the  $\beta$ -hydride as well as the  $\beta$ -methyl elimination.<sup>20, 33</sup> The first one takes place *via* hydride transfer to the metal center or a coordinated monomer unit, going along with a cleavage of the  $M-C$   $\sigma$ -bond ending up with a  $\pi$ -coordinated polymeryl substituent. The polymer chain is set free after dissociation/associative displacement of the  $\pi$ -coordinated intermediate.<sup>23-24, 69-70</sup> The  $\beta$ -methyl elimination

proceeds quite similarly following a unimolecular mechanism of methyl transfer to the metal center.  $M-C$   $\sigma$ -bond disruption leads to the  $\pi$ -coordinated intermediate.<sup>71-76</sup> The major hurdle for both elimination pathways is of thermodynamic nature, since the conversion of double bonds to  $C-C$  single bonds during chain propagation is exothermic. From a kinetic point of view, the processes of  $M-C$  bond cleavage represent an essential energetic contribution to the rate determining step of both elimination pathways.<sup>67</sup> At low polymerization temperatures, a larger enthalpic contribution to the activation barrier facilitates the catalysis of longer averaged chain lengths. Therefore, the polypropylenes produced by the hafnocene catalyst possess distinctly higher molecular weights than the ones of the zirconium analog. Consequently, the 30 years legend of the “hafnium-effect” originates from a higher enthalpic contribution to the activation barrier in the case of  $M-C$  bond conversion. At elevated temperatures, the large entropic contribution to the activation barrier for **2-Zr** enables longer averaged chain lengths compared to the polymers of **2-Hf**. The presented temperature dependent differences in the molecular weights of polypropylenes produced with isostructural Zr- and Hf-complexes were already reported for other metallocene catalysts.<sup>15</sup> The analog findings support our presented theory that the observed trends of the molecular weights indeed arise from intrinsic differences in the  $M-C$  bonds, which are expressed by different enthalpic and entropic contributions to the activation barrier. The significantly shorter molecular weights using **3-Ti** are hardly comparable to the results of the group IV analogs. Unknown side reactions, which deactivate the catalytically active complexes, prevent a proper comparison at this point.

Investigation of the olefinic end group composition facilitated the determination and quantification of chain release reactions. Since complexes **2-Zr** and **2-Hf** were both capable of producing high molecular weight polypropylene, unsaturated end groups could only be identified *via*  $^1H$  NMR spectroscopy at high polymerization temperatures and low monomer concentrations (Figure 8).



**Figure 8.** Determination of olefinic end groups *via*  $^1H$  NMR spectroscopy (140 °C  $C_6D_5Br$ ) of polypropylene (entry 5, 11, 17;  $T_p = 90$  °C) catalyzed with **3-Ti** (black), **2-Zr** (red) and **2-Hf** (blue).

The most prominent olefinic end groups were vinylidene (Figure 8, orange) as well as allylic end groups (Figure 8, green) deriving from  $\beta$ -hydride and  $\beta$ -methyl elimination. Especially for **2-Zr** inter-

nal end groups (Figure 8, purple) as a result of allylic C–H bond activation were also observed. In low amounts internal end groups being generated by a cascade mechanism of elimination and reinsertion reactions (Figure 8, grey) were detected as well.<sup>15, 25, 77</sup> According to Figure 9, chain release using **3-Ti** almost exclusively proceeded *via*  $\beta$ -hydride elimination revealing the highest selectivity towards vinylidene endgroups of all three metal centers. The process of  $\beta$ -hydride elimination was also the most favored chain release reaction for **2-Zr**, whereupon **2-Hf** exhibited a predominant selectivity toward allylic end groups as a consequence of  $\beta$ -methyl elimination. An increase of the polymerization temperature from 90 °C to 110 °C under isobar conditions further accelerated the  $\beta$ -methyl elimination pathway for **2-Hf**. Under analog change of the polymerization conditions a significant decrease of internal end groups as a result of allylic C–H bond activation was observed with **2-Zr**, whereas all other chain release processes became more favored.

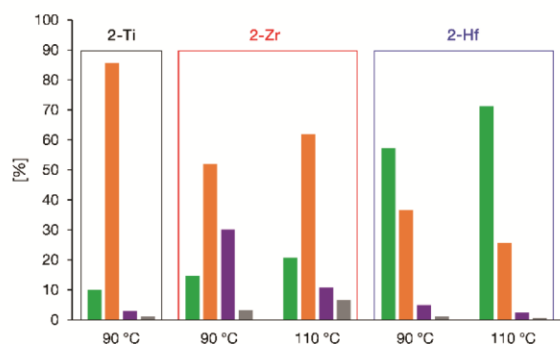


**Figure 9.** Olefinic end group composition with respect to the applied metal center (entry 5, 11-12, 17-18).

An accurate regio-chemistry is indispensable in the coordinative polymerization of propene to control the resulting polymer properties. Complexes **3-Ti**, **2-Zr** and **2-Hf** reveal a very concise regioselective behavior since neither 2,1-erythro nor 3,1 isomerization regio defects were detected *via* standard <sup>13</sup>C {<sup>1</sup>H} NMR spectroscopy (s. Experimental). The observed accurate regioselective behavior is in line with previous results of metallocenes bearing this rigid 2,4,7-substituted complex framework.<sup>14, 20, 33</sup>

The applied rigid metallocene framework is also responsible for the accurate stereoselectivity of **3-Ti**, **2-Zr** and **2-Hf** following the mechanism of enantiomorphic site control.<sup>78-80</sup> The tacticity was determined by the mole percentage ratio of the *mmmm*-pentad to the sum of all pentads. With respect to the signal to noise ratio the maximum isotacticity was determined to be at least 99% *mmmm*. Tacticities of the produced polypropylenes with all three complexes are provided in Figure 10. In the range of 0 - 50 °C only the *mmmm*-sequence is detectable indicating a precise stereoselective behavior of all three catalysts. Isolated stereo errors (*mmmr*, *mmrr*, *mrrm*), caused by the cascade reaction of chain end epimerization, were observed when the temperature was raised and the monomer concentration was lowered.<sup>20, 33</sup>

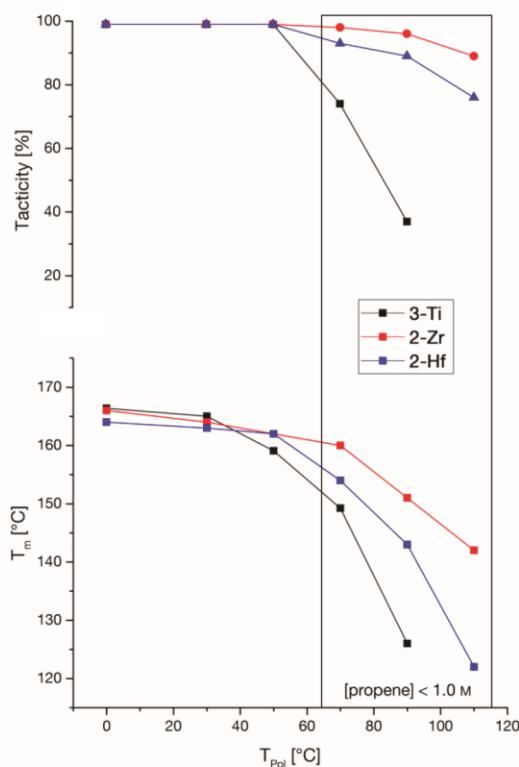


**Figure 10.** Tacticities (top) and melting transitions (bottom) of polypropylenes produced with complexes **3-Ti**, **2-Zr** and **2-Hf** (see Table 2 for details on reaction conditions).

The effect of metal exchange on the stereoselectivity became particularly obvious at elevated polymerization temperatures when epimerization occurred. At this juncture, the most accurate stereoselective behavior was observed with **2-Zr** followed by **2-Hf**, whereupon the one of **3-Ti** was most susceptible toward high temperatures. The process of chain end epimerization is known to occur *via* a cascade reaction of  $\beta$ -hydride elimination, rotation and unspecific reinsertion.<sup>81-83</sup> The elimination steps in the epimerization process are herein identified to be rate determining. Consequently, the M–C bond also constitutes an essential role regarding the stereochemistry of our isostructural group IV metallocene catalysts. At elevated temperatures the entropic contribution to the activation barrier becomes progressively important. Consequently, less epimerization takes place for the zirconocene catalyst leading to an improved stereoregularity of in the respective polymers. For the catalysis with **2-Hf** and **3-Ti**, comprising less pronounced entropic terms to the activation energy, epimerization is accelerated at high polymerization temperatures.

The melting behavior of polypropylenes is predominantly influenced by the stereo- and regioregularity of the polymer samples (Figure 10). Additionally, the molecular weight possesses an important role in the case of overall short chain lengths.<sup>84</sup> Accordingly, melting transition of polymers produced at high temperatures with **2-Zr** outperformed the ones of **2-Hf** and **3-Ti**, due to higher stereoselectivities. The melting points of the polypropylenes produced at 90 °C and 110 °C revealed additional influence of the averaged chain length beside the present tacticity. At low temperatures **3-Ti** tended to produce polymers comprising the highest melting transitions. This may be explained by the significantly lower molecular weights enabling faster rearrangement of the polymer chains under the adjusted conditions of the DSC-measurements.<sup>34,85</sup>

## CONCLUSION

The present report addresses the impact of varied group IV metal centers in isostructural complexes on fundamental metallocene chemistry. In this context, the electronic *M*–C bond properties were examined together with the kinetic behavior and the catalytic abilities in the polymerization of propene. All investigations were based on a *C*<sub>2</sub>-symmetric –SiMe<sub>2</sub>- bridged (2-methyl-4-[(3',5'-Me)-phenyl]-7-methoxy) substituted bisindenyl metallocene complex framework representing the state of the art catalyst class for high melting, high molecular weight <sup>3</sup>PP.

The first part of this multidisciplinary study discloses the electron density distribution of the *M*–C (methyl)  $\sigma$ -bond by high resolution single-crystal X-ray diffraction analysis. Processing of theoretical and experimentally derived data suggested significant differences in the group IV *M*–C bonding situation. While the Ti–C bond possesses substantial covalent character, the Hf–C bond is mainly determined by ionic interactions. Single-crystal X-ray diffraction analysis additionally disclosed a severely different behavior of the Zr–C and Hf–C bond under increasing external pressure. Whereas the more covalent Zr–C bond is hardly compressible, the distance of the ionic Hf–C bond is considerably reduced, if an external force is applied.

To elucidate the impact of varying *M*–C bond characteristics on the actual chemical behavior, *M*–C bond conversion was investigated kinetically in the second part. All three methylated complex were examined in a model reaction with <sup>1</sup>BuOH under conditions pseudo first order at varying temperatures. Provided by the Eyring equation, enthalpic and entropic contributions to the activation energy were determined. The obtained results suggested an enthalpically dominated activation barrier for the conversion of the Ti–C and Hf–C bond, while the activation enthalpy of the Zr analog was significantly lower. A more explicit ionic character of the Hf–C compared to the Zr–C bond is therefore made responsible, whereas the activation enthalpy for the Ti–C bond conversion may additionally be amplified by the high covalent content of this bond. Steric interactions, leading back to different sizes of the metal centers as well as varying *M*–C bond polarization, were identified to determine the individual entropic contributions to the activation energy.

The third part of our multidisciplinary study addresses the catalytic behavior of isostructural metallocenes in the polymerization of propene. In this context, the catalyst activity and the main polymer characteristics were correlated to essential sub-processes within the

whole polymerization process, all comprising *M*–C bond disruption in the rate determining step. As a result, the hafnocene complex was the most active one at elevated polymerization temperatures and revealed the highest molecular weights of all three complexes at low polymerization temperatures. Both findings originate in the large enthalpic contribution to the activation barrier and elucidate the “hafnium-effect” when addressing extraordinarily high molecular weight polymers. On the contrary, the maximum productivity of the zirconocene catalyst was already reached at moderate temperatures, which was in line with a significantly lower enthalpic contribution. Regarding the stereoregularity at elevated polymerization temperatures and low monomer concentrations, the zirconocene complex outperformed the Ti and Hf analogs. This observation is a result of the large entropic contribution to the activation barrier thereby sufficiently suppressing undesired chain end epimerization.

Examination of the electron density of the *M*–C bond in isostructural group IV metallocenes represents the first experimental contribution disclosing fundamental differences in the electronic composition of this crucial moiety. Additional investigation of the particular kinetic characteristics facilitated the direct correlation between varying electronic binding situations and the individual chemical behavior. As a consequence, typical peculiarities applying zirconium and hafnium in the coordinative polymerization of olefins can be clearly explained, verifying the 30 years legend of different Zr–C and Hf–C bond strengths in metallocene catalysis.

## EXPERIMENTAL SECTION

**General.** All reactions containing air- and moisture-sensitive compounds were performed under argon atmosphere using standard Schlenk or glovebox techniques. All chemicals, unless otherwise stated, were purchased from Aldrich, Acros or VWR and used as received. Dry toluene, *n*-pentane, and dichloromethane were obtained from an MBraun MB-SPS-800 solvent purification system. Dry *n*-hexane was obtained by distillation of a solvent/so-dium/benzophenone mixture. Deuterated benzene was dried over 3 Å molecular sieve; deuterated dichloromethane and tetrachloroethane were refluxed over CaH<sub>2</sub> and distilled prior to use. Propene (99.5% by Westfalen AG) was purified by passage through two columns filled with BASF catalyst (R3-11) and molecular sieve 3-4 Å. Elemental analysis were conducted with a EURO EA (HEKA tech) instrument equipped with a CHNS combustion analyzer.

<sup>1</sup>H and <sup>13</sup>C {<sup>1</sup>H} NMR measurements were recorded on a Bruker ARX-300, AV-400, AV-500C or AV-500 spectrometer at ambient temperature, unless otherwise stated. Chemical shifts  $\delta$  are reported in ppm relative to tetramethylsilane and calibrated to the residual <sup>1</sup>H or <sup>13</sup>C signal of the deuterated solvent. Polymer spectra were measured with an ARX-300 spectrometer at 140 °C in bromobenzene-*d*<sub>5</sub> with 50-60 mg/mL.

Gel permeation Chromatography (GPC) was performed with a PL-GPC 220 instrument equipped with 2 × Olexis 300 × 7.5 mm columns and triple detection *via* differential refractive index detector, PL-BV 400 HT viscometer and light scattering (Precision Detectors Model 2040; 15°, 90°). Measurements were performed at 160 °C using 1,2,4-trichlorobenzene (TCB; 30 mg BHT/L) with a constant flow rate of 1 mL/min and a calibration set with narrow

MWD polystyrene (PS) and polyethylene (PE) standards. Samples were prepared dissolving 0.9–1.1 mg polymer in 1.0 mL stabilized TCB for 10–15 min at 160 °C immediately before each measurement.

Differential Scanning Calorimetry (DSC) analysis was conducted on a DSC Q2000 instrument. 3–8 mg of the polymer were sealed into a DSC aluminum pan and heated from 20 °C to 200 °C with 10 °C/min. After holding the temperature for 2 min the sample was cooled down to 20 °C with 10 °C/min and heated up again in the same manner. The reported values are those determined in the second heating cycle.

**Synthesis.** Synthesis procedures and characterization of all new compounds are provided in the supporting information. The synthesis of ligand **1**, complex **2-Hf**, **2-Ti** and **3-Ti** were conducted according to literature known procedures.<sup>14, 20, 33</sup>

**NMR-kinetics.** Reactions pseudo first order of complex **3-Ti**, **3-Zr** and **3-Hf** (3.0 μmol, 1.0 eq.) with 100 eq. of <sup>t</sup>BuOH in 0.5 mL C<sub>2</sub>Cl<sub>4</sub>D<sub>2</sub> were measured on Bruker ARX-300 spectrometer at elevated temperatures. All components were added into a J. Young valve NMR tube at room temperature in the glovebox. The NMR tube was subsequently lifted into the preheated spectrometer and spectra were recorded following the concerted decay of the M–(Me)<sub>2</sub>-signal after the temperature was adjusted (±0.1 °C).

**X-ray Diffraction and Multipolar Refinements.** For all four compounds an Independent Atom Model (IAM) refinement was carried out using SHELXL.<sup>86–87</sup>

Crystal Data for **3-Ti**:  $M_r = 660.79$ ,  $T = 100$  K,  $\lambda$  (Mo,  $K_{\alpha}$ ) = 0.71073 Å, orange rhombus 0.373 × 0.217 × 0.159 mm<sup>3</sup>, monoclinic space group  $C2/c$ ,  $a = 25.970(3)$  Å,  $b = 9.8085(10)$  Å,  $c = 18.2911(19)$  Å,  $\beta = 133.594(2)^\circ$ ,  $V = 3374.4(6)$  Å<sup>3</sup>,  $Z = 4$ ,  $F(000) = 1408$ ,  $D_{\text{calcd}} = 1.301$  g/cm<sup>3</sup>,  $\mu = 0.326$  mm<sup>-1</sup>, total/unique reflections: 213626/ 16548, completeness 99.8 %,  $2.356^\circ < \theta < 48.532^\circ$ ,  $\sin(\theta_{\text{max}})/\lambda = 1.054$  Å<sup>-1</sup>,  $R_1 = 2.67$  %,  $wR_2 = 8.81$  %,  $Goof = 1.065$ , residual density: 0.728/-0.355 e/Å<sup>3</sup> for 14574 reflections  $I > 2\sigma(I)$ .

Crystal Data for **3-Zr**:  $M_r = 704.11$ ,  $T = 100$  K,  $\lambda$  (Mo,  $K_{\alpha}$ ) = 0.71073 Å, yellow rhombus 0.491 × 0.244 × 0.124 mm<sup>3</sup>, monoclinic space group  $C2/c$ ,  $a = 26.3358(10)$  Å,  $b = 9.8386(4)$  Å,  $c = 18.4303(13)$  Å,  $\beta = 134.1270(10)^\circ$ ,  $V = 3427.8(3)$  Å<sup>3</sup>,  $Z = 4$ ,  $F(000) = 1480$ ,  $D_{\text{calcd}} = 1.364$  g/cm<sup>3</sup>,  $\mu = 0.392$  mm<sup>-1</sup>, total/unique reflections: 257387/18486, completeness 98.7 %,  $2.334^\circ < \theta < 50.938^\circ$ ,  $\sin(\theta_{\text{max}})/\lambda = 1.093$  Å<sup>-1</sup>,  $R_1 = 2.16$  %,  $wR_2 = 6.52$  %,  $Goof = 1.052$ , residual density: 1.276/-0.385 e/Å<sup>3</sup> for 16489 reflections  $I > 2\sigma(I)$ .

Crystal Data for **3-Hf**:  $M_r = 791.38$ ,  $T = 100$  K,  $\lambda$  (Mo,  $K_{\alpha}$ ) = 0.71073 Å, yellow rhombus 0.222 × 0.168 × 0.138 mm<sup>3</sup>, monoclinic space group  $C2/c$ ,  $a = 26.2522(9)$  Å,  $b = 9.8608(3)$  Å,  $c = 18.4145(6)$  Å,  $\beta = 134.0260(10)^\circ$ ,  $V = 3427.5(2)$  Å<sup>3</sup>,  $Z = 4$ ,  $F(000) = 1608$ ,  $D_{\text{calcd}} = 1.534$  g/cm<sup>3</sup>,  $\mu = 3.12$  mm<sup>-1</sup>, total/unique reflections: 283251/ 19718, completeness 99.5 %,  $2.330^\circ < \theta < 52.327^\circ$ ,  $\sin(\theta_{\text{max}})/\lambda = 1.114$  Å<sup>-1</sup>,  $R_1 = 1.77$  %,  $wR_2 = 4.40$  %,  $Goof = 1.101$ , residual density: +4.226/-0.973 e/Å<sup>3</sup> for 18382 reflections  $I > 2\sigma(I)$ .

Crystal Data for **2-Zr**:  $M_r = 744.95$ ,  $T = 123$  K,  $\lambda$  (Mo,  $K_{\alpha}$ ) = 0.71073 Å, red rhombus 0.557 × 0.271 × 0.204 mm<sup>3</sup>, monoclinic space group  $C2/c$ ,  $a = 26.275(4)$  Å,  $b = 9.7814(12)$  Å,  $c = 18.385(2)$  Å,  $\beta = 133.821(12)^\circ$ ,  $V = 3409.2(10)$  Å<sup>3</sup>,  $Z = 4$ ,  $F(000) = 1544$ ,  $D_{\text{calcd}}$

= 1.451 g/cm<sup>3</sup>,  $\mu = 0.55$  mm<sup>-1</sup>, total/unique reflections: 43478/4056, completeness 99.9%,  $3.07^\circ < \theta < 27.87^\circ$ ,  $\sin(\theta_{\text{max}})/\lambda = 0.658$  Å<sup>-1</sup>,  $R_1 = 2.38$  %,  $wR_2 = 6.10$  %,  $Goof = 1.079$ , residual density: +0.379/-0.251 e/Å<sup>3</sup> for 3748 reflections  $I > 2\sigma(I)$ .

A multipole model was then adopted to describe the aspherical charge density deformation of  $\rho(\mathbf{r})$  for **3-Ti**, **3-Zr** and **3-Hf**. The deformation density was described by a multipole model<sup>88</sup> based on products of spherical harmonics multiplied with Slater-type radial functions with energy-optimized exponents and using the XD program<sup>89</sup> Topological analyses of the experimental density was accomplished in the framework of the quantum theory of atoms in molecules (QTAIM<sup>37</sup>). The final agreement factors were  $R_1 = 1.91$  [1.50] {1.42}% and  $wR_2 = 3.25$  [2.37] {2.26}% for 14917 [16879] {18591} reflections ( $F_o > 3\sigma(F_o)$ ) and 461 [486] {473} parameters ( $N_{\text{ref}}/N_{\text{var}} = 32.4$  [34.7] {39.3}), while the residual electron density distribution was almost featureless with the exception of **3-Hf** with the minimum and maximum values of +0.212/-0.200 [+0.268/-0.188] {+0.907/-0.424} e/Å<sup>3</sup> ( $\sin(\theta/\lambda) < 0.8$  Å<sup>-1</sup>), for **3-Ti**, [**3-Zr**] and [**3-Hf**], respectively. Further details are provided in the Supporting Information Chapter 12–18 and CCDC XX (**3-Ti**), XX (**3-Zr**), XX (**3-Ti**) and XX (**2-Zr**) contain the supplementary crystallographic data for this paper. These data can be obtained free of charge from The Cambridge Crystallographic Data Centre via:

www.ccdc.cam.ac.uk/data\_request/cif.

**High-Pressure X-ray Diffraction.** A modified Merrill-Bassett diamond anvil cell (DAC) was applied in case of **3-Hf** to vary the pressure between 0 and 4.0(1) GPa.<sup>90–91</sup> A Boehler-Platte DAC was employed for **3-Zr** to investigate the pressure range of 0 to 3.0(1) GPa.<sup>92</sup> The DACs were equipped with conical type Boehler anvils with a culet diameter of 600 μm.<sup>93</sup> In both cases stainless-steel gaskets pre-indented to 80 μm were employed and the borehole varied between 270 μm (**3-Zr**) and 280 μm (**3-Hf**). Each pressure chamber was loaded in an Ar-glovebox with a plate-like single crystal, three ruby spheres and Daphne 7575, which served as pressure transmitting medium (hydrostatic limit: 3.9–4.0 GPa).<sup>94</sup> The dimensions of the single crystals were 140 × 110 × 40 μm<sup>3</sup> (**3-Zr**) and 130 × 120 × 40 μm<sup>3</sup> (**3-Hf**). The pressure was determined by the ruby fluorescence method.<sup>95</sup>

Intensity data of **3-Hf** were collected on a Bruker D8 goniometer equipped with an APEX2 CCD-detector and a mirror-focused Ag  $K_{\alpha}$  source ( $\lambda = 0.56087$  Å). Intensity data collection of **3-Zr** was conducted at the XS04-material science beamline of the Swiss Lightsource (SLS) of the Paul Scherrer Institute, Switzerland.<sup>96–97</sup> The precise wavelength of the monochromatic synchrotron beam ( $\lambda = 0.56087$  Å) was calibrated by collection of the NIST SRM 660a standard and a refinement of the lattice parameters of LaB<sub>6</sub>. A Detris 6M was employed as detector.

For both compounds the collected frames were imported in the CrysAlis<sup>Pro</sup> software for indexing and data reduction steps including an empirical absorption correction with the implemented SCALE3 ABSPACK module.<sup>98</sup> The evolution of the cell parameters with pressure as well as the results of the structure refinements via SHELXL are listed in Table S8\* and S9\* in the Supporting Information.<sup>87</sup> The

relevant data and refinement results can be found in the supplementary crystallographic data CCDC XX to XX. These data can be obtained free of charge from The Cambridge Crystallographic Data Centre via [www.ccdc.cam.ac.uk/data\\_request/cif](http://www.ccdc.cam.ac.uk/data_request/cif). More detailed information regarding the HP single crystal diffraction experiments and the pressure dependency of the crystal structures of **3-Hf** and **3-Hf** are given in the Supporting Information

**Computational Details.** The geometries of **3-Ti**, **3-Zr** and **3-Hf** have been optimized with ADF<sup>99-101</sup> at the BP86-level of theory in combination with an all-electron TZ2P basis set<sup>102</sup> and the ZORA<sup>103-105</sup> Hamiltonian to describe scalar relativistic effects. The local C<sub>2</sub>-symmetry was kept throughout all calculations and the minimum of the potential energy surface has been verified by calculating vibrational frequencies. The analysis of the electron density in the framework of the QTAIM was carried out with ADF<sup>106-107</sup>.  $L(\mathbf{r})$  maps were calculated with DenProp<sup>108</sup>, while the bond paths, MO maps,  $\eta(\mathbf{r})$  maps and  $\eta(\mathbf{r})$  lines were determined with DGrid<sup>109</sup>, zero flux surfaces were determined with critic2 (git commit 25e6df9)<sup>110-111</sup>.

The theoretical support of the kinetical measurements have been performed with the Gaussian09 suite<sup>112</sup> of programs. The pure density functional BP86<sup>113-114</sup> together with the TZVP<sup>115</sup> basis set for all atoms except Zr and Hf have been used. The latter ones were described with a LANL2DZ-ECP<sup>116</sup>. Dispersion effects were correlated with Grimme's GD3BJ<sup>117</sup> algorithm, while solvation effects (tetrachloroethane) were introduced using the PCM<sup>118</sup> formalism. All reported energies are  $\Delta G$  values (kJ/mol) relative to the starting material in solution at 298.15 K.

**Polymerization.** All polymerization reactions were performed in a 1.1 L Büchi steel autoclave equipped with a paddle agitator, temperature sensor and a heating/cooling jacket attached to a cryo-/thermostat unit (Thermo Scientific HAAKE DynaMax). Ar-pressure for all manipulations was set on 1.3 bar. Prior to the polymerization the autoclave was equipped with 300 mL of dry toluene and 2.0 mL of 1.1 M TIBA solution in toluene and heated up to 90 °C. After maintaining the temperature for 15 min the scrubbing solution was released. For the polymerization reaction the autoclave was charged with 280 mL of dry toluene and 2.0 mL of 1.1 M TIBA solution in toluene. The metallocene complex (1.0 eq., **3-Ti**, **2-Zr** or **2-Hf**) was dissolved in 10 mL toluene and preactivated with 200 eq. of TIBA at 60 °C for 1 h (**3-Ti** is just dissolved in 10 mL toluene). After the desired temperature was adjusted the activated metallocene solution was transferred into the autoclave and was pressurized with propene. When the system was equilibrated and stable the polymerization was started adding 5.0 eq. of [Ph<sub>3</sub>C][B(C<sub>6</sub>F<sub>5</sub>)<sub>4</sub>], dissolved in 10 mL of toluene, to the autoclave via a pressure burette ( $p_{\text{pol}} + 1.0$  bar). The propene consumption was monitored using a gas flow meter (Bronkhorst F-111C-HA-33P). Temperature, pressure, time and total propene consumption were recorded as well. The polymerization reaction was quenched with 2.0 mL of methanol and the reaction mixture was poured into 1.0 L acidified methanol. Precipitated polymer was removed from the autoclave and all combined polymer was washed exhaustively and dried at 70 °C *in vacuo* overnight.

## ASSOCIATED CONTENT

### Supporting Information.

Synthesis procedures of new compounds, <sup>1</sup>H NMR and <sup>13</sup>C {<sup>1</sup>H} NMR spectra of all key compounds **1-3**, kinetic measurements, UV VIS spectra, <sup>13</sup>C {<sup>1</sup>H} NMR spectra of polypropylenes for tacticity determination, <sup>1</sup>H NMR spectra of polypropylenes for olefinic end group determination, SC-XRD and high-pressure SC-XRD data including theoretical processing and computational data of the kinetic investigation (coordinates, absolute energies).

This material is available free of charge via the Internet at <http://pubs.acs.org>.

## AUTHOR INFORMATION

### Corresponding Author

\* E-mail: [rieger@tum.de](mailto:rieger@tum.de). Tel.: +49-89-289-13570. Fax: +49-89-289-13562

### Notes

The authors declare no competing financial interest.

## ACKNOWLEDGMENT

We are exceptionally grateful to the WACKER Chemie AG for continued financial support. The authors thank Philipp Pahl and Daniel Wendel for proofreading the manuscript and valuable discussions.

## REFERENCES

1. Natta, G.; Pino, P.; Mazzanti, G.; Giannini, U., *J. Am. Chem. Soc.* **1957**, *79*, 2975-2976.
2. Breslow, D. S.; Newburg, N. R., *J. Am. Chem. Soc.* **1957**, *79*, 5072-5073.
3. Ziegler, K.; Holzkamp, E.; Breil, H.; Martin, H., *Angew. Chem.* **1955**, *67*, 541-547.
4. Natta, G., *Angew. Chem.* **1956**, *68*, 393-403.
5. Sinn, H.; Kaminsky, W.; Vollmer, H.-J.; Woldt, R., *Angew. Chem., Int. Ed.* **1980**, *19*, 390-392.
6. Kaminsky, W.; Miri, M.; Sinn, H.; Woldt, R., *Makromol. Chem., Rapid Commun.* **1983**, *4*, 417-421.
7. Kaminsky, W.; Külper, K.; Brintzinger, H. H.; Wild, F. R. W. P., *Angew. Chem., Int. Ed.* **1985**, *24*, 507-508.
8. Ewen, J. A.; Haspelslach, L.; Atwood, J. L.; Zhang, H., *J. Am. Chem. Soc.* **1987**, *109*, 6544-6545.
9. Resconi, L.; Cavallo, L.; Fait, A.; Piemontesi, F., *Chem. Rev.* **2000**, *100*, 1253-1345.
10. Baier, M. C.; Zuideveld, M. A.; Mecking, S., *Angew. Chem., Int. Ed.* **2014**, *53*, 9722-9744.
11. Bochmann, M., *Organometallics* **2010**, *29*, 4711-4740.
12. Rieger, B.; Troll, C.; Preuschen, J., *Macromolecules* **2002**, *35*, 5742-5743.
13. Busico, V.; Cipullo, R.; Pellicchia, R.; Talarico, G.; Razavi, A., *Macromolecules* **2009**, *42*, 1789-1791.
14. Schöbel, A.; Herdtweck, E.; Parkinson, M.; Rieger, B., *Chem.-Eur. J.* **2012**, *18*, 4129-4129.
15. Schöbel, A.; Lanzinger, D.; Rieger, B., *Organometallics* **2013**, *32*, 427-437.
16. Bryliakov, K. P.; Talsi, E. P.; Voskoboynikov, A. Z.; Lancaster, S. J.; Bochmann, M., *Organometallics* **2008**, *27*, 6333-6342.
17. Kaminsky, W.; Engehausen, R.; Zoumis, K.; Spaleck, W.; Rohrmann, J., *Makromol. Chem.* **1992**, *193*, 1643-1651.
18. Razavi, A.; Peters, L.; Nafpliotis, L., *J. Mol. Catal. A: Chem.* **1997**, *115*, 129-154.

19. Bryliakov, K. P.; Babushkin, D. E.; Talsi, E. P.; Voskoboinikov, A. Z.; Gritzko, H.; Schröder, L.; Damrau, H.-R. H.; Wieser, U.; Schaper, F.; Brintzinger, H. H., *Organometallics* **2005**, *24*, 894-904.
20. Machat, M. R.; Jandl, C.; Rieger, B., *Organometallics* **2017**, *36*, 1408-1418.
21. Deisenhofer, S.; Feifel, T.; Kukral, J.; Klinga, M.; Leskelä, M.; Rieger, B., *Organometallics* **2003**, *22*, 3495-3501.
22. Machat, M. R.; Lanzinger, D.; Drees, M.; Altmann, P. J.; Herdtweck, E.; Rieger, B., *Macromolecules* **2018**, *51*, 914-929.
23. Laine, A.; Linnolahti, M.; Pakkanen, T. A.; Severn, J. R.; Kokko, E.; Pakkanen, A., *Organometallics* **2010**, *29*, 1541-1550.
24. Laine, A.; Linnolahti, M.; Pakkanen, T. A.; Severn, J. R.; Kokko, E.; Pakkanen, A., *Organometallics* **2011**, *30*, 1350-1358.
25. Resconi, L.; Piemontesi, F.; Franciscano, G.; Abis, L.; Fiorani, T., *J. Am. Chem. Soc.* **1992**, *114*, 1025-1032.
26. Shannon, R. D.; Prewitt, C. T., *Acta Crystallogr. B* **1969**, *25*, 925-946.
27. Shannon, R., *Acta Crystallogr. A* **1976**, *32*, 751-767.
28. Reiher, M.; Wolf, A., *Relativistic Quantum Chemistry - The Fundamental Theory of Molecular Science*, Wiley, 2nd Edition, **2015**, p. 623.
29. Schock, L. E.; Marks, T. J., *J. Am. Chem. Soc.* **1988**, *110*, 7701-7715.
30. Dias, A. R.; Salema, M. S.; Martinho Simões, J. A.; Pattiasina, J. W.; Teuben, J. H., *J. Organomet. Chem.* **1988**, *346*, C4-C6.
31. Simoes, J. A. M.; Beauchamp, J. L., *Chem. Rev.* **1990**, *90*, 629-688.
32. While the given bond enthalpies of Hf–C and Zr–C constitute an average of the first and second metal-methyl cleavages, the given bond enthalpy of Ti–C exclusively refers to the first metal-methyl cleavage.
33. Machat, M. R.; Lanzinger, D.; Pöthig, A.; Rieger, B., *Organometallics* **2017**, *36*, 399-408.
34. Tranchida, D.; Mileva, D.; Resconi, L.; Rieger, B.; Schöbel, A., *Macromol. Chem. Phys.* **2015**, *216*, 2171-2178.
35. Shaltout, R. M.; Corey, J. Y.; Rath, N. P., *J. Organomet. Chem.* **1995**, *503*, 205-212.
36. Moehring, P. C.; Coville, N. J., *Coord. Chem. Rev.* **2006**, *250*, 18-35.
37. Bader, R. F. W., *Atoms in Molecules - A Quantum Theory*, Clarendon Press Oxford, **1994**.
38. Bader, R. F. W.; MacDougall, P. J.; Lau, C. D. H., *J. Am. Chem. Soc.* **1984**, *106*, 1594-1605.
39. Scherer, W.; Sirsch, P.; Grosche, M.; Spiegler, M.; Mason, S. A.; Gardiner, M. G., *Chemical Communications* **2001**, 2072-2073.
40. Scherer, W.; Sirsch, P.; Shorokhov, D.; McGrady, G. S.; Mason, S. A.; Gardiner, M. G., *Chem. Eur. J.*, **2002**, *8*, 2324-2334.
41. Scherer, W.; Sirsch, P.; Shorokhov, D.; Tafipolsky, M.; McGrady, G. S.; Gullo, E., *Chem. Eur. J.*, **2003**, *9*, 6057-6070.
42. McGrady, G. S.; Downs, A. J.; Bednall, N. C.; McKean, D. C.; Thiel, W.; Jonas, V.; Frenking, G.; Scherer, W., *J. Phys. Chem. A* **1997**, *101*, 1951-1968.
43. Bader, R. F. W.; Gillespie, R. J.; Martin, F., *Chemical Physics Letters*, **1998**, *290*, 488-494.
44. McGrady, G. S.; Haaland, A.; Verne, H. P.; Volden, H. V.; Downs, A. J.; Shorokhov, D.; Eicklerling, G.; Scherer, W. *Chem. Eur. J.*, **2005**, *11*, 4921-4934.
45. Brown, I. D.; Klages, P.; Skowron, A., *Acta Cryst. B*, **2003**, *59*, 439-448.
46. Liu, A. Y.; Cohen, M. L., *Science*, **1989**, *245*, 841-842.
47. This relationship has been coined into an empirical formula where the bulk modulus  $B = (19.71 + 220) \times d^{-3.5}$  increases with decreasing bond distance  $d$  (as a measure of the bond strength) and decreasing bond ionicity.
48. Solution calorimetric studies by T. Marks and coworker have determined the individual bond dissociation energies  $D_1(M-C) - D_2(M-C)$  for the methyl complexes  $(C_5Me_5)MMe_3$  ( $M = Zr, Hf$ ). All three individual Hf-C bond enthalpies were larger than the corresponding Zr-C bond enthalpies. However, the differences of the respective  $D(Hf-C)$  and  $D(Zr-C)$  values were rather small (0.1 - 6.8%); Schock, L.E.; Marks, T.J., *J. Am. Chem. Soc.* **1988**, *110*, 7701-7715.
49. The isolated (M–C) stretching frequencies of **3-M** were computed by fitting the M–C potential energy surface (PES) with the harmonic oscillator model. (See, the Supporting Information S\* for further information).
50. Arne Haaland, *Molecules and Models*, Oxford, **2007**, p. 69.
51. Contreras-García, J.; Mori-Sánchez, P.; Silvi, B.; Recio, J. M., *J. Chem. Theory Comput.* **2009**, *5*, 2108-2114.
52. Becke, A. D. & Edgecombe, K. E., *J. Chem. Phys.*, **1990**, *92*, 5397-5403.
53. Silvi, B.; Savin, A., *Nature* **1994**, *371*, 683-686.
54. Bader, R. F. W.; Johnson, S.; Tang, T. H.; Popelier, P. L. A., *J. Am. Chem. Soc.*, **1996**, *118*, 15398-15415.
55. Gillespie, R. J.; Noury, S.; Pilmé, J.; Silvi, B., *Inorg. Chem.* **2004**, *43*, 3248-3256.
56. We, note, that only in case of **3-Ti** ligand-directed maxima (denoted LD in Figure 4) occur in the M-shell of titanium. In case of **3-Zr** and **3-Hf** solely four ligand-opposed (LO) maxima occur in the outermost core shell of the respective metal atoms.
57. Uddin, J.; Morales, C. M.; Maynard, J. H.; Landis, C. R., *Organometallics* **2006**, *25*, 5566-5581.
58. Bryliakov, K. P.; Semikolenova, N. V.; Zakharov, V. A.; Talsi, E. P., *J. Organomet. Chem.* **2003**, *683*, 23-28.
59. Lee, M. H.; Han, Y.; Kim, D.-h.; Hwang, J.-W.; Do, Y., *Organometallics* **2003**, *22*, 2790-2796.
60. Cossee, P., *Tetrahedron Letters* **1960**, *1*, 12-16.
61. Cossee, P., *Tetrahedron Letters* **1960**, *1*, 17-21.
62. Arlman, E. J.; Cossee, P., *Journal of Catalysis* **1964**, *3*, 99-104.
63. Cossee, P., *Journal of Catalysis* **1964**, *3*, 80-88.
64. Dawoodi, Z.; Green, M. L. H.; Mtetwa, V. S. B.; Prout, K., *Chem. Commun.* **1982**, 1410-1411.
65. Brookhart, M.; Green, M. L. H., *J. Organomet. Chem.* **1983**, *250*, 395-408.
66. Ehm, C.; Budzelaar, P. H. M.; Busico, V., *J. Organomet. Chem.* **2015**, *775*, 39-49.
67. Rappé, A. K.; Skiff, W. M.; Casewit, C. J., *Chem. Rev.* **2000**, *100*, 1435-1456.
68. Resconi, L.; Fait, A.; Piemontesi, F.; Colonna, M.; Rychlicki, H.; Zeigler, R., *Macromolecules* **1995**, *28*, 6667-6676.
69. Resconi, L.; Piemontesi, F.; Camurati, I.; Balboni, D.; Sironi, A.; Moret, M.; Rychlicki, H.; Zeigler, R., *Organometallics* **1996**, *15*, 5046-5059.
70. Cavallo, L.; Guerra, G., *Macromolecules* **1996**, *29*, 2729-2737.
71. Eshuis, J. J. W.; Tan, Y. Y.; Meetsma, A.; Teuben, J. H.; Renkema, J.; Evens, G. G., *Organometallics* **1992**, *11*, 362-369.
72. Guo, Z.; Swenson, D. C.; Jordan, R. F., *Organometallics* **1994**, *13*, 1424-1432.
73. Hajela, S.; Bercaw, J. E., *Organometallics* **1994**, *13*, 1147-1154.
74. Yang, P.; Baird, M. C., *Organometallics* **2005**, *24*, 6005-6012.
75. Yang, P.; Baird, M. C., *Organometallics* **2005**, *24*, 6013-6018.
76. Suzuki, Y.; Yasumoto, T.; Mashima, K.; Okuda, J., *J. Am. Chem. Soc.* **2006**, *128*, 13017-13025.
77. Resconi, L., *J. Mol. Catal. A: Chem.* **1999**, *146*, 167-178.

78. Castonguay, L. A.; Rappe, A. K., *J. Am. Chem. Soc.* **1992**, *114*, 5832-5842.
79. Longo, P.; Grassi, A.; Pellicchia, C.; Zambelli, A., *Macromolecules* **1987**, *20*, 1015-1018.
80. Dahlmann, M.; Erker, G.; Nissinen, M.; Fröhlich, R., *J. Am. Chem. Soc.* **1999**, *121*, 2820-2828.
81. Busico, V.; Cipullo, R., *J. Am. Chem. Soc.* **1994**, *116*, 9329-9330.
82. Busico, V.; Caporaso, L.; Cipullo, R.; Landriani, L.; Angelini, G.; Margonelli, A.; Segre, A. L., *J. Am. Chem. Soc.* **1996**, *118*, 2105-2106.
83. Busico, V.; Brita, D.; Caporaso, L.; Cipullo, R.; Vacatello, M., *Macromolecules* **1997**, *30*, 3971-3977.
84. Busico, V.; Cipullo, R., *Prog. Polym. Sci.* **2001**, *26*, 443-533.
85. Gahleitner, M.; Bachner, C.; Ratajski, E.; Rohaczek, G.; Neißl, W., *J. Appl. Polym. Sci.* **1999**, *73*, 2507-2515.
86. Sheldrick, G. M., *Acta Crystallogr. Sect. A* **2008**, *64*, 112-122.
87. Sheldrick, G. M., *Acta Crystallogr. Sect. C* **2015**, *71*, 3-8.
88. Hansen, N. K.; Coppens, P., *Acta Crystallogr. Sect. A* **1978**, *34*, 909-921.
89. Volkov, A.; Macchi, P.; Farrugia, L. J.; Gatti, C.; Mallinson, P.; Richter, R.; Koritsanszky, T. XD2006 (version 5.42) A computer program for multipole refinement, topological analysis of charge densities, and evaluation of intermolecular energies from experimental or theoretical structure factors; **2006**.
90. Merrill, L.; Bassett, W. A., *Rev. Sci. Instrum.* **1974**, *45*, 290-294.
91. Moggach, S. A.; Allan, D. R.; Parsons, S.; Warren, J. E., *J. Appl. Crystallogr.* **2008**, *41*, 249-251.
92. Boehler, R., *Rev. Sci. Instrum.* **2006**, *77*, 115103.
93. Boehler, R.; De Hantsetters, K., *High Press. Res.* **2004**, *24*, 391-396.
94. Murata, K.; Aoki, S., *Rev. High Press. Sci. Technol.* **2016**, *26*, 3-7.
95. Piermarini, G. J.; Block, S.; Barnett, J. D.; Forman, R. A., *J. Appl. Phys.* **1975**, *46*, 2774-2780.
96. Willmott, P. R.; Meister, D.; Leake, S. J.; Lange, M.; Bergamaschi, A.; Böge, M.; Calvi, M.; Cancellieri, C.; Casati, N.; Cervellino, A.; Chen, Q.; David, C.; Flechsig, U.; Gozzo, F.; Henrich, B.; Jäggi-Spielmann, S.; Jakob, B.; Kalichava, I.; Karvinen, P.; Krempasky, J.; Lüdeke, A.; Lüscher, R.; Maag, S.; Quitmann, C.; Reinle-Schmitt, M. L.; Schmidt, T.; Schmitt, B.; Streun, A.; Vartiainen, L.; Vitins, M.; Wang, X.; Wulschleger, R., *J. Synchrotron Radiat.* **2013**, *20*, 667-682.
97. Meixner, P.; Batke, K.; Fischer, A.; Schmitz, D.; Eickerling, G.; Kalter, M.; Ruhland, K.; Eichele, K.; Barquera-Lozada, J. E.; Casati, N. P. M.; Montisci, F.; Macchi, P.; Scherer, W., *J. Phys. Chem. A* **2017**, *121*, 7219-7235.
98. CrysAlisPro 1.17.1.38.43. **2015**, Rigaku OD.
99. Velde, G.; Bickelhaupt, F. M.; Baerends, E. J.; Fonseca Guerra, C.; van Gisbergen, S. J. A.; Snijders, J. G.; Ziegler, T., *J. Comput. Chem.* **2001**, *22*, 931.
100. Guerra, C. F.; Snijders, J. G.; Velde, G. te; Baerends, E., *J. Theor. Chem. Acc.* **1998**, *99*, 391.
101. ADF2014; Theoretical Chemistry, Vrije Universiteit: Amsterdam, The Netherlands <http://www.scm.com>.
102. van Lenthe, E.; Baerends, E. J., *J. Comput. Chem.* **2003**, *24*, 1142.
103. van Lenthe, E.; Baerends, E. J.; Snijders, J. G., *J. Chem. Phys.* **1993**, *99*, 4597.
104. van Lenthe, E.; Baerends, E. J.; Snijders, J. G., *J. Chem. Phys.* **1994**, *101*, 9783.
105. van Lenthe, E.; Ehlers, A.; Baerends, E.-J., *J. Chem. Phys.* **1999**, *110*, 8943.
106. Rodríguez, J. I.; Köster, A. M.; Ayers, P. W.; Santos-Valle, A.; Vela, A.; Merino, G., *J. Comput. Chem.* **2009**, *30*, 1082.
107. Rodríguez, J. I.; Bader, R. F. W.; Ayers, P. W.; Michel, C.; Götz, A. W.; Bo, C., *Chem. Phys. Lett.* **2009**, *472*, 149.
108. Volkov, A.; Koritsanszky, T.; Chodkiewicz, M.; King, H. F., *J. Comput. Chem.* **2009**, *30*, 1379.
109. Kohout, M. Dgrid v4.6e; Radebeul, **2011**.
110. A. Otero-de-la-Roza et al., *Comput. Phys. Commun.* **2014**, *185*, 1007-1018.
111. A. Otero-de-la-Roza et al., *Comput. Phys. Commun.* **2009**, *180*, 157-166.
112. Gaussian 09, Revision E.03, Frisch, M. J.; Trucks, G. W.; Schlegel, H. B.; Scuseria, G. E.; Robb, M. A.; Cheeseman, J. R.; Scalmani, G.; Barone, V.; Petersson, G. A.; Nakatsuji, H.; Li, X.; Caricato, M.; Marenich, A. V.; Bloino, J.; Janesko, B. G.; Gomperts, R.; Mennucci, B.; Hratchian, H. P.; Ortiz, J. V.; Izmaylov, A. F.; Sonnenberg, J. L.; Williams-Young, D.; Ding, F.; Lipparini, F.; Egidi, F.; Goings, J.; Peng, B.; Petrone, A.; Henderson, T.; Ranasinghe, D.; Zakrzewski, V. G.; Gao, J.; Rega, N.; Zheng, G.; Liang, W.; Hada, M.; Ehara, M.; Toyota, K.; Fukuda, R.; Hasegawa, J.; Ishida, M.; Nakajima, T.; Honda, Y.; Kitao, O.; Nakai, H.; Vreven, T.; Throssell, K.; Montgomery, J. A., Jr.; Peralta, J. E.; Ogliaro, F.; Bearpark, M. J.; Heyd, J. J.; Brothers, E. N.; Kudin, K. N.; Staroverov, V. N.; Keith, T. A.; Kobayashi, R.; Normand, J.; Raghavachari, K.; Rendell, A. P.; Burant, J. C.; Iyengar, S. S.; Tomasi, J.; Cossi, M.; Millam, J. M.; Klene, M.; Adamo, C.; Cammi, R.; Ochterski, J. W.; Martin, R. L.; Morokuma, K.; Farkas, O.; Foresman, J. B.; Fox, D. J. Gaussian, Inc., Wallingford CT, **2016**.
113. Becke A. D., *Phys. Rev. A* **1988**, *38*, 309-3100.
114. Perdew J. P., *Phys. Rev. B*, **1986**, *33*, 8822-8824.
115. Schaefer, A.; Huber C.; Ahlrichs, R., *J. Chem. Phys.*, **1994**, *100*, 5829-5835.
116. Hay, P. J.; Ward, W. R., *J. Chem. Phys.* **1985**, *82*, 270-283.
117. Grimme, S.; Ehrlich, S.; Goerigk, L., *J. Comp. Chem.*, **2011**, *32*, 1456-1465.
118. Tomasi, J.; Mennucci, B.; Cammi, R., *Chem. Rev.*, **2005**, *105*, 2999-3093.

## 7. High-Melting, Elastic Polypropylene

- Title:** “High-Melting, Elastic Polypropylene: A One-Pot, One-Catalyst Strategy toward Propylene-Based Thermoplastic Elastomers”
- Status:** Full Paper, Published online February 2<sup>nd</sup>, 2018
- Journal:** Macromolecules, 2018, Volume 51, 914 – 929
- Publisher:** American Chemical Society
- DOI:** 10.1021/acs.macromol.7b02679
- Authors:** Martin R. Machat, Dominik Lanzinger, Markus Drees, Philipp J. Altmann, Eberhardt Herdtweck, and Bernhard Rieger<sup>d</sup>

**Content:** The focus of this comparative study is directed toward the production of high-temperature stable ( $T_m \sim 140$  °C) elastic polypropylenes in a simple one-pot, one-catalyst approach. By the formation of tailored <sup>e</sup>PP-<sup>i</sup>PP block structures embedded in a matrix of high molecular weight atactic polypropylenes, a propylene based thermoplastic elastomer with exceptional mechanical characteristics was generated. These findings were facilitated by the elucidation of different stereocontrol mechanisms, which collectively impact the final tacticities, using EBFI-type metallocenes: Beside the enantiofacial discrimination of the dual-site system, the impact of possible chain migration, chain end epimerization and the interconversion between different chelate ring conformers was investigated in-depth. In this context, the occurrence of two different five-membered chelate ring conformers, catalyzing mainly isotactic (II-forward) or atactic (Y-backward) sequences, is considered to be the genesis of this variable stereocontrol mechanism. By accurately adjusting the interplay of chain propagation, chain release, and interconversion between the isoselective and nonselective conformation during the polymerization process the formation of high-melting <sup>e</sup>PP was facilitated.

---

<sup>b</sup> M. Machat planned and executed most of the experiments, developed the concept toward the formation of high-melting elastic polypropylenes and wrote the manuscript. D. Lanzinger developed the synthesis of some complexes, evaluated some catalysts and the respective polymer properties and contributed with fruitful mental input. P. J. Altmann and E. Herdtweck conducted all SC XRD-measurements and managed the processing of the respective data. M. Drees performed all DFT-calculations concerning the free energy differences and barrier heights of the chelate ring conformers. All work was performed under the supervision of B. Rieger.

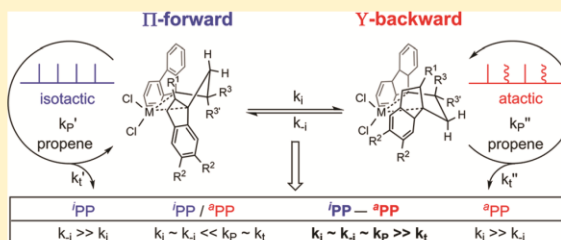
## High-Melting, Elastic Polypropylene: A One-Pot, One-Catalyst Strategy toward Propylene-Based Thermoplastic Elastomers

Martin R. Machat,<sup>†</sup> Dominik Lanzinger,<sup>†</sup> Markus Drees,<sup>‡</sup> Philipp J. Altmann,<sup>§</sup> Eberhardt Herdtweck,<sup>§</sup> and Bernhard Rieger<sup>\*,†,‡</sup>

<sup>†</sup>Wacker-Lehrstuhl für Makromolekulare Chemie, Catalysis Research Center, <sup>‡</sup>Chair of Inorganic and Metal–Organic Chemistry, Catalysis Research Center, and <sup>§</sup>Catalysis Research Center, Technische Universität München, 85748 Garching bei München, Germany

### Supporting Information

**ABSTRACT:** This contribution provides the simple one-pot, one-catalyst synthesis of high-melting ( $T_m \sim 140$  °C), high-molecular-weight, elastic polypropylene (PP) offering an excellent reversible deformation behavior. The produced propylene-based thermoplastic elastomers contain of <sup>i</sup>PP–<sup>a</sup>PP block structures embedded in an amorphous polypropylene matrix which is enabled by the variable stereoselective behavior of ethylene-bridged fluorenylindenyl (EBFI) *ansa*-metallocene complexes. For the tailored synthesis of these high-melting PPs the intricate interplay of various mechanisms, which collectively define the stereoregularity of the produced polypropylenes, was examined, and a decisive impact of different chelate ring conformers was elucidated. In this connection, the accurate adjustment of conformational interconversion with respect to the chain propagation and termination rate facilitated a directed switching between iso- and unselective polypropylene sequences in the catalytic production of highly temperature-stable, elastic polypropylene.



## INTRODUCTION

Just a few years after the initial discovery of propylene polymerization in 1956<sup>1</sup> first research was conducted by Natta and co-workers addressing elastic properties in polypropylene materials.<sup>2</sup> In the late 1980s, scientists of DuPont reported on high molecular weight elastic polypropylene (PP) produced along with isotactic polypropylene as an ether-soluble fraction using metal oxide supported group IV metal compounds.<sup>3,4</sup> Back in those days, the application of metallocene complexes for tailored polypropylene structures received accretive attention evoking several successful approaches toward the directed synthesis of <sup>i</sup>PP. In this context, the group of Chien et al. developed a series of  $C_1$ -symmetric indenylcyclopentadienyl-based *ansa*-metallocene complexes in the early 1990s comprising different cyclopentadienyl derivatives and chiral methylene bridges.<sup>5–7</sup> Additional approaches toward PP with elastic properties were conducted by Collins et al. applying a bridged,  $C_1$ -symmetric metallocene framework,<sup>8,9</sup> whereas the directed synthesis of <sup>a</sup>PP–<sup>i</sup>PP block structures using unbridged bis(2-phenylindenyl)zirconium dichloride with an oscillating stereocontrol mechanism constituted a breakthrough regarding the synthesis of pure propene-based elastomers.<sup>10,11</sup> In the past decade, the concept of tailored polyolefin block structures even passed the threshold toward industrial application regarding the implementation of a chain shuttling mechanism into the polymerization setup using two catalysts of different selectivity in combination with a chain shuttling agent.<sup>12</sup> An alternative approach to design polyolefin block structures is provided by a

living coordinative polymerization mechanism and facilitates a variety of promising polyolefin products.<sup>13–15</sup> However, the economic inefficiency to be limited to one polymer chain per catalyst molecule displays the major drawback auf this strategy.<sup>16</sup>

Developed in the 1990s, ethylene-bridged fluorenylindenyl (EBFI) *ansa*-metallocenes still represent one of the most flexible dual-site catalyst systems for the stereoselective synthesis of polypropylenes with a unique tacticity range from completely atactic to isotactic.<sup>17–21</sup> This remarkable variation of the stereoselectivity enables the formation of elastic and thermoplastic materials because, apart from the molecular weights, the mechanical properties of polypropylene are mainly determined by its microstructure.<sup>22,23</sup> Especially the formation of high molecular weight, elastic polypropylene using hafnium-based EBFI-type *ansa*-metallocenes led to a new class of polypropylene elastomers with exceptional mechanical characteristics.<sup>20</sup> However, the restricted temperature stability of these polymers displayed an unresolved issue to this day.<sup>18,24</sup> Accordingly, this contribution addresses the still imperfect amalgamation of elasticity in combination with high-melting characteristics regarding the catalysis of pure propylene-based thermoplastic elastomers. Therefore, a comprehensive investigation of three novel (IV, V<sub>a</sub>, V<sub>b</sub>) and four literature known

Received: December 18, 2017

Revised: January 21, 2018

Published: February 2, 2018

(I<sub>Hf</sub>, I<sub>Zr</sub>, II, III) EBFI-type *ansa*-metallocene complexes in the polymerization of propylene with concerted focus on the two most substantial polymerization parameters ( $T_p$  and [propene]) was conducted. Facilitated by this detailed analysis, elucidation of the intricate interplay of different mechanisms which collectively determine the resulting stereoregularity of the produced polypropylenes was targeted.

In order to gain such a comprehensive understanding, all mechanisms which theoretically impact the stereoselectivity of  $C_1$ -symmetric EBFI-type *ansa*-metallocene catalysts must be considered: The first obvious peculiarity of these EBFI-type *ansa*-metallocenes is the dual-site character, which provides two different enantiofacial selectivities since the chemical environment of both coordination sites is unequal.<sup>18,21</sup> In the case of a basic EBFI–metallocene framework the enantiofacial discrimination of a coordinating monomer at the inward site proceeds quite accurate, whereas the enantiofacial selectivity of a coordinating monomer unit at the outward site is considered to take place less explicit. If no chain migration occurs, monomer insertions strictly alternate between the monomer inward and outward sites, thereby determining the respective stereoregularity.<sup>18,25</sup> However, if the polymer chain migrates from the sterically crowded inward to the less crowded outward site before every second insertion step, predominantly isotactic polypropylene is generated through a chain-back-skip/chain-migration mechanism (Figure 1).<sup>26,27</sup> The chain-back-skip

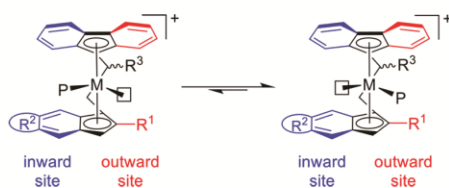


**Figure 1.** Ground states before propene coordination at the inward and outward site using dual-site EBFI-type metallocenes (M: Zr, Hf; P: polymeryl).

mechanism is known to considerably impact the stereoselectivity of the resulting polypropylenes and is mainly influenced by the counterplay between the monomer concentration, correlated to the chain propagation mechanism, and the rate of the polymeryl shift.<sup>21,27</sup> Its occurrence is experimentally verified by the catalytic performance of several  $C_1$ -symmetric EBFI-type metallocene complexes in the polymerization of propene and has been subject of detailed theoretical investigation.<sup>21,26,28,29</sup>

Furthermore, the stereoregularity of the produced polypropylenes is impacted by the cascade process of chain end epimerization. The process is considered to proceed via several elimination, rotation, and reinsertion steps, thereby randomizing the stereoinformation on the last inserted monomer unit. The epimerization process especially occurs at high polymerization temperatures and low monomer concentrations.<sup>30–33</sup> To additionally complicate the situation, an impact of two different chelate ring conformations on the stereoselective polymerization behavior has been reported for  $C_1$ -symmetric EBFI-type metallocenes with a substituted ethylene bridge (Figure 2).<sup>17</sup> In this context, through chelation of the metal center by the ethylene bridged ligands the respective metallocene complexes build up five-membered ring structures, occurring as  $\Pi$ -forward and Y-backward chelate ring con-

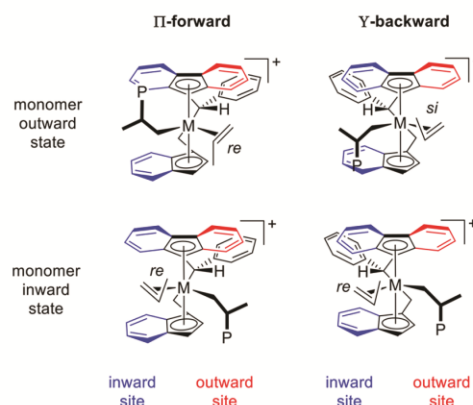


**Figure 2.** Preferred monomer coordination at the outward and inward sites using bridge-substituted EBFI complexes (VI:  $R^1 = R^2 = H$ ;  $R^3 = C_6H_5$ , M = Zr, Hf, P = polymeryl) determined by the calculated energy differences of the *re*- and *si*-coordinated monomer.<sup>26</sup>

formers.<sup>34,35</sup> According to the notation first introduced by Brintzinger et al., the  $\Pi$ -conformation places the opposite substituents 5-H<sub>Flu</sub> and the 4-H<sub>Ind</sub> in a forward position to minimize the distance between both groups, while the Y-conformer leads to a backward arrangement with the maximal distance between both substituents.<sup>36</sup> In addition, substituents at the ethylene bridge generally favor the equatorial over the axial position and thereby determine the final conformation.<sup>17</sup> Consequently, the preferred conformations are defined by the configuration of the bridge substituent and the indenyl unit. The theoretical investigations of fluorenyl-indenyl *ansa*-metallocenes with a phenyl-substituted ethylene bridge (VI) by Guerra et al. suggest significant differences of the enantiofacial discrimination of both chelate ring conformers with respect to the monomer coordination at the inward and outward sites (Figure 2).<sup>26</sup>

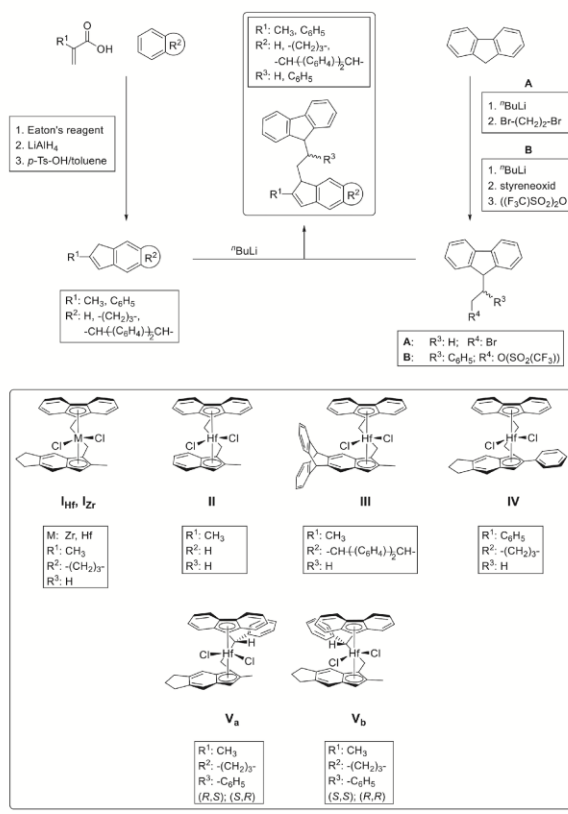
The results suggest a high enantioselectivity (*re*) in the monomer inward state for the  $\Pi$ -forward (VI<sub>f</sub>, (R)-phenyl-(S)-indenyl) and Y-backward (VI<sub>b</sub>, (S)-phenyl-(S)-indenyl) chelate ring conformations. At the monomer outward state, a moderate selectivity of the  $\Pi$ -forward conformer for the analogous enantioface (*re*) was calculated, leading to a relatively isospecific polymer. For the Y-backward conformer, a slight selectivity toward the coordination of the opposite enantioface (*si*) is suggested, resulting in a hemi-isospecific or even syndiotactic polymer, if a strictly alternating insertion occurs. In this context, the enantiomers of both diastereomers reveal analogous conformational preferences resulting in an identical stereoselective polymerization behavior. For a conclusive picture on the entire stereoselective process, a possible migration of the polymeryl chain, dependent on the present conformation, needs to be considered as well. But although the conformational impact on the stereoregularities using bridge-substituted EBFI-type metallocenes has been investigated in previous studies,<sup>17,26</sup> the impact of conformational preferences on the stereoregular behavior of unsubstituted ( $R^3$ : H) EBFI-type metallocenes was generally neglected. Therefore, this contribution claims to shed light on the actual mechanisms that essentially impact the overall stereoregularities of polypropylenes produced with the catalyst class of EBFI-type metallocenes. Provoked by the profound understanding of the entire stereoregulative process, a novel route for the formation of

high-melting ( $T_m \sim 140$  °C) propylene-based thermoplastic elastomers is presented in this report.

## RESULTS AND DISCUSSION

**Synthesis.** EBFI-type ligand structures with different substitution patterns at the indenyl moiety and the ethylene bridge were synthesized according to established or adapted literature procedures (Scheme 1).<sup>17–19,37</sup> Various residues in

**Scheme 1. Synthesis Route to EBFI-Type Metallocene Complexes of Varying Substitution Pattern at the Indenyl Moiety and the Ethylene Bridge**



positions 2, 5, and 6 of the indenyl fragment were introduced using different acrylic acid derivatives in combination with different benzene derivatives in a one-pot synthesis through an acylation reaction followed by a Nazarov cyclization reaction. The obtained indanone derivatives were reduced and eliminated to form the respective indene derivatives. Substituted and unsubstituted ethylene bridges were attached to the fluorenyl unit by reacting lithiated fluorene with 1,2-dibromoethane or styrene oxide. For the latter reaction, the alcohol is converted into an appropriate leaving group, and the fluorenyl substrates are finally reacted with the lithiated indene derivatives to yield EBFI-type ligand structures with various substitution patterns. The desired metallocenes were obtained by a salt metathesis reaction of the lithiated ligands and MCl<sub>4</sub> (M: Zr, Hf) in a toluene/1,4-dioxane mixture. Complex V was composed of the diastereomers V<sub>a</sub> and V<sub>b</sub> and was isolated as a 2:1 mixture. The diastereomer V<sub>a</sub> itself consists of a racemic mixture of the (R)-phenyl-(S)-indenyl (depicted in Scheme 1)

and the (S)-phenyl-(R)-indenyl enantiomers, whereas the diastereomer V<sub>b</sub> consists of the (S)-phenyl-(S)-indenyl (depicted in Scheme 1) and the (R)-phenyl-(R)-indenyl enantiomers.

**Structural Evaluation (Solid State).** Single crystals of complexes II, III, IV, and V suitable for X-ray diffraction analysis were obtained by diffusion of pentane into a saturated solution of the complex in toluene. The solid-state structures of I<sub>Zr</sub> (CCDC 1192206) and I<sub>Hf</sub> (CCDC 291959) are already known in the literature.<sup>18,38</sup> The crystal structures of V<sub>a</sub> and V<sub>b</sub> were determined by the XRD analysis of one single crystal (V<sub>a</sub>/V<sub>b</sub> = 2/1) containing both diastereomers crystallized in a single unit cell. ORTEP-style representations of all new complex structures (II–V; CCDC 1578809, 1578808, 1580068, and 1578810) are provided in the Supporting Information. Important bond lengths and angles are depicted in Table 1.

**Table 1. Characteristic Angles and Distances of the Solid-State Structures I–V**

	$\beta^a$ (deg)	$\delta^b$ (deg)	M–Ind <sub>Centroid</sub> (Å)	M–Flu <sub>Centroid</sub> (Å)	preferred conformer
I <sub>Hf</sub> <sup>38</sup>	59.8	36.3	2.203	2.252	Y
I <sub>Zr</sub> <sup>18</sup>	60.2	37.2	2.226	2.267	Y
II	60.5	38.2	2.192	2.275	Y
III	62.0	35.0	2.185	2.276	Y
IV	60.6	−41.4	2.203	2.271	Π
V <sub>a</sub>	60.0	−19.6	2.184	2.266	Π
V <sub>b</sub>	59.5	32.5	2.247	2.244	Y

<sup>a</sup>Bite angle.<sup>39,40</sup> <sup>b</sup>Dihedral angle (fluorenyl–ethylene bridge–indenyl).

In the solid state, the smallest bite angles were observed for complexes I and V, which had an identical substitution pattern at the indenyl fragment, whereas the largest bite angle was observed for complex III, bearing the bulkiest steric demand at the indenyl fragment. The distance between the metal center and the chelating ligand was decreased when switching from zirconium (I<sub>Zr</sub>) to hafnium (I<sub>Hf</sub>). The bond lengths from the metal center to the fluorenyl ligand were shorter than those to the indenyl ligand, except for complex V<sub>b</sub>, which had almost identical distances between the metal center and the fluorenyl and indenyl frameworks. A significant twist of the 2-phenyl substituent was observed for complex IV, leading to an angle of 36.4° between the phenyl group and the indenyl fragment. This phenomenon was considered to be a result of reaching the energetic minimum in a coplanar structure by maximized delocalization, interfering with the reduction of steric interactions by rotation of the 2-phenyl substituent.

The exhaustive experimental and theoretical investigations of ethylene-bridged bisindenyl *ansa*-metallocene (EBI) complexes have underlined the existence of dynamic conformational changes between the Π-forward and Y-backward conformation in solution.<sup>34,35</sup> Accordingly, the application of an unsubstituted, bipartite ethylene bridge in EBFI-type metallocenes also provokes the appearance of two different conformations. From an energetic point of view, one conformer is energetically more favored but a possible interconversion takes place in solution. Consequently, the particularly preferred conformations are observable for the substituted (V<sub>a</sub> and V<sub>b</sub>) and unsubstituted (I–IV) EBFI-type complexes in the solid state (Figure 3) being additionally indicated by the dihedral angle (Table 1). In the case of the diastereomers V<sub>a</sub> and V<sub>b</sub>, the configuration of the bulky phenyl substituent attached to the ethylene bridge

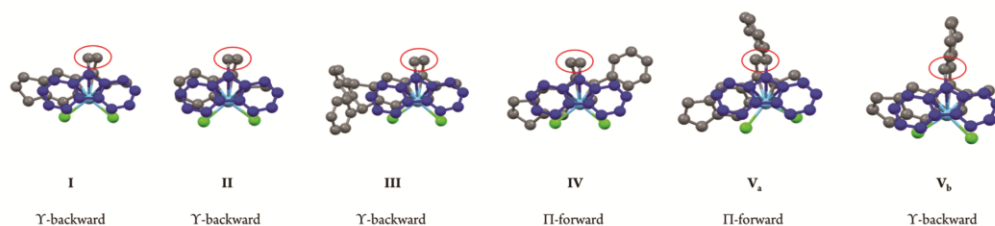


**Figure 3.** Preferred  $\Pi$ - and Y-chelate ring conformers of EBFI-type metallocenes in the solid state with the fluorenyl fragment in blue on top and the ethylene bridge marked in red.

determines the overall conformation, assuring an equatorial position. In this context, an (*R/S*)-phenyl-(*S/R*)-indenyl configuration leads to a  $\Pi$ -forward conformation ( $V_a$ ), whereas a Y-backward arrangement is obtained with an (*R/S*)-phenyl-(*R/S*)-indenyl configuration ( $V_b$ ). In the case of an unsubstituted ethylene bridge, the differences in the steric demand of the indenyl fragment are responsible for the preferred conformations of complexes I–IV. If the ethylene bridge is unsubstituted, the 2-methyl substituent ( $R^1$ ) at the indenyl moiety leads to a Y-backward conformation of the respective metallocenes (I–III). Differences in positions 5 and 6 of the indenyl fragment ( $R^2$ ) may have a less significant impact on the resulting ring conformation. As illustrated in Figure 4, the difference in steric encumbrance between the

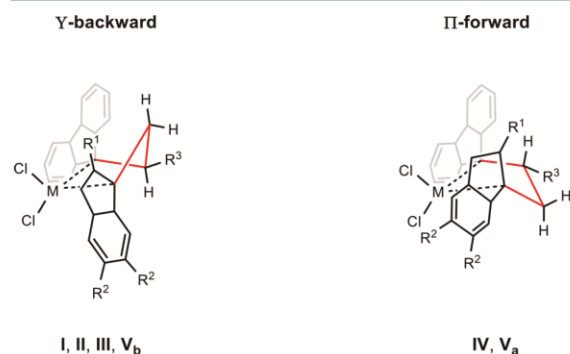


**Figure 4.** Molecular representation of preferred  $\Pi$ - and Y-chelate ring conformers of EBFI-type metallocene complexes. The  $\eta^5$ -coordination is omitted for clarity. The dashed M–C bond represents a visualization of the five-membered ring.

substituted benzene unit of the indenyl fragment ( $R^2$ ) and the 2-methyl/phenyl substituent at the Cp moiety ( $R^1$ ) determines the preference of the  $\Pi$ - or Y-chelate ring conformers if no bridge substituent ( $R^3$ ; H) is present. In the case of 2-methyl substitution ( $R^1$ ), an equatorial position is preferred, which forces the benzene unit of the indenyl in an axial position (Figure 4, left). Replacement of the methyl group by a phenyl unit, triggers a change in conformation. The benzene unit of the indenyl fragment is in this case oriented in the energetically preferred equatorial position (Figure 4, right). Regarding the present chemical environment, the 2-methyl group appears to be more sterically demanding than the phenyl unit. This observation can be explained by the possible twist of the phenyl group resulting in a minimized steric interaction with the surrounding chemical environment.

**Structural Evaluation (DFT Calculations).** Although the solid-state structures of EBFI-type metallocenes disclosed

different preferences for the  $\Pi$ - and Y-chelate ring conformer depending on the substitution pattern, these observations just serve as indications for the actual behavior in solution. In addition, the relevant catalytically active species may significantly differ from the precatalytic bis-chlorinated metallocene structures with respect to the preferred chelate ring conformers because a cationic metallocene structure bearing an alkyl/polymeryl substituent and a noncoordinating anion needs to be considered. To verify the preferred conformations on a molecular level in solution, taking the catalytically active cationic structures  $L_2M^+(\text{Bu})^+$  into consideration, density function theory (DFT) calculations (see Experimental Section and Supporting Information for details) on the free energy differences and the barrier heights were conducted with complexes I–V (Tables 2 and 3).

**Table 2.** Free Energy Differences and Barrier Heights between the Ring Conformers of Each Metallocene (I–V)

	$\Delta G(\Pi)^a$ (kcal/mol)	$\Delta G(\text{TS})^a$ (kcal/mol)	preferred conformer
$I_{\text{Hf}}$	+1.58	+4.09	Y
$I_{\text{Zr}}$	+1.40	+4.04	Y
II	+1.36	+3.97	Y
III	+1.42	+3.98	Y
IV	−1.00	+3.69	$\Pi$
$V_a$	−3.38 <sup>b</sup>	N/A <sup>c</sup>	$\Pi$
$V_b$	+6.27 <sup>b</sup>	N/A <sup>c</sup>	Y

<sup>a</sup>All energies are relative to the Y conformer. <sup>b</sup>Energy difference between  $V_b(\text{Y})$  and  $V_a(\Pi)$ :  $V_b(\text{Y})$  is 1.49 kcal/mol more exergonic. <sup>c</sup>Transition state searches followed the wrong eigenfrequency; because of the higher energy difference of both conformers, it should be reasonably higher than for the other metallocenes.

**Table 3.** Free Energy Differences and Barrier Heights between the Ring Conformers of Each Metallocene (I–V) in the Catalytically Active, Cationic Structure of the Type  $L_2M^+(\text{Bu})^+$

	$\Delta G(\Pi)^a$ (kcal/mol)	$\Delta G(\text{TS})^a$	preferred conformer
$I_{\text{Hf}}$	+0.94	+3.10	Y
$I_{\text{Zr}}$	+0.95	+3.47	Y
II	+1.05	+4.14	Y
III	+1.16	+3.43	Y
IV	+1.33	+4.38	Y
$V_a$	−2.73 <sup>b</sup>	N/A <sup>c</sup>	$\Pi$
$V_b$	+4.48 <sup>b</sup>	N/A <sup>c</sup>	Y

<sup>a</sup>All energies are relative to the Y conformer. <sup>b</sup>Energy difference between  $V_b(\text{Y})$  and  $V_a(\Pi)$ :  $V_b(\text{Y})$  is 1.49 kcal/mol more exergonic. <sup>c</sup>Transition state searches followed the wrong eigenfrequency; because of the higher energy difference of both conformers, it should be reasonably higher than for the other metallocenes.

Table 4. Conditions and Results for the Polymerization of Propene with Complexes I–V in Toluene<sup>a</sup>

entry	catalyst	$T_p^b$	$n^c$	$[C_3]^d$	$T_m^e$	$mmmm^f$	$M_n^g$	$\bar{D}^h$	$P^i$
1	I <sub>Hf</sub>	0	2.5	2.14	–	24	1300	2.2	1100
2	I <sub>Hf</sub>	15	2.5	2.14	–	27	200	1.7	1200
3	I <sub>Hf</sub>	30	2.5	2.14	–	29	190	1.7	1500
4	I <sub>Hf</sub>	45	5.0	0.50	–	32	13	1.8	700
5	I <sub>Hf</sub>	45	2.5	1.01	–	38	57	2.2	2400
6	I <sub>Hf</sub>	45	2.5	1.58	–	37	120	1.6	4600
7	I <sub>Hf</sub>	45	2.5	2.14	–	36	160	2.0	5900
8	I <sub>Hf</sub>	60	2.5	2.14	–	37	60	2.0	11000
9	I <sub>Hf</sub>	75	2.5	2.14	–	38	9	1.9	16000
10	I <sub>Zr</sub>	0	2.5	2.14	–	18	170	2.2	3800
11	I <sub>Zr</sub>	15	2.5	2.14	–	25	160	1.7	4600
12	I <sub>Zr</sub>	30	2.5	2.14	–	40	150	1.7	17000
13	I <sub>Zr</sub>	45	2.5	0.50	–	60	27	1.9	7200
14	I <sub>Zr</sub>	45	2.5	1.01	–	56	69	2.0	34000
15	I <sub>Zr</sub>	45	2.5	1.58	–	53	82	1.9	23000
16	I <sub>Zr</sub>	45 <sup>j</sup>	2.5	2.14	–	50	140	1.7	27000
17	I <sub>Zr</sub>	60 <sup>j</sup>	2.5	2.14	–	55	33	2.3	40000
18	I <sub>Zr</sub>	75 <sup>j</sup>	1.3	2.14	–	58	7	2.4	23000
19	II	0	2.5	2.14	–	15	1300	2.1	1200
20	II	15	2.5	2.14	–	16	350	2.2	1100
21	II	30	2.5	2.14	–	18	290	2.3	1600
22	II	45	5.0	0.50	–	21	16	2.0	800
23	II	45	2.5	1.01	–	25	81	1.7	2700
24	II	45	2.5	1.58	–	24	110	1.9	2300
25	II	45	2.5	2.14	–	23	190	1.7	4900
26	II	60	2.5	2.14	–	28	37	1.7	12000
27	II	75	2.5	2.14	–	28	5	2.2	8900
28	III	0	2.5	2.14	–	11	1200	2.4	940
29	III	15	2.5	2.14	–	17	290	1.8	1300
30	III	30	2.5	2.14	–	21	77	1.9	5400
31	III	45	5.0	0.50	–	21	9	1.9	710
32	III	45	2.5	1.01	–	30	16	2.0	4900
33	III	45	2.5	1.58	–	28	37	2.1	5200
34	III	45	2.5	2.14	–	25	57	1.9	6900
35	III	60	2.5	2.14	–	28	12	2.0	6800
36	III	75	2.5	2.14	–	30	4	1.9	7200
37	IV	0	2.5	2.14	116	74	1100	1.5	1400
38	IV	15	2.5	2.14	113	69	130	1.8	1500
39	IV	30	2.5	2.14	113	67	92	1.7	1400
40	IV	45	5.0	0.50	–	30	3	1.6	260
41	IV	45	2.5	1.01	–	38	9	1.9	2900
42	IV	45	2.5	1.58	–	56	19	1.7	2500
43	IV	45	2.5	2.14	110	63	30	1.6	1900
44	IV	60	2.5	2.14	87	57	8	1.6	3500
45	IV	75	2.5	2.14	–	43	2	1.5	3500
46	V <sub>a</sub>	0	2.5	2.14	149	93	1200	2.0	1300 <sup>k</sup>
47	V <sub>a</sub>	15	2.5	2.14	146	88	140	2.0	1400 <sup>k</sup>
48	V <sub>a</sub>	30	2.5	2.14	140	86	120	2.2	2800 <sup>k</sup>
49	V <sub>a</sub>	45	2.5	0.50	116	58	15	1.5	1700 <sup>k</sup>
50	V <sub>a</sub>	45	2.5	1.01	127	60	36	2.1	5500 <sup>k</sup>
51	V <sub>a</sub>	45	2.5	1.58	133	62	45	2.2	5500 <sup>k</sup>
52	V <sub>a</sub>	45	2.5	2.14	137	74	61	2.1	6900 <sup>k</sup>
53	V <sub>a</sub>	60	2.5	2.14	127	69	19	1.9	12000 <sup>k</sup>
54	V <sub>a</sub>	75 <sup>j</sup>	2.5	2.14	114	65	11	1.6	26000 <sup>k</sup>
55	V <sub>b</sub>	0	2.5	2.14	–	3	1200	1.4	1300 <sup>k</sup>
56	V <sub>b</sub>	15	2.5	2.14	–	6	760	1.5	1400 <sup>k</sup>
57	V <sub>b</sub>	30	2.5	2.14	–	11	330	1.7	2800 <sup>k</sup>
58	V <sub>b</sub>	45	2.5	0.50	–	14	13	2.1	1700 <sup>k</sup>
59	V <sub>b</sub>	45	2.5	1.01	–	13	35	1.9	5500 <sup>k</sup>
60	V <sub>b</sub>	45	2.5	1.58	–	13	57	1.7	5500 <sup>k</sup>
61	V <sub>b</sub>	45	2.5	2.14	–	14	77	1.7	6900 <sup>k</sup>

Table 4. continued

entry	catalyst	$T_p^b$	$n^c$	$[C_3]^d$	$T_m^e$	$mmmm^f$	$M_n^g$	$\bar{D}^h$	$P^i$
62	$V_b$	60	2.5	2.14	–	19	16	2.2	12000 <sup>k</sup>
63	$V_b$	75 <sup>j</sup>	2.5	2.14	–	26	5	2.2	26000 <sup>k</sup>

<sup>a</sup> $V_{\text{toluene}}$ : 300 mL,  $t_p$ : 30 min, scavenger (TIBA): 2.2 mmol; “–”  $\triangleq$  “not determined”. <sup>b</sup> $T_p$  in  $^{\circ}\text{C} \pm 2$ . <sup>c</sup>In  $\mu\text{mol}$ . <sup>d</sup>Concentration of propene [mol/L] (estimated by the equation of Busico). <sup>e</sup>In  $^{\circ}\text{C}$ . <sup>f</sup>In %, determined via  $^{13}\text{C}$  { $^1\text{H}$ } NMR spectroscopy assuming the enantiomorphic site model. <sup>g</sup>In  $\text{kg mol}^{-1}$ . <sup>h</sup> $\bar{D}$ :  $M_w/M_n$ . <sup>i</sup> $P$  in  $\text{kg}_{\text{PP}} \cdot [\text{mol}_M \cdot (\text{mol/L}) \cdot \text{h}]^{-1}$ . <sup>j</sup> $T_p$  in  $^{\circ}\text{C} \pm 5$ . <sup>k</sup> $P$  of the complex mixture  $V_a/V_b = 2/1$ .

In this context, the calculated results for the preferred ring conformation considering a precatalytic bis-chlorinated substitution pattern were all in line with our findings in the solid state. Although the free energy differences between both conformations were determined to be 1–2 kcal/mol for all complexes without a phenyl substituent at the ethylene bridge (I–IV), significantly higher energy differences were observed when a bridge substituent was present ( $V_a$  and  $V_b$ ). The barrier heights of the possible interconversion are suggested to be approximately 4 kcal/mol for complex I–IV, whereas the ones of  $V_a$  and  $V_b$  were expected to be significantly higher. In general, quite similar results were observed with the catalytically active, cationic structures of the type  $L_2M(\text{tBu})^+$ . The only significant difference was observed with complex IV because the preferred conformation switches from  $\Pi$ -forward to  $Y$ -backward. This computationally derived result was unexpected and is not in line with our additional experimental findings. However, as the differences are small, this could just be a mathematical artifact. Furthermore, the additional impact of the counteranion or aluminum alkyls which both interact with the catalytically active cationic structure under experimental conditions may lead to a change of the preferred conformation. Regarding the interconversion between both possible conformations, the dihedral angle along the ethylene bridge was the most important geometric parameter that changed. The calculated dihedral angles of complexes I–V in the precatalytic and cationic states are provided in the Supporting Information (Tables S10 and S11). For the precatalytic, bis-chlorinated structures and the catalytically active, cationic structures of the type  $L_2M(\text{tBu})^+$ , the dihedral angles of both conformations were found to be similar. The determined dihedral angles of the preferred conformations in the solid state (Table 1) are also in good agreement with the calculated results. The most significant differences between the complexes I–V were observed if there was a phenyl substituent at the ethylene bridge. In this context, steric repulsion between the phenyl unit and the residual ligand framework significantly reduces the dihedral angle in the nonpreferred conformation of the complexes  $V_a$  and  $V_b$  compared to the dihedral angles obtained with complexes I–IV.

Considering the presented computational results, the presence of a preferred chelate ring conformer considering all applied EBFI-type complexes I–V is evident; in addition, there is a possibility of interconversion between the preferred and nonpreferred conformations in a dynamic equilibrium. The energy barrier height determines the interconversion frequency, whereas the free energy differences are accountable for the overall population of the preferred and nonpreferred chelate ring conformers. Consequently, the energetically preferred conformation generally dominates in solution at low temperatures, whereas a theoretical 1:1 mixture of both conformers in a dynamic equilibrium is estimated at high temperatures.

**Catalytic Evaluation.** All synthesized EBFI complexes I–V were examined in the polymerization of propene under

identical conditions. Activation of the bis-chlorinated structures was conducted *via in situ* alkylation with 200 equiv of triisobutylaluminum (TIBA) for 1 h at 60  $^{\circ}\text{C}$  followed by subsequent addition of 5.0 equiv of  $[\text{Ph}_3\text{C}][\text{B}(\text{C}_6\text{F}_5)_4]$  to start the polymerization reaction. The polymerization behavior of all complexes I–V was analyzed between 0 and 75  $^{\circ}\text{C}$  in steps of 15  $^{\circ}\text{C}$  using identical monomer concentrations (2.14 M) and at various monomer concentrations between 0.50 and 2.14 M with a constant polymerization temperature (45  $^{\circ}\text{C}$ ). Details of the reaction conditions and the polymerization results are provided in Table 4.

All complexes revealed similar trends of the productivity at varying polymerization temperatures; moderate activities were observed at low temperatures, which increased significantly with increasing polymerization temperature. At temperatures below 75  $^{\circ}\text{C}$ , the productivities of the zirconocene complex ( $I_{Zr}$ ) were considerably higher compared to the hafnium analogue  $I_{Hf}$  as well as all other hafnium-based complexes; however, at 75  $^{\circ}\text{C}$ , the productivity of the isostructural hafnocene system exceeded that of  $I_{Zr}$ , which had already reached its maximum at approximately 60  $^{\circ}\text{C}$ . Complexes  $I_{Hf}$  and V, comprising an identical substitution pattern at the indenyl moiety, appeared to be the most active hafnium-based catalysts, whereas the hafnocene complex IV displayed the lowest catalytic activities. Increasing the monomer concentration at a constant polymerization temperature accelerated the productivities of all the presented catalyst systems (I–V). For the polymerization with complex V especially at low polymerization temperatures, a macroscopic mixture of “PP and ‘PP was observed (Figure S36). Therefore, all polymers produced with the mixture of diastereomers V were separated by a Soxhlet extraction with *n*-pentane. The pentane soluble fraction was attributed to the catalytic activity of complex  $V_b$  and the insoluble residue to the catalytic activity of complex  $V_a$ . The pentane-soluble and -insoluble fractions were assigned to the respective diastereomers of complex V analogous to reported EBFI-type complexes with unsubstituted indenyl and fluorenyl moieties and a phenyl-substituted ethylene bridge (VI,  $R^1 = R^2 = \text{H}$ ;  $R^3 = \text{C}_6\text{H}_5$ ).<sup>17</sup>

**Molecular Weights.** The molecular weights of polypropylenes are generally defined by the rate ratio of propagation and chain release. Regarding our produced polymers, the molar mass distributions were predominantly found in the range of 1.5–2.5 ( $\bar{D}$ :  $M_w/M_n$ ). For all hafnocene complexes molecular weights ( $M_n$ ) exceeding 1000 kDa were observed at 0  $^{\circ}\text{C}$ , whereas the ones of the zirconocene complex  $I_{Zr}$  were approximately 7 times lower (Figure 5). An increase in the polymerization temperature led to a severe decrease in the molecular weights of the polypropylenes produced with all the hafnocene systems, resulting in comparable chain lengths of the Zr- and Hf-analogues ( $I_{Zr}$  and  $I_{Hf}$ ). Although most of the produced polypropylenes with complexes I–V at moderate to elevated temperatures were in a comparable range, a significant decrease in the molecular weights was observed with the

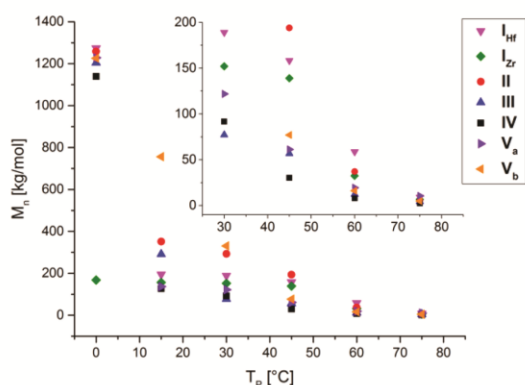


**Figure 5.** Average molecular weights of the polypropylenes produced with I–V at a constant monomer concentration (2.14 M) and varying polymerization temperature.

replacement of the 2-methyl with a 2-phenyl substituent ( $R^1$ ) at the indenyl framework (I vs IV).

If the polymerization temperature was kept constant and the monomer concentration was varied, the molecular weights of the polymers of all the catalyst systems I–V distinctly increased with increasing monomer concentration (Figure 6). In analogy

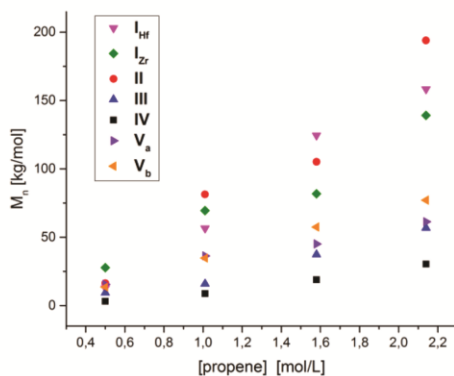


**Figure 6.** Average molecular weights of polypropylenes produced with I–V at constant polymerization temperature (45 °C) and varying monomer concentration.

to the results at varied polymerization temperature, the lowest molecular weights were observed with the 2-phenyl-substituted EBFI-type complex IV. The molecular weights of the polypropylenes produced with III and V increased moderately, whereas the most significant impact of the monomer concentration was observed with complexes I and II.

**Olefinic End Groups.** The chain release reactions are known to be crucial for the average molecular weight of the produced polypropylenes. Examination of the occurring termination reactions was conducted via high temperature  $^1\text{H}$  NMR spectroscopy of polypropylene samples produced at different polymerization temperatures ([propene]: 2.14 M, 45–75 °C) and at varying monomer concentrations ([propene]: 2.14–0.50 M, 45 °C) with catalysts I–V (Figure 7 and Table S1). For all the hafnium-based metallocene catalysts  $\text{I}_{\text{Hf}}$ –V the  $\beta$ -methyl elimination mechanism (Figure 7, green) was identified to be the most favored elimination process leading to a release of polymer chains bearing allylic end groups. In

addition, vinylidene end groups as a result of  $\beta$ -hydride elimination (Figure 7, orange) and internal end groups caused by allylic C–H bond activation (Figure 7, purple) were detected.<sup>41,42</sup> Switching from the hafnocene complex  $\text{I}_{\text{Hf}}$  to the zirconium analogue  $\text{I}_{\text{Zr}}$  the selectivity toward chain release via  $\beta$ -methyl elimination significantly decreased.<sup>43</sup> The highest selectivity toward the process of  $\beta$ -methyl elimination was observed with complex IV, which generated polypropylenes with up to 95% allylic chain ends. For all complexes I–V the  $\beta$ -methyl elimination process was accelerated with increasing temperature. This is in line with previous results of  $C_2$ -symmetric hafnocenes and may be explained by a higher estimated activation barrier for the process of  $\beta$ -methyl elimination considering the notable energy difference for C–C vs C–H bond cleavage.<sup>40,44</sup> For complexes  $\text{I}_{\text{Zr}}$ , II, and  $\text{V}_a$  significant amounts of internal end groups were detected, especially at lower polymerization temperatures and increased monomer concentrations. If the monomer concentration was lowered at a constant polymerization temperature, the amount of allylic chain ends significantly increased for complexes  $\text{I}_{\text{Zr}}$ –V, whereas the selectivity toward vinylidene and internal end groups considerably decreased. Because the  $\beta$ -hydride elimination process is suggested to be bimolecular and a unimolecular process is energetically more favored for the  $\beta$ -methyl elimination, it becomes obvious that higher monomer concentrations lower the selectivity toward allylic chain ends.<sup>27,45</sup> In line with all other metallocene catalysts, complex  $\text{I}_{\text{Hf}}$  exhibited a high selectivity toward allylic chain ends at low monomer concentrations (0.50 M). However, the selectivity toward allylic chain ends was surprisingly low at 1.01 M and again substantially increased with a further increasing monomer concentration.

**Stereoregularity.** A particular interest was directed to the stereoregularity of the polypropylenes. Therefore, the tacticity of all the polymers produced with complexes I–V was examined. The temperature-dependent stereoselective behavior of all the complexes, offering stereoregularities between 3% and 93% *mmmm*, is visualized in Figure 8. The polymers of complexes I–III and  $\text{V}_b$  revealed generally low tacticities, which significantly increase with increasing the polymerization temperature. Comparing these four ligand structures, the stereoselectivity of  $\text{V}_b$  was generally the lowest and those of II and III were considerably higher, while the highest stereoselectivities were observed with  $\text{I}_{\text{Hf}}$  and  $\text{I}_{\text{Zr}}$ . For the latter ligand framework, the zirconocene analogue  $\text{I}_{\text{Zr}}$  had a distinctly higher temperature dependency on its stereoregularity than the hafnium complex  $\text{I}_{\text{Hf}}$ . In contrast, the polypropylenes produced with IV and especially  $\text{V}_a$  were highly isotactic, but a significant decrease in the tacticity was observed at elevated temperatures.

In previous contributions, two main mechanisms have been proposed to explain the opposing trends in tacticity. For the increased stereoregularity at higher polymerization temperatures, the chain-back-skip mechanism served as a plausible explanation because an accelerated back-skip of the polymeryl chain from the “aspecific” to the “specific” site occurs.<sup>18,43,46,47</sup> In the case of decreasing stereoselectivity with increasing temperature, the cascade reaction of chain-end epimerization was held responsible, which is in analogy to the trend of  $C_2$ -symmetric complexes.<sup>30,40,48</sup> Considering the general similarities of the applied catalysts, which are all based on the identical  $C_1$ -symmetric EBFI-type framework, such extreme differences

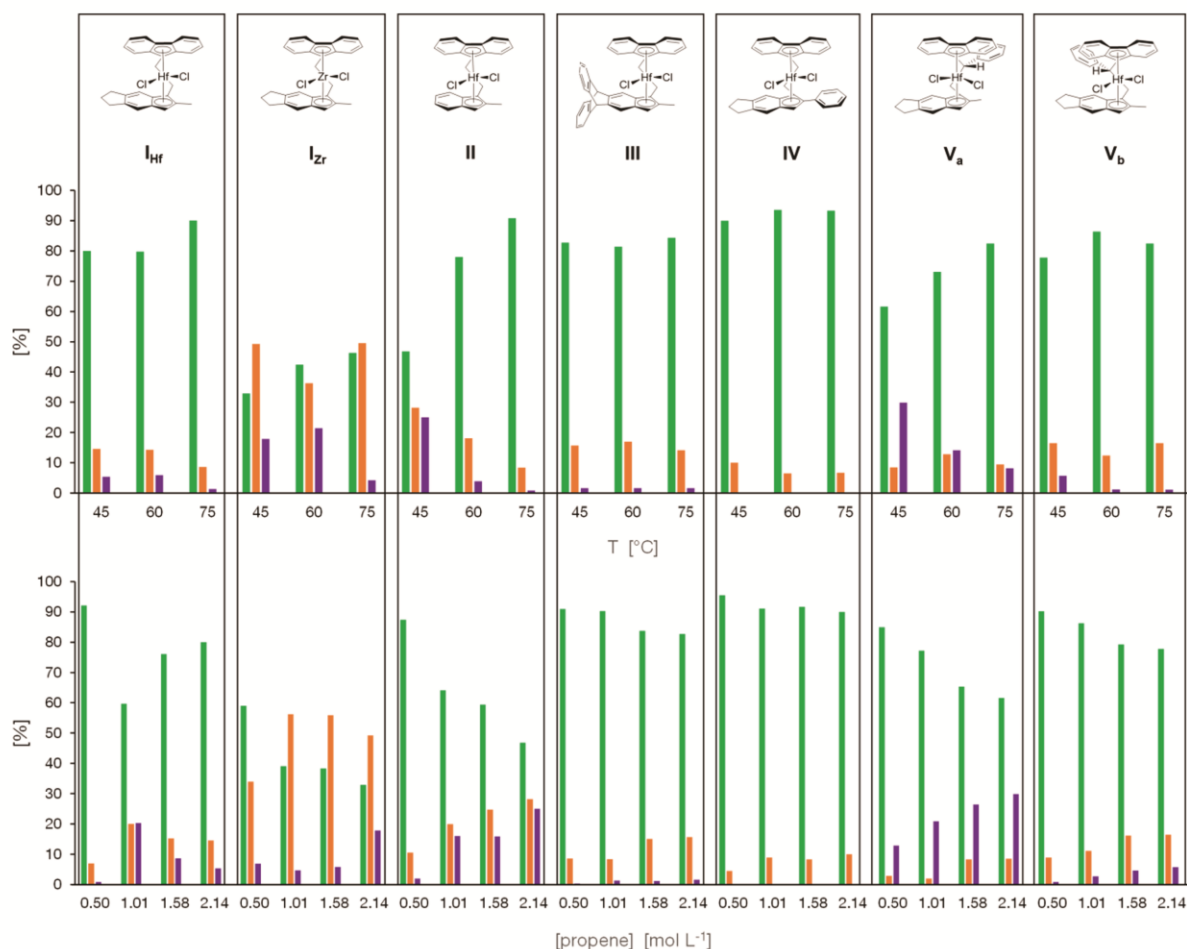


**Figure 7.** Determination of olefinic end-group composition of polypropylenes produced with I–V via  $^1\text{H}$  NMR spectroscopy (300 MHz, 140 °C,  $\text{C}_6\text{D}_5\text{Br}$ , Table S1). The relative amounts of allylic chain ends (green), vinylidene chain ends (orange) and internal double bonds (purple) are visualized. The assignment of olefinic end groups in the  $^1\text{H}$  NMR spectrum is provided in the Supporting Information (Figure S32). The results at constant monomer concentration (2.14 M) and varying polymerization temperature are depicted on the top, and the ones at constant polymerization temperature (45 °C) and varying monomer concentration are depicted at the bottom.

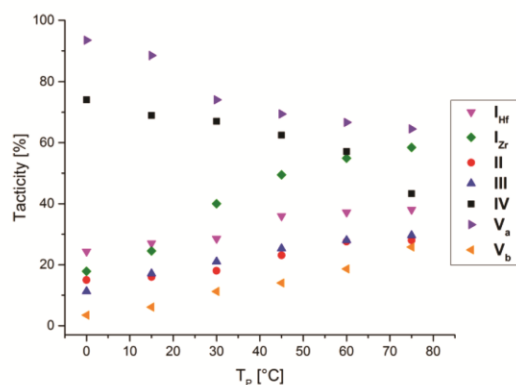


**Figure 8.** Tacticities (% *mmmm*) of polypropylene produced with I–V at constant monomer concentration (2.14 M) and varied polymerization temperature determined via  $^{13}\text{C}$   $\{^1\text{H}\}$  NMR spectroscopy (300 MHz, 140 °C,  $\text{C}_6\text{D}_5\text{Br}$ , Table 4).

in the counterplay of chain-end epimerization and chain-backskip mechanism seem rather unlikely.

Previous experimental and computational results of EBFI-type complexes with unsubstituted indenyl and fluorenyl moieties and a phenyl-substituted ethylene bridge (VI) revealed a significant impact of different chelate ring conformations on the tacticity of the resulting polypropylenes (Figure 2).<sup>17,26</sup> Detailed comparison of these findings with the results of Figure 8 strongly suggested a fundamental impact of different chelate ring conformations on the resulting tacticity of the polypropylenes. In this context, an impact of the  $\Pi$ -forward and  $\text{Y}$ -backward conformations is expected not only for the bridge-substituted complexes  $\text{V}_a$  and  $\text{V}_b$  but also for complexes I–IV comprising unsubstituted ethylene bridges. While the stereoregular behaviors of I–III and  $\text{V}_b$  were similar to those of the  $\text{Y}$ -backward conformer of complex VI, the tacticity trends of the predominantly isotactic polypropylenes produced with IV and  $\text{V}_a$  were comparable to those of the  $\Pi$ -forward chelate ring conformer of complex VI.<sup>17</sup> Considering the preferred conformations of complexes I–V, the determined stereo-

regularities of the produced polymers were all in line with the preferred chelate ring conformers observed in the solid state and verified by DFT calculations (Figure 3 and Tables 2 and 3). Because one conformer is energetically more favored, the energy barrier between both states determines a possible interconversion, leading to a dynamic equilibrium of both conformations in solution. Although a considerable energy barrier between both conformers is suggested in the case of bulky substituents at the ethylene bridge (V and VI), smaller energy barriers are observed in the case of an unsubstituted ethylene bridge (I–IV). Accordingly, an interconversion between both conformers may already occur at ambient temperature for complexes I–IV, whereas elevated temperatures are necessary for a significant interconversion using complexes V and VI.

By estimating similar enantiofacial selectivities for the inward and outward site of the  $\Pi$ -forward and Y-backward chelate ring conformations of the reference system (EBFI complex VI, Figure 2) and our investigated EBFI complexes I–V, two conformations, catalyzing mainly isoselective or nonselective sequences, are expected to exist for all complexes I–VI of this catalyst class. Consequently, the observed stereoselectivities regarding low polymerization temperatures are predominantly catalyzed by the preferred chelate ring conformation, whereas accelerated interconversion and a convergence to a 1:1 mixture occur when the temperature rises. If a substituted ethylene bridge in the EBFI-type metallocene framework (V and VI) is applied compared to an unsubstituted one (I–IV), the energy barrier for a possible interconversion between both conformations is considerably higher. Therefore, the preferred conformation is highly populated for both complexes V<sub>a</sub> and V<sub>b</sub> at low to moderate temperatures, and interconversion to the nonpreferred conformation is rather unlikely. Some interconversion going along with an increased population of the disfavored ring conformation is suggested to occur at elevated temperatures because the stereoregularities of both diastereomers (V<sub>a</sub> and V<sub>b</sub>) converge. If the EBFI-type complexes with unsubstituted ethylene bridge (I–IV) are applied, interconversion of the preferred and less preferred conformation is suggested to already occur at lower polymerization temperatures. Consequently, complexes I–III appear in a preferred Y-backward ring conformation, catalyzing mainly atactic polypropylene; however, the tacticity increased at elevated temperatures because the population of the disfavored  $\Pi$ -forward conformation increases. The analogous principle is suggested for complex IV, starting with a preference for the  $\Pi$ -forward conformation at low polymerization temperatures and assuming an accelerated population of the disfavored Y-backward ring conformation through a decrease in the tacticities of the produced polymers at higher temperatures. Although we believe that the major trends of the observed stereoselectivities are determined by the interplay of both chelate ring conformations, an additional impact of the chain-back-skip mechanism and the process of chain-end epimerization on the presented temperature-dependent tacticities should not be excluded.

To evaluate the impact of both mentioned mechanisms, the stereoregularities of the polymers produced at 45 °C at various monomer concentrations were investigated (Figure 9). The chain-back-skip mechanism, describing the possible migration of the polymeryl chain from the sterically crowded inward to the less crowded outward coordination site (Figure 1), generally leads to lower tacticities in the case of higher

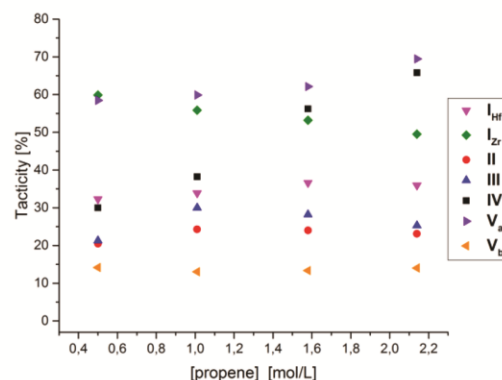


**Figure 9.** Tacticities (% *mmm*) of polypropylenes produced with I–V at constant polymerization temperature (45 °C) and varying monomer concentration determined via <sup>13</sup>C {<sup>1</sup>H} NMR spectroscopy (300 MHz, 140 °C, C<sub>6</sub>D<sub>3</sub>Br, Table 4).

monomer concentrations, whereas the cascade reaction of chain end epimerization significantly lowers the stereoregularities in the case of low monomer concentrations.

Accordingly, the polymers produced with complexes IV and V<sub>a</sub> were mainly influenced by the process of chain-end epimerization, since a consistent trend of increasing tacticity with increased monomer concentration was observed. Both complexes prefer the  $\Pi$ -forward chelate ring conformation which catalyzes isotactic enriched polypropylene. As a result, the epimerization mechanism usually observed with the application of C<sub>2</sub>-symmetric metallocene catalysts distinctly impacts the stereoselective behavior at varied monomer concentrations.<sup>30,40,48</sup> On the contrary, the polypropylene catalysis with complex I<sub>Zr</sub> is one of the most prominent examples being dominated by the chain-back-skip mechanism.<sup>18,19,21</sup> To our surprise, the tacticities of the polymers produced with the hafnium analogue I<sub>Hf</sub> were far less influenced by the chain-back-skip mechanism. Consequently, the stereoregularities were less dependent on changes in the monomer concentration, and the tacticity trends were very similar to those of hafnocene complexes II and III. In all three cases, the isotacticities tended to be lower for small (0.50 M) and large (2.14 M) monomer concentrations but substantially higher at monomer concentrations in between these values. These findings suggest a superordinated impact of the chain-end epimerization mechanism at low monomer concentrations and a superordinated impact of the chain-back-skip mechanism at high monomer concentrations. Regarding complex V<sub>b</sub>, the impact of the monomer concentration on the tacticities of the respective polypropylenes was negligible. The overall low impact of the chain-back-skip mechanism on the catalytic performance of the applied hafnocene complexes may be partially explained by the applied polymerization temperature. Previous studies have demonstrated a more explicit impact of this mechanism if lower polymerization temperatures were used.<sup>19,21</sup>

The general mechanism of chain-end epimerization is known to be a cascade reaction of  $\beta$ -hydride elimination and several rotation and reinsertion steps.<sup>30</sup> Epimerization via a metallocene allyl dihydrogen intermediate has also been suggested in the literature, although further experimental investigations with deuterium-labeled propene have excluded this pathway at least using C<sub>2</sub>-symmetric *rac*-EBI metallocenes.<sup>42,49</sup> The latter

pathway via an allyl dihydrogen intermediate is also considered unlikely in the present study using EBFI-type metallocenes, since no internal double bonds as a result of allylic C–H bond activation were observed using complex IV. From the observations made in the present study, the results of complex IV suggest an epimerization process based on  $\beta$ -methyl elimination. The highest selectivities toward allylic chain ends were observed in combination with the generally lowest molecular weights, indicating an exceptionally high occurrence of the  $\beta$ -methyl elimination pathway. In addition, the most significant impact of the process of chain-end epimerization on the resulting tacticities of the produced polymers was identified. All combined findings lead to the conclusion, that chain-end epimerization via  $\beta$ -methyl elimination represents the most plausible explanation. Keeping in mind the results depicted in Figure 7 at low monomer concentrations, the selectivity toward chain release via  $\beta$ -methyl elimination was extraordinarily high for all hafnium-based catalysts  $I_{\text{Hf}}-V$ , which suggests a general epimerization mechanism through  $\beta$ -methyl elimination if hafnium is combined with an EBFI framework.

The polypropylenes produced with all the catalysts (I–V) were highly regioregular under all applied conditions. Neither 2,1-threo or erythro nor 3,1-isomerization defects were detected by standard  $^{13}\text{C}$  NMR spectroscopy (see Experimental Section).<sup>27,50</sup> Because no significant differences in the regioselectivities of all the applied complexes were observed, the melting behavior of the produced polymers should mainly depend on the stereoregularities. In the case of short average chain lengths, the molecular weight possesses a distinct impact on the melting transitions as well.<sup>51</sup> Using EBFI-type complexes in the polymerization of propene, melting transitions up to 149 °C were detected with complex  $V_a$  (Table 4). A comparison of the melting transitions of the mainly isotactic polymers produced with complexes IV and  $V_a$  revealed significantly higher melting points for the polypropylenes of complex  $V_a$  at comparable degrees of the overall tacticity. Comparing the results of Table 4, entry 37 (IV,  $T_p$ : 0 °C, 2.14 M, 1100 kg/mol) and Table 4, entry 52 ( $V_a$ ,  $T_p$ : 45 °C, 2.14 M, 61 kg/mol), both polypropylenes exhibited 74% isotactic sequences (*mmmm*). Whereas a melting transition of 116 °C was observed for the polymer of complex IV, the polypropylene of complex  $V_a$  revealed a melting transition of 137 °C. This observation indicated distinct differences in the microstructure of the produced polymers because the stereoregularity of crystallizable sequences within a polymer chain determines the type and size of crystalline spherulites, thereby essentially defining the melting transition.<sup>24,52</sup> Accordingly, a quite uniform distribution of stereodeficits is expected for complex IV, whereas sequences with less stereodeficits are expected for complex  $V_a$ , alternating with sequences of particularly lower stereoselectivity. This hypothesis was supported by additional differential scanning calorimetry (DSC) data, providing a distinctly higher melting enthalpy for the polymer of complex IV (IV: 52 J/g vs  $V_a$ : 39 J/g) and the detection of a glass transition exclusively for the polymer of complex  $V_a$  (–4 °C). Consequently, we believe that the observed differences in the microstructures of the analyzed polypropylenes originate from the different energy barriers between preferred and non-preferred chelate ring conformation. Higher interconversion frequencies and a more uniform microstructure in the case of unsubstituted ethylene bridge (IV,  $T_p$ : 0 °C) are suggested compared to the formation of blocklike structures within a polymer chain by slower interconversion frequencies in the case

of a substituted ethylene bridge ( $V_a$ ,  $T_p$ : 45 °C). Based on the present observations, the tailored synthesis of high-melting polypropylene block structures, comprising different stereoregular properties by an appropriate adjustment of the dynamic conformational interconversion, represents the final objective of this study.

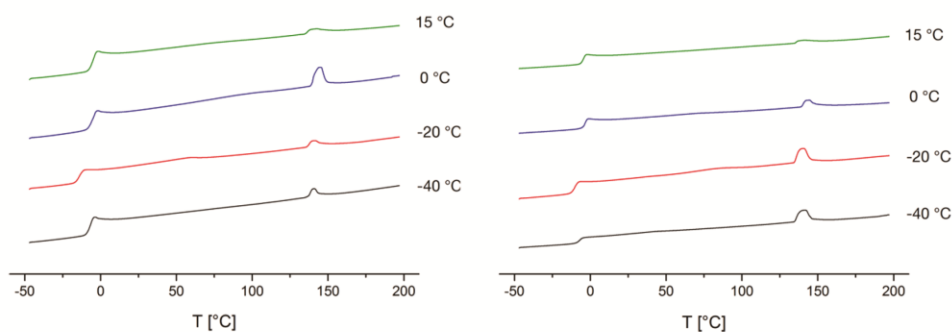
**High-Melting, Elastic Polypropylene.** The synthesis of polymer block structures via a coordinative polymerization of olefins is known to be a highly challenging task because statistical distributions are generally favored. However, it facilitates the synthesis of new polymers with unique properties based on well-studied and largely available monomer units. One of the most prominent examples for the generation of olefin-based block structures is introduced by Arriola et al., where the block copolymers are synthesized by chain shuttling between two catalysts comprising different monomer selectivities.<sup>12</sup> The application of a living/“quasi-living”-type coordinative polymerization mechanism can also be utilized for the synthesis of tailored block structures. The synthesis of PE/PP multiblock copolymers, recently introduced by the group of Coates, herein represents a highlighted example.<sup>15</sup> Regarding the formation of stereoblock copolymers based on polypropylene, the synthesis of elastic polypropylene through an oscillating stereocontrol mechanism using unbridged bis(2-phenylindenyl)zirconium dichloride depicts a prominent example.<sup>10</sup> Although today the overall mechanism is considered more complex, the basic principle of block formation is assumed to proceed by a dynamic isomerization equilibrium switching between two catalytically active isomers comprising different stereoselectivities.<sup>10,53</sup> In the case of EBFI-type complexes, the presence of two different chelate ring conformers enables the catalysis of polypropylene with isotactic and/or atactic sequences. By a possible dynamic interconversion between both chelate ring conformations, the formation of tailored “PP–iPP” block structures within one polymer chain becomes feasible. Considering mainly atactic polypropylene bearing isolated isotactic sequences, crystallization of these isotactic sequences leads to a physically cross-linked network in an otherwise amorphous matrix.<sup>54</sup> Based on this fundamental principle of thermoplastic elastomers (TPE), our complexes (I–V) were examined for the production of high-melting, elastic polypropylene. Since high molecular weights are indispensable to ensure a covalent connection between both stereoblocks, low polymerization temperatures are essential (Figure 5). The main component needs to be of amorphous nature, which led to a complex favoring the unselective Y-backward ring conformation (Figure 8). In addition, interconversion between both conformations must proceed under the applied conditions, which excluded any complexes with ethylene bridge substituents. In the case of an optimized interconversion frequency between both conformations, the produced isotactic sequences should be of an appropriate length and distribution to facilitate a slightly cross-linked, elastomeric network.

Complex  $V_a$  demonstrated the general capability to catalyze high-melting, isotactic polypropylenes (~150 °C) with a 2-methyl and 5,6-cycloalkyl substitution pattern at the indenyl moiety of the EBFI framework, if the isoselective  $\Pi$ -forward conformation is present. Consequently, we investigated the bridge unsubstituted analogues  $I_{\text{Hf}}$  and  $I_{\text{Zr}}$  for the synthesis of a high-melting thermoplastic elastomer (TPE) based on propene. Therefore, polypropylenes were synthesized at –20 and –40 °C and compared to the results obtained at 0 and 15 °C (Table 5). All polymers produced at –20 and –40 °C as well as the

**Table 5.** Conditions and Results for the Polymerization of Propene at Low Temperatures with Complexes  $I_{Hf}$  and  $I_{Zr}$  in Toluene<sup>a</sup>

entry	catalyst	$T_p^b$	fraction <sup>c</sup>	$T_g^d$	$T_m^d$	$\Delta H_m^e$	<i>mmmm</i> <sup>f</sup>	$M_n^g$	$D^h$
1	$I_{Hf}$	-40		-7	140	1.1	28	250	3.3
2	$I_{Hf}$	-20		-11	139	1.4	27	280	2.3
3	$I_{Hf}$	-20	residue (16 wt %)	-5	141	17	49	180	2.4
4	$I_{Hf}$	-20	pentane (84 wt %)	-7	—	—	25	210	2.3
5 <sup>i</sup>	$I_{Hf}$	0		-4	144	4.0	24	1300	2.2
6 <sup>i</sup>	$I_{Hf}$	15		-4	138	1.0	27	200	1.7
7	$I_{Zr}$	-40		-7	140	5.9	18	180	2.0
8	$I_{Zr}$	-20		-10	139	4.1	31	170	1.9
9	$I_{Zr}$	-20	residue (20 wt %)	-7	140	20	59	120	2.1
10	$I_{Zr}$	-20	pentane (80 wt %)	-7	—	—	26	160	1.8
11 <sup>i</sup>	$I_{Zr}$	0		-4	142	2.5	18	170	2.2
12 <sup>i</sup>	$I_{Zr}$	15		-4	137	1.0	25	160	1.7
13 <sup>i</sup>	$V_b$	0		-7	—	—	3	1200	1.4

<sup>a</sup> $V_{\text{toluene}}$ : 80 mL;  $n$ : 5.0  $\mu\text{mol}$ ;  $[C_3]$  not defined (see Experimental Section); scavenger (TIBA): 2.2 mmol; “—”  $\triangleq$  “not observed”. <sup>b</sup> $T_p$  in  $^\circ\text{C}$ . <sup>c</sup>Fractions after Soxhlet extraction of entries 2 and 8. <sup>d</sup> $T_g$  in  $^\circ\text{C}$ , determined after tempering of the polymer samples. <sup>e</sup>Melting enthalpy in  $\text{J/g}$ . <sup>f</sup>In %, determined via  $^{13}\text{C}$   $\{^1\text{H}\}$  NMR spectroscopy assuming the enantiomorphic site model. <sup>g</sup>In  $\text{kg mol}^{-1}$ . <sup>h</sup> $D$ :  $M_w/M_n$ . <sup>i</sup>Polymers of Table 4, entries 1, 2, 10, 11, and 55,  $[C_3]$ : 2.14 M.

**Figure 10.** Heat flow (exo-down) of tempered polypropylene samples produced with  $I_{Hf}$  (left) and  $I_{Zr}$  (right) at 15, 0, -20, and -40  $^\circ\text{C}$  (see Table 5 and Experimental Section for details).

polypropylenes produced at 0 and 15  $^\circ\text{C}$  were predominantly of amorphous and elastic nature with overall tacticities between 18% and 31% *mmmm*. However, the average molecular weights of the polymers produced with  $I_{Hf}$  at 0  $^\circ\text{C}$  and those produced at even lower temperatures differed significantly. The larger molecular weights of polymers produced at 0  $^\circ\text{C}$  were herein attributed to a higher monomer concentration compared to the polymerization reactions at -20 and -40  $^\circ\text{C}$ , owing to the necessary differences with respect to the polymerization setup (see Experimental Section). In contrast, there was a negligible correlation between the average chain lengths of the polypropylenes produced with  $I_{Zr}$  and the applied polymerization temperature and procedure. To identify chain sequences of distinctly differing stereoregular nature produced with either  $I_{Hf}$  or  $I_{Zr}$ , the polymers synthesized at -20  $^\circ\text{C}$  were separated via Soxhlet extraction with pentane (Table 5, entries 3, 4, 9, and 10). In both cases, the extracted polymer was completely amorphous and had an observable glass transition at -7  $^\circ\text{C}$ . In contrast, semicrystalline polymer samples with defined melting and glass transitions ( $\sim 141$   $^\circ\text{C}$  and -6  $^\circ\text{C}$ ) were observed via DSC analysis of the residues. In addition,  $^{13}\text{C}$  NMR spectroscopy revealed tacticities of 49% *mmmm* ( $I_{Hf}$ ) and 59% *mmmm* ( $I_{Zr}$ ), thereby proving the covalent connection of atactic and isotactic block sequences within a polymer chain, because the melting transitions need to derive from PP

sequences with significantly higher isotacticity. Consequently,  $i$ PP blocks covalently bond and embedded in a generally atactic matrix were obtained.

To identify the degree of physical cross-linking in the amorphous polymer network, all polypropylenes were tempered and examined via DSC analysis. Figure 10 provides the dependency of melting transitions and glass transition temperatures of polypropylene samples produced with  $I_{Hf}$  and  $I_{Zr}$  at different polymerization temperatures. According to the amorphous nature of the polymers, all depicted heat flow curves show distinct glass transitions between -4 and -11  $^\circ\text{C}$  (Table 5). The observed glass transitions are in a typical range for polypropylene materials but generally constitute a considerable limitation regarding the application of pure propylene-based polymers in cold weather climates. However, there exist strategies to adjust the melting transitions by adding small amounts of ethylene to the propylene feed.<sup>55–57</sup> Nevertheless, the focus was primarily directed toward the melting temperatures of the produced polypropylenes in the present contribution. Accordingly, after tempering of the polymer samples melting transitions at approximately 140  $^\circ\text{C}$  were detected. The largest melting enthalpies were obtained for the polypropylenes produced with  $I_{Hf}$  at 0  $^\circ\text{C}$  (Table 5, entry 5) and with  $I_{Zr}$  at -20 to -40  $^\circ\text{C}$  (Table 5, entries 7 and 8), indicating the largest content of crystalline domains. In this

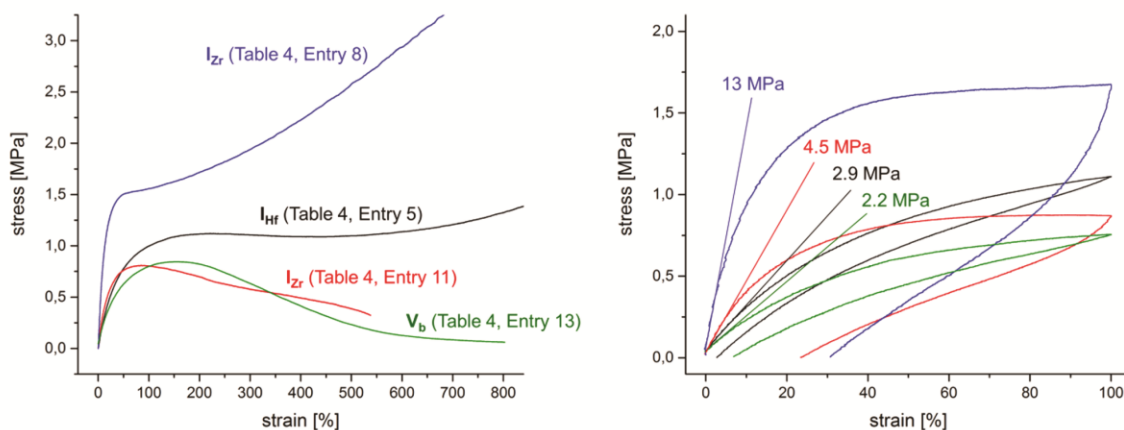


**Figure 11.** Stress–strain (left) and cyclic stress–strain (right) hysteresis curves of compression-molded polypropylene specimen (see the Experimental Section for details on specimen fabrication). The Young modulus of all samples is determined at the initial region of linear stress–strain behavior.

context, the crystalline portions within the polymer sample need to derive from isotactic regions in the polypropylene microstructure with an estimated isotacticity  $>85\%$  *mmmm*, taking the results of complex  $V_a$  into consideration. If the polymerization temperature is reduced, the population of the disfavored chelate ring conformation, the interconversion frequencies, and the chain propagation rate decrease. Although the absolute impact of the temperature on all three parameters is hard to predict, optimized conditions for enhanced physical cross-linking are disclosed by the DSC measurements. For the polymers produced at  $15\text{ }^\circ\text{C}$ , the melting enthalpies at approximately  $140\text{ }^\circ\text{C}$  were rather low. It is suggested that the interconversion frequencies were too high that a proper formation of block structures was not obtained. The largest amount of cross-linking caused by crystalline domains was obtained at higher temperatures for  $I_{Hf}$  compared to the zirconium analogue. If the polymerization temperatures were too low, the population of the nonpreferred  $\Pi$ -chelate ring conformer became negligible, resulting in the exclusive formation of atactic polypropylene. Since the covalent connection of amorphous and crystalline regions is essential for the mechanical properties of the thermoplastic elastomer, high molecular weights are considered indispensable.

To investigate the overall impact of varying molar masses and different degrees of crystallinity on the mechanical properties, linear and cyclic stress–strain measurements were conducted (Figure 11). The stress–strain behavior of high-molecular-weight polypropylene (Figure 11, black:  $I_{Hf}$ ,  $M_n$ : 1300 kg/mol) with considerable physical cross-linking ( $T_m$ :  $144\text{ }^\circ\text{C}$ ,  $\Delta H_m$ :  $4.0\text{ J/g}$ ) and no cross-linking (Figure 11, green:  $V_b$ ,  $M_n$ : 1200 kg/mol) was compared to that of moderate-molecular-weight polymers comprising lower (Figure 11, red:  $I_{Zr}$ ,  $M_n$ : 170 kg/mol,  $T_m$ :  $142\text{ }^\circ\text{C}$ ,  $\Delta H_m$ :  $2.5\text{ J/g}$ ) and higher (Figure 11, blue:  $I_{Zr}$ ,  $M_n$ : 170 kg/mol,  $T_m$ :  $139\text{ }^\circ\text{C}$ ,  $\Delta H_m$ :  $4.1\text{ J/g}$ ) amounts of physical cross-linking. The polymer obtained with catalyst  $I_{Hf}$  (Figure 11, black) displayed ideal elastic behavior, whereas that obtained with  $I_{Zr}$  ( $T_p$ :  $-20\text{ }^\circ\text{C}$ , Figure 11, blue) revealed considerable plastomeric behavior, which was disclosed by strain-induced crystallization at higher strain rates. In contrast, the polypropylenes of complex  $V_b$  (Figure 11, green) and  $I_{Zr}$  ( $T_p$ :  $0\text{ }^\circ\text{C}$ , Figure 11, red) exhibited decreasing stress when the strain was substantially increased, indicating stress-induced

creeping of the polymer chains because the polymer network was not sufficiently cross-linked. In line with previous observations, a significant dependency of the degree of crystallinity on the Young's modulus is observed.<sup>58</sup> In this context, physical cross-linking may be facilitated in the case of lower average molecular weights, keeping in mind that the investigated specimens were not tempered before the measurements.<sup>59</sup> More importantly, the results of cyclic stress–strain hysteresis curves emphasize the necessity of high-molecular-weight polymers when addressing elastic polymer materials, in order to ensure high recovery rates, resulting in low amounts of irreversible deformation. In addition to the improved cross-linking of crystalline and amorphous regions with higher molecular weight polymers, stress-induced creeping of polymer chains is prohibited by increased amounts of entanglements in the polymer network.

The outstanding mechanical properties of elastic polypropylenes produced with  $I_{Hf}$  have already been highlighted in previous studies.<sup>20</sup> Furthermore, the investigation of the mechanical behavior by tensile tests of high-molecular-weight elastic polypropylenes was reported as a typically cross-linked rubber material.<sup>24</sup> Since the samples possessed predominantly amorphous nature, the cross-linking was estimated to derive from entanglements caused by the high-molecular-weight polymer chains and some crystallinity deriving from statistically occurring isotactic enriched sequences.<sup>20,21,52</sup> Consequently, the temperature stability of these polymers was rather limited due to the low melting transitions. Accordingly, this contribution provides a unique strategy toward the synthesis of high-melting ( $T_m \sim 140\text{ }^\circ\text{C}$ ), elastic polypropylene in a simple one-pot, one-catalyst synthesis. In this connection, the elucidation of the intricate stereoregularity process using EBFI-type catalysts in the polymerization of propene facilitated the directed adjustment of the chain propagation and termination rate in combination with an appropriate population and interconversion frequency of both chelate ring conformers. Tensile tests underlined the necessity of extraordinarily high molecular weights, which are only accessible by hafnium-based catalysts, and an adequate amount of physical cross-linking. Considering the simple polymerization setup in order to generate these high-melting PPs, and the tremendous industrial demand of elastic, olefin-based polymer materials,

the presented strategy certainly displays a highly interesting and novel route for the production of tailored  ${}^i\text{PP}-{}^t\text{PP}$  block structures building up a new generation of high-temperature-stable propylene-based elastomers. Nevertheless, continuative studies are currently conducted to optimize the applicability of the present production process especially pertaining to the required low polymerization temperatures and to evaluate further setup parameters including bulk polymerization techniques.

## CONCLUSION

This report addresses the formation of elastic polypropylene using EBFI-type *ansa*-metallocenes, which have so far proven their capability concerning the outstanding mechanical properties, even though the amalgamation of elasticity in combination with high-melting characteristics has not yet been fulfilled. Accordingly, several novel and literature known EBFI-type *ansa*-metallocene complexes (Zr, Hf) with a varied 2,5,6-indenyl substitution pattern containing a substituted and unsubstituted ethylene bridge were examined referring to their catalytic behavior in the polymerization of propene. We investigated the impact of different applied polymerization temperatures and monomer concentrations on the polymer properties focusing on the chain release mechanisms and the stereoregularities of the produced polypropylenes. The obtained results provoked particular interest toward possible chelate ring conformers occurring in an EBFI–metallocene framework in the  $\Pi$ -forward and Y-backward conformation. X-ray diffraction analysis of the hafnocenes II–V in combination with the reported solid-state structures of complexes  $\text{I}_{\text{Zr}}$  and  $\text{I}_{\text{Hf}}$  disclosed the preference of one particular chelate ring conformation dependent on the different indenyl (I–IV) and ethylene bridge (V) substitution patterns. Verification of the preferred conformation including the catalytically relevant, optimized  $\text{L}_2\text{M}(\text{Bu})^+$  complex structures (I–V) was carried out by DFT calculations addressing the free energy differences and the barrier heights of interconversion of both chelate ring conformers. In accordance with previous experimental and computational studies on similar bridge-substituted EBFI-type metallocenes, an isoselective  $\Pi$ -forward conformation and a nonselective Y-backward conformation are proposed for the bridge-substituted as well as the unsubstituted EBFI-type metallocenes (I–V). Consequently, the temperature-dependent population of preferred and nonpreferred ring conformations determines the tacticities and dominate the usually accountable mechanisms of chain-end epimerization and chain migration mechanism. Nevertheless, the additional impact of these two mechanisms was elucidated by polymerization experiments at constant temperature and varied monomer concentrations with complexes I–V. The results revealed significant differences depending on the substitution pattern and the metal center. Considering major results of the determined molecular weights, the occurring chain release mechanisms, and the cascade process of chain end epimerization, a modified epimerization mechanism via a  $\beta$ -methyl elimination pathway is proposed. More importantly, the presence of a tacticity-determining preferred chelate ring conformer and the dynamic equilibrium between both conformations during the polymerization reaction opens up the opportunity to synthesize defined  ${}^i\text{PP}-{}^t\text{PP}$  block structures. In this context, an appropriately adjusted interplay of chain propagation, chain release, and interconversion between the isoselective and nonselective conformation facilitated the formation of high-melting ( $T_m \sim$

140 °C), elastic polypropylene in a simple one-pot, one-catalyst approach. Examination of the mechanical behavior disclosed an indispensable interaction between physical cross-linking and high-molecular-weight polymer chains to ensure high elasticity in combination with proper recovery rates.

## EXPERIMENTAL SECTION

**General.** All reactions involving air- and moisture-sensitive compounds were performed under an argon atmosphere using standard Schlenk or glovebox techniques. All chemicals, unless otherwise stated, were purchased from Aldrich, Acros, or VWR and used as received. Dry toluene, dichloromethane, *n*-pentane, and *n*-hexane were purified with an MBraun MB-SPS-800 solvent purification system. Deuterated dichloromethane was refluxed over  $\text{CaH}_2$  and distilled prior to use. Propene (99.5% by Westfalen AG) was purified by passing it through two columns filled with BASF catalyst (R3–11) and molecular sieves 3–4 Å. Elemental analysis was conducted with a EURO EA (HEKA tech) instrument equipped with a CHNS combustion analyzer.

NMR ( ${}^1\text{H}$  and  ${}^{13}\text{C}$  { ${}^1\text{H}$ }) measurements were recorded on a Bruker AV400 or AV500C spectrometer at ambient temperature. Chemical shifts  $\delta$  were reported in ppm relative to tetramethylsilane and calibrated to the residual  ${}^1\text{H}$  or  ${}^{13}\text{C}$  signal of the deuterated solvent. The NMR spectra of the polymers were measured with an ARX-300 spectrometer at 140 °C with 50–60 mg/mL in bromobenzene- $d_5$ .

Gel permeation chromatography (GPC) was performed with a PL-GPC 220 instrument equipped with 2  $\times$  Olexis 300  $\times$  7.5 mm columns and triple detection using a differential refractive index detector, a PL-BV 400 HT viscometer, and light scattering (Precision Detectors Model 2040; 15° and 90°). Measurements were performed at 160 °C using 1,2,4-trichlorobenzene (TCB; 30 mg BHT/L) with a constant flow rate of 1 mL/min and a calibration set with narrow MWD polystyrene (PS) and polyethylene (PE) standards. Samples were prepared by dissolving 0.9–1.1 mg polymer in 1.0 mL of stabilized TCB for 10–15 min at 160 °C immediately before each measurement.

Differential scanning calorimetry (DSC) was conducted on a DSC Q2000 instrument. Between 3 and 8 mg of the polymer was sealed into a DSC aluminum pan and heated from 20 to 200 °C at a rate of 10 °C/min. After holding the temperature for 2 min, the sample was cooled down to –50 °C at a rate of 10 °C/min and heated up again in the same manner. The reported values are those determined during the second heating cycle. For tempering experiments, the polymer samples were kept at a constant temperature at 10 °C below the melting point for 60 min. The temperature was reduced at a rate of 1 °C/min for an additional 30 min and then cooled down to –50 °C at a rate of 10 °C/min. The polymer was heated up to 200 °C at a rate of 10 °C/min (analyzed exo-down curves) and cooled again to –50 °C at a rate of 10 °C/min.

Stress–strain measurements were performed on a ZwickRoell machine with a strain rate of 4 mm/min and analyzed with testXpert II software. Specimen (dog bone shape, 50 mm long, 4 mm wide (smallest distance)) were cut out of a compression-molded polymer film produced at 150 °C and 150 bar for 1 h.

**Synthesis.** The synthesis procedures and characterization of all new compounds are provided in the Supporting Information. The synthesis of complexes I–III and all the other known compounds were conducted according to reported procedures.<sup>17–19,37</sup>

**Polymerization.** All polymerization reactions between 0 and 90 °C were performed in a 1.1 L Büchi steel autoclave equipped with a paddle agitator, temperature sensor, and a heating/cooling jacket attached to a cryo-/thermostat unit (Thermo Scientific HAAKE DynaMax). The Ar pressure for all manipulations was set to 1.3 bar. Prior to polymerization the autoclave was equipped with 300 mL of dry toluene and 2.0 mL of 1.1 M TIBA solution in toluene and heated up to 90 °C. After maintaining the temperature for 15 min the scrubbing solution was released. For the polymerization, the autoclave was charged with 280 mL of dry toluene and 2.0 mL of 1.1 M TIBA solution in toluene. The metallocene complex (1.0 equiv) was

dissolved in 10 mL of toluene and preactivated with 200 equiv of TIBA at 60 °C for 1 h. After the desired temperature was adjusted, the alkylated metallocene solution was transferred into the autoclave and was pressurized with propene. When the system was equilibrated and stable, the polymerization was started by adding 5.0 equiv of  $[\text{Ph}_3\text{C}][\text{B}(\text{C}_6\text{F}_5)_4]$  dissolved in 10 mL of toluene to the autoclave using a pressure buret ( $p_{\text{pol}} + 1.0$  bar). The propene consumption was monitored using a gas flow meter (Bronkhorst F-111C-HA-33P). Temperature, pressure, time, and total propene consumption were recorded as well. The polymerization reaction was quenched with 2.0 mL of methanol, and the reaction mixture was poured into 1.0 L of acidified methanol. The precipitated polymer was removed from the autoclave, and all the combined polymer was washed and dried at 70 °C *in vacuo* overnight. For complex V, the  $^4\text{PP}/\text{PP}$  mixture was separated by Soxhlet extraction with *n*-pentane for 3 days. The pentane-soluble fraction was attributed to the catalytic activity of complex  $\text{V}_b$ , and the insoluble residue was attributed to the catalytic activity of complex  $\text{V}_a$ .

Polymerization reactions below 0 °C were performed in a 100 mL Schlenk flask. The metallocene complex (1.0 equiv) was dissolved with 10 mL of toluene and preactivated with 200 equiv of TIBA at 60 °C for 1 h. After the *in situ* alkylation was complete, 2.0 mL of 1.1 M TIBA solution in toluene was added, and the volume was increased by adding an additional 60 mL of toluene. The flask was then placed into an isopropanol cooling bath equipped with a Julabo cryostat unit (model FT902) at the desired temperature and stirred for 15 min to ensure isothermal conditions. The Ar supply was stopped, and propene was bubbled through the solution for 15 min with a flow of approximately 1000 mL/min. The polymerization reaction was started by adding 5.0 equiv of  $[\text{Ph}_3\text{C}][\text{B}(\text{C}_6\text{F}_5)_4]$  dissolved in 10 mL of toluene. After a few minutes, when the viscosity of the reaction mixture started to prevent proper stirring, the polymerization reaction was quenched with 2.0 mL of methanol and the reaction mixture was poured into 300 mL of acidified methanol. The precipitated polymer was filtered, washed, and dried at 70 °C *in vacuo* overnight.

**DFT Calculations.** All calculations were performed with the software package Gaussian16, RevA.03.<sup>60</sup> The GGA functional BP86<sup>61,62</sup> was used together with the basis set TZVP<sup>63</sup> for elements C, H, and Cl and the ECP containing LANL2DZ basis set<sup>64</sup> for Hf and Zr. Dispersion corrections were modeled by the GD3BJ method.<sup>65,66</sup> All calculation were conducted in the gas phase, whereas the reported  $\Delta H$  or  $\Delta G$  values were accountable for a temperature of 298.15 K and taken out from the relevant frequency calculations after the optimization.

## ■ ASSOCIATED CONTENT

### Supporting Information

The Supporting Information is available free of charge on the ACS Publications website at DOI: 10.1021/acs.macromol.7b02679.

Synthesis procedures of new compounds,  $^1\text{H}$  NMR and  $^{13}\text{C}$   $\{^1\text{H}\}$  NMR spectra of all key compounds I–V,  $^{13}\text{C}$   $\{^1\text{H}\}$  NMR spectra of polypropylenes for tacticity determination,  $^1\text{H}$  NMR spectra of polypropylenes for olefinic end-group determination, SC-XRD data and computational data (PDF)

X-ray crystallographic data of compounds II–V (CIF)

## ■ AUTHOR INFORMATION

### Corresponding Author

\*E-mail rieger@tum.de; Tel +49-89-289-13570; Fax +49-89-289-13562 (B.R.).

### ORCID

Bernhard Rieger: 0000-0002-0023-884X

### Notes

The authors declare no competing financial interest.

## ■ ACKNOWLEDGMENTS

We are exceptionally grateful to the WACKER Chemie AG for their continued financial support. A big thank you to Andreas Eisele and his work on new EBFI-type ligand structures during his Master Thesis at the WACKER-Chair of Macromolecular Chemistry. We also thank Dr. Alexander Poethig as head of the SC-XRD laboratory of the Catalysis Research Center. The authors thank Philipp Pahl and Daniel Wendel for proofreading the manuscript and valuable discussions.

## ■ REFERENCES

- (1) Natta, G. Stereospezifische Katalysen und isotaktische Polymere. *Angew. Chem.* **1956**, *68*, 393–403.
- (2) Natta, G. Properties of isotactic, atactic, and stereoblock homopolymers, random and block copolymers of  $\alpha$ -olefins. *J. Polym. Sci.* **1959**, *34*, 531–549.
- (3) Collette, J. W.; Tullock, C. W.; MacDonald, R. N.; Buck, W. H.; Su, A. C. L.; Harrell, J. R.; Mulhaupt, R.; Anderson, B. C. Elastomeric polypropylenes from alumina-supported tetraalkyl Group IVB catalysts. 1. Synthesis and properties of high molecular weight stereoblock homopolymers. *Macromolecules* **1989**, *22*, 3851–3858.
- (4) Collette, J. W.; Ovenall, D. W.; Buck, W. H.; Ferguson, R. C. Elastomeric polypropylenes from alumina-supported tetraalkyl group IVB catalysts. 2. Chain microstructure, crystallinity, and morphology. *Macromolecules* **1989**, *22*, 3858–3866.
- (5) Mallin, D. T.; Rausch, M. D.; Lin, Y. G.; Dong, S.; Chien, J. C. W. rac-[Ethylidene(1-*eta*-5-tetramethylcyclopentadienyl)(1-*eta*-5-indenyl)]dichlorotitanium and its homopolymerization of propylene to crystalline-amorphous block thermoplastic elastomers. *J. Am. Chem. Soc.* **1990**, *112*, 2030–2031.
- (6) Chien, J. C. W.; Llinas, G. H.; Rausch, M. D.; Lin, G. Y.; Winter, H. H.; Atwood, J. L.; Bott, S. G. Two-state propagation mechanism for propylene polymerization catalyzed by rac-[anti-ethylidene(1-*eta*-5-tetramethylcyclopentadienyl)(1-*eta*-5-indenyl)] dimethyltitanium. *J. Am. Chem. Soc.* **1991**, *113*, 8569–8570.
- (7) Llinas, G. H.; Day, R. O.; Rausch, M. D.; Chien, J. C. W. Ethylidene(1-*eta*-5-tetramethylcyclopentadienyl)(1-*eta*-5-indenyl)-dichlorozirconium: synthesis, molecular structure, and polymerization catalysis. *Organometallics* **1993**, *12*, 1283–1288.
- (8) Gauthier, W. J.; Corrigan, J. F.; Taylor, N. J.; Collins, S. Elastomeric Poly(propylene): Influence of Catalyst Structure and Polymerization Conditions on Polymer Structure and Properties. *Macromolecules* **1995**, *28*, 3771–3778.
- (9) Bravakis, A. M.; Bailey, L. E.; Pigeon, M.; Collins, S. Synthesis of Elastomeric Poly(propylene) Using Unsymmetrical Zirconocene Catalysts: Marked Reactivity Differences of “Rac”- and “Meso”-like Diastereomers. *Macromolecules* **1998**, *31*, 1000–1009.
- (10) Coates, G. W.; Waymouth, R. M. Oscillating Stereocontrol: A Strategy for the Synthesis of Thermoplastic Elastomeric Polypropylene. *Science* **1995**, *267*, 217–219.
- (11) Maciejewski Petoff, J. L.; Agoston, T.; Lal, T. K.; Waymouth, R. M. Elastomeric Polypropylene from Unbridged 2-Arylindenyl Zirconocenes: Modeling Polymerization Behavior Using ansa-Metallocene Analogues. *J. Am. Chem. Soc.* **1998**, *120*, 11316–11322.
- (12) Arriola, D. J.; Carnahan, E. M.; Hustad, P. D.; Kuhlman, R. L.; Wenzel, T. T. Catalytic Production of Olefin Block Copolymers via Chain Shuttling Polymerization. *Science* **2006**, *312*, 714–719.
- (13) Domski, G. J.; Rose, J. M.; Coates, G. W.; Bolig, A. D.; Brookhart, M. Living alkene polymerization: New methods for the precision synthesis of polyolefins. *Prog. Polym. Sci.* **2007**, *32*, 30–92.
- (14) Hustad, P. D. Frontiers in Olefin Polymerization: Reinventing the World’s Most Common Synthetic Polymers. *Science* **2009**, *325*, 704–707.
- (15) Eagan, J. M.; Xu, J.; Di Girolamo, R.; Thurber, C. M.; Macosko, C. W.; LaPointe, A. M.; Bates, F. S.; Coates, G. W. Combining polyethylene and polypropylene: Enhanced performance with PE/PP multiblock polymers. *Science* **2017**, *355*, 814–816.

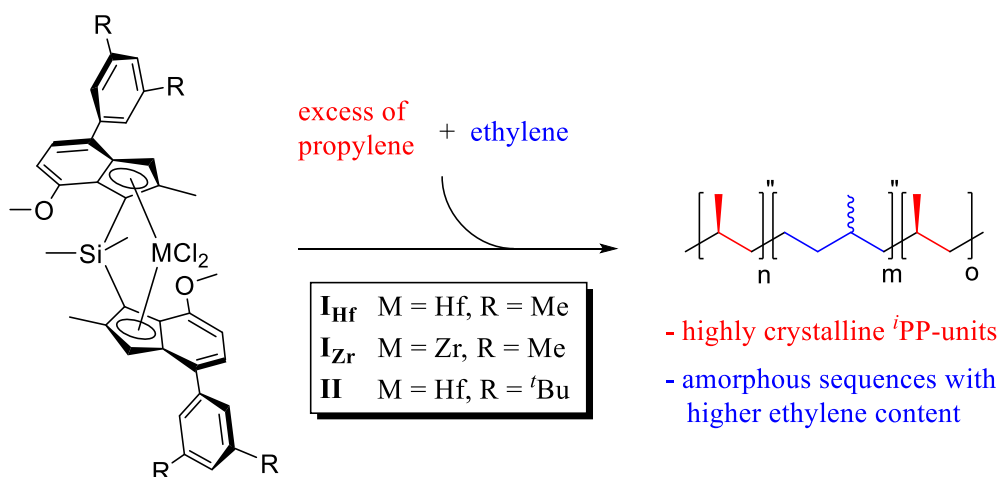
- (16) Busico, V. Metal-catalysed olefin polymerisation into the new millennium: a perspective outlook. *Dalton Transactions* **2009**, 8794–8802.
- (17) Rieger, B.; Jany, G.; Fawzi, R.; Steimann, M. Unsymmetric ansa-Zirconocene Complexes with Chiral Ethylene Bridges: Influence of Bridge Conformation and Monomer Concentration on the Stereoselectivity of the Propene Polymerization Reaction. *Organometallics* **1994**, *13*, 647–653.
- (18) Dietrich, U.; Hackmann, M.; Rieger, B.; Klinga, M.; Leskelä, M. Control of Stereoerror Formation with High-Activity “Dual-Side” Zirconocene Catalysts: A Novel Strategy To Design the Properties of Thermoplastic Elastic Polypropenes. *J. Am. Chem. Soc.* **1999**, *121*, 4348–4355.
- (19) Kukral, J.; Lehmus, P.; Feifel, T.; Troll, C.; Rieger, B. Dual-Side ansa-Zirconocene Dichlorides for High Molecular Weight Isotactic Polypropene Elastomers. *Organometallics* **2000**, *19*, 3767–3775.
- (20) Rieger, B.; Troll, C.; Preuschen, J. Ultrahigh Molecular Weight Polypropene Elastomers by High Activity “Dual-Side” Hafnocene Catalysts. *Macromolecules* **2002**, *35*, 5742–5743.
- (21) Cobzaru, C.; Hild, S.; Boger, A.; Troll, C.; Rieger, B. Dual-side” catalysts for high and ultrahigh molecular weight homopolypropylene elastomers and plastomers. *Coord. Chem. Rev.* **2006**, *250*, 189–211.
- (22) Hatanaka, T.; Mori, H.; Terano, M. Study of thermo-oxidative degradation of molten state polypropylenes with a variety of tacticities. *Polym. Degrad. Stab.* **1999**, *64*, 313–319.
- (23) Madkour, T. M.; Soldera, A. Tacticity induced molecular microstructure dependence of the configurational properties of metallocene-synthesized polypropylenes. *Eur. Polym. J.* **2001**, *37*, 1105–1113.
- (24) Boger, A.; Heise, B.; Troll, C.; Marti, O.; Rieger, B. Mechanical and temperature dependant properties, structure and phase transitions of elastic polypropylenes. *Eur. Polym. J.* **2007**, *43*, 634–643.
- (25) Dahlmann, M.; Erker, G.; Nissinen, M.; Fröhlich, R. Direct Experimental Observation of the Stereochemistry of the First Propene Insertion Step at an Active Homogeneous Single-Component Metallocene Ziegler Catalyst. *J. Am. Chem. Soc.* **1999**, *121*, 2820–2828.
- (26) Guerra, G.; Cavallo, L.; Moscardi, G.; Vacatello, M.; Corradini, P. Back-Skip of the Growing Chain at Model Complexes for the Metallocene Polymerization Catalysis. *Macromolecules* **1996**, *29*, 4834–4845.
- (27) Resconi, L.; Cavallo, L.; Fait, A.; Piemontesi, F. Selectivity in Propene Polymerization with Metallocene Catalysts. *Chem. Rev.* **2000**, *100*, 1253–1345.
- (28) Cavallo, L.; Guerra, G.; Vacatello, M.; Corradini, P. A possible model for the stereospecificity in the syndiospecific polymerization of propene with group 4a metallocenes. *Macromolecules* **1991**, *24*, 1784–1790.
- (29) van der Leek, Y.; Angermund, K.; Reffke, M.; Kleinschmidt, R.; Goretzki, R.; Fink, G. On the Mechanism of Stereospecific Polymerization—Development of a Universal Model to Demonstrate the Relationship Between Metallocene Structure and Polymer Microstructure. *Chem. - Eur. J.* **1997**, *3*, 585–591.
- (30) Busico, V.; Cipullo, R. Influence of Monomer Concentration on the Stereospecificity of 1-Alkene Polymerization Promoted by C<sub>2</sub>-symmetric ansa-Metallocene Catalysts. *J. Am. Chem. Soc.* **1994**, *116*, 9329–9330.
- (31) Busico, V.; Caporaso, L.; Cipullo, R.; Landriani, L.; Angelini, G.; Margonelli, A.; Segre, A. L. Propene Polymerization Promoted by C<sub>2</sub>-Symmetric Metallocene Catalysts: From Atactic to Isotactic Polypropene in Consequence of an Isotope Effect. *J. Am. Chem. Soc.* **1996**, *118*, 2105–2106.
- (32) Busico, V.; Brita, D.; Caporaso, L.; Cipullo, R.; Vacatello, M. Interfering Effects of Growing Chain Epimerization on Metallocene-Catalyzed Isotactic Propene Polymerization. *Macromolecules* **1997**, *30*, 3971–3977.
- (33) Busico, V.; Cipullo, R.; Caporaso, L.; Angelini, G.; Segre, A. L. C<sub>2</sub>-symmetric ansa-metallocene catalysts for propene polymerization: Stereoselectivity and enantioselectivity. *J. Mol. Catal. A: Chem.* **1998**, *128*, 53–64.
- (34) Piemontesi, F.; Camurati, I.; Resconi, L.; Balboni, D.; Sironi, A.; Moret, M.; Zeigler, R.; Piccolrovazzi, N. Crystal Structures and Solution Conformations of the Meso and Racemic Isomers of (Ethylenebis(1-indenyl))zirconium Dichloride. *Organometallics* **1995**, *14*, 1256–1266.
- (35) Linnolahti, M.; Pakkanen; Tapani, A.; Leino, R.; Luttikhedde; Hendrik, J. G.; Wilén, C.-E.; Näsman; Jan, H. Conformational Preferences of Racemic Ethylene-Bridged Bis(indenyl)-Type Zirconocenes: An ab initio Hartree–Fock Study. *Eur. J. Inorg. Chem.* **2001**, *2001*, 2033–2040.
- (36) Schäfer, A.; Karl, E.; Zsolnai, L.; Huttner, G.; Brintzinger, H.-H. ansa-Metallocene derivatives: XII. Diastereomeric derivatisation and enantiomer separation of ethylenebis(tetrahydronindenyl)-titanium and -zirconium dichlorides. *J. Organomet. Chem.* **1987**, *328*, 87–99.
- (37) Deisenhofer, S. Entwicklung neuer Zriconocen- und Hafnocen-Katalysatorarchitekturen und deren Verwendung in der metallocenkatalysierten Olefinpolymerisation, Dissertation, Universität Ulm, Anorganische Chemie II, 2002.
- (38) Nedorezova, P. M.; Veksler, E. N.; Novikova, E. S.; Optov, V. A.; Baranov, A. O.; Aladyshev, A. M.; Tsvetkova, V. I.; Shklyaruk, B. F.; Krut'ko, D. P.; Churakov, A. V.; Kuz'mina, L. G.; Howard, J. A. K. Synthesis of elastomeric polypropylene in bulk using C1-symmetric ansa-metallocenes. New aspects of the synthesis of 1-(fluoren-9-yl)-2-(2-methyl-5,6-dihydrocyclopenta [f]-1H-inden-1-yl)ethane and complexes of zirconium and hafnium with this ligand. *Russ. Chem. Bull.* **2005**, *54*, 400–413.
- (39) Moehring, P. C.; Coville, N. J. Group 4 metallocene polymerisation catalysts: quantification of ring substituent steric effects. *Coord. Chem. Rev.* **2006**, *250*, 18–35.
- (40) Machat, M. R.; Lanzinger, D.; Pöthig, A.; Rieger, B. Ultrarigid Indenyl-based Hafnocene Complexes for the Highly Ioselective Polymerization of Propene: Tunable Polymerization Performance Adopting Various Sterically Demanding 4-Aryl Substituents. *Organometallics* **2017**, *36*, 399–408.
- (41) Resconi, L.; Camurati, I.; Sudmeijer, O. Chain transfer reactions in propylene polymerization with zirconocene catalysts. *Top. Catal.* **1999**, *7*, 145–163.
- (42) Resconi, L. On the mechanisms of growing-chain-end isomerization and transfer reactions in propylene polymerization with isospecific, C<sub>2</sub>-symmetric zirconocene catalysts. *J. Mol. Catal. A: Chem.* **1999**, *146*, 167–178.
- (43) Schöbel, A.; Lanzinger, D.; Rieger, B. Polymerization Behavior of C1-Symmetric Metallocenes (M = Zr, Hf): From Ultrahigh Molecular Weight Elastic Polypropylene to Useful Macromonomers. *Organometallics* **2013**, *32*, 427–437.
- (44) Sini, G.; Macgregor, S. A.; Eisenstein, O.; Teuben, J. H. Why Is β-Me Elimination Only Observed in d<sup>0</sup> Early-Transition-Metal Complexes? An Organometallic Hyperconjugation Effect with Consequences for the Termination Step in Ziegler-Natta Catalysis. *Organometallics* **1994**, *13*, 1049–1051.
- (45) Caporaso, L.; De Rosa, C.; Talarico, G. The relationship between catalyst precursors and chain end groups in homogeneous propene polymerization catalysis. *J. Polym. Sci., Part A: Polym. Chem.* **2010**, *48*, 699–708.
- (46) Cobzaru, C.; Deisenhofer, S.; Harley, A.; Troll, C.; Hild, S.; Rieger, B. Novel High and Ultrahigh Molecular Weight Poly(propylene) Plastomers by Asymmetric Hafnocene Catalysts. *Macromol. Chem. Phys.* **2005**, *206*, 1231–1240.
- (47) Thomas, E. J.; Rausch, M. D.; Chien, J. C. W. New C<sub>1</sub> Symmetric Ziegler–Natta Type Zirconocenes for the Production of Isotactic Polypropylene. *Organometallics* **2000**, *19*, 4077–4083.
- (48) Machat, M. R.; Jandl, C.; Rieger, B. Titanocenes in Olefin Polymerization: Sustainable Catalyst System or an Extinct Species? *Organometallics* **2017**, *36*, 1408–1418.
- (49) Yoder, J. C.; Bercaw, J. E. Chain Epimerization during Propylene Polymerization with Metallocene Catalysts: Mechanistic Studies Using a Doubly Labeled Propylene. *J. Am. Chem. Soc.* **2002**, *124*, 2548–2555.

- (50) Schöbel, A.; Herdtweck, E.; Parkinson, M.; Rieger, B. Cover Picture: Ultra-Rigid Metallocenes for Highly Iso- and Regiospecific Polymerization of Propene: The Search for the Perfect Polypropylene Helix. *Chem. - Eur. J.* **2012**, *18*, 4129–4129.
- (51) Busico, V.; Cipullo, R. Microstructure of polypropylene. *Prog. Polym. Sci.* **2001**, *26*, 443–533.
- (52) Hild, S.; Boger, A.; Troll, C.; Rieger, B. Nucleation and Crystallization of Low Isotactic Polypropylenes with Statistically Distributed Stereoerrors. *Polym. J.* **2009**, *41*, 993–1004.
- (53) Busico, V.; Cipullo, R.; Kretschmer, W. P.; Talarico, G.; Vacatello, M.; Van Axel Castelli, V. Oscillating<sup>†</sup> Metallocene Catalysts: How Do They Oscillate? *Angew. Chem., Int. Ed.* **2002**, *41*, 505–508.
- (54) Hu, Y.; Krejchi, M. T.; Shah, C. D.; Myers, C. L.; Waymouth, R. M. Elastomeric Polypropylenes from Unbridged (2-Phenylindene)-zirconocene Catalysts: Thermal Characterization and Mechanical Properties. *Macromolecules* **1998**, *31*, 6908–6916.
- (55) Voegelé, J.; Troll, C.; Rieger, B. Zirconocene-catalyzed propene-ethene copolymer elastomers: Kinetic investigations at low ethene concentration and characterization of microstructure. *Macromol. Chem. Phys.* **2002**, *203*, 1918–1925.
- (56) Cheng, C. Y.; Datta, S.; Agarwal, P. K. Elastic fibers and articles made therefrom, including crystalline and crystallizable polymers of propylene. US 6,342,565 B1, 2002.
- (57) Datta, S.; Gadkari, A. C.; Cozewith, C. Thermoplastic polymer blends of isotactic polypropylene and alpha-olefin/propylene copolymers. WO 99/07788, 1999.
- (58) Hild, S.; Cobzaru, C.; Troll, C.; Rieger, B. Elastomeric Poly(propylene) from “Dual-side” Metallocenes: Reversible Chain Transfer and its Influence on Polymer Microstructure. *Macromol. Chem. Phys.* **2006**, *207*, 665–683.
- (59) Gahleitner, M.; Bachner, C.; Ratajski, E.; Rohaczek, G.; Neißl, W. Effects of the catalyst system on the crystallization of polypropylene\*. *J. Appl. Polym. Sci.* **1999**, *73*, 2507–2515.
- (60) Frisch, M. J.; Trucks, G. W.; Schlegel, H. B.; Scuseria, G. E.; Robb, M. A.; Cheeseman, J. R.; Scalmani, G.; Barone, V.; Petersson, G. A.; Nakatsuji, H.; Li, X.; Caricato, M.; Marenich, A. V.; Bloino, J.; Janesko, B. G.; Gomperts, R.; Mennucci, B.; Hratchian, H. P.; Ortiz, J. V.; Izmaylov, A. F.; Sonnenberg, J. L.; Williams-Young, D.; Ding, F.; Lipparini, F.; Egidi, F.; Goings, J.; Peng, B.; Petrone, A.; Henderson, T.; Ranasinghe, D.; Zakrzewski, V. G.; Gao, J.; Rega, N.; Zheng, G.; Liang, W.; Hada, M.; Ehara, M.; Toyota, K.; Fukuda, R.; Hasegawa, J.; Ishida, M.; Nakajima, T.; Honda, Y.; Kitao, O.; Nakai, H.; Vreven, T.; Throssell, K.; Montgomery, J. A., Jr.; Peralta, J. E.; Ogliaro, F.; Bearpark, M. J.; Heyd, J. J.; Brothers, E. N.; Kudin, K. N.; Staroverov, V. N.; Keith, T. A.; Kobayashi, R.; Normand, J.; Raghavachari, K.; Rendell, A. P.; Burant, J. C.; Iyengar, S. S.; Tomasi, J.; Cossi, M.; Millam, J. M.; Klene, M.; Adamo, C.; Cammi, R.; Ochterski, J. W.; Martin, R. L.; Morokuma, K.; Farkas, O.; Foresman, J. B.; Fox, D. *Gaussian 16, Revision A.03*; Gaussian, Inc.: Wallingford, CT, 2016.
- (61) Becke, A. D. Density-functional exchange-energy approximation with correct asymptotic behavior. *Phys. Rev. A: At., Mol., Opt. Phys.* **1988**, *38*, 3098–3100.
- (62) Perdew, J. P. Density-functional approximation for the correlation energy of the inhomogeneous electron gas. *Phys. Rev. B: Condens. Matter Mater. Phys.* **1986**, *33*, 8822–8824.
- (63) Godbout, N.; Salahub, R.; Andzelm, J.; Wimmer, E. Optimization of Gaussian-type basis sets for local spin density functional calculations. Part I. Boron through neon, optimization technique and validation. *Can. J. Chem.* **1992**, *70*, 560–571.
- (64) Hay, P. J.; Wadt, W. R. Ab initio effective core potentials for molecular calculations. Potentials for the transition metal atoms Sc to Hg. *J. Chem. Phys.* **1985**, *82*, 270–283.
- (65) Grimme, S.; Ehrlich, S.; Goerigk, L. Effect of the damping function in dispersion corrected density functional theory. *J. Comput. Chem.* **2011**, *32*, 1456–1465.
- (66) Perdew, J. P. Density-functional approximation for the correlation energy of the inhomogeneous electron gas. *Phys. Rev. B: Condens. Matter Mater. Phys.* **1986**, *33*, 8822–8824.

## 8. Excursus: New Microstructures in Olefin-Based Polymers

### 8.1 Ethylene – Propylene Copolymerization Using State of the Art *i*PP-Catalysts

From an industrial point of view, ethylene and propylene homopolymers represent the two most important polymer classes today. However, even the copolymerization of both monomer units facilitates the formation of several commercial products. Beside the synthesis of amorphous ethylene/propylene copolymers using vanadium based catalysts, the application of heterogeneous ZN-catalysts and numerous metallocenes has been established over the last decades.<sup>116-118</sup> Recent investigation on the copolymerization of ethylene and propylene using a C<sub>2</sub>-symmetric dimethylsilyl-bridged 2-methyl-4-phenyl bisindenyl *ansa*-zirconocene system (Spaleck-type)<sup>119</sup> revealed a random distribution of both comonomers similar to the applied feed composition.<sup>118</sup> While randomly distributed ethylene/propylene copolymers comprise elastomeric properties, with the incorporation of just small amounts of ethylene into a PP-network the impact strength can be improved significantly compared to plain polypropylene.<sup>120</sup> In the present study, the influence of small ethylene contents in the monomer feed was investigated using highly regio- and stereospecific C<sub>2</sub>-symmetric *ansa*-metallocenes (Scheme 11). By the simultaneous formation of highly crystalline *i*PP-sequences and amorphous regions comprising randomly distributed ethylene units the production of olefin-based thermoplastic elastomers was targeted.



Scheme 11. Copolymerization of ethylene with excess of propylene using highly regio- and stereoselective C<sub>2</sub>-symmetric metallocenes.

**Table 2. Conditions and results for the copolymerization of ethylene and propylene with complexes I–II in toluene.<sup>a</sup>**

entry	catalyst	C <sub>2</sub> /C <sub>3</sub> -mixture <sup>b</sup>	M <sub>n</sub> <sup>c</sup>	Đ <sup>d</sup>	T <sub>m</sub> <sup>e</sup>	T <sub>m</sub> <sup>f</sup>	P <sup>g</sup>
1	<b>I<sub>Hf</sub></b>	0/1	970	1.5	163	170	15000
2	<b>I<sub>Hf</sub></b>	0.02/1	310	1.7	159	166	12000
3	<b>I<sub>Hf</sub></b>	0.04/1	230	2.0	148	156	13000
4	<b>I<sub>Hf</sub></b>	0.06/1	160	1.8	141	147	13000
5	<b>I<sub>Hf</sub></b>	0.08/1	180	1.9	138	141	10000
6	<b>I<sub>Hf</sub></b>	0.10/1	130	2.3	128	129	13000
7	<b>I<sub>Hf</sub></b>	0.20/1	210	2.2	109	111	10000
8	<b>I<sub>Zr</sub></b>	0/1	510	1.9	164		29000
9	<b>I<sub>Zr</sub></b>	0.04/1	330	2.1	145	151	16000
10	<b>I<sub>Zr</sub></b>	0.10/1	270	1.9	122	128	16000
11	<b>II</b>	0/1	2600	1.3	170		13000
12	<b>II</b>	0.04/1	650	3.0	147	154	18000
13	<b>II</b>	0.10/1	1100	1.6	126	132	20000

<sup>a</sup>t<sub>p</sub>: 30 min, T<sub>p</sub>: 30 °C ± 5 °C, [monomer]: 1.65 M, V<sub>toluene</sub>: 300 mL, scavenger (TIBA): 2.2 mmol, Activated with TIBA (200 eq., 60 °C, 1h) / [Ph<sub>3</sub>C][ B(C<sub>6</sub>F<sub>5</sub>)<sub>4</sub>] (5.0 eq.). <sup>b</sup>Mixture of propylene and ethylene in the feed. <sup>c</sup>In kg mol<sup>-1</sup>. <sup>d</sup>Đ: M<sub>w</sub>/M<sub>n</sub>. <sup>e</sup>T<sub>m</sub> in °C. <sup>f</sup>Annealed sample (10 °C below T<sub>m</sub> for 1 h) [°C]. <sup>g</sup>P in kg<sub>PP</sub>·[mol<sub>M</sub>·(mol/L)·h]<sup>-1</sup>.

Three different catalysts (**I<sub>Hf</sub>**, **I<sub>Zr</sub>** and **II**) were investigated at identical polymerization temperature (30 °C) and olefin concentration (1.65 M) and varied composition of the monomer feed (Table 2). While an increasing ethylene concentration in the monomer feed led to a slight decrease of the productivity of **I<sub>Hf</sub>**, the productivity of the zirconium analog decreased more distinctly and the one of the sterically more demanding hafnocene (**II**) increased. For all three complexes, the average molecular weights dropped if ethylene was added to the monomer feed, which was in line with the results of first-generation ZN-catalysts under similar conditions.<sup>120</sup> In contrast to heterogeneous ZN-catalysts, narrow polydispersities were observed in all cases. However, with the incorporation of increasing ethylene content into the copolymer, the melting transitions decreased significantly. Furthermore, an analog trend was observed when the melting transitions of tempered copolymers were investigated. If an ideal TPE-network would have been generated, phase separation would have excluded amorphous, ethylene enriched sequences from the crystalline regions and the melting transition would have remained relatively constant. Consequently, the incorporation of ethylene interrupted the, otherwise perfect, isotactic polypropylene sequences thereby impacting the size and quality of macroscopic crystalline spherulites which in total lowered the observable melting transitions. To analyze the actual microstructure of the produced polyolefins, sequence distributions were investigated *via* <sup>13</sup>C {<sup>1</sup>H} NMR spectroscopy (Figure 9).

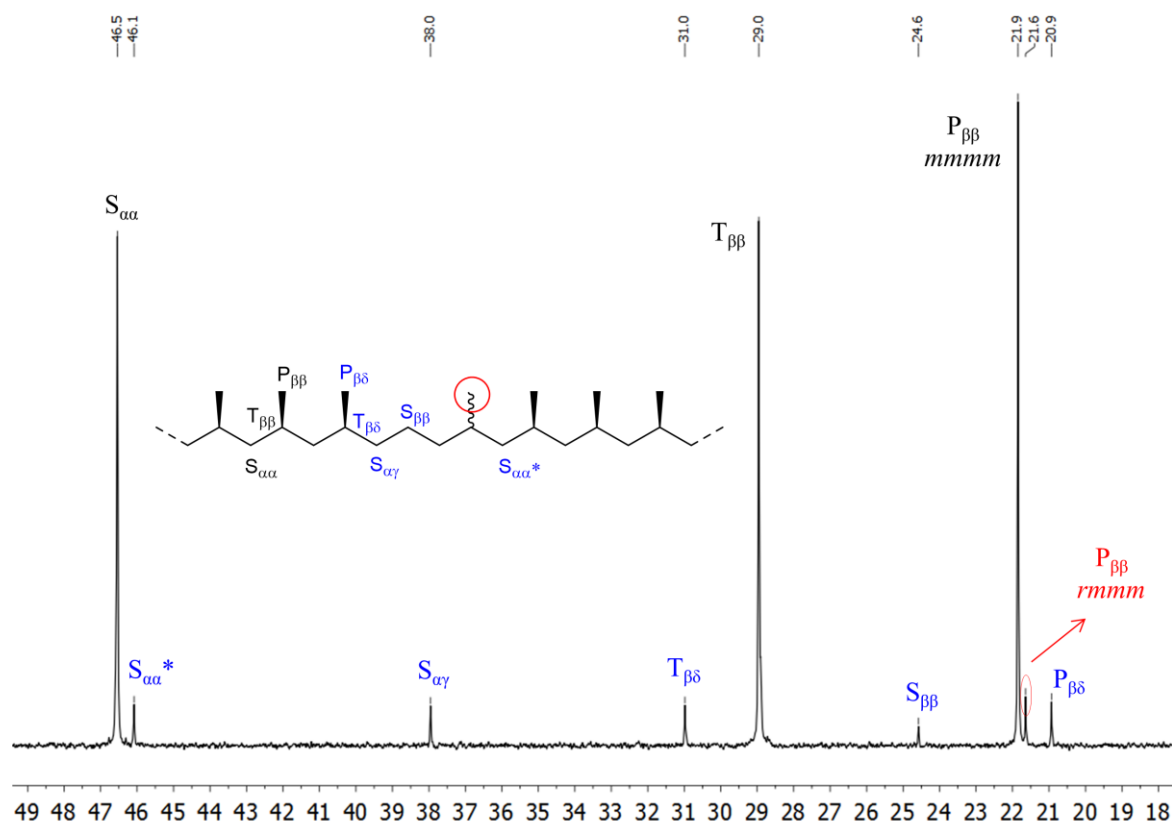


**Figure 9.** Sequence determination of ethylene/propylene copolymers *via*  $^{13}\text{C}$   $\{^1\text{H}\}$  NMR spectroscopy (the spectrum of entry 5 displays a representative example for all copolymers of Table 2 (except entry 7)).<sup>121-122</sup>

For all copolymers produced at an ethylene/propylene composition between 0.02/1 to 0.10/1 with catalysts **I<sub>Hf</sub>**, **I<sub>Zr</sub>** and **II**, the predominant formation of isotactic polypropylene sequences was found *via*  $^{13}\text{C}$   $\{^1\text{H}\}$  NMR spectroscopy. In addition, isolated ethylene units within an *i*PP matrix were detected, followed by a subsequent stereo-unselective propylene insertion (*rmmm*-pentad). However, neither alternating ethylene/propylene sequences, nor consecutive ethylene units were present in the produced ethylene/propylene copolymers until the ethylene/propylene composition in the feed was raised to 0.20/1 (Table 2, entry 7). The random distribution of ethylene units within the *i*PP-sequences indicates a similar monomer/comonomer selectivity of all three complexes (**I<sub>Hf</sub>**, **I<sub>Zr</sub>** and **II**) and is in line with the results of the related Spaleck-type complex structure.<sup>118</sup> However, the random distribution of ethylene hinders a proper separation of amorphous and crystalline domains, which is indispensable for high-melting TPE-characteristics. Nevertheless, the impact of varying ethylene/propylene feed composition on the mechanical properties of all produced polyolefins using different metallocene complexes was additional matter of investigation (Figure 10 and Figure 11).

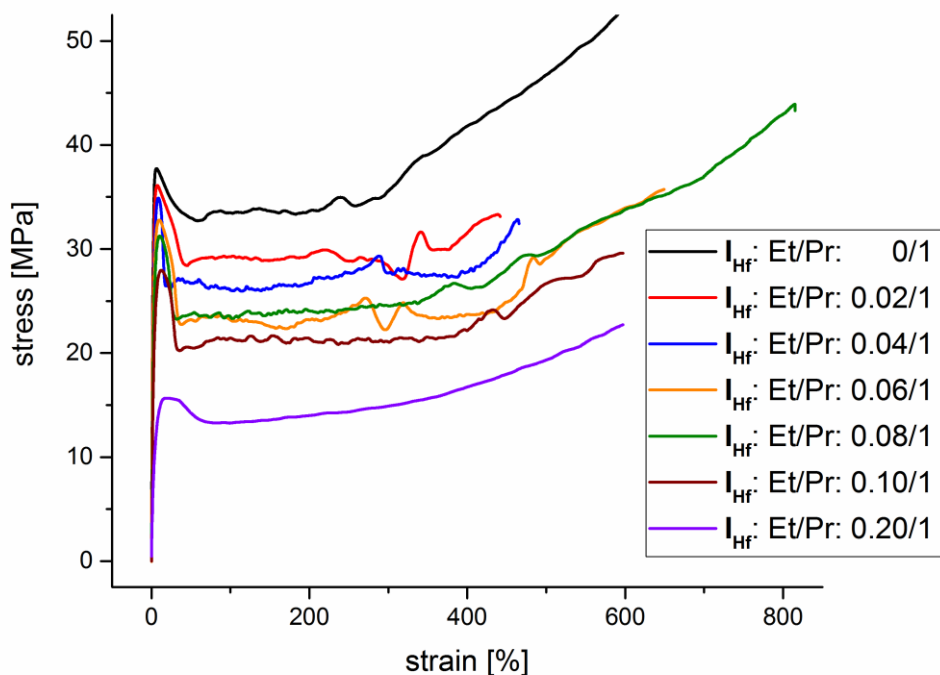


Figure 10. Stress-strain hysteresis curve of compression molded (200 °C, 50 bar, 1 h) polyolefin specimen (dog bone shape, 50.0 mm long, 4.0 mm wide) produced with complex  $I_{Hf}$  at different ethylene/propylene feed compositions.

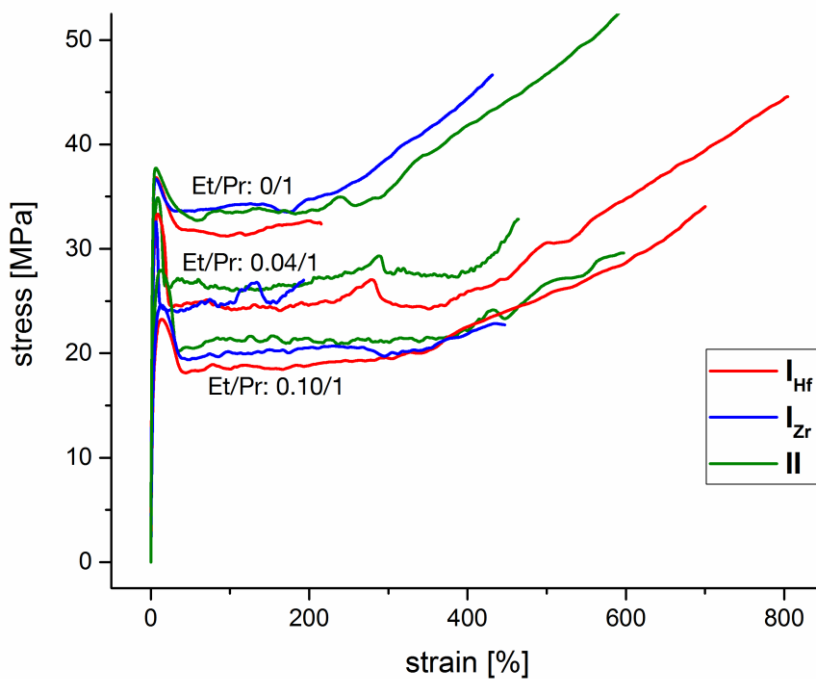


Figure 11. Stress-strain hysteresis curve of compression molded (200 °C, 50 bar, 1 h) polyolefin specimen (dog bone shape, 50.0 mm long, 4.0 mm wide) produced with complex  $I_{Hf}$ ,  $I_{Zr}$  and II at three different ethylene/propylene feed compositions.

**Table 3. Mechanical parameters of produced polyolefins specimen determined on a ZwickRoell machine with testXpert II software.<sup>a</sup>**

entry	catalyst	C <sub>2</sub> /C <sub>3</sub> -mixture <sup>b</sup>	E <sup>c</sup>	σ <sub>plateau</sub> <sup>d</sup>	λ <sub>plateau</sub> <sup>e</sup>	σ <sub>rupture</sub> <sup>f</sup>	λ <sub>rupture</sub> <sup>g</sup>
1	<b>I<sub>Hf</sub></b>	0/1	1630	37.7	6.4	53.4	600
2	<b>I<sub>Hf</sub></b>	0.02/1	1530	36.1	7.2	33.3	440
3	<b>I<sub>Hf</sub></b>	0.04/1	1200	34.9	8.9	32.9	640
4	<b>I<sub>Hf</sub></b>	0.06/1	1160	32.8	9.9	35.7	650
5	<b>I<sub>Hf</sub></b>	0.08/1	1060	31.3	10.6	43.3	820
6	<b>I<sub>Hf</sub></b>	0.10/1	800	27.9	12.5	29.6	600
7	<b>I<sub>Hf</sub></b>	0.20/1	360	15.7	19.0	30.7	820
8	<b>I<sub>Zr</sub></b>	0/1	1400	36.8	6.7	32.4	220
9	<b>I<sub>Zr</sub></b>	0.04/1	1250	33.3	8.8	44.6	800
10	<b>I<sub>Zr</sub></b>	0.10/1	690	23.3	13.8	34.1	700
11	<b>II</b>	0/1	1520	36.7	6.4	46.7	430
12	<b>II</b>	0.04/1	1280	32.6	6.6	27.0	170
13	<b>II</b>	0.10/1	710	24.6	13.7	22.7	450

<sup>a</sup>Compression molded polyolefin specimen (dog bone shape, 50.0 mm long, 4.0 mm wide), measured with a strain rate of 4.0 mm/min. <sup>b</sup>Mixture of propylene and ethylene in the feed. <sup>c</sup>Young's modulus [MPa]. <sup>d</sup>Yield strength [MPa]. <sup>e</sup>Strain before reduction in area [%]. <sup>f</sup>Stress at rupture [MPa]. <sup>g</sup>Strain at rupture [%].

Table 3 provides all relevant mechanical parameters given by the stress-strain hysteresis curves of Figure 10 and Figure 11. Irrespective of the applied metallocene catalyst, the young modulus and the yield strength decrease with increasing ethylene content in the monomer feed whereas the maximum strain before irreversible deformation increases. However, despite these differences, all produced polyolefins still provide a classical thermoplastic stress-strain behavior with a pronounced yield point, necking and strain-induced crystallization. Regarding the respective stress and strain values at rupture, the obtained results were less consistent. Unavoidable differences in the specimen fabrication including potential polymer degradation certainly limit the reproducibility of reliable data at rupture.

By comparison of the mechanical properties of the produced ethylene/propylene copolymers with plain polypropylenes of varying stereoregularity, the impact of isolated ethylene units within a <sup>i</sup>PP network is compared to the impact of isolated stereoerrors within a predominantly isotactic polypropylene matrix. With the application of C<sub>1</sub>-symmetric EBFI-type metallocenes, the formation of elastic and thermoplastic polypropylenes is feasible due to a flexible stereoselective polymerization behavior (see Chapter 7). Therefore, Figure 12 provides the mechanical examination of polypropylenes with varying stereoregularity and average chain length.<sup>115</sup>

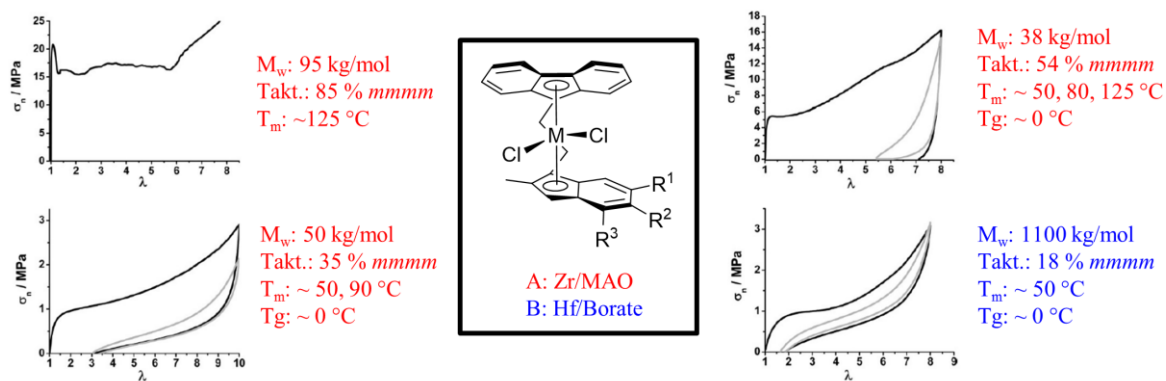
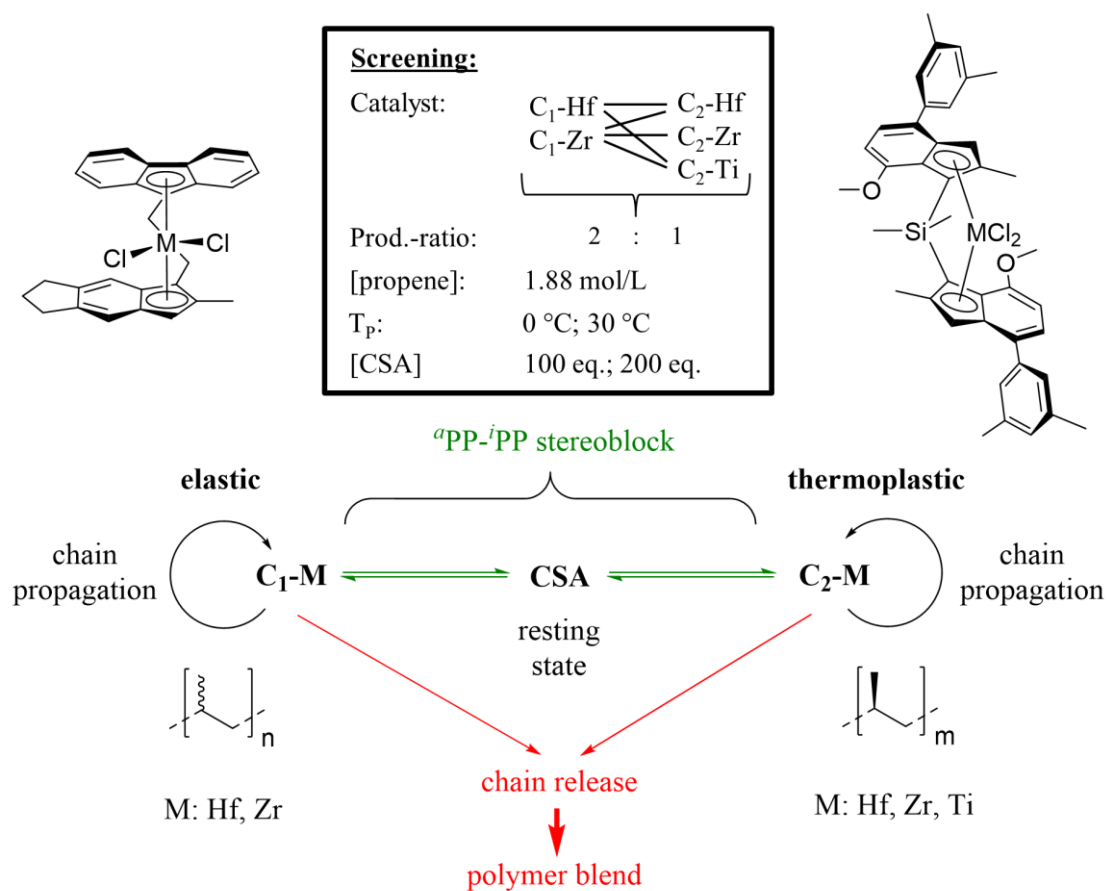


Figure 12. Stress-strain hysteresis curve of compression molded polypropylene specimen produced with  $C_1$ -symmetric EBFI-type catalysts.<sup>115</sup>

While the stress-strain behavior of moderately isotactic polypropylene (85 % *mmmm*) is of clearly thermoplastic nature (Figure 12: left side, on top), the one of isotactic enriched polypropylene (54 % *mmmm*, Figure 12: right side, on top) exhibits a significantly lower yield strength and a less pronounced yield point, which vanishes in the case of predominantly amorphous polypropylene samples (Figure 12: left and right side, underneath). By comparison of these findings with the ones of our produced copolymers, polyolefins of larger propylene and rather small ethylene content reveal quite analog mechanical properties compared to isotactic polypropylenes comprising isolated stereoerrors (Figure 12: left side, on top). In this context, the random incorporation of “the other” comonomer (ethylene) just as the random formation of an isolated stereoerror interrupts the otherwise isotactic polypropylene sequence and certainly impacts the type and amount of crystallinity of the respective polyolefin morphology. Accordingly, the presented approach facilitates the formation of perfect, high-melting  $\text{PP}$  just as thermoplastic materials with a higher impact strength and increased flexibility. The simple addition of ethylene to the propylene feed herein conveniently replaces a costly catalyst exchange for the production of plain polypropylene comprising similar characteristics.

8.2  $^a$ PP –  $^i$ PP Copolymers via Chain Shuttling

In 2006, a research group of the Dow Chemical Company established a new and convenient strategy toward the formation of defined polyolefin block structures.<sup>123</sup> By the directed application of a chain shuttling agent (CSA), polymer chains were transferred between two catalysts comprising different selectivities. The initial approach, which even passed the threshold toward industrial application, based on a copolymerization of ethylene and 1-octene using two living coordinative polymerization catalysts of high and low comonomer selectivity that facilitated the formation of amorphous and crystalline domains. With the addition of  $\text{ZnEt}_2$  (CSA), growing polymeryl chains were transferred to the zinc center, and transferred back from the zinc center to an active catalyst species. As a result, polyolefin blocks of different monomer selectivity were generated and covalently linked to each other.<sup>123-127</sup> Since the initial discovery, this principle was extended toward several catalyst mixtures comprising different comonomer- or stereoselectivities.<sup>128-131</sup>



Scheme 12. Illustrated chain shuttling setup and conditions using a rigid,  $\text{C}_2$ -symmetric *ansa*-metallocene complex and a  $\text{C}_1$ -symmetric EBFI-type *ansa*-metallocene complex.

Accordingly, this chapter provides the evaluation of our state of the art  $C_2$ -symmetric, rigid *ansa*-metallocenes (**C<sub>2</sub>-M**) in a chain shuttling polymerization setup (Scheme 12). In this connection, high-melting, highly stereo- and regioregular <sup>1</sup>PP-sequences should be linked to an amorphous PP-network. For a first, fundamental evaluation  $C_1$ -symmetric EBFI-type metallocenes (**C<sub>1</sub>-M**) were applied as second catalyst system for the synthesis of atactic polypropylene sequences. For ideal chain-shuttling conditions, living-type polymerization catalysts are generally applied. Since both catalysts do not provide a catalytic conversion of propylene in a living manner, pseudo-living conditions are imitated using low polymerization temperatures.<sup>132</sup> However, elevated temperatures in turn enhance the rate of chain transfer. In the process of chain shuttling, polymer chains need to be transferred from the group IV metal center to the zinc reagent and back from the zinc reagent to a group IV metal center. Consequently, the role of the group IV metal center and the respective M–C  $\sigma$ -bond properties are considered crucial. Therefore, the application of isostructural  $C_2$ -symmetric group IV metallocenes (**C<sub>2</sub>-Ti**, **C<sub>2</sub>-Zr** and **C<sub>2</sub>-Hf**) was screened in combination with isostructural  $C_1$ -symmetric group IV metallocenes (**C<sub>1</sub>-Zr** and **C<sub>1</sub>-Hf**) and  $ZnEt_2$  as a chain shuttling agent. Details on the screening conditions are provided in Scheme 12. Chapter 6 (**C<sub>2</sub>-M**) and Chapter 7 (**C<sub>1</sub>-M**) provide further information on the catalytic behavior of all applied catalysts in the homopolymerization of propylene.

Beside the combination of different group IV metal centers, the polymerization temperature (0 °C, 30 °C) and the amount of CSA ( $[ZnEt_2]:[C_2-M] = 100, 200$  eq.) was varied. However, after precipitation and drying of all produced polymers any applied combination provided the formation of macroscopic <sup>1</sup>PP/ <sup>2</sup>PP blends. Soxhlet extraction of all blends with methanol, *n*-pentane, *n*-hexane and *n*-heptane (each solvent 24 h) led to a pentane soluble fraction (~50–70 wt.%) and a insoluble fraction (~30–50 wt.%).

Comparison of the molecular weights of the produced polypropylenes in the presence and absence of  $ZnEt_2$  revealed a significant drop of the average chain length if a chain transfer agent was applied (Figure 13). Accordingly, an interaction of the chain transfer agent was observed with all applied  $C_1$ - and  $C_2$ -symmetric complexes (**C<sub>1</sub>-M** and **C<sub>2</sub>-M**). The most significant impact of the CSA on the molecular weights was generally observed for the hafnocene complexes (**C<sub>1</sub>-Hf** and **C<sub>2</sub>-Hf**), whereas the lowest impact was observed with the titanocene catalyst (**C<sub>2</sub>-Ti**). In addition, an accelerated decrease of the molecular weights was in most cases monitored at lower polymerization temperatures and increased CSA concentration.

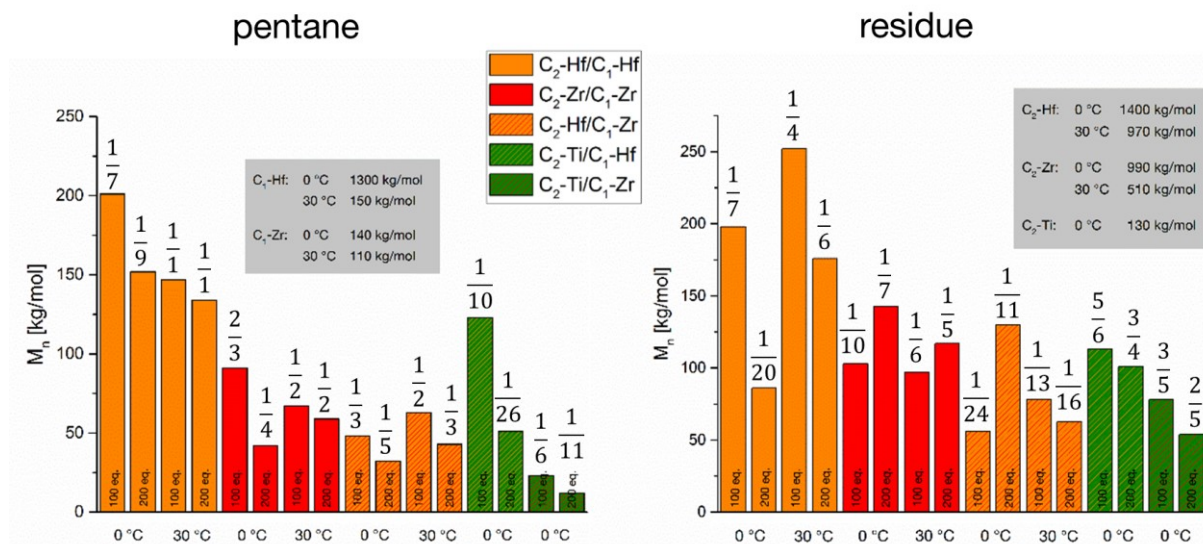


**Figure 13.** Molecular weights of the polypropylenes produced under the presence of a chain transfer reagent. The pentane soluble fraction is compared to the plain catalytic behavior of  $C_1\text{-M}$  and the residue to the catalytic behavior of  $C_2\text{-M}$ . The quotient of the molecular weights under the presence/absence of the chain transfer agent is additionally given.

Since the residual polymer properties (e. g. tacticities, polydispersities) of the pentane soluble fraction were identical to those of the homopolymer of ( $C_1\text{-M}$ ) the focus was directed toward the residues of the Soxhlet extraction in order to evaluate the general suitability of  $C_2\text{-M}$  in a chain shuttling setup. In this connection,  $i\text{PP}-a\text{PP}$  block structures are rather expected in the residue than in the extract due to physical crosslinking of the  $i\text{PP}$ -segments. Therefore, additional polymer analysis mainly focused on differences between the residues of the Soxhlet extraction and the homopolymers produced with the respective  $C_2\text{-M}$  catalysts.

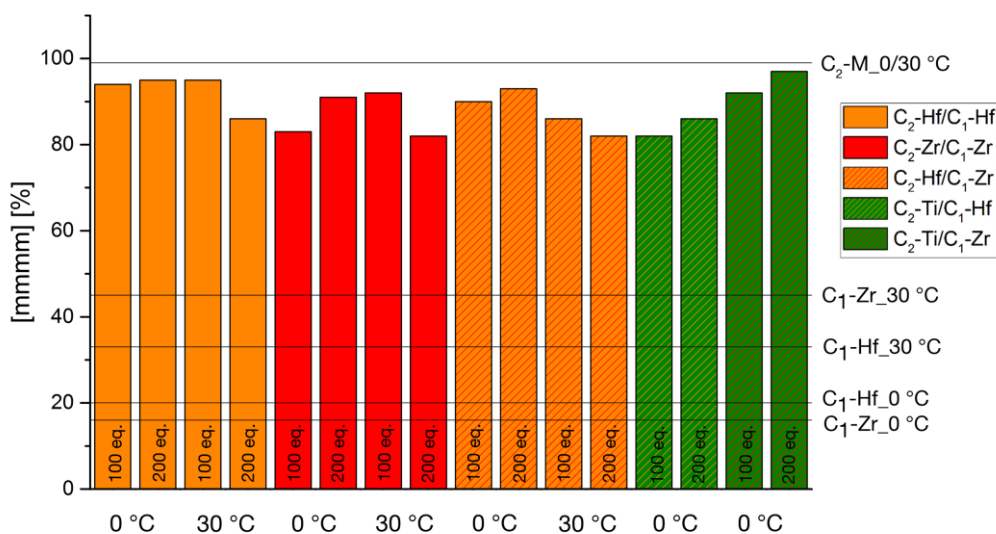


**Figure 14.** Tacticities of the pentane-extracted residues determined via  $^{13}\text{C}\{^1\text{H}\}$  NMR spectroscopy (300 MHz, 140 °C,  $\text{C}_6\text{D}_5\text{Br}$ ). The results of each particular catalyst in a standard propylene polymerization setup are indicated by horizontal lines.

If chain shuttling occurred in the present polymerization setup,  $i$ PP- $a$ PP block structures in the residue would lead to a significant decrease of the, otherwise perfect, overall isotacticity. Therefore, Figure 14 provides the determined tacticities of the residues, which all deviate significantly from the expected tacticities of  $C_2$ -M. Especially at higher polymerization temperatures and CSA concentrations, the tendency toward decreased isotacticities is higher, which indicates the presence of  $i$ PP- $a$ PP block structures embedded in a matrix of isotactic polypropylene. However, tacticities  $> 80\%$  clearly underline the predominant occurrence of plain  $i$ PP in the residue.

If a significant amount of atactic sequences is covalently linked to the crystalline residue, a decrease of the melting enthalpy, regarding the melting transition at  $\sim 160$ – $165\text{ }^\circ\text{C}$ , is considered. Accordingly, Figure 15 provides the determined melting enthalpies of the pentane-extracted polymer samples with additional visualization of the expected region for the homopolymerization results by just using  $C_2$ -M. While higher polymerization temperatures led to lower melting enthalpies, the amount of CSA had no defined impact in this regard. In addition, lower melting enthalpies were observed with the application of zirconium as well as hafnium, whereas the results with  $C_2$ -Ti suggested no significant occurrence of chain shuttling if a titanocene complex was involved.

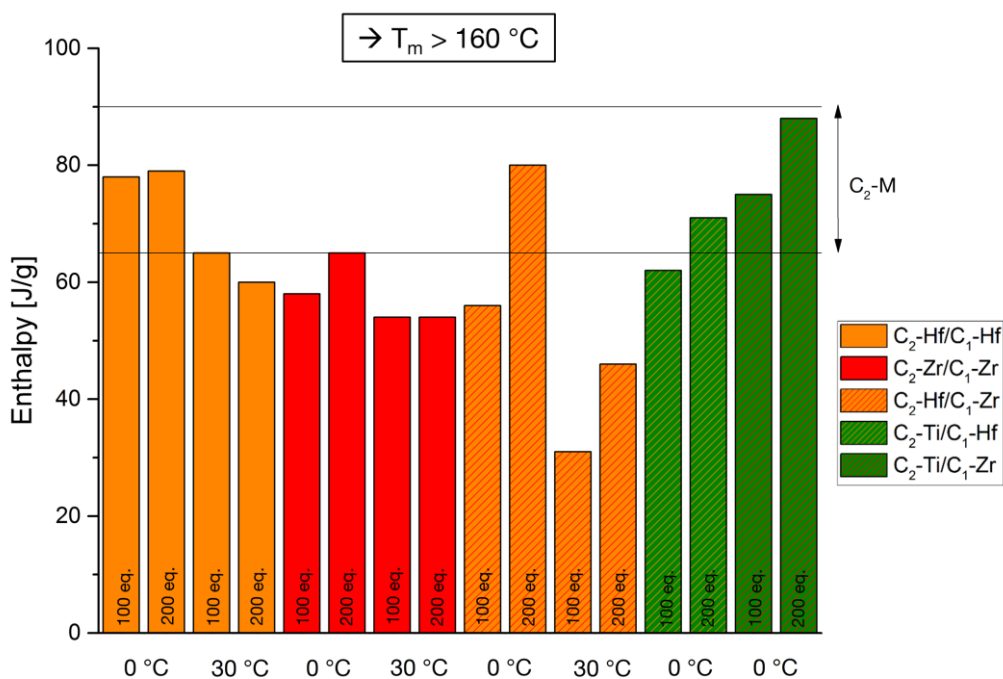


Figure 15. Melting enthalpies of the melting transition between 160 to 165 °C of the pentane-extracted polymer samples.

Since a severe impact of  $\text{ZnEt}_2$  on the molecular weights of the produced polymers was observed, the transfer of polymer chains from the metallocene catalyst to the chain transfer agent is evident. However, if the chain transfer agent acts as a real chain shuttling agent, the transfer of polymer chains from the zinc-species back to a metallocene catalyst must occur as well. Due to the assumed appearance of some isolated  $i\text{PP}$ - $^a\text{PP}$  block structures embedded in an  $i\text{PP}$ -matrix more distributed polydispersities are expected compared to the results of  $\text{C}_2\text{-M}$  (Figure 16).

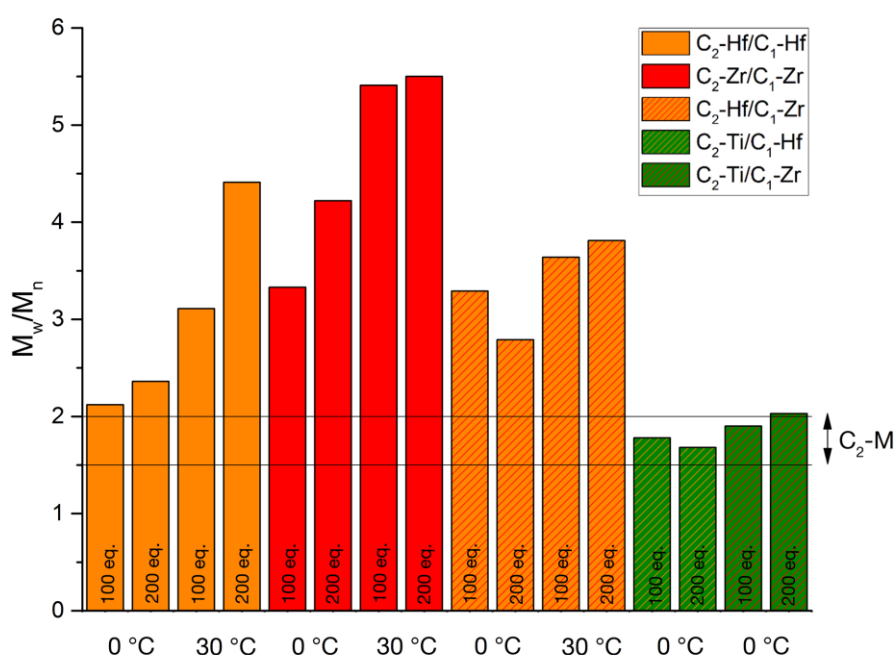


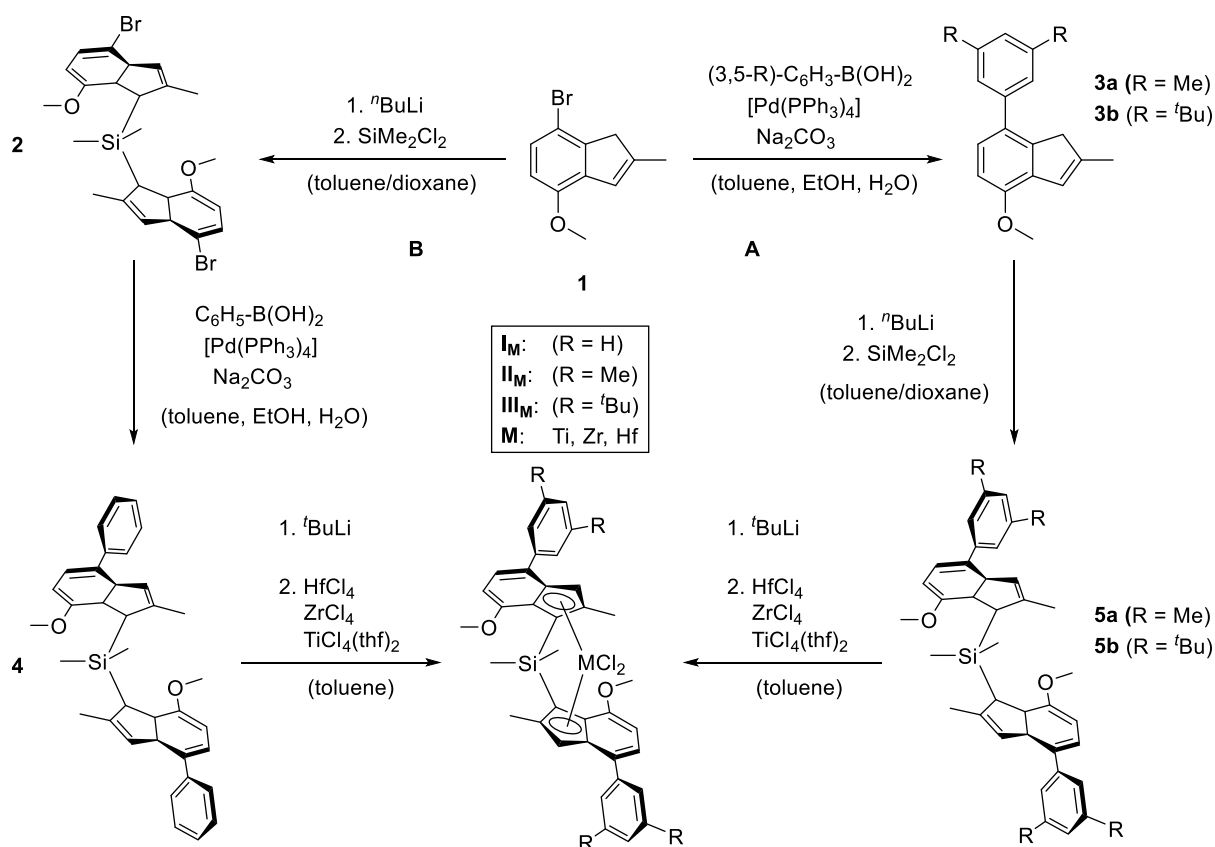
Figure 16. Polydispersities of the pentane-extracted polymer samples.

According to Figure 16, especially the application of zirconium or hafnium in combination with higher polymerization temperatures and CSA concentrations increases the molecular weight distributions of the pentane-extracted residues. In this connection, there is again no indication for chain shuttling if a titanocene complex is applied. However, increased polydispersities just indicate that different type of polymers are present. Accordingly, based on the above presented findings three different types of polypropylenes can be expected in the residue. If no chain transfer to the zinc reagent occurs, plain isotactic polypropylenes with molecular weights determined by standard chain release reactions analog to a homopolymerization with  $\text{C}_2\text{-M}$  should be observed. If a chain transfer occurs, chain propagation has been interrupted at some point and the polymer chain rests on a transfer agent. If no further chain transfer back to a catalyst takes place, the polymeryl-CSA adduct is hydrolyzed in the precipitation step and rather short  $i\text{PP}$ -chains are generated. Only if the

isotactic polymer chain gets transferred from the CSA to a  $C_1\text{-M}$ -catalyst the formation of  $i\text{PP-}a\text{PP}$  block structures occurs. Although improved results, in most cases, are observed with the application of zirconium- and hafnium-based catalysts at higher polymerization temperatures and increased CSA concentrations, the general formation of atactic and isotactic homopolymers is far too high in the presented chain shuttling setup for a satisfying result. Also the application of even higher CSA concentrations (400 eq.) and a more polar solvent (chlorobenzene instead of toluene) did not lead to any significant improvement. Therefore, the general problem is attributed to the low solubility of the produced  $i\text{PP}$ -sequences under the applied polymerization conditions. Due to the high accuracy of the stereo- and regiocontrol mechanism, the isotactic polypropylene already precipitates at a very early state in the polymerization setup and is no longer available for any chain shuttling process. In addition, the sterically crowded complex framework of  $C_2\text{-M}$  hinders a transfer of polymer sequences from the CSA to the isoselective complex. To improve the solubility of  $i\text{PP}$ -sequences and the transfer rate of the polymer chains the polymerization temperature needs to be increased. But since such a change of the polymerization conditions would cause a severe decrease of the molecular weights in line with a significant increase of the productivities, the necessary living character would be lost completely. Hence, it is concluded that the suitability of our extraordinarily precise  $C_2$ -symmetric metallocene complexes ( $C_2\text{-M}$ ) in a chain shuttling polymerization setup is rather limited.

## 9. Summary and Outlook

In 2012, the *Rieger* group developed the catalytic benchmark system (Scheme 13, **III<sub>Hf</sub>**) for the synthesis of regio- and stereodeflect free, ultra-high molecular weight isotactic polypropylene.<sup>23-24</sup> Driven by its extraordinarily precise catalytic performance, the essential structural key factors were elucidated as part of this thesis. Therefore, further strategies for the synthesis of 2,4,7-substituted bisindenyl *ansa*-metallocene complexes comprising a varied steric demand of the 4-aryl substituent were developed. Beside the literature-known synthesis route to **III<sub>Hf</sub>** (Pathway A) the synthesis of **II<sub>Hf</sub>** (Pathway A) and **I<sub>Hf</sub>** (Pathway B) were established. Accordingly, Figure 17 provides the impact of varying 4-aryl substituents on the coordination gap aperture of the respective metallocenes.



**Scheme 13.** Synthetic strategies toward 2,4,7-substituted metallocene complexes with varied 4-aryl substituents.

Detailed structural evaluation of **I<sub>Hf</sub>** – **III<sub>Hf</sub>** disclosed the presence of opposing intramolecular forces within the entire *ansa*-metallocene framework, which leads to a generally high structural rigidity using sterically demanding 4-aryl substituents. Further catalytic examination of complexes **I<sub>Hf</sub>** – **III<sub>Hf</sub>** revealed a more sufficient temperature stability of the metallocene catalyst in combination with an accelerated prevention of chain release and

epimerization reactions if a higher steric demand of the 4-aryl substituent was provided. Consequently, the increasing rigidity in the complex framework is considered crucial for an optimized polymerization behavior. Facilitated by the profound analysis of these structure-property relationships, we believe that the developed substitution pattern, which provokes the presented rigidity concept and enables the formation of almost perfect *i*PP, will contribute to a more directed development of the next generation of polypropylene catalysts.

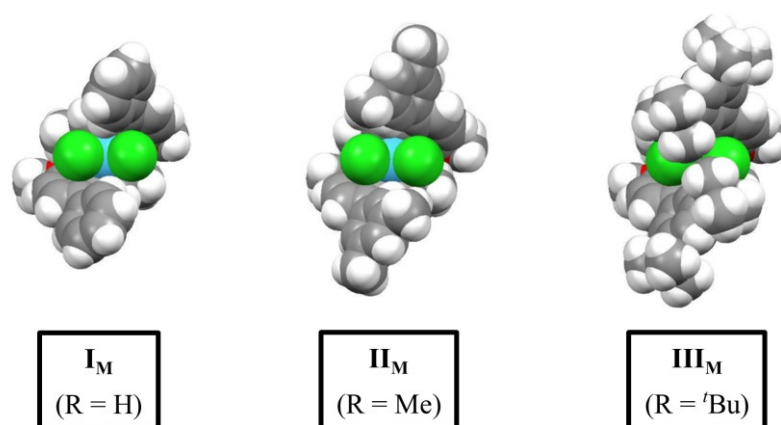
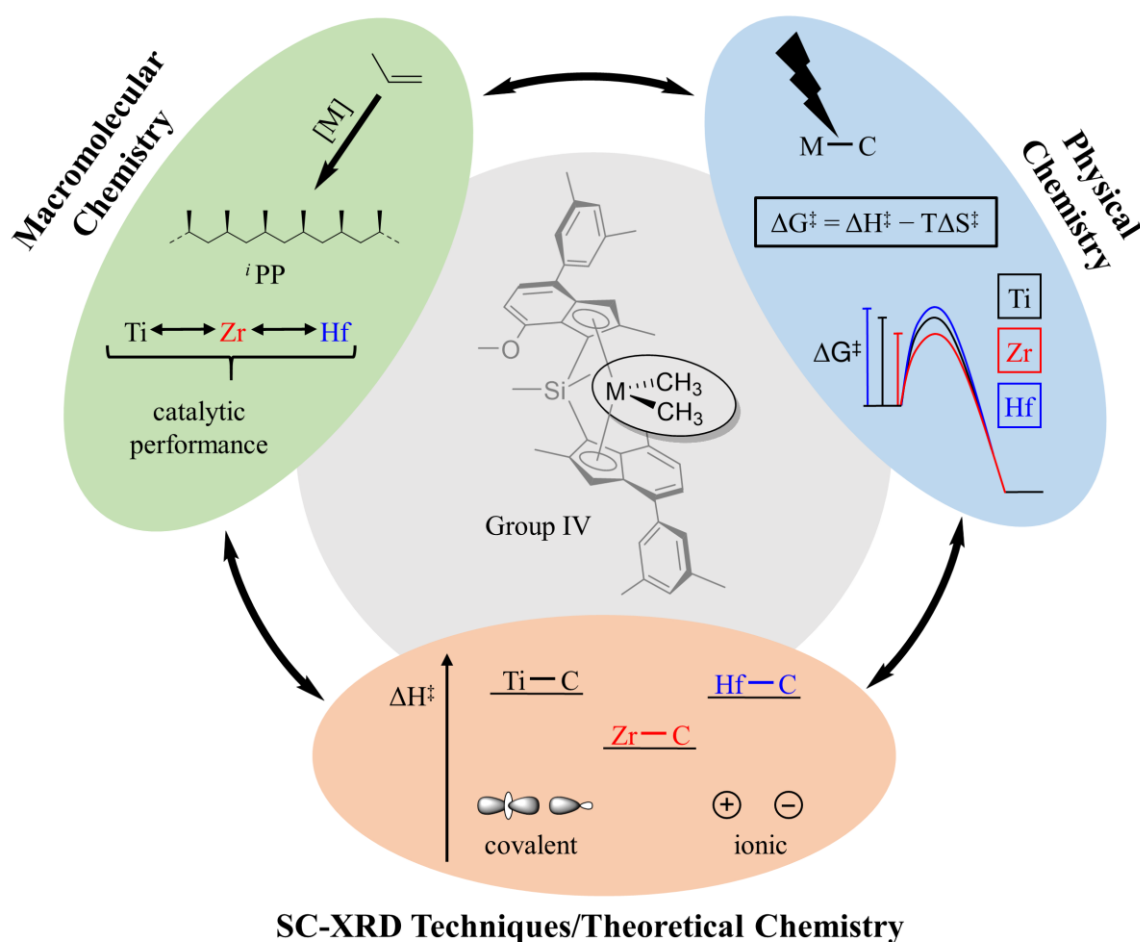


Figure 17. Space filling representation of **I<sub>Hf</sub>** – **III<sub>Hf</sub>** illustrating the effect of different 4-aryl substituents on the coordination gap aperture.

Inspired by the exceptional catalytic precision of this complex framework, the scope was expanded toward the application of isostructural titanocenes in the polymerization of propylene. Since titanium based metallocene catalysts are generally known to undergo fast catalyst deactivation, usually by reduction of the  $\text{Ti}^{+IV}$  metal center,<sup>101</sup> the present ligand structure promises an improved catalyst stability by the prevention of undesired deactivation reactions. Screening of the ligand substitution pattern (Scheme 13), different activation strategies and varying polymerization conditions did indeed disclose optimized conditions for the catalytic production of narrow molecular weight distributed, high-melting ( $T_m > 170\text{ }^\circ\text{C}$ ) isotactic polypropylene. Transformation of the bischlorinated complex **III<sub>Ti</sub>** to the bismethylated derivative, prior to the activation with  $[\text{Ph}_3\text{C}][\text{B}(\text{C}_6\text{F}_5)_4]$ , herein represents the most suitable activation strategy that led to the most stable and active titanocene catalyst for the polymerization of propylene known to this date. Although the catalytic performance of this state of the art titanocene catalyst is still significantly exceeded by the zirconium and hafnium analogs, the application of titanium in metallocene catalysis should not be completely disregarded in future catalyst development. In contrast to the higher homologs, titanium is still one of the most abundant elements on this planet, is cheap and well available

and it has already proven its capability in the polymerization of olefins using heterogeneous ZN-catalysts.

For a comparative picture of isostructural group IV metallocene catalysts (**II**), the zirconocene analog (**II<sub>Zr</sub>**) was synthesized and evaluated catalytically in an identical manner to **II<sub>Hf</sub>** and **II<sub>Ti</sub>** (Figure 18). Moreover, the essential structural and chemical differences of varying group IV metal centers became a central objective of this thesis. In this context, the M–C  $\sigma$ -bond is considered decisive regarding several catalytic sub-processes which altogether determine the catalytic activity and the final polymer properties. Therefore, a synthetic strategy toward isostructural group IV metallocenes (**II**) with a bismethylated substitution pattern was developed.



**Figure 18.** Multidisciplinary approach disclosing the role of the group IV metal center in the catalytic conversion of olefins.

For a fundamental analysis of the M–C  $\sigma$ -bond characteristics, the electronic properties of this crucial moiety were elucidated experimentally *via* high resolution single-crystal X-ray diffraction analysis and additional theoretical processing (Figure 18). While the Ti–C bond revealed substantial covalent character, the Hf–C bond exhibited a dominating ionic nature. In

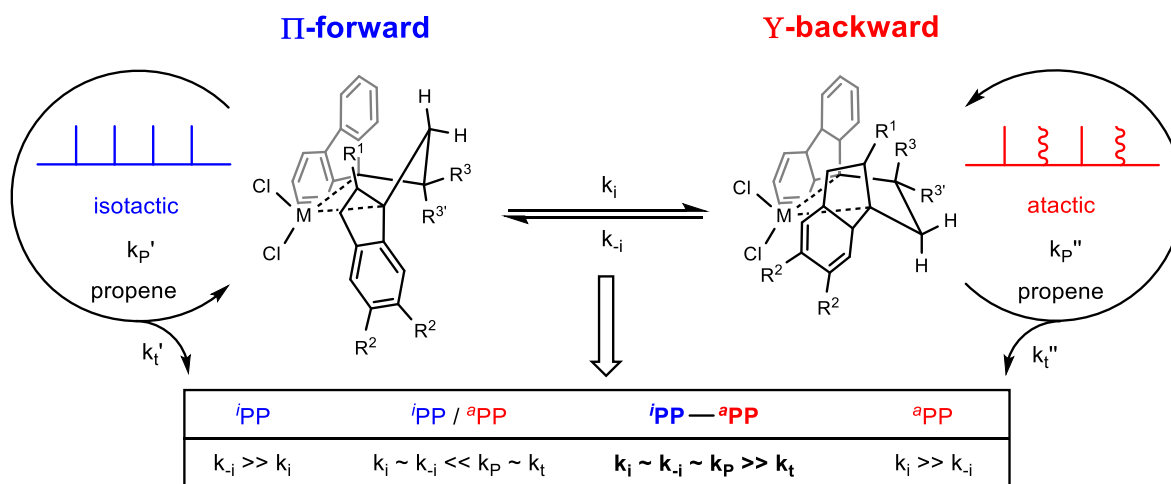
addition, further single-crystal X-ray diffraction analysis under high pressure uncovered a Zr–C bond with significantly more distinct covalent properties than the Hf–C bond. Furthermore, the chemical M–C  $\sigma$ -bond characteristics were investigated by kinetic examination of M–C bond conversion (Figure 18). The covalent Ti–C and ionic Hf–C bond both comprise a large enthalpic contribution to the activation barrier; whereas the enthalpic impact for M–C  $\sigma$ -bond conversion of the Zr moiety is significantly lower. However, for the conversion of the Zr–C bond the entropic contribution to the activation barrier is explicitly higher. Correlation of these findings with the catalytic abilities of the isostructural group IV metallocenes (**II**) for the first time facilitated a concrete connection between experimentally and theoretically determined fundamental electronic and kinetic differences and the corresponding catalytic performance. The capability of hafnium-based catalysts to produce significantly higher molecular weight PP herein became clearly explainable by the presented new insights, as did the temperature dependency of the catalytic activity and of the stereoregularities when applying different group IV metal centers in the polymerization of propene.

We believe that our pioneering study on fundamental electronic and chemical differences of these group IV metallocenes in combination with their state of the art catalytic behavior has the potential to revolutionize the prospective use of the group IV metals in the polymerization of olefins. The choice to apply the “right” metal center has usually been driven by assumptions, experiences and, in most instances, a simple trial and error principle. Facilitated by our new perspective, differences regarding the application of the group IV metals in isostructural metallocene complexes are more concretely ascribed and more conveniently interpretable regarding each particular field of application. Our presented findings even elucidate the severe chemical differences between zirconium and hafnium, a unique pair in the periodic table of elements that due to the lanthanide contraction possesses almost identical geometric parameters. However, further systematic studies should be performed which address the application of further ligand structures in order to completely segregate the impact of the group IV metal center from the influence of the surrounding framework. Nevertheless, in times where a more systematic and directed development in research attracts accretive attention, the presented novel insights on group IV metallocene chemistry will certainly enable a better differentiation and more precise application of these metals in the huge field of polyolefin catalysis. In addition, the strategy established in this pioneering study must also be considered highly relevant regarding other pairs and groups of metals in the periodic table of elements which are involved in other fundamental catalytic processes.

Further projects of this thesis shifted the focus from metallocene development and its particular characteristics to the respective polymers and their properties. In this connection, the formation of polyolefin block structures is an intensively investigated but also highly challenging task, since monomer/comonomer incorporation and stereoselective polymerization behavior are both generally statistical processes. Nevertheless, certain strategies exist, like chain-shuttling,<sup>123</sup> an oscillating stereocontrol mechanism,<sup>18</sup> or the application of a living/“quasi-living”-type coordinative polymerization mechanism,<sup>133</sup> in order to produce defined olefin-based block copolymers. Inspired by these strategies, this thesis provides an alternative route for the formation of tailored *a*PP-*i*PP block structures, thereby generating a new polymer class of high-melting, elastic polypropylenes.

Hafnium-based EBFI-type metallocene complexes have proven their exceptional capability regarding the production of high molecular weight, elastic polypropylene.<sup>20</sup> But despite the outstanding mechanical characteristics, the restricted temperature stability of these polymers presents, to this day, an unresolved issue. In line with these findings, the amalgamation of elasticity with high-melting characteristics in relation to the catalysis of pure propylene-based thermoplastic elastomers must still be considered imperfect.<sup>19, 115</sup>

Therefore, the intricate interplay of all mechanisms which impact the final stereoregularity using EBFI-type metallocenes was elucidated. Beside the enantiofacial discrimination of the dual-site system, the impact of possible chain migration, chain end epimerization and especially the interconversion between different chelate ring conformers was investigated in-depth. Accordingly, several novel as well as literature-known EBFI-type metallocenes of varying 2,5,6-indenyl substitution patterns were examined in the polymerization of propene in order to identify a decisive impact of both chelate ring conformations on the final tacticities (Scheme 14). It could be shown that one conformer is energetically favored and interconverts with the disfavored chelate ring conformer in a dynamic equilibrium. In this context, detailed adjustment of all polymerization parameters in order to optimize the interconversion kinetics in correlation with the chain propagation and termination rate finally facilitated the formation of defined *a*PP-*i*PP block structures embedded in a matrix of *a*PP. The result was a physically crosslinked, high molecular weight, high-melting ( $T_m \sim 140\text{ }^\circ\text{C}$ ), propylene-based thermoplastic elastomer with an excellent reversible deformation behavior, produced in a simple one-pot, one-catalyst synthesis.

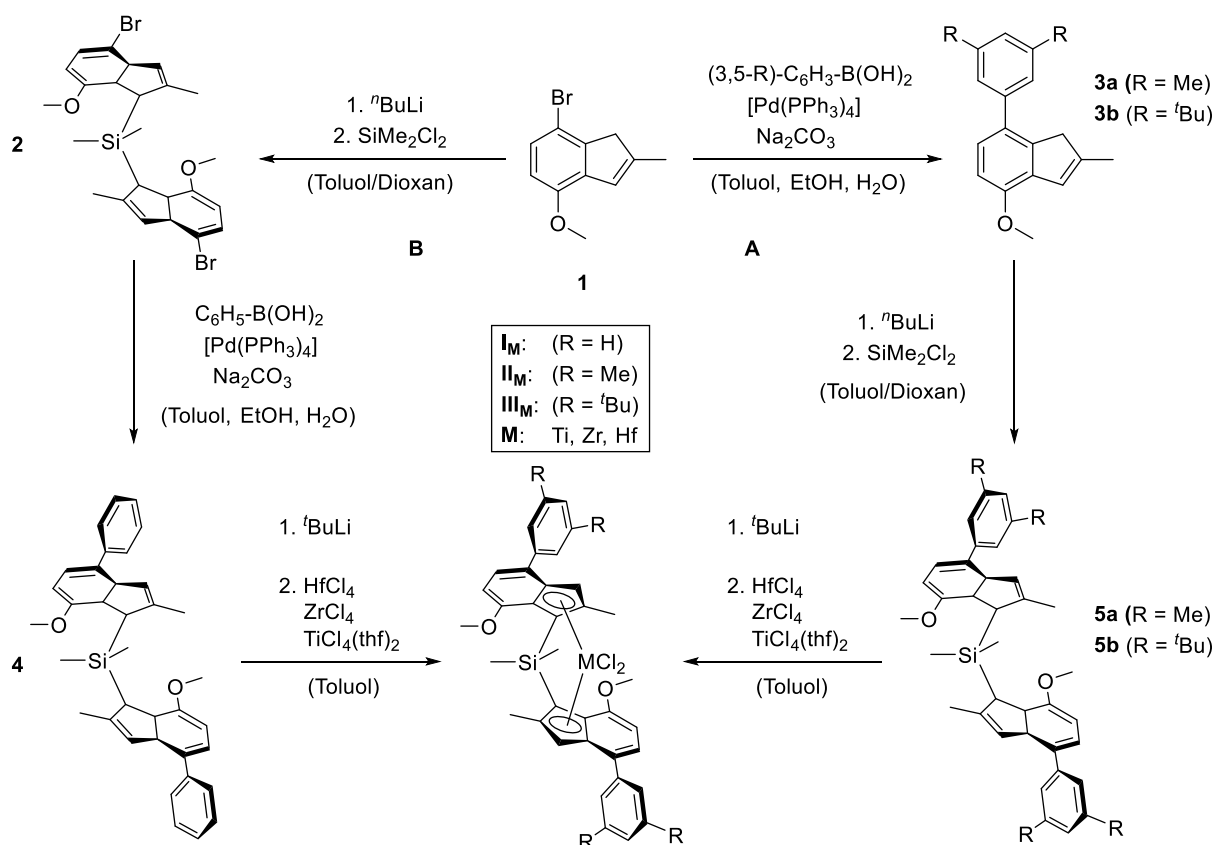


**Scheme 14.** Molecular representation of the isoselective  $\Pi$ -forward and nonselective  $Y$ -backward chelate ring conformer of EBFI-type metallocene complexes. Both conformations undergo dynamic interconversion according to the particular free energy differences and the barrier heights.

The application of a hafnium-based EBFI-type metallocene for the directed synthesis of high-melting, elastic polypropylenes certainly represents an outstanding example of the simple formation of block structures *via* a one-pot, one-catalyst approach. In addition, the evaluated mechanical characteristics disclose the production of a thermoplastic elastomer with excellent recovery rates due to a high proportion of reversible deformation. However, the necessity of low polymerization temperatures during the production process constitutes the main drawback concerning its industrial application. In this context, additional investigation of the most suitable reaction conditions in combination with other EBFI-type metallocenes may facilitate the production of a high-melting, propylene-based, thermoplastic elastomer under industrially relevant conditions applying this simple one-pot, one-catalyst strategy.

## 10. Zusammenfassung und Ausblick

Der von *Rieger et al.* im Jahre 2012 entwickelte Metallocen-Komplex (Schema 15, **III<sub>Hf</sub>**) entspricht bis heute dem Maß aller Dinge, was die Synthese von ultra-hochmolekularem, isotaktischem Polypropylen angeht.<sup>23-24</sup> Von dieser nahezu perfekten Katalyse getragen, sollen in der vorliegenden Arbeit die entscheidenden, strukturellen Schlüsselfaktoren ermittelt werden. In diesem Zuge wurden alternative Strategien zur Synthese von 2,4,7-substituierten bis-Indenyl *ansa*-Metallocen-Komplexen entwickelt, welche einen unterschiedlichen sterischen Anspruch des 4-Aryl-Substituenten aufweisen. Neben der bereits literaturbekannten Syntheseroute für **III<sub>Hf</sub>** (Route A) wurden die Synthesen von **II<sub>Hf</sub>** (Route A) und von **I<sub>Hf</sub>** (Route B) entwickelt. In diesem Zusammenhang bietet Abbildung 19 eine aufschlussreiche Darstellung des sterischen Einflusses der 4-Aryl-Substituenten auf den Koordinationswinkel (cga).



Schema 15. Synthesewege zu 2,4,7-substituierten Metallocen-Komplexen mit variierendem 4-Aryl-Substituent am Indenyl.

Durch die detaillierte strukturelle Analyse der Komplexe **I<sub>Hf</sub>** – **III<sub>Hf</sub>** wurde ein Gegenpiel unterschiedlicher intramolekularer Kräfte im gesamten Metallocen-Gerüst aufgedeckt, welches die generelle Rigidität dieser Komplexe verursacht. Eine zusätzliche Untersuchung

des Polymerisationsverhaltens aller drei Hafnocen-Komplexe zeigte eine gesteigerte Temperaturstabilität des Metallocen-Katalysators, sowie eine Verringerung von Kettenfreisetzungs- und Kettenendepimerisierungsreaktionen im Falle eines größeren sterischen Anspruchs des 4-Aryl-Substituenten. In diesem Zusammenhang wird die zunehmende Rigidität im Metallocen-Gerüst durch den vergrößerten sterischen Anspruch des 4-Aryl-Substituenten als entscheidend angesehen. Im Hinblick auf die durchgeführte Studie sind wir der Überzeugung, dass unsere detaillierte Analyse der Struktur-Wirkungsbeziehungen nicht nur das optimale katalytische System für die Herstellung von fast perfektem isotaktischem Polypropylen herausgearbeitet hat, sondern wesentlich zur Entwicklung der zukünftigen Generationen von homogenen Polypropylen-Katalysatoren beitragen kann.

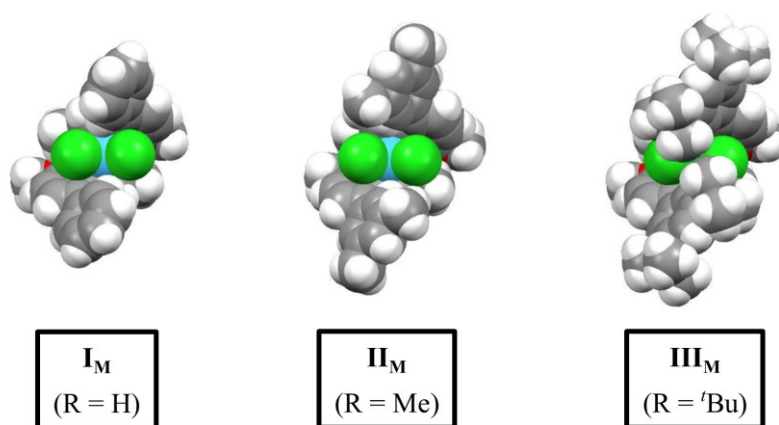


Abbildung 19. *Space filling* Abbildung von I<sub>Hf</sub> – III<sub>Hf</sub> zur Verdeutlichung des Einflusses des 4-Aryl Substituenten auf den Öffnungswinkel (*cga*) der *ansa*-Metallocene.

Inspiriert durch das quasi perfekte katalytische Verhalten dieses Metallocen-Gerüsts, wurde im Zuge der vorliegenden Arbeit die Palette der verwendeten Zentralmetalle um das Titan erweitert. Da Titanocene in der Polymerisation von Olefinen zur schnellen Deaktivierung des katalytisch aktiven Komplexes neigen,<sup>101</sup> verspricht das entwickelte Ligandensystem (Schema 15) eine verbesserte Katalysatorstabilität durch die Verhinderung unerwünschter Nebenreaktionen. Durch das Testen unterschiedlicher Ligand-Substitutionen, verschiedener Aktivierungsstrategien und unterschiedlicher Polymerisationsbedingungen konnten in der Tat optimierte Bedingungen für die katalytische Umsetzung von Propen mit Titan-basierten Metallocenen gefunden werden. Hierbei wurden hochschmelzende ( $T_m > 170$  °C), isotaktische Polypropylene mit enger Polydispersität generiert. In diesem Zusammenhang wurde das bismethylierte Derivat („L<sub>2</sub>TiMe<sub>2</sub>“) von III<sub>Ti</sub> („L<sub>2</sub>TiCl<sub>2</sub>“) in Kombination mit [Ph<sub>3</sub>C][B(C<sub>6</sub>F<sub>5</sub>)<sub>4</sub>] als, bis heute, stabilster und katalytisch aktivster Titanocen-basierter Katalysator für die Umsetzung von Propen ermittelt. Obwohl die katalytische

Leistungsfähigkeit immer noch von den isostrukturellen Zirkon- und Hafniumkomplexen übertroffen wird, sollten Titanocene in der Polymerisation von Olefinen auch in Zukunft nicht komplett außer Acht gelassen werden. Im Gegensatz zu den beiden höheren Homologen weist das Element Titan eine der größten Häufigkeiten auf unserem Planeten auf, ist entsprechend gut verfügbar und günstig und hat zudem seine Fähigkeiten in der heterogenen Polymerisation von Olefinen mit ZN-Systemen bereits sehr erfolgreich unter Beweis gestellt.

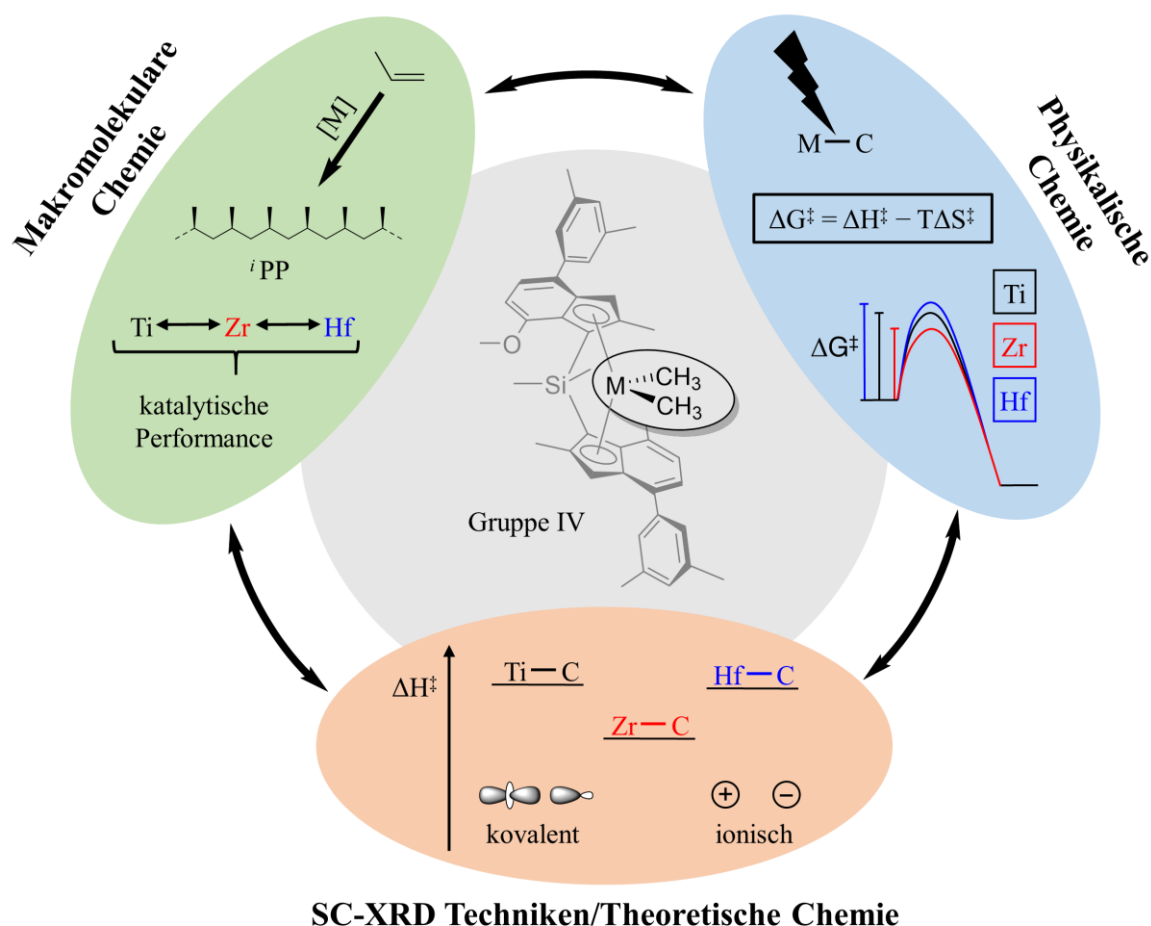


Abbildung 20. Visualisierung des multidisziplinären Ansatzes zur Aufklärung der Rolle der Gruppe IV Metalle in der katalytischen Umsetzung von Olefinen.

Für ein vergleichendes Bild isostruktureller Gruppe IV Metallocene wurde neben den Komplexen  $\mathbf{II}_{Hf}$  und  $\mathbf{II}_{Ti}$  das Zirkon-Analog  $\mathbf{II}_{Zr}$  synthetisiert und unter identischen Bedingungen katalytisch evaluiert. Zusätzlich zu dem katalytischen Verhalten rückten die essentiellen strukturellen und chemischen Unterschiede bei der Verwendung von Gruppe IV Metallen zunehmend in den Fokus dieser Arbeit (Abbildung 20). In diesem Zusammenhang wird der M-C  $\sigma$ -Bindung eine entscheidende Rolle zugesprochen, da sie in zahlreichen katalytischen Subprozessen beteiligt ist, welche in ihrer Gesamtheit sowohl die katalytische Aktivität, als auch die resultierenden Polymereigenschaften festlegen. Entsprechend wurden

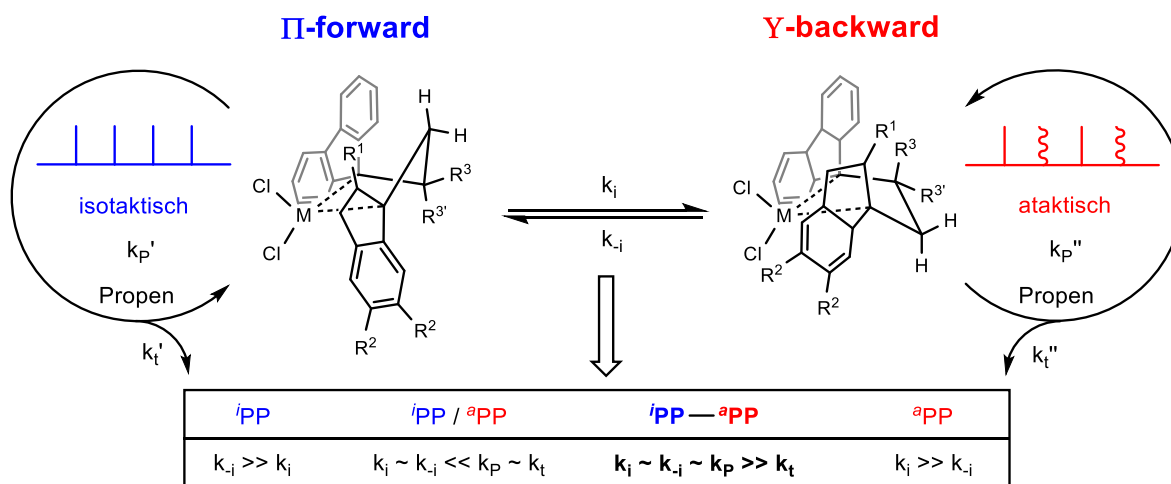
synthetische Strategien entwickelt, welche die Herstellung von isostrukturellen (II) bismethylierten Gruppe IV Metallocenen ermöglicht. Für eine fundamentale Analyse der M–C  $\sigma$ -Bindung wurden die elektronischen Eigenschaften dieser essentiellen Einheit erstmalig experimentell mittels hochaufgelöster Einkristall-Röntgenstrukturanalyse und weiterführenden theoretischen Berechnungen aufgeklärt (Abbildung 20). Während die Ti–C Bindung einen wesentlichen kovalenten Charakter aufweist, ist die Hf–C Bindung von starker ionischer Natur. Zusätzliche Einkristall-Röntgenstrukturanalyse unter hohem Druck offenbarte eine Zr–C Bindung mit signifikant höheren kovalenten Charakter als die Hf–C Bindung. Abgesehen davon wurde zusätzlich das elementare chemische Verhalten der M–C  $\sigma$ -Bindung untersucht, indem die Umsetzung dieser Einheit kinetisch analysiert wurde. In diesem Zusammenhang zeigten die kovalentere Ti–C und die stark ionische Hf–C Bindung einen ausgeprägten enthalpischen Beitrag zur Aktivierungsenergie, wohingegen der enthalpische Beitrag für die Umsetzung der Zr–C Bindung deutlich geringer ausfiel. Allerdings war für die Umsetzung der Zr–C Bindung der entropische Beitrag zur Aktivierungsbarriere wesentlich höher. Eine Korrelation dieser Ergebnisse mit dem katalytischen Verhalten aller drei isostruktureller Komplexe (II) der Gruppe IV ließ erstmalig Rückschlüsse von experimentell beobachteten, elektronischen und chemischen Unterschieden in den M–C  $\sigma$ -Bindungen auf das resultierende katalytische Verhalten zu. Entsprechend können hierbei die außergewöhnlich hohen Molekulargewichte in Kombination mit dem „Hafnium-Effekt“ anschaulich erläutert werden, genauso wie wesentliche Unterschiede in der Temperaturabhängigkeit der katalytischen Aktivität und der Stereoregularitäten bei der Verwendung der verschiedenen Gruppe IV Zentralmetalle in der Polymerisation von Propen.

In unseren Augen birgt die durchgeführte Pionierstudie über die grundlegenden elektronischen und chemischen Eigenschaften der M–C Bindung isostruktureller Metallocene, in Kombination mit dem katalytischen Verhalten, durchaus das Potential, die Rolle der Gruppe IV Metalle in der Polymerisation von Olefinen zu revolutionieren. Die klassische Suche nach dem „richtigen“ Metallzentrum, welche in der Regel von Vermutungen, von praktischen Erfahrungen und oftmals von einfachem, systematischem Ausprobieren geprägt gewesen ist, wird hierbei um neue, wesentliche Erkenntnisse bereichert. Unsere Ergebnisse eröffnen hierbei eine neue Perspektive, welche eine vereinfachte Interpretation in Bezug auf das am besten geeignete Zentralmetall für jeden spezifischen Anwendungsbereich ermöglicht. Die dargestellten Untersuchungen lösen sogar die entscheidenden chemischen Unterschiede von Zirkon und Hafnium auf, einem einmaligen Pärchen im Periodensystem der Elemente, welches, aufgrund der Lanthanoidenkontraktion,

quasi identische geometrische Parameter aufweist. Allerdings soll nicht unerwähnt bleiben, dass nur mit der Durchführung weiterer, systematischer Studien, welche sich mit isostrukturellen Verbindungen der Gruppe IV in Kombination mit anderen Ligandstrukturen beschäftigen, der explizite Einfluss der Gruppe IV Metalle in seiner absoluten Form zweifelsfrei sichergestellt werden kann. Nichtsdestotrotz werden die neuen Einblicke in die Chemie der Gruppe IV Metalle, in Zeiten einer zunehmenden Systematisierung und Strukturierung von zukünftigen Entwicklungsfeldern, eine präzisere Anwendung dieser Metalle auf dem gewaltigen Feld der Polyolefinkatalyse ermöglichen. Zusätzlich kann das entwickelte Prinzip dieser Pionierstudie, mit Blick auf andere Elementgruppierungen mit einem gemeinsamen katalytischen Hintergrund, als Vorlage dienen, um einen neuen und fundierteren Einblick in die jeweilige Materie zu erlangen.

In weiterführenden Projekten dieser Arbeit wechselte der Fokus von der fundamentalen Chemie der Metallocene zu den synthetisierbaren Polymeren und ihren Eigenschaften. Im Bereich der Polyolefine stellt die Herstellung von definierten Blockstrukturen ein außerordentlich interessantes Forschungsfeld dar, welches allerdings auch große Herausforderungen mit sich bringt. Durch das statistische Verhalten beim Einbau von Monomer/Comonomer in einer Copolymerisationsreaktion von unterschiedlichen Olefinen, sowie bei der statistischen Verteilung von Stereofehlern im Bereich der generellen Stereoselektivität, ist die Ausbildung von Blockstrukturen generell nicht begünstigt. Nichtsdestotrotz existieren einzelne Strategien wie das *chain-shuttling*,<sup>123</sup> ein Mechanismus mit oszillierender Stereokontrolle,<sup>18</sup> oder die Anwendung eines lebenden/“quasi-lebenden“ koordinativen Polymerisationsmechanismus,<sup>133</sup> um die Herstellung von definierten Polyolefin-Blockstrukturen zu ermöglichen. Inspiriert durch diese unterschiedlichen Strategien wurde im Zuge der vorliegenden Arbeit eine alternative Route für die Herstellung von maßgeschneiderten *PP-*i*PP* Blockstrukturen entwickelt, welche eine neue Klasse von hochschmelzenden, elastischen Polypropylenen darstellt.

Hafnium-basierte EBFI-Metallocene haben bereits in vorangegangenen Studien ihre außergewöhnlichen Fähigkeiten in der Produktion von hochmolekularem, elastischem Polypropylen unter Beweis gestellt.<sup>20</sup> Allerdings stellt bis heute die eingeschränkte Temperaturstabilität dieser Polymere, trotz der hervorzuhebenden mechanischen Eigenschaften, ein ungelöstes Problem dar.<sup>19, 115</sup> Dieses Problem steht sinnbildlich für den bisher unvollendeten Ansatz, in der katalytischen Herstellung von Propen-basierten Elastomeren ein elastisches Verhalten mit hochschmelzenden Eigenschaften zu kombinieren.



**Schema 16. Molekulare Abbildung der isoselektiven  $\Pi$ -forward und unselektiven Y-backward Ringkonformation von EBFI-Metallocenen. Beide Konformationen gehen in Abhängigkeit der energetischen Grundzustände und der Energiebarriere in einem dynamischen Gleichgewicht ineinander über.**

Um dieser Problematik auf den Grund zu gehen, soll das komplexe Zusammenspiel der zahlreichen Mechanismen, welche alle in ihrer Gesamtheit die resultierende Stereoregularität der EBFI-Metallocene bestimmen, aufgelöst werden. Neben den unterschiedlichen enantiofacialen Selektivitäten des dual-site Systems wurden der Einfluss einer möglichen Kettenmigration, einer Kettenendepimerisierung und insbesondere der Einfluss der zwei Konformationsisomere auf die Taktizität im Detail untersucht. Entsprechend wurde im Zuge dieser Arbeit das Polymerisationsverhalten von zahlreichen neuen und literaturbekannten EBFI-Metallocenen mit variierendem 2,5,6-Indenyl Substitutionsmuster ausführlich analysiert und ein wesentlicher Einfluss beider Ringkonformationen auf die finalen Stereoregularitäten identifiziert (Schema 16). Bei allen Komplexen ist stets eines der beiden Konformere energetisch bevorzugt und liegt mit der weniger bevorzugten Konformation in einem dynamischen Gleichgewicht vor. Durch die genaue Anpassung von allen Polymerisationsparametern war es gelungen, den Konformationswechsel, in Bezug auf die Kettenwachstums- und Abbruchgeschwindigkeit, so zu optimieren, dass  $aPP-iPP$  Blockstrukturen hergestellt werden konnten, die in einer Matrix von ataktischem Polypropylen vorliegen. Das Resultat ist ein physikalisch vernetztes, hochmolekulares und hochschmelzendes ( $T_m \sim 140\text{ }^\circ\text{C}$ ) thermoplastisches Elastomer, welches ein exzellentes reversibles Verformungsverhalten aufweist und in einer simplen einstufigen Synthese hergestellt wird.

Die Verwendung von EBFI-Metallocenen für die gezielte Herstellung von hochschmelzenden, elastischen Polypropylenen stellt in ihrem einfachen Setup, bestehend aus nur einem angewendeten Katalysator in einer einzigen Reaktion, sicherlich ein

hervorzuhebendes Beispiel für die Herstellung von Blockstrukturen dar. Außerdem haben mechanische Untersuchungen der entsprechenden Polymereigenschaften die Herstellung eines thermoplastischen Elastomers hervorgehoben, welches ein exzellentes reversibles Verformungsverhalten aufweist. Allerdings stellt die Notwendigkeit, bei relativ niedrigen Polymerisationstemperaturen zu arbeiten, bis dato den größten Nachteil für eine potentielle industrielle Anwendung dar. In diesem Zusammenhang versprechen zusätzliche Untersuchungen, die eine weitere Optimierung der Polymerisationsbedingungen in Kombination mit anderen EBFI-Metallocen-Komplexen adressieren, einen verbesserten Syntheseweg von hochschmelzenden, Propylen-basierten, thermoplastischen Elastomeren unter industriell relevanten Bedingungen.

11. Bibliography

1. Steinborn, D., *Grundlagen der Metallorganischen Komplexkatalyse*, Vieweg-Teubner, **2010**, 4-7.
2. [http://www.plasticseurope.org/documents/document/20161014113313-plastics\\_the\\_facts\\_2016\\_final\\_version.pdf](http://www.plasticseurope.org/documents/document/20161014113313-plastics_the_facts_2016_final_version.pdf), status: october, **2017**.
3. Ziegler, K.; Holzkamp, E.; Breil, H.; Martin, H., *Angew. Chem.* **1955**, *67*, 541-547.
4. Busico, V., *Dalton Transactions* **2009**, 8794-8802.
5. Resconi, L.; Cavallo, L.; Fait, A.; Piemontesi, F., *Chem. Rev.* **2000**, *100*, 1253-1345.
6. Hild, S.; Cobzaru, C.; Troll, C.; Rieger, B., *Macromol. Chem. Phys.* **2006**, *207*, 665-683.
7. [http://www.plasticseurope.org/documents/document/20150227150049-final\\_plastics\\_the\\_facts\\_2014\\_2015\\_260215.pdf](http://www.plasticseurope.org/documents/document/20150227150049-final_plastics_the_facts_2014_2015_260215.pdf), status: october, **2017**.
8. Natta, G., *Angew. Chem.* **1956**, *68*, 393-403.
9. Elias, H.-G., *Makromoleküle - Band 3: Industrielle Polymere und Synthesen*, Wiley-VCH, **2001**, 167-169.
10. Breslow, D. S.; Newburg, N. R., *J. Am. Chem. Soc.* **1957**, *79*, 5072-5073.
11. Natta, G.; Pino, P.; Mazzanti, G.; Giannini, U., *J. Am. Chem. Soc.* **1957**, *79*, 2975-2976.
12. Sinn, H.; Kaminsky, W.; Vollmer, H.-J.; Woldt, R., *Angew. Chem., Int. Ed.* **1980**, *19*, 390-392.
13. Wild, F. R. W. P.; Zsolnai, L.; Huttner, G.; Brintzinger, H. H., *J. Organomet. Chem.* **1982**, *232*, 233-247.
14. Kaminsky, W.; Külper, K.; Brintzinger, H. H.; Wild, F. R. W. P., *Angew. Chem., Int. Ed.* **1985**, *24*, 507-508.
15. Wild, F. R. W. P.; Wasiucionek, M.; Huttner, G.; Brintzinger, H. H., *J. Organomet. Chem.* **1985**, *288*, 63-67.
16. Ewen, J. A., *J. Am. Chem. Soc.* **1984**, *106*, 6355-6364.
17. Ewen, J. A.; Jones, R. L.; Razavi, A.; Ferrara, J. D., *J. Am. Chem. Soc.* **1988**, *110*, 6255-6256.
18. Coates, G. W.; Waymouth, R. M., *Science* **1995**, *267*, 217-219.
19. Dietrich, U.; Hackmann, M.; Rieger, B.; Klinga, M.; Leskelä, M., *J. Am. Chem. Soc.* **1999**, *121*, 4348-4355.
20. Rieger, B.; Troll, C.; Preuschen, J., *Macromolecules* **2002**, *35*, 5742-5743.
21. Okuda, J., *Chemische Berichte* **1990**, *123*, 1649-1651.
22. Baier, M. C.; Zuideveld, M. A.; Mecking, S., *Angew. Chem., Int. Ed.* **2014**, *53*, 9722-9744.
23. Schöbel, A.; Herdtweck, E.; Parkinson, M.; Rieger, B., *Chem.-Eur. J.* **2012**, *18*, 4129-4129.
24. Tranchida, D.; Mileva, D.; Resconi, L.; Rieger, B.; Schöbel, A., *Macromol. Chem. Phys.* **2015**, *216*, 2171-2178.
25. Wang, B., *Coord. Chem. Rev.* **2006**, *250*, 242-258.
26. Brintzinger, H. H.; Fischer, D.; Mülhaupt, R.; Rieger, B.; Waymouth, R. M., *Angew. Chem., Int. Ed.* **1995**, *34*, 1143-1170.
27. Moehring, P. C.; Coville, N. J., *Coord. Chem. Rev.* **2006**, *250*, 18-35.
28. Shaltout, R. M.; Corey, J. Y.; Rath, N. P., *J. Organomet. Chem.* **1995**, *503*, 205-212.
29. Bryant, P. L.; Harwell, C. R.; Mrse, A. A.; Emery, E. F.; Gan, Z.; Caldwell, T.; Reyes, A. P.; Kuhns, P.; Hoyt, D. W.; Simeral, L. S.; Hall, R. W.; Butler, L. G., *J. Am. Chem. Soc.* **2001**, *123*, 12009-12017.

30. Stellbrink, J.; Niu, A.; Allgaier, J.; Richter, D.; Koenig, B. W.; Hartmann, R.; Coates, G. W.; Fetters, L. J., *Macromolecules* **2007**, *40*, 4972-4981.
31. Pédeutour, J.-N.; Radhakrishnan, K.; Cramail, H.; Deffieux, A., *Macromol. Rapid Commun.* **2001**, *22*, 1095-1123.
32. Busico, V.; Cipullo, R.; Pellecchia, R.; Talarico, G.; Razavi, A., *Macromolecules* **2009**, *42*, 1789-1791.
33. Pédeutour, J.-N.; Cramail, H.; Deffieux, A., *J. Mol. Catal. A: Chem.* **2001**, *174*, 81-87.
34. Pédeutour, J.-N.; Cramail, H.; Deffieux, A., *J. Mol. Catal. A: Chem.* **2001**, *176*, 87-94.
35. Bryliakov, K. P.; Talsi, E. P.; Voskoboynikov, A. Z.; Lancaster, S. J.; Bochmann, M., *Organometallics* **2008**, *27*, 6333-6342.
36. Chien, J. C. W.; Tsai, W. M.; Rausch, M. D., *J. Am. Chem. Soc.* **1991**, *113*, 8570-8571.
37. Chen, E. Y.-X.; Marks, T. J., *Chem. Rev.* **2000**, *100*, 1391-1434.
38. Bochmann, M., *Organometallics* **2010**, *29*, 4711-4740.
39. Yang, X.; Stern, C. L.; Marks, T. J., *J. Am. Chem. Soc.* **1994**, *116*, 10015-10031.
40. Chien, J. C. W.; Song, W.; Rausch, M. D., *Macromolecules* **1993**, *26*, 3239-3240.
41. Mathis, D.; Couzijn, E. P. A.; Chen, P., *Organometallics* **2011**, *30*, 3834-3843.
42. Cossee, P., *Tetrahedron Letters* **1960**, *1*, 12-16.
43. Cossee, P., *Tetrahedron Letters* **1960**, *1*, 17-21.
44. Arlman, E. J.; Cossee, P., *Journal of Catalysis* **1964**, *3*, 99-104.
45. Cossee, P., *Journal of Catalysis* **1964**, *3*, 80-88.
46. Dawoodi, Z.; Green, M. L. H.; Mtetwa, V. S. B.; Prout, K., *Chem. Commun.* **1982**, 1410-1411.
47. Brookhart, M.; Green, M. L. H., *J. Organomet. Chem.* **1983**, *250*, 395-408.
48. Rappé, A. K.; Skiff, W. M.; Casewit, C. J., *Chem. Rev.* **2000**, *100*, 1435-1456.
49. Laine, A.; Linnolahti, M.; Pakkanen, T. A.; Severn, J. R.; Kokko, E.; Pakkanen, A., *Organometallics* **2010**, *29*, 1541-1550.
50. Laine, A.; Linnolahti, M.; Pakkanen, T. A.; Severn, J. R.; Kokko, E.; Pakkanen, A., *Organometallics* **2011**, *30*, 1350-1358.
51. Ehm, C.; Budzelaar, P. H. M.; Busico, V., *J. Organomet. Chem.* **2015**, *775*, 39-49.
52. Bochmann, M., *J. Organomet. Chem.* **2004**, *689*, 3982-3998.
53. Guerra, G.; Longo, P.; Cavallo, L.; Corradini, P.; Resconi, L., *J. Am. Chem. Soc.* **1997**, *119*, 4394-4403.
54. Resconi, L.; Camurati, I.; Sudmeijer, O., *Topics in Catalysis* **1999**, *7*, 145-163.
55. Zhou, Z.; Stevens, J. C.; Klosin, J.; Kümmerle, R.; Qiu, X.; Redwine, D.; Cong, R.; Taha, A.; Mason, J.; Winniford, B.; Chauvel, P.; Montañez, N., *Macromolecules* **2009**, *42*, 2291-2294.
56. Grassi, A.; Zambelli, A.; Resconi, L.; Albizzati, E.; Mazzocchi, R., *Macromolecules* **1988**, *21*, 617-622.
57. Rieger, B.; Mu, X.; Mallin, D. T.; Chien, J. C. W.; Rausch, M. D., *Macromolecules* **1990**, *23*, 3559-3568.
58. Zambelli, A.; Locatelli, P.; Bajo, G.; Bovey, F. A., *Macromolecules* **1975**, *8*, 687-689.
59. Zambelli, A.; Locatelli, P.; Zannoni, G.; Bovey, F. A., *Macromolecules* **1978**, *11*, 923-924.
60. Baugh, L. S.; Canich, J. A. M., *Stereoselective Polymerization with Single-Site Catalysts*, CRC Press - Taylor & Francis Group, **2008**, 9-15.
61. Kawamura-Kuribayashi, H.; Koga, N.; Morokuma, K., *J. Am. Chem. Soc.* **1992**, *114*, 2359-2366.
62. Kawamura-Kuribayashi, H.; Koga, N.; Morokuma, K., *J. Am. Chem. Soc.* **1992**, *114*, 8687-8694.
63. Yoshida, T.; Koga, N.; Morokuma, K., *Organometallics* **1996**, *15*, 766-777.

64. Dahlmann, M.; Erker, G.; Nissinen, M.; Fröhlich, R., *J. Am. Chem. Soc.* **1999**, *121*, 2820-2828.
65. Busico, V.; Cipullo, R., *J. Am. Chem. Soc.* **1994**, *116*, 9329-9330.
66. Busico, V.; Caporaso, L.; Cipullo, R.; Landriani, L.; Angelini, G.; Margonelli, A.; Segre, A. L., *J. Am. Chem. Soc.* **1996**, *118*, 2105-2106.
67. Busico, V.; Brita, D.; Caporaso, L.; Cipullo, R.; Vacatello, M., *Macromolecules* **1997**, *30*, 3971-3977.
68. Busico, V.; Cipullo, R.; Caporaso, L.; Angelini, G.; Segre, A. L., *J. Mol. Catal. A: Chem.* **1998**, *128*, 53-64.
69. Resconi, L., *J. Mol. Catal. A: Chem.* **1999**, *146*, 167-178.
70. Yoder, J. C.; Bercaw, J. E., *J. Am. Chem. Soc.* **2002**, *124*, 2548-2555.
71. Guerra, G.; Cavallo, L.; Moscardi, G.; Vacatello, M.; Corradini, P., *Macromolecules* **1996**, *29*, 4834-4845.
72. Kukral, J.; Lehmus, P.; Feifel, T.; Troll, C.; Rieger, B., *Organometallics* **2000**, *19*, 3767-3775.
73. Song, F.; Lancaster, S. J.; Cannon, R. D.; Schormann, M.; Humphrey, S. M.; Zuccaccia, C.; Macchioni, A.; Bochmann, M., *Organometallics* **2005**, *24*, 1315-1328.
74. Kukral, J.; Lehmus, P.; Klinga, M.; Leskelä, M.; Rieger, B., *Eur. J. Inorg. Chem.* **2002**, *2002*, 1349-1356.
75. Cobzaru, C.; Hild, S.; Boger, A.; Troll, C.; Rieger, B., *Coord. Chem. Rev.* **2006**, *250*, 189-211.
76. Rieger, B.; Jany, G.; Fawzi, R.; Steimann, M., *Organometallics* **1994**, *13*, 647-653.
77. Linnolahti, M.; Pakkanen, Tapani A.; Leino, R.; Luttikhedde, Hendrik J. G.; Wilén, C.-E.; Näsman, Jan H., *Eur. J. Inorg. Chem.* **2001**, *2001*, 2033-2040.
78. Cavallo, L.; Guerra, G., *Macromolecules* **1996**, *29*, 2729-2737.
79. Caporaso, L.; De Rosa, C.; Talarico, G., *J. Polym. Sci., Part A, Polym. Chem.* **2010**, *48*, 699-708.
80. Talarico, G.; Budzelaar, P. H. M., *J. Am. Chem. Soc.* **2006**, *128*, 4524-4525.
81. Talarico, G.; Budzelaar, P. H. M., *Organometallics* **2008**, *27*, 4098-4107.
82. Resconi, L.; Piemontesi, F.; Camurati, I.; Balboni, D.; Sironi, A.; Moret, M.; Rychlicki, H.; Zeigler, R., *Organometallics* **1996**, *15*, 5046-5059.
83. Hajela, S.; Bercaw, J. E., *Organometallics* **1994**, *13*, 1147-1154.
84. Yang, P.; Baird, M. C., *Organometallics* **2005**, *24*, 6013-6018.
85. Suzuki, Y.; Yasumoto, T.; Mashima, K.; Okuda, J., *J. Am. Chem. Soc.* **2006**, *128*, 13017-13025.
86. Sini, G.; Macgregor, S. A.; Eisenstein, O.; Teuben, J. H., *Organometallics* **1994**, *13*, 1049-1051.
87. Resconi, L.; Piemontesi, F.; Franciscono, G.; Abis, L.; Fiorani, T., *J. Am. Chem. Soc.* **1992**, *114*, 1025-1032.
88. Eshuis, J. J. W.; Tan, Y. Y.; Meetsma, A.; Teuben, J. H.; Renkema, J.; Evens, G. G., *Organometallics* **1992**, *11*, 362-369.
89. Resconi, L.; Piemontesi, F.; Camurati, I.; Sudmeijer, O.; Nifant'ev, I. E.; Ivchenko, P. V.; Kuz'mina, L. G., *J. Am. Chem. Soc.* **1998**, *120*, 2308-2321.
90. Chirik, P. J.; Dalleska, N. F.; Henling, L. M.; Bercaw, J. E., *Organometallics* **2005**, *24*, 2789-2794.
91. Resconi, L.; Bossi, S.; Abis, L., *Macromolecules* **1990**, *23*, 4489-4491.
92. Schöbel, A.; Lanzinger, D.; Rieger, B., *Organometallics* **2013**, *32*, 427-437.
93. Holleman, A. F.; Wiberg, E.; Wiberg, N., *Lehrbuch der Anorganischen Chemie* **2007**, Walter de Gruyter & Co: Berlin, 102. Edition.
94. Shannon, R. D.; Prewitt, C. T., *Acta Crystallogr. B* **1969**, *25*, 925-946.
95. Shannon, R., *Acta Crystallogr. A* **1976**, *32*, 751-767.

96. Kaminsky, W.; Miri, M.; Sinn, H.; Woldt, R., *Makromol. Chem., Rapid Commun.* **1983**, *4*, 417-421.
97. Mallin, D. T.; Rausch, M. D.; Lin, Y. G.; Dong, S.; Chien, J. C. W., *J. Am. Chem. Soc.* **1990**, *112*, 2030-2031.
98. Llinas, G. H.; Dong, S. H.; Mallin, D. T.; Rausch, M. D.; Lin, Y. G.; Winter, H. H.; Chien, J. C. W., *Macromolecules* **1992**, *25*, 1242-1253.
99. Llinas, G. H.; Day, R. O.; Rausch, M. D.; Chien, J. C. W., *Organometallics* **1993**, *12*, 1283-1288.
100. Lee, M. H.; Han, Y.; Kim, D.-h.; Hwang, J.-W.; Do, Y., *Organometallics* **2003**, *22*, 2790-2796.
101. Bryliakov, K. P.; Babushkin, D. E.; Talsi, E. P.; Voskoboynikov, A. Z.; Gritzo, H.; Schröder, L.; Damrau, H.-R. H.; Wieser, U.; Schaper, F.; Brintzinger, H. H., *Organometallics* **2005**, *24*, 894-904.
102. Miyake, S.; Okumura, Y.; Inazawa, S., *Macromolecules* **1995**, *28*, 3074-3079.
103. Bravakis, A. M.; Bailey, L. E.; Pigeon, M.; Collins, S., *Macromolecules* **1998**, *31*, 1000-1009.
104. Machat, M. R.; Jandl, C.; Rieger, B., *Organometallics* **2017**, *36*, 1408-1418.
105. Razavi, A.; Peters, L.; Nafpliotis, L., *J. Mol. Catal. A: Chem.* **1997**, *115*, 129-154.
106. Kaminsky, W.; Engehausen, R.; Zoumis, K.; Spaleck, W.; Rohrmann, J., *Makromol. Chem.* **1992**, *193*, 1643-1651.
107. Ewen, J. A.; Zambelli, A.; Longo, P.; Sullivan, J. M., *Macromol. Rapid Commun.* **1998**, *19*, 71-73.
108. Razavi, A.; Atwood, J. L., *J. Organomet. Chem.* **1993**, *459*, 117-123.
109. Ewen, J. A.; Haspelslach, L.; Atwood, J. L.; Zhang, H., *J. Am. Chem. Soc.* **1987**, *109*, 6544-6545.
110. Schock, L. E.; Marks, T. J., *J. Am. Chem. Soc.* **1988**, *110*, 7701-7715.
111. Dias, A. R.; Salema, M. S.; Martinho Simões, J. A.; Pattiasina, J. W.; Teuben, J. H., *J. Organomet. Chem.* **1988**, *346*, C4-C6.
112. Simoes, J. A. M.; Beauchamp, J. L., *Chem. Rev.* **1990**, *90*, 629-688.
113. Schöbel, A., *Differences of Zirconocenes and Hafnocenes*, Dissertation, TU München, WACKER-Lehrstuhl für Makromolekulare Chemie **2012**.
114. Lanzinger, D., *New Microstructures in Olefin-Based Polymers*, Dissertation, TU München, WACKER-Lehrstuhl für Makromolekulare Chemie **2015**.
115. Boger, A.; Heise, B.; Troll, C.; Marti, O.; Rieger, B., *European Polymer Journal* **2007**, *43*, 634-643.
116. Fan, W.; Leclerc, M. K.; Waymouth, R. M., *J. Am. Chem. Soc.* **2001**, *123*, 9555-9563.
117. Reybuck, S. E.; Meyer, A.; Waymouth, R. M., *Macromolecules* **2002**, *35*, 637-643.
118. Lu, L.; Niu, H.; Dong, J.-Y.; Zhao, X.; Hu, X., *Journal of Applied Polymer Science* **2010**, *118*, 3218-3226.
119. Spaleck, W.; Kueber, F.; Winter, A.; Rohrmann, J.; Bachmann, B.; Antberg, M.; Dolle, V.; Paulus, E. F., *Organometallics* **1994**, *13*, 954-963.
120. Voegelé, J.; Troll, C.; Rieger, B., *Macromol. Chem. Phys.* **2002**, *203*, 1918-1925.
121. Kakugo, M.; Naito, Y.; Mizunuma, K.; Miyatake, T., *Macromolecules* **1982**, *15*, 1150-1152.
122. Wang, W.-J.; Zhu, S., *Macromolecules* **2000**, *33*, 1157-1162.
123. Arriola, D. J.; Carnahan, E. M.; Hustad, P. D.; Kuhlman, R. L.; Wenzel, T. T., *Science* **2006**, *312*, 714-719.
124. Alfano, F.; Boone, H. W.; Busico, V.; Cipullo, R.; Stevens, J. C., *Macromolecules* **2007**, *40*, 7736-7738.
125. Zintl, M.; Rieger, B., *Angew. Chem., Int. Ed.* **2007**, *46*, 333-335.

126. Hustad, P. D.; Kuhlman, R. L.; Arriola, D. J.; Carnahan, E. M.; Wenzel, T. T., *Macromolecules* **2007**, *40*, 7061-7064.
127. Hustad, P. D.; Kuhlman, R. L.; Carnahan, E. M.; Wenzel, T. T.; Arriola, D. J., *Macromolecules* **2008**, *41*, 4081-4089.
128. Zhang, W.; Sita, L. R., *J. Am. Chem. Soc.* **2008**, *130*, 442-443.
129. Valente, A.; Mortreux, A.; Visseaux, M.; Zinck, P., *Chem. Rev.* **2013**, *113*, 3836-3857.
130. Descour, C.; Macko, T.; Cavallo, D.; Parkinson, M.; Hubner, G.; Spoelstra, A.; Villani, M.; Duchateau, R., *J. Polym. Sci., Part A, Polym. Chem.* **2014**, *52*, 1422-1434.
131. Theurkauff, G.; Roisnel, T.; Waassenaar, J.; Carpentier, J.-F.; Kirillov, E., *Macromol. Chem. Phys.* **2014**, *215*, 2035-2047.
132. Coates, G. W.; Hustad, P. D.; Reinartz, S., *Angew. Chem., Int. Ed.* **2002**, *41*, 2236-2257.
133. Eagan, J. M.; Xu, J.; Di Girolamo, R.; Thurber, C. M.; Macosko, C. W.; LaPointe, A. M.; Bates, F. S.; Coates, G. W., *Science* **2017**, *355*, 814-816.

## 12. Appendix

### 12.1 Supporting Information – Chapter 4: *Striving for Perfection: High Molecular Weight, High-Melting <sup>1</sup>PP*

#### Ultra-Rigid Indenyl-based Hafnocene Complexes for the Highly Isoselective Polymerization of Propene: Tunable Polymerization Performance Adopting Various Sterically Demanding 4-Aryl Substituents

Martin R. Machat,<sup>†</sup> Dominik Lanzinger,<sup>‡</sup> Alexander Pöthig,<sup>§</sup> and Bernhard Rieger<sup>\*,†</sup>

<sup>†</sup>Wacker-Lehrstuhl für Makromolekulare Chemie, Technische Universität München, Lichtenbergstraße 4, 85748 Garching bei München, Germany

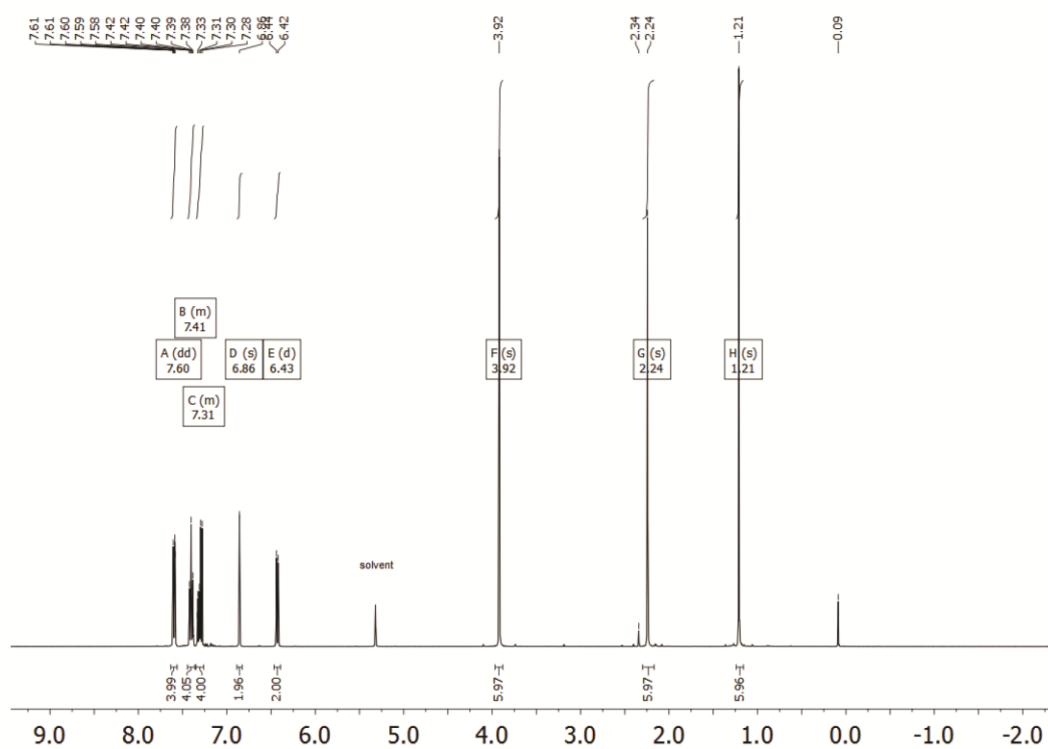
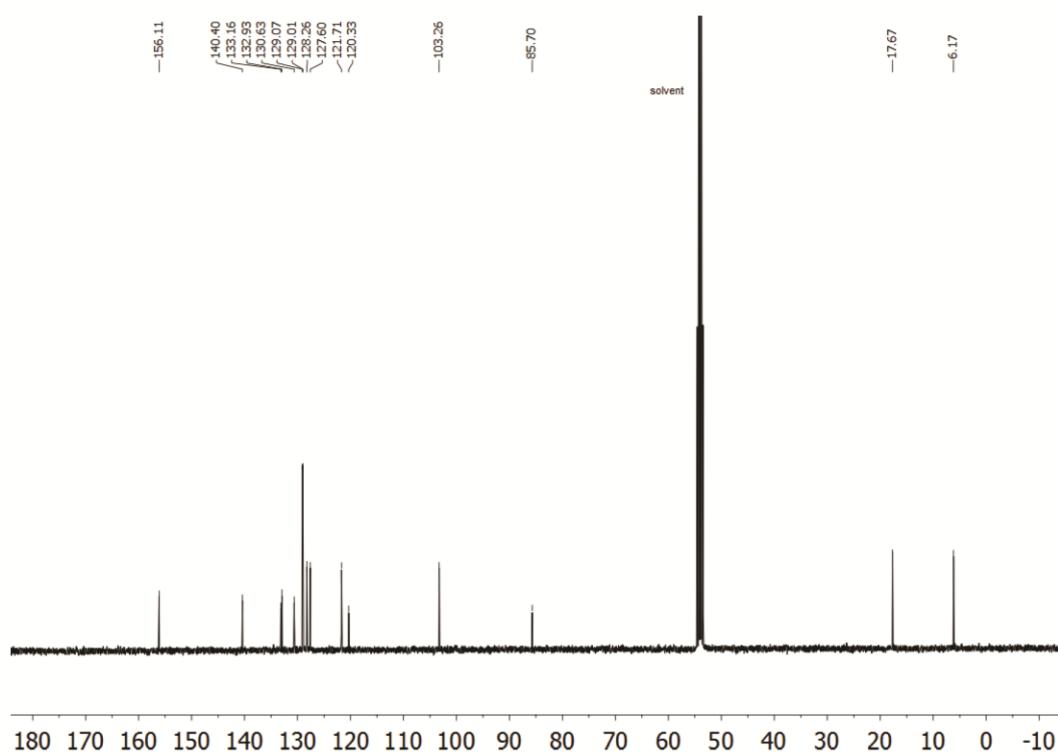
<sup>‡</sup>Advanced Materials & Systems Research, BASF SE, GCP/PM-B001, 67056 Ludwigshafen am Rhein, Germany

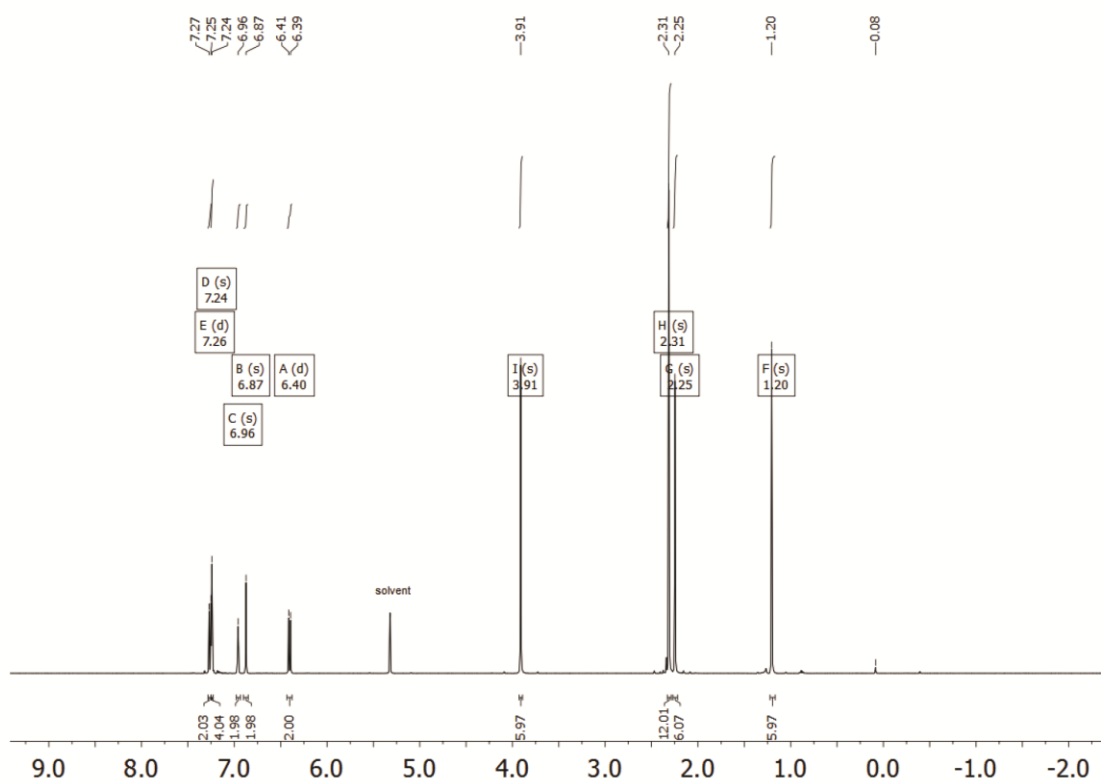
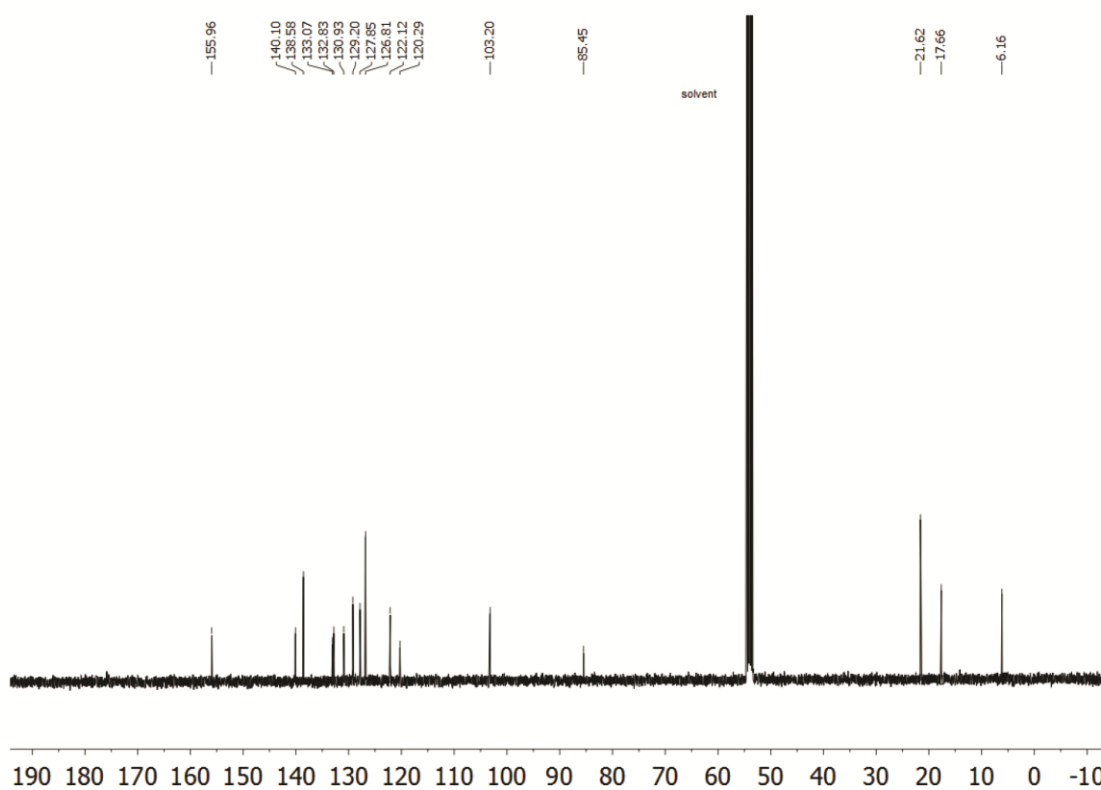
<sup>§</sup>Catalysis Research Center, Technische Universität München, Ernst-Otto-Fischer Straße 1, 85748 Garching bei München, Germany

## Supporting information

### Table of contents:

1. Synthesis – <sup>1</sup> H NMR and <sup>13</sup> C NMR spectra .....	2
2. UV VIS-spectra for the preactivation with 200 eq. TIBA .....	4
3. Olefinic end group analysis <i>via</i> <sup>1</sup> H NMR .....	6
4. Tacticity determination <i>via</i> <sup>13</sup> C NMR of polymers at elevated temperatures.....	7
5. Temperature dependent consumption of propene for <b>I-III</b> .....	14
6. Single Crystal XRD (SC-XRD) data .....	16

1. Synthesis –  $^1\text{H}$  NMR and  $^{13}\text{C}$  NMR spectraFigure S1.  $^1\text{H}$  NMR spectrum of **I** in  $\text{CD}_2\text{Cl}_2$ .Figure S2.  $^{13}\text{C}$  NMR spectrum of **I** in  $\text{CD}_2\text{Cl}_2$ .

Figure S3. <sup>1</sup>H NMR spectrum of **II** in CD<sub>2</sub>Cl<sub>2</sub>.Figure S4. <sup>13</sup>C NMR spectrum of **II** in CD<sub>2</sub>Cl<sub>2</sub>.

## 2. UV VIS-spectra for the preactivation with 200 eq. TIBA

UV VIS spectra were obtained using a Varian Cary 50 spectrophotometer with a sealed UV quartz cuvette (1 mm) at 60 °C. A  $8.0 \cdot 10^{-4}$  M complex (**I-III**) solution is measured first, subsequently adding 200 eq. 1.1 M TIBA- solution in toluene. The reaction is followed the commonly applied activation time of one hour. In all three cases the initial absorbance maxima is significantly shifted to lower wavelength indicating a substitution reaction between chloride and alkyl substituents resulting in an increase of the HOMO-LUMO gap (Figure S1-S3).<sup>[1]</sup>

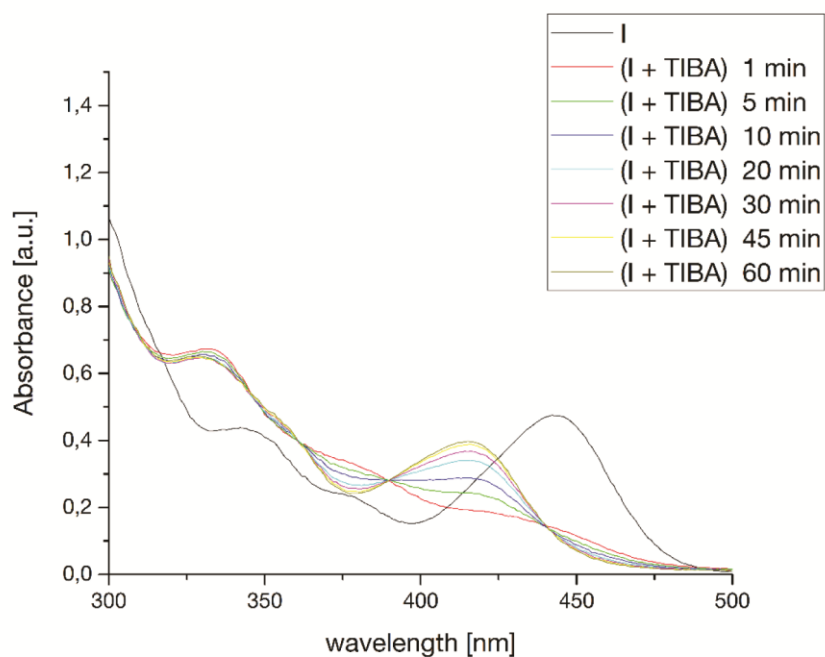


Figure S5. UV VIS investigation of the *in situ* alkylation of complex **I** with 200 eq. TIBA.

[1] I. Schöbel, A.; Lanzinger, D.; Rieger, B., *Organometallics* **2013**, 32 (2), 427.

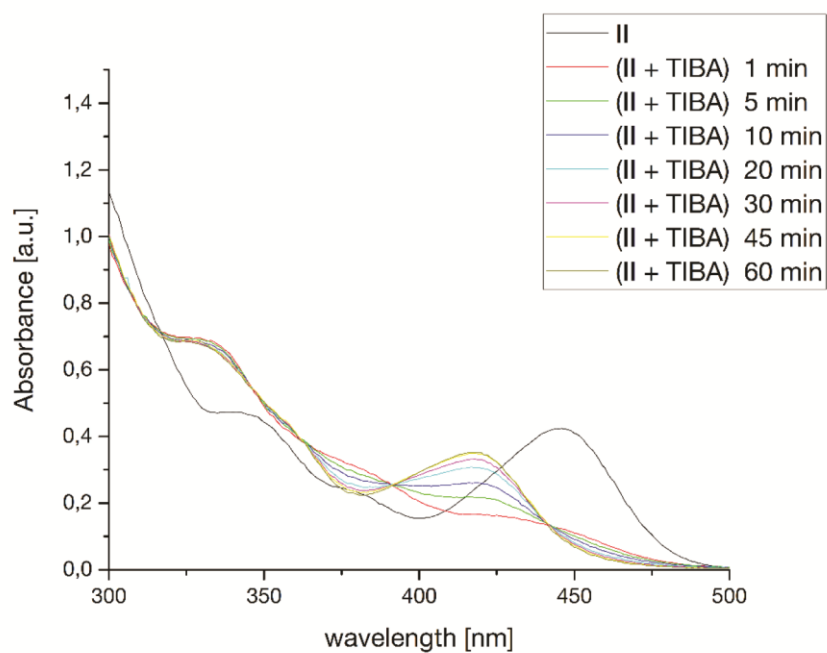


Figure S6. UV VIS investigation of the *in situ* alkylation of complex **II** with 200 eq. TIBA.

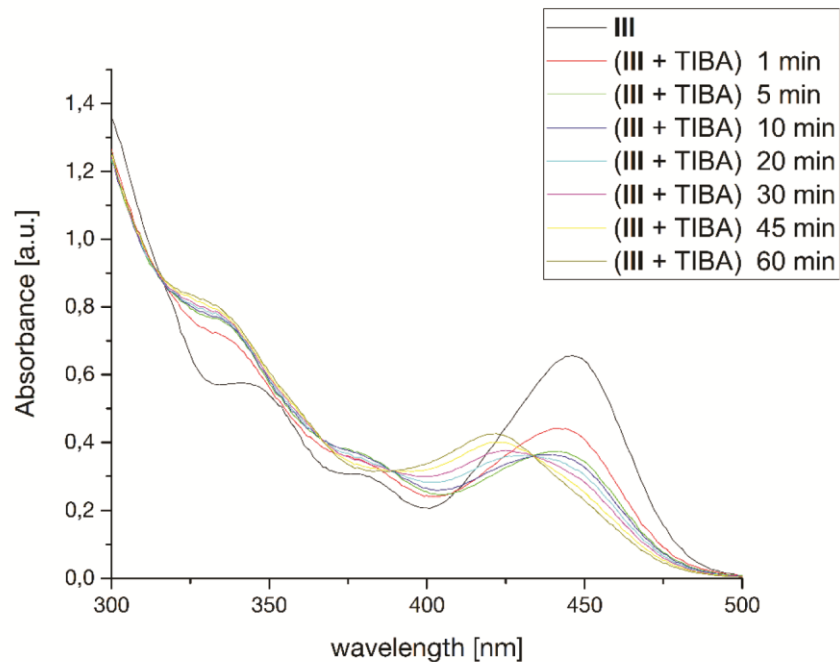
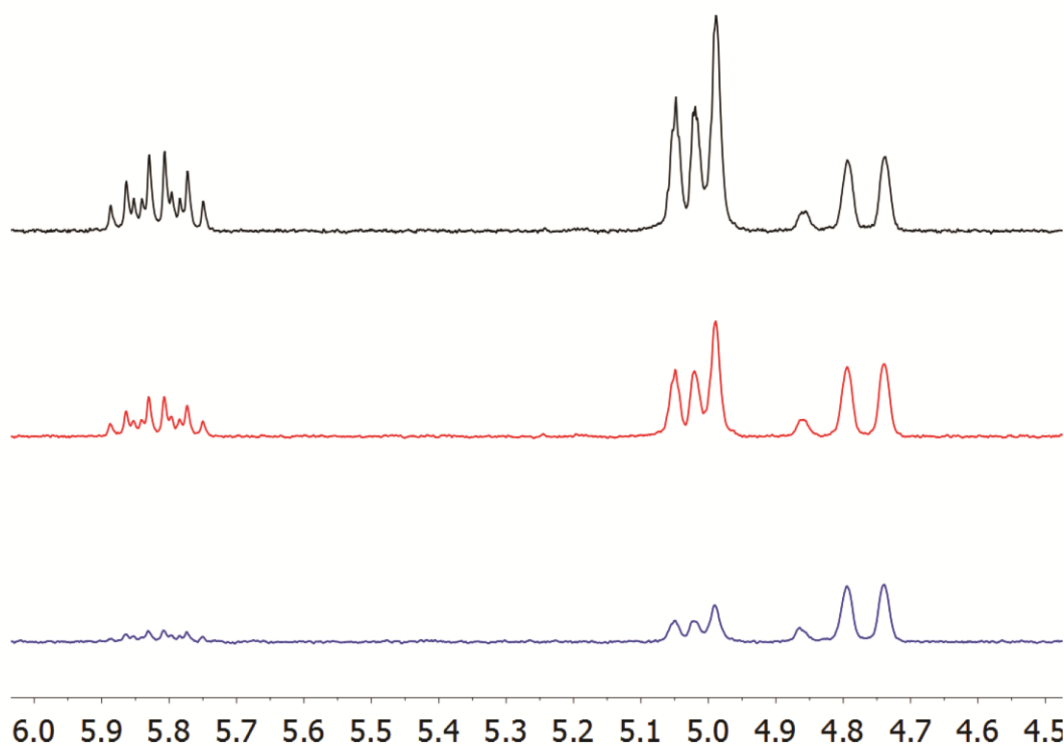
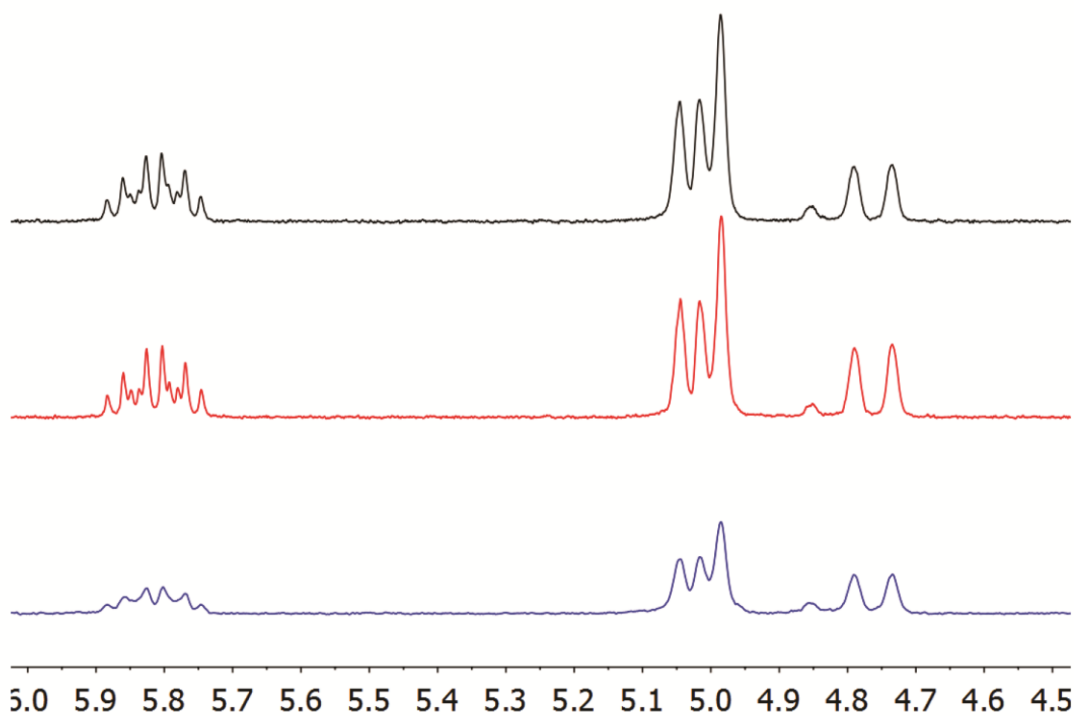


Figure S7. UV VIS investigation of the *in situ* alkylation of complex **III** with 200 eq. TIBA.

3. Olefinic end group analysis *via*  $^1\text{H}$  NMRFigure S8.  $^1\text{H}$  NMR spectrum of the polymers produced at  $90\text{ }^\circ\text{C}$  (entry 5(black), 11(red), 17(blue)) in  $\text{C}_6\text{D}_5\text{Br}$  at  $140\text{ }^\circ\text{C}$ .Figure S9.  $^1\text{H}$  NMR spectrum of the polymers produced at  $110\text{ }^\circ\text{C}$  (entry 5(black), 11(red), 17(blue)) in  $\text{C}_6\text{D}_5\text{Br}$  at  $140\text{ }^\circ\text{C}$ .

4. Tacticity determination *via*  $^{13}\text{C}$  NMR of polymers at elevated temperatures

All  $^{13}\text{C}$  NMR measurements were conducted in  $\text{C}_6\text{D}_5\text{Br}$  at  $140\text{ }^\circ\text{C}$ . All chemical shifts are internally referenced to the methyl signal of the isotactic pentad *mmmm* at  $21.85\text{ ppm}$ . The tacticity distribution was quantified *via* integration of the methyl region between  $22.0 - 19.7\text{ ppm}$ . The relative content of isotactic *mmmm* pentad is reported as mole fraction (in percentage) with respect to all steric pentads.

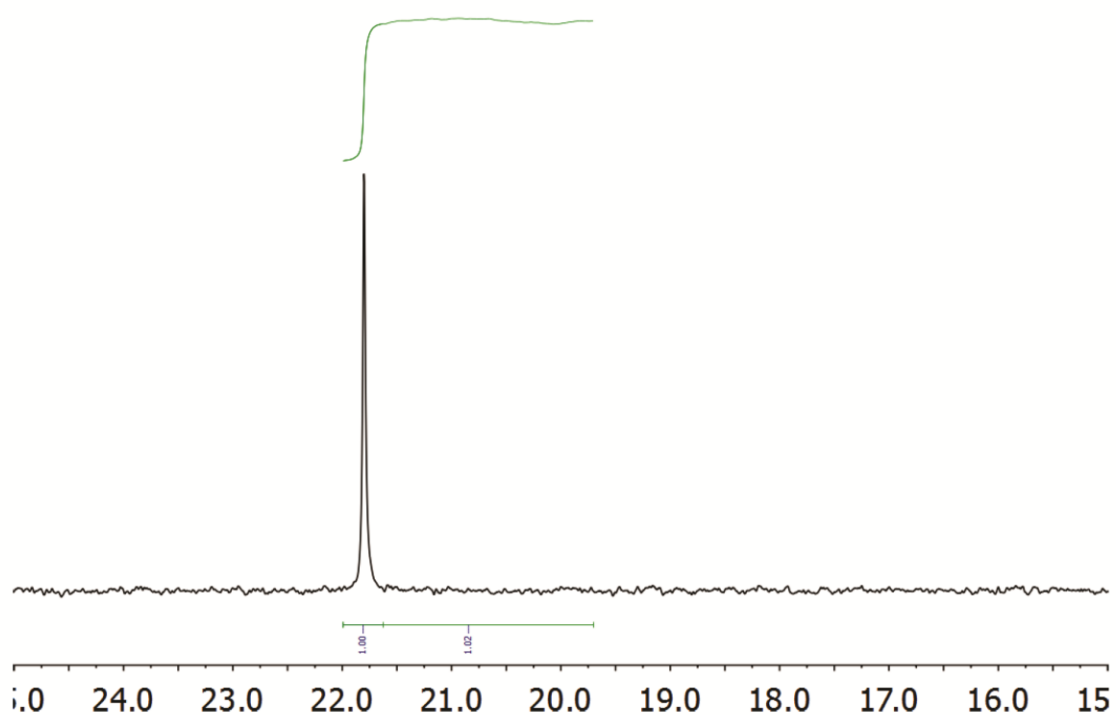


Figure S10. Pentad distribution of entry 3 in the  $^{13}\text{C}$  NMR spectrum.

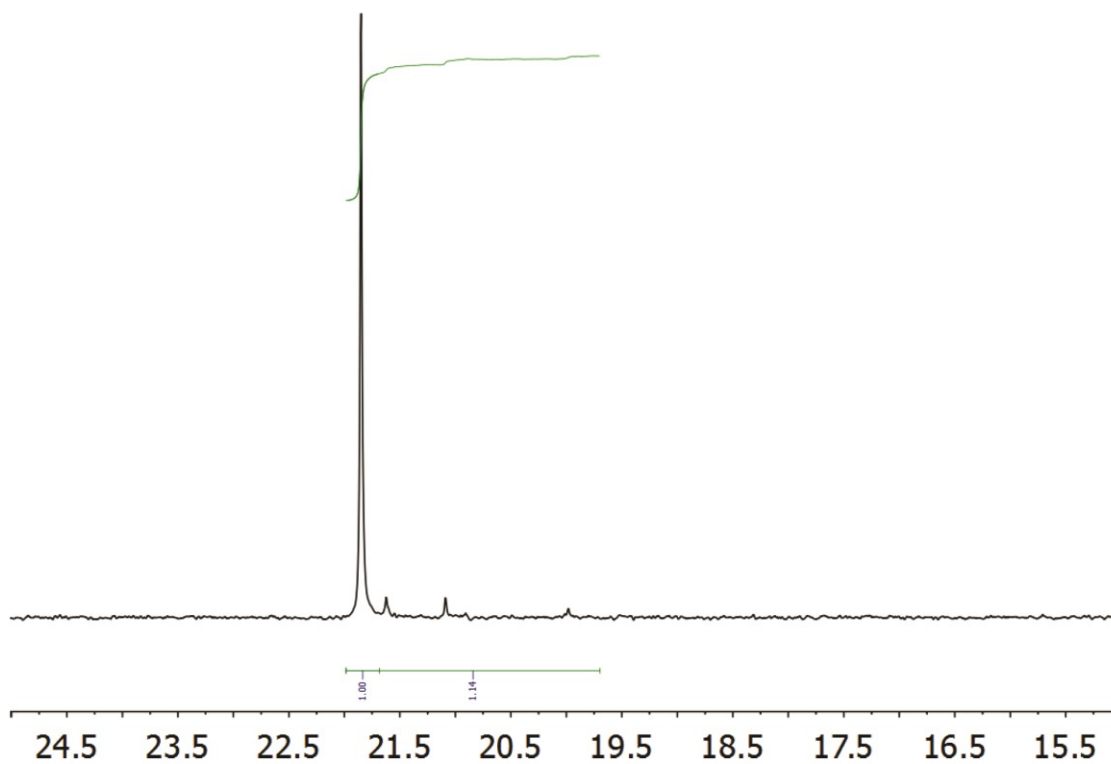


Figure S11. Pentad distribution of entry 4 in the  $^{13}\text{C}$  NMR spectrum.

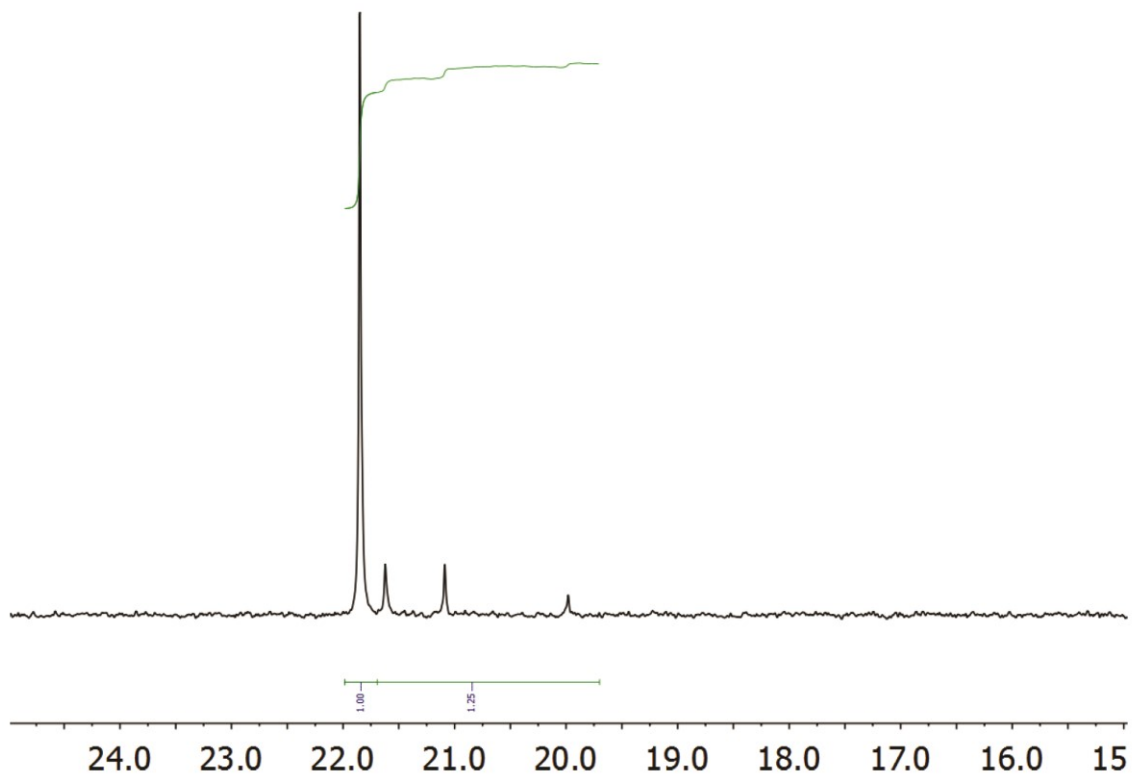


Figure S12. Pentad distribution of entry 5 in the  $^{13}\text{C}$  NMR spectrum.

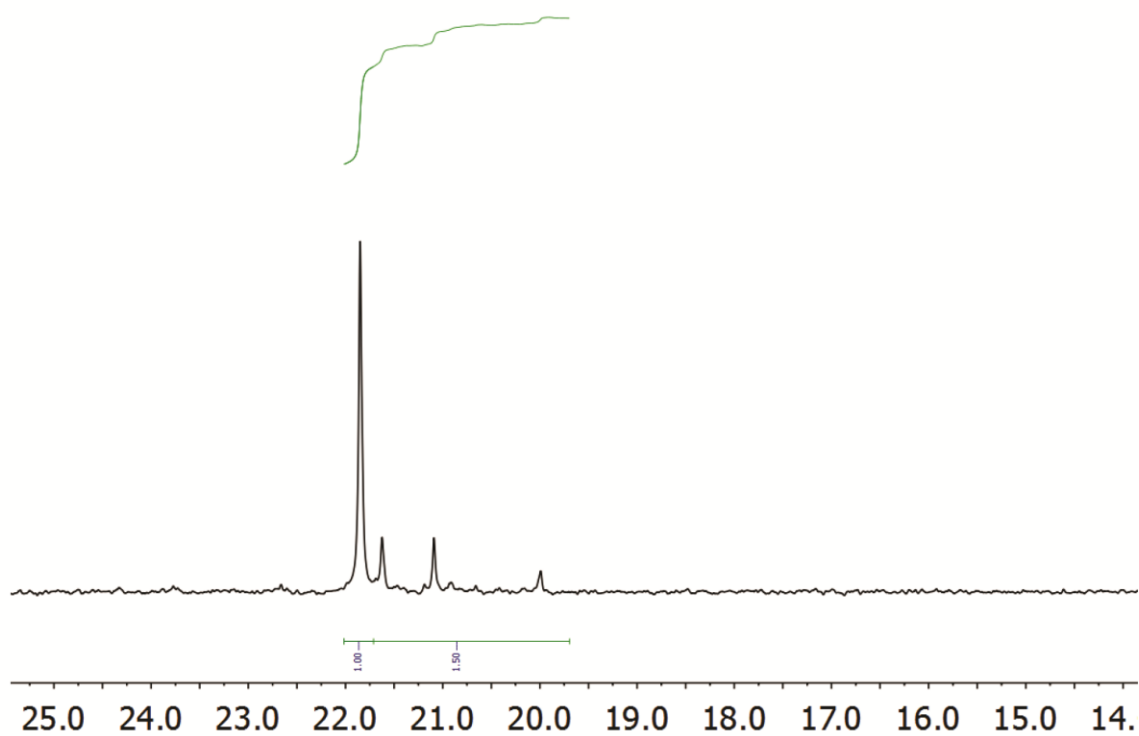


Figure S13. Pentad distribution of entry 6 in the  $^{13}\text{C}$  NMR spectrum.

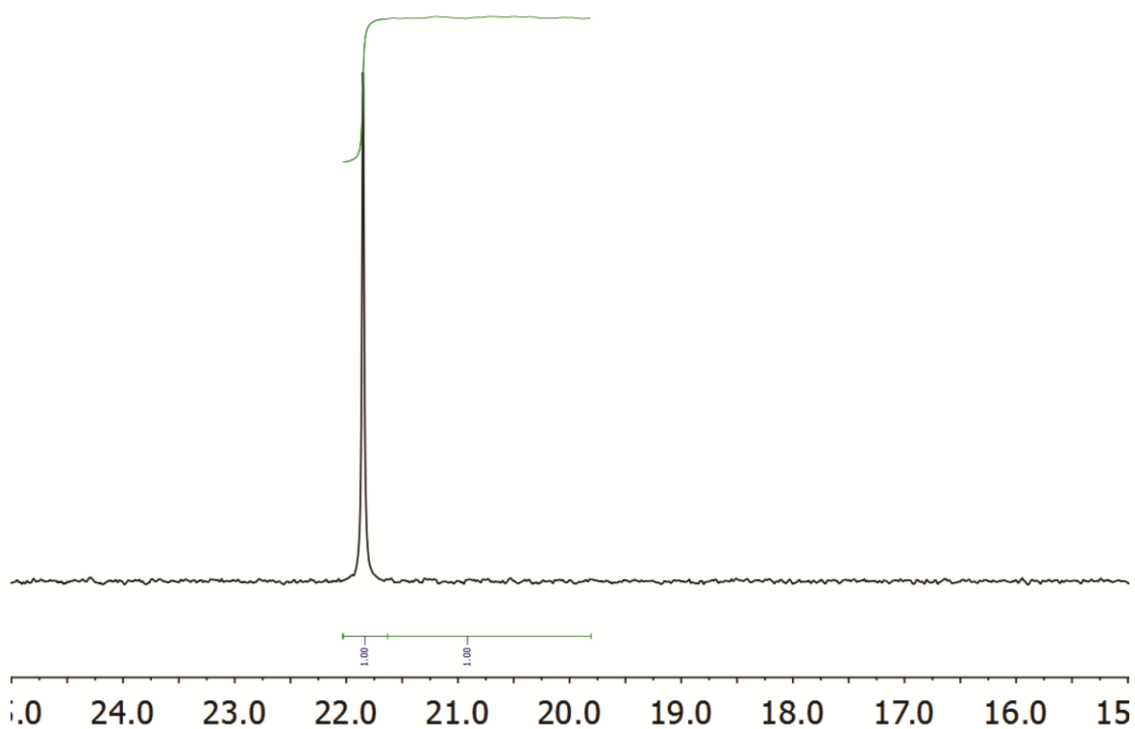


Figure S14. Pentad distribution of entry 9 in the  $^{13}\text{C}$  NMR spectrum.

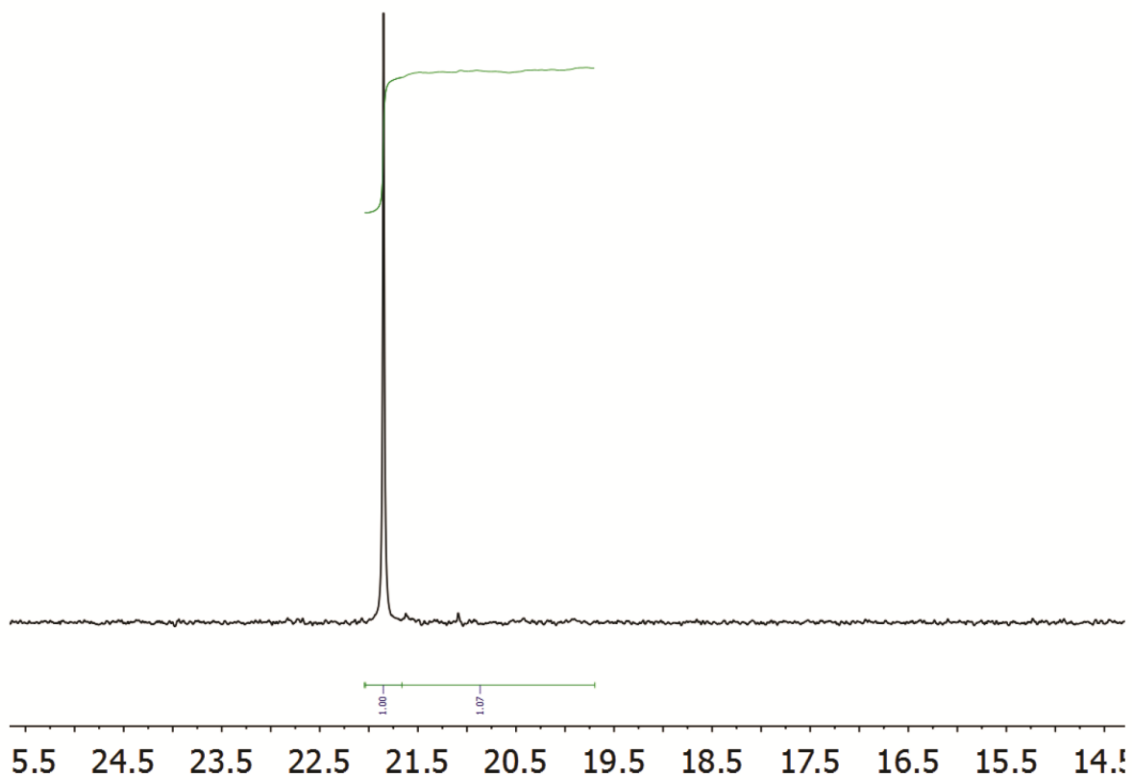


Figure S15. Pentad distribution of entry 10 in the  $^{13}\text{C}$  NMR spectrum.

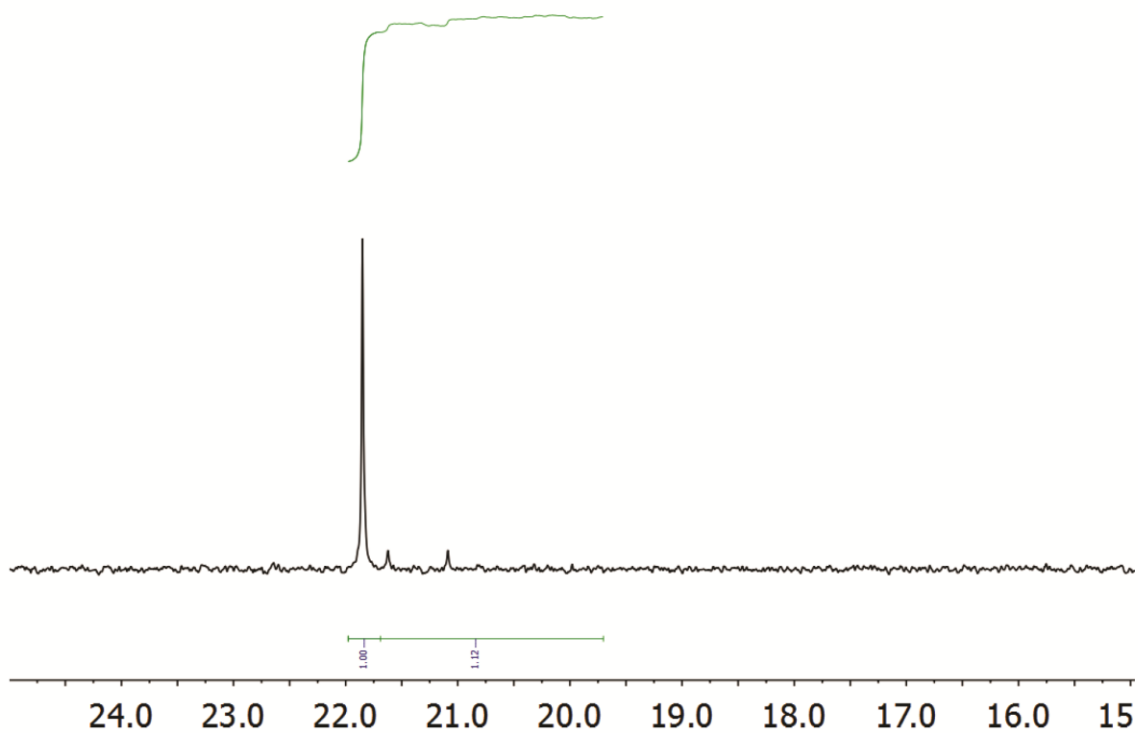


Figure S16. Pentad distribution of entry 11 in the  $^{13}\text{C}$  NMR spectrum.

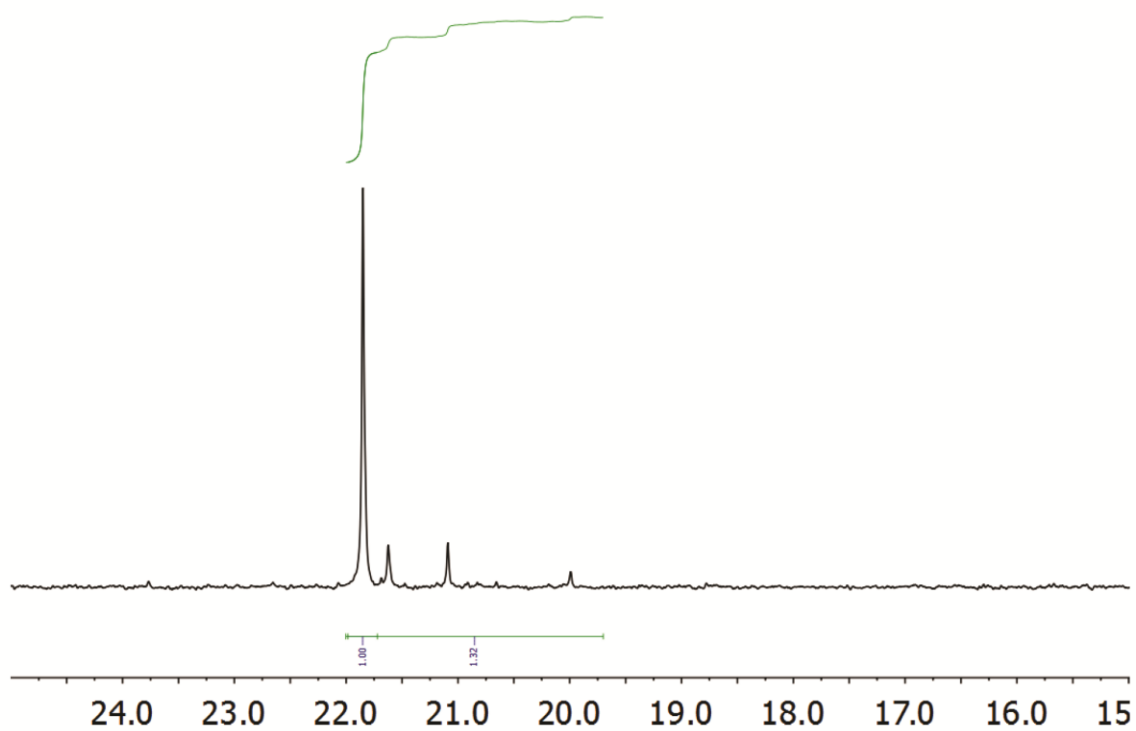


Figure S17. Pentad distribution of entry 12 in the  $^{13}\text{C}$  NMR spectrum.

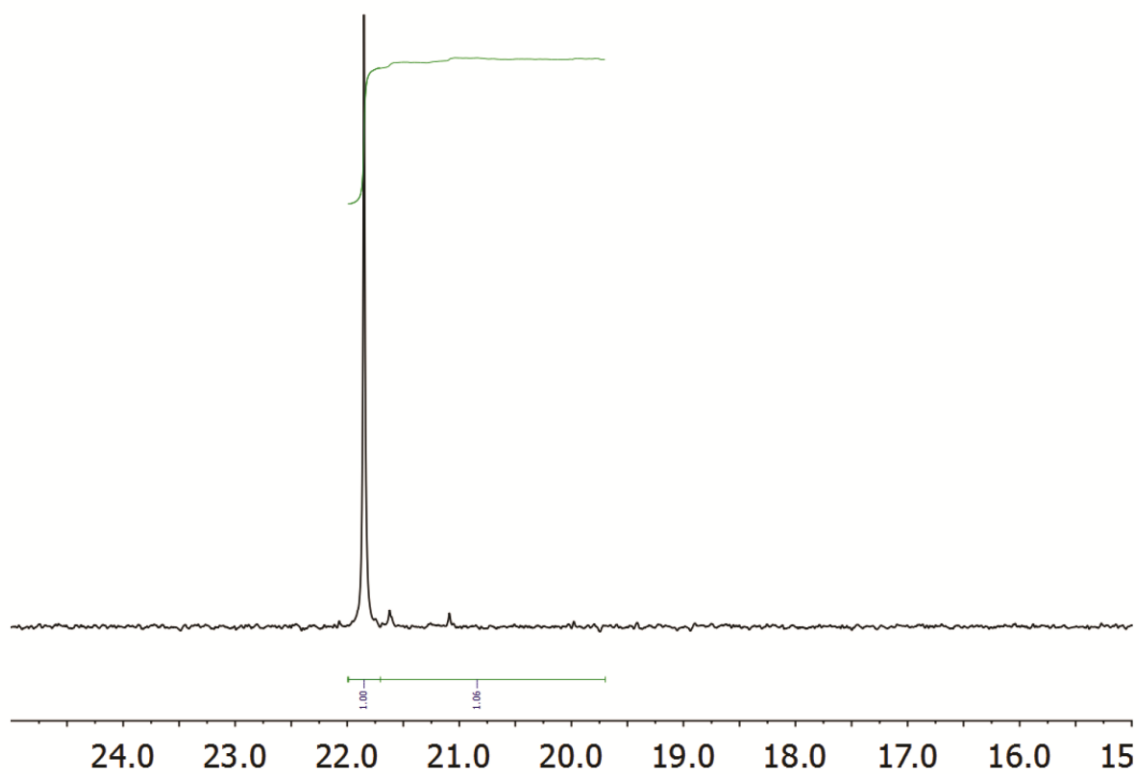


Figure S18. Pentad distribution of entry 17 in the  $^{13}\text{C}$  NMR spectrum.

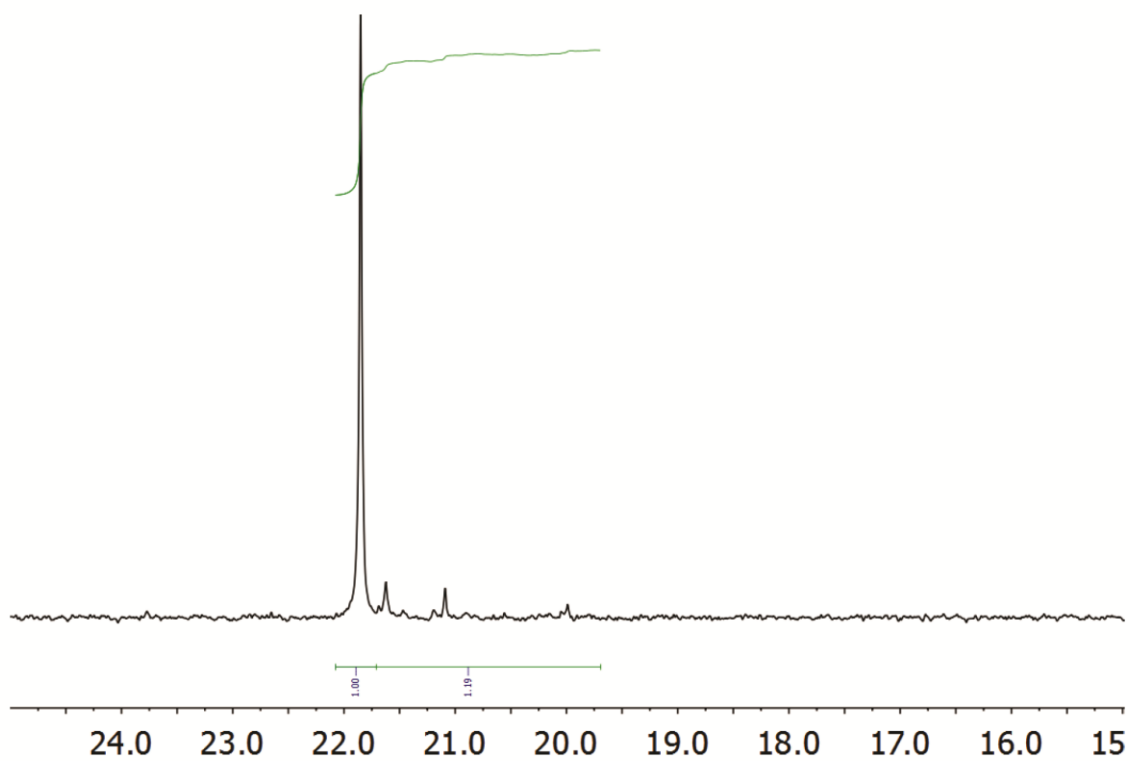


Figure S19. Pentad distribution of entry 18 in the  $^{13}\text{C}$  NMR spectrum.

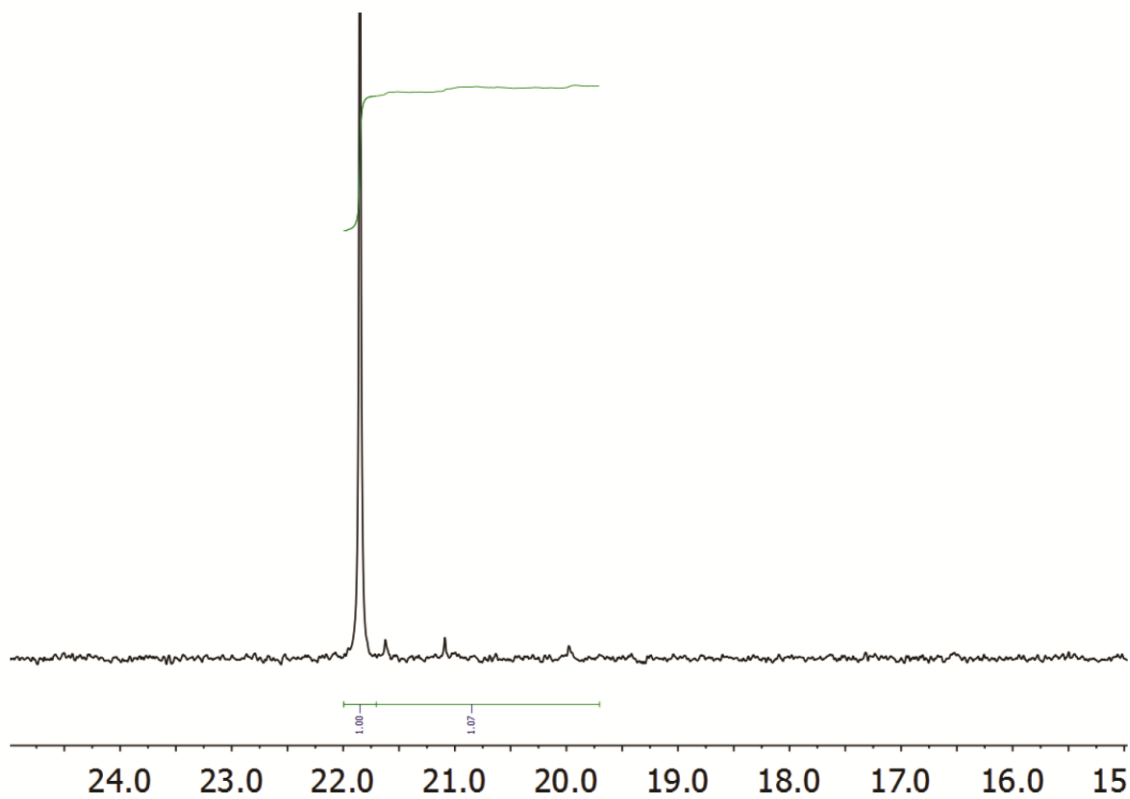


Figure S20. Pentad distribution of entry 19 in the  $^{13}\text{C}$  NMR spectrum.

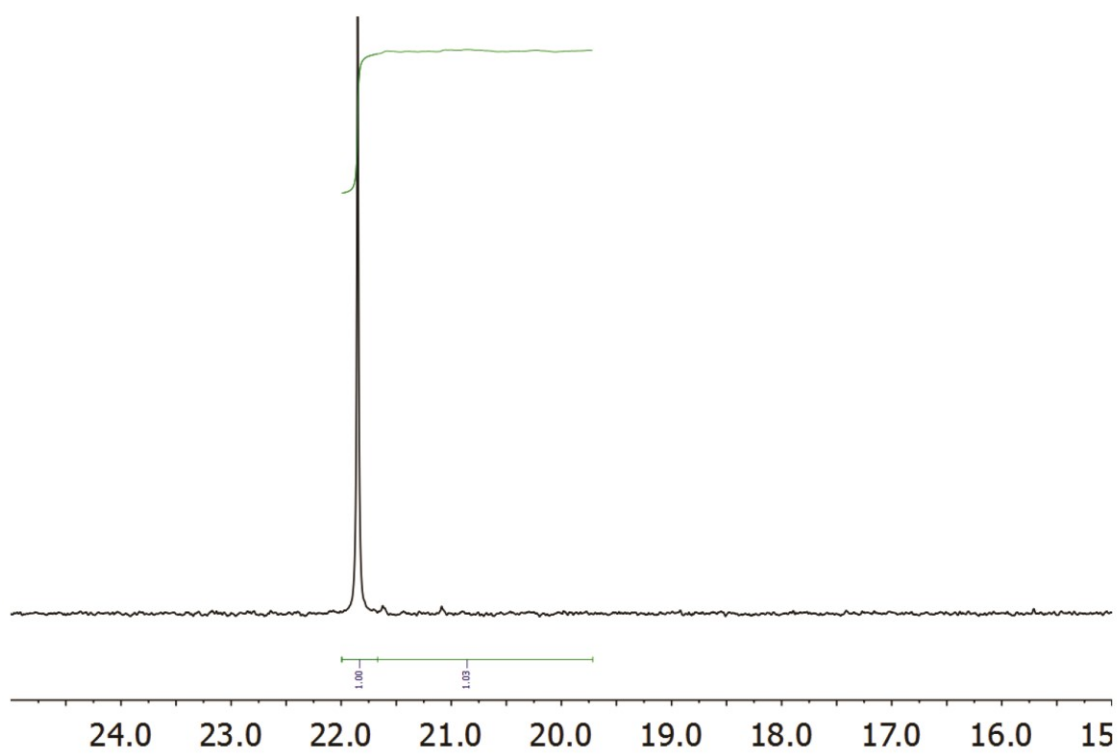


Figure S21. Pentad distribution of entry 20 in the  $^{13}\text{C}$  NMR spectrum.

## 5. Temperature dependent consumption of propene for I-III

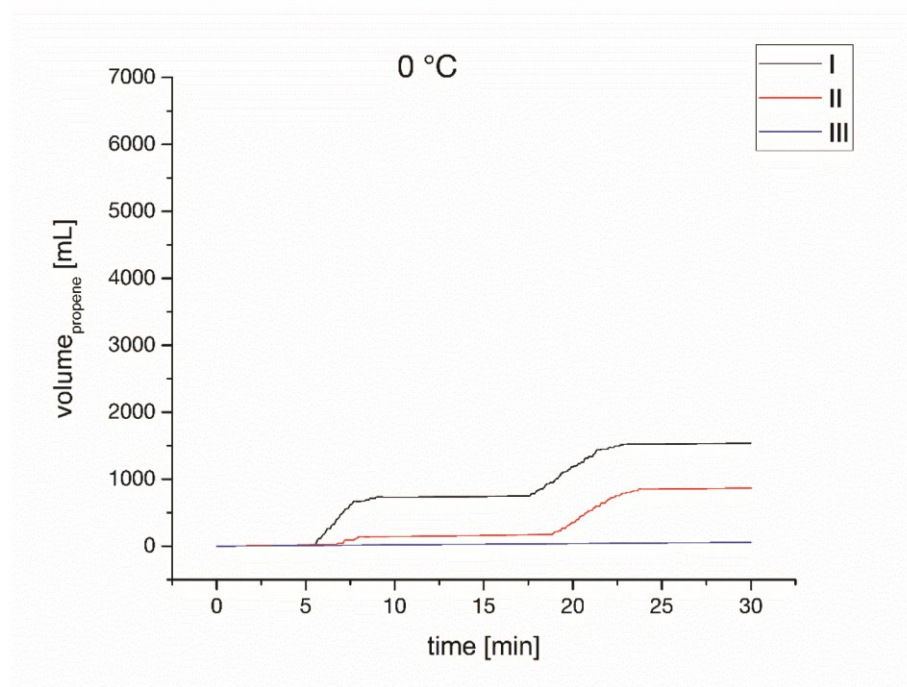


Figure S22. Time dependent consumption of propene for entry 1, 7 and 13.

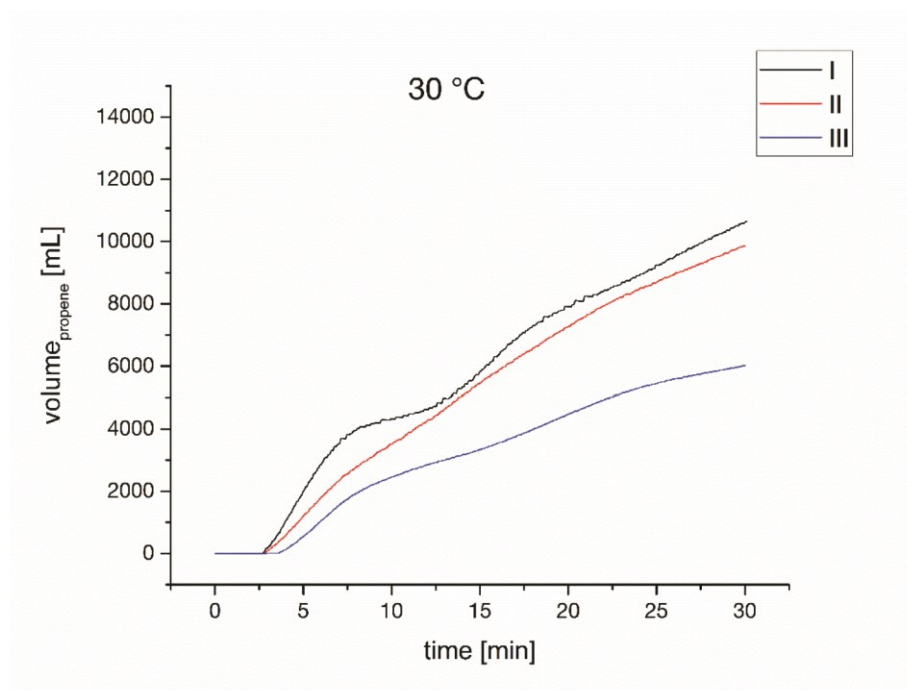


Figure S23. Time dependent consumption of propene for entry 2, 8 and 14.

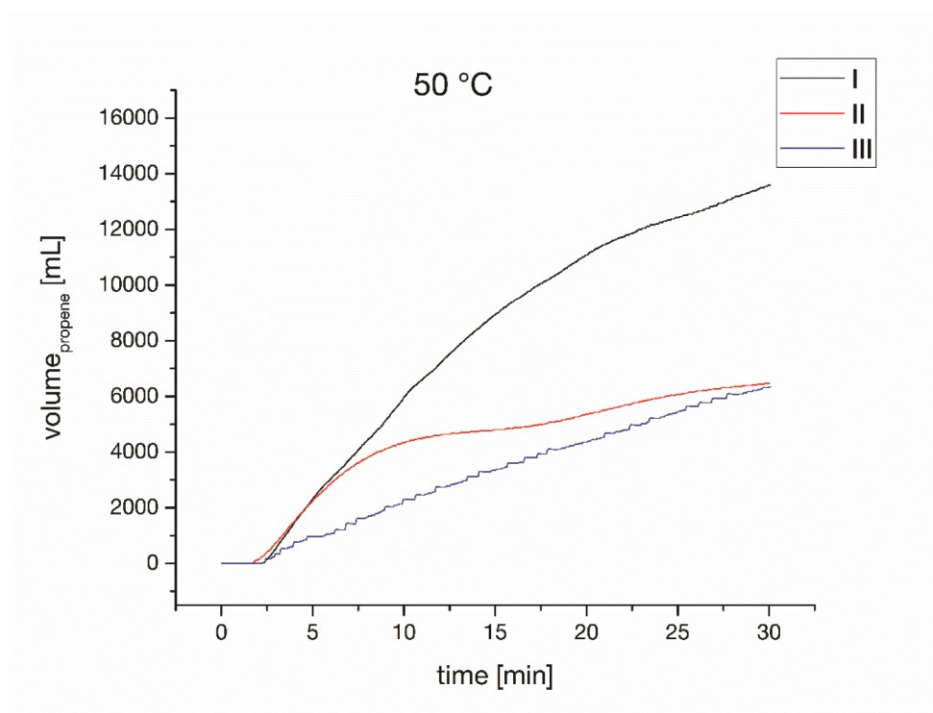


Figure S24. Time dependent consumption of propene for entry 3, 9 and 15.

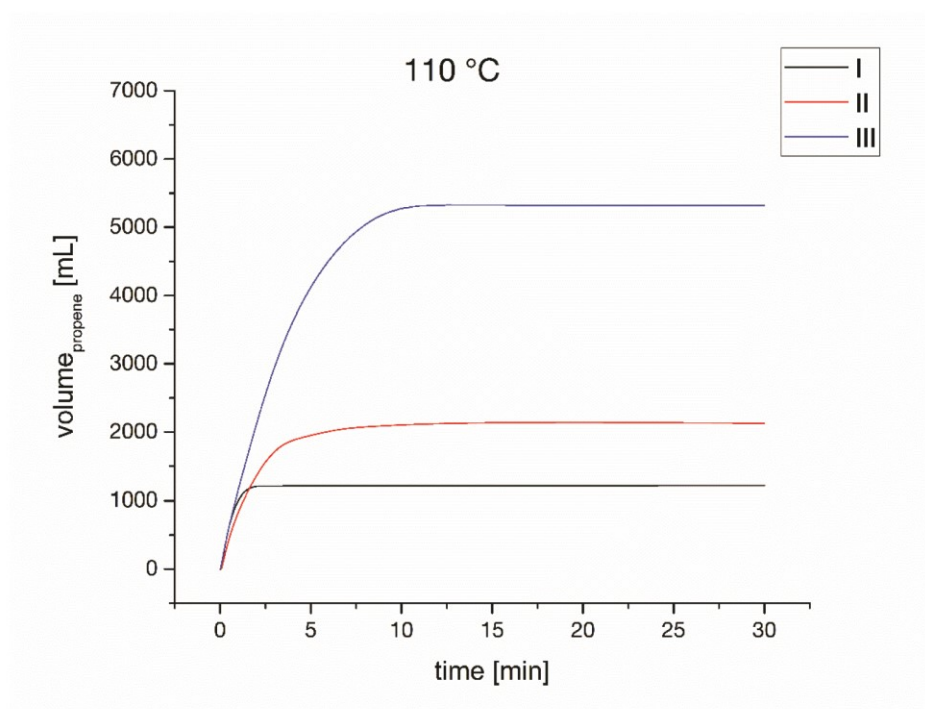


Figure S25. Time dependent consumption of propene for entry 6, 12 and 18.

## 6. Single Crystal XRD (SC-XRD) data

## Compound I (CCDC 1508946)

A clear intense yellow-orange fragment-like specimen of  $C_{39}H_{37}Cl_2HfO_2Si$ , approximate dimensions 0.135 mm x 0.152 mm x 0.206 mm, was used for the X-ray crystallographic analysis. The X-ray intensity data were measured on a Bruker Kappa APEX II CCD system equipped with a MONTELE mirror monochromator and a Mo FR591 rotating anode ( $\lambda = 0.71073 \text{ \AA}$ ).

A total of 2419 frames were collected. The total exposure time was 1.34 hours. The frames were integrated with the Bruker SAINT software package using a narrow-frame algorithm. The integration of the data using a triclinic unit cell yielded a total of 39782 reflections to a maximum  $\theta$  angle of  $25.36^\circ$  ( $0.83 \text{ \AA}$  resolution), of which 6021 were independent (average redundancy 6.607, completeness = 99.2%,  $R_{int} = 2.66\%$ ) and 5845 (97.08%) were greater than  $2\sigma(F^2)$ . The final cell constants of  $a = 10.5902(2) \text{ \AA}$ ,  $b = 11.3762(3) \text{ \AA}$ ,  $c = 14.2613(3) \text{ \AA}$ ,  $\alpha = 78.6260(10)^\circ$ ,  $\beta = 82.1580(10)^\circ$ ,  $\gamma = 80.8410(10)^\circ$ , volume =  $1653.10(6) \text{ \AA}^3$ , are based upon the refinement of the XYZ-centroids of 9744 reflections above  $20 \sigma(I)$  with  $5.105^\circ < 2\theta < 50.70^\circ$ . Data were corrected for absorption effects using the multi-scan method (SADABS). The ratio of minimum to maximum apparent transmission was 0.840. The calculated minimum and maximum transmission coefficients (based on crystal size) are 0.5420 and 0.6580.

The final anisotropic full-matrix least-squares refinement on  $F^2$  with 440 variables converged at  $R1 = 1.31\%$ , for the observed data and  $wR2 = 3.20\%$  for all data. The goodness-of-fit was 1.056. The largest peak in the final difference electron density synthesis was  $0.420 \text{ e}/\text{\AA}^3$  and the largest hole was  $-0.382 \text{ e}/\text{\AA}^3$  with an RMS deviation of  $0.060 \text{ e}/\text{\AA}^3$ . On the basis of the final model, the calculated density was  $1.638 \text{ g}/\text{cm}^3$  and  $F(000)$ , 814  $e^-$ .

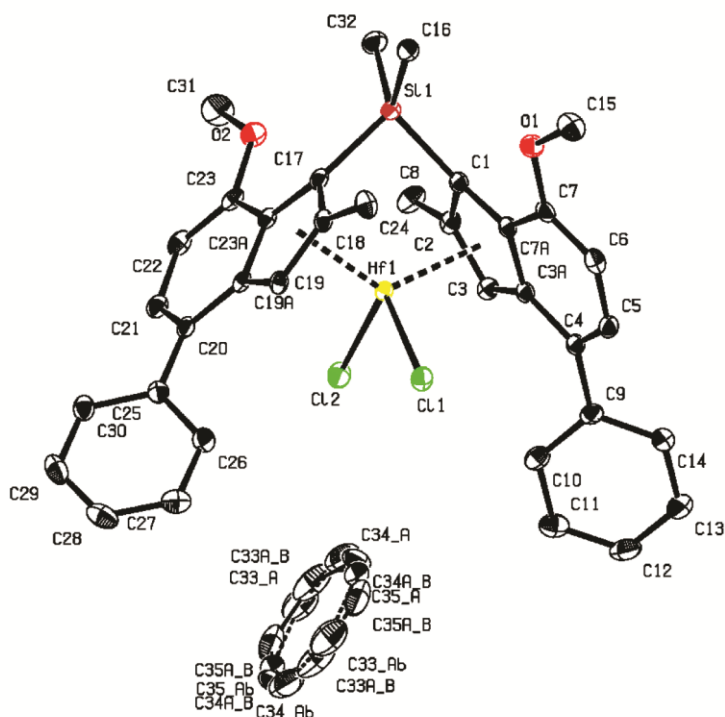


Figure S22. ORTEP drawing with 50% ellipsoids for compound I.

**Table S2. Sample and crystal data, data collection and structure refinement for compound I.**

Identification code	MacMa2 AP6191-123	
Chemical formula	C <sub>39</sub> H <sub>37</sub> Cl <sub>2</sub> HfO <sub>2</sub> Si	
Formula weight	815.16	
Temperature	123(2) K	
Wavelength	0.71073 Å	
Crystal size	0.135 x 0.152 x 0.206 mm	
Crystal habit	clear intense yellow-orange fragment	
Crystal system	triclinic	
Space group	P -1	
Unit cell dimensions	a = 10.5902(2) Å	α = 78.6260(10)°
	b = 11.3762(3) Å	β = 82.1580(10)°
	c = 14.2613(3) Å	γ = 80.8410(10)°
Volume	1653.10(6) Å <sup>3</sup>	
Z	2	
Density (calculated)	1.638 g/cm <sup>3</sup>	
Absorption coefficient	3.388 mm <sup>-1</sup>	
F(000)	814	
Diffractometer	Bruker Kappa APEX II CCD	
Radiation source	FR591 rotating anode, Mo	
Theta range for data collection	1.84 to 25.36°	
Index ranges	-12<=h<=12, -13<=k<=13, -17<=l<=17	
Reflections collected	39782	
Independent reflections	6021 [R(int) = 0.0266]	
Coverage of independent reflections	99.2%	
Absorption correction	multi-scan	
Max. and min. transmission	0.6580 and 0.5420	
Refinement method	Full-matrix least-squares on F <sup>2</sup>	
Refinement program	SHELXL-2014 (Sheldrick, 2014)	
Function minimized	Σ w(F <sub>o</sub> <sup>2</sup> - F <sub>c</sub> <sup>2</sup> ) <sup>2</sup>	
Data / restraints / parameters	6021 / 72 / 440	
Goodness-of-fit on F <sup>2</sup>	1.056	
Δ/σ <sub>max</sub>	0.001	
Final R indices	5845 data; I>2σ(I)	R1 = 0.0131, wR2 = 0.0316
	all data	R1 = 0.0138, wR2 = 0.0320
Weighting scheme	w=1/[σ <sup>2</sup> (F <sub>o</sub> <sup>2</sup> )+(0.0124P) <sup>2</sup> +1.1212P] where P=(F <sub>o</sub> <sup>2</sup> +2F <sub>c</sub> <sup>2</sup> )/3	
Largest diff. peak and hole	0.420 and -0.382 eÅ <sup>-3</sup>	
R.M.S. deviation from mean	0.060 eÅ <sup>-3</sup>	

## Compound II (CCDC 1508945)

A clear intense yellow-orange fragment-like specimen of  $C_{20}H_{21}ClHf_{0.50}OSi_{0.50}$ , approximate dimensions 0.091 mm x 0.150 mm x 0.261 mm, was used for the X-ray crystallographic analysis. The X-ray intensity data were measured on a Bruker Kappa APEX II CCD system equipped with a MONTEL mirror monochromator and a Mo FR591 rotating anode ( $\lambda = 0.71073 \text{ \AA}$ ).

A total of 3231 frames were collected. The total exposure time was 1.79 hours. The frames were integrated with the Bruker SAINT software package using a narrow-frame algorithm. The integration of the data using a monoclinic unit cell yielded a total of 33351 reflections to a maximum  $\theta$  angle of  $25.38^\circ$  ( $0.83 \text{ \AA}$  resolution), of which 3122 were independent (average redundancy 10.683, completeness = 99.8%,  $R_{\text{int}} = 2.65\%$ ) and 3101 (99.33%) were greater than  $2\sigma(F^2)$ . The final cell constants of  $a = 26.2052(6) \text{ \AA}$ ,  $b = 9.7908(2) \text{ \AA}$ ,  $c = 18.3890(4) \text{ \AA}$ ,  $\beta = 133.875(2)^\circ$ , volume =  $3401.03(15) \text{ \AA}^3$ , are based upon the refinement of the XYZ-centroids of 316 reflections above  $20 \sigma(I)$  with  $4.655^\circ < 2\theta < 56.22^\circ$ . Data were corrected for absorption effects using the multi-scan method (SADABS). The ratio of minimum to maximum apparent transmission was 0.886. The calculated minimum and maximum transmission coefficients (based on crystal size) are 0.4800 and 0.7540.

The final anisotropic full-matrix least-squares refinement on  $F^2$  with 214 variables converged at  $R1 = 1.24\%$ , for the observed data and  $wR2 = 3.19\%$  for all data. The goodness-of-fit was 1.096. The largest peak in the final difference electron density synthesis was  $0.357 \text{ e}/\text{\AA}^3$  and the largest hole was  $-0.323 \text{ e}/\text{\AA}^3$  with an RMS deviation of  $0.056 \text{ e}/\text{\AA}^3$ . On the basis of the final model, the calculated density was  $1.625 \text{ g}/\text{cm}^3$  and  $F(000)$ , 1672 e.

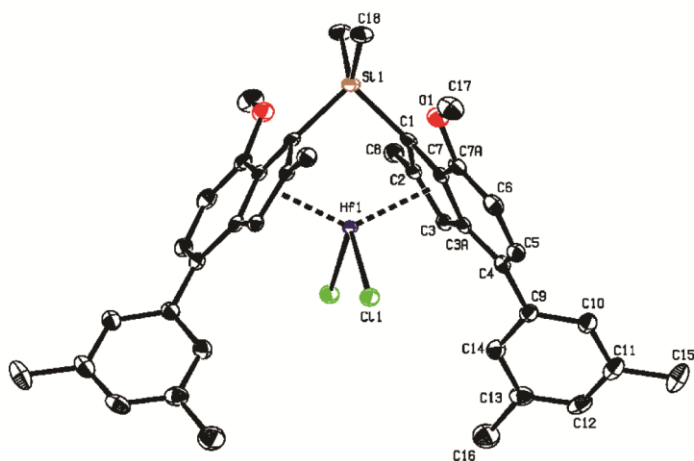


Figure S23. ORTEP drawing with 50% ellipsoids for compound II.

**Table S3. Sample and crystal data, data collection and structure refinement for compound II.**

Identification code	MacMa1 AP6190-123	
Chemical formula	C <sub>20</sub> H <sub>21</sub> ClHf <sub>0.50</sub> OSi <sub>0.50</sub>	
Formula weight	416.11	
Temperature	123(2) K	
Wavelength	0.71073 Å	
Crystal size	0.091 x 0.150 x 0.261 mm	
Crystal habit	clear intense yellow-orange fragment	
Crystal system	monoclinic	
Space group	C 1 2/c 1	
Unit cell dimensions	a = 26.2052(6) Å	α = 90°
	b = 9.7908(2) Å	β = 133.875(2)°
	c = 18.3890(4) Å	γ = 90°
Volume	3401.03(15) Å <sup>3</sup>	
Z	8	
Density (calculated)	1.625 g/cm <sup>3</sup>	
Absorption coefficient	3.295 mm <sup>-1</sup>	
F(000)	1672	
Diffractometer	Bruker Kappa APEX II CCD	
Radiation source	FR591 rotating anode, Mo	
Theta range for data collection	2.16 to 25.38°	
Index ranges	-31 ≤ h ≤ 30, -11 ≤ k ≤ 11, -22 ≤ l ≤ 21	
Reflections collected	33351	
Independent reflections	3122 [R(int) = 0.0265]	
Coverage of independent reflections	99.8%	
Absorption correction	multi-scan	
Max. and min. transmission	0.7540 and 0.4800	
Refinement method	Full-matrix least-squares on F <sup>2</sup>	
Refinement program	SHELXL-2014 (Sheldrick, 2014)	
Function minimized	Σ w(F <sub>o</sub> <sup>2</sup> - F <sub>c</sub> <sup>2</sup> ) <sup>2</sup>	
Data / restraints / parameters	3122 / 0 / 214	
Goodness-of-fit on F <sup>2</sup>	1.096	
Δ/σ <sub>max</sub>	0.001	
Final R indices	3101 data;  >2σ(I)	R1 = 0.0124, wR2 = 0.0318
	all data	R1 = 0.0125, wR2 = 0.0319
Weighting scheme	w = 1/[σ <sup>2</sup> (F <sub>o</sub> <sup>2</sup> ) + (0.0110P) <sup>2</sup> + 6.5072P] where P = (F <sub>o</sub> <sup>2</sup> + 2F <sub>c</sub> <sup>2</sup> )/3	
Absolute structure parameter	0.0(0)	
Largest diff. peak and hole	0.357 and -0.323 eÅ <sup>-3</sup>	
R.M.S. deviation from mean	0.056 eÅ <sup>-3</sup>	

12.2 Supporting Information – Chapter 5: Titanocenes in Olefin Polymerization: Sustainable Catalyst System or an Extinct Species?

## Titanocenes in Olefin Polymerization – Sustainable Catalyst System or an Extinct Species?

Martin R. Machat<sup>†</sup>, Christian Jandl<sup>‡</sup>, and Bernhard Rieger<sup>\*†</sup>

<sup>†</sup>Wacker-Lehrstuhl für Makromolekulare Chemie, Catalysis Research Center, Technische Universität München, Lichtenbergstraße 4, 85748 Garching bei München, Germany

<sup>‡</sup>Catalysis Research Center, Technische Universität München, Ernst-Otto-Fischer Straße 1, 85748 Garching bei München, Germany

### Table of contents:

1. Polymerization conditions and results.....	S2
2. Synthesis – <sup>1</sup> H and <sup>13</sup> C spectra.....	S4
3. EPR spectra.....	S8
4. UV/VIS spectra for the preactivation with 200 eq. of TIBA.....	S9
5. Tacticity determination <i>via</i> <sup>13</sup> C NMR of polymers at elevated temperatures.....	S10
6. Single crystal XRD (SC-XRD) data .....	S16
7. References.....	S25

## 1. Polymerization conditions and results

All polymerization results and conditions are listed in Table S1. All experiments are ordered as follows:

1. Catalyst (I-V)
2. Reaction temperature ( $T_p$ )
3. Reaction time (t)
4. Monomer concentration ( $C_3$ )
5. Scavenger concentration

**Table S1. Conditions and results for the polymerization of propene with I-V in toluene.**

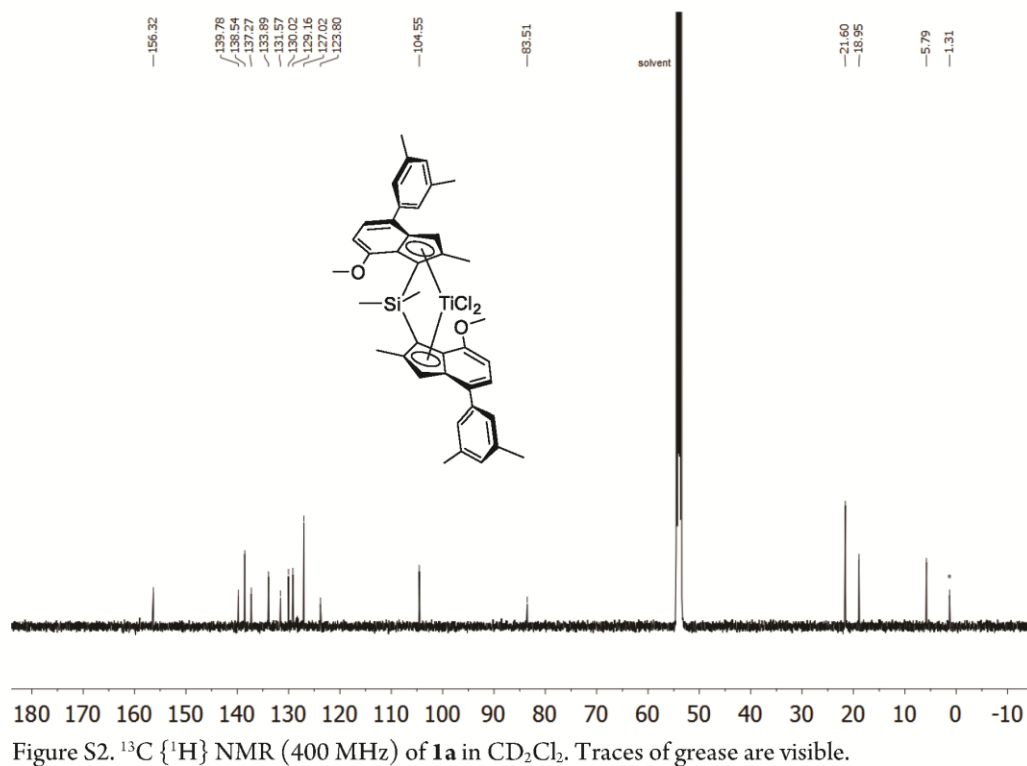
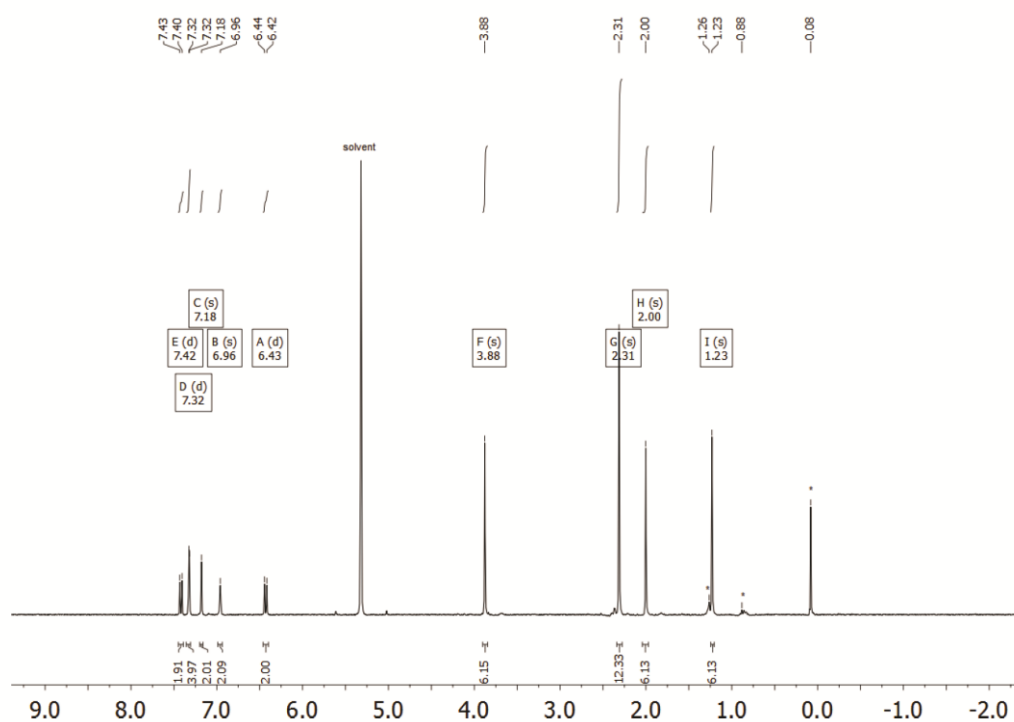
Entry	Catalyst	$T_p^a$	$n^b$	$t^c$	$[C_3]^d$	$T_m^e$	Mmmm <sup>f</sup>	$M_n^g$	$\bar{D}^h$	$P^i$
S-1	I	-10	2	30	1.88	167	-	150	1.6	340
S-2	I	0	2	5	1.88	-	-	-	-	350
S-3	I	0	2	30	1.88	167	-	110	1.9	300
S-4	I	0	2	80	1.88	-	-	-	-	200
S-5	I	0	2	150	1.88	-	-	-	-	110
S-6	I	15	2	30	1.88	166	-	84	2.7	120
S-7	I	30	2	30	1.88	164	-	62	2.7	100
S-8	I	50	5	30	0.31	151	95	8	2.5	190
S-9	I	50	5	30	0.74	157	98	21	2.9	260
S-10	I	50	5	30	1.18	159	≥99	30	2.2	130
S-11	I	50	5	30	1.88	162	≥99	49	1.7	80
S-12	II	-10	2	30	1.88	165	-	160	1.5	120
S-13	II	0	2	5	1.88	-	-	-	-	280
S-14	II	0	2	30	1.88	165	-	120	1.7	74
S-15	II	0	2	80	1.88	-	-	-	-	42
S-16	II	0	2	150	1.88	-	-	-	-	27
S-17	II	15	2	30	1.88	164	-	98	1.5	48
S-18	II	30	2	30	1.88	162	≥99	82	1.6	42
S-19	II	50	2	30	1.88	160	98	45	1.8	16
S-20	III	-10	2	30	1.88	168	-	160	1.6	1 400
S-21	III	0	2	5	1.88	-	-	-	-	5 800
S-22	III	0	2	30	1.88	166	-	130	1.7	1 300
S-23 <sup>j</sup>	III	0	2	30	1.88	-	-	-	-	1 100
S-24 <sup>k</sup>	III	0	2	30	1.88	-	-	-	-	860
S-25 <sup>l</sup>	III	0	2	30	1.88	-	-	-	-	11
S-26	III	0	2	80	1.88	-	-	-	-	800
S-27	III	0	2	150	1.88	-	-	-	-	470
S-28	III	15	2	30	1.88	166	-	93	1.7	740

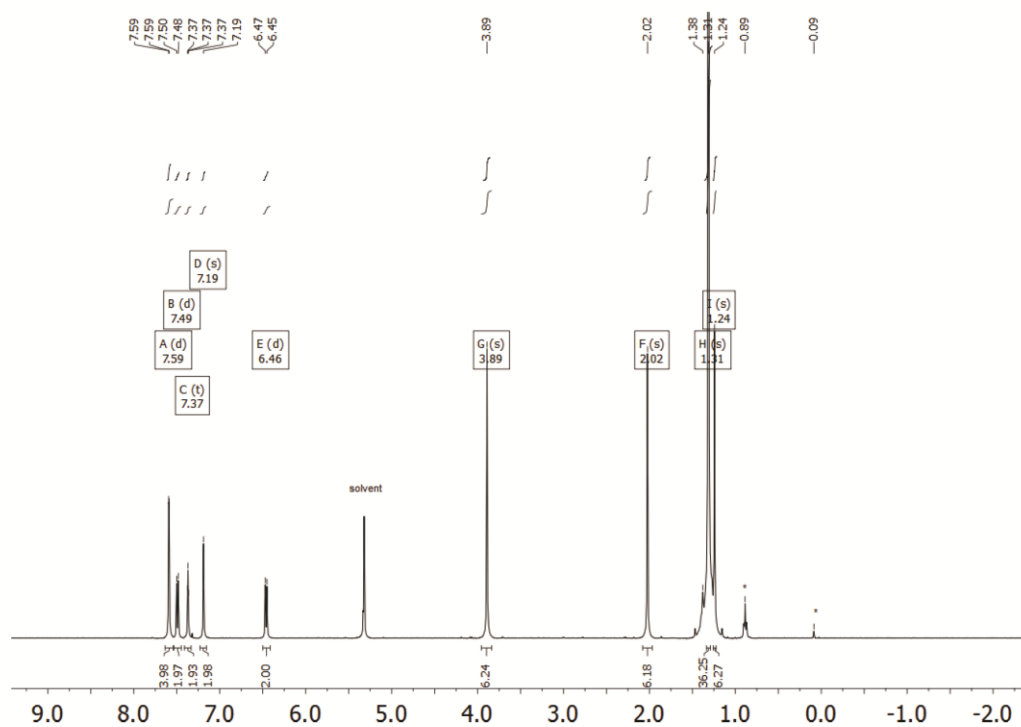
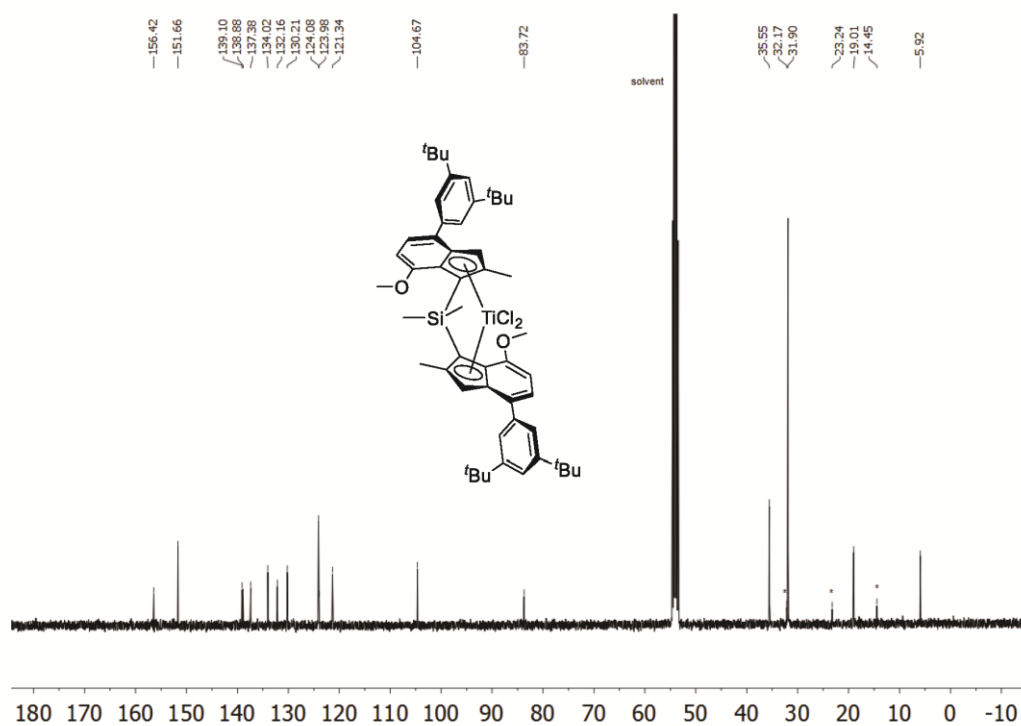
S2

Appendix

S-29	III	30	2	30	1.88	164	-	64	1.7	430
S-30 <sup>i</sup>	III	30	2	30	1.88	-	-	-	-	420
S-31 <sup>k</sup>	III	30	2	30	1.88	-	-	-	-	370
S-32	III	50	2	30	1.88	162	-	35	1.7	66
S-33 <sup>j</sup>	III	50	2	30	1.88	-	-	-	-	180
S-34 <sup>k</sup>	III	50	2	30	1.88	-	≥99	-	-	350
S-35	IV	-10	2	30	1.88	170	-	200	2.2	300
S-36	IV	0	2	5	1.88	-	-	-	-	900
S-37	IV	0	2	30	1.88	169	-	190	1.8	270
S-38	IV	0	2	80	1.88	-	-	-	-	290
S-39	IV	0	2	150	1.88	-	-	-	-	350
S-40	IV	15	2	30	1.88	168	-	140	2.0	160
S-41	IV	30	2	30	1.88	166	-	130	1.7	160
S-42	IV	50	5	30	0.31	160	98	19	1.7	580
S-43	IV	50	5	30	0.74	160	≥99	42	1.7	390
S-44	IV	50	5	30	1.18	162	≥99	52	1.7	250
S-45	IV	50	5	30	1.88	165	≥99	56	2.0	150
S-46	V	-10	2	30	1.88	170	-	190	2.0	3 700
S-47	V	0	2	5	1.88	-	-	-	-	8 500
S-48	V	0	2	30	1.88	169	-	170	2.2	2 200
S-49	V	0	2	80	1.88	-	-	-	-	1 000
S-50	V	0	2	150	1.88	-	-	-	-	640
S-51	V	15	2	30	1.88	169	-	150	1.7	1 800
S-52	V	30	2	30	1.88	166	-	120	1.6	1 100
S-53	V	50	2	30	1.88	165	≥99	60	1.5	330

$V_{\text{toluene}}$ : 300 mL, scavenger (TIBA): 2.2 mmol, “-“  $\triangleq$  “not defined”. <sup>a</sup>  $T_p$  in °C  $\pm$  1 °C. <sup>b</sup> In  $\mu\text{mol}$ . <sup>c</sup> Time [min]. <sup>d</sup> Concentration of propene [mol/L] (estimated by the equation of Busico).<sup>[1]</sup> <sup>e</sup> In °C. <sup>f</sup> In %, determined *via*  $^{13}\text{C}\{^1\text{H}\}$  NMR spectroscopy assuming the enantiomorphic site model. <sup>g</sup> In  $\text{kg mol}^{-1}$ . <sup>h</sup> D:  $M_w/M_n$ . <sup>i</sup> P in  $\text{kgPP} \cdot [\text{mol}_M(\text{mol/L})\cdot\text{h}]^{-1}$ . <sup>j</sup> scavenger (TIBA): 1.1 mmol. <sup>k</sup> scavenger (TIBA): 0.55 mmol. <sup>l</sup> scavenger (TMA): 2.2 mmol.

2. Synthesis –  $^1\text{H}$  and  $^{13}\text{C}$  spectra

Figure S3.  $^1\text{H}$  NMR (400 MHz) spectrum of **1b** in  $\text{CD}_2\text{Cl}_2$  with traces of *n*-hexane and grease.Figure S4.  $^{13}\text{C}$   $\{^1\text{H}\}$  NMR (400 MHz) spectrum of **1b** in  $\text{CD}_2\text{Cl}_2$  with traces of *n*-hexane.

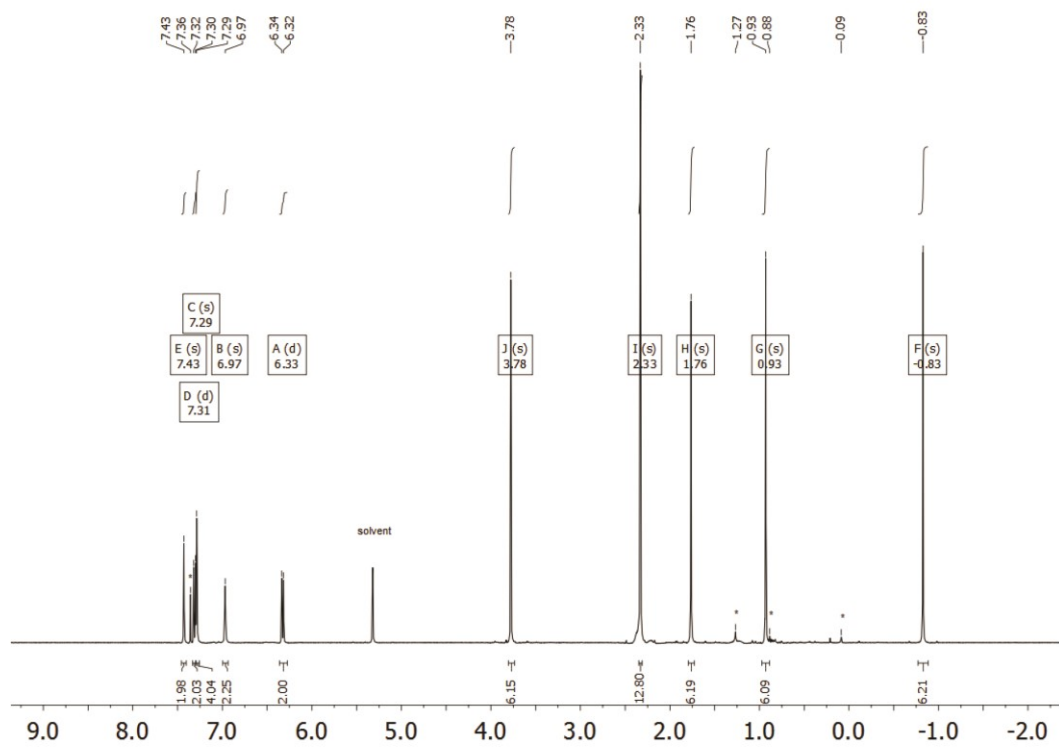


Figure S5.  $^1\text{H}$  NMR (400 MHz) spectrum of **2a** in  $\text{CD}_2\text{Cl}_2$ . Traces of benzene, *n*-pentane and grease are visible.

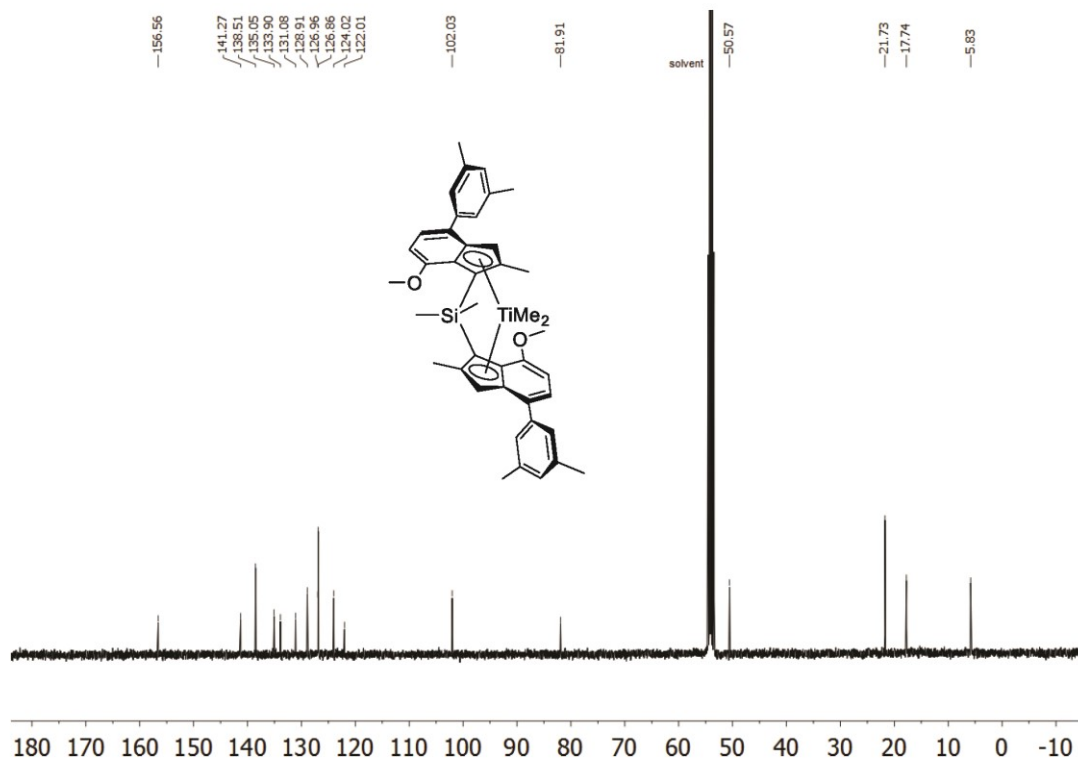
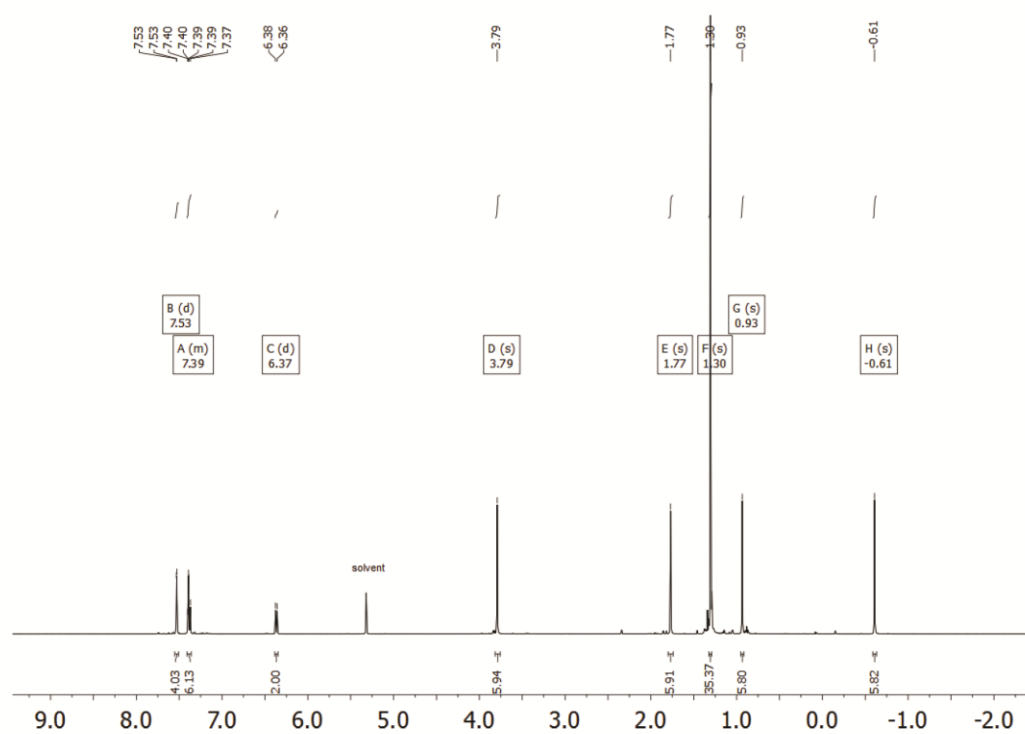
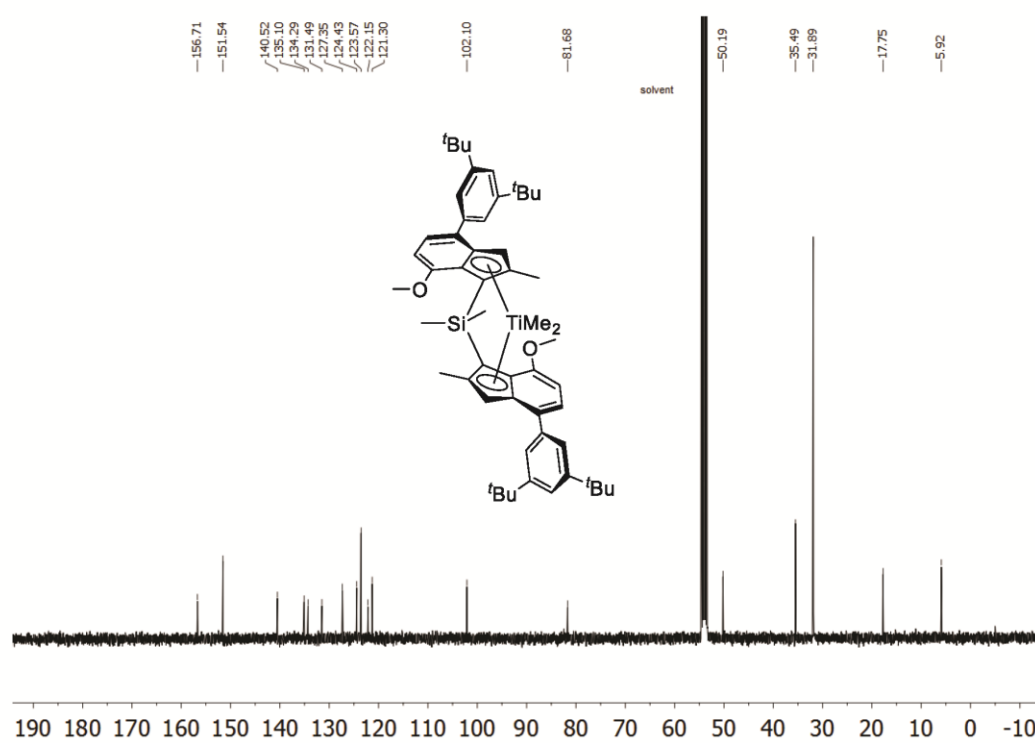


Figure S6.  $^{13}\text{C}$   $\{^1\text{H}\}$  NMR (400 MHz) spectrum of **2a** in  $\text{CD}_2\text{Cl}_2$ .

Figure S7. <sup>1</sup>H NMR (400 MHz) spectrum of **2b** in CD<sub>2</sub>Cl<sub>2</sub>.Figure S8. <sup>13</sup>C {<sup>1</sup>H} NMR (400 MHz) spectrum of **2b** in CD<sub>2</sub>Cl<sub>2</sub>.

## 3. EPR spectra

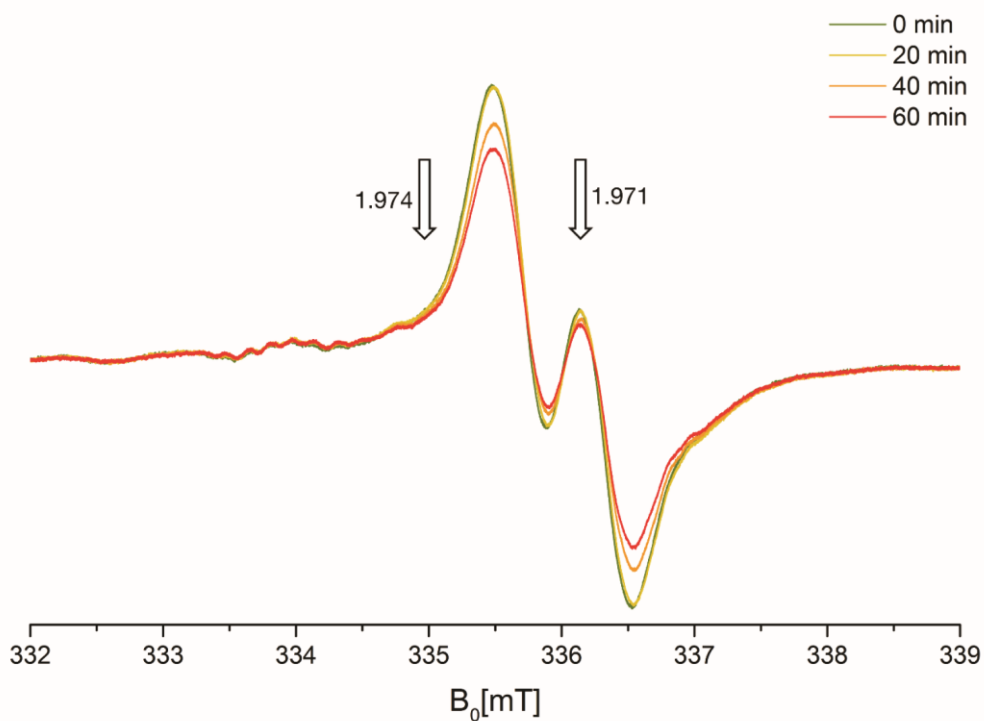


Figure S9. Time dependent EPR-spectra of **1b** in toluene ( $1 \cdot 10^{-4}$  M) with 200 eq. TIBA at 15 °C. Two partially overlapping type of signals ( $g = 1.971$ ,  $a_H = 6.6$  G;  $g = 1.974$ ,  $a_H = 14.3$  G,  $a_{Al} = 1.7$  G) can be assigned to mono- and bimetallic complex structures. The latter signal seems to be less pronounced compared to **1a**, most presumably due to increased steric interaction of the Al-compound with the ligand framework.

## 4. UV/VIS spectra for the preactivation with 200 eq. of TIBA

UV/VIS spectra were obtained using a Varian Cary 50 spectrophotometer with a sealed UV quartz cuvette (1 mm). A  $8.0 \cdot 10^{-4}$  M complex solution is measured first, subsequently adding 200 eq. 1.1 M TIBA- solution in toluene. The reaction is followed for one hour at room temperature. In both cases the initial absorbance maxima between 350 – 400 nm immediately vanish indicating a substitution reaction between chloride and alkyl substituents resulting in an increase of the HOMO-LUMO gap (Figure S10-S11).

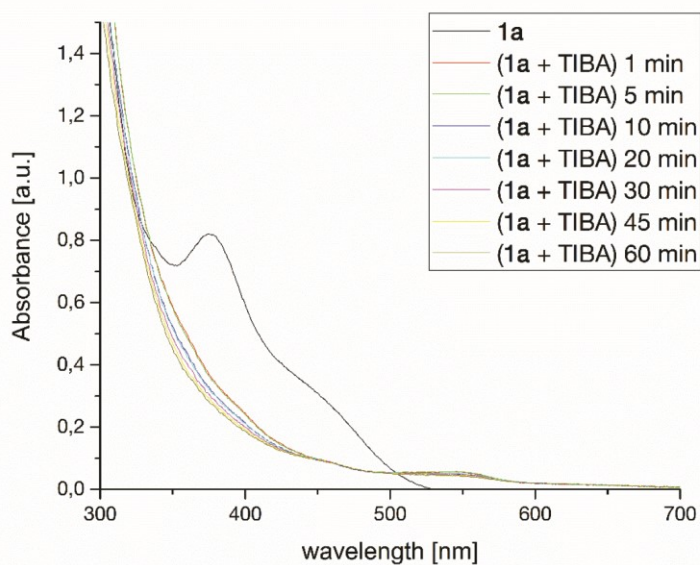


Figure S10. UV/VIS spectra of the *in situ* alkylation of **1a** with 200 eq. TIBA at room temperature.

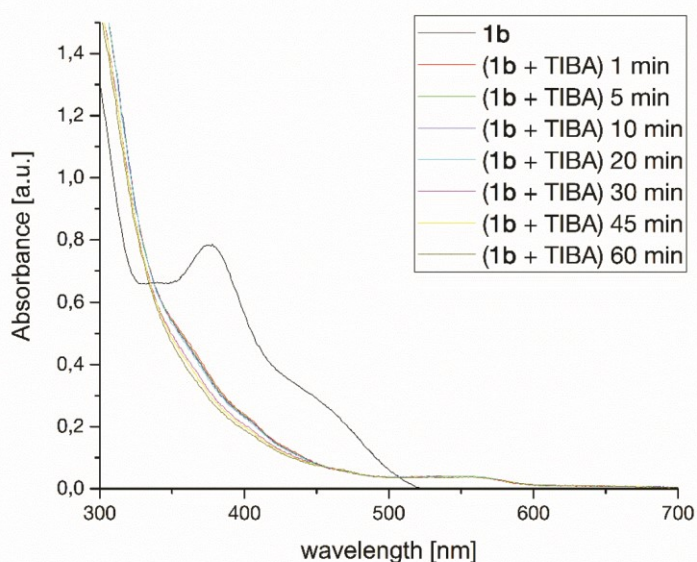


Figure S11. UV/VIS spectra of the *in situ* alkylation of **1b** with 200 eq. TIBA at room temperature.

5. Tacticity determination *via*  $^{13}\text{C}$  NMR of polymers at elevated temperatures

All  $^{13}\text{C}$   $\{^1\text{H}\}$  NMR measurements were conducted in  $\text{C}_6\text{D}_5\text{Br}$  at  $140\text{ }^\circ\text{C}$ . All chemical shifts are internally referenced to the methyl signal of the isotactic pentad *mmmm* at 21.85 ppm. The tacticity distribution was quantified *via* integration of the methyl region between 22.0 – 19.7 ppm. The relative content of isotactic *mmmm* pentad is reported as mole fraction (in percentage) with respect to the sum of all steric pentads.

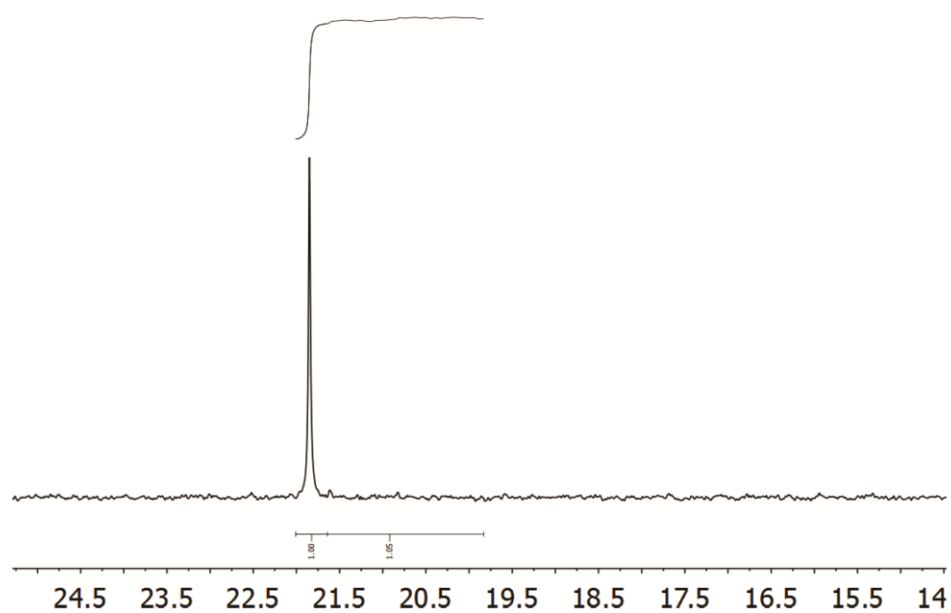


Figure S12. Pentad distribution of entry 8 in the  $^{13}\text{C}$   $\{^1\text{H}\}$  NMR (300 MHz) spectrum.

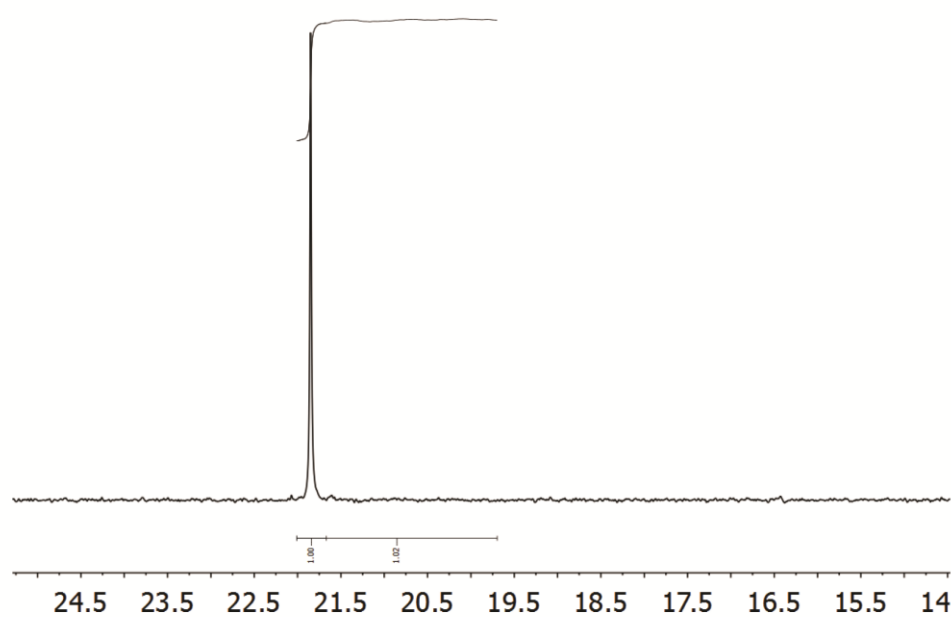


Figure S13. Pentad distribution of entry 9 in the  $^{13}\text{C}$   $\{^1\text{H}\}$  NMR (300 MHz) spectrum.

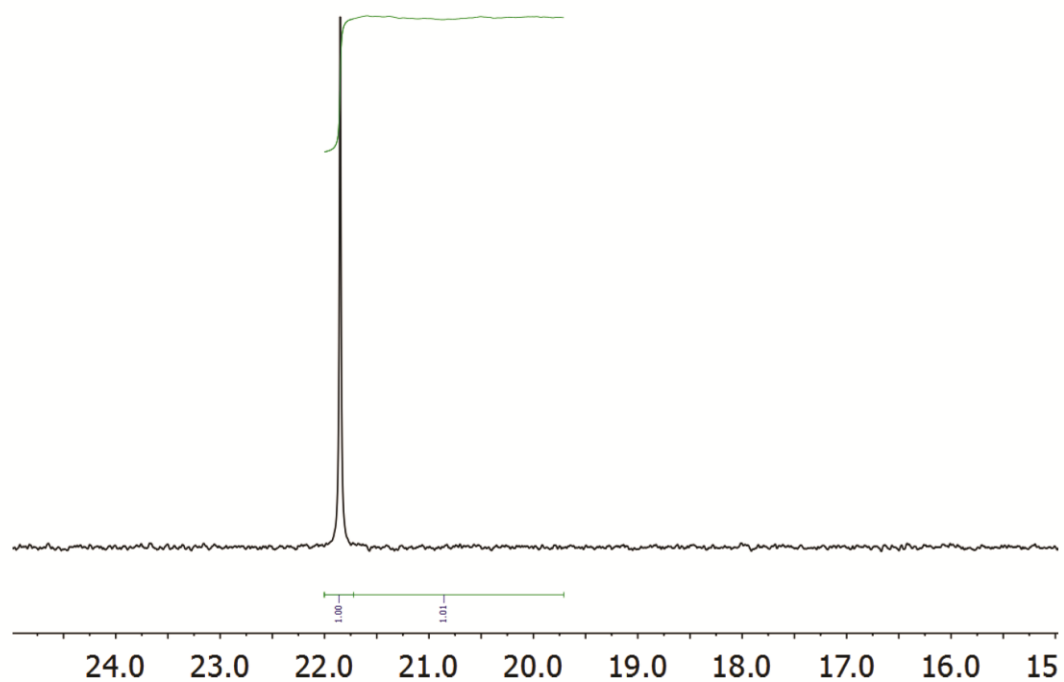


Figure S14. Pentad distribution of entry 10 in the  $^{13}\text{C}$   $\{^1\text{H}\}$  NMR (300 MHz) spectrum.

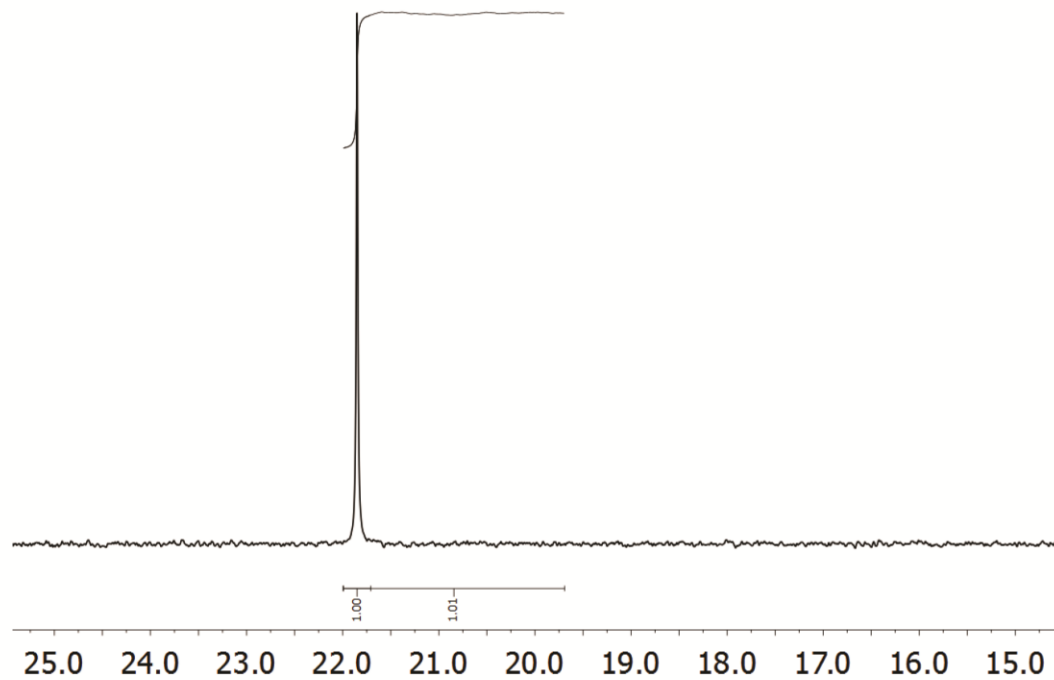


Figure S15. Pentad distribution of entry 11 in the  $^{13}\text{C}$   $\{^1\text{H}\}$  NMR (300 MHz) spectrum.

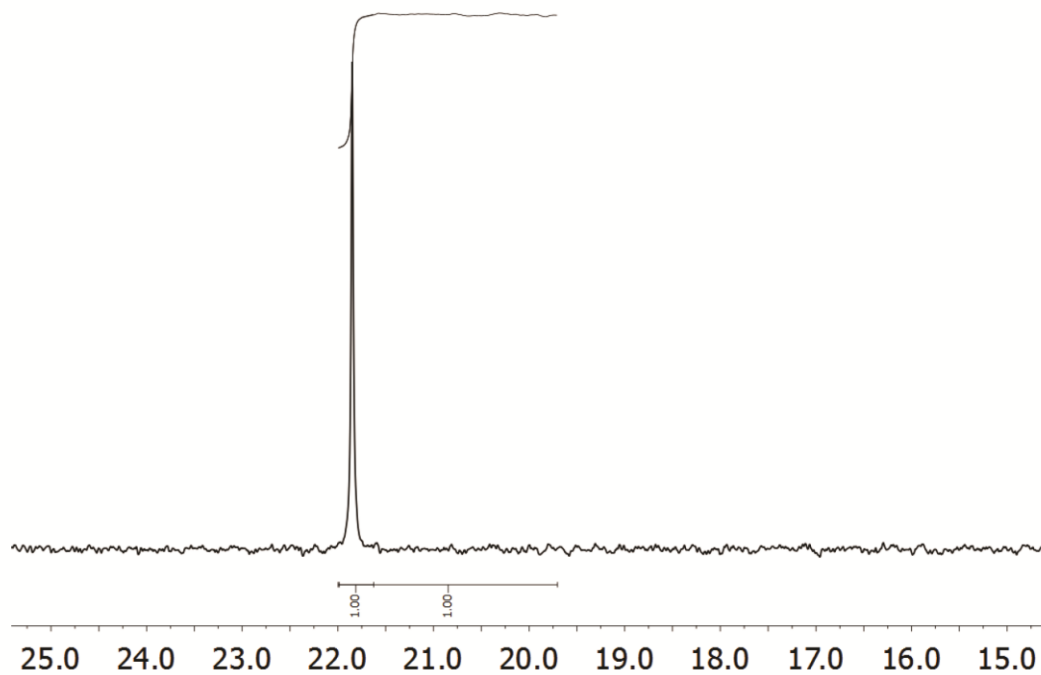


Figure S16. Pentad distribution of entry 18 in the  $^{13}\text{C}$   $\{^1\text{H}\}$  NMR (300 MHz) spectrum.

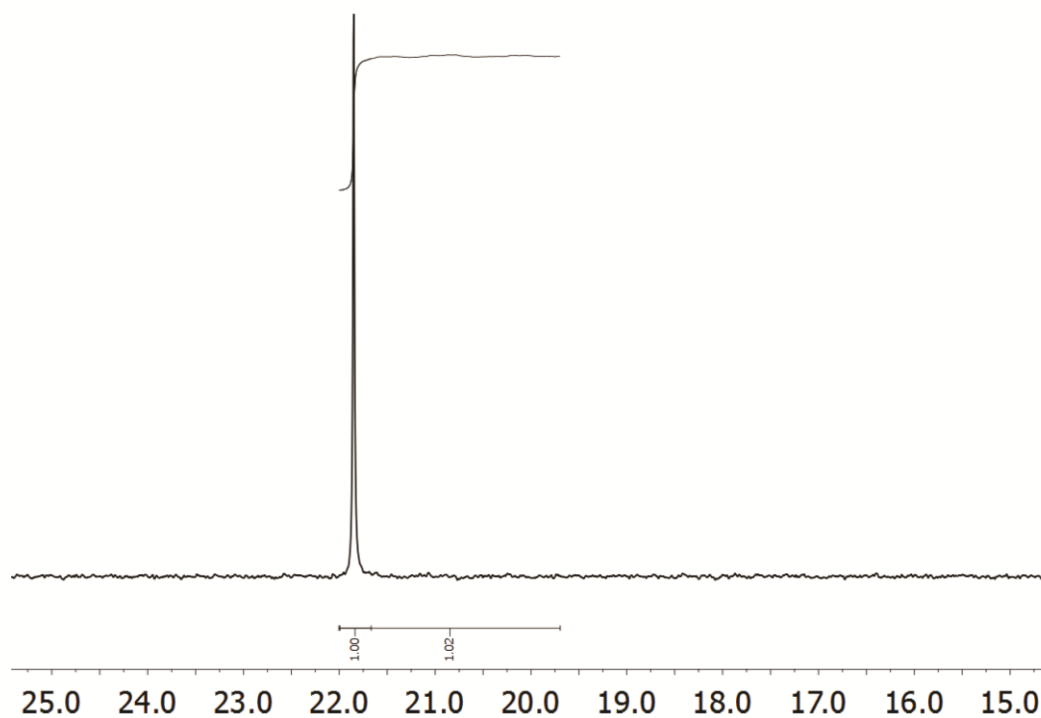


Figure S17. Pentad distribution of entry 19 in the  $^{13}\text{C}$   $\{^1\text{H}\}$  NMR (300 MHz) spectrum.

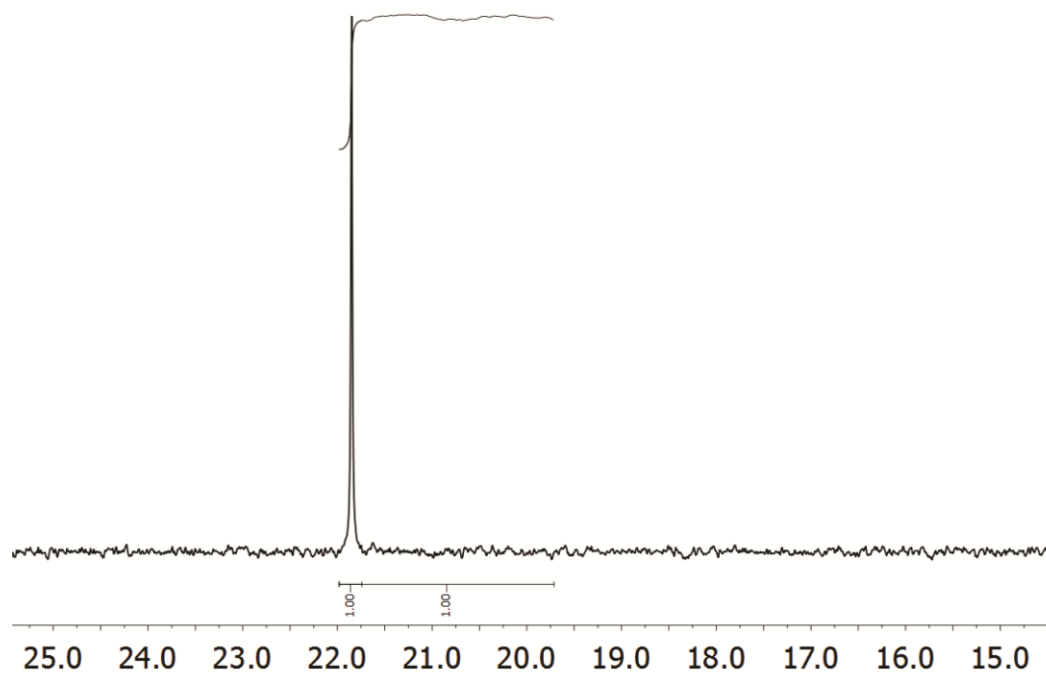


Figure S18. Pentad distribution of entry 34 in the  $^{13}\text{C}$   $\{^1\text{H}\}$  NMR (300 MHz) spectrum.

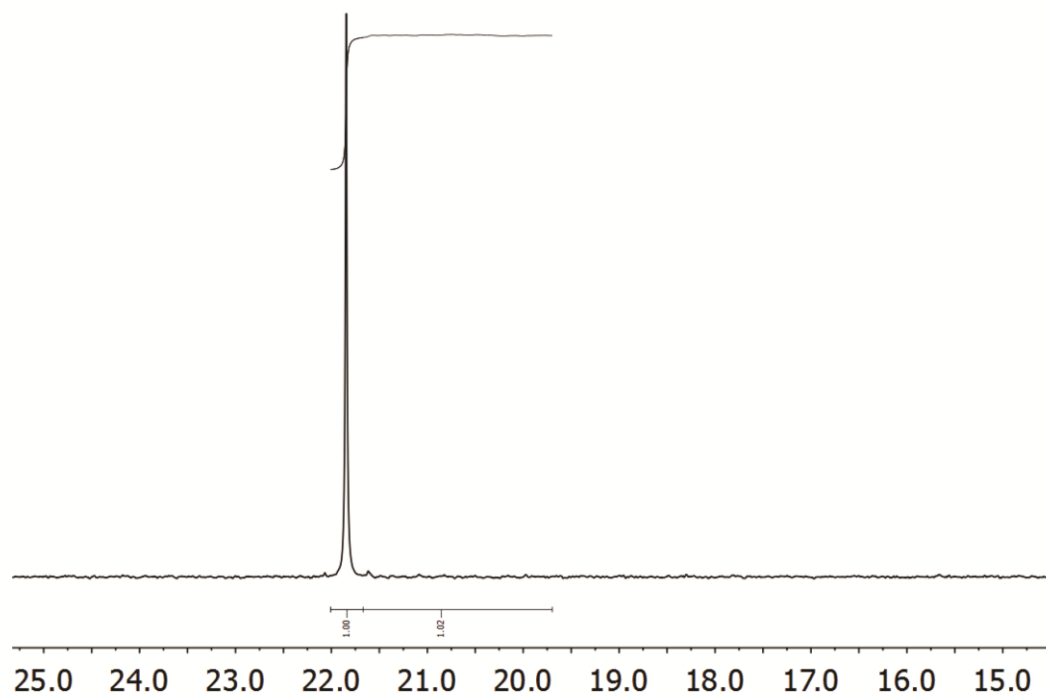


Figure S19. Pentad distribution of entry 42 in the  $^{13}\text{C}$   $\{^1\text{H}\}$  NMR (300 MHz) spectrum.

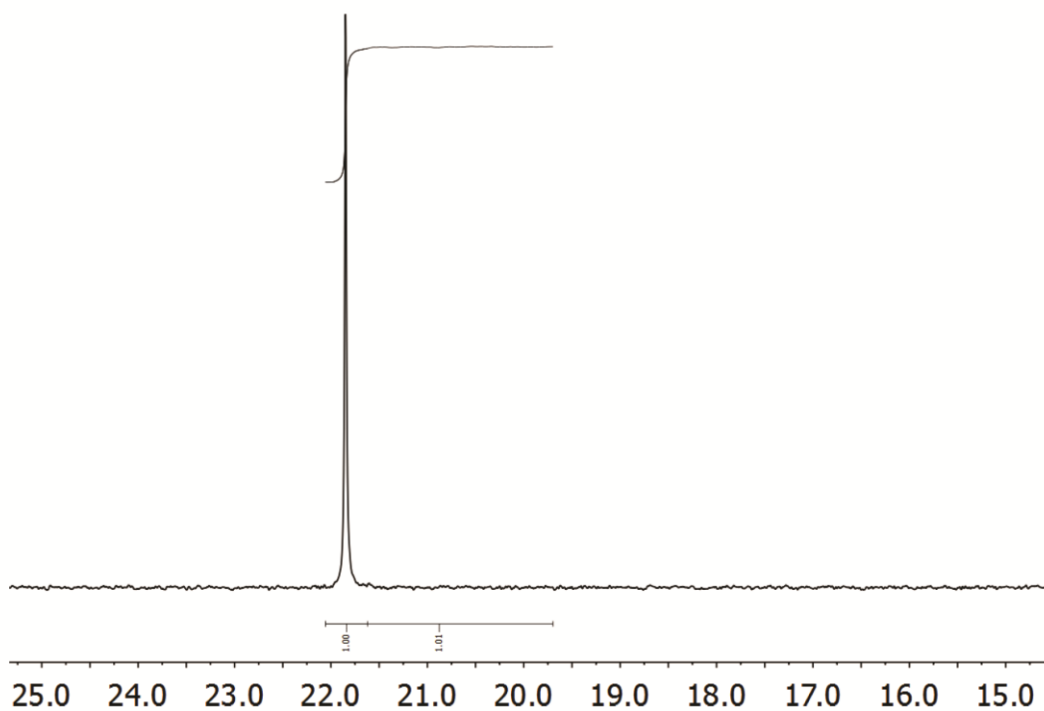


Figure S20. Pentad distribution of entry 43 in the  $^{13}\text{C}$   $\{^1\text{H}\}$  NMR (300 MHz) spectrum.

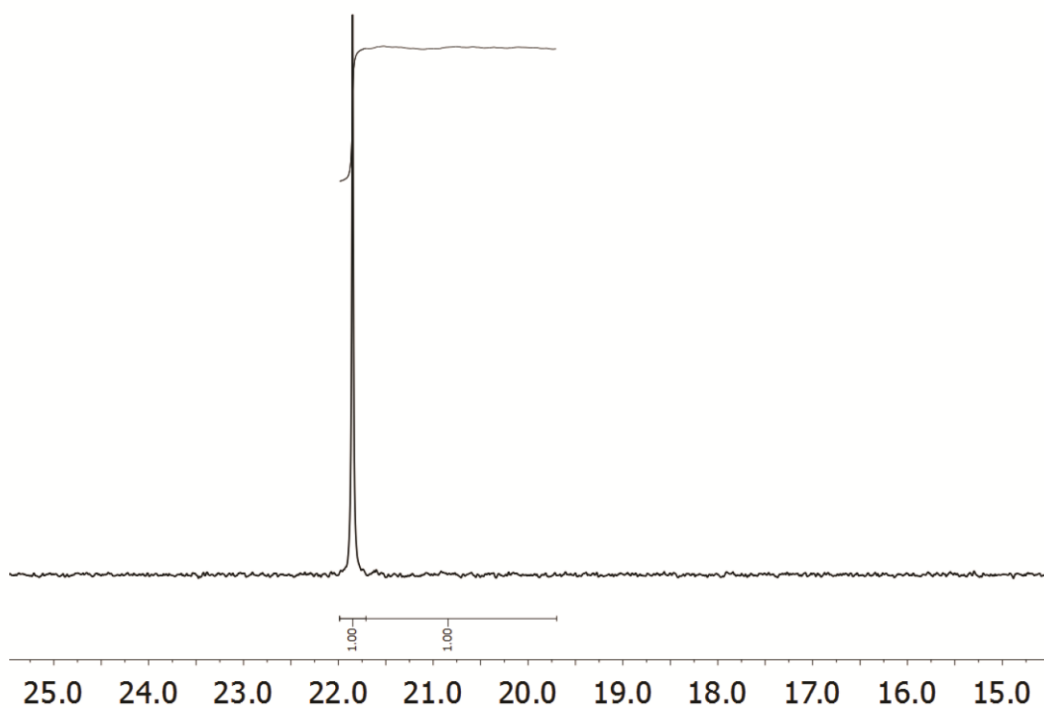


Figure S21. Pentad distribution of entry 44 in the  $^{13}\text{C}$   $\{^1\text{H}\}$  NMR (300 MHz) spectrum.

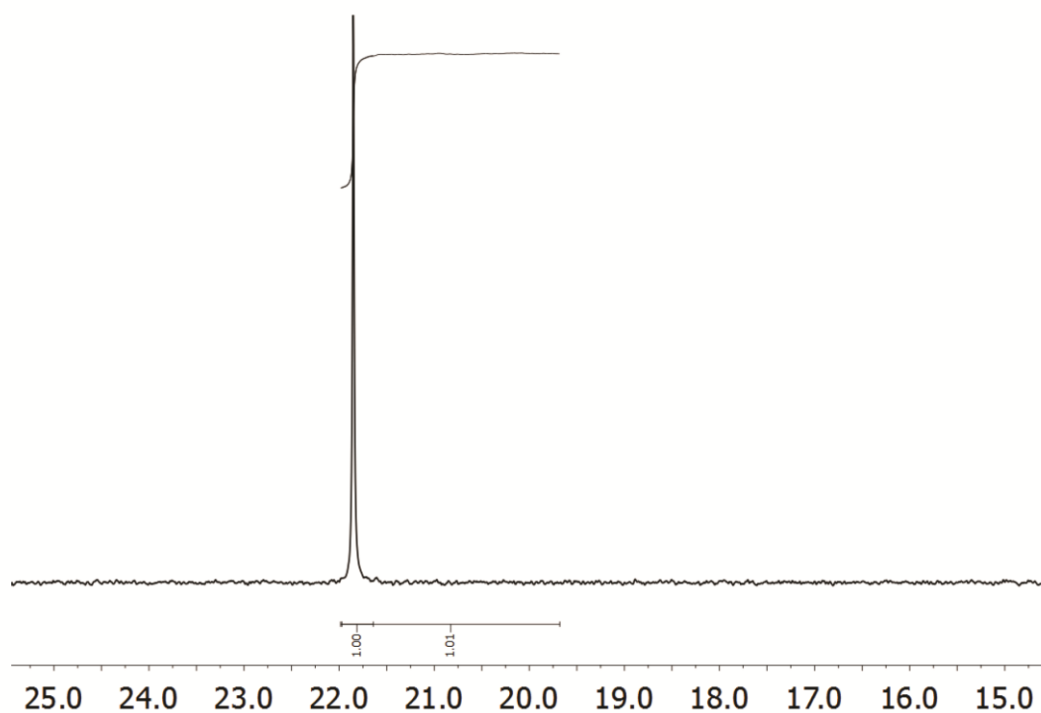


Figure S22. Pentad distribution of entry 45 in the  $^{13}\text{C}$   $\{^1\text{H}\}$  NMR (300 MHz) spectrum.

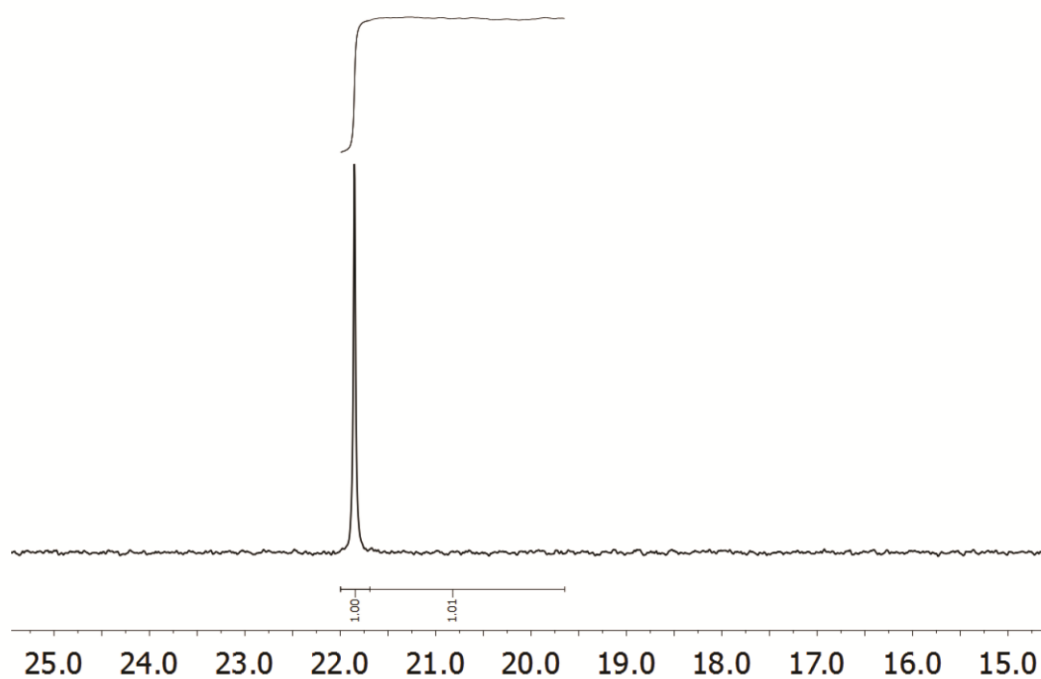


Figure S23. Pentad distribution of entry 53 in the  $^{13}\text{C}$   $\{^1\text{H}\}$  NMR (300 MHz) spectrum.

## 6. Single crystal XRD (SC-XRD) data

### General

Data were collected on single crystal X-ray diffractometers equipped with a CCD detector (APEX II,  $\kappa$ -CCD), a fine-focus sealed tube and a Triumph monochromator (**1a**), or a CCD detector (APEX II,  $\kappa$ -CCD), a FR591 rotating anode and a Montel mirror optic (**2a**) using the APEX II software package or with a CMOS detector (APEX III,  $\kappa$ -CMOS), an IMS microsource (**2b**) or a TXS rotating anode (**1b**) and a Helios optic using the APEX III software package.<sup>[2]</sup> All measurements used MoK $\alpha$  radiation ( $\lambda = 0.71073 \text{ \AA}$ ). The crystals were fixed on the top of a glass fiber with perfluorinated ether, transferred to the diffractometer and frozen under a stream of cold nitrogen. A matrix scan was used to determine the initial lattice parameters. Reflections were merged and corrected for Lorentz and polarization effects, scan speed and background using SAINT.<sup>[3]</sup> Absorption corrections, including odd and even ordered spherical harmonics were performed using SADABS.<sup>[3]</sup> Space group assignments were based upon systematic absences,  $E$  statistics, and successful refinement of the structures. Structures were solved using SHELXS-97 or SHELXT with the aid of successive difference Fourier maps, and were refined against all data using SHELXL-2014 in conjunction with SHELXLE.<sup>[4] [5] [6]</sup> Hydrogen atoms were calculated in ideal positions as follows: Methyl hydrogen atoms were refined as part of rigid rotating groups, with a C–H distance of 0.98  $\text{\AA}$  and  $U_{\text{iso(H)}} = 1.5 \cdot U_{\text{eq(C)}}$ . Other H atoms were placed in calculated positions and refined using a riding model with methylene and aromatic C–H distances of 0.99  $\text{\AA}$  and 0.95  $\text{\AA}$ , respectively, other C–H distances of 1.00  $\text{\AA}$  and  $U_{\text{iso(H)}} = 1.2 \cdot U_{\text{eq(C)}}$ . Non-hydrogen atoms were refined with anisotropic displacement parameters. Full-matrix least-squares refinements were carried out by minimizing  $\sum w(F_o^2 - F_c^2)^2$  with the SHELXL-97 weighting scheme.<sup>[5]</sup> Neutral atom scattering factors for all atoms and anomalous dispersion corrections for the non-hydrogen atoms were taken from *International Tables for Crystallography*.<sup>[7]</sup> Images were created with PLATON and Mercury.<sup>[8] [9]</sup> Crystallographic Data are also deposited at the Cambridge Crystallographic Data Centre (CCDC 1531610-1531613) and are available free of charge via [www.ccdc.cam.ac.uk/data\\_request/cif](http://www.ccdc.cam.ac.uk/data_request/cif).

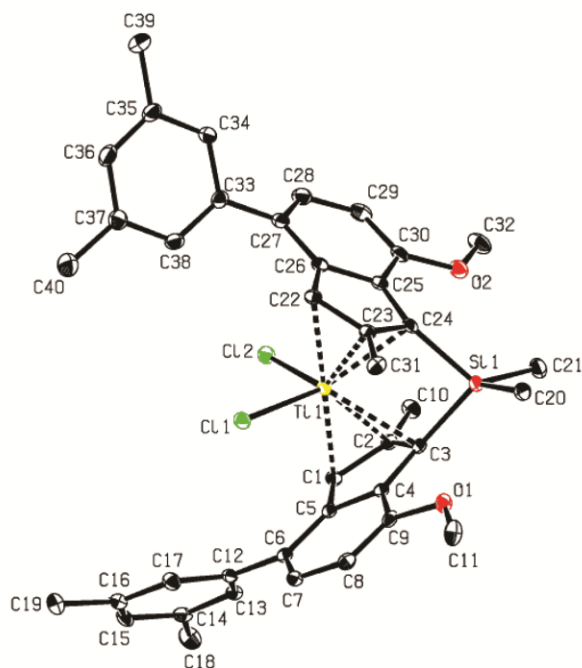
Compound **1a** (CCDC 1531611)

Figure S24. ORTEP style representation of **1a** with ellipsoids drawn at 50% probability level. Hydrogen atoms are omitted for clarity.

Diffractometer operator C. Jandl  
 scanspeed 10 s per frame  
 dx 35mm  
 3355 frames measured in 10 data sets  
 phi-scans with delta\_phi = 0.5  
 omega-scans with delta\_omega = 0.5

Table S2. Sample and crystal data, data collection and structure refinement for **1a**.

*Crystal data*

$C_{40}H_{42}Cl_2O_2SiTi$	$F(000) = 736$
$M_r = 701.60$	
Triclinic, $P$	$D_x = 1.379 \text{ Mg m}^{-3}$
Hall symbol: $-P 1$	Melting point: ? K
$a = 8.9690 (4) \text{ \AA}$	Mo $K\alpha$ radiation, $\lambda = 0.71073 \text{ \AA}$
$b = 12.5726 (6) \text{ \AA}$	Cell parameters from 9923 reflections
$c = 15.2414 (8) \text{ \AA}$	$\theta = 2.3\text{--}28.1^\circ$
$\alpha = 88.736 (2)^\circ$	$\mu = 0.48 \text{ mm}^{-1}$
$\beta = 85.302 (2)^\circ$	$T = 100 \text{ K}$

$\gamma = 80.633 (2)^\circ$	Fragment, black
$V = 1690.00 (14) \text{ \AA}^3$	$0.28 \times 0.12 \times 0.09 \text{ mm}$
$Z = 2$	

*Data collection*

<u>Bruker APEX-II CCD diffractometer</u>	<u>7460</u> independent reflections
Radiation source: <u>fine-focus sealed tube</u>	<u>6133</u> reflections with $i > 2\sigma(i)$
<u>Triumph optic monochromator</u>	$R_{\text{int}} = 0.041$
Detector resolution: <u>16</u> pixels $\text{mm}^{-1}$	$\theta_{\text{max}} = 27.1^\circ$ , $\theta_{\text{min}} = 2.1^\circ$
<u>phi- and omega-rotation scans</u>	$h = -11 \ 11$
Absorption correction: <u>multi-scan SADABS, Bruker, 2012</u>	$k = -16 \ 16$
$T_{\text{min}} = 0.709$ , $T_{\text{max}} = 0.746$	$l = -19 \ 19$
<u>61001</u> measured reflections	

*Refinement*

Refinement on $F^2$	Secondary atom site location: <u>difference Fourier map</u>
Least-squares matrix: <u>full</u>	Hydrogen site location: <u>inferred from neighbouring sites</u>
$R[F^2 > 2\sigma(F^2)] = 0.032$	<u>H-atom parameters constrained</u>
$wR(F^2) = 0.080$	$W = 1/[\Sigma^2(FO^2) + (0.0333P)^2 + 1.3606P]$ <u>WHERE <math>P = (FO^2 + 2FC^2)/3</math></u>
$S = 1.01$	$(\Delta/\sigma)_{\text{max}} \leq 0.001$
<u>7460</u> reflections	$\Delta\rho_{\text{max}} = 0.35 \text{ e \AA}^{-3}$
<u>425</u> parameters	$\Delta\rho_{\text{min}} = -0.30 \text{ e \AA}^{-3}$
<u>0</u> restraints	Extinction correction: <u>none</u>
<u>0</u> constraints	Extinction coefficient: <u>-</u>
Primary atom site location: <u>structure-invariant direct methods</u>	

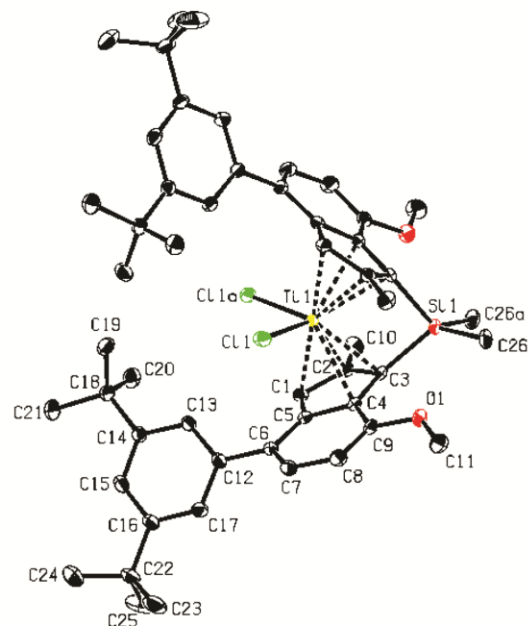
Compound **1b** (CCDC 1531612)

Figure S25. ORTEP style representation of **1b** with ellipsoids drawn at 50% probability level. Hydrogen atoms are omitted for clarity.

Diffractometer operator C. Jandl  
 scanspeed 20 s per frame  
 dx 40 mm  
 3124 frames measured in 11 data sets  
 phi-scans with  $\Delta\phi = 0.5$   
 omega-scans with  $\Delta\omega = 0.5$   
 shutterless mode

Table S3. Sample and crystal data, data collection and structure refinement for **1b**.

## Crystal data

<u><math>C_{52}H_{66}Cl_2O_2SiTi</math></u>	
$M_r = 869.91$	$D_x = 1.218 \text{ Mg m}^{-3}$
<u>Orthorhombic, <math>Pbcn</math></u>	Melting point: ? K
Hall symbol: <u><math>-P 2_n 2ab</math></u>	<u>Mo <math>K\alpha</math></u> radiation, $\lambda = 0.71073 \text{ \AA}$
$a = 17.0174 (9) \text{ \AA}$	Cell parameters from <u>9415</u> reflections
$b = 13.5503 (9) \text{ \AA}$	$\theta = 2.8\text{--}28.1^\circ$
$c = 20.5662 (15) \text{ \AA}$	$\mu = 0.36 \text{ mm}^{-1}$
$V = 4742.4 (5) \text{ \AA}^3$	$T = 101 \text{ K}$
$Z = 4$	<u>Rhombus, black</u>

$F(000) = 1856$	$0.22 \times 0.10 \times 0.08$ mm
<i>Data collection</i>	
<u>Bruker Photon CMOS diffractometer</u>	<u>4851</u> independent reflections
Radiation source: <u>TXS rotating anode</u>	<u>4266</u> reflections with $I > 2\sigma(I)$
<u>Helios optic monochromator</u>	$R_{\text{int}} = 0.071$
Detector resolution: <u>16 pixels mm<sup>-1</sup></u>	$\theta_{\text{max}} = 26.4^\circ$ , $\theta_{\text{min}} = 2.2^\circ$
<u>phi- and omega-rotation scans</u>	$h = -19 \ 21$
Absorption correction: <u>multi-scan SADABS 2014/5, Bruker</u>	$k = -16 \ 16$
$T_{\text{min}} = 0.665$ , $T_{\text{max}} = 0.746$	$l = -25 \ 25$
<u>109546</u> measured reflections	

*Refinement*

Refinement on $F^2$	Secondary atom site location: <u>difference Fourier map</u>
Least-squares matrix: <u>full</u>	Hydrogen site location: <u>inferred from neighbouring sites</u>
$R[F^2 > 2\sigma(F^2)] = 0.037$	<u>H-atom parameters constrained</u>
$wR(F^2) = 0.101$	$W = 1/[\Sigma^2(F\text{O}^2) + (0.0372P)^2 + 5.2017P]$ <u>WHERE <math>P = (F\text{O}^2 + 2FC^2)/3</math></u>
$S = 1.13$	$(\Delta/\sigma)_{\text{max}} = 0.001$
<u>4851</u> reflections	$\Delta\rho_{\text{max}} = 0.44 \text{ e \AA}^{-3}$
<u>272</u> parameters	$\Delta\rho_{\text{min}} = -0.45 \text{ e \AA}^{-3}$
<u>0</u> restraints	Extinction correction: <u>none</u>
<u>0</u> constraints	Extinction coefficient: <u>-</u>
Primary atom site location: <u>intrinsic phasing</u>	

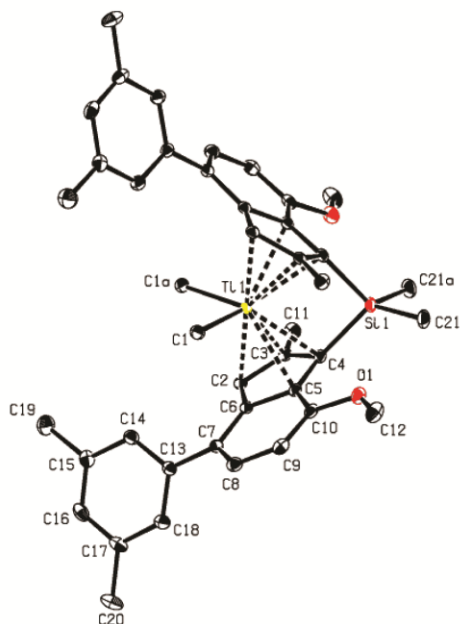
Compound **2a** (CCDC 1531610)

Figure S26. ORTEP style representation of **2a** with ellipsoids drawn at 50% probability level. Hydrogen atoms are omitted for clarity.

Diffractometer operator C. Jandl  
 scanspeed 10 s per frame  
 dx 55 mm  
 4857 frames measured in 12 data sets  
 phi-scans with  $\Delta\phi = 0.5$   
 omega-scans with  $\Delta\omega = 0.5$

Table S4. Sample and crystal data, data collection and structure refinement for **2a**.

*Crystal data*

<u><math>C_{42}H_{48}O_2SiTi</math></u>	
$M_r = 660.76$	$D_x = 1.299 \text{ Mg m}^{-3}$
Monoclinic, $C2/c$	Melting point: ? K
Hall symbol: $-C 2yc$	Mo $K\alpha$ radiation, $\lambda = 0.71073 \text{ \AA}$
$a = 26.0058 (18) \text{ \AA}$	Cell parameters from 9344 reflections
$b = 9.8108 (7) \text{ \AA}$	$\theta = 2.3\text{--}37.8^\circ$
$c = 18.285 (2) \text{ \AA}$	$\mu = 0.33 \text{ mm}^{-1}$
$\beta = 133.589 (2)^\circ$	$T = 100 \text{ K}$
$V = 3379.0 (5) \text{ \AA}^3$	Fragment, red
$Z = 4$	$0.37 \times 0.30 \times 0.27 \text{ mm}$

$F(000) = \underline{1408}$

#### Data collection

<u>Bruker APEX-II CCD diffractometer</u>	<u>4196</u> independent reflections
Radiation source: <u>rotating anode FR591</u>	<u>4057</u> reflections with $i > 2\sigma(i)$
<u>MONTEL optic monochromator</u>	$R_{\text{int}} = \underline{0.031}$
Detector resolution: <u>16 pixels mm<sup>-1</sup></u>	$\theta_{\text{max}} = \underline{28.3}^\circ$ , $\theta_{\text{min}} = \underline{2.2}^\circ$
<u>phi- and <math>\omega</math>-rotation scans</u>	$h = \underline{-34}$ $\underline{34}$
Absorption correction: <u>multi-scan SADABS, Bruker, 2012</u>	$k = \underline{-13}$ $\underline{13}$
$T_{\text{min}} = \underline{0.717}$ , $T_{\text{max}} = \underline{0.747}$	$l = \underline{-24}$ $\underline{24}$
<u>40929</u> measured reflections	

#### Refinement

Refinement on $F^2$	Secondary atom site location: <u>difference Fourier map</u>
Least-squares matrix: <u>full</u>	Hydrogen site location: <u>inferred from neighbouring sites</u>
$R[F^2 > 2\sigma(F^2)] = \underline{0.030}$	<u>H-atom parameters constrained</u>
$wR(F^2) = \underline{0.088}$	$W = 1/[\Sigma^2(FO^2) + (0.0484P)^2 + 3.438P]$ <u>WHERE <math>P = (FO^2 + 2FC^2)/3</math></u>
$S = \underline{1.06}$	$(\Delta/\sigma)_{\text{max}} = \underline{0.001}$
<u>4196</u> reflections	$\Delta\rho_{\text{max}} = \underline{0.48} \text{ e } \text{\AA}^{-3}$
<u>215</u> parameters	$\Delta\rho_{\text{min}} = \underline{-0.23} \text{ e } \text{\AA}^{-3}$
<u>0</u> restraints	Extinction correction: <u>none</u>
<u>0</u> constraints	Extinction coefficient: <u>-</u>
Primary atom site location: <u>structure-invariant direct methods</u>	

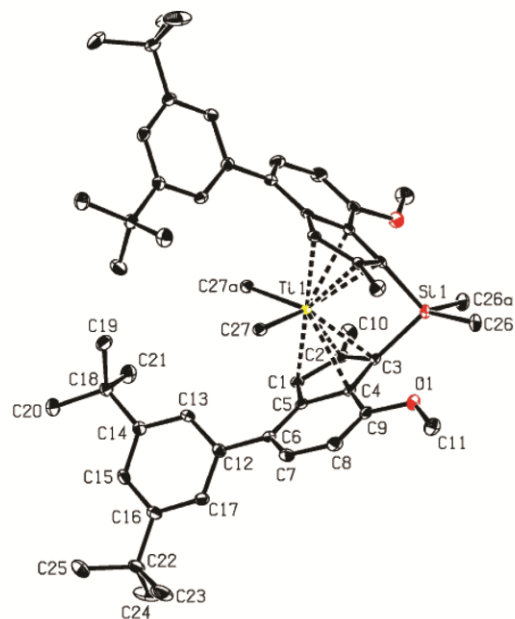
Compound **2b** (CCDC 1531613)

Figure S27. ORTEP style representation of **2b** with ellipsoids drawn at 50% probability level. Hydrogen atoms are omitted for clarity.

Diffractometer operator C. Jandl  
 scanspeed 30 s per frame  
 dx 40 mm  
 1949 frames measured in 8 data sets  
 phi-scans with  $\Delta\phi = 0.5$   
 omega-scans with  $\Delta\omega = 0.5$   
 shutterless mode

Table S5. Sample and crystal data, data collection and structure refinement for **2b**.

*Crystal data*

$C_{54}H_{72}O_2SiTi$	
$M_r = 829.08$	$D_x = 1.150 \text{ Mg m}^{-3}$
Orthorhombic, <i>Pbcn</i>	Melting point: ? K
Hall symbol: $-P\ 2n\ 2ab$	Mo $K\alpha$ radiation, $\lambda = 0.71073 \text{ \AA}$
$a = 17.0522 (7) \text{ \AA}$	Cell parameters from 9973 reflections
$b = 13.6012 (6) \text{ \AA}$	$\theta = 2.4\text{--}26.4^\circ$
$c = 20.6542 (9) \text{ \AA}$	$\mu = 0.24 \text{ mm}^{-1}$
$V = 4790.3 (4) \text{ \AA}^3$	$T = 100 \text{ K}$
$Z = 4$	Fragment, red

$F(000) = 1792$	$0.18 \times 0.16 \times 0.12$ mm
-----------------	-----------------------------------

*Data collection*

<u>Bruker Photon CMOS diffractometer</u>	<u>4716</u> independent reflections
Radiation source: <u>IMS microsource</u>	<u>4243</u> reflections with $I > 2\sigma(I)$
<u>Helios optic monochromator</u>	$R_{\text{int}} = 0.047$
Detector resolution: <u>16 pixels mm<sup>-1</sup></u>	$\theta_{\text{max}} = 26.0^\circ$ , $\theta_{\text{min}} = 2.3^\circ$
<u>phi- and omega-rotation scans</u>	$h = -21 \ 21$
Absorption correction: <u>multi-scan SADABS 2016/2, Bruker</u>	$k = -16 \ 16$
$T_{\text{min}} = 0.719$ , $T_{\text{max}} = 0.745$	$l = -25 \ 25$
<u>135373</u> measured reflections	

*Refinement*

Refinement on $F^2$	Secondary atom site location: <u>difference Fourier map</u>
Least-squares matrix: <u>full</u>	Hydrogen site location: <u>inferred from neighbouring sites</u>
$R[F^2 > 2\sigma(F^2)] = 0.034$	H-atom parameters constrained
$wR(F^2) = 0.087$	$W = 1/[\Sigma^2(FO^2) + (0.0397P)^2 + 3.5861P]$ WHERE $P = (FO^2 + 2FC^2)/3$
$S = 1.03$	$(\Delta/\sigma)_{\text{max}} = 0.001$
<u>4716</u> reflections	$\Delta\rho_{\text{max}} = 0.28 \text{ e \AA}^{-3}$
<u>273</u> parameters	$\Delta\rho_{\text{min}} = -0.40 \text{ e \AA}^{-3}$
<u>0</u> restraints	Extinction correction: <u>none</u>
<u>0</u> constraints	Extinction coefficient: <u>-</u>
Primary atom site location: <u>intrinsic phasing</u>	

## 7. References

- [1] Busico, V.; Brita, D.; Caporaso, L.; Cipullo, R.; Vacatello, M., *Macromolecules* **1997**, *30*, 3971.
- [2] a) Bruker AXS Inc., *APEX suite of crystallographic software, APEX 2 Version 2014-9.0*, Bruker, Madison, Wisconsin, USA, **2014**.  
b) Bruker AXS Inc., *APEX suite of crystallographic software, APEX 3 Version 2015-5.2*, Bruker, Madison, Wisconsin, USA, **2015**.
- [3] a) Bruker AXS Inc., *SAINT, Version 8.27b and SADABS, Version 2012/1*, Bruker, Madison, Wisconsin, USA, **2012**.  
b) Bruker AXS Inc., *SAINT, Version 8.34A and SADABS, Version 2014/5*, Bruker, Madison, Wisconsin, USA, **2014**.
- [4] a) Sheldrick, G. M.; SHELXS97. University of Göttingen, Germany, **1997**.  
b) Sheldrick, G. M.; *Acta Cryst. A* **2015**, *71*, 3–8.
- [5] Sheldrick, G. M.; *Acta Cryst. C* **2015**, *71*, 3–8.
- [6] Huebschle, C. B.; Sheldrick, G. M.; Dittrich, B.; *J. Appl. Cryst.* **2011**, *44*, 1281–1284.
- [7] Wilson, A. J. C.; (Ed.) *International Tables for Crystallography, Vol. C, Tables 6.1.1.4 (pp. 500-502), 4.2.6.8 (pp. 219-222), and 4.2.4.2 (pp. 193-199)*, Kluwer Academic Publishers, Dordrecht, The Netherlands, **1992**.
- [8] Spek, A. L.; *Acta Cryst. D* **2009**, *65*, 148-155.
- [9] Macrae, C. F.; Edgington, P. R.; McCabe, P.; Pidcock, E.; Shields, G. P.; Taylor, R.; Towler, M.; van de Streek, J.; *J. Appl. Cryst.* **2006**, *39*, 453–457.

## 12.3 Supporting Information – Chapter 6: *Behind the Scenes of Group IV Metallocene Catalysis: Examination of the Metal–Carbon Bond*

### Behind the Scenes of Group IV Metallocene Catalysis: Examination of the Metal–Carbon Bond

Martin R. Machat<sup>†</sup>, Andreas Fischer<sup>†</sup>, Dominik Schmitz<sup>†</sup>, Marcel Vöst<sup>†</sup>, Markus Drees<sup>§</sup>, Christian Jandl<sup>§</sup>, Alexander Pöthig<sup>§</sup>, Nicola P. M. Casati<sup>‡</sup>, Wolfgang Scherer<sup>\*†</sup>, and Bernhard Rieger<sup>\*†</sup>

<sup>†</sup>Wacker-Lehrstuhl für Makromolekulare Chemie, Catalysis Research Center, Technische Universität München, Lichtenbergstraße 4, 85748 Garching bei München, Germany

<sup>‡</sup>Lehrstuhl für Chemische Physik und Materialwissenschaften, Institut für Physik, Universität Augsburg, Universitätsstraße 1, 86159 Augsburg, Germany

<sup>‡</sup>Paul Scherrer Institut, WLG/229, 5232 Villigen PSI, Switzerland

<sup>§</sup>Catalysis Research Center, Technische Universität München, Ernst-Otto-Fischer Straße 1, 85748 Garching bei München, Germany

Metallocene – zirconium – hafnium – group IV chemistry – bond strength – bond compressibility – electron density – electron localization – lanthanide contraction – ionic character – covalent character – enthalpy – entropy – polyolefin catalysis – propene polymerization – polypropylene – high melting transition – stereoselectivity

#### Table of contents:

1. Synthesis – Procedures.....	3
2. Synthesis – <sup>1</sup> H NMR and <sup>13</sup> C NMR spectra.....	4
3. Kinetic measurements.....	10
4. UV VIS spectra for the prealkylation of complexes <b>2</b> with 200 eq. of TIBA .....	15
5. Olefinic end group analysis <i>via</i> <sup>1</sup> H NMR spectroscopy.....	17
6. Tacticity determination <i>via</i> <sup>13</sup> C { <sup>1</sup> H} NMR spectroscopy.....	18
7. ORTEP representations of 3-Zr, 2-Zr, 3-Ti and 3-Hf.....	22
8. Computational data of 3-Ti, 3-Zr and 3-Hf.....	26
9. Crystallographic Studies of <b>3</b> under High-Pressure (HP).....	30
10. Crystallographic Studies of <b>3</b> under HP: Crystal Data and Selected Bond Distances and Angles.....	33
11. Overview of the Structural Changes in <b>3</b> with increasing Pressure.....	38
12. High resolution charge density refinement details of 3-Ti, 3-Zr and 3-Hf.....	46
13. Experimental d-orbital populations at the metal center of 3-Ti, 3-Zr and 3-Hf.....	49
14. Residual electron density maps of 3-Ti, 3-Zr and 3-Hf.....	49
15. Scaling and drk plots of 3-Ti, 3-Zr and 3-Hf.....	51
16. Topological parameters of selected bonds of selected atoms of 3-Ti, 3-Zr and 3-Hf.....	52

17.	Integrated AIM charges of selected atoms of 3-Ti, 3-Zr and 3-Hf.....	54
18.	Critical points of the Laplacian of the electron density of selected atoms of 3-Ti, 3-Zr and 3-Hf .....	55
	$\angle$ CC1-M-CC1 .....	55
19.	Critical points of the ELI-D of the outer shell of selected atoms 3-Ti, 3-Zr and 3-Hf.....	56
	$\angle$ CC1-M-CC1 (ELI-D) .....	56
20.	Experimental and theoretical Laplacian maps of 3-Zr and 3-Hf.....	57
21.	Experimental and theoretical Laplacian 3D-isosurface plot of 3-Zr .....	59
22.	Theoretical ELI-D 3D-isosurface plots of 3-Ti, 3-Zr and 3-Hf.....	61
23.	Kinetic measurements – theoretical verification .....	63
24.	References .....	86

## 1. Synthesis – Procedures

*rac*-Dimethylsilanediybis[4-(3',5'-dimethylphenyl)-7-methoxy-2-methylindenyl]zirconium dichloride (**2-Zr**)

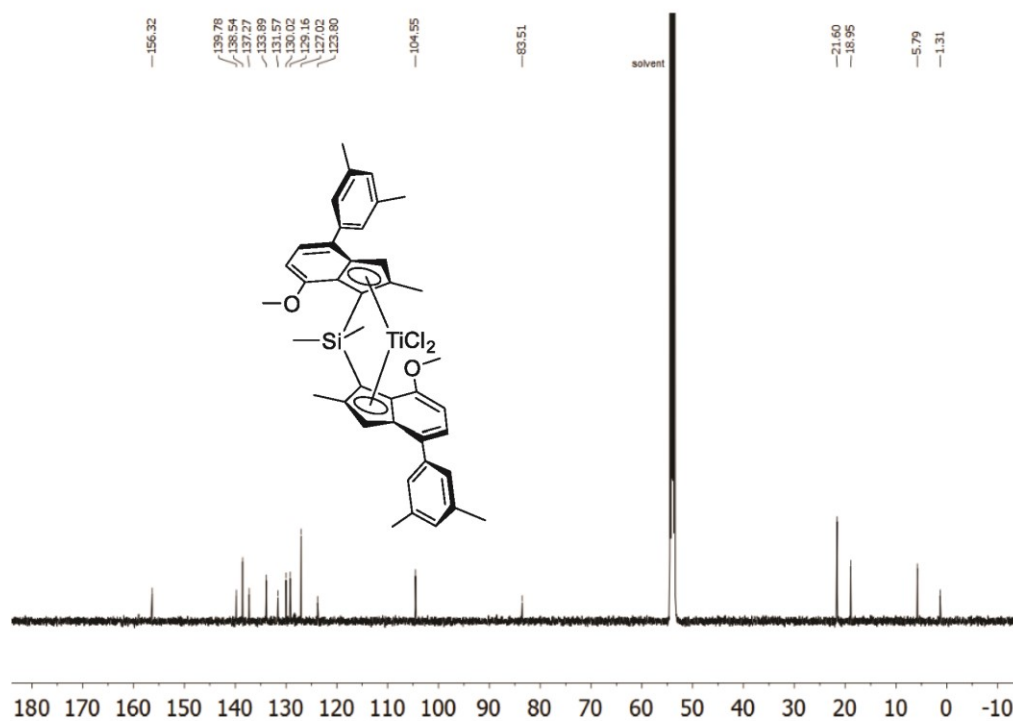
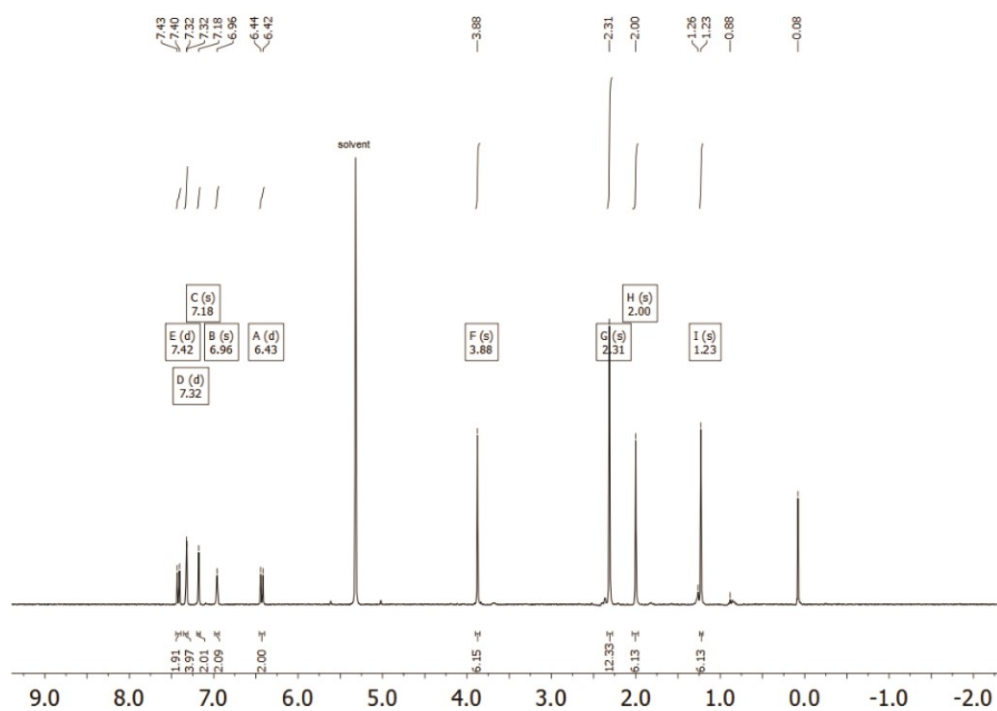
0.86 g (1.47 mmol, 1.00 eq.) of bis[4-(3',5'-dimethylphenyl)-7-methoxy-2-methylindenyl]dimethyl silane were dissolved in 40 mL dry toluene, cooled down to  $-78\text{ }^{\circ}\text{C}$  and 1.73 mL (2.94 mmol, 2.00 eq.) 1.7 M  $t\text{BuLi}$  solution in pentane were added dropwise. After maintaining the temperature for one hour the reaction mixture was stirred for additional 3 h at room temperature. The yellow suspension was cooled down to  $0\text{ }^{\circ}\text{C}$  and subsequently transferred *via cannulae* to a suspension of 343 mg (1.47 mmol, 1.00 eq.)  $\text{ZrCl}_4$  in 20 mL dry toluene at  $-78\text{ }^{\circ}\text{C}$ . The reaction mixture was allowed to unfreeze overnight resulting in an orange to red suspension. The suspension was filtered, the solvent of the filtrate was distilled off and the residue was washed with dry pentane ( $2 \times 65\text{ mL}$ ) and a 1:2 toluene/pentane-mixture (150 mL). After recrystallization in a toluene/pentane mixture 160 mg (15 %) of orange crystalline powder were obtained containing the pure *rac*-isomer. Anal. Calcd for  $\text{C}_{40}\text{H}_{42}\text{Cl}_2\text{O}_2\text{SiZr}$ : C, 64.49; H, 5.68; Cl, 9.52; O, 4.30; Si, 3.77; Zr, 12.25. Found: C, 64.62; H, 5.78.  $^1\text{H NMR}$  (400 MHz,  $\text{CD}_2\text{Cl}_2$ , 298 K):  $\delta$  (ppm) = 7.30 (d,  $^3J = 7.8\text{ Hz}$ , 2H, H-Ar), 7.26 (s, 4H, H-Ar'), 6.96 (m, 4H, H-Ar',  $-\text{CH}=\text{}$ ), 6.42 (d,  $^3J = 7.8\text{ Hz}$ , 2H, H-Ar), 3.90 (s, 6H,  $-\text{OCH}_3$ ), 2.32 (s, 12H, Ar'- $\text{CH}_3$ ), 2.16 (s, 6H,  $-\text{CH}_3$ ), 1.21 (s, 6H, Si- $\text{CH}_3$ ).  $^{13}\text{C}\{^1\text{H}\}$  NMR (100 MHz,  $\text{CD}_2\text{Cl}_2$ )  $\delta$  156.0, 140.0, 138.6, 135.5, 133.6, 131.3, 129.3, 127.9, 126.8, 123.9, 121.8, 103.7, 84.4, 21.6, 17.9, 6.2.

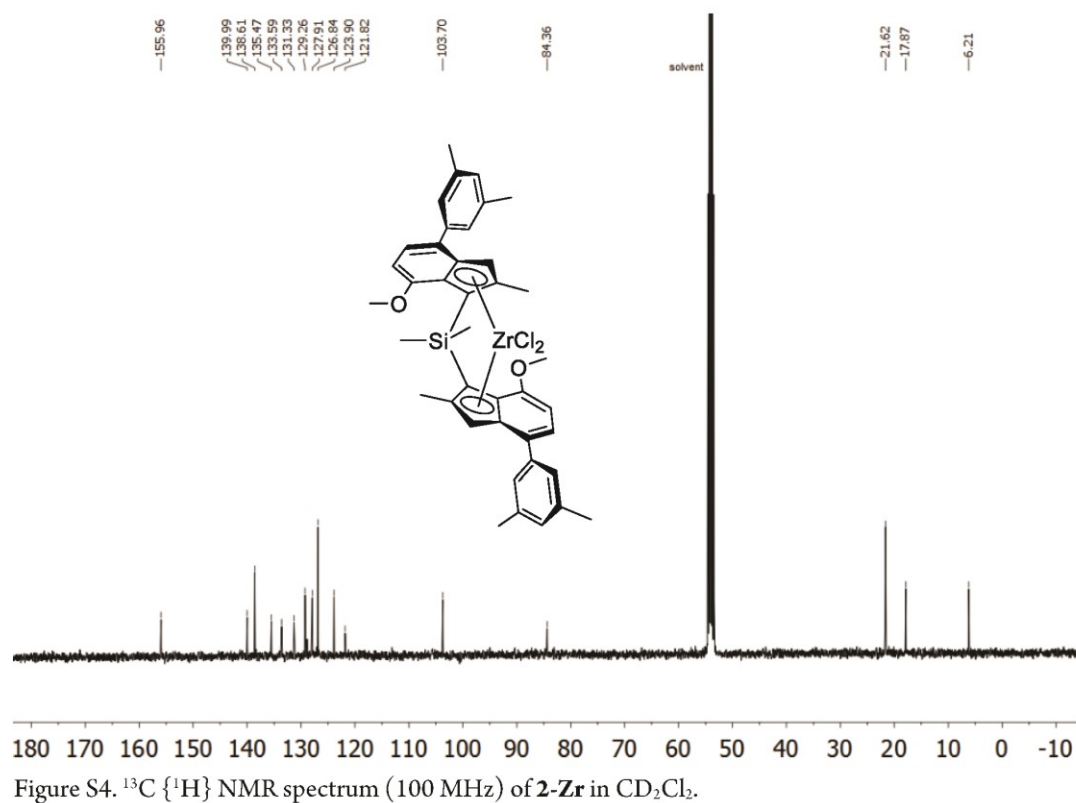
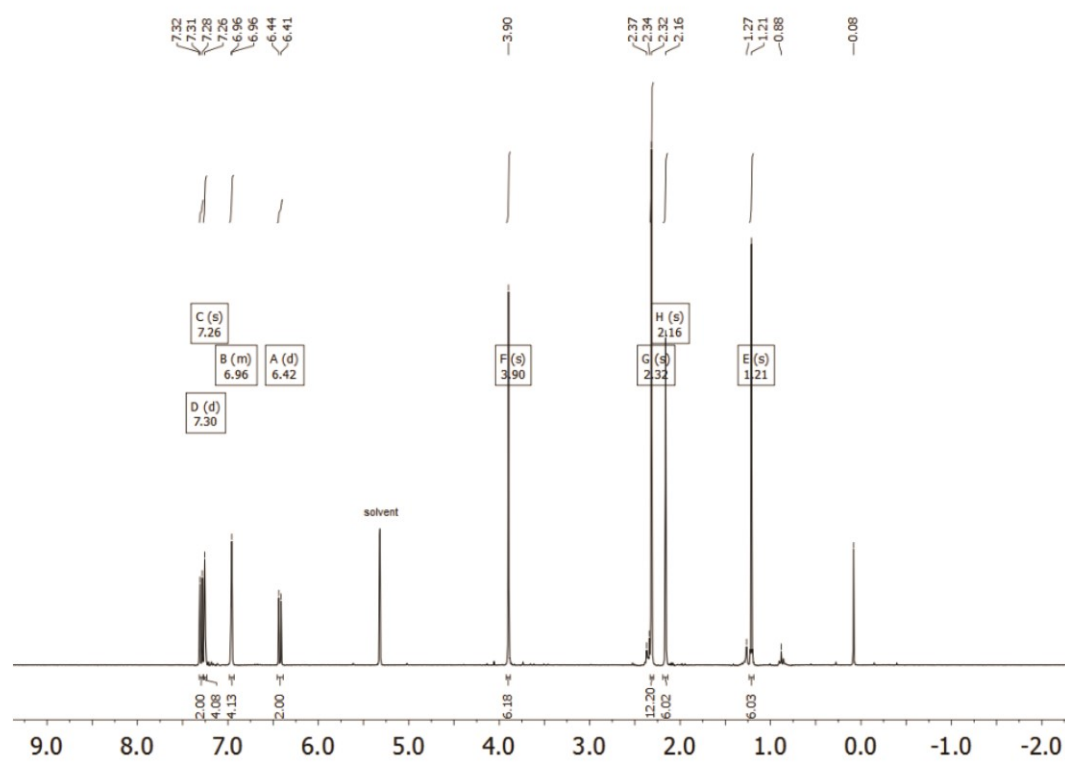
*rac*-Dimethylsilanediybis[4-(3',5'-dimethylphenyl)-7-methoxy-2-methylindenyl]dimethyl zirconium (**3-Zr**)

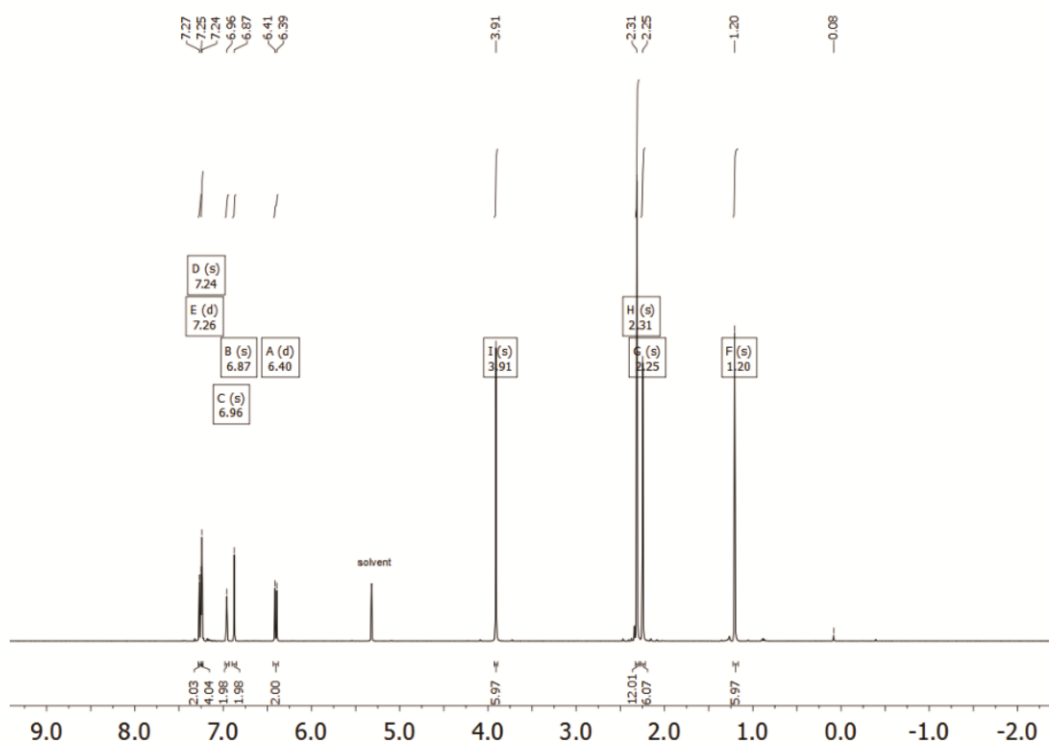
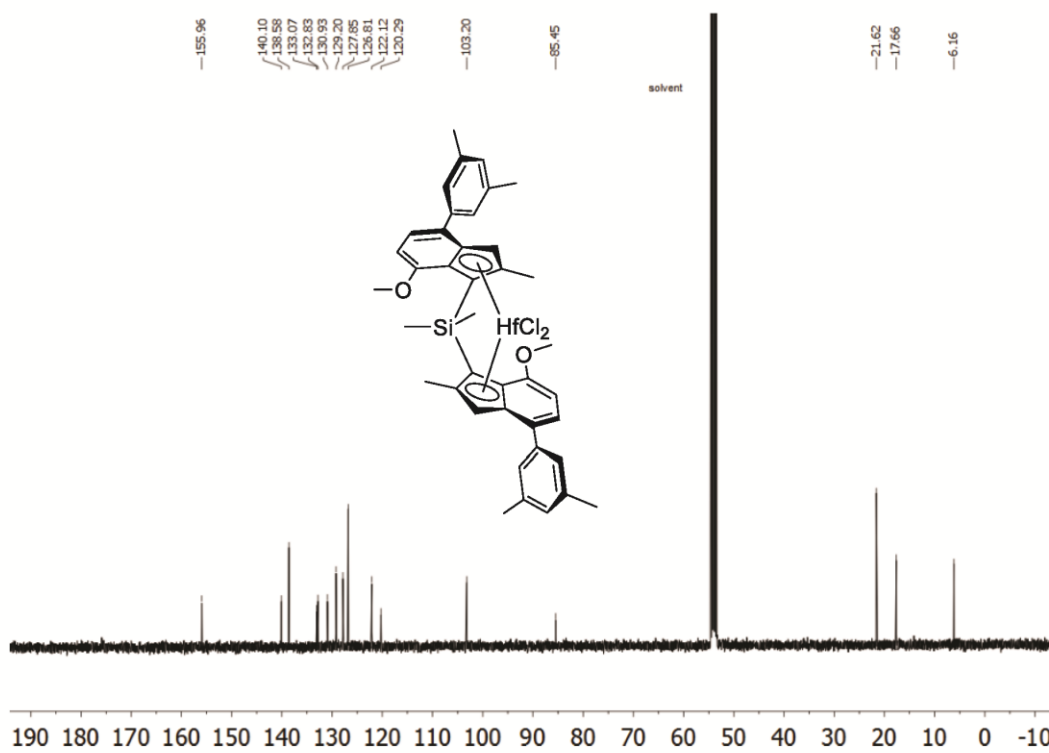
41.1 mg (55.2  $\mu\text{mol}$ , 1.00 eq.) of **2-Zr** were dissolved in 5.0 mL dry benzene and 46.0  $\mu\text{L}$  (138  $\mu\text{mol}$ , 2.50 eq.) 3.0 M MeMgBr solution in diethyl ether were added. After stirring the yellow reaction mixture for 6 h at  $40\text{ }^{\circ}\text{C}$  the filtrate was isolated and the solvent was removed *in vacuo*. After recrystallization in a dry toluene/*n*-pentane mixture 25.3 mg (65%) of yellow crystalline solid **3-Zr** were isolated. Crystals suitable for high resolution X-ray diffraction analysis were obtained by diffusion of *n*-pentane into a saturated benzene solution at  $6\text{ }^{\circ}\text{C}$ . Anal. Calcd for  $\text{C}_{42}\text{H}_{48}\text{O}_2\text{SiZr}$ : C, 71.64; H, 6.87; O, 4.54; Si, 3.99; Zr, 12.96. Found: C, 71.62; H, 6.79.  $^1\text{H NMR}$  (400 MHz,  $\text{CD}_2\text{Cl}_2$ , 298 K):  $\delta$  (ppm) = 7.23 (d,  $^3J = 7.8\text{ Hz}$ , 2H, H-Ar), 7.20 (s, 4H, H-Ar'), 6.97 (s, 2H,  $-\text{CH}=\text{}$ ), 6.96 (s, 2H, H-Ar'), 6.36 (d,  $^3J = 7.8\text{ Hz}$ , 2H, H-Ar), 3.83 (s, 6H,  $-\text{OCH}_3$ ), 2.32 (s, 12H, Ar'- $\text{CH}_3$ ), 1.99 (s, 6H,  $-\text{CH}_3$ ), 1.01 (s, 6H, Si- $\text{CH}_3$ ), -1.17 (s, 6H, Zr- $\text{CH}_3$ ).  $^{13}\text{C}\{^1\text{H}\}$  NMR (100 MHz,  $\text{CD}_2\text{Cl}_2$ )  $\delta$  156.2, 140.9, 138.5, 134.7, 130.9, 130.1, 129.0, 126.7, 125.6, 121.3, 116.7, 102.1, 79.2, 34.2, 21.7, 17.4, 6.2.

*rac*-Dimethylsilanediybis[4-(3',5'-dimethylphenyl)-7-methoxy-2-methylindenyl]dimethyl hafnium (**3-Hf**)

90.0 mg (108  $\mu\text{mol}$ , 1.00 eq.) of **2-Hf** were dissolved in 10 mL dry benzene and 180  $\mu\text{L}$  (540  $\mu\text{mol}$ , 5.00 eq.) 3.0 M MeMgBr solution in diethyl ether were added. After stirring the reaction mixture for 18 h at  $50\text{ }^{\circ}\text{C}$  the slightly yellow solution was separated from the brownish residue and the solvent of the filtrate was removed *in vacuo*. After recrystallization in a dry toluene/*n*-pentane mixture 47.9 mg (56%) of yellow crystalline solid **3-Hf** were isolated. Crystals suitable for high resolution X-ray diffraction analysis were obtained by diffusion of *n*-pentane into a saturated benzene solution at  $6\text{ }^{\circ}\text{C}$ . Anal. Calcd for  $\text{C}_{42}\text{H}_{48}\text{O}_2\text{SiHf}$ : C, 63.74; H, 6.11; Hf, 22.55; O, 4.04; Si, 3.55. Found: C, 63.83; H, 6.10.  $^1\text{H NMR}$  (400 MHz,  $\text{CD}_2\text{Cl}_2$ , 298 K):  $\delta$  (ppm) = 7.22 (d,  $^3J = 7.8\text{ Hz}$ , 2H, H-Ar), 7.20 (s, 4H, H-Ar'), 6.96 (s, 2H, H-Ar'), 6.89 (s, 2H,  $-\text{CH}=\text{}$ ), 6.36 (d,  $^3J = 7.8\text{ Hz}$ , 2H, H-Ar), 3.85 (s, 6H,  $-\text{OCH}_3$ ), 2.32 (s, 12H, Ar'- $\text{CH}_3$ ), 2.05 (s, 6H,  $-\text{CH}_3$ ), 1.03 (s, 6H, Si- $\text{CH}_3$ ), -1.35 (s, 6H, Zr- $\text{CH}_3$ ).  $^{13}\text{C}\{^1\text{H}\}$  NMR (100 MHz,  $\text{CD}_2\text{Cl}_2$ )  $\delta$  156.2, 141.0, 138.5, 133.2, 130.6, 130.0, 128.9, 126.7, 125.8, 120.9, 115.8, 101.9, 81.3, 40.0, 21.7, 17.3, 6.2.

2. Synthesis –  $^1\text{H}$  NMR and  $^{13}\text{C}$  NMR spectra



Figure S5. <sup>1</sup>H NMR spectrum (400 MHz) spectrum of **2-Hf** in CD<sub>2</sub>Cl<sub>2</sub>. Traces of grease are visible.<sup>2</sup>Figure S6. <sup>13</sup>C {<sup>1</sup>H} NMR spectrum (100 MHz) of **2-Hf** in CD<sub>2</sub>Cl<sub>2</sub>.<sup>2</sup>

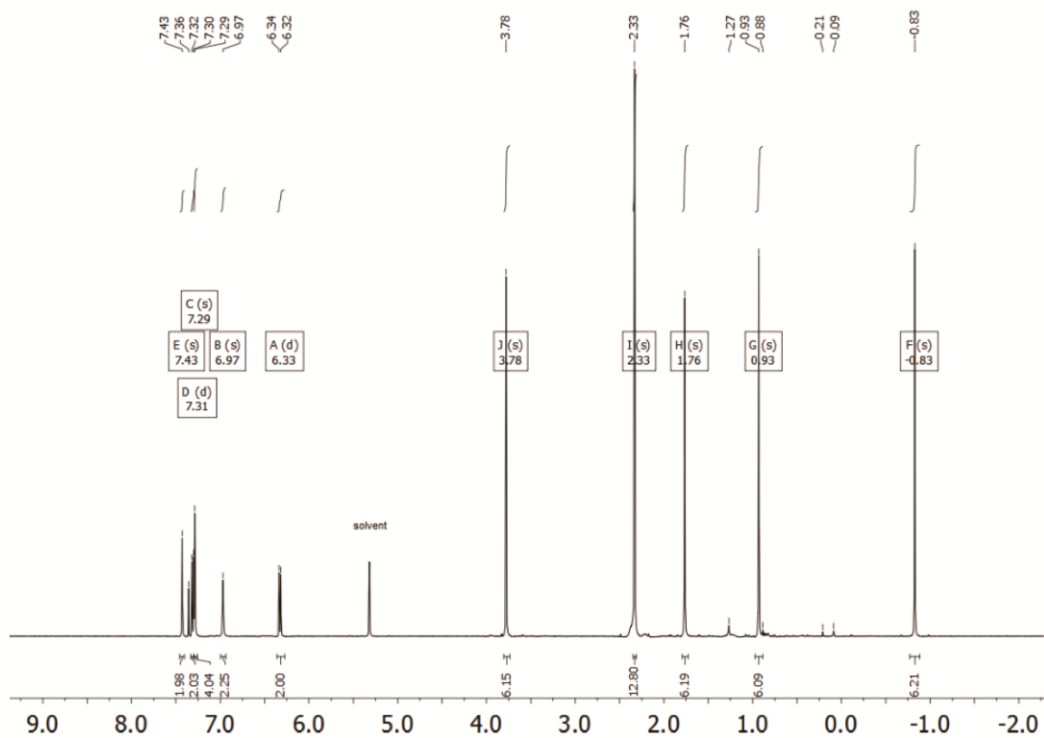


Figure S7.  $^1\text{H}$  NMR spectrum (400 MHz) of **3-Ti** in  $\text{CD}_2\text{Cl}_2$ . Traces of benzene, *n*-pentane and grease are visible.<sup>1</sup>

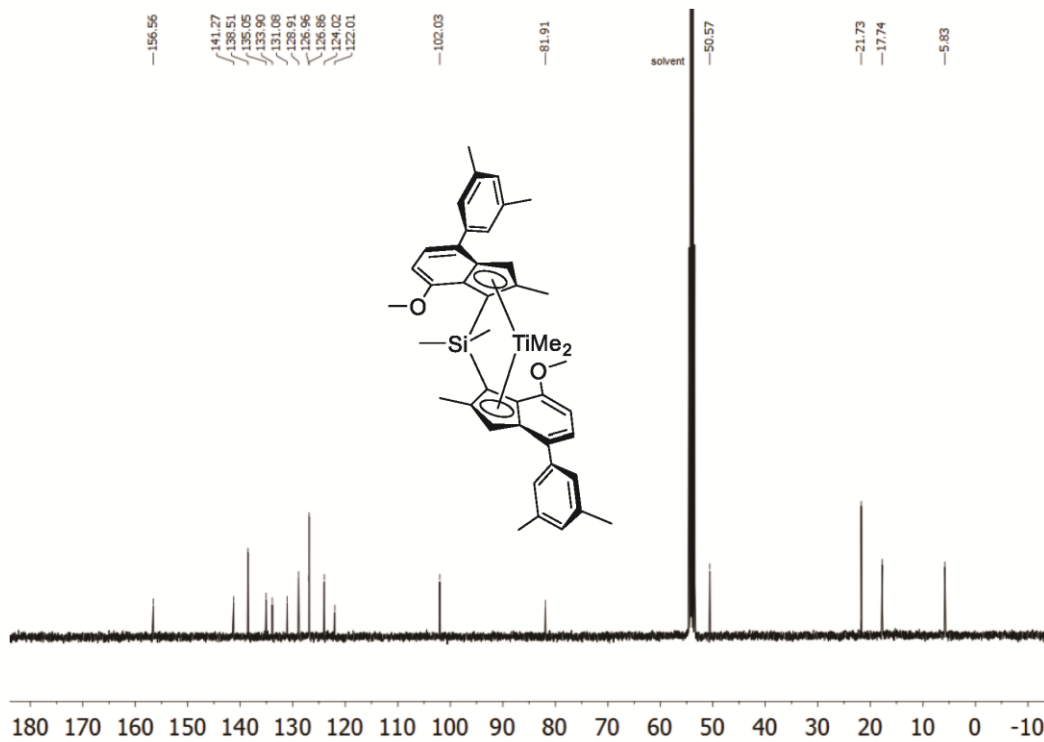
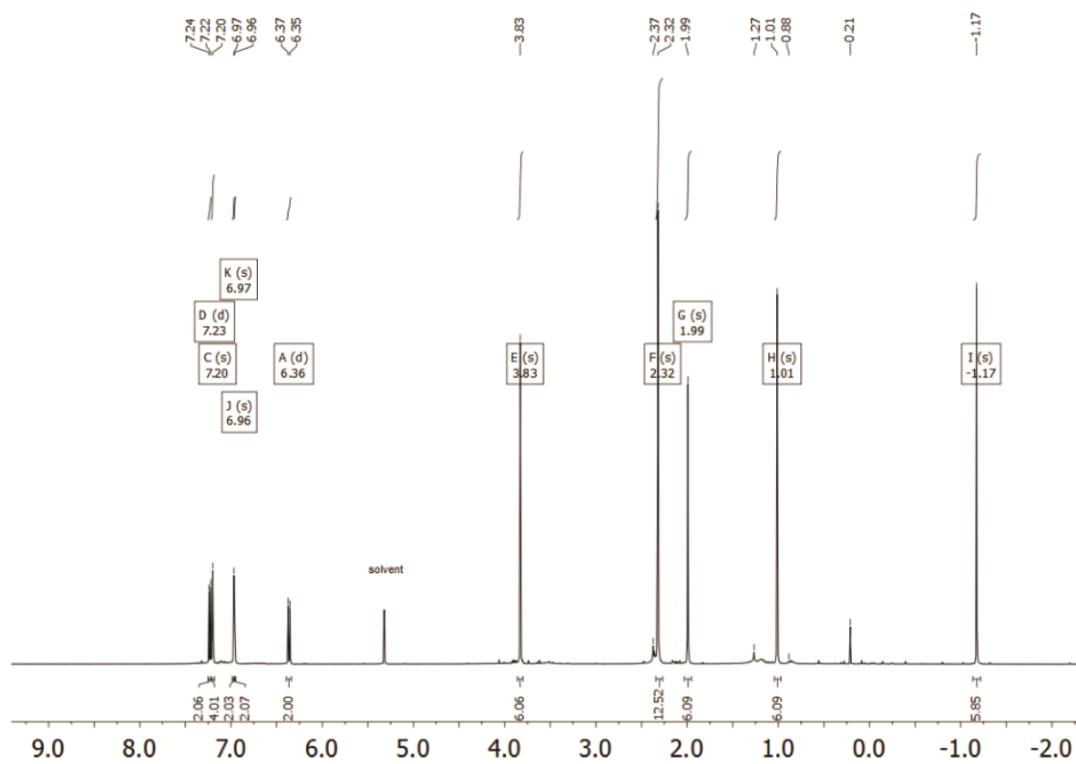
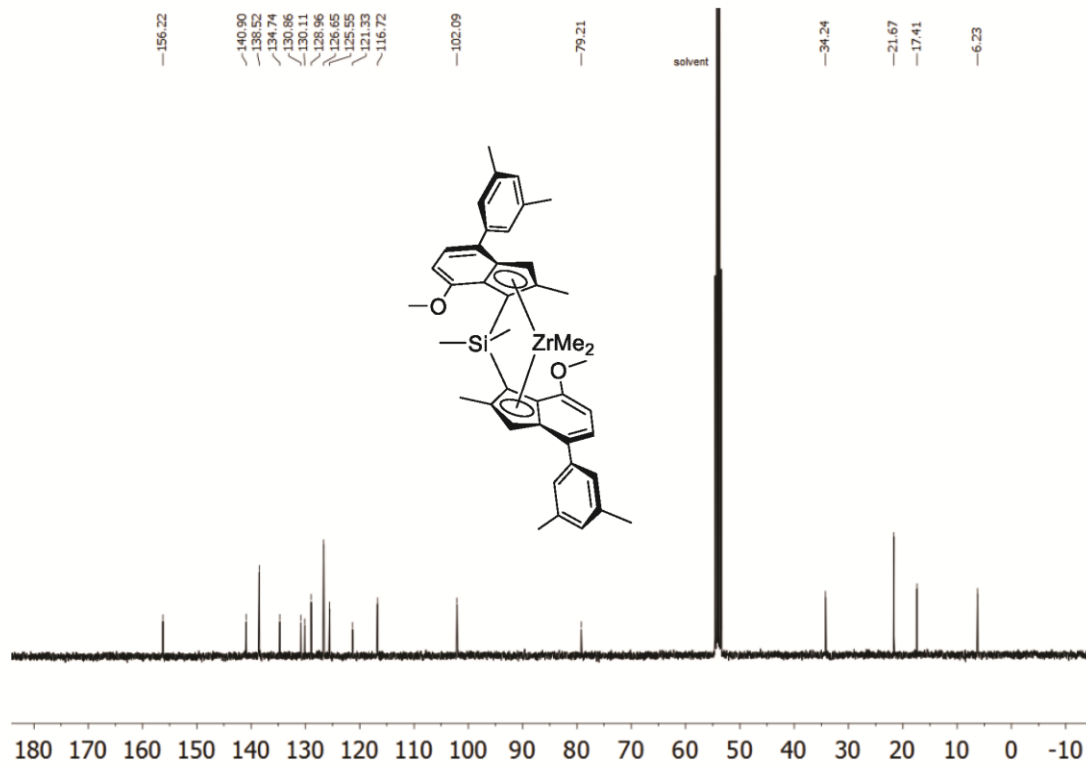
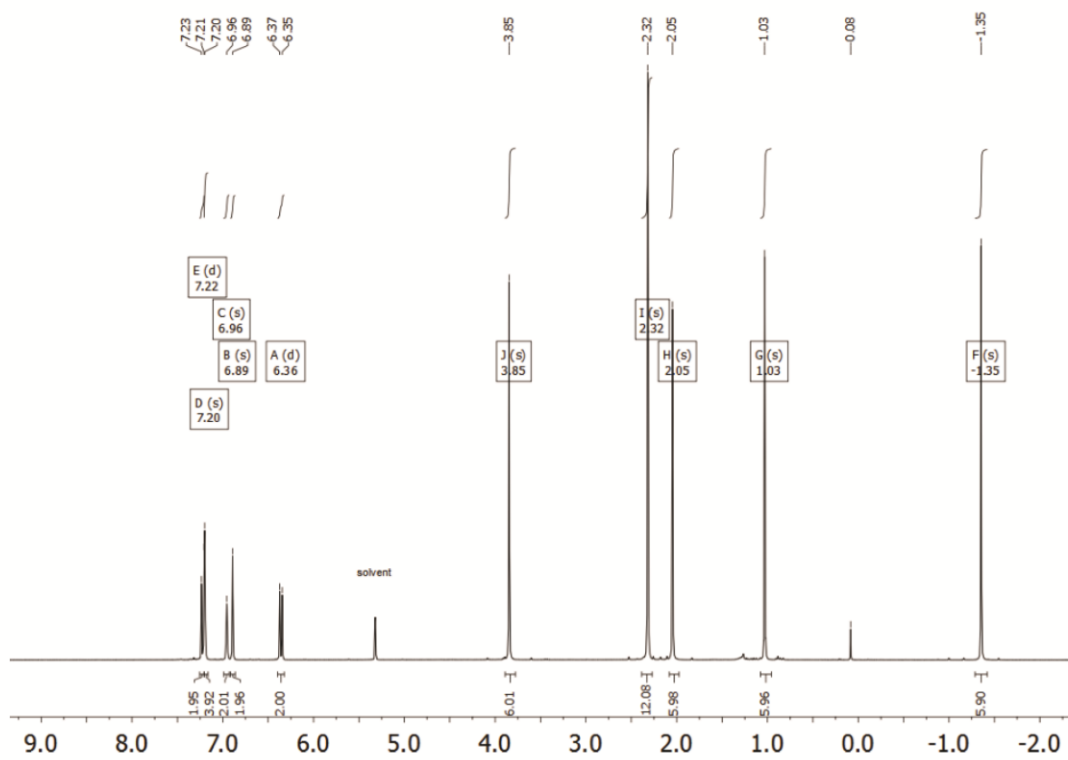
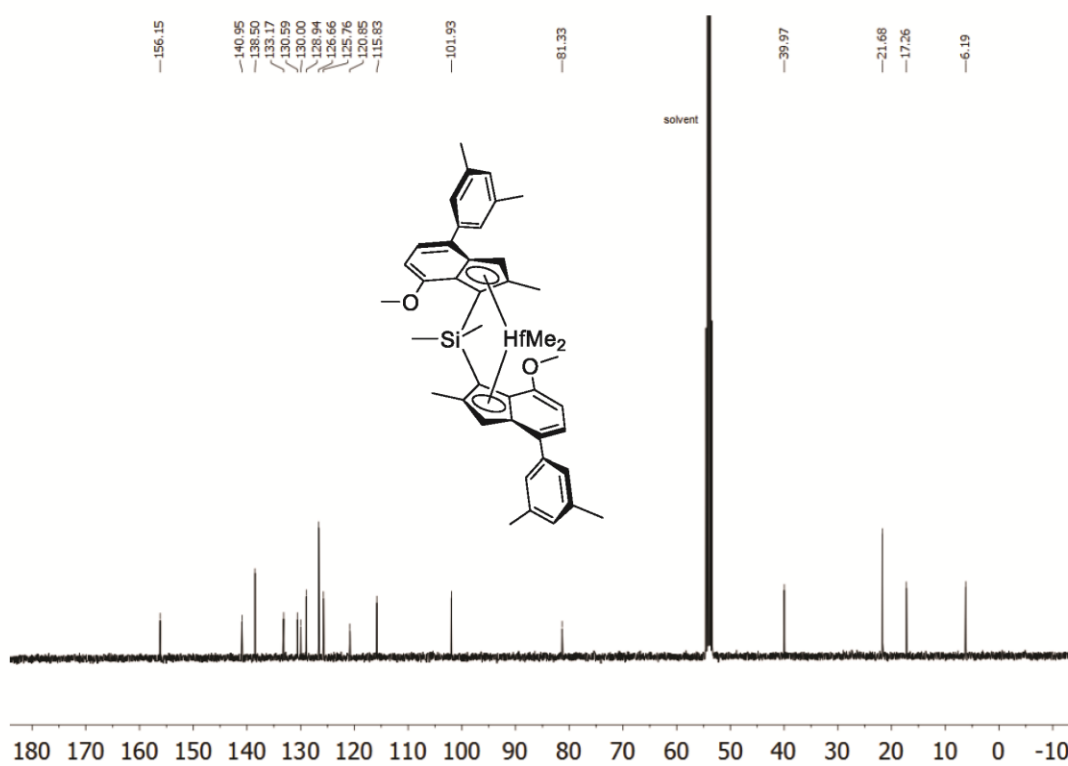


Figure S8.  $^{13}\text{C} \{^1\text{H}\}$  NMR spectrum (100 MHz) of **3-Ti** in  $\text{CD}_2\text{Cl}_2$ .<sup>1</sup>

Figure S9.  $^1\text{H}$  NMR spectrum (400 MHz) of 3-Zr in  $\text{CD}_2\text{Cl}_2$ . Traces of *n*-pentane and toluene are visible.Figure S10.  $^{13}\text{C}$   $\{^1\text{H}\}$  NMR spectrum (100 MHz) of 3-Zr in  $\text{CD}_2\text{Cl}_2$ .

Figure S11.  $^1\text{H}$  NMR spectrum (400 MHz) of **3-Hf** in  $\text{CD}_2\text{Cl}_2$ . Traces of *n*-pentane and grease are visible.Figure S12.  $^{13}\text{C}$   $\{^1\text{H}\}$  NMR spectrum (100 MHz) of **3-Hf** in  $\text{CD}_2\text{Cl}_2$ .

## 3. Kinetic measurements

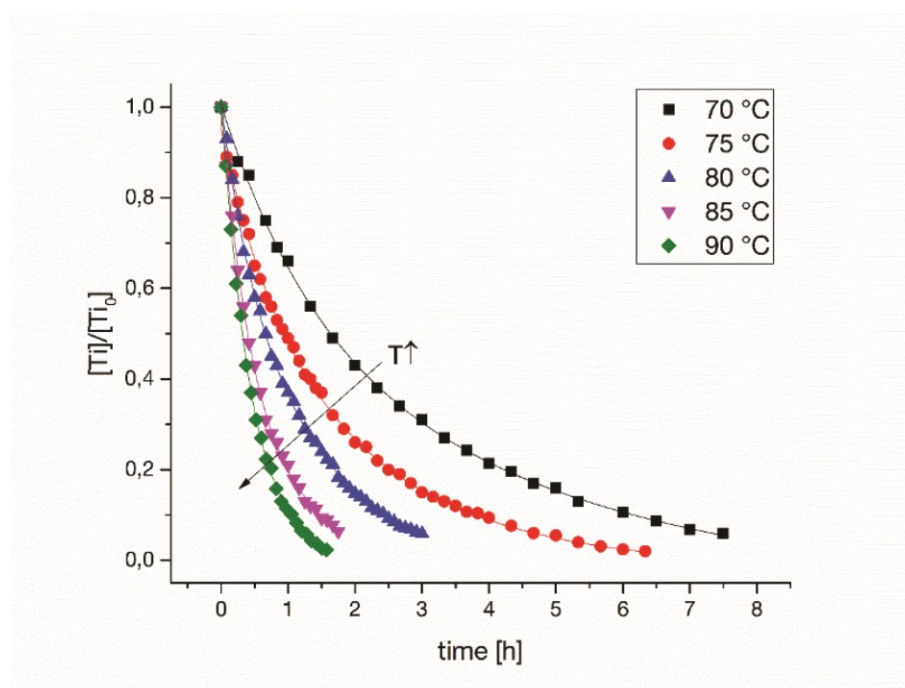


Figure S13. Decay of the  $\text{Ti}(\text{CH}_3)_2$  signal in a reaction pseudo first order with 100 eq.  $t\text{BuOH}$  at elevated temperatures monitored *via*  $^1\text{H}$  NMR spectroscopy.

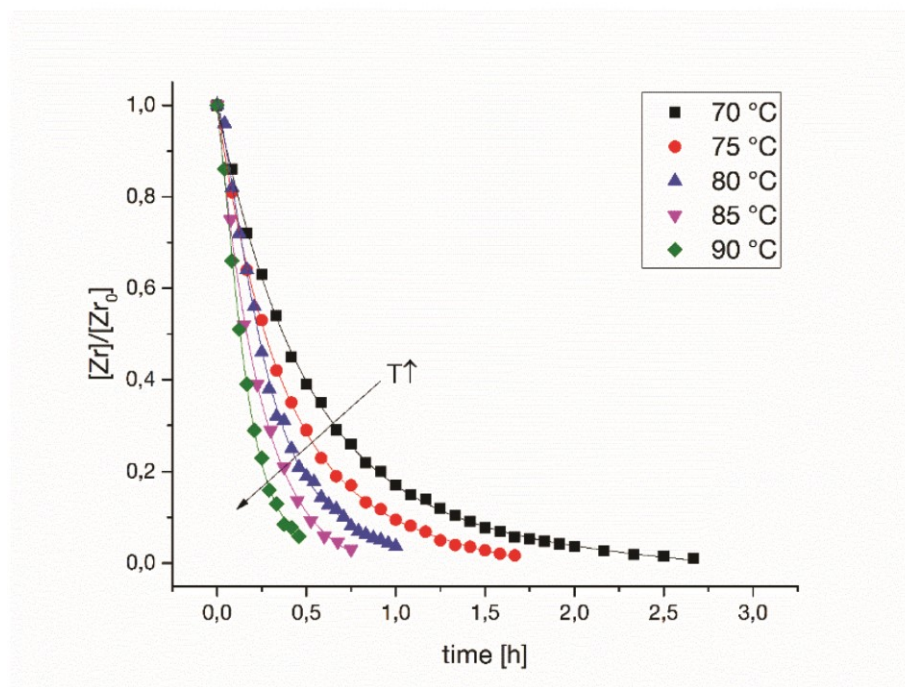


Figure S14. Decay of the  $\text{Zr}(\text{CH}_3)_2$  signal in a reaction pseudo first order with 100 eq.  $t\text{BuOH}$  at elevated temperatures monitored *via*  $^1\text{H}$  NMR spectroscopy.

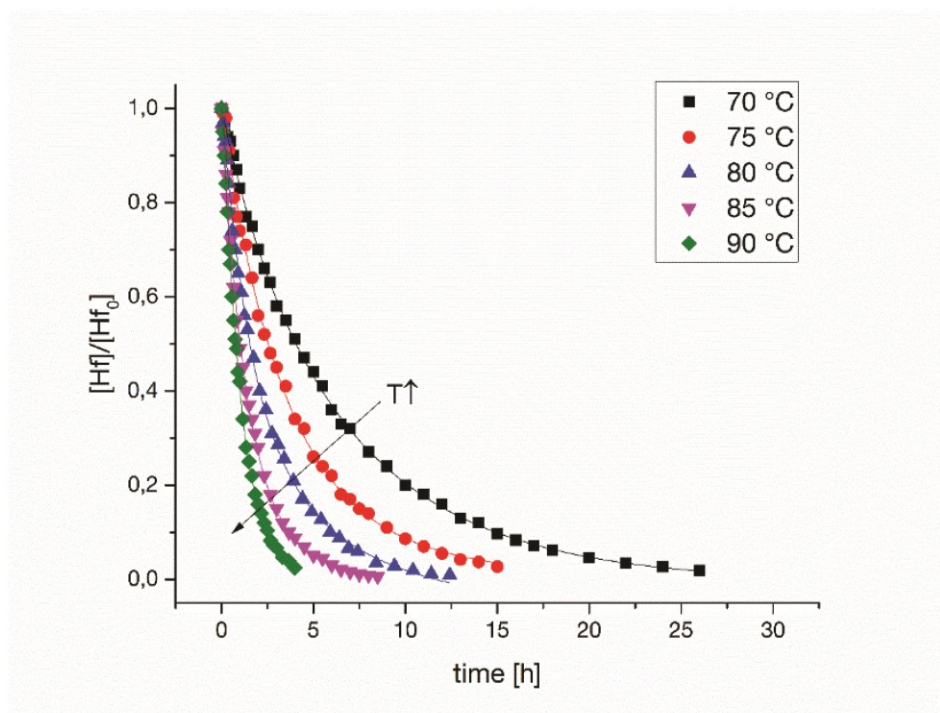


Figure S15. Decay of the  $\text{Hf}(\text{CH}_3)_2$  signal in a reaction pseudo first order with 100 eq.  $t\text{BuOH}$  at elevated temperatures monitored *via*  $^1\text{H}$  NMR spectroscopy.

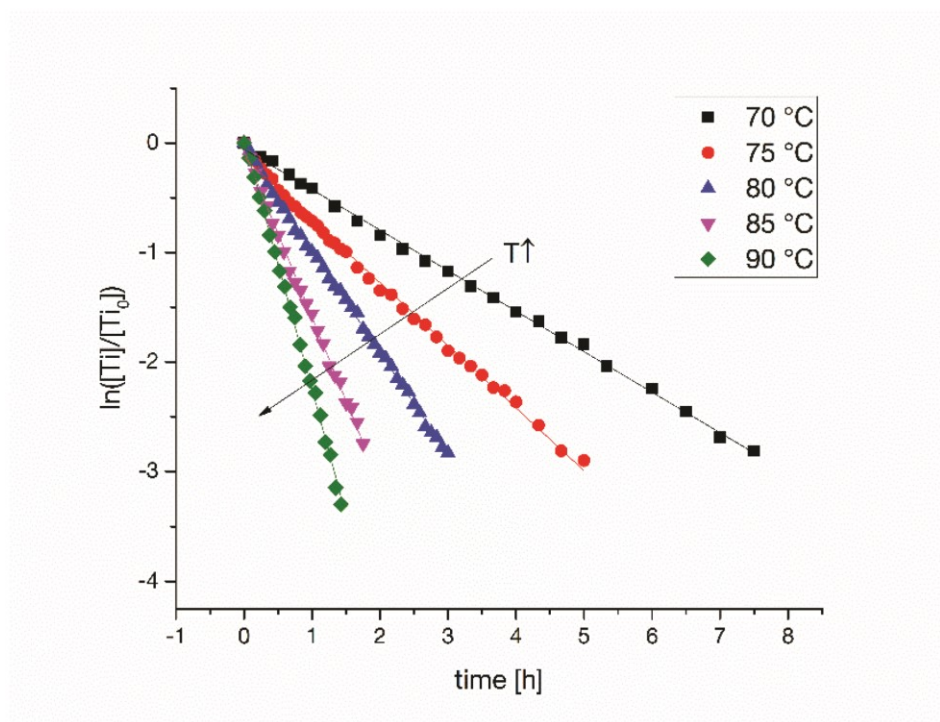
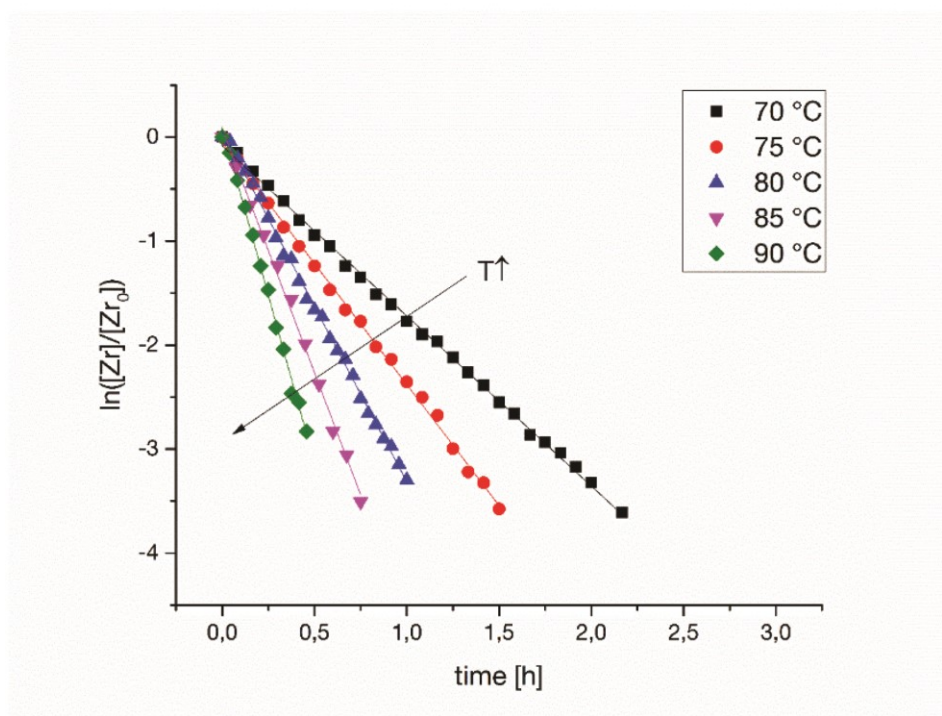
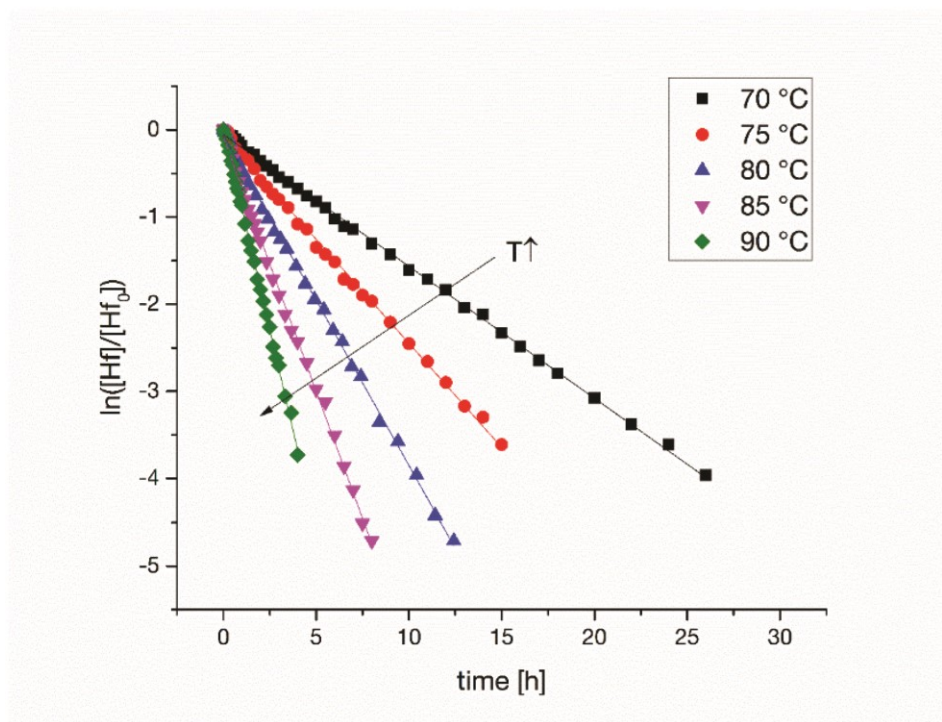


Figure S16. Logarithmic plot of the  $\text{Ti}(\text{CH}_3)_2$  signal as a function of reaction time.

Figure S17. Logarithmic plot of the  $Zr(CH_3)_2$  signal as a function of reaction time.Figure S18. Logarithmic plot of the  $Hf(CH_3)_2$  signal as a function of reaction time.

**Table S1. Determined rate constants of the logarithmic plots.**

<i>Complex</i>	<i>Temperature [°C]</i>	<i>Rate constant<sup>a</sup> [s<sup>-1</sup>]</i>	<i>Deviation<sup>b</sup> [s<sup>-1</sup>]</i>
<b>3-Ti</b>	70	1.03 E-4	8.72 E-7
<b>3-Ti</b>	75	1.63 E-4	1.29 E-6
<b>3-Ti</b>	80	2.59 E-4	2.49 E-6
<b>3-Ti</b>	85	4.24 E-4	5.01 E-6
<b>3-Ti</b>	90	6.54 E-4	8.67 E-6
<b>3-Zr</b>	70	4.56 E-4	2.98 E-6
<b>3-Zr</b>	75	6.58 E-4	6.95 E-6
<b>3-Zr</b>	80	9.41 E-4	8.60 E-6
<b>3-Zr</b>	85	1.30 E-3	2.56 E-5
<b>3-Zr</b>	90	1.79 E-3	3.55 E-5
<b>3-Hf</b>	70	4.21 E-5	2.18 E-7
<b>3-Hf</b>	75	6.64 E-5	5.85 E-7
<b>3-Hf</b>	80	1.05 E-4	6.97 E-7
<b>3-Hf</b>	85	1.63 E-4	1.23 E-6
<b>3-Hf</b>	90	2.57 E-4	1.75 E-6

<sup>a</sup>Slope of the logarithmic plots. <sup>b</sup>Determined by the square root of reduced chi square.

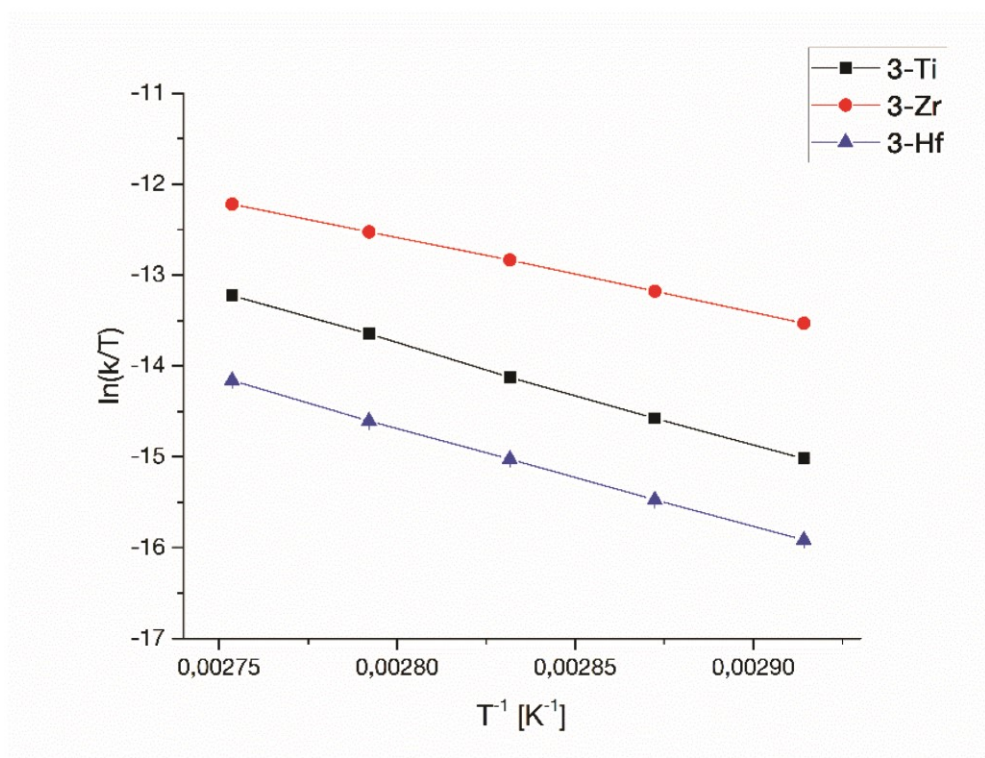


Figure S19. Eyring plots of the reaction of **3-Ti**, **3-Zr** and **3-Hf** with *t*-BuOH between 70 °C and 90 °C.

**Table S2. Enthalpy and entropy of activation determined by the Eyring equation.**

Complex	Enthalpy [kJ·mol <sup>-1</sup> ]	Entropy [J·(mol·K) <sup>-1</sup> ]
<b>3-Ti</b>	93.3 ± 1.3	-50.7 ± 3.7
<b>3-Zr</b>	67.9 ± 0.7	-112 ± 1.9
<b>3-Hf</b>	90.5 ± 0.7	-66.3 ± 2.0

4. UV VIS spectra for the prealkylation of complexes **2** with 200 eq. of TIBA

UV VIS spectra were recorded using a Varian Cary 50 spectrophotometer with a sealed UV quartz cuvette (1 mm). A  $8.0 \cdot 10^{-4}$  M complex solution (**2**) was measured first. Subsequently 200 eq. 1.1 M TIBA solution in toluene were added. The reaction of **2-Zr** and **2-Hf** with TIBA is monitored at 60 °C for one hour *via* UV Vis spectroscopy. In both cases the initial absorbance maxima is significantly shifted to lower wavelength indicating an increase of the HOMO-LUMO gap. This observation suggests a substitution reaction between chloride and alkyl substituents (Figure S20-S21).

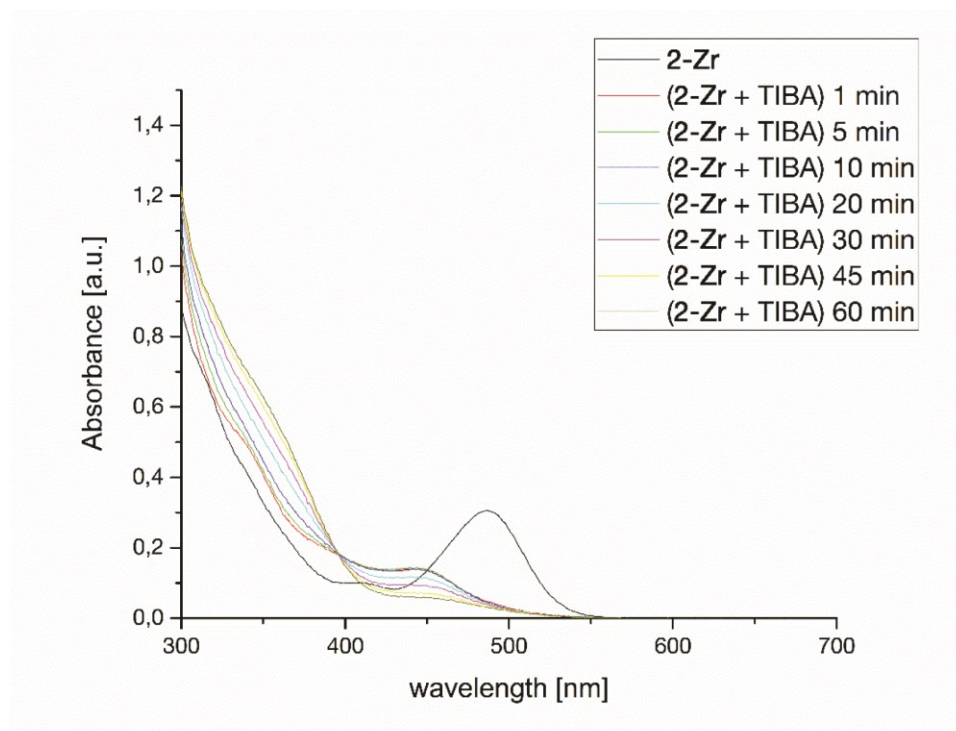


Figure S20. UV VIS spectra of the *in situ* alkylation of **2-Zr** with 200 eq. TIBA at 60 °C.

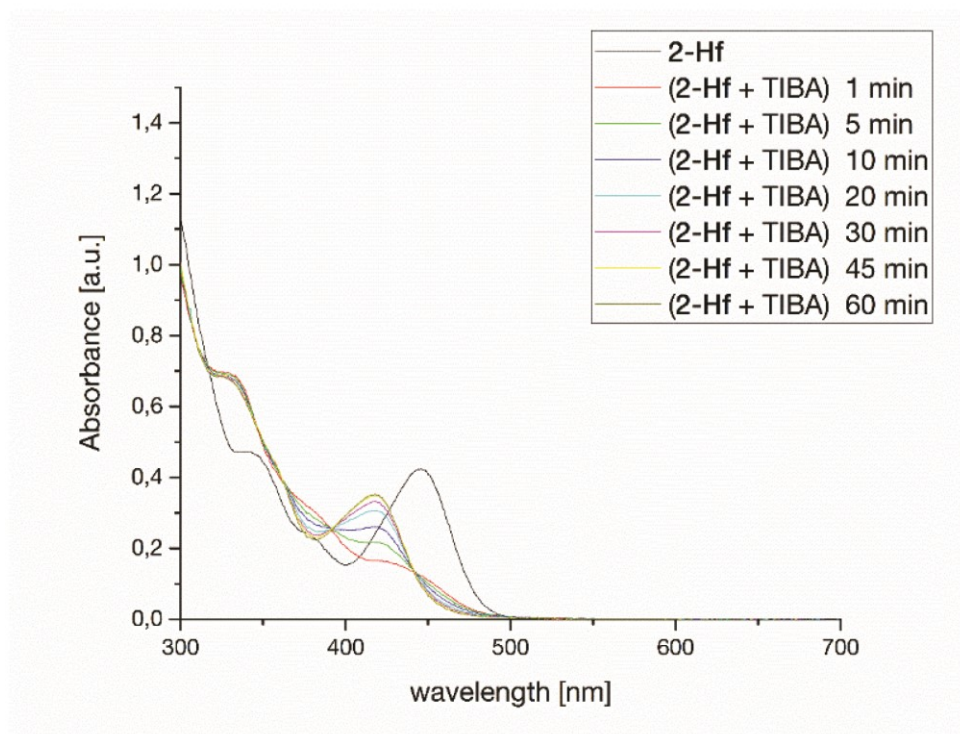


Figure S21. UV VIS spectra of the *in situ* alkylation of 2-Hf with 200 eq. TIBA at 60 °C.<sup>2</sup>

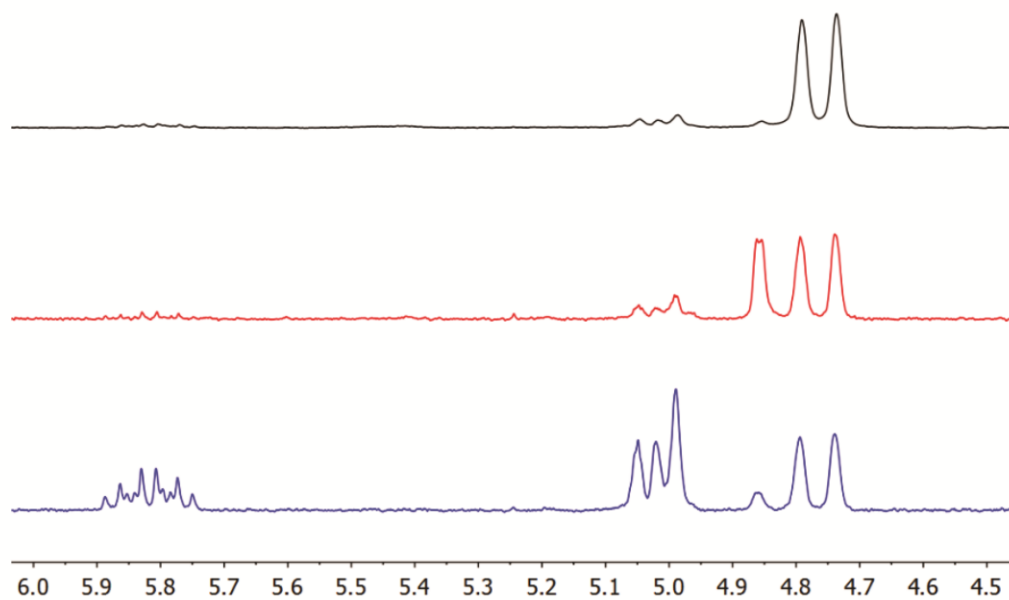
5. Olefinic end group analysis *via*  $^1\text{H}$  NMR spectroscopy

Figure S22.  $^1\text{H}$  NMR spectrum (300 MHz) of the polymers produced at 90 °C (entry 5(black), 11(red), 17(blue)) in  $\text{C}_6\text{D}_5\text{Br}$  at 140 °C.

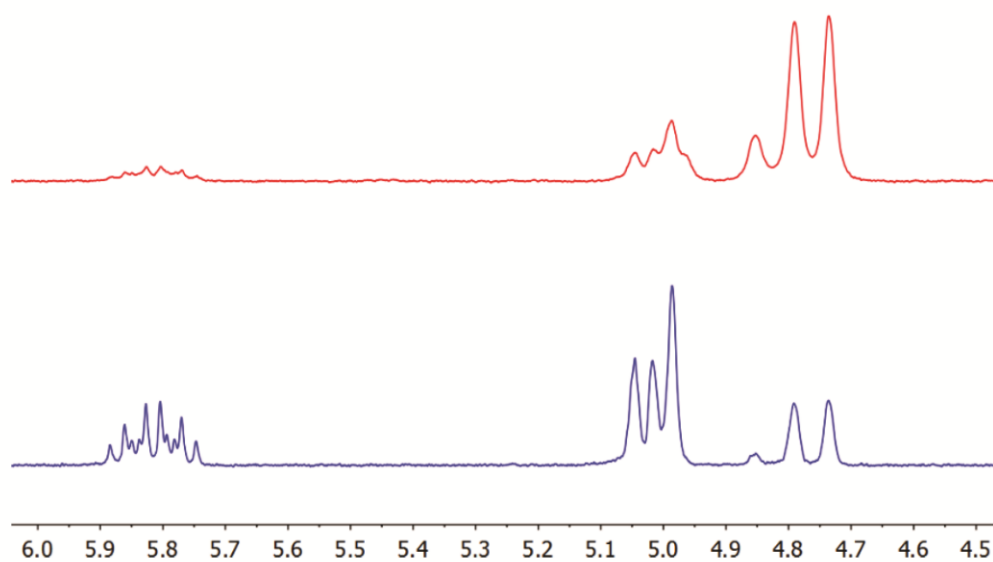


Figure S23.  $^1\text{H}$  NMR spectrum (300 MHz) of the polymers produced at 110 °C (11(red), 17(blue)) in  $\text{C}_6\text{D}_5\text{Br}$  at 140 °C.

6. Tacticity determination *via*  $^{13}\text{C}$   $\{^1\text{H}\}$  NMR spectroscopy

All  $^{13}\text{C}$   $\{^1\text{H}\}$  NMR measurements were conducted in  $\text{C}_6\text{D}_5\text{Br}$  at  $140^\circ\text{C}$ . All chemical shifts are internally referenced on the methyl signal of the isotactic pentad *mmmm* at 21.85 ppm. The tacticity distribution was quantified *via* integration of the methyl region between 22.0 – 19.7 ppm. The relative content of isotactic *mmmm* pentad is reported as mole fraction (in percentage) with respect to all steric pentads.

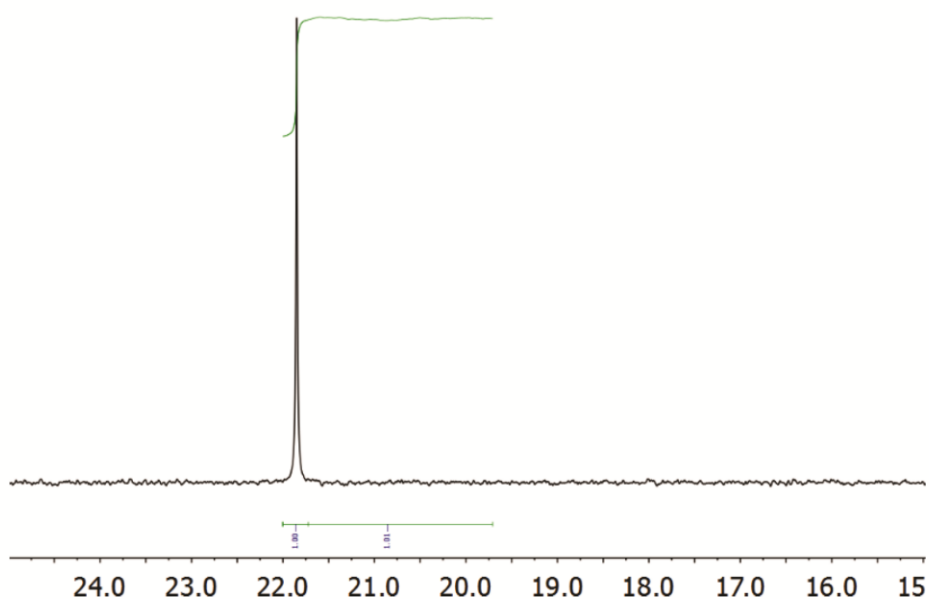


Figure S24. Pentad distribution of entry 3 in the  $^{13}\text{C}$   $\{^1\text{H}\}$  NMR spectrum (75 MHz).

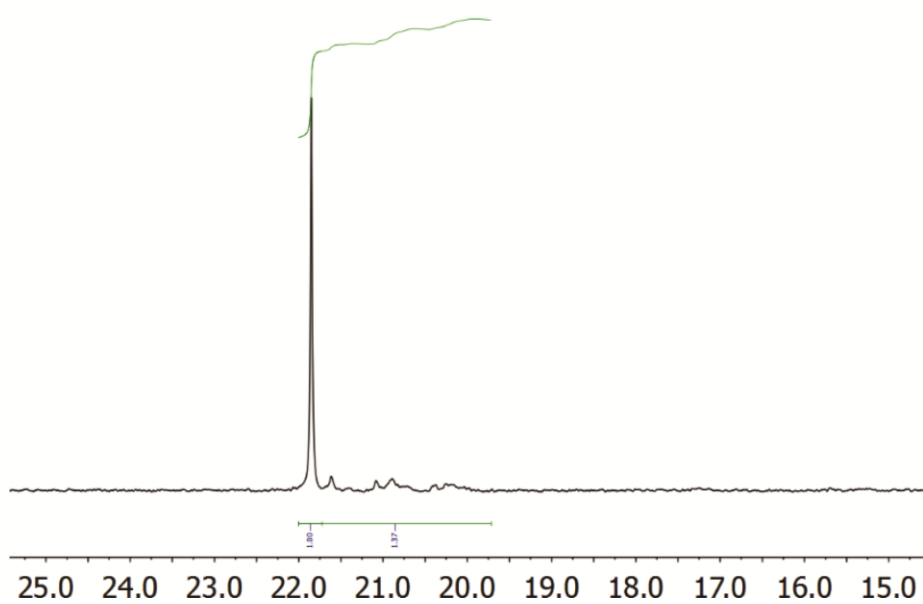


Figure S25. Pentad distribution of entry 4 in the  $^{13}\text{C}$   $\{^1\text{H}\}$  NMR spectrum (75 MHz).

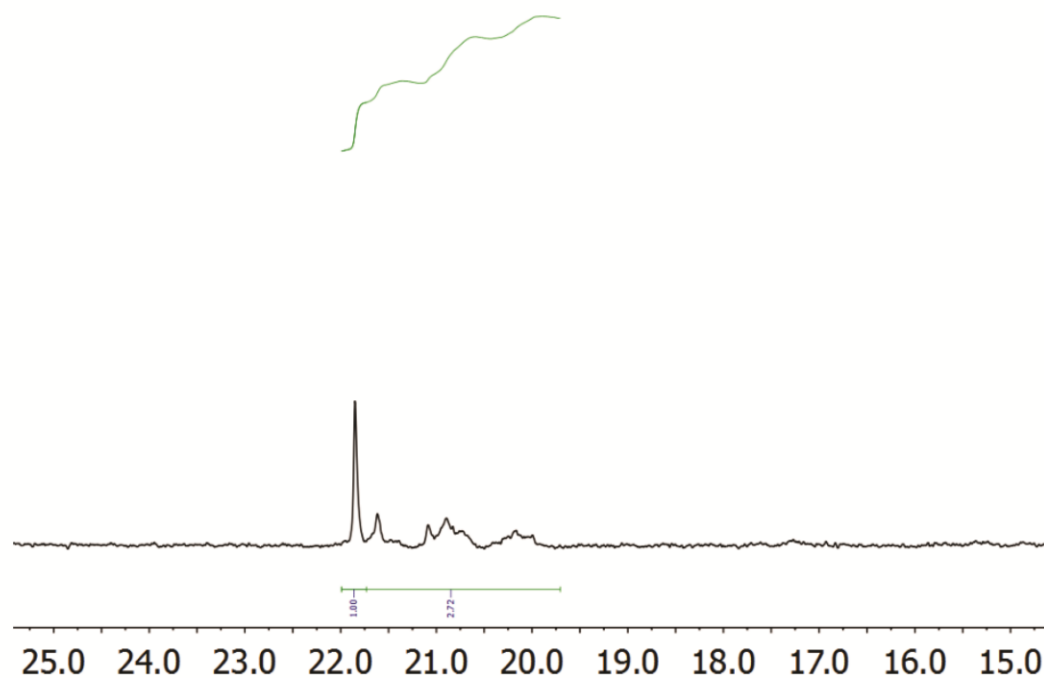


Figure S26. Pentad distribution of entry 5 in the  $^{13}\text{C}$   $\{^1\text{H}\}$  NMR spectrum (75 MHz).

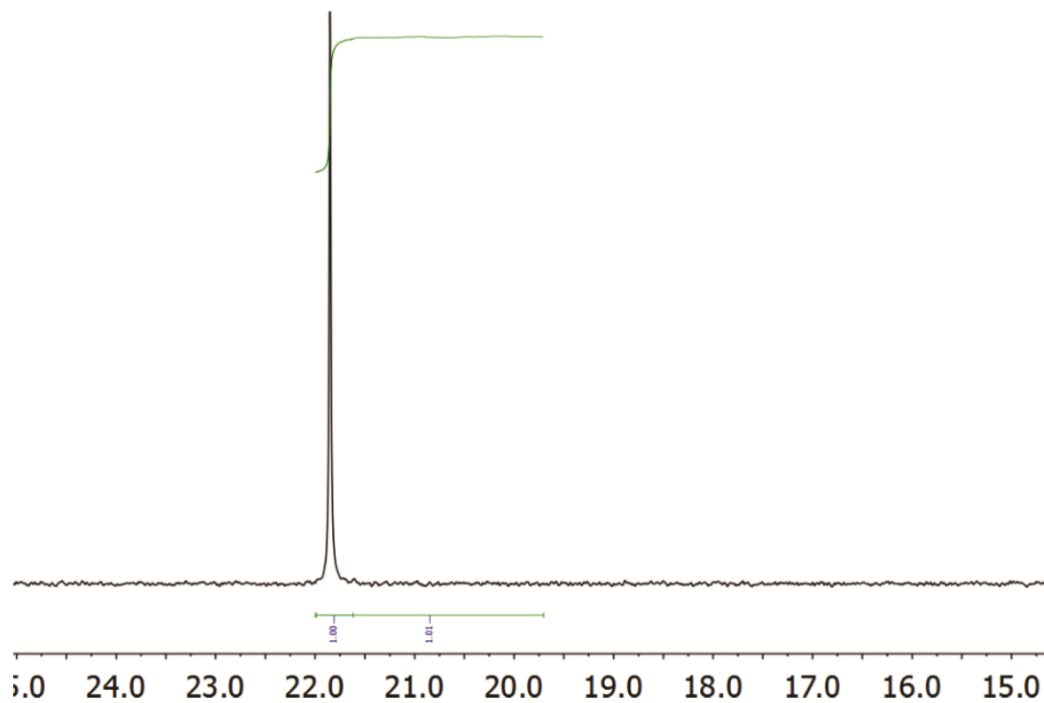


Figure S27. Pentad distribution of entry 9 in the  $^{13}\text{C}$   $\{^1\text{H}\}$  NMR spectrum (75 MHz).

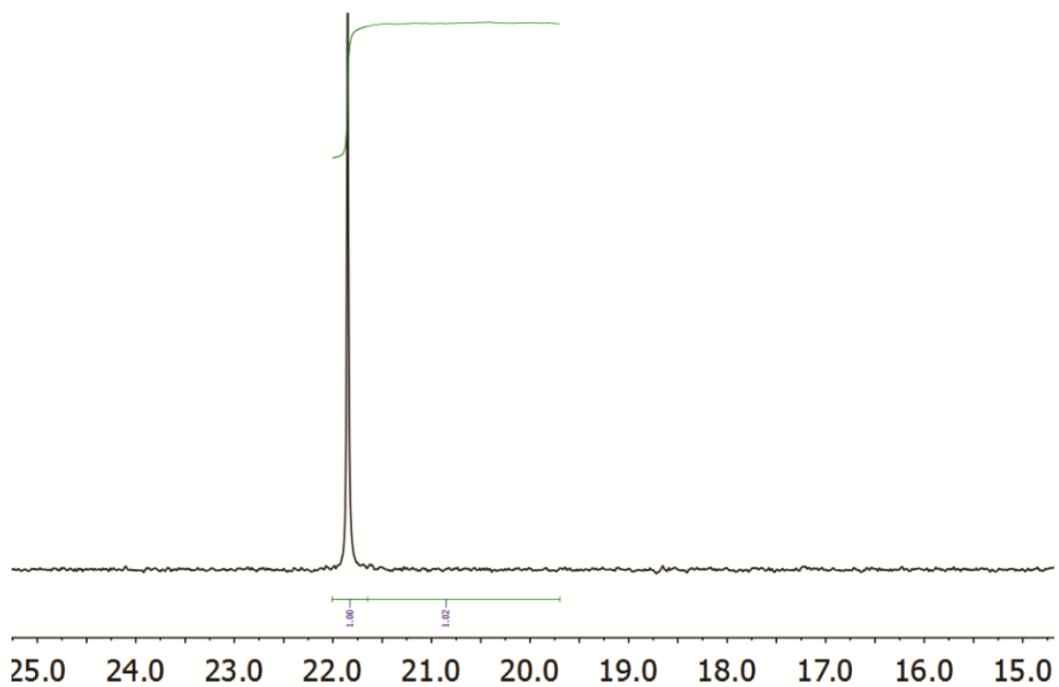


Figure S28. Pentad distribution of entry 10 in the  $^{13}\text{C}$   $\{^1\text{H}\}$  NMR spectrum (75 MHz).

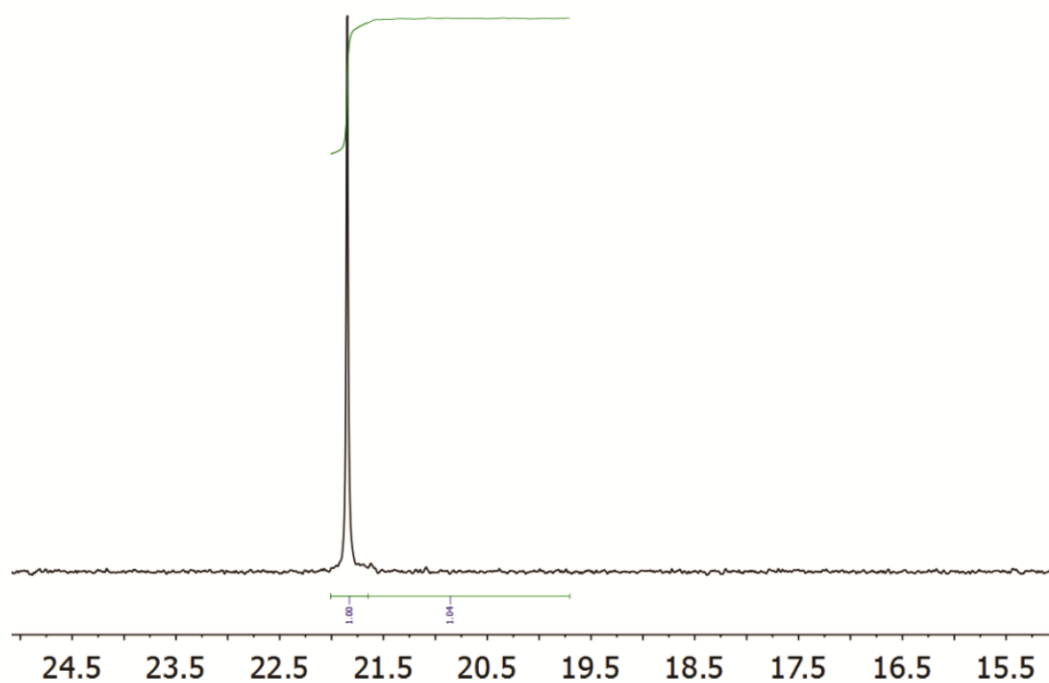


Figure S29. Pentad distribution of entry 11 in the  $^{13}\text{C}$   $\{^1\text{H}\}$  NMR spectrum (75 MHz).

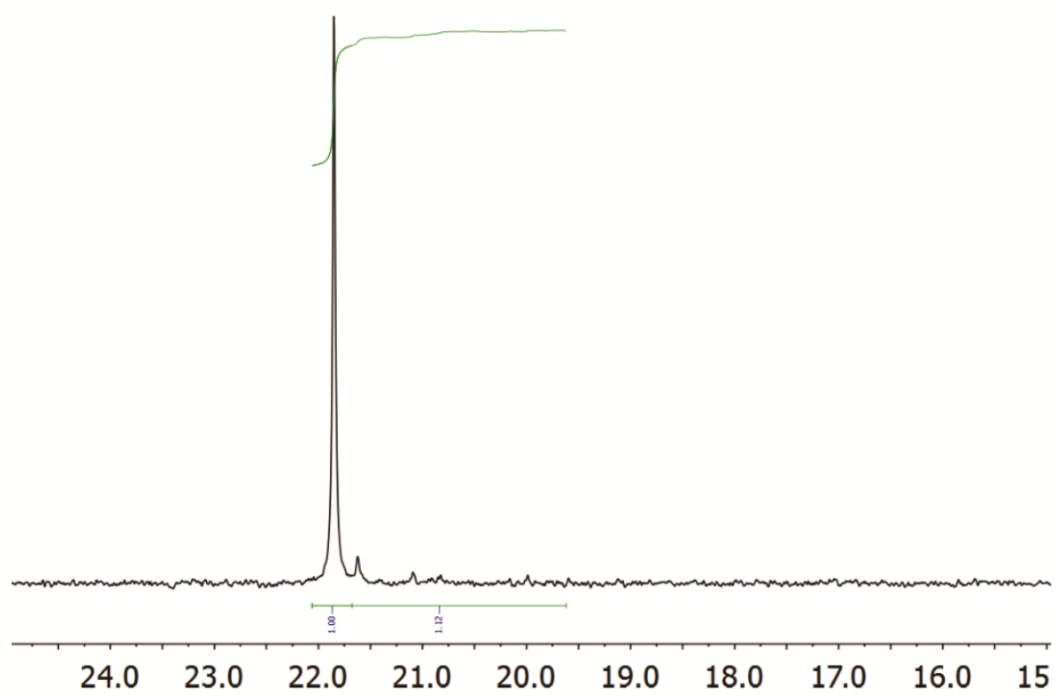


Figure S30. Pentad distribution of entry 12 in the  $^{13}\text{C}$   $\{^1\text{H}\}$  NMR spectrum (75 MHz).



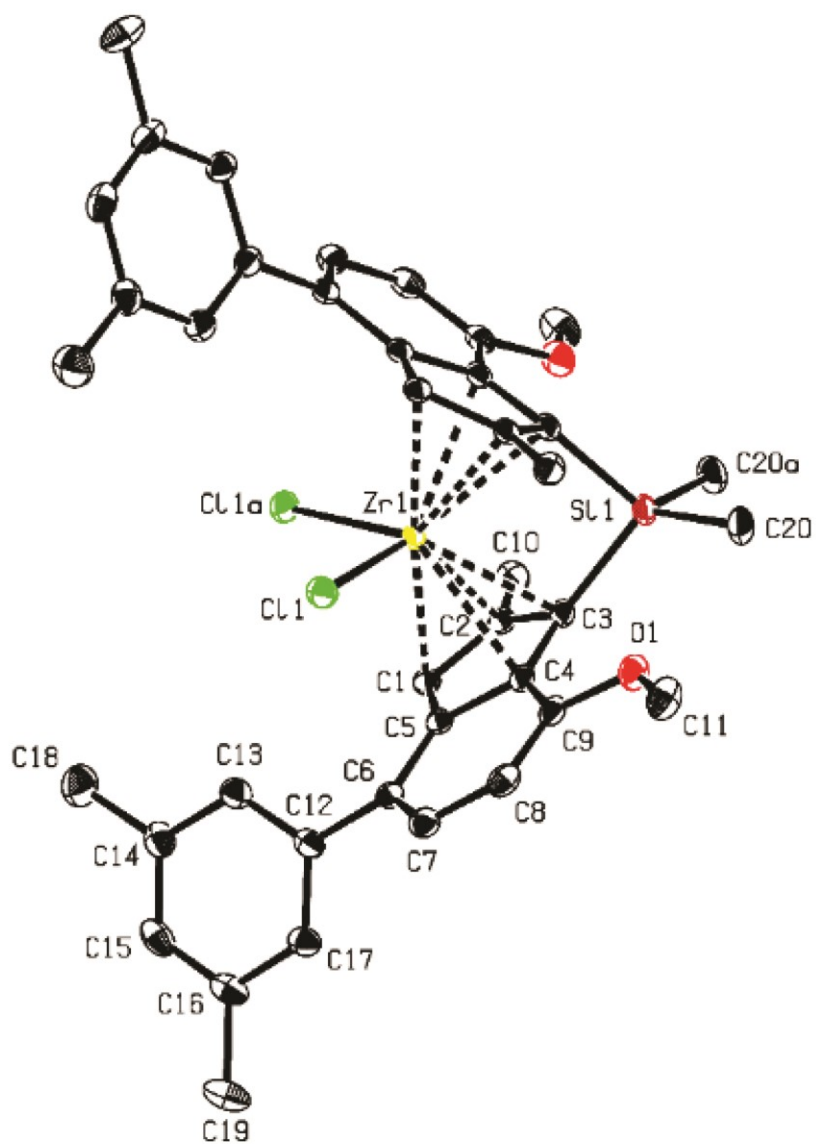


Figure S32. ORTEP style representation of **2-Zr** with ellipsoids drawn at 50 % probability level. Hydrogen atoms are omitted for clarity.

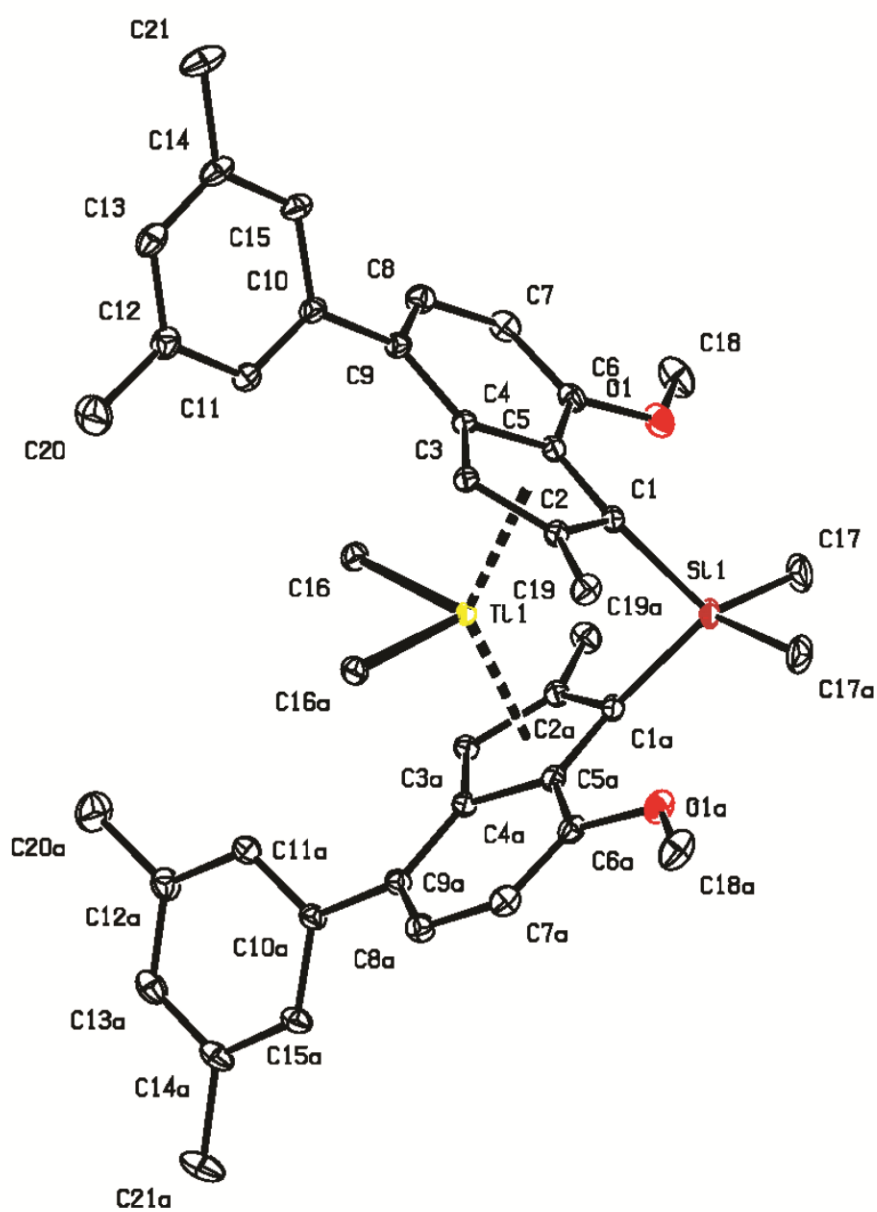


Figure S33. ORTEP style representation of 3-Ti with ellipsoids drawn at 50 % probability level. Hydrogen atoms are omitted for clarity.

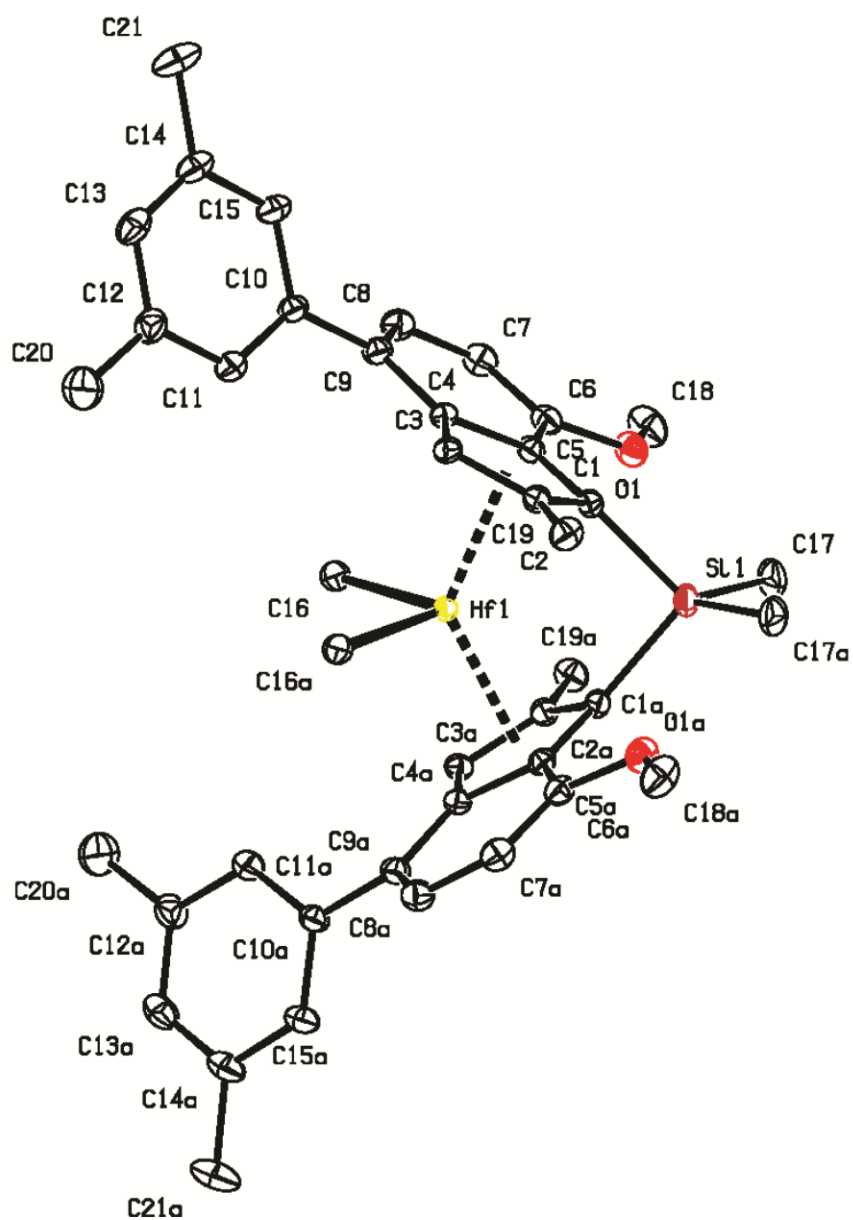


Figure S34. ORTEP style representation of 3-Hf with ellipsoids drawn at 50 % probability level. Hydrogen atoms are omitted for clarity.

## 8. Computational data of 3-Ti, 3-Zr and 3-Hf

Table S3. Optimized geometry for 3-Ti.

Ti	0.000000	0.000000	0.353236	H	-2.151384	-1.158658	4.378929
C	1.178493	1.068003	-1.086679	H	-1.523414	0.043817	5.526636
C	-1.178493	-1.068003	-1.086679	H	-0.753080	-1.550777	5.397291
C	-2.119106	1.353561	0.375459	C	2.126673	4.195180	3.459783
C	2.119106	-1.353561	0.375459	H	1.475650	5.108282	1.237621
C	-1.983047	0.602327	1.561426	C	-2.126673	-4.195180	3.459783
C	1.983047	-0.602327	1.561426	H	-1.475650	-5.108282	1.237621
C	-0.853395	1.095907	2.319822	H	0.159184	5.292885	-0.815693
C	0.853395	-1.095907	2.319822	C	-2.113605	2.670821	-2.612690
C	-0.370108	2.245286	1.575787	C	-2.317115	5.000122	-2.023348
C	0.370108	-2.245286	1.575787	H	-0.159184	-5.292885	-0.815693
C	-1.160845	2.403027	0.369345	C	2.113605	-2.670821	-2.612690
C	1.160845	-2.403027	0.369345	C	2.317115	-5.000122	-2.023348
H	1.855631	1.782489	-0.594400	H	2.963865	4.293089	2.751800
H	-1.855631	-1.782489	-0.594400	H	2.512072	3.917242	4.445489
H	0.513634	1.641400	-1.745380	H	1.592397	5.154552	3.528640
H	-0.513634	-1.641400	-1.745380	H	-2.963865	-4.293089	2.751800
H	1.784840	0.390149	-1.700581	H	-2.512072	-3.917242	4.445489
H	-1.784840	-0.390149	-1.700581	H	-1.592397	-5.154552	3.528640
H	-2.899783	1.205911	-0.362546	C	-2.864069	2.883012	-3.772469
H	2.899783	-1.205911	-0.362546	H	-1.715516	1.675579	-2.415743
C	-2.970410	-0.469551	1.931296	C	-3.077876	5.241872	-3.173098
C	2.970410	0.469551	1.931296	H	-2.122186	5.819727	-1.329591
Si	0.000000	0.000000	3.616598	C	2.864069	-2.883012	-3.772469
C	0.586404	3.260433	1.883411	H	1.715516	-1.675579	-2.415743
C	-0.586404	-3.260433	1.883411	C	3.077876	-5.241872	-3.173098
C	-0.988756	3.513300	-0.515083	H	2.122186	-5.819727	-1.329591
C	0.988756	-3.513300	-0.515083	C	-3.341079	4.174370	-4.038012
H	-2.504402	-1.394219	2.285794	C	-3.135416	1.753840	-4.736690
H	-3.597226	-0.714192	1.065545	C	-3.633425	6.617899	-3.450184
H	-3.632803	-0.107630	2.732092	C	3.341079	-4.174370	-4.038012
H	2.504402	1.394219	2.285794	C	3.135416	-1.753840	-4.736690
H	3.597226	0.714192	1.065545	C	3.633425	-6.617899	-3.450184
H	3.632803	0.107630	2.732092	H	-3.931303	4.351380	-4.940445
C	1.241050	0.752720	4.821519	H	-2.599749	1.906944	-5.685276
C	-1.241050	-0.752720	4.821519	H	-4.205240	1.684047	-4.978657
O	1.240966	3.140630	3.078863	H	-2.815283	0.789119	-4.324982
C	0.756513	4.324021	1.013071	H	-2.935291	7.404001	-3.133825
O	-1.240966	-3.140630	3.078863	H	-4.575284	6.780020	-2.904014
C	-0.756513	-4.324021	1.013071	H	-3.845162	6.756533	-4.518002
C	-0.017548	4.437137	-0.164018	H	3.931303	-4.351380	-4.940445
C	-1.821433	3.720655	-1.723249	H	2.599749	-1.906944	-5.685276
C	0.017548	-4.437137	-0.164018	H	4.205240	-1.684047	-4.978657
C	1.821433	-3.720655	-1.723249	H	2.815283	-0.789119	-4.324982
H	2.151384	1.158658	4.378929	H	2.935291	-7.404001	-3.133825
H	1.523414	-0.043817	5.526636	H	4.575284	-6.780020	-2.904014
H	0.753080	1.550777	5.397291	H	3.845162	-6.756533	-4.518002

Table S4. Optimized geometry for 3-Zr.

Zr	0.000000	0.000000	0.248025	H	2.152156	1.155691	4.350385
C	-1.324639	-1.130339	-1.211982	H	1.515147	-0.042636	5.497739
C	1.324639	1.130339	-1.211982	H	0.748218	1.553396	5.357995
C	2.179893	-1.442079	0.397224	C	-2.242128	-4.134643	3.373773
C	-2.179893	1.442079	0.397224	H	-1.561642	-5.074250	1.174108
C	2.037072	-0.683963	1.578815	C	2.242128	4.134643	3.373773
C	-2.037072	0.683963	1.578815	H	1.561642	5.074250	1.174108
C	0.868328	-1.130734	2.311728	H	-0.199544	-5.309099	-0.844515
C	-0.868328	1.130734	2.311728	C	2.167284	-2.755870	-2.603407
C	0.365411	-2.269653	1.554813	C	2.329463	-5.081897	-1.988013
C	-0.365411	2.269653	1.554813	H	0.199544	5.309099	-0.844515
C	1.179394	-2.455574	0.365874	C	-2.167284	2.755870	-2.603407
C	-1.179394	2.455574	0.365874	C	-2.329463	5.081897	-1.988013
H	-2.069112	-1.775873	-0.721405	H	-3.062917	-4.216513	2.644755
H	2.069112	1.775873	-0.721405	H	-2.646406	-3.840690	4.347218
H	-0.709318	-1.779393	-1.853030	H	-1.735497	-5.107262	3.462937
H	0.709318	1.779393	-1.853030	H	3.062917	4.216513	2.644755
H	-1.874062	-0.431951	-1.861772	H	2.646406	3.840690	4.347218
H	1.874062	0.431951	-1.861772	H	1.735497	5.107262	3.462937
H	2.985189	-1.325193	-0.320272	C	2.939213	-2.987921	-3.744976
H	-2.985189	1.325193	-0.320272	H	1.778061	-1.753867	-2.422673
C	3.036724	0.373148	1.961035	C	3.112409	-5.343469	-3.118732
C	-3.036724	-0.373148	1.961035	H	2.109112	-5.891806	-1.290506
Si	0.000000	0.000000	3.581361	C	-2.939213	2.987921	-3.744976
C	-0.633009	-3.252983	1.836204	H	-1.778061	1.753867	-2.422673
C	0.633009	3.252983	1.836204	C	-3.112409	5.343469	-3.118732
C	0.991342	-3.562632	-0.521510	H	-2.109112	5.891806	-1.290506
C	-0.991342	3.562632	-0.521510	C	3.406797	-4.287511	-3.987290
H	2.579578	1.322354	2.260261	C	3.240943	-1.872783	-4.716296
H	3.710716	0.570578	1.119151	C	3.655673	-6.729037	-3.370613
H	3.648576	0.024354	2.806130	C	-3.406797	4.287511	-3.987290
H	-2.579578	-1.322354	2.260261	C	-3.240943	1.872783	-4.716296
H	-3.710716	-0.570578	1.119151	C	-3.655673	6.729037	-3.370613
H	-3.648576	-0.024354	2.806130	H	4.015024	-4.479932	-4.874401
C	-1.239083	-0.752464	4.788682	H	2.682206	-2.005015	-5.654876
C	1.239083	0.752464	4.788682	H	4.308011	-1.848350	-4.977442
O	-1.319640	-3.106278	3.010333	H	2.967897	-0.894622	-4.302356
C	-0.811180	-4.315250	0.966042	H	2.914741	-7.501595	-3.125623
O	1.319640	3.106278	3.010333	H	4.543854	-6.923245	-2.750221
C	0.811180	4.315250	0.966042	H	3.951650	-6.858491	-4.419173
C	-0.012575	-4.457526	-0.190397	H	-4.015024	4.479932	-4.874401
C	1.844227	-3.793812	-1.710783	H	-2.682206	2.005015	-5.654876
C	0.012575	4.457526	-0.190397	H	-4.308011	1.848350	-4.977442
C	-1.844227	3.793812	-1.710783	H	-2.967897	0.894622	-4.302356
H	-2.152156	-1.155691	4.350385	H	-2.914741	7.501595	-3.125623
H	-1.515147	0.042636	5.497739	H	-4.543854	6.923245	-2.750221
H	-0.748218	-1.553396	5.357995	H	-3.951650	6.858491	-4.419173

Table S5. Optimized geometry for 3-Hf.

Hf	0.000000	0.000000	0.222116	H	-2.158623	-1.144455	4.328839
C	1.271028	1.120314	-1.247690	H	-1.514931	0.050344	5.476090
C	-1.271028	-1.120314	-1.247690	H	-0.757485	-1.550408	5.337591
C	-2.157109	1.428497	0.357122	C	2.217300	4.145562	3.382077
C	2.157109	-1.428497	0.357122	H	1.553149	5.084369	1.174975
C	-2.019110	0.668791	1.541095	C	-2.217300	-4.145562	3.382077
C	2.019110	-0.668791	1.541095	H	-1.553149	-5.084369	1.174975
C	-0.863903	1.127263	2.286512	H	0.202809	5.317307	-0.851932
C	0.863903	-1.127263	2.286512	C	-2.149233	2.759538	-2.630007
C	-0.360200	2.267194	1.533886	C	-2.321546	5.082170	-2.004145
C	0.360200	-2.267194	1.533886	H	-0.202809	-5.317307	-0.851932
C	-1.165703	2.450168	0.338405	C	2.149233	-2.759538	-2.630007
C	1.165703	-2.450168	0.338405	C	2.321546	-5.082170	-2.004145
H	1.985168	1.805145	-0.762600	H	3.045843	4.232430	2.662535
H	-1.985168	-1.805145	-0.762600	H	2.611855	3.852949	4.359892
H	0.653549	1.738697	-1.916353	H	1.703663	5.114948	3.465881
H	-0.653549	-1.738697	-1.916353	H	-3.045843	-4.232430	2.662535
H	1.860857	0.437054	-1.877782	H	-2.611855	-3.852949	4.359892
H	-1.860857	-0.437054	-1.877782	H	-1.703663	-5.114948	3.465881
H	-2.955417	1.306833	-0.367001	C	-2.923020	2.993337	-3.769839
H	2.955417	-1.306833	-0.367001	H	-1.755629	1.758449	-2.453945
C	-3.017092	-0.394033	1.913715	C	-3.106632	5.345294	-3.133022
C	3.017092	0.394033	1.913715	H	-2.105267	5.889633	-1.302523
S	0.000000	0.000000	3.559907	C	2.923020	-2.993337	-3.769839
C	0.630205	3.256515	1.825907	H	1.755629	-1.758449	-2.453945
C	-0.630205	-3.256515	1.825907	C	3.106632	-5.345294	-3.133022
C	-0.978633	3.562488	-0.543376	H	2.105267	-5.889633	-1.302523
C	0.978633	-3.562488	-0.543376	C	-3.396605	4.291938	-4.006183
H	-2.558691	-1.334115	2.237867	C	-3.222983	1.880442	-4.744277
H	-3.668302	-0.610250	1.058600	C	-3.657323	6.729373	-3.377114
H	-3.653164	-0.038621	2.738032	C	3.396605	-4.291938	-4.006183
H	2.558691	1.334115	2.237867	C	3.222983	-1.880442	-4.744277
H	3.668302	0.610250	1.058600	C	3.657323	-6.729373	-3.377114
H	3.653164	0.038621	2.738032	H	-4.006638	4.485454	-4.891848
C	1.243153	0.746792	4.767662	H	-2.687586	2.031783	-5.693404
C	-1.243153	-0.746792	4.767662	H	-4.294882	1.836486	-4.982576
O	1.305001	3.111916	3.007167	H	-2.921832	0.904749	-4.344293
C	0.809678	4.320660	0.959266	H	-2.919031	7.504322	-3.131598
O	-1.305001	-3.111916	3.007167	H	-4.543964	6.916661	-2.752391
C	-0.809678	-4.320660	0.959266	H	-3.957866	6.861828	-4.424005
C	0.017629	4.461442	-0.202874	H	4.006638	-4.485454	-4.891848
C	-1.830245	3.795136	-1.733130	H	2.687586	-2.031783	-5.693404
C	-0.017629	-4.461442	-0.202874	H	4.294882	-1.836486	-4.982576
C	1.830245	-3.795136	-1.733130	H	2.921832	-0.904749	-4.344293
H	2.158623	1.144455	4.328839	H	2.919031	-7.504322	-3.131598
H	1.514931	-0.050344	5.476090	H	4.543964	-6.916661	-2.752391
H	0.757485	1.550408	5.337591	H	3.957866	-6.861828	-4.424005

Furthermore, theoretical force constants  $k$  of the M-C bond have been calculated with ADF using the same level of theory and basis set. The potential energy surface has been sampled by 21 single point calculations around the ground state geometry by simply moving the methyl groups along the M-C vector. The maximum displacements were 0.02 Å. Two scenarios were tested, (i) the symmetric variation of the bond length preserving the molecular  $C_2$  symmetry and (ii) the asymmetric variation of the bond length which scans only the variation of one M-C bond and thus falls back to  $C_1$  symmetry. These scenarios are termed  $C_1$  and  $C_2$  in

Table S6. The force constants were finally determined by fitting with a polynomial of the 2<sup>nd</sup> order and successive curve analysis.

Table S6. *M-C* force constants. Values in square brackets are simply half the value for better comparison with the  $C_1$  case.

	$k$ [N/m] ( $C_1$ )	$k$ [N/m] ( $C_2$ )
3-Ti	150.3	313.3 [156.7]
3-Zr	149.4	311.7 [155.9]
3-Hf	168.0	351.5 [175.75]

## 9. Crystallographic Studies of **3** under High-Pressure (HP)

**High-Pressure Preparation:** A requirement for collecting diffraction data at elevated pressures is a hydrostatic and inert pressure-transmitting medium (PTM). Therefore, single crystals of **3-Ti**, **3-Zr** and **3-Hf** were tested concerning the reactivity or dissolution in the two nonpolar PTM of choice with a reasonably high hydrostatic limit: 1:1 volume mixture of iso-pentane: *n*-pentane (limit: 7 GPa) and Daphne 7575 (limit: 3.9-4 GPa).<sup>3,4</sup> Due to the air-sensitivity of **3** all testing steps and the actual loading of the single crystals into the diamond anvils (DAC) were performed in an Ar-glovebox. The behavior of the **3-Zr** and **3-Hf** crystals were similar, showing no hints of reaction with Daphne 7575 but a rougher surface after being in contact with isopentane: *n*-pentane indicating a slight solvation of the surface. The **3-Ti** crystals reacted differently and showed instantaneously the similar optical changes after being in contact with both PTM: A darkening of the color and creation of a few tiny cracks in the crystals. Nevertheless, single crystals of **3-Ti** were loaded subsequently with both PTMs in a DAC and intensity diffraction data was collected. For both PTMs the obtained diffraction data was of exceptionally low quality including insufficient scattering power and multiple domains. Finally, perfluoro-2-butyltetrahydrofuran (FC-75) was tested as PTM, which has a hydrostatic limit of 1.2 GPa.<sup>5</sup> However, the obtained intensity data from a crystal surrounded by this PTM contained the same diffraction issues. We like to note that the low diffraction quality of the single crystals being in contact with these PTM has not necessarily to be related to a severe reaction of **3-Ti** with these PTMs. The diminished crystal quality might be also based on the light sensitivity of **3-Ti** combined with the rather light-intensive loading procedure of the pressure chamber. Accordingly, no data collection of **3-Ti** at high pressures were feasible. In case of **3-Zr** and **3-Hf** Daphne 7575 served as PTM.

**X-ray data collection:** In order to generate the high pressures two different types of DACs were employed. In case of **3-Zr** a Boehler-Plate DAC was used and for **3-Hf** a modified Merrill-Bassett DAC with tungsten carbide seats was applied.<sup>6-9</sup> In both cases, the culet diameter of the conical (Boehler-Almax) anvils was 0.6 mm.<sup>8</sup> For both compounds, the stainless steel gasket was pre-indented from initially 250  $\mu\text{m}$  to 80  $\mu\text{m}$ . The diameter of the borehole was 270 and 280  $\mu\text{m}$  for **3-Zr** and **3-Hf**, respectively. The pressure chamber were loaded in an Ar-filled glovebox with a single crystal, three ruby spheres for the pressure determination via the ruby fluorescence method, and Daphne 7575 as PTM. The size of the clear, yellowish and trapezoidally shaped single crystals were 140 x 110 x 40  $\mu\text{m}^3$  (**3-Zr**) and 130 x 120 x 40  $\mu\text{m}^3$  (**3-Hf**).

The pressure was determined with an estimated precision of  $\pm 0.1$  GPa by the ruby fluorescence method.<sup>10</sup> In case of **3-Hf** the combination of a diode pumped solid-state laser (CNI MGL-FN\_532nm-50mW) and a fiber optic spectrometer (Ocean Optics HR2000+) was employed. For **3-Zr** an *Almax eaysLab* Optiprex PLS photoluminescence system was used.

Intensity diffraction data of **3-Hf** were collected with a *Bruker* SMART-APEX diffractometer with a D8 goniometer and an APEX II CCD detector using mirror optics monochromated Ag  $K\alpha$  radiation ( $\lambda = 0.56087$  Å; Incoatec I $\mu$ S 1.0). The data collections were based on  $\omega$  scans with 0.5° steps with a fixed sample detector distance of 6 cm. The theta dependent exposure times varied between 15 s ( $2\theta = 0^\circ$ ), 30 s ( $2\theta = \pm 14^\circ$ ) and 60 s ( $2\theta = \pm 28^\circ$ ).

To compensate for the reduced scattering power of **3-Zr** the higher brilliance of the synchrotron beam at the X04SA Material Science-beamline of the Paul Scherrer Institute, Switzerland, was employed.<sup>11-13</sup> A photon

energy of 25 keV for the monochromated beam (square of  $200 \times 200 \mu\text{m}^2$ ) was used corresponding to a precise wavelength of  $\lambda = 0.49616 \text{ \AA}$ , which was verified by the refinement of the lattice parameters of NIST SRM 660a LaB6 powder standard in a capillary. A Dectris Pilatus 6M single-photon counting detector was employed for the collection of the intensity diffraction data during the single crystal experiment.<sup>13</sup> The distance between the sample and detector was fixed to 200.15 mm. The alignment of the entire setup was verified by a standard single crystal diffraction experiment on NIST SRM 1990 ruby single-crystal standard.<sup>14</sup>

The precise alignment of the DAC to the primary beam was achieved by centering the hole of the gasket to the centre of the beam with a *xyz*-motor equipped on the cradle's  $\phi$ -circle.<sup>12,13,15</sup> The modified single-crystal high pressure setup on the beamline allowed only  $\phi$ -scans. In order to increase the redundancy and completeness the circular shaped Boehler-Plate DAC was mounted for each pressure point on two different positions, which were approximately  $120^\circ$  separated. This  $120^\circ$  rotation of the DAC mimics a  $\chi$  rotation. However, for each rotation the DAC had to be detached from the cradle's  $\phi$ -circle and centered again after the rotation to the primary beam. Therefore, the orientation matrix *UB* of the single crystal was not only rotated about  $120^\circ$  in  $\chi$  between these two mounting positions but also slight deviations in  $\phi$  due to slight inaccuracies during the alignment are expected. This led to an individual data reduction of each mounting position. For each mounting position two  $\phi$ -scans separated by  $0.2^\circ$  in  $\phi$  with a stepsize of  $0.5^\circ$  were performed. The exposure time per frame was 5 s.

The collected frames were imported into *CrysAlis<sup>Pro</sup>* software.<sup>16</sup> Obvious diamond reflections were rejected before the integration, data reduction and empirical absorption correction of the imported diffraction data were performed. Typically, the data reduction contained 2200 frames for **3-Hf** and 290 frames per mounting position for **3-Zr**. In case of **3-Zr** the data sets of different mounting positions but same pressure were finally merged via Sortav applying a single scale factor for each individual reduced data set.<sup>17,18</sup>

The more accurately determined cell parameters in terms of standard uncertainties of the two mounting positions were used for the merged datasets. The space group of the compounds (Int. Tables No. 15) allows different choices regarding the cell setting. In case of the DAC experiments with the limitations of the restricted reciprocal space the choice of the conventional *I2/a* cell setting produces slightly more accurate cell parameters than the more often applied unconventional cell setting *C2/c* for these compounds.<sup>1,2,19,20</sup> Therefore, the conventional setting *I2/a* with the shorter translation vectors in the *ac*-plane and a monoclinic angle  $\beta$  closer to  $90^\circ$  for the cell at  $P = 0.0001 \text{ GPa}$  is applied during the high-pressure studies. In order to trace the pressure dependency of the cell parameters the rough alignment of the orientation matrix of the single-crystal was remained and adapted to the elevated pressure points and the different alignment. The pressure evolution of the cell parameters and the fixed principal direction of the translation vectors yield minor crystallographic alerts like acute monoclinic angle, *i.e.*  $\beta < 90^\circ$ , for  $a > c$  which were of obvious reasons not corrected.

The crystal structures were solved by SHELXS-2014 using the structure expansion method and refined by SHELXL-2014.<sup>21,22</sup> The anomalous dispersion coefficients  $f'$  and  $f''$  for the applied wavelength  $\lambda = 0.49616 \text{ \AA}$  at the PSI were calculated by the FPRIME code in the XDISP module of the WINGX-suite.<sup>18,23</sup> To obtain a better match with the absorption coefficient  $\mu$  estimated by *CrysAlis<sup>Pro</sup>* software the photon interaction cross-sections were derived from the Henke tables via the *Computational Crystallography Toolbox* implemented in the *Olex2*-suite.<sup>16,24-26</sup>

For consistency, the same labelling scheme for all non-hydrogen atoms was applied for **3-Zr** and **3-Hf** (see Fig. SXb). In case of **3-Zr** anisotropic displacement parameters (ADP) were used for all non-hydrogen atoms. For **3-Hf** the aromatic carbon atoms of the connected cyclopentadienyl (Cp) and phenyl (Ph) are treated isotropically. The remaining non-hydrogen atoms were refined anisotropically. However, the ADPs of the carbons in the remaining Ph as well as the terminal carbons connected to Si or O were restrained by the enhanced 'rigid-bond' instruction RIGU.<sup>27</sup> For both compound, measured reflections with too (i) low or (ii) high intensity compared to the model and an unambiguous relation of this intensity difference due to position of the reflections on the frames, *i.e.* (i) in a partially shaded area or (ii) close to a tail of a diamond reflection, were finally omitted from the refinement.

All H atoms were assigned geometrically with a riding model with isotropic displacement parameters equal to 1.5 times  $U_{eq}$  of the corresponding C atom for terminal CH<sub>3</sub> groups or 1.2 times  $U_{eq}$  of the attached C in the Cp- and Ph-rings. The terminal methyl groups were allowed to rotate along the C—Hf/Zr/Si/O/C axis during the least-square refinement to achieve the best possible position of the constrained hydrogens.

In order to track the evolution of the intermolecular distances a Hirshfeld surface analysis is applied employing *CrystalExplorer17*.<sup>28,29</sup> On the Hirshfeld surfaces, the normalized contact distances  $d_{norm}$  are mapped indicating longer or shorter intermolecular distances than the sum of the van der Waals radii of the participating atoms in the neighbouring molecules in the crystal.<sup>28,30</sup>

Key parameters of the data reduction and refinement for the high-pressure studies on **3-Zr** and **3-Hf** are summarized in Table S7 and Table S8, respectively. The evolution of the cell parameters with increasing pressure is shown in Figure S36. The pressure dependency of volume is described by a least square fit of a 3<sup>rd</sup> order Vinet equation of state (EoS) applying the EoSFit7-GUI suite.<sup>31-34</sup> The obtained fitting parameters are listed in Table S13. The pressure dependency of selected bond distances and angles following labeling scheme (Figure S35) are briefly summarized in Table S9 to Table S12 and depicted in Figure S37 to Figure S39, respectively. Figure S40 indicates the packing of the molecules in the crystal system. Figure S41 to Figure S43 show the evolution of the Hirshfeld surfaces of **3-Zr** and **3-Hf** with increasing pressure.

10. Crystallographic Studies of **3** under HP: Crystal Data and Selected Bond Distances and AnglesTable S7: Crystallographic data and parameters from the X-ray data reduction and refinement of the **3-Zr** structure at the four different pressure points between 0 and 3.0(1) GPa collected at the PSI.

<i>Crystal Parameters</i>				
Formula, FW [g mol <sup>-1</sup> ]	C <sub>42</sub> H <sub>48</sub> O <sub>2</sub> ZrSi, 704.11,			
F000	1480.0			
Crystal system, space group, Z:	Monoclinic, I2/a, 4			
<b>P [GPa]</b>	<b>0</b>	<b>1.2(1)</b>	<b>1.8(1)</b>	<b>3.0(1)</b>
<i>a</i> [Å]	18.503(3)	18.026(2)	17.887(2)	17.685(2)
<i>b</i> [Å]	9.85906(12)	9.56487(7)	9.49549(8)	9.41697(9)
<i>c</i> [Å]	18.7642(3)	18.1779(2)	17.9728(2)	17.6556(3)
$\beta$ [°]	90.492(3)	89.158(3)	88.701(3)	87.902(3)
<i>V</i> [Å <sup>3</sup> ]	3423.0(6)	3133.9(4)	3051.8(4)	2938.4(4)
Reflections (cell)	4888	5584	5321	4794
$\lambda$ [Å]	0.49616			
$\rho_{\text{calc}}$ [g cm <sup>-3</sup> ]	1.366	1.492	1.533	1.592
$\mu$ [mm <sup>-1</sup> ]	0.744	0.813	0.835	0.867
<i>T</i> <sub>min</sub> , <i>T</i> <sub>max</sub>	0.93719, 1.000	0.95308, 1.000	0.95463, 1.000	0.94473, 1.000
$\theta$ range [°]	1.629-22.425 -8 ≤ <i>h</i> ≤ 10	1.683-22.431 -8 ≤ <i>h</i> ≤ 9	1.693-22.436 -8 ≤ <i>h</i> ≤ 9	1.711-22.437 -8 ≤ <i>h</i> ≤ 10
Index ranges	-15 ≤ <i>k</i> ≤ 15 -28 ≤ <i>l</i> ≤ 28	-14 ≤ <i>k</i> ≤ 14 -27 ≤ <i>l</i> ≤ 27	-14 ≤ <i>k</i> ≤ 14 -27 ≤ <i>l</i> ≤ 27	-14 ≤ <i>k</i> ≤ 14 -27 ≤ <i>l</i> ≤ 27
Reflections	19013	17242	17211	16375
Coverage to 0.65 Å [%]	41.2	39.1	39.3	41.3
<i>I</i> / $\sigma$ ( <i>I</i> )	34.6	44.4	46.5	47.6
Average redundancy	7.2	7.4	7.5	7.1
<i>R</i> <sub>int</sub>	0.0549	0.0508	0.0483	0.0446
<i>R</i> <sub>sigma</sub>	0.0288	0.0225	0.0215	0.0210
Unique reflections	2690	2338	2291	2313
Reflections <i>I</i> > 2 $\sigma$ ( <i>I</i> )	2513	2247	2184	2185
Parameters (restraints)	215 (0)	215 (0)	215 (0)	215 (0)
Goodness-of-Fit on <i>F</i> <sup>2</sup>	1.061	1.081	1.062	1.094
<i>R</i> <sub>1</sub> [ <i>I</i> > 2 $\sigma$ ( <i>I</i> )],	0.0293	0.0277	0.0267	0.0311
( <i>R</i> <sub>1</sub> all data)	0.0317	0.0288	0.0282	0.0332
<i>wR</i> <sub>2</sub> [ <i>I</i> > 2 $\sigma$ ( <i>I</i> )],	0.0762	0.0731	0.0698	0.0796
( <i>wR</i> <sub>2</sub> all data)	0.0778	0.0736	0.0708	0.0806
Largest diff. peak and hole [e Å <sup>-3</sup> ]	0.179 and -0.297	0.209 and -0.222	0.266 and -0.244	0.271 and -0.416
CCDC number				

Table S8: Crystallographic data and parameters from the X-ray data reduction and refinement of the **3-Hf** structure at the five different pressure points between 0 and 4.0(1) GPa collected with I $\mu$ S system.

<b>Crystal Parameters:</b>					
Formula, FW [g mol <sup>-1</sup> ]	C <sub>42</sub> H <sub>48</sub> O <sub>2</sub> HfSi, 791.38,				
F000	1608.0				
Crystal system, space group, Z:	Monoclinic, I2/a, 4				
<b>P [GPa]</b>	<b>0</b>	<b>1.1(1)</b>	<b>2.1(1)</b>	<b>3.3(1)</b>	<b>4.0(1)</b>
<i>a</i> [Å]	18.499(8)	18.117(9)	17.830(7)	17.636(8)	17.492(8)
<i>b</i> [Å]	9.8948(3)	9.6368(3)	9.4989(3)	9.4100(3)	9.3924(3)
<i>c</i> [Å]	18.7755(6)	18.2893(7)	17.9061(6)	17.5509(6)	17.3845(6)
$\beta$ [°]	90.731(7)	89.649(8)	88.708(7)	87.700(9)	87.215(10)
<i>V</i> [Å <sup>3</sup> ]	3436.5(14)	3193.0(15)	3032.0(12)	2910.3(14)	2825.7(14)
Reflections (cell)	19690	18299	17462	15778	15491
$\lambda$ [Å]	0.56087				
$\rho_{\text{calc}}$ [g cm <sup>-3</sup> ]	1.530	1.646	1.734	1.806	1.843
$\mu$ [mm <sup>-1</sup> ]	1.680	1.808	1.904	1.984	2.024
<i>T</i> <sub>min</sub> , <i>T</i> <sub>max</sub>	0.94307, 1.000	0.89082, 1.000	0.95137, 1.000	0.88856, 1.000	0.89803, 1.000
$\theta$ range [°]	1.712–21.979	1.757–22.033	1.795–21.977	1.833–22.028	1.851–21.995
	$-7 \leq h \leq 7$	$-7 \leq h \leq 7$	$-7 \leq h \leq 7$	$-7 \leq h \leq 7$	$-7 \leq h \leq 7$
Index ranges	$-13 \leq k \leq 13$	$-12 \leq k \leq 12$			
	$-25 \leq l \leq 25$	$-24 \leq l \leq 24$	$-23 \leq l \leq 23$	$-23 \leq l \leq 23$	$-23 \leq l \leq 23$
Reflections	26623	24561	23389	22219	21960
Coverage to 0.75 Å [%]	37.0	37.2	37.5	37.4	37.1
<i>I</i> / $\sigma$ ( <i>I</i> )	42.6	45.5	56.5	52.1	55.6
Average redundancy	16.5	16.2	16.3	15.9	16.3
<i>R</i> <sub>int</sub>	0.0611	0.0601	0.0499	0.0528	0.0507
<i>R</i> <sub>sigma</sub>	0.0235	0.0220	0.0177	0.192	0.0180
Unique reflections	1583	1489	1411	1366	1320
Reflections <i>I</i> > 2 $\sigma$ ( <i>I</i> )	1451	1419	1326	1234	1194
Parameters (restraints)	170 (42)	170 (42)	170 (42)	170 (42)	170 (42)
Goodness-of-Fit on <i>F</i> <sup>2</sup>	1.068	1.131	1.080	1.121	1.095
<i>R</i> <sub>1</sub> [ <i>I</i> > 2 $\sigma$ ( <i>I</i> )],	0.0248	0.0213	0.0210	0.0215	0.0219
( <i>R</i> <sub>1</sub> all data)	0.0311	0.0239	0.0245	0.0271	0.0273
<i>wR</i> <sub>2</sub> [ <i>I</i> > 2 $\sigma$ ( <i>I</i> )],	0.0501	0.0455	0.0460	0.0448	0.0474
( <i>wR</i> <sub>2</sub> all data)	0.0519	0.0462	0.0472	0.0467	0.0490
Largest diff. peak and hole [e Å <sup>-3</sup> ]	0.321 and -0.314	0.295 and -0.309	0.317 and -0.261	0.289 and -0.234	0.363 and -0.224
CCDC number					

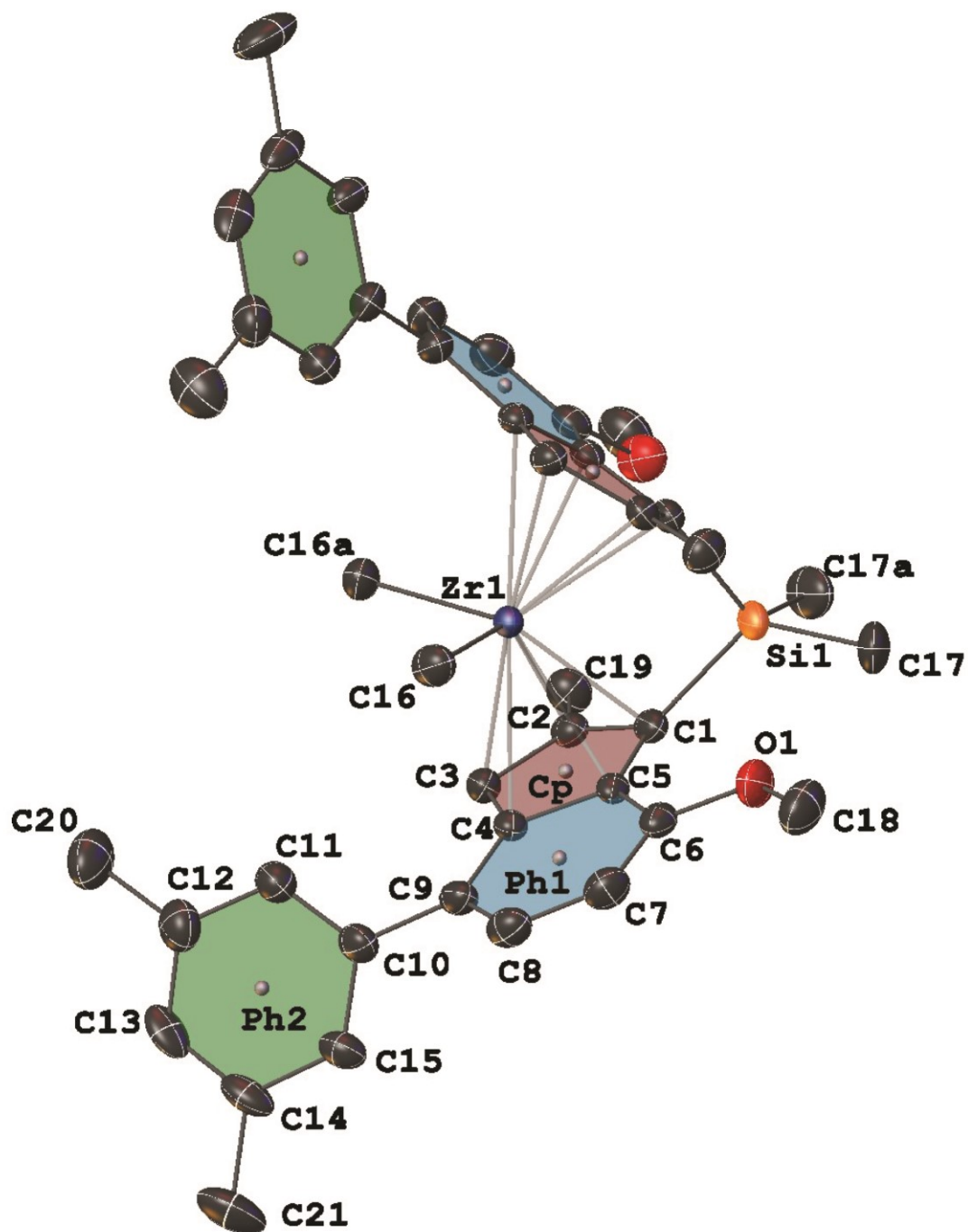


Figure S35: Labeling scheme of the unconstrained refined atoms. Atomic displacement ellipsoids are drawn at 50 % probability level. Cp, Ph1 and Ph2 are the calculated centroids by Olex2 of mean plane spanned by the Cp- and Ph-rings of the Shelxl-14 refined C1 to C5, C4 to C9 and C10 to C15 atoms, respectively.<sup>26</sup> The structural model is form **3-Zr** at  $P = 1.2(1)$  GPa.

Table S9: Pressure dependency of selected heteroatomic bond distances of **3-Zr** with estimated standard uncertainties (esd).

Distances [Å]				
<b>P [GPa]</b>	<b>0</b>	<b>1.2(1)</b>	<b>1.8(1)</b>	<b>3.0(1)</b>
Zr1—C16	2.272(3)	2.260(3)	2.264(3)	2.255(4)
Zr1—Cp	2.2670(15)	2.2430(15)	2.2335(16)	2.2213(18)
Zr1—C1	2.495(2)	2.483(2)	2.481(2)	2.474(3)
Zr1—C2	2.533(4)	2.526(4)	2.530(4)	2.527(5)
Zr1—C3	2.601(5)	2.576(5)	2.561(5)	2.567(6)
Zr1—C4	2.669(3)	2.634(3)	2.618(3)	2.595(3)
Zr1—C5	2.5713(18)	2.2500(17)	2.5253(17)	2.503(2)
Si1—C1	1.909(3)	1.897(3)	1.896(3)	1.890(3)
Si1—C17	1.881(4)	1.876(4)	1.875(4)	1.870(5)
O1—C6	1.364(4)	1.353(4)	1.350(4)	1.351(5)
O1—Cl8	1.423(7)	1.436(7)	1.429(7)	1.423(7)

Table S10: Pressure dependency of selected heteroatomic bond distances of **3-Hf** with esds.

Distances [Å]					
<b>P [GPa]</b>	<b>0</b>	<b>1.1(1)</b>	<b>2.1(1)</b>	<b>3.3(1)</b>	<b>4.0(1)</b>
Hf1—C16	2.262(8)	2.253(7)	2.239(6)	2.226(7)	2.219(7)
Hf1—Cp	2.254(4)	2.236(3)	2.228(4)	2.214(4)	2.205(4)
Hf1—C1	2.494(6)	2.487(5)	2.485(5)	2.481(5)	2.479(6)
Hf1—C2	2.508(9)	2.514(9)	2.515(9)	2.519(9)	2.520(10)
Hf1—C3	2.581(11)	2.563(10)	2.555(11)	2.546(11)	2.538(12)
Hf1—C4	2.656(7)	2.629(6)	2.611(6)	2.587(7)	2.573(7)
Hf1—C5	2.568(4)	2.539(4)	2.521(4)	2.495(4)	2.479(4)
Si1—C1	1.906(7)	1.902(6)	1.904(6)	1.903(6)	1.898(7)
Si1—C17	1.878(9)	1.880(8)	1.880(8)	1.866(8)	1.866(9)
O1—C6	1.358(9)	1.357(8)	1.352(8)	1.356(9)	1.359(9)
O1—Cl8	1.441(14)	1.433(12)	1.414(12)	1.421(13)	1.413(13)

Table S11: Pressure dependency of selected bond angles of **3-Zr** with esds.

Angle [°]				
<i>P</i> [GPa]	<b>0</b>	<b>1.2(1)</b>	<b>1.8(1)</b>	<b>3.0(1)</b>
bite	59.20(19)	57.95(15)	56.09(19)	56.9(2)
Cp—Zr1—Cpa	129.46(5)	129.68(5)	129.70(5)	129.73(6)
C16—Zr1—C16a	97.13(17)	96.91(17)	96.63(16)	95.78(19)
C1—Si1—C1a	96.85(14)	96.53(15)	96.63(15)	96.25(18)
Cp—Si1—Cpa	82.32(5)	81.67(5)	81.43(5)	81.05(6)
Si1—C1—Cp	161.39(17)	161.05(16)	160.63(17)	160.61(19)
Twist: Ph1—Ph2	46.75(15)	47.02(15)	46.80(15)	46.89(17)

Table S12: Pressure dependency of selected bond angles of **3-Hf** with esds.

Angle [°]					
<i>P</i> [GPa]	<b>0</b>	<b>1.1(1)</b>	<b>2.1(1)</b>	<b>3.3(1)</b>	<b>4.0(1)</b>
bite	58.7(5)	57.6(4)	56.7(4)	55.9(5)	55.6(5)
Cp—Hf1—Cpa	129.39(12)	129.63(11)	129.78(11)	129.74(11)	129.46(12)
C16—Hf1—C16a	96.7(4)	96.6(3)	96.1(3)	94.8(3)	94.2(4)
C1—Si1—C1a	96.8(4)	96.5(3)	96.7(3)	96.7(4)	96.3(4)
Cp—Si1—Cpa	81.89(13)	81.30(11)	81.08(12)	80.72(12)	80.32(13)
Si1—C1—Cp	161.0(4)	160.7(4)	160.1(4)	159.7(4)	159.7(4)
Twist: Ph1—Ph2	46.2(3)	46.5(3)	46.6(3)	46.7(3)	46.7(3)

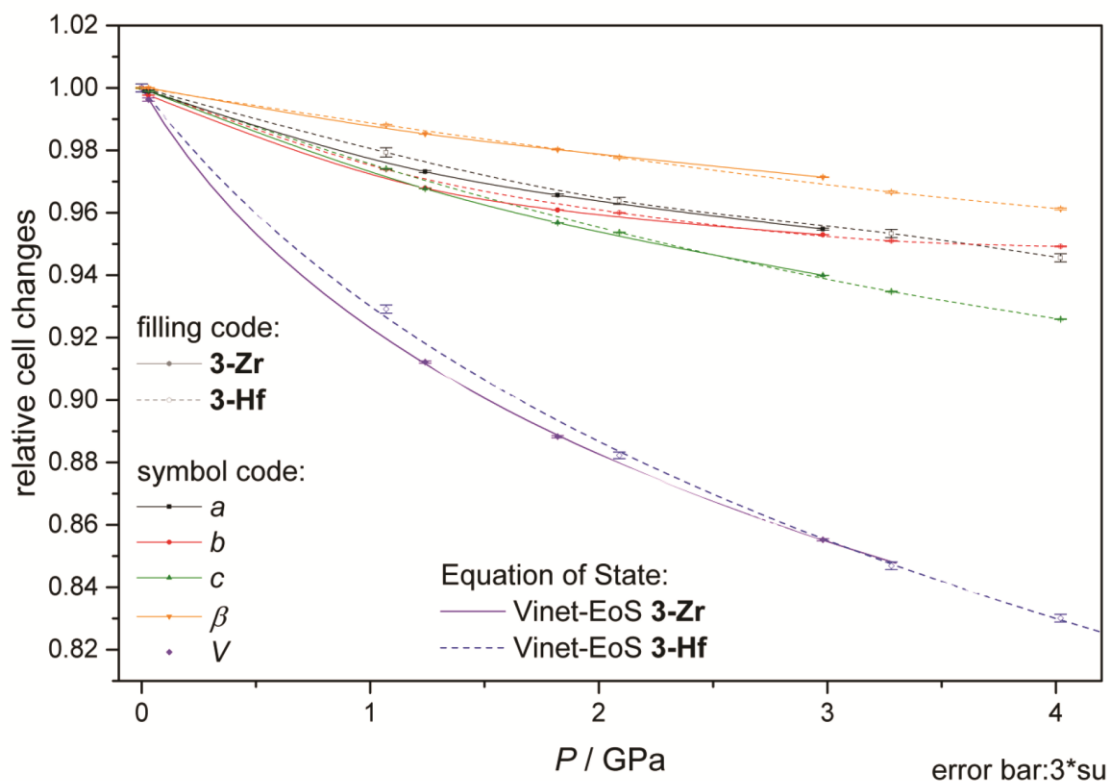
11. Overview of the Structural Changes in **3** with increasing Pressure

Figure S36: Evolution of the lattice parameters with increasing pressure normalized to the values at 0.0(1) GPa. The error bars, which represent three times the estimated standard uncertainty, are roughly of the size of the symbols. For the volume the pressure dependency is fitted by the 3rd order Vinet equation of state (EoS) applying the EoSFit7-GUI suite.<sup>31-34</sup>

Table S13: Obtained parameters from fitting of the 3<sup>rd</sup> order Vinet-EoS to the experimental  $P - V$ -data.  $V_0$  is the initial volume,  $K_0$  is the Bulk modulus at  $P = 0$  GPa and  $K'_0$  is the first partial derivative of  $K_0$  with respect to  $P$ .

Parameter	3-Zr	3-Hf
$V_0 / \text{\AA}$	3436 (14)	3436.5 (15)
$K_0 / \text{GPa}$	8.0 (16)	10.3 (12)
$K'_0$	11 (3)	8.1 (14)

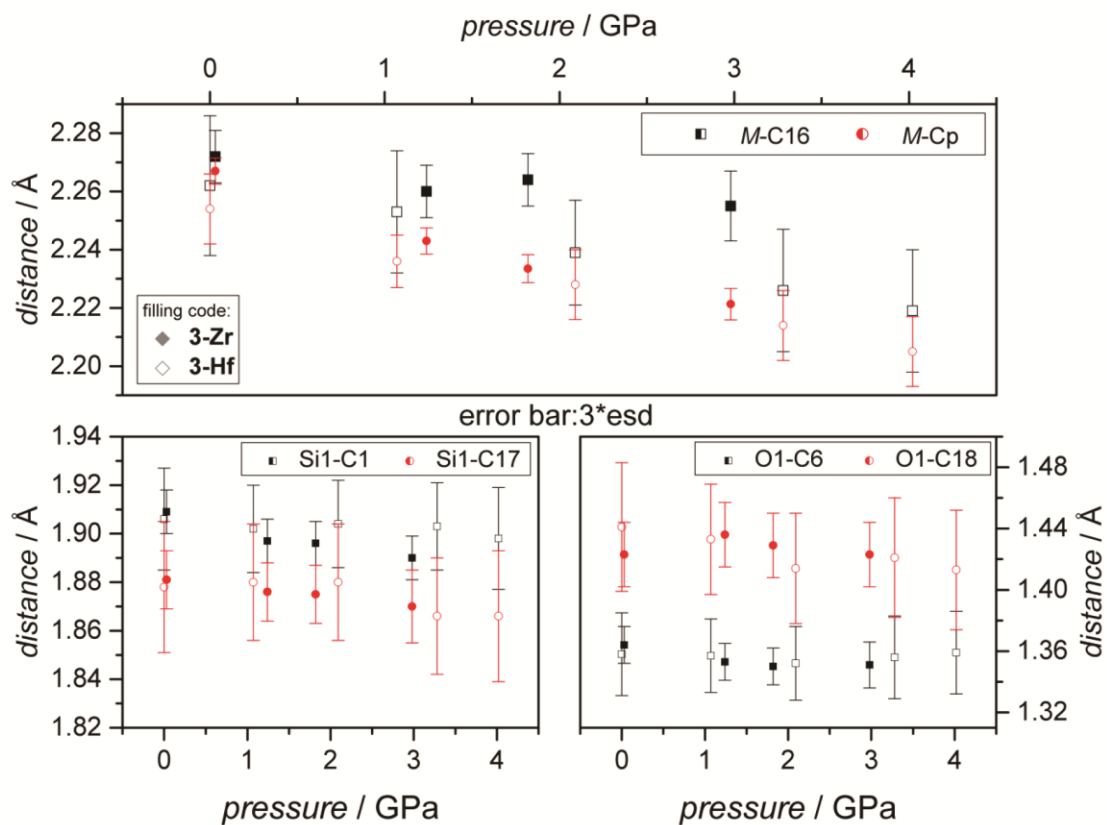


Figure S37: Evolution of the M—C16, M—Cp, Si1—C1, Si1—C17, O1—C6 and O1—C18 bond distances with increasing pressure. The error bars represent 3 times the esd of the structure refinement.

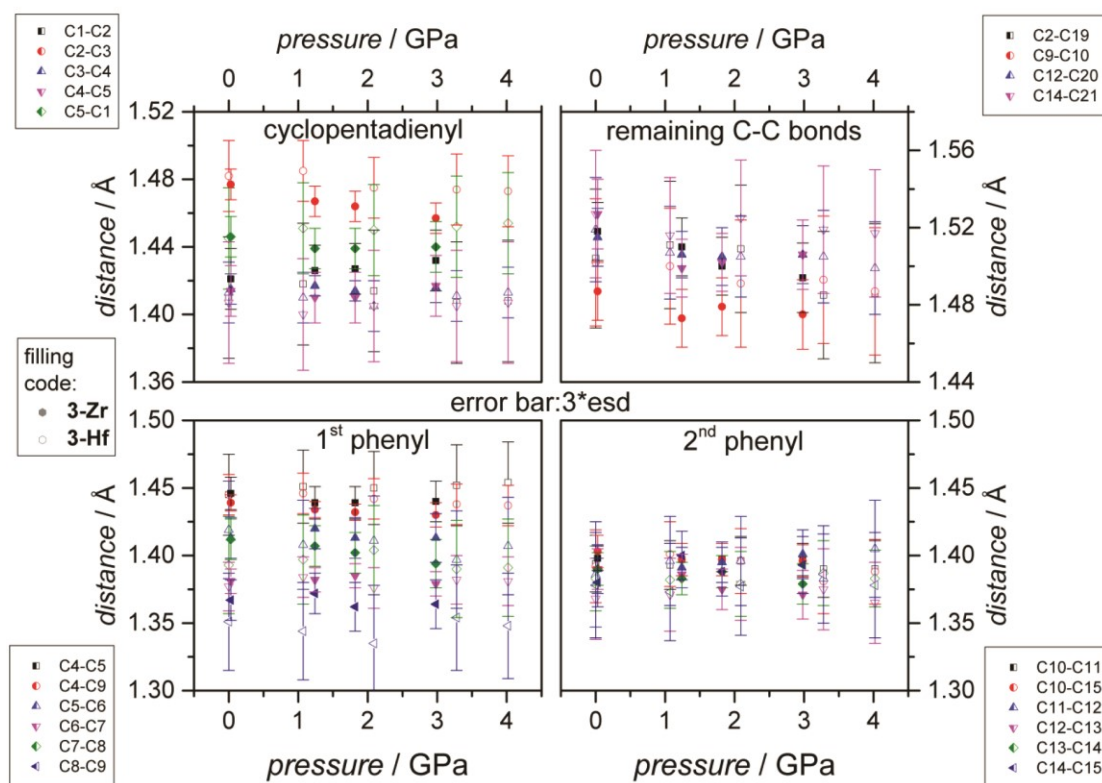


Figure S38: Evolution of the C—C bond distances in with increasing pressure. The error bars represent 3 times the esd of the structure refinement.

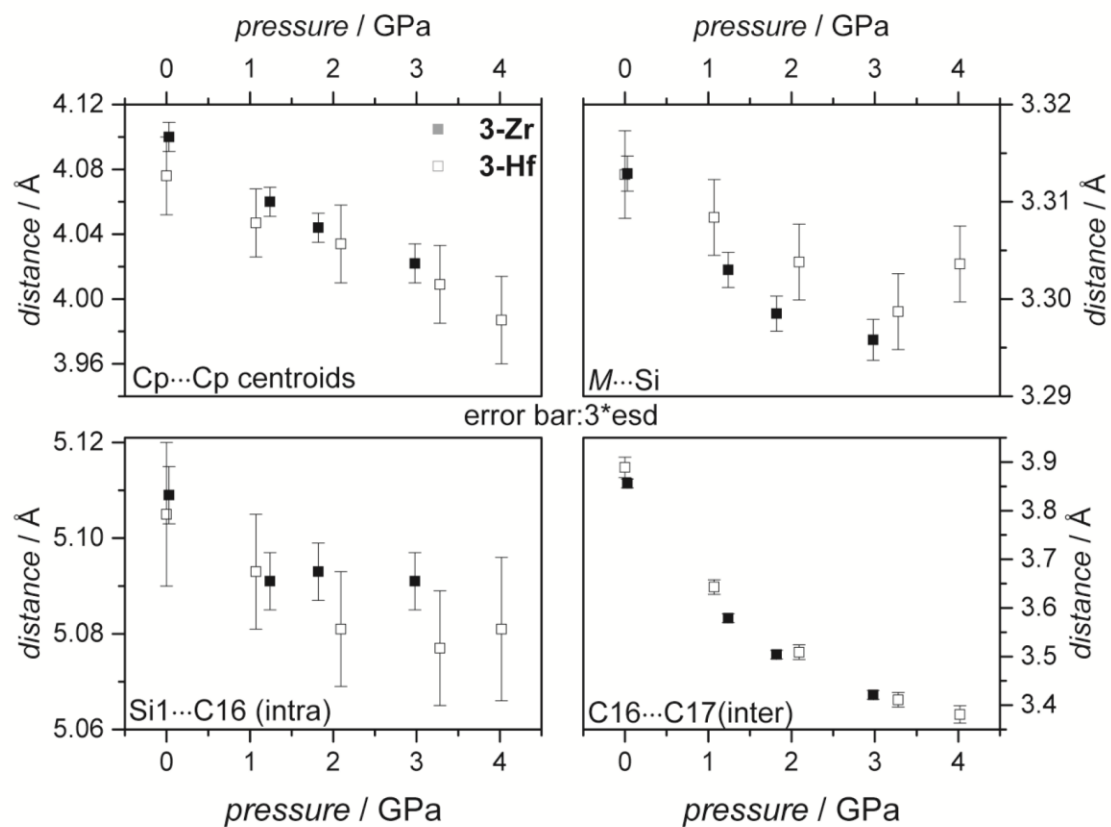


Figure S39: Evolution of the Cp...Cp, M...Si1, Si1...C16 and C16...C17 distances with increasing pressure. The error bars represent 3 times the esd of the structure refinement.

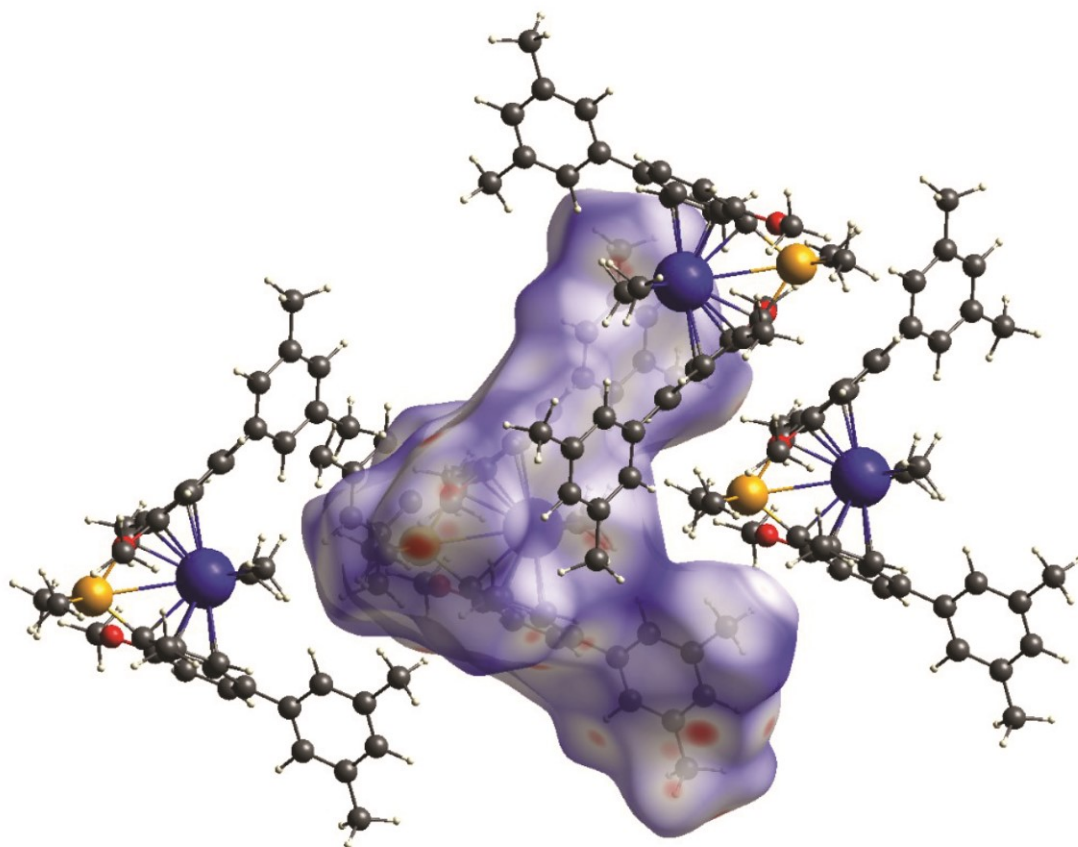


Figure S40: Section of the crystal packing. The V-shaped molecules are stacked along the  $b$ -axis. For the molecule in the middle the Hirshfeld surface is plotted.<sup>28,29</sup>

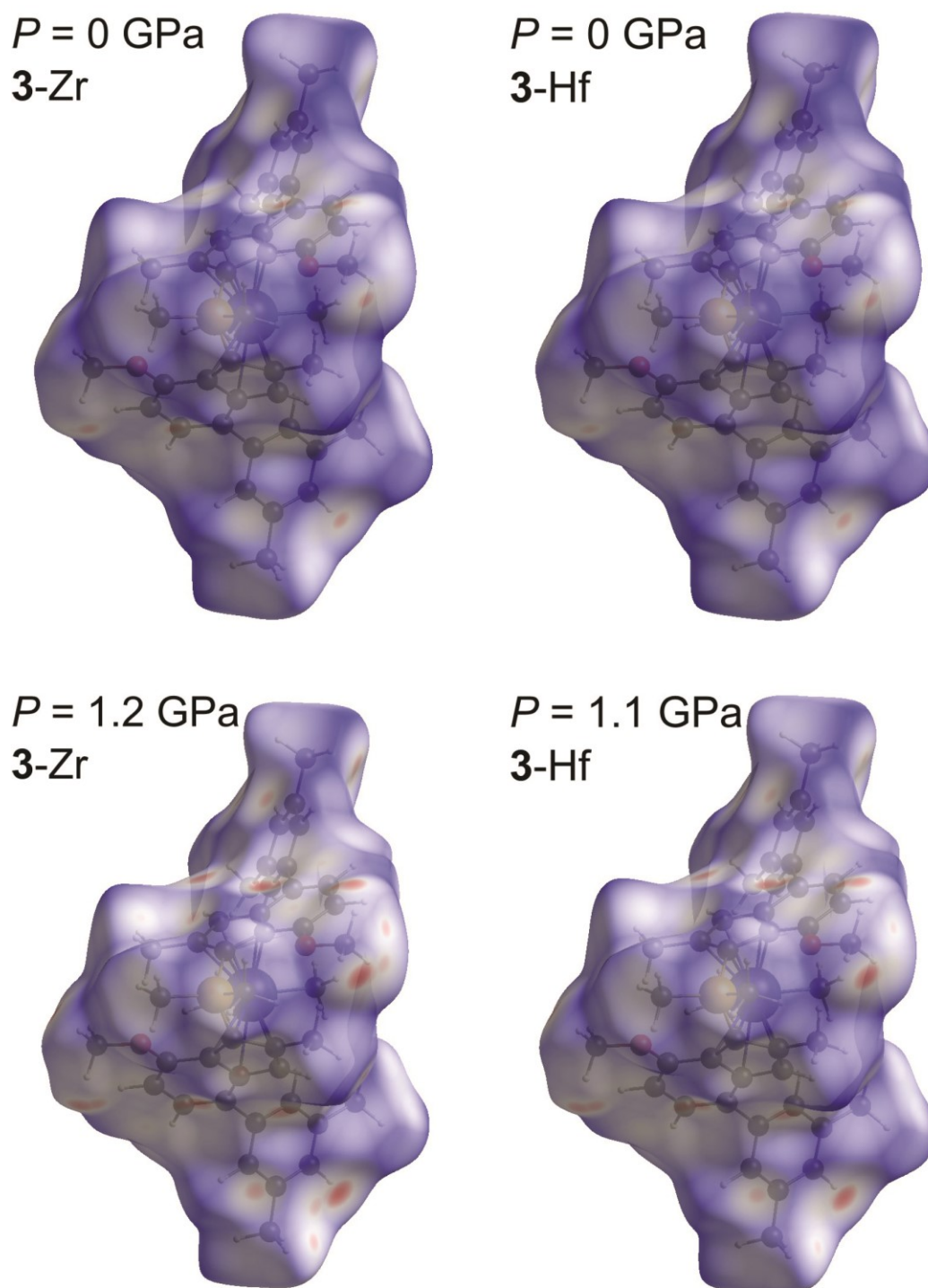


Figure S41: Evolution of the Hirshfeld surfaces with increasing pressure. The normalized contact distance  $d_{\text{norm}}$  is mapped on the surface.<sup>28,30</sup> Color coding ranges from blue over white to red.<sup>28,30</sup> Blue color indicates longer intermolecular distances than the sum of the van der Waals radii (vdW). Red color represents a shorter distance than the sum of the vdW-radii. Pressure range: 0 -1.2 GPa

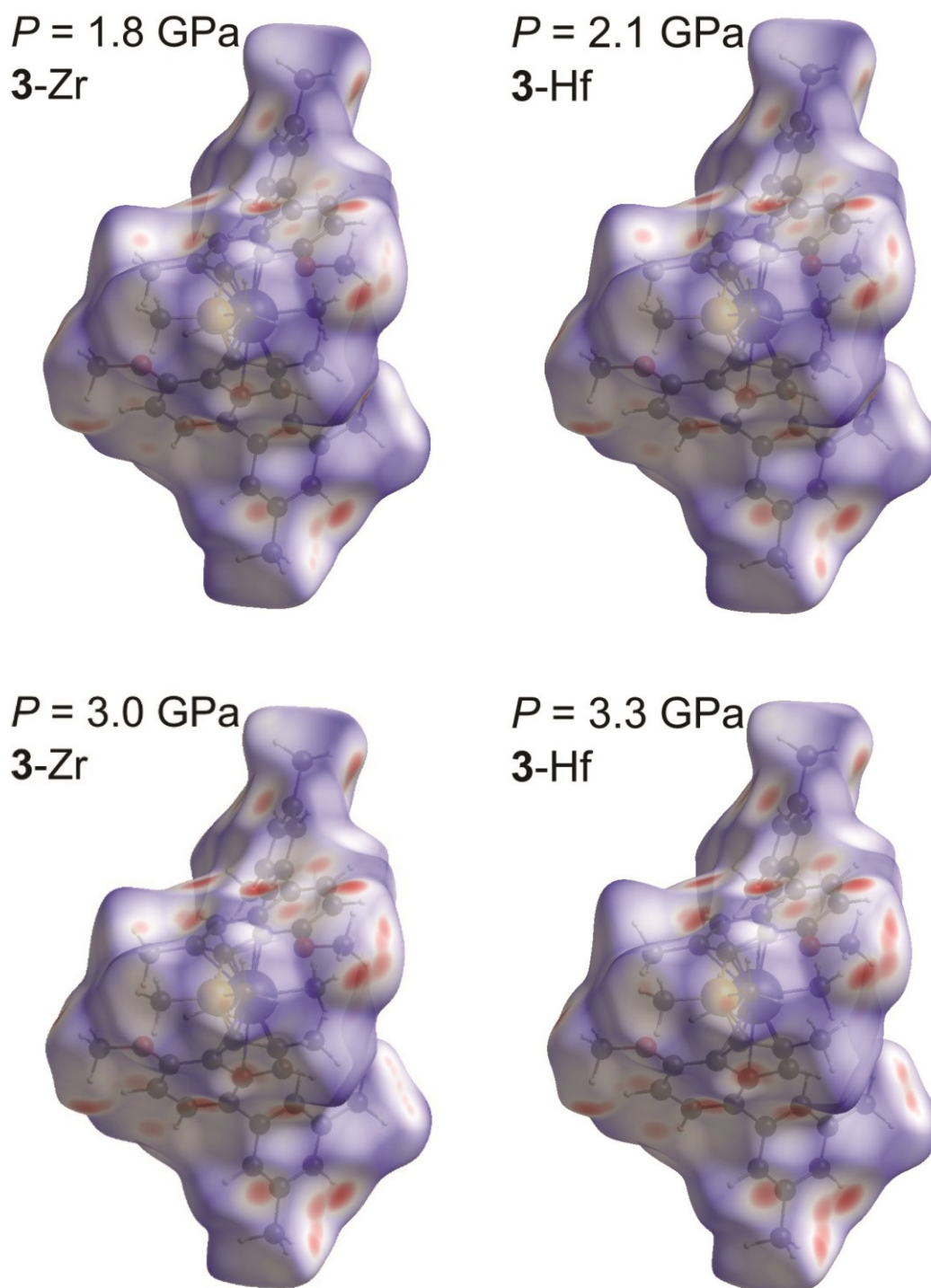


Figure S42: Evolution of the Hirshfeld surfaces with increasing pressure. The normalized contact distance  $d_{\text{norm}}$  is mapped on the surface.<sup>28,30</sup> Color coding ranges from blue over white to red.<sup>28,30</sup> Blue color indicates longer intermolecular distances than the sum of the van der Waals radii (vdW). Red color represents a shorter distance than the sum of the vdW-radii. Pressure range: 1.8 -3.3 GPa

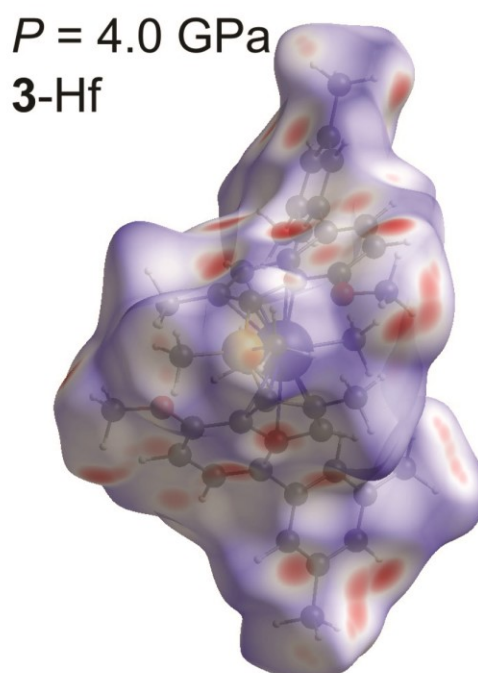


Figure S43: Hirshfeld surface of **3-Hf** at  $P = 4$  GPa. The normalized contact distance  $d_{\text{norm}}$  is mapped on the surface.<sup>28,30</sup> Color coding ranges from blue over white to red.<sup>28,30</sup> Blue color indicates longer intermolecular distances than the sum of the van der Waals radii (vdW). Red color represents a shorter distance than the sum of the vdW-radii.

## 12. High resolution charge density refinement details of 3-Ti, 3-Zr and 3-Hf

First, an independent atom model (IAM) refinement for 3-Ti [3-Zr] {3-Hf} was carried out using SHELXL<sup>21,22</sup>. Anisotropic thermal parameters were introduced to describe the thermal motion of all non-hydrogen atoms. The refinement finally converged at  $R_1 = 2.67$  [2.16] {1.77}%,  $wR_2 = 8.81$  [6.52] {4.40} and  $Goof = 1.065$  [1.052] {1.101} for all reflections  $F_o > 4\sigma(F_o)$  and 215 [215] {215} parameters. Analyzing the residual electron density  $\Delta\rho(r)$ , the deepest holes were -0.355 [-0.385] {-0.973} and the highest peaks were 0.728 [1.276] {4.226}. A multipole model was then adopted to describe the aspherical charge density deformation of  $\rho(\mathbf{r})$ .

According to a method proposed by Stewart,<sup>35</sup> the electron density  $\rho(\mathbf{r})$  in a crystal is described by a sum of aspherical pseudoatoms at the nuclear positions  $\{\mathbf{R}_j\}$ .

$$\rho(\mathbf{r}) = \sum_j \rho_j(\mathbf{r} - \mathbf{R}_j)$$

Based on the Hansen-Coppens formalism,<sup>36</sup> the pseudoatom density  $\rho_{at}$  is expressed in terms of multipoles:

$$\rho_{at}(\mathbf{r}) = P_c \rho_{core}(r) + P_v \kappa^3 \rho_{valence}(\kappa r) + \sum_{l=0}^{l_{max}} \kappa^{l^3} R_l(\kappa r) \sum_{m=0}^l P_{lm\pm} d_{lm\pm}(\theta, \phi)$$

In the refinement of our best model the multipole expansion was truncated at the hexadecapole level ( $l_{max} = 4$ ) for M and Si and at the octupolar level ( $l_{max} = 3$ ) for carbon and oxygen. A bond-directed dipole and quadrupole ( $l_{max} = 2$ ) was introduced for all hydrogen atoms. Core and spherical valence densities were constructed using relativistic wave functions, which are expanded over Slater-type basis functions, as implemented in the databank-file of Volkov and Macchi (VM) provided by the XD2006 suite of programs.<sup>37</sup> Single- $\xi$  functions were also taken from the VM databank. The valence configuration of the central M atoms were selected based on the refinements of theoretical structure factors and its extracted QTAIM charges in comparison with the ones obtained directly from the wavefunction.

The atomic coordinates and thermal displacement parameters of all non-hydrogen atoms were optimized along with all multipolar parameters using all data with  $\sin\theta/\lambda < 1.0543$  [1.0925] {1.1137}  $\text{\AA}^{-1}$ . During the multipolar refinements the hydrogen positions were restrained with fixed C-H bond distances  $r(\text{C-H}) = 1.10$   $\text{\AA}$  for hydrogen atoms bonded to  $sp^3$  hybridized carbons atoms and  $r(\text{C-H}) = 1.08$   $\text{\AA}$  for hydrogen atoms bonded to  $sp^2$  hybridized carbon atoms, and their isotropic thermal parameters were related to  $1.5 \times U_{eq}(\text{C})$  for methyl ( $sp^3$ ) groups and  $1.2 \times U_{eq}(\text{C})$  for all other ( $sp^2$ ) groups.

To reduce the number of independently populated multipole parameters a chemically constrained model was employed. For all Me groups a local  $C_{3v}$  pseudo symmetry was imposed and for the oxygen atom as well as C(6)-C(9) a local  $C_s$  symmetry was assumed. Furthermore, the dimethylphenyl group was assumed to be  $C_{2v}$ -symmetric and all parameters breaking that symmetry have not been refined or constrained to be the same. In contrast to that, all five carbon atoms that are part of the indenyl group and coordinated to the central metal atom were kept fully flexible in order to take the M-C interactions upon coordination into account.

In addition, after a multipole model had been applied for all atoms, the thermal motion of the M and Si atoms for 3-Zr and 3-Hf were described by an anharmonic model, using the Gram-Charlier expansion<sup>38</sup> up to the fourth order. First, all multipolar parameters were kept fixed, and only the positional and thermal parameters of these atoms were refined, to avoid correlation between multipole- and anharmonic thermal parameters. In the next step both multipolar parameters as well as all thermal displacement parameters (also anharmonic parameters) were refined simultaneously. The validity of the thermal displacement parameters was carefully

checked for negative probability density regions in a cube of 2 Å base length around the respective atom using the XDPDF routine. For 3-Zr and Zr(1) no negative region was found whereas for Si(1) a small fraction of 0.020% of the integrated volume was negative. For 3-Hf no negative region was found, despite the higher degree of anharmonic motion.

Individual sets radial scaling parameters ( $\kappa$ ,  $\kappa'$ ) were adopted for the M, Si and O atoms, the C atoms of methyl ligands, the C atoms of the methyl group at the Si atom, the C atoms of the remaining methyl groups and finally one set for all the remaining C atoms (7 sets in total) to adjust the spherical atomic density as well as deformation density contributions. The  $\kappa$ - and  $\kappa'$ -values for the hydrogen atoms was kept fixed at the default value of 1.20 and 1.20 at all times, respectively. The total charge of the asymmetric unit was constrained to zero during all refinements.

In order to obtain reference parameters for the multipolar refinements, simplified model systems have been calculated based on the experimental structural parameters for, where the 4-(3',5'-dimethylphenyl)-7-methoxy-2-methylindenyl structural fragment has been replaced by a simple cyclopentadienyl fragment. Hydrogen positions were pre-optimized using Gaussian09 Rev. C<sup>39</sup> at the B3LYP/6-311G++(2d,2p) level of theory. For the metal atoms the LANL2TZ(f) basis including effective core potentials (ECP) were used.<sup>40</sup> The resulting coordinates were then used for an all-electron calculations with ADF at the PBE/QZ4P level of theory for consistency reasons with the VM database as employed in the XD2006 suite of programs. The theoretical structure factors have been calculated with DENPROP using a similar strategy as described elsewhere.<sup>41,42</sup>

Comparing selected multipolar populations of the Ti-atom in 3-Ti between experiment and theory shows very good agreement (i.e. H42+ = -0.123(7) and -0.119(1) or H40 = -0.100(8) and -0.096(1) for experiment and theory, respectively, justifying the use of theoretically obtained parameters of the multipolar model in cases where a refinement on the experimental data is hindered by anharmonic motion.

For 3-Zr, the  $\kappa$ - and  $\kappa'$ -parameter were taken from the refinement of the theoretical structure factors of the simplified model system.

Due to the severe bias of anharmonic motion in 3-Hf, all multipolar parameters (charge, populations,  $\kappa$ - and  $\kappa'$ -parameters) of the Hf atom were fixed and their values taken from the refinement of the theoretical structure factors of the simplified model system. Furthermore the  $\kappa'$  parameter of the Si atom was kept at the default value of 1.0.

The final agreement factors were  $R_1 = 1.91 [1.50] \{1.42\}\%$  and  $wR_2 = 3.25 [2.37] \{2.26\}\%$  for 14917 [16879] {18591} reflections ( $F_o > 3\sigma(F_o)$ ) and 461 [486] {473} parameters ( $N_{\text{ref}} / N_{\text{var}} = 32.4 [34.7] \{39.3\}$ ). The final multipole population parameters, the local coordinate system, fractional coordinates, bond distances, angles and dihedral angles are given in the crystallographic information file (CIF). The residual electron density distribution was almost featureless with the minimum and maximum values of +0.212/-0.200 [+0.268/-0.188] {+0.907/-0.424} e/Å<sup>3</sup> throughout the unit cell using a 0.025Å grid using the XDFFT routine ( $\sin(\theta/\lambda) < 0.8 \text{ \AA}^{-1}$ ). The residual electron density values at the full resolution, which are +0.502/-0.270 [+0.771/-0.307] {+1.606/-1.868}, are somewhat higher, especially for 3-Zr and 3-Hf due to anharmonic motion.

All refinements were carried out with the full-matrix least-square program XDLSM of the XD2006 suite of programs, the quantity minimized was  $\epsilon = \sum w_1 (|F_o| - k|F_c|)^2$ , where  $k$  is a scale factor, based on all reflections with  $F_o > 3\sigma(F_o)$ . Weights were taken as  $w_1 = 1/\sigma^2(F_o)$  and  $w_2 = 1/\sigma^2(F_o^2)$ . For sufficient convergence, the all  $\kappa$ -parameters were fixed in the final refinement. Convergence was assumed when a maximal shift/esd  $< 10^{-11}$

was achieved. For the topological analysis, critical points of the electron density were searched by using the XDPROP module of the XD2006 suite of programs, which was also used to calculate the bond paths.

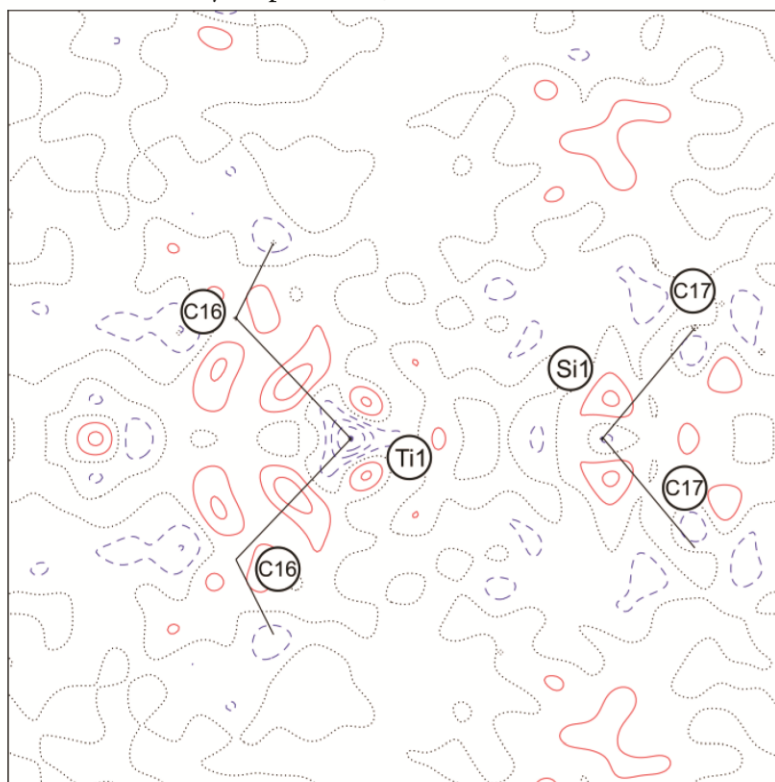
CCDC ?? [] {} contains the supplementary crystallographic data for this paper. These data can be obtained free of charge from The Cambridge Crystallographic Data Centre via [www.ccdc.cam.ac.uk/data\\_request/cif](http://www.ccdc.cam.ac.uk/data_request/cif).

## 13. Experimental d-orbital populations at the metal center of 3-Ti, 3-Zr and 3-Hf

Table S14: d-orbital populations derived from refined multipole populations at the metal center.

3-Ti	3-Zr	3-Hf
$z^2 = 0.26143 (0.00649)$	$z^2 = 0.38030 (0.01057)$	$z^2 = 0.36587 (0.00000)$
$xz = 0.30655 (0.00657)$	$xz = 0.36569 (0.01060)$	$xz = 0.41839 (0.00000)$
$yz = 0.66097 (0.00662)$	$yz = 0.64711 (0.01079)$	$yz = 0.70021 (0.00000)$
$x^2-y^2 = 0.34364 (0.00660)$	$x^2-y^2 = 0.21959 (0.01086)$	$x^2-y^2 = 0.44990 (0.00000)$
$xy = 0.33672 (0.00660)$	$xy = 0.40371 (0.01085)$	$xy = 0.45555 (0.00000)$

## 14. Residual electron density maps of 3-Ti, 3-Zr and 3-Hf

Figure S44: Residual density map of 3-Ti (data cut-off at  $\sin\theta/\lambda = 0.8 \text{ \AA}^{-1}$ ; contour level intervals =  $\pm 0.05 \text{ e/\AA}^3$ , positive red, negative blue) in the Ti(1), Si(1), C(16) plane.

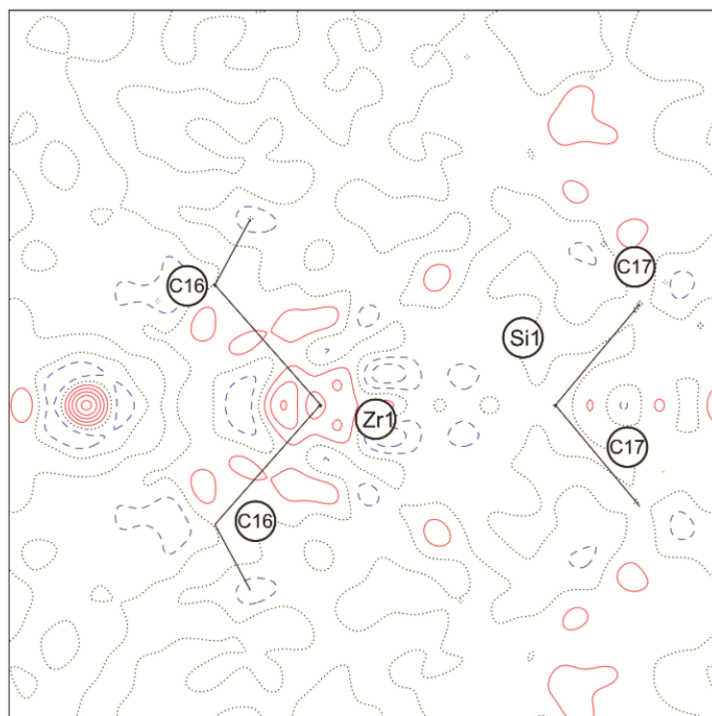


Figure S45: Residual density map of **3-Zr** (data cut-off at  $\sin\theta/\lambda = 0.8 \text{ \AA}^{-1}$ ; contour level intervals =  $\pm 0.05 \text{ e/\AA}^3$ , positive red, negative blue) in the Zr(1), Si(1), C(16) plane.

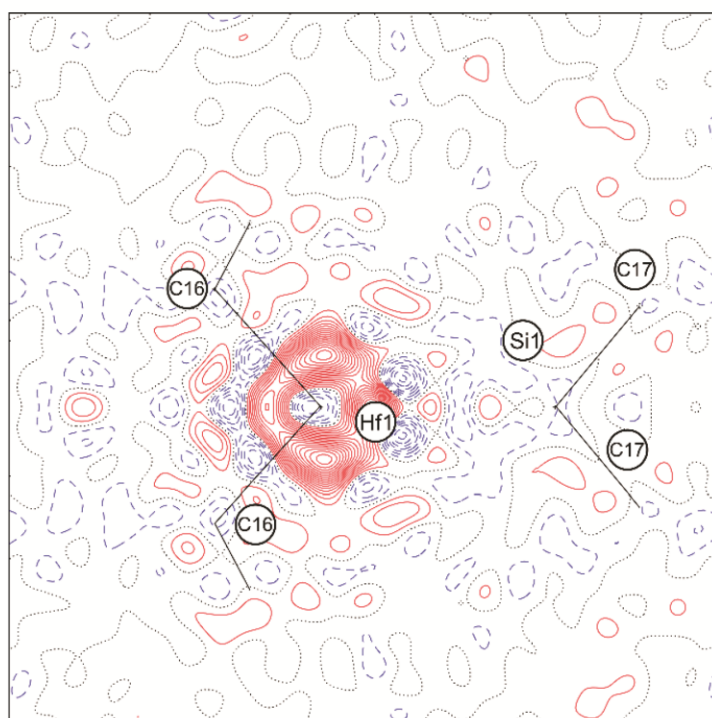


Figure S46: Residual density map of **3-Hf** (data cut-off at  $\sin\theta/\lambda = 0.8 \text{ \AA}^{-1}$ ; contour level intervals =  $\pm 0.05 \text{ e/\AA}^3$ , positive red, negative blue) in the Ti(1), Si(1), C(16) plane.

15. Scaling and drk plots of 3-Ti, 3-Zr and 3-Hf

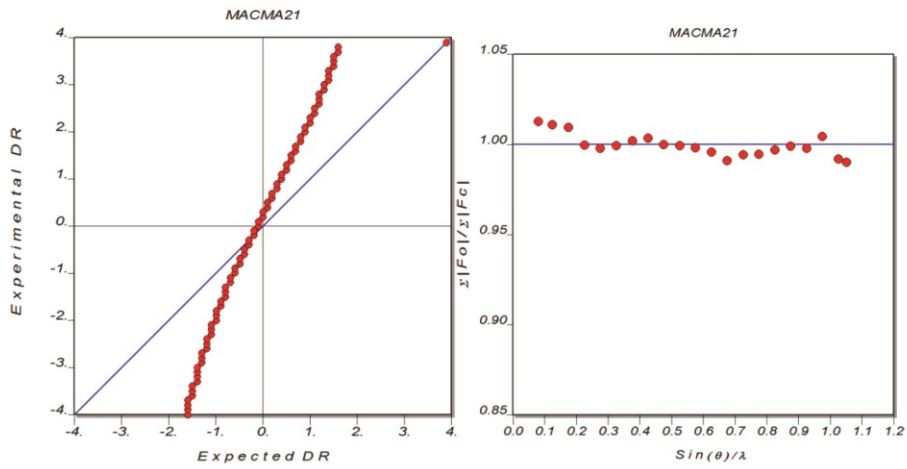


Figure S47: DRK-plot (left) and scaling-plot (right) of 3-Ti.

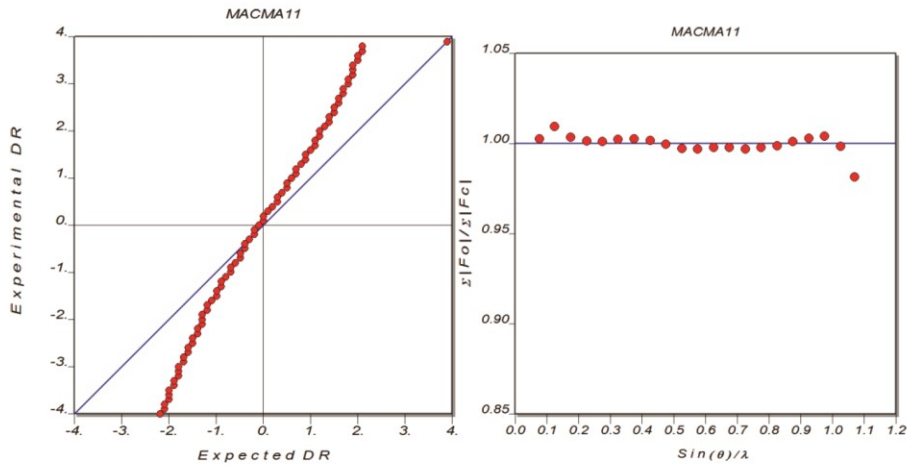


Figure S48: DRK-plot (left) and scaling-plot (right) of 3-Zr.

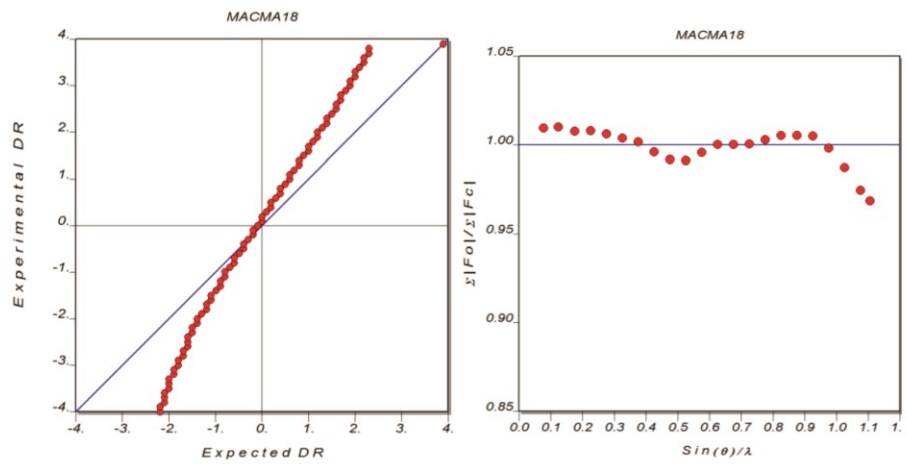


Figure S49: DRK-plot (left) and scaling-plot (right) of 3-Hf.

16. Topological parameters of selected bonds of selected atoms of 3-Ti, 3-Zr and 3-Hf

Table S15: Topological parameters of selected bonds in **3-Ti** in experiment and theory (ADF).

Bond	Method	Distance [Å]	$\rho(\mathbf{r}_c)$ [e/Å <sup>3</sup> ]	$\nabla^2\rho(\mathbf{r}_c)$ [e/Å <sup>5</sup> ]	$r_1$ [Å]	$r_2$ [Å]	$\epsilon$
Ti(1)-C(16)	Exp.	2.1527(3)	0.531( 3)	5.470( 3)	1.0696	1.0831	0.06
188	DFT <sup>a</sup>	2.1454	0.662	1.110	1.0895	1.0559	0.048
Si(1)-C(1)	Exp.	1.8908(4)	0.807( 8)	-0.844( 27)	0.7994	1.0922	0.11
145	DFT <sup>a</sup>	1.9002	0.778	2.088	0.7507	1.1507	0.098
Si(1)-C(17)	Exp.	1.8730(4)	0.930( 8)	-3.604( 26)	0.8118	1.0636	0.06
193	DFT <sup>a</sup>	1.8864	0.825	1.359	0.7471	1.1400	0.011
C(1)-C(2)	Exp.	1.4438(4)	1.849( 7)	-12.076( 18)	0.7002	0.7441	0.22
201	DFT <sup>a</sup>	1.4474	1.850	-14.878	0.7152	0.7325	0.187
C(2)-C(3)	Exp.	1.4074(4)	2.063( 8)	-17.136( 18)	0.7099	0.6979	0.25
200	DFT <sup>a</sup>	1.4105	2.019	-18.236	0.7071	0.7036	0.220
C(3)-C(4)	Exp.	1.4178(4)	2.031( 8)	-17.113( 19)	0.7048	0.7137	0.22
217	DFT <sup>a</sup>	1.4212	1.974	-17.803	0.7044	0.7171	0.167
C(4)-C(5)	Exp.	1.4415(4)	1.939( 7)	-14.964( 17)	0.7146	0.7271	0.22
141	DFT <sup>a</sup>	1.4511	1.875	-15.915	0.7232	0.7281	0.150
C(5)-C(1)	Exp.	1.4527(4)	1.806( 8)	-11.614( 20)	0.7769	0.6771	0.20
133	DFT <sup>a</sup>	1.4520	1.825	-14.787	0.7400	0.7122	0.156

Table S16: Topological parameters of selected bonds in **3-Zr** in experiment and theory (ADF).

Bond	Method	Distance [Å]	$\rho(\mathbf{r}_c)$ [e/Å <sup>3</sup> ]	$\nabla^2\rho(\mathbf{r}_c)$ [e/Å <sup>5</sup> ]	$r_1$ [Å]	$r_2$ [Å]	$\epsilon$
Zr(1)-C(16)	Exp.	2.2654(3)	0.584( 4)	4.166( 4)	1.1762	1.0904	0.12
117	DFT <sup>a</sup>	2.2724	0.629	1.481	1.1841	1.0883	0.020
Si(1)-C(1)	Exp.	1.8999(4)	0.834( 8)	-0.351( 28)	0.7784	1.1217	0.05
202	DFT <sup>a</sup>	1.9091	0.767	1.894	0.7538	1.1561	0.100
Si(1)-C(17)	Exp.	1.8725(3)	0.922( 9)	-0.855( 31)	0.7637	1.1097	0.23
133	DFT <sup>a</sup>	1.8866	0.825	1.344	0.7472	1.1401	0.015
C(1)-C(2)	Exp.	1.4473(4)	1.892( 8)	-13.955( 20)	0.7072	0.7405	0.17
139	DFT <sup>a</sup>	1.4501	1.839	-14.682	0.7155	0.7347	0.191
C(2)-C(3)	Exp.	1.4095(4)	2.082( 9)	-18.200( 21)	0.7071	0.7026	0.27
186	DFT <sup>a</sup>	1.4111	2.015	-18.101	0.7085	0.7028	0.227
C(3)-C(4)	Exp.	1.4217(3)	2.027( 9)	-17.553( 21)	0.7169	0.7058	0.23
206	DFT <sup>a</sup>	1.4245	1.958	-17.457	0.7053	0.7195	0.173
C(4)-C(5)	Exp.	1.4439(4)	1.928( 8)	-15.691( 20)	0.7220	0.7224	0.17
178	DFT <sup>a</sup>	1.4528	1.865	-15.685	0.7242	0.7288	0.158
C(5)-C(1)	Exp.	1.4576(4)	1.814( 8)	-12.801( 20)	0.7658	0.6925	0.19
173	DFT <sup>a</sup>	1.4570	1.805	-14.364	0.7432	0.7140	0.163

Table S17: Topological parameters of selected bonds in **3-Hf** in experiment and theory (ADF).

Bond	Method	Distance [Å]	$\rho(\mathbf{r}_c)$ [e/Å <sup>3</sup> ]	$\nabla^2\rho(\mathbf{r}_c)$ [e/Å <sup>5</sup> ]	$r_1$ [Å]	$r_2$ [Å]	$\varepsilon$
Hf(1)-C(16)	Exp.	2.2443(5)	0.680( 6)	4.383( 6)	1.1623	1.0820	0.09
170	DFT <sup>a</sup>	2.2430	0.665	2.018	1.1733	1.0697	0.036
Si(1)-C(1)	Exp.	1.8988(6)	0.787( 15)	2.227( 53)	0.7668	1.1329	0.15
217	DFT <sup>a</sup>	1.9075	0.769	1.912	0.7532	1.1552	0.088
Si(1)-C(17)	Exp.	1.8725(8)	0.919( 16)	-0.265( 58)	0.7628	1.1098	0.02
224	DFT <sup>a</sup>	1.8873	0.824	1.326	0.7474	1.1406	0.014
C(1)-C(2)	Exp.	1.4455(6)	1.921( 14)	-16.117( 34)	0.6651	0.7813	0.15
190	DFT <sup>a</sup>	1.4493	1.840	-14.679	0.7151	0.7344	0.194
C(2)-C(3)	Exp.	1.4119(7)	2.012( 14)	-18.280( 32)	0.6803	0.7323	0.30
229	DFT <sup>a</sup>	1.4135	2.004	-17.902	0.7097	0.7040	0.226
C(3)-C(4)	Exp.	1.4201(6)	2.023( 15)	-19.516( 32)	0.6851	0.7361	0.20
192	DFT <sup>a</sup>	1.4237	1.959	-17.474	0.7050	0.7191	0.175
C(4)-C(5)	Exp.	1.4444(7)	1.880( 14)	-15.738( 30)	0.7294	0.7151	0.21
218	DFT <sup>a</sup>	1.4531	1.864	-15.677	0.7243	0.7289	0.157
C(5)-C(1)	Exp.	1.4576(6)	1.826( 14)	-14.509( 32)	0.7798	0.6783	0.16
188	DFT <sup>a</sup>	1.4559	1.808	-14.426	0.7425	0.7136	0.163

## 17. Integrated AIM charges of selected atoms of 3-Ti, 3-Zr and 3-Hf

List of the QTAIM-charges  $Q$  given in [ $e$ ] and  $L(\Omega)$ :  $L(\mathbf{r}) = -\nabla^2\rho(\mathbf{r})$  integrated over the atomic basins in [a.u.]; experimental values based on the multipolar refinements of the electron density; theoretical values based on DFT optimized structures.

Table S18. Theoretical (ADF) and experimental QTAIM charges of 3-Ti, 3-Zr and 3-Hf.

Basin		$Q$		$L(\Omega)$		$Q$		$L(\Omega)$	
		<i>3-Ti</i>		<i>3-Zr</i>		<i>3-Hf</i>			
<b>M(1)</b>	Exp.	1.648	<0.001	1.746	0.004	1.636	0.003		
	DFT <sup>g</sup>	1.649	-0.010	1.939	-0.002	2.024	0.001		
<b>Si(1)</b>	Exp.	2.349	-0.006	2.433	-0.008	2.454	-0.010		
	DFT <sup>g</sup>	2.663	-0.003	2.652	-0.003	2.649	-0.004		
<b>C(16)</b>	Exp.	-0.773	0.002	-1.189	0.008	-1.223	0.002		
	DFT <sup>g</sup>	-0.324	-0.020	-0.385	-0.004	-0.406	-0.006		
<b>H(16A)</b>	Exp.	0.192	<0.001	0.264	<0.001	0.321	<0.001		
	DFT <sup>g</sup>	-0.051	0.006	-0.053	-0.001	-0.049	<0.001		
<b>H(16B)</b>	Exp.	0.192	<0.001	0.266	<0.001	0.322	<0.001		
	DFT <sup>g</sup>	-0.031	0.007	-0.037	0.006	-0.034	0.007		
<b>H(16C)</b>	Exp.	0.194	<0.001	0.270	<0.001	0.324	<0.001		
	DFT <sup>g</sup>	-0.031	0.007	-0.031	-0.001	-0.031	<0.001		
<b>C(17)</b>	Exp.	-1.135	0.004	-1.093	0.003	-1.417	<0.001		
	DFT <sup>g</sup>	-0.607	-0.006	-0.600	-0.003	-0.600	-0.002		
<b>H(17A)</b>	Exp.	0.124	<0.001	0.181	<0.001	0.182	0.001		
	DFT <sup>g</sup>	0.002	-0.001	0.003	<0.001	0.002	-0.001		
<b>H(17B)</b>	Exp.	0.121	<0.001	0.176	<0.001	0.171	<0.001		
	DFT <sup>g</sup>	-0.015	0.006	-0.017	0.005	-0.017	<0.001		
<b>H(17C)</b>	Exp.	0.122	<0.001	0.179	<0.001	0.170	<0.001		
	DFT <sup>g</sup>	-0.015	0.001	-0.018	-0.001	-0.017	0.005		
<b>C(1)</b>	Exp.	-0.485	0.003	-0.684	0.005	-0.707	0.003		
	DFT <sup>g</sup>	-0.779	-0.002	-0.793	-0.003	-0.794	-0.004		
<b>C(2)</b>	Exp.	-0.101	<0.001	-0.130	<0.001	-0.218	<0.001		
	DFT <sup>g</sup>	-0.123	<0.001	-0.121	-0.001	-0.129	0.002		
<b>C(3)</b>	Exp.	-0.222	<0.001	-0.319	<0.001	-0.258	<0.001		
	DFT <sup>g</sup>	-0.128	0.006	-0.152	0.004	-0.152	-0.001		
<b>C(4)</b>	Exp.	-0.002	0.001	-0.072	<0.001	-0.088	0.001		
	DFT <sup>g</sup>	-0.062	0.003	-0.087	0.003	-0.089	0.004		
<b>C(5)</b>	Exp.	-0.227	-0.002	-0.146	-0.001	-0.213	0.001		
	DFT <sup>g</sup>	-0.095	<0.001	-0.114	-0.001	-0.118	-0.001		

## 18. Critical points of the Laplacian of the electron density of selected atoms of 3-Ti, 3-Zr and 3-Hf

Table S19: Critical points of the Laplacian of the electron density and their distance to the nuclei for 3-Ti, 3-Zr and 3-Hf in experiment and theory (ADF).

		3-Ti		3-Zr		3-Hf	
		$\nabla^2\rho$	r	$\nabla^2\rho$	r	$\nabla^2\rho$	r
trans-LICC (CC1)	Exp.	-287.64	0.4066	-30.77	0.6009	-	-
	DFT <sup>a</sup>	-299.77	0.4026	-32.21	0.5924	-	-
BCC (CC2)	Exp.	-258.00	0.4079	-25.71	0.6013	-	-
	DFT <sup>a</sup>	-234.54	0.4087	-16.01	0.5989	-	-
trans-LICC(Cp) (CC3)	Exp.	-201.37	0.4109	-16.13	0.6029	-	-
	DFT <sup>a</sup>	-246.49	0.4067	-25.31	0.5927	-	-
BCC(Me) (CC4)	Exp.	-26.84	0.4940	-27.00	0.4965	-33.21	0.4913
	DFT <sup>a</sup>	-17.91	0.4920	-18.32	0.4903	-19.36	0.4886

Table S20: Selected angles of the charge concentrations with respect to the metal center.

		3-Ti	3-Zr	3-Hf
$\angle C-M-C$ (reference)	Exp.	92.79(1)	97.24(1)	96.00(2)
	DFT <sup>a</sup>	95.69	100.05	98.12
$\angle CC1-M-CC1$	Exp.	91.20	87.84	-
	DFT <sup>a</sup>	95.96	100.28	-
$\angle CC2-M-CC2$	Exp.	88.08	85.11	-
	DFT <sup>a</sup>	80.25	64.80	-
$\angle CC3-M-CC3$	Exp.	172.81	176.88	-
	DFT <sup>a</sup>	153.37	143.53	-

## 19. Critical points of the ELI-D of the outer shell of selected atoms 3-Ti, 3-Zr and 3-Hf

The ELI-D cannot be extracted from experimental charge density refinements. Therefore, only theoretical values are given.

Table S21. Critical points of the ELI-D in the valence shell and their distance to the nuclei for 3-Ti, 3-Zr and 3-Hf in theory (ADF).

		3-Ti		3-Zr		3-Hf	
		ELI-D	r	ELI-D	r	ELI-D	r
trans-LICC (ELI-D)	DFT <sup>a</sup>	1.676	0.5381	1.526	0.7168	1.229	0.7491
cis-LICC (ELI-D)	DFT <sup>a</sup>	1.563	0.5263	-	-	-	-
trans-LICC(Cp) (ELI-D)	DFT <sup>a</sup>	1.574	0.5334	1.483	0.7063	1.185	0.7227
LICC(Me) (CC4) (ELI-D)	DFT <sup>a</sup>	1.772	0.7477	1.779	0.7417	1.780	0.7296

Table S22. Selected angles of the critical points in the ELI-D with respect to the metal center.

$\angle$ CC1-M-CC1 (ELI-D)	DFT <sup>a</sup>	96.59	101.71	99.90
$\angle$ CC2-M-CC2 (ELI-D)	DFT <sup>a</sup>	83.75	-	-
$\angle$ CC3-M-CC3 (ELI-D)	DFT <sup>a</sup>	153.67	140.20	140.53

## 20. Experimental and theoretical Laplacian maps of 3-Zr and 3-Hf

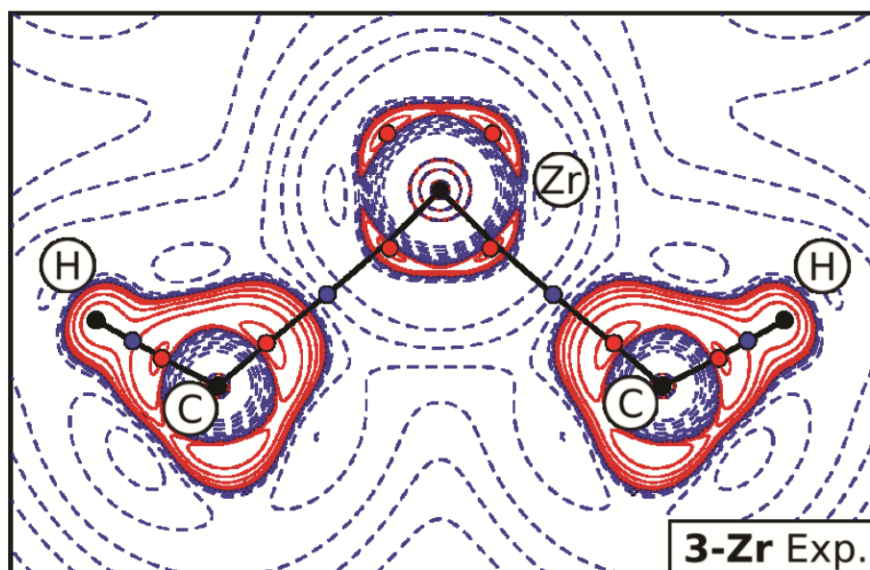


Figure S50: Experimental  $L(\mathbf{r}) = -\nabla^2\rho(\mathbf{r})$  map of 3-Zr in the plane defined by  $M$  and the two methyl ligands; positive (red, solid) and negative (blue, dashed)  $L(\mathbf{r})$  contour lines were drawn at  $\pm 2.0 \times 10^n$ ,  $\pm 4.0 \times 10^n$ ,  $\pm 8.0 \times 10^n$   $\text{e}/\text{\AA}^5$  with  $n = \pm 2, \pm 1, 0$ . Bond paths are displayed as black solid lines. Bond critical points and charge concentrations are drawn as blue and red filled circles, respectively.

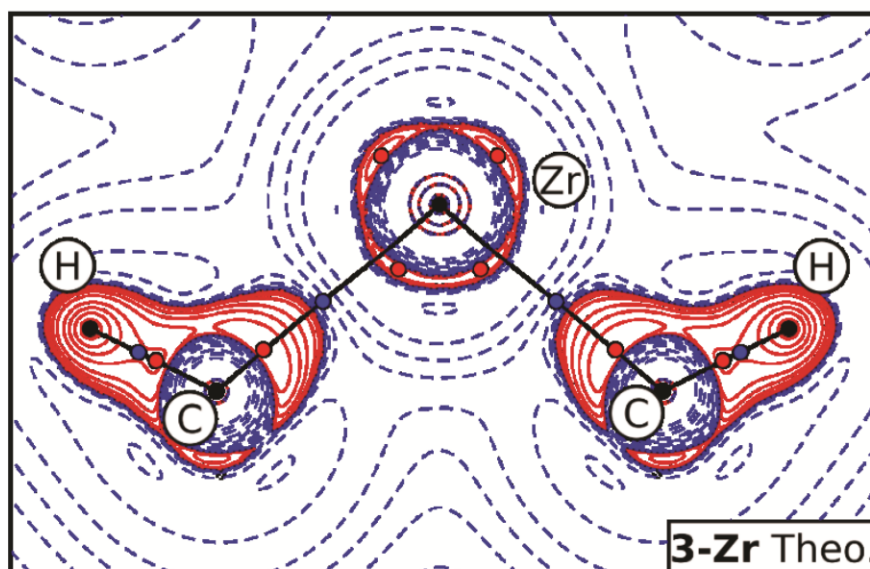


Figure S51: Theoretical (ADF)  $L(\mathbf{r}) = -\nabla^2\rho(\mathbf{r})$  map of 3-Zr in the plane defined by  $M$  and the two methyl ligands; positive (red, solid) and negative (blue, dashed)  $L(\mathbf{r})$  contour lines were drawn at  $\pm 2.0 \times 10^n$ ,  $\pm 4.0 \times 10^n$ ,  $\pm 8.0 \times 10^n$   $\text{e}/\text{\AA}^5$  with  $n = \pm 2, \pm 1, 0$ . Bond paths are displayed as black solid lines. Bond critical points and charge concentrations are drawn as blue and red filled circles, respectively.

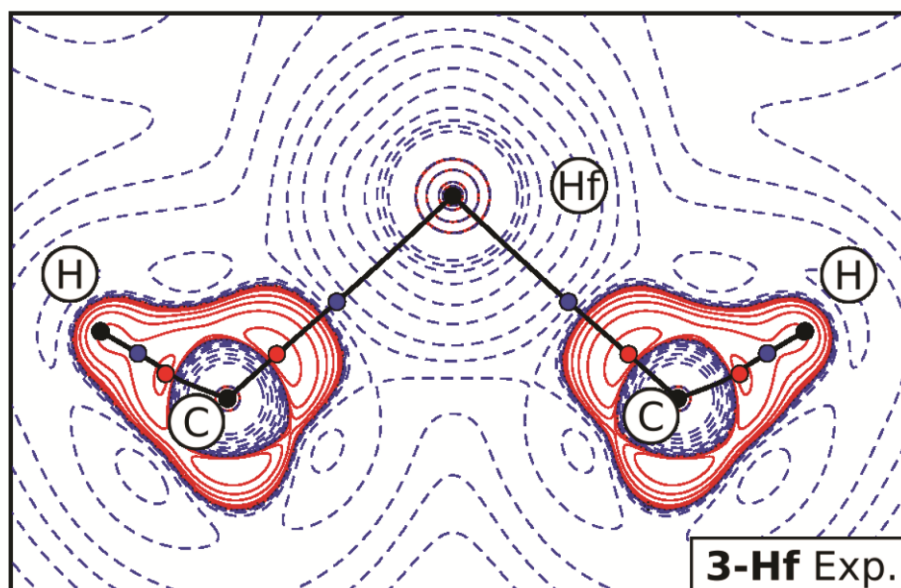


Figure S52: Experimental  $L(\mathbf{r}) = -\nabla^2\rho(\mathbf{r})$  map of **3-Hf** in the plane defined by  $M$  and the two methyl ligands; positive (red, solid) and negative (blue, dashed)  $L(\mathbf{r})$  contour lines were drawn at  $\pm 2.0 \times 10^n$ ,  $\pm 4.0 \times 10^n$ ,  $\pm 8.0 \times 10^n$   $e/\text{\AA}^5$  with  $n = \pm 2, \pm 1, 0$ . Bond paths are displayed as black solid lines. Bond critical points and charge concentrations are drawn as blue and red filled circles, respectively.

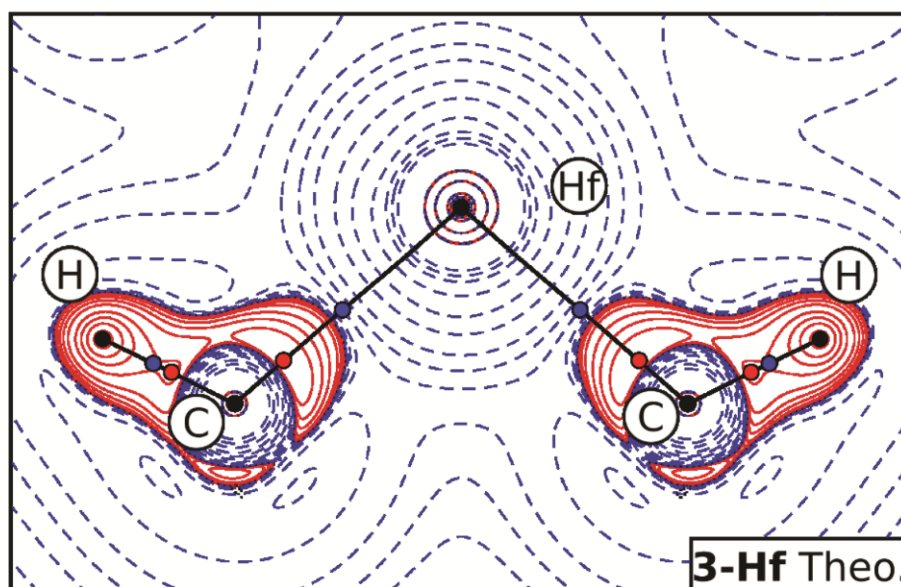


Figure S53: Theoretical (ADF)  $L(\mathbf{r}) = -\nabla^2\rho(\mathbf{r})$  map of **3-Zr** in the plane defined by  $M$  and the two methyl ligands; positive (red, solid) and negative (blue, dashed)  $L(\mathbf{r})$  contour lines were drawn at  $\pm 2.0 \times 10^n$ ,  $\pm 4.0 \times 10^n$ ,  $\pm 8.0 \times 10^n$   $e/\text{\AA}^5$  with  $n = \pm 2, \pm 1, 0$ . Bond paths are displayed as black solid lines. Bond critical points and charge concentrations are drawn as blue and red filled circles, respectively.

## 21. Experimental and theoretical Laplacian 3D-isosurface plot of 3-Zr

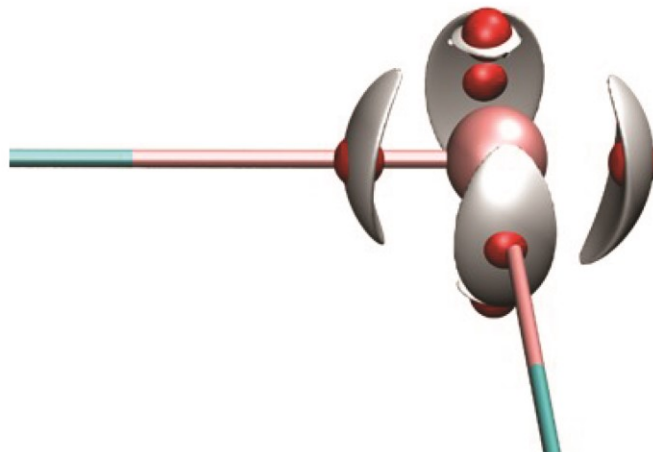


Figure S54: Experimental 3D isosurface plot of the Laplacian ( $\nabla^2\rho = -192e/\text{\AA}^5$ ) of 3-Ti at the metal center. Ti-Me bonds shown as sticks. The position of valence shell charge concentration maxima are shown as red spheres.

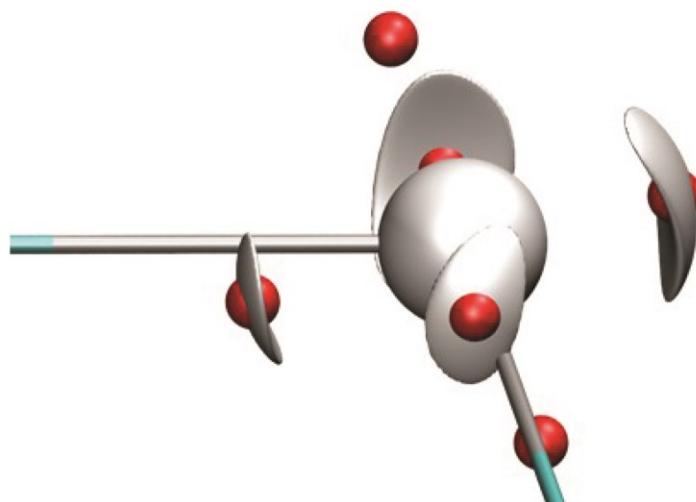


Figure S55: Experimental 3D isosurface plot of the Laplacian ( $\nabla^2\rho = -14.94e/\text{\AA}^5$ ) of 3-Zr at the metal center. Zr-Me bonds shown as sticks. The position of valence shell charge concentration maxima are shown as red spheres.

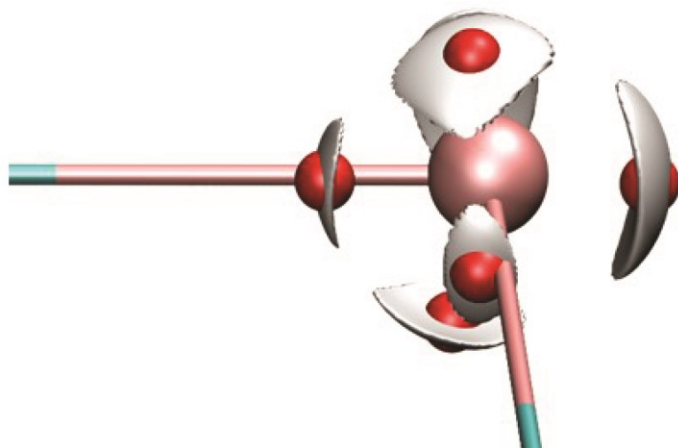


Figure S56: Theoretical 3D isosurface plot of the Laplacian ( $\nabla^2\rho = -214e/\text{\AA}^3$ ) of 3-Ti at the metal center. Ti-Me bonds shown as sticks. The position of valence shell charge concentration maxima are shown as red spheres.

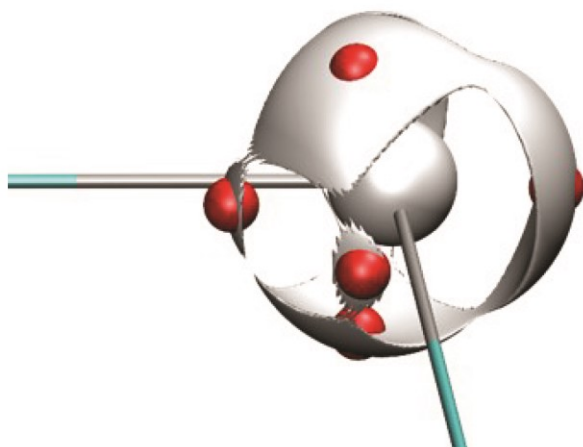


Figure S57: Theoretical 3D isosurface plot of the Laplacian ( $\nabla^2\rho = -214e/\text{\AA}^3$ ) of 3-Zr at the metal center. Zr-Me bonds shown as sticks. The position of valence shell charge concentration maxima are shown as red spheres.

22. Theoretical ELI-D 3D-isosurface plots of 3-Ti, 3-Zr and 3-Hf

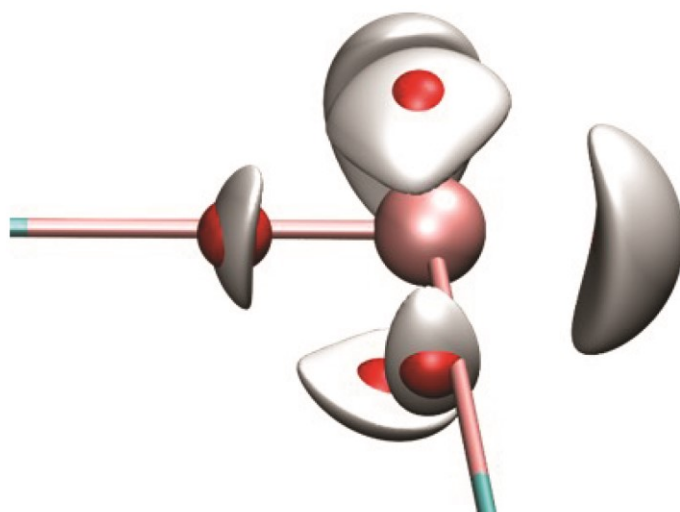


Figure S58: Theoretical 3D isosurface plot of the ELI-D (value: 1.52) of 3-Ti at the metal center. Ti-Me bonds shown as sticks. The position of valence shell maxima are shown as red spheres.

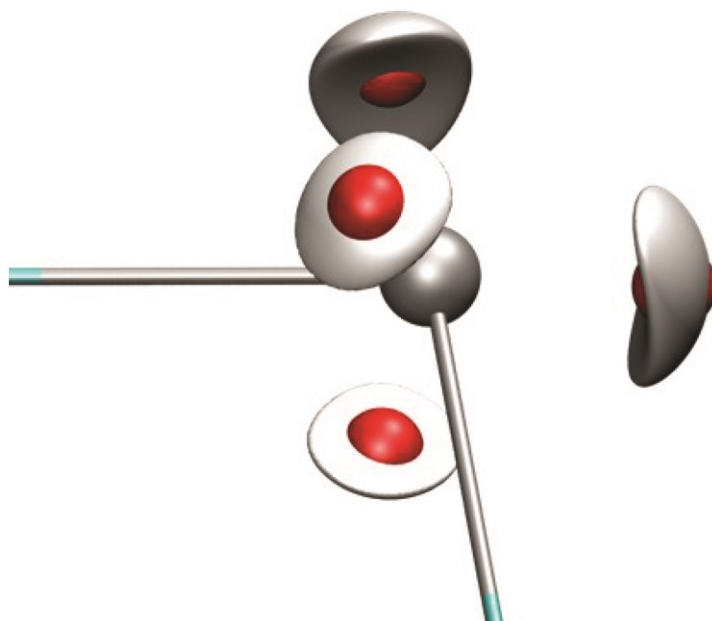


Figure S59: Theoretical 3D isosurface plot of the ELI-D (value: 1.45) of 3-Zr at the metal center. Zr-Me bonds shown as sticks. The position of valence shell maxima are shown as red spheres.

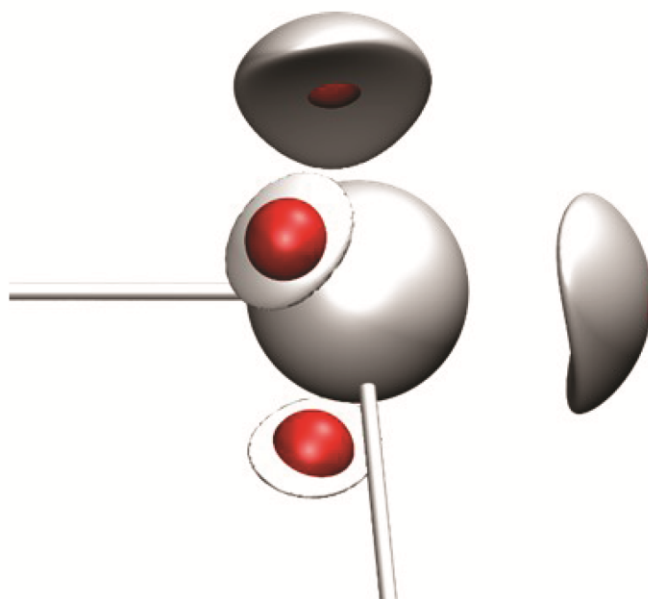
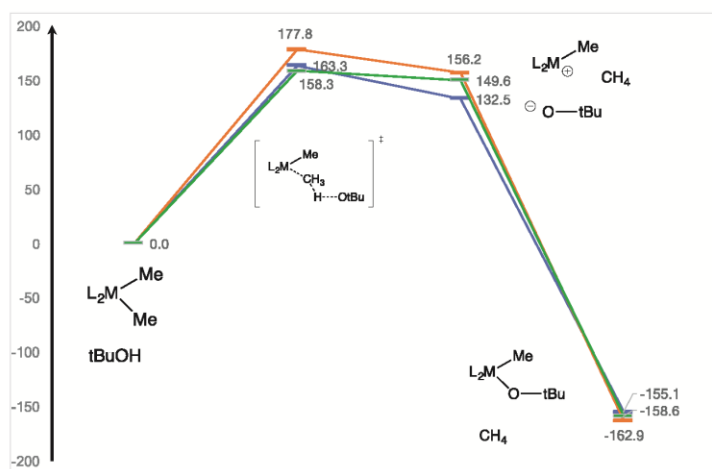


Figure S60: Theoretical 3D isosurface plot of the ELL-D (value: 1.18) of 3-Hf at the metal center. Hf-Me bonds shown as sticks. The position of valence shell maxima are shown as red spheres.

## 23. Kinetic measurements – theoretical verification



Scheme S1. Calculated free energies  $\Delta G$  (kJ/mol) in solution along the proposed pathway (green: M=Ti; blue: M=Zr; orange: M=Hf). Note: The 4-aryl groups on each of the sandwich rings have been replaced by methyl for saving computing time and resources.

XYZ coordinates and absolute energies for each species:

Methane



Figure S61. Molecular representation of methane.

Table S24. Calculated values of methane.

Center Number	Atomic Number	Atomic Type	Coordinates (Angstroms)		
			X	Y	Z
1	6	0	0.000000	0.000000	0.000000
2	1	0	0.633778	0.633778	0.633778
3	1	0	-0.633778	-0.633778	0.633778
4	1	0	-0.633778	0.633778	-0.633778
5	1	0	0.633778	-0.633778	-0.633778

HF= -40.5316364 / NImag=0  
Sum of electronic and thermal Enthalpies= -40.484428  
Sum of electronic and thermal Free Energies= -40.505587

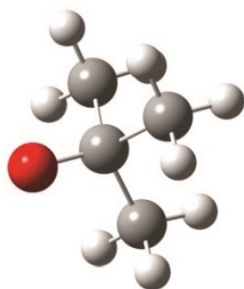
<sup>t</sup>Bu-OHFigure S62. Molecular representation of <sup>t</sup>BuOH.Table S25. Calculated values of <sup>t</sup>BuOH.

Center Number	Atomic Number	Atomic Type	Coordinates (Angstroms)		
			X	Y	Z
1	6	0	0.674402	1.265773	-0.527440
2	6	0	-0.007463	-0.000055	0.010230
3	1	0	0.192364	2.164454	-0.115380
4	1	0	1.740031	1.282302	-0.247386
5	1	0	0.614259	1.309022	-1.625638
6	6	0	0.683248	-1.260858	-0.527924
7	6	0	-1.498663	-0.005082	-0.329293
8	1	0	0.207481	-2.163112	-0.116402
9	1	0	0.623660	-1.303978	-1.626151
10	1	0	1.748955	-1.270106	-0.247752
11	1	0	-1.644548	-0.004925	-1.418876
12	1	0	-1.983855	-0.899925	0.087554
13	1	0	-1.989988	0.885892	0.088645
14	8	0	0.048819	-0.000112	1.468786
15	1	0	0.991937	0.002608	1.717655

HF= -233.7745988 / NImag=0

Sum of electronic and thermal Enthalpies= -233.635642

Sum of electronic and thermal Free Energies= -233.672636

<sup>t</sup>BuO<sup>-</sup>Figure S63. Molecular representation of <sup>t</sup>BuO<sup>-</sup>.Table S26. Calculated values of <sup>t</sup>BuO<sup>-</sup>.

Center Number	Atomic Number	Atomic Type	Coordinates (Angstroms)		
			X	Y	Z
1	6	0	0.464340	-1.377953	-0.433886
2	6	0	-0.000785	0.000124	0.141008

3	1	0	1.476984	-1.603783	-0.059253
4	1	0	-0.213602	-2.169358	-0.071873
5	1	0	0.485512	-1.417325	-1.539746
6	6	0	-1.419792	0.291723	-0.448623
7	6	0	0.969474	1.086971	-0.428534
8	1	0	-1.770461	1.270593	-0.079623
9	1	0	-1.455372	0.303061	-1.554775
10	1	0	-2.124134	-0.476073	-0.086446
11	1	0	1.011805	1.111766	-1.534211
12	1	0	0.651759	2.081563	-0.072360
13	1	0	1.987744	0.901820	-0.046350
14	8	0	-0.016207	-0.000932	1.508107

HF= -233.2497064 / NImag=0  
 Sum of electronic and thermal Enthalpies= -233.125392  
 Sum of electronic and thermal Free Energies= -233.161595

**3-Hf (4-Aryl ↔ Me)**

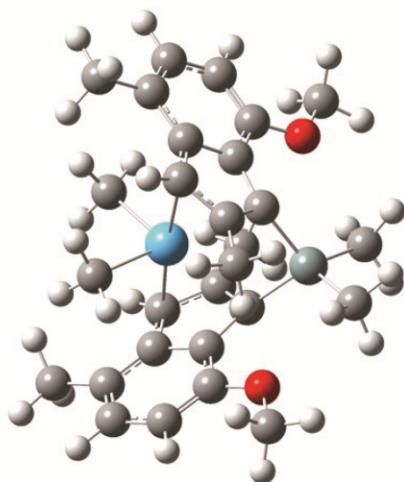


Figure S64. Molecular representation of **3-Hf**.

Table S27. Calculated values of **3-Hf**.

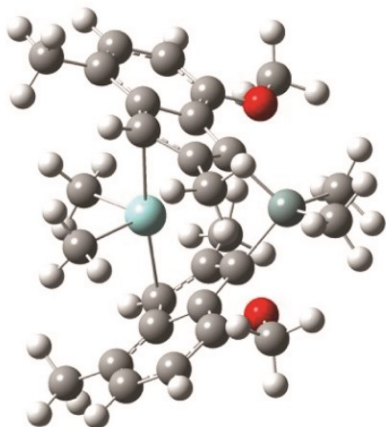
Center Number	Atomic Number	Atomic Type	Coordinates (Angstroms)		
			X	Y	Z
1	72	0	-0.000006	0.827401	-0.000008
2	14	0	-0.000002	-2.514000	-0.000018
3	8	0	3.230243	-1.899649	-0.864927
4	6	0	1.254038	2.359430	-1.065784
5	1	0	0.671670	2.910337	-1.821278
6	1	0	2.133950	1.917083	-1.563246
7	1	0	1.632864	3.085415	-0.327231
8	6	0	1.049001	0.716768	2.335638
9	1	0	0.789496	1.456941	3.087372
10	6	0	0.341918	-0.490375	2.108238
11	6	0	0.974388	-1.235008	1.037166
12	6	0	2.144371	-0.454090	0.670637
13	6	0	2.184604	0.753734	1.474598
14	6	0	3.233103	1.713098	1.363232

S65

## Appendix

---

15	6	0	4.237114	1.434775	0.457299
16	1	0	5.061746	2.141663	0.335878
17	6	0	4.255006	0.242903	-0.318288
18	1	0	5.100761	0.066812	-0.982119
19	6	0	3.240310	-0.695391	-0.215686
20	6	0	-0.866312	-0.867397	2.918533
21	1	0	-1.191495	-0.011196	3.524391
22	1	0	-0.623888	-1.696577	3.602081
23	1	0	-1.712788	-1.190069	2.301505
24	6	0	4.323340	-2.188912	-1.747723
25	1	0	4.112118	-3.180700	-2.162633
26	1	0	5.278713	-2.210994	-1.199583
27	1	0	4.382427	-1.449896	-2.563378
28	6	0	0.956411	-3.711934	-1.112525
29	1	0	1.707717	-4.243360	-0.510084
30	1	0	1.461571	-3.255896	-1.966220
31	1	0	0.228301	-4.451337	-1.484287
32	8	0	-3.230161	-1.899669	0.864952
33	6	0	-1.254058	2.359417	1.065778
34	1	0	-0.671694	2.910324	1.821275
35	1	0	-2.133967	1.917062	1.563239
36	1	0	-1.632889	3.085404	0.327230
37	6	0	-1.049025	0.716784	-2.335648
38	1	0	-0.789532	1.456967	-3.087376
39	6	0	-0.341931	-0.490357	-2.108270
40	6	0	-0.974387	-1.235006	-1.037200
41	6	0	-2.144368	-0.454098	-0.670649
42	6	0	-2.184621	0.753732	-1.474597
43	6	0	-3.233129	1.713084	-1.363208
44	6	0	-4.237120	1.434743	-0.457257
45	1	0	-5.061755	2.141625	-0.335812
46	6	0	-4.254985	0.242867	0.318324
47	1	0	-5.100720	0.066769	0.982180
48	6	0	-3.240283	-0.695418	0.215695
49	6	0	0.866292	-0.867353	-2.918587
50	1	0	1.191452	-0.011140	-3.524441
51	1	0	0.623871	-1.696529	-3.602139
52	1	0	1.712782	-1.190016	-2.301575
53	6	0	-4.323208	-2.188950	1.747804
54	1	0	-4.111943	-3.180730	2.162711
55	1	0	-5.278608	-2.211058	1.199710
56	1	0	-4.382273	-1.449930	2.563457
57	6	0	-0.956446	-3.711898	1.112499
58	1	0	-1.707761	-4.243317	0.510062
59	1	0	-1.461602	-3.255835	1.966185
60	1	0	-0.228354	-4.451311	1.484277
61	6	0	3.203853	2.962449	2.196797
62	1	0	3.188280	2.729876	3.274416
63	1	0	4.079469	3.594412	1.994789
64	1	0	2.297532	3.556185	1.987223
65	6	0	-3.203905	2.962442	-2.196761
66	1	0	-2.297584	3.556184	-1.987201
67	1	0	-3.188353	2.729880	-3.274383
68	1	0	-4.079521	3.594397	-1.994730
HF=-1578.2383043 / NImag=0					
Sum of electronic and thermal Enthalpies=				-1577.654785	
Sum of electronic and thermal Free Energies=				-1577.755477	

**3-Zr** (4-Aryl ↔ Me)Figure S65. Molecular representation of **3-Zr**.Table S28. Calculated values of **3-Zr**.

Center Number	Atomic Number	Atomic Type	Coordinates (Angstroms)		
			X	Y	Z
1	40	0	0.000065	0.932916	0.000051
2	14	0	-0.000088	-2.410606	0.000054
3	8	0	-3.228017	-1.797944	0.875803
4	6	0	-1.295986	2.442346	1.115857
5	1	0	-0.725931	2.978067	1.890515
6	1	0	-2.180412	1.978155	1.581564
7	1	0	-1.658098	3.173500	0.373476
8	6	0	-1.071031	0.802710	-2.355412
9	1	0	-0.817391	1.539489	-3.112746
10	6	0	-0.358843	-0.398566	-2.123228
11	6	0	-0.980829	-1.136635	-1.039773
12	6	0	-2.157241	-0.361773	-0.678916
13	6	0	-2.202539	0.842349	-1.487318
14	6	0	-3.247225	1.804007	-1.369677
15	6	0	-4.245858	1.529319	-0.455595
16	1	0	-5.067826	2.238424	-0.329168
17	6	0	-4.260026	0.339713	0.322264
18	1	0	-5.100192	0.167104	0.994084
19	6	0	-3.244898	-0.598794	0.217035
20	6	0	0.853447	-0.772858	-2.927641
21	1	0	1.171824	0.079794	-3.542033
22	1	0	0.621675	-1.612614	-3.602037
23	1	0	1.701316	-1.080085	-2.304252
24	6	0	-4.313216	-2.081233	1.770276
25	1	0	-4.097143	-3.069296	2.191557
26	1	0	-5.273196	-2.109144	1.230550
27	1	0	-4.366332	-1.335552	2.580236
28	6	0	-0.953790	-3.609167	1.114393
29	1	0	-1.703937	-4.143414	0.512956
30	1	0	-1.459829	-3.153175	1.967521
31	1	0	-0.223595	-4.346196	1.486916
32	8	0	3.227689	-1.798069	-0.876036
33	6	0	1.296235	2.442269	-1.115724
34	1	0	0.726223	2.978055	-1.890370

S67

35	1	0	2.180625	1.978020	-1.581443
36	1	0	1.658407	3.173376	-0.373325
37	6	0	1.071181	0.802600	2.355484
38	1	0	0.817613	1.539391	3.112831
39	6	0	0.358922	-0.398638	2.123339
40	6	0	0.980799	-1.136725	1.039842
41	6	0	2.157239	-0.361931	0.678927
42	6	0	2.202660	0.842172	1.487348
43	6	0	3.247399	1.803766	1.369653
44	6	0	4.245943	1.529038	0.455483
45	1	0	5.067933	2.238106	0.328993
46	6	0	4.259975	0.339453	-0.322414
47	1	0	5.100049	0.166838	-0.994344
48	6	0	3.244800	-0.598999	-0.217122
49	6	0	-0.853340	-0.772869	2.927820
50	1	0	-1.171648	0.079803	3.542219
51	1	0	-0.621561	-1.612625	3.602214
52	1	0	-1.701248	-1.080079	2.304485
53	6	0	4.312692	-2.081369	-1.770741
54	1	0	4.096441	-3.069366	-2.192086
55	1	0	5.272770	-2.109433	-1.231196
56	1	0	4.365733	-1.335611	-2.580635
57	6	0	0.953490	-3.609312	-1.114239
58	1	0	1.703559	-4.143635	-0.512771
59	1	0	1.459604	-3.153410	-1.967368
60	1	0	0.223212	-4.346261	-1.486755
61	6	0	-3.219800	3.055429	-2.200590
62	1	0	-3.202467	2.826011	-3.278756
63	1	0	-4.096962	3.685004	-1.997778
64	1	0	-2.315205	3.650773	-1.987987
65	6	0	3.220107	3.055181	2.200583
66	1	0	2.315529	3.650579	1.988056
67	1	0	3.202842	2.825753	3.278748
68	1	0	4.097288	3.684710	1.997712
HF=-1575.9089236 / NImag=0					
Sum of electronic and thermal Enthalpies=				-1575.325709	
Sum of electronic and thermal Free Energies=				-1575.426397	

**3-Ti (4-Aryl ↔ Me)**

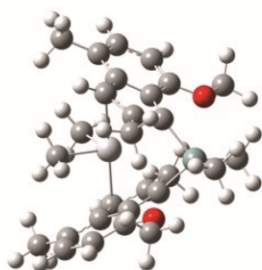


Figure S66. Molecular representation of **3-Ti**.

Table S29. Calculated values of **3-Ti**.

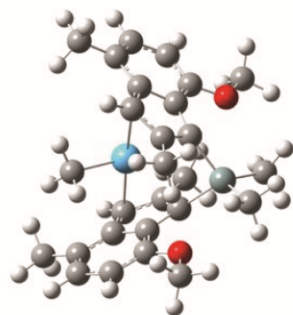
Center Number	Atomic Number	Atomic Type	Coordinates (Angstroms)		
			X	Y	Z
1	22	0	-0.000003	0.925251	-0.000012

S68

Appendix

---

2	14	0	0.000002	-2.354791	0.000034
3	8	0	-3.244853	-1.754648	0.804600
4	6	0	-1.188904	2.423745	0.990659
5	1	0	-2.059362	1.953306	1.477012
6	1	0	-1.559005	3.124592	0.228933
7	1	0	-0.612600	2.979964	1.741659
8	6	0	-0.972926	0.925238	-2.270503
9	1	0	-0.695111	1.678234	-3.001831
10	6	0	-0.273617	-0.284825	-2.052143
11	6	0	-0.941295	-1.049006	-1.019301
12	6	0	-2.113125	-0.273956	-0.664381
13	6	0	-2.132412	0.945303	-1.446867
14	6	0	-3.184153	1.900506	-1.351480
15	6	0	-4.207991	1.610606	-0.471390
16	1	0	-5.036185	2.315034	-0.359300
17	6	0	-4.245452	0.405936	0.284980
18	1	0	-5.108750	0.219054	0.922729
19	6	0	-3.231859	-0.533866	0.186055
20	6	0	0.940107	-0.656124	-2.853444
21	1	0	1.758476	-1.045635	-2.239107
22	1	0	1.309822	0.219991	-3.402865
23	1	0	0.683460	-1.435362	-3.589473
24	6	0	-4.358727	-2.058061	1.656129
25	1	0	-4.430726	-1.338822	2.488280
26	1	0	-4.162781	-3.061080	2.050958
27	1	0	-5.302190	-2.060137	1.087219
28	6	0	-0.960336	-3.552679	1.109609
29	1	0	-1.469013	-3.095991	1.961284
30	1	0	-0.233690	-4.291602	1.485359
31	1	0	-1.708737	-4.086690	0.505791
32	8	0	3.244770	-1.754657	-0.804623
33	6	0	1.188873	2.423730	-0.990735
34	1	0	2.059339	1.953289	-1.477073
35	1	0	1.558961	3.124612	-0.229037
36	1	0	0.612557	2.979911	-1.741754
37	6	0	0.972939	0.925304	2.270486
38	1	0	0.695133	1.678320	3.001797
39	6	0	0.273619	-0.284759	2.052158
40	6	0	0.941290	-1.048973	1.019335
41	6	0	2.113117	-0.273940	0.664385
42	6	0	2.132435	0.945324	1.446861
43	6	0	3.184212	1.900489	1.351479
44	6	0	4.208039	1.610555	0.471388
45	1	0	5.036256	2.314956	0.359297
46	6	0	4.245453	0.405891	-0.284994
47	1	0	5.108740	0.218986	-0.922753
48	6	0	3.231831	-0.533879	-0.186067
49	6	0	-0.940102	-0.656024	2.853479
50	1	0	-1.758480	-1.045541	2.239160
51	1	0	-1.309801	0.220109	3.402881
52	1	0	-0.683457	-1.435245	3.589527
53	6	0	4.358615	-2.058104	-1.656178
54	1	0	4.430622	-1.338862	-2.488326
55	1	0	4.162624	-3.061113	-2.051009
56	1	0	5.302090	-2.060218	-1.087288
57	6	0	0.960365	-3.552680	-1.109518
58	1	0	1.469038	-3.095994	-1.961198
59	1	0	0.233735	-4.291621	-1.485259
60	1	0	1.708775	-4.086667	-0.505689
61	6	0	-3.137647	3.160927	-2.167809
62	1	0	-3.093926	2.942758	-3.247587
63	1	0	-4.019796	3.788303	-1.980124
64	1	0	-2.238558	3.754317	-1.927770
65	6	0	3.137752	3.160908	2.167813
66	1	0	3.094024	2.942736	3.247590
67	1	0	4.019923	3.788253	1.980129
68	1	0	2.238684	3.754331	1.927778
HF=-2378.837271 / NImag=0					
Sum of electronic and thermal Enthalpies=				-2378.252721	
Sum of electronic and thermal Free Energies=				-2378.352156	

**3-Hf<sup>+</sup> cation (4-Aryl ↔ Me)**Figure S67. Molecular representation of **3-Hf<sup>+</sup>** cation.Table S30. Calculated values of **3-Hf<sup>+</sup>** cation.

Center Number	Atomic Number	Atomic Type	Coordinates (Angstroms)		
			X	Y	Z
1	6	0	3.133162	0.678903	0.240883
2	6	0	2.032528	0.444498	-0.644506
3	6	0	2.108668	-0.705670	-1.527201
4	6	0	3.180008	-1.639330	-1.476070
5	6	0	4.176784	-1.383698	-0.551953
6	6	0	4.167528	-0.242833	0.291392
7	6	0	0.965857	-0.642951	-2.383212
8	6	0	0.254010	0.560447	-2.115167
9	6	0	0.860893	1.241240	-0.992457
10	72	0	-0.076576	-0.865724	-0.114439
11	6	0	1.228024	-2.413651	0.858270
12	6	0	-0.942052	0.981538	-2.918677
13	14	0	-0.105396	2.479011	0.112287
14	6	0	0.840543	3.647618	1.255794
15	6	0	3.198385	-2.829119	-2.391314
16	8	0	3.107972	1.853538	0.927794
17	6	0	4.210957	2.142121	1.806247
18	6	0	-0.959325	-0.934340	2.290011
19	6	0	-0.297244	0.303607	2.107987
20	6	0	-0.984595	1.082822	1.090266
21	6	0	-2.137571	0.282085	0.711584
22	6	0	-2.103883	-0.977483	1.444662
23	6	0	-3.039668	-2.032287	1.200359
24	6	0	-4.023459	-1.775132	0.262679
25	6	0	-4.135600	-0.528400	-0.411995
26	6	0	-3.235510	0.503255	-0.182596
27	6	0	0.879009	0.698613	2.949411
28	6	0	-2.963131	-3.315871	1.977711
29	8	0	-3.323924	1.747145	-0.725022
30	6	0	-4.435414	2.021376	-1.598623
31	6	0	-1.138773	3.678959	-0.915655
32	1	0	-0.654880	-1.702723	2.994134
33	1	0	-4.768031	-2.544393	0.044883
34	1	0	-4.974935	-0.380369	-1.090457
35	1	0	1.287482	-0.180319	3.464400
36	1	0	0.556142	1.423324	3.713504
37	1	0	1.681066	1.167660	2.372510
38	1	0	-4.313268	3.065064	-1.905943
39	1	0	-5.389998	1.897058	-1.065151
40	1	0	-4.412992	1.366278	-2.483823
41	1	0	-1.883504	4.155830	-0.261668
42	1	0	-1.660195	3.251355	-1.773204

43	1	0	-0.449124	4.460508	-1.273322
44	1	0	0.680777	-3.000724	1.610621
45	1	0	2.129204	-1.999377	1.335980
46	1	0	1.574493	-3.099696	0.065936
47	1	0	0.736814	-1.333409	-3.192821
48	1	0	5.023237	-2.070323	-0.477166
49	1	0	5.016434	-0.078506	0.953645
50	1	0	-1.241544	0.178035	-3.604044
51	1	0	-0.692227	1.867182	-3.522740
52	1	0	-1.803778	1.247726	-2.295165
53	1	0	3.980331	3.114727	2.253385
54	1	0	5.153486	2.204140	1.241473
55	1	0	4.296349	1.378986	2.595690
56	1	0	1.590606	4.198631	0.670099
57	1	0	1.341735	3.176834	2.103528
58	1	0	0.105268	4.373091	1.639740
59	1	0	-3.112895	-3.134785	3.054546
60	1	0	-3.730926	-4.025368	1.641675
61	1	0	-1.979411	-3.799391	1.871746
62	1	0	2.331220	-3.486546	-2.207016
63	1	0	3.148863	-2.524073	-3.449052
64	1	0	4.110042	-3.423773	-2.247495
HF=-1538.1536482 / NImag=0					
Sum of electronic and thermal Enthalpies= -1537.605478					
Sum of electronic and thermal Free Energies= -1537.701444					

**3-Zr<sup>+</sup> cation (4-Aryl ↔ Me)**

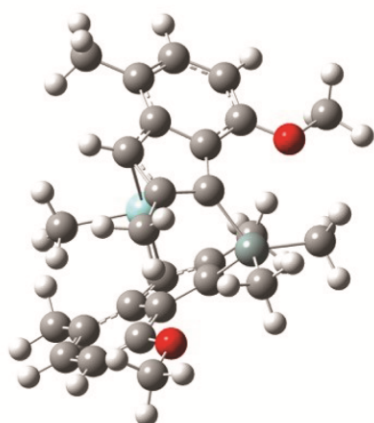


Figure S68. Molecular representation of 3-Zr<sup>+</sup> cation.

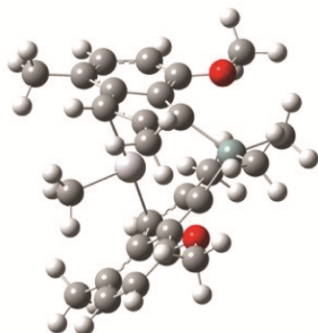
Table S31. Calculated values of 3-Zr<sup>+</sup> cation.

Center Number	Atomic Number	Atomic Type	Coordinates (Angstroms)		
			X	Y	Z
1	6	0	3.133537	0.581704	0.261141
2	6	0	2.047168	0.359758	-0.642584
3	6	0	2.144207	-0.766538	-1.551370
4	6	0	3.217897	-1.697241	-1.505128
5	6	0	4.197875	-1.460211	-0.558189
6	6	0	4.171264	-0.336626	0.308068
7	6	0	1.012612	-0.692035	-2.419089
8	6	0	0.279699	0.491017	-2.125980

## Appendix

---

9	6	0	0.867010	1.147557	-0.977997
10	40	0	-0.103199	-0.996999	-0.175830
11	6	0	1.261603	-2.493669	0.851571
12	6	0	-0.916926	0.914780	-2.926657
13	14	0	-0.116465	2.360954	0.138254
14	6	0	0.809283	3.512394	1.315926
15	6	0	3.257630	-2.864130	-2.449358
16	8	0	3.092610	1.741379	0.973768
17	6	0	4.181154	2.013679	1.874464
18	6	0	-1.005879	-1.076112	2.265965
19	6	0	-0.328843	0.153184	2.095423
20	6	0	-1.005877	0.948962	1.081946
21	6	0	-2.166583	0.166715	0.695144
22	6	0	-2.147131	-1.099433	1.417049
23	6	0	-3.090496	-2.143389	1.158970
24	6	0	-4.069921	-1.868466	0.222331
25	6	0	-4.166660	-0.614996	-0.443586
26	6	0	-3.255655	0.404742	-0.204893
27	6	0	0.847374	0.529170	2.944348
28	6	0	-3.025645	-3.437036	1.920810
29	8	0	-3.325289	1.651877	-0.744105
30	6	0	-4.428319	1.942873	-1.622498
31	6	0	-1.136009	3.578380	-0.883406
32	1	0	-0.710880	-1.855202	2.962674
33	1	0	-4.820676	-2.628858	-0.005283
34	1	0	-5.000829	-0.454032	-1.125490
35	1	0	1.258455	-0.361108	3.437605
36	1	0	0.524303	1.234330	3.726790
37	1	0	1.647332	1.014600	2.378438
38	1	0	-4.289789	2.985049	-1.928186
39	1	0	-5.387324	1.831965	-1.093869
40	1	0	-4.411382	1.288370	-2.508306
41	1	0	-1.890016	4.044864	-0.232619
42	1	0	-1.644706	3.165391	-1.755630
43	1	0	-0.440658	4.365340	-1.217532
44	1	0	0.696192	-3.089485	1.582887
45	1	0	2.138523	-2.053896	1.348512
46	1	0	1.628731	-3.157800	0.050906
47	1	0	0.798347	-1.365864	-3.246860
48	1	0	5.045485	-2.145573	-0.484161
49	1	0	5.008958	-0.183830	0.987266
50	1	0	-1.200316	0.124252	-3.633723
51	1	0	-0.677406	1.818815	-3.507367
52	1	0	-1.786819	1.153145	-2.302471
53	1	0	3.940569	2.974853	2.340736
54	1	0	5.131831	2.091907	1.325375
55	1	0	4.258352	1.232656	2.647168
56	1	0	1.564890	4.078692	0.752334
57	1	0	1.300562	3.027804	2.161778
58	1	0	0.065064	4.226912	1.703403
59	1	0	-3.177810	-3.268965	2.999389
60	1	0	-3.797191	-4.137051	1.573397
61	1	0	-2.044801	-3.925980	1.812021
62	1	0	2.391390	-3.531182	-2.298283
63	1	0	3.225174	-2.532226	-3.499683
64	1	0	4.170113	-3.457547	-2.305402
HF=-1535.8341356 / NImag=0					
Sum of electronic and thermal Enthalpies=				-1535.286000	
Sum of electronic and thermal Free Energies=				-1535.381372	

**3-Ti<sup>+</sup> cation (4-Aryl ↔ Me)**Figure S69. Molecular representation of **3-Ti<sup>+</sup>** cation.Table S32. Calculated values of **3-Ti<sup>+</sup>** cation.

Center Number	Atomic Number	Atomic Type	Coordinates (Angstroms)		
			X	Y	Z
1	6	0	3.089654	0.550232	-0.000336
2	6	0	1.927139	0.249323	-0.775766
3	6	0	1.907257	-1.003288	-1.507308
4	6	0	2.993985	-1.914710	-1.503800
5	6	0	4.095337	-1.554965	-0.739959
6	6	0	4.149505	-0.351404	0.001092
7	6	0	0.659890	-1.055273	-2.199779
8	6	0	-0.026412	0.168075	-2.007584
9	6	0	0.707014	0.991665	-1.064846
10	22	0	0.016686	-0.892532	0.120368
11	6	0	1.246138	-2.384731	1.019751
12	6	0	-1.274421	0.493089	-2.769451
13	14	0	-0.167240	2.350381	-0.027835
14	6	0	0.858551	3.584848	0.962507
15	6	0	2.912091	-3.209370	-2.257087
16	8	0	3.102540	1.753529	0.627240
17	6	0	4.281721	2.117919	1.372300
18	6	0	-0.821055	-0.957116	2.334766
19	6	0	-0.262534	0.328777	2.134306
20	6	0	-0.985939	1.014362	1.079001
21	6	0	-2.062574	0.116426	0.706864
22	6	0	-1.928943	-1.122859	1.451961
23	6	0	-2.742907	-2.265343	1.188393
24	6	0	-3.742048	-2.097019	0.243065
25	6	0	-3.992882	-0.855881	-0.400755
26	6	0	-3.195451	0.253333	-0.158730
27	6	0	0.917326	0.823737	2.912262
28	6	0	-2.530606	-3.545493	1.945977
29	8	0	-3.431835	1.503190	-0.634368
30	6	0	-4.602919	1.700617	-1.451258
31	6	0	-1.260747	3.478961	-1.074244
32	1	0	-0.483230	-1.677102	3.071733
33	1	0	-4.399483	-2.937504	0.008639
34	1	0	-4.851517	-0.780120	-1.066115
35	1	0	1.732059	1.168637	2.263693
36	1	0	1.304595	0.028722	3.561827
37	1	0	0.620448	1.675688	3.543060
38	1	0	-4.545029	1.103047	-2.374355

S73

39	1	0	-4.608026	2.766928	-1.698493
40	1	0	-5.513420	1.439363	-0.891349
41	1	0	-1.800371	3.002327	-1.894648
42	1	0	-0.602006	4.255911	-1.494428
43	1	0	-1.993228	3.973474	-0.419452
44	1	0	2.302003	-2.393082	0.721545
45	1	0	0.738845	-3.216222	0.476156
46	1	0	1.166293	-2.572450	2.093650
47	1	0	0.324311	-1.861877	-2.849032
48	1	0	4.962550	-2.218318	-0.708104
49	1	0	5.057019	-0.124912	0.558635
50	1	0	-1.986926	1.091134	-2.198688
51	1	0	-1.774298	-0.427341	-3.099357
52	1	0	-1.003591	1.070571	-3.668251
53	1	0	4.471876	1.398794	2.183516
54	1	0	4.064623	3.105047	1.792979
55	1	0	5.156927	2.179038	0.708390
56	1	0	1.452428	3.169477	1.778052
57	1	0	0.151064	4.320753	1.377492
58	1	0	1.536628	4.115381	0.278001
59	1	0	-2.714325	-3.403249	3.023269
60	1	0	-3.206290	-4.332590	1.586449
61	1	0	-1.494701	-3.907433	1.844431
62	1	0	2.667090	-3.046008	-3.318323
63	1	0	3.860009	-3.760110	-2.201846
64	1	0	2.119288	-3.852826	-1.838509

HF= -2338.7553392 / NImag=0  
Sum of electronic and thermal Enthalpies= -2338.206367  
Sum of electronic and thermal Free Energies= -2338.300619

### 3-Hf<sup>+</sup> – <sup>t</sup>BuO<sup>-</sup> ion pair

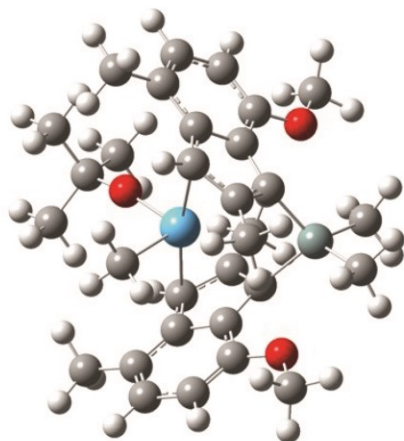


Figure S70. Molecular representation of the 3-Hf<sup>+</sup> – <sup>t</sup>BuO<sup>-</sup> ion pair.

*Appendix*

Table S33. Calculated values of the **3-Hf<sup>+</sup> – <sup>t</sup>BuO<sup>-</sup>** ion pair.

Center Number	Atomic Number	Atomic Type	Coordinates (Angstroms)		
			X	Y	Z
1	72	0	0.060965	0.508875	0.255142
2	14	0	-1.141061	-2.561312	-0.575090
3	8	0	2.188666	-2.905863	-1.223930
4	6	0	0.682877	-0.592013	2.553183
5	1	0	0.610887	-0.019686	3.474359
6	6	0	-0.375772	-1.339743	1.976824
7	6	0	0.084292	-1.977538	0.763181
8	6	0	1.494558	-1.627118	0.654625
9	6	0	1.861025	-0.793375	1.784239
10	6	0	3.187289	-0.319989	1.990429
11	6	0	4.139321	-0.711601	1.070272
12	1	0	5.174035	-0.380352	1.192099
13	6	0	3.829591	-1.556737	-0.030663
14	1	0	4.635322	-1.859998	-0.698121
15	6	0	2.540730	-2.024217	-0.236678
16	6	0	-1.728214	-1.422268	2.625731
17	1	0	-1.821180	-0.644482	3.395623
18	1	0	-1.858674	-2.400815	3.115809
19	1	0	-2.553379	-1.300205	1.915829
20	6	0	3.211501	-3.321711	-2.138955
21	1	0	2.717155	-3.995379	-2.847882
22	1	0	4.017235	-3.860799	-1.615233
23	1	0	3.635737	-2.459650	-2.679348
24	6	0	-0.524793	-3.710195	-1.949480
25	1	0	-0.078883	-4.608197	-1.496545
26	1	0	0.207180	-3.273440	-2.631414
27	1	0	-1.409308	-4.022710	-2.528595
28	8	0	-4.066554	-1.112637	0.349665
29	6	0	-0.911502	1.933731	1.710511
30	1	0	-0.304869	2.050879	2.622164
31	1	0	-1.926996	1.623801	2.005997
32	1	0	-0.997121	2.922566	1.231995
33	6	0	-0.824368	1.291210	-2.004563
34	1	0	-0.276533	2.051017	-2.554638
35	6	0	-0.570817	-0.105180	-2.080507
36	6	0	-1.523835	-0.815807	-1.251345
37	6	0	-2.402842	0.202966	-0.715504
38	6	0	-1.968034	1.507234	-1.184904
39	6	0	-2.663905	2.707890	-0.855766
40	6	0	-3.799525	2.576711	-0.082843
41	1	0	-4.366950	3.470013	0.191108
42	6	0	-4.283727	1.313031	0.356609
43	1	0	-5.212982	1.279144	0.923819
44	6	0	-3.614866	0.142153	0.041224
45	6	0	0.493481	-0.680641	-2.972439
46	1	0	1.114886	0.126369	-3.381308
47	1	0	0.033769	-1.214779	-3.818913
48	1	0	1.150962	-1.389904	-2.455737
49	6	0	-5.279603	-1.216055	1.107587
50	1	0	-5.444312	-2.289187	1.255230
51	1	0	-6.129213	-0.782242	0.556262
52	1	0	-5.181754	-0.717207	2.085766
53	6	0	-2.537893	-3.592670	0.182154
54	1	0	-3.361464	-3.686003	-0.540805
55	1	0	-2.944020	-3.205431	1.118702
56	1	0	-2.125747	-4.598780	0.364317
57	6	0	3.496741	0.549329	3.175705
58	1	0	3.278398	0.029592	4.123416
59	1	0	4.554269	0.847732	3.185841
60	1	0	2.883001	1.465135	3.164037
61	6	0	-2.147677	4.037153	-1.327459
62	1	0	-1.165425	4.259581	-0.877804
63	1	0	-2.006764	4.053693	-2.420733
64	1	0	-2.836707	4.849180	-1.057136
65	8	0	1.572321	1.643497	-0.079224
66	6	0	2.525132	2.549850	-0.626984

67	6	0	1.794580	3.825588	-1.069414
68	6	0	3.552381	2.886990	0.462234
69	6	0	3.206905	1.863460	-1.817126
70	1	0	1.047444	3.596203	-1.840866
71	1	0	1.279884	4.282003	-0.210949
72	1	0	2.504473	4.558778	-1.480881
73	1	0	4.081824	1.977555	0.772909
74	1	0	4.284901	3.618711	0.088941
75	1	0	3.045098	3.315895	1.338721
76	1	0	3.995814	2.503232	-2.240265
77	1	0	3.652126	0.912350	-1.491145
78	1	0	2.469567	1.652561	-2.604941
HF=-1771.5478942 / NImag=0					
Sum of electronic and thermal Enthalpies=				-1770.871818	
Sum of electronic and thermal Free Energies=				-1770.984579	

**3-Zr<sup>+</sup> - <sup>t</sup>BuO<sup>-</sup> ion pair**

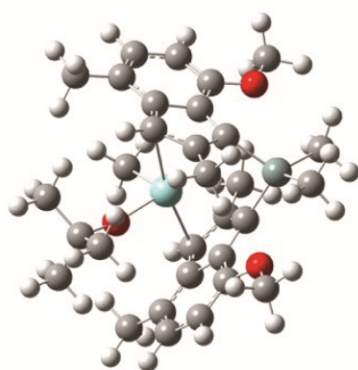


Figure S71. Molecular representation of the 3-Zr<sup>+</sup> - <sup>t</sup>BuO<sup>-</sup> ion pair.

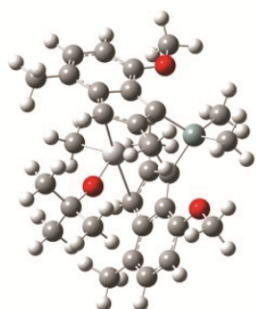
Table S34. Calculated values of the 3-Zr<sup>+</sup> - <sup>t</sup>BuO<sup>-</sup> ion pair.

Center Number	Atomic Number	Atomic Type	Coordinates (Angstroms)		
			X	Y	Z
1	40	0	0.074013	0.558583	0.288828
2	14	0	-1.150363	-2.491813	-0.588853
3	8	0	2.180700	-2.838184	-1.228385
4	6	0	0.668157	-0.606861	2.596189
5	1	0	0.593624	-0.052104	3.527979
6	6	0	-0.391105	-1.333539	1.997863
7	6	0	0.070468	-1.945693	0.770809
8	6	0	1.485388	-1.607228	0.681562
9	6	0	1.849097	-0.795279	1.827376
10	6	0	3.173482	-0.320560	2.042016
11	6	0	4.128242	-0.696892	1.117887
12	1	0	5.161844	-0.364723	1.246181
13	6	0	3.821558	-1.523179	0.002591
14	1	0	4.628452	-1.813026	-0.669428
15	6	0	2.531922	-1.983376	-0.217340
16	6	0	-1.749379	-1.417493	2.633668
17	1	0	-1.838542	-0.662089	3.425992
18	1	0	-1.897582	-2.408644	3.092510
19	1	0	-2.566839	-1.263060	1.921019

## Appendix

20	6	0	3.206640	-3.236296	-2.147873
21	1	0	2.712766	-3.888933	-2.876551
22	1	0	4.006183	-3.793190	-1.633347
23	1	0	3.639041	-2.363435	-2.663874
24	6	0	-0.530716	-3.623957	-1.975662
25	1	0	-0.095334	-4.531303	-1.531102
26	1	0	0.210263	-3.184243	-2.645726
27	1	0	-1.412642	-3.922247	-2.566174
28	8	0	-4.068612	-1.036584	0.354179
29	6	0	-0.918539	1.962438	1.794859
30	1	0	-0.320103	2.044728	2.714643
31	1	0	-1.940724	1.647794	2.057040
32	1	0	-0.979006	2.957670	1.326839
33	6	0	-0.819851	1.376628	-1.980455
34	1	0	-0.271703	2.140819	-2.524680
35	6	0	-0.578177	-0.019170	-2.076993
36	6	0	-1.526046	-0.735065	-1.246093
37	6	0	-2.398879	0.282654	-0.696135
38	6	0	-1.956934	1.589959	-1.149161
39	6	0	-2.638173	2.790817	-0.794261
40	6	0	-3.769654	2.657118	-0.014707
41	1	0	-4.325746	3.550890	0.280031
42	6	0	-4.263611	1.390863	0.404463
43	1	0	-5.189375	1.355736	0.977285
44	6	0	-3.607264	0.219204	0.064840
45	6	0	0.486983	-0.592242	-2.968952
46	1	0	1.093958	0.217098	-3.394667
47	1	0	0.030548	-1.147324	-3.803411
48	1	0	1.158291	-1.283610	-2.444904
49	6	0	-5.283045	-1.142582	1.109825
50	1	0	-5.457788	-2.216715	1.237206
51	1	0	-6.128003	-0.690439	0.566187
52	1	0	-5.181079	-0.663245	2.097235
53	6	0	-2.560885	-3.527125	0.136705
54	1	0	-3.380915	-3.594970	-0.593121
55	1	0	-2.968914	-3.158445	1.079821
56	1	0	-2.159629	-4.541271	0.297239
57	6	0	3.478258	0.546214	3.230314
58	1	0	3.227823	0.038101	4.176167
59	1	0	4.541924	0.820615	3.260420
60	1	0	2.887079	1.476514	3.199170
61	6	0	-2.110991	4.123261	-1.244605
62	1	0	-1.123434	4.326966	-0.797469
63	1	0	-1.977091	4.158656	-2.338276
64	1	0	-2.789532	4.937349	-0.954766
65	8	0	1.621134	1.715775	-0.011602
66	6	0	2.578523	2.603002	-0.581295
67	6	0	1.861544	3.891382	-1.009505
68	6	0	3.634197	2.917759	0.487895
69	6	0	3.220206	1.902509	-1.785512
70	1	0	1.092391	3.672492	-1.762433
71	1	0	1.374431	4.357688	-0.140264
72	1	0	2.573746	4.611983	-1.439150
73	1	0	4.141738	1.994093	0.794032
74	1	0	4.381204	3.626485	0.098758
75	1	0	3.154312	3.364553	1.370843
76	1	0	4.002646	2.531175	-2.236621
77	1	0	3.665021	0.948818	-1.466571
78	1	0	2.456963	1.693152	-2.548669

HF= -1769.2167771 / NImag=0  
Sum of electronic and thermal Enthalpies= -1768.540769  
Sum of electronic and thermal Free Energies= -1768.652525

**3-Ti<sup>+</sup> – <sup>t</sup>BuO<sup>-</sup> ion pair**Figure S72. Molecular representation of the 3-Ti<sup>+</sup> – <sup>t</sup>BuO<sup>-</sup> ion pair.Table S35. Calculated values of the 3-Ti<sup>+</sup> – <sup>t</sup>BuO<sup>-</sup> ion pair.

Center Number	Atomic Number	Atomic Type	Coordinates (Angstroms)		
			X	Y	Z
1	22	0	-0.259769	0.687811	0.149067
2	14	0	-0.687259	-2.422433	-0.582872
3	8	0	-3.874421	-1.725907	0.475985
4	6	0	-1.158415	1.936978	1.639809
5	1	0	-2.139791	1.556215	1.959376
6	1	0	-1.293533	2.939918	1.206451
7	1	0	-0.481888	2.006230	2.503110
8	6	0	-1.322822	1.404747	-1.866278
9	1	0	-0.958102	2.297028	-2.366960
10	6	0	-0.796477	0.097278	-2.037079
11	6	0	-1.538450	-0.831591	-1.209168
12	6	0	-2.591997	-0.047557	-0.598951
13	6	0	-2.452034	1.336777	-0.999374
14	6	0	-3.340836	2.356706	-0.555922
15	6	0	-4.365644	1.962451	0.282085
16	1	0	-5.072065	2.709467	0.653262
17	6	0	-4.559749	0.606943	0.667328
18	1	0	-5.416837	0.360337	1.292636
19	6	0	-3.705643	-0.392313	0.225997
20	6	0	0.367462	-0.195355	-2.939426
21	1	0	1.161180	-0.766996	-2.439594
22	1	0	0.800067	0.745241	-3.305935
23	1	0	0.039118	-0.780218	-3.813287
24	6	0	-4.954967	-2.109816	1.337646
25	1	0	-4.852990	-1.646023	2.332420
26	1	0	-4.885779	-3.199328	1.428890
27	1	0	-5.928376	-1.834760	0.900477
28	6	0	-1.732608	-3.714743	0.326291
29	1	0	-2.134536	-3.380687	1.285667
30	1	0	-1.079829	-4.585912	0.501193
31	1	0	-2.571733	-4.035360	-0.308188
32	8	0	2.587875	-2.194447	-1.486115
33	6	0	1.086139	-0.367277	2.554276
34	1	0	1.004059	0.139229	3.515076
35	6	0	0.018468	-1.007298	1.895182
36	6	0	0.489960	-1.535072	0.613719
37	6	0	1.922447	-1.240108	0.585711
38	6	0	2.277203	-0.526732	1.790709
39	6	0	3.596517	-0.077778	2.051926
40	6	0	4.564118	-0.379911	1.100947

## Appendix

---

41	1	0	5.598333	-0.065659	1.265135
42	6	0	4.254927	-1.093606	-0.082207
43	1	0	5.056798	-1.309273	-0.787612
44	6	0	2.950891	-1.509507	-0.351207
45	6	0	-1.305053	-1.240403	2.575616
46	1	0	-2.159935	-1.234342	1.893033
47	1	0	-1.475725	-0.471132	3.340776
48	1	0	-1.302080	-2.221542	3.079765
49	6	0	3.601080	-2.448003	-2.464996
50	1	0	4.035408	-1.508189	-2.844519
51	1	0	3.097279	-2.976762	-3.282511
52	1	0	4.403439	-3.083583	-2.055933
53	6	0	0.003720	-3.422598	-2.034400
54	1	0	0.562777	-2.842626	-2.772124
55	1	0	-0.858597	-3.895698	-2.532860
56	1	0	0.660066	-4.219544	-1.655602
57	6	0	-3.128510	3.782203	-0.978489
58	1	0	-3.142273	3.886848	-2.075855
59	1	0	-3.902843	4.440507	-0.561223
60	1	0	-2.146183	4.152534	-0.637902
61	6	0	3.921831	0.661901	3.323837
62	1	0	3.748228	0.031831	4.212163
63	1	0	4.973274	0.982250	3.337069
64	1	0	3.291283	1.558271	3.443477
65	8	0	1.153393	1.717162	-0.175768
66	6	0	2.067797	2.750005	-0.551694
67	6	0	1.300215	3.844623	-1.301755
68	6	0	2.668881	3.294184	0.751087
69	6	0	3.150896	2.124378	-1.437247
70	1	0	0.909359	3.461368	-2.254640
71	1	0	0.458247	4.205470	-0.693419
72	1	0	1.965444	4.693167	-1.519832
73	1	0	3.178104	2.482582	1.287295
74	1	0	3.395944	4.091211	0.535674
75	1	0	1.875268	3.702622	1.393181
76	1	0	3.896405	2.882487	-1.720535
77	1	0	3.654098	1.309688	-0.899196
78	1	0	2.704592	1.713838	-2.354326
HF= -2572.1420675 / NImag=0					
Sum of electronic and thermal Enthalpies=				-2571.465965	
Sum of electronic and thermal Free Energies=				-2571.579595	

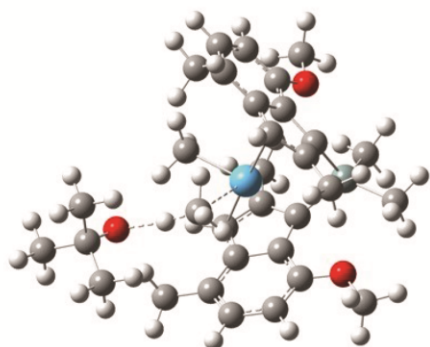
Transition state (3-Hf): H-transfer to methyl group

Figure S73. Molecular representation of the transition state (3-Hf): H-transfer to methyl group.

Table S36. Calculated values of the transition state (3-Hf): H-transfer to methyl group.

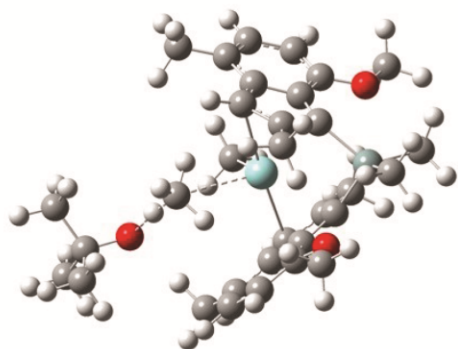
Center Number	Atomic Number	Atomic Type	Coordinates (Angstroms)		
			X	Y	Z
1	6	0	-0.160580	3.293470	-0.244542
2	6	0	0.125538	2.228836	0.667384
3	6	0	-0.986047	1.677728	1.431063
4	6	0	-2.327896	2.159119	1.305557
5	6	0	-2.529915	3.152678	0.361720
6	6	0	-1.473923	3.714683	-0.402544
7	6	0	-0.438726	0.692590	2.302764
8	6	0	0.964935	0.646752	2.126760
9	6	0	1.357779	1.569575	1.073231
10	72	0	0.067482	-0.194540	-0.040019
11	6	0	-0.682983	-1.991414	1.056170
12	14	0	2.992061	1.351341	0.100108
13	6	0	3.625887	2.778590	-0.965570
14	6	0	1.843318	-0.215295	2.986594
15	6	0	-3.429525	1.586242	2.137783
16	8	0	0.919098	3.877806	-0.842412
17	6	0	0.675603	4.983368	-1.728212
18	6	0	2.154036	-1.498418	-0.637956
19	6	0	2.837967	-2.379712	0.259248
20	6	0	2.483778	-3.720129	0.294043
21	6	0	1.472638	-4.239930	-0.556060
22	6	0	0.795712	-3.456387	-1.471417
23	6	0	1.150988	-2.079539	-1.511489
24	6	0	0.690431	-1.034191	-2.365795
25	6	0	1.430838	0.144740	-2.094747
26	6	0	2.327949	-0.089481	-0.978913
27	8	0	3.859112	-1.830300	0.976549
28	6	0	4.593445	-2.690527	1.864419
29	6	0	-0.279569	-3.990022	-2.374166
30	6	0	1.256728	1.391847	-2.912099
31	6	0	4.453750	1.025274	1.253026
32	6	0	-2.244791	-0.132571	-1.162744

S80

## Appendix

---

33	8	0	-4.203038	-0.996765	0.680168
34	6	0	-5.466301	-1.142908	0.112782
35	6	0	-5.980288	0.210101	-0.455184
36	6	0	-5.429110	-2.176838	-1.045622
37	6	0	-6.474306	-1.640610	1.180313
38	1	0	-3.098400	-0.399929	-0.437274
39	1	0	-1.766087	0.811832	-0.810789
40	1	0	-1.607455	-1.038267	-1.251356
41	1	0	-0.997644	0.095762	3.017503
42	1	0	-3.536469	3.552840	0.219395
43	1	0	-1.705240	4.531226	-1.085546
44	1	0	2.567103	-0.805880	2.413848
45	1	0	1.227091	-0.905824	3.577087
46	1	0	2.414797	0.414521	3.686509
47	1	0	0.045194	4.679051	-2.579123
48	1	0	1.662559	5.290763	-2.090407
49	1	0	0.198431	5.818085	-1.191694
50	1	0	3.716217	3.680653	-0.342712
51	1	0	3.013089	3.021717	-1.834924
52	1	0	4.634357	2.496441	-1.308831
53	1	0	-0.682408	-2.915040	0.460338
54	1	0	-1.734052	-1.744536	1.303503
55	1	0	-0.153856	-2.198619	1.998311
56	1	0	-0.038156	-1.137963	-3.166489
57	1	0	1.238118	-5.304832	-0.485961
58	1	0	3.004255	-4.405446	0.961566
59	1	0	1.158472	2.294101	-2.298966
60	1	0	0.363461	1.304298	-3.544929
61	1	0	2.127881	1.534534	-3.570838
62	1	0	3.933599	-3.120148	2.634704
63	1	0	5.345952	-2.049552	2.336091
64	1	0	5.089556	-3.498976	1.305375
65	1	0	4.253936	0.342093	2.080111
66	1	0	4.760335	2.001082	1.663263
67	1	0	5.292407	0.622153	0.666517
68	1	0	-4.299776	2.258764	2.143221
69	1	0	-3.764776	0.602286	1.717021
70	1	0	-3.107080	1.428239	3.179010
71	1	0	-0.062047	-3.776525	-3.433121
72	1	0	-0.389700	-5.076461	-2.257869
73	1	0	-1.254824	-3.526515	-2.146958
74	1	0	-2.569726	0.077974	-2.188836
75	1	0	-6.025650	0.956265	0.353532
76	1	0	-5.280609	0.583256	-1.219938
77	1	0	-6.982075	0.129595	-0.912391
78	1	0	-5.063732	-3.144355	-0.665884
79	1	0	-6.419403	-2.334062	-1.508456
80	1	0	-4.733409	-1.834196	-1.828327
81	1	0	-7.491892	-1.780240	0.774292
82	1	0	-6.129098	-2.601320	1.595506
83	1	0	-6.526350	-0.912415	2.005564
HF= -1811.9627347 / NImag=1 (-79.9630 cm <sup>-1</sup> )					
Sum of electronic and thermal Enthalpies=				-1811.241180	
Sum of electronic and thermal Free Energies=				-1811.360399	

Transition state (**3-Zr**): H-transfer to methyl groupFigure S74. Molecular representation of the transition state (**3-Zr**): H-transfer to methyl group.Table S37. Calculated values of the transition state (**3-Zr**): H-transfer to methyl group.

Center Number	Atomic Number	Atomic Type	Coordinates (Angstroms)		
			X	Y	Z
1	6	0	2.387254	-0.130276	-0.975160
2	6	0	2.196743	-1.540987	-0.646618
3	6	0	1.200224	-2.106135	-1.537142
4	6	0	0.764154	-1.050833	-2.395212
5	6	0	1.520120	0.114385	-2.111671
6	6	0	0.825976	-3.476899	-1.506141
7	6	0	1.474888	-4.271623	-0.578397
8	6	0	2.475584	-3.766638	0.290938
9	6	0	2.848727	-2.430130	0.263973
10	40	0	0.092135	-0.209191	-0.070334
11	6	0	-0.639054	-2.027845	1.069831
12	8	0	3.859265	-1.894841	1.007115
13	6	0	4.560742	-2.765957	1.910890
14	6	0	-0.237892	-3.996579	-2.430684
15	6	0	1.368073	1.371868	-2.916699
16	14	0	3.042058	1.304605	0.121031
17	6	0	4.487645	0.961155	1.289579
18	6	0	0.178059	2.220678	0.670563
19	6	0	-0.093062	3.285371	-0.244054
20	6	0	-1.402661	3.717694	-0.410408
21	6	0	-2.471494	3.152863	0.332760
22	6	0	-2.285771	2.147621	1.268261
23	6	0	-0.944026	1.672220	1.419085
24	6	0	-0.410708	0.686854	2.301123
25	6	0	0.991709	0.628769	2.136108
26	6	0	1.399824	1.543345	1.079344
27	8	0	0.994432	3.859265	-0.838496
28	6	0	0.764195	4.964872	-1.727806
29	6	0	-3.406836	1.546063	2.055063
30	6	0	1.857309	-0.240680	2.999855
31	6	0	3.701265	2.732689	-0.927744

S82

## Appendix

---

32	6	0	-2.339571	-0.230659	-1.168235
33	8	0	-4.349510	-1.067135	0.620669
34	6	0	-5.649442	-1.099972	0.121095
35	6	0	-6.050435	0.271963	-0.490579
36	6	0	-5.778406	-2.185185	-0.981687
37	6	0	-6.647705	-1.438403	1.257943
38	1	0	-3.255640	-0.550386	-0.543248
39	1	0	-1.680005	-1.123603	-1.167894
40	1	0	-2.539931	0.022702	-2.215165
41	1	0	-0.980315	0.096521	3.013079
42	1	0	-3.475970	3.552190	0.174241
43	1	0	-1.621994	4.538707	-1.092088
44	1	0	2.558989	-0.858161	2.427300
45	1	0	1.230899	-0.906331	3.607876
46	1	0	2.453705	0.384011	3.683273
47	1	0	0.133087	4.664639	-2.579658
48	1	0	1.755079	5.261731	-2.088084
49	1	0	0.293952	5.805836	-1.194883
50	1	0	3.089595	3.001230	-1.790177
51	1	0	4.703081	2.437031	-1.278839
52	1	0	3.810714	3.622965	-0.290903
53	1	0	-0.620683	-2.946533	0.467386
54	1	0	-1.689862	-1.786852	1.318104
55	1	0	-0.094417	-2.214903	2.006071
56	1	0	0.045563	-1.143784	-3.206552
57	1	0	1.224320	-5.333225	-0.514372
58	1	0	2.971826	-4.458643	0.969869
59	1	0	1.238596	2.264736	-2.294397
60	1	0	0.503025	1.287716	-3.587886
61	1	0	2.264149	1.533152	-3.536585
62	1	0	3.876419	-3.190805	2.662242
63	1	0	5.307665	-2.134842	2.404310
64	1	0	5.062643	-3.578037	1.362369
65	1	0	4.278892	0.263065	2.101725
66	1	0	4.787533	1.929991	1.720886
67	1	0	5.335075	0.569953	0.707324
68	1	0	-4.279252	2.215731	2.058531
69	1	0	-3.736465	0.574070	1.605274
70	1	0	-3.111989	1.358077	3.099233
71	1	0	0.006442	-3.789186	-3.484998
72	1	0	-0.366865	-5.080978	-2.314659
73	1	0	-1.210665	-3.517601	-2.226887
74	1	0	-1.981936	0.683763	-0.650165
75	1	0	-5.975656	1.057291	0.277851
76	1	0	-5.360929	0.533061	-1.309213
77	1	0	-7.079043	0.274927	-0.891587
78	1	0	-5.496238	-3.165786	-0.565780
79	1	0	-6.801617	-2.258960	-1.390527
80	1	0	-5.089662	-1.956206	-1.810801
81	1	0	-7.692900	-1.481604	0.904123
82	1	0	-6.388940	-2.413841	1.699708
83	1	0	-6.580554	-0.675636	2.050150
HF= -1809.6403007 / NImag=1 (-47.9336 cm <sup>-1</sup> )					
Sum of electronic and thermal Enthalpies=			-1808.918957		
Sum of electronic and thermal Free Energies=			-1809.036851		

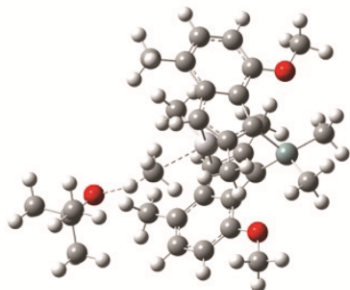
Transition state (3-Ti): H-transfer to methyl group

Figure S75. Molecular representation of the transition state (3-Ti): H-transfer to methyl group.

Table S38. Calculated values of the transition state (3-Ti): H-transfer to methyl group.

Center Number	Atomic Number	Atomic Type	Coordinates (Angstroms)		
			X	Y	Z
1	6	0	1.187726	1.677483	0.914651
2	6	0	-0.223308	1.950238	0.729445
3	6	0	-0.992123	1.164318	1.681711
4	6	0	-0.050301	0.410063	2.440263
5	6	0	1.257334	0.743159	2.024293
6	6	0	-2.410501	1.254196	1.785689
7	6	0	-3.027476	2.154190	0.929799
8	6	0	-2.311564	2.953119	0.004108
9	6	0	-0.929164	2.872715	-0.101109
10	22	0	0.298089	-0.375319	0.155894
11	6	0	0.145450	-2.201699	1.319526
12	8	0	-0.163903	3.674292	-0.897545
13	6	0	-0.840584	4.635937	-1.724794
14	6	0	-3.196368	0.378036	2.713688
15	6	0	2.469678	0.212081	2.729141
16	14	0	2.626310	1.857371	-0.323622
17	6	0	2.647642	3.283436	-1.562972
18	6	0	2.191694	0.196065	-1.155759
19	6	0	2.491966	-1.153199	-0.706991
20	6	0	1.537873	-2.071463	-1.292818
21	6	0	0.643308	-1.290938	-2.076845
22	6	0	1.057455	0.064558	-2.044766
23	6	0	1.597336	-3.478358	-1.090572
24	6	0	2.629354	-3.942391	-0.298276
25	6	0	3.611165	-3.079284	0.260433
26	6	0	3.570222	-1.709940	0.048910
27	6	0	0.390036	1.120409	-2.877765
28	6	0	0.566684	-4.377527	-1.710797
29	8	0	4.535023	-0.833414	0.453901
30	6	0	5.645339	-1.359303	1.199662
31	6	0	4.289552	2.071498	0.548235
32	6	0	-2.050761	-0.731411	-0.661821
33	8	0	-4.486869	-1.438408	0.507301
34	6	0	-5.703555	-1.328546	-0.162318
35	6	0	-6.637782	-2.496682	0.246725
36	6	0	-6.405105	0.013116	0.177816
37	6	0	-5.487267	-1.390159	-1.698405
38	1	0	-3.117787	-0.842990	-0.229209
39	1	0	-1.783229	0.338733	-0.637493

S84

## Appendix

---

40	1	0	-1.501518	-1.403864	0.038475
41	1	0	-0.283498	-0.258758	3.262543
42	1	0	-4.113421	2.262233	0.969615
43	1	0	-2.865904	3.663229	-0.608254
44	1	0	3.242022	-0.152024	2.045158
45	1	0	2.184456	-0.609412	3.399385
46	1	0	2.921776	1.009080	3.341041
47	1	0	-1.524654	4.139151	-2.431113
48	1	0	-0.049578	5.154381	-2.277150
49	1	0	-1.400266	5.357579	-1.109672
50	1	0	2.589041	4.237814	-1.019543
51	1	0	1.857004	3.268938	-2.315565
52	1	0	3.623244	3.241971	-2.074279
53	1	0	-0.084381	-3.067938	0.686146
54	1	0	-0.601635	-2.135363	2.121281
55	1	0	1.138310	-2.361860	1.770621
56	1	0	-0.171159	-1.678945	-2.681223
57	1	0	2.718440	-5.014629	-0.107510
58	1	0	4.429355	-3.521854	0.827060
59	1	0	0.162443	2.035431	-2.320294
60	1	0	-0.545979	0.731580	-3.300351
61	1	0	1.047210	1.404361	-3.715294
62	1	0	5.305333	-1.831085	2.135419
63	1	0	6.279385	-0.496101	1.428440
64	1	0	6.210829	-2.089104	0.599480
65	1	0	4.426895	1.480695	1.455982
66	1	0	4.375853	3.139605	0.806335
67	1	0	5.101474	1.823903	-0.151046
68	1	0	-3.996602	0.947315	3.210789
69	1	0	-3.690245	-0.421754	2.115374
70	1	0	-2.565648	-0.077557	3.488922
71	1	0	0.560445	-4.285682	-2.809154
72	1	0	0.753382	-5.429341	-1.455803
73	1	0	-0.448217	-4.117248	-1.364675
74	1	0	-2.004910	-1.129982	-1.676605
75	1	0	-4.848747	-0.552858	-2.021188
76	1	0	-4.980558	-2.331139	-1.965180
77	1	0	-6.438910	-1.335110	-2.253778
78	1	0	-6.807087	-2.472646	1.335156
79	1	0	-7.618173	-2.449177	-0.258552
80	1	0	-6.161689	-3.458053	-0.003866
81	1	0	-7.379517	0.125642	-0.328651
82	1	0	-6.569339	0.082599	1.265039
83	1	0	-5.758291	0.852010	-0.123548
HF=			-2612.5716875	/ NImag=1	(-45.0558 cm <sup>-1</sup> )
Sum of electronic and thermal Enthalpies=					-2611.848659
Sum of electronic and thermal Free Energies=					-2611.964497

## 24. References

- (1) Machat, M. R.; Jandl, C.; Rieger, B. *Organometallics* **2017**, *36* (7), 1408.
- (2) Machat, M. R.; Lanzinger, D.; Pöthig, A.; Rieger, B. *Organometallics* **2017**, *36* (2), 399.
- (3) Piermarini, G. J.; Block, S.; Barnett, J. D. *J. Appl. Phys.* **1973**, *44* (12), 5377.
- (4) Murata, K.; Aoki, S. *Rev. High Press. Sci. Technol.* **2016**, *26* (1), 3.
- (5) Varga, T.; Wilkinson, A. P.; Angel, R. J. *Rev. Sci. Instrum.* **2003**, *74* (10), 4564.
- (6) Boehler, R. *Rev. Sci. Instrum.* **2006**, *77* (11), 115103.
- (7) Merrill, L.; Bassett, W. A. *Rev. Sci. Instrum.* **1974**, *45* (2), 290.
- (8) Boehler, R.; De Hantsetters, K. *High Press. Res.* **2004**, *24* (3), 391.
- (9) Moggach, S. A.; Allan, D. R.; Parsons, S.; Warren, J. E. *J. Appl. Crystallogr.* **2008**, *41* (2), 249.
- (10) Piermarini, G. J.; Block, S.; Barnett, J. D.; Forman, R. A. *J. Appl. Phys.* **1975**, *46* (6), 2774.
- (11) Willmott, P. R.; Meister, D.; Leake, S. J.; Lange, M.; Bergamaschi, A.; Böge, M.; Calvi, M.; Cancellieri, C.; Casati, N.; Cervellino, A.; Chen, Q.; David, C.; Flechsig, U.; Gozzo, F.; Henrich, B.; Jäggi-Spielmann, S.; Jakob, B.; Kalichava, I.; Karvinen, P.; Krempasky, J.; Lüdeke, A.; Lüscher, R.; Maag, S.; Quitmann, C.; Reinle-Schmitt, M. L.; Schmidt, T.; Schmitt, B.; Streun, A.; Vartiainen, I.; Vitins, M.; Wang, X.; Wulschleger, R. *J. Synchrotron Radiat.* **2013**, *20* (5), 667.
- (12) Fisch, M.; Lanza, A.; Macchi, P.; Casati, N. *J. Appl. Crystallogr.* **2015**, *48* (6), 1956.
- (13) Meixner, P.; Batke, K.; Fischer, A.; Schmitz, D.; Eickerling, G.; Kalter, M.; Ruhland, K.; Eichele, K.; Barquera-Lozada, J. E.; Casati, N. P. M.; Montisci, F.; Macchi, P.; Scherer, W. *J. Phys. Chem. A* **2017**, *121* (38), 7219.
- (14) Wong-Ng, W.; Siegrist, T.; DeTitta, G. T.; Finger, L. W.; Evans, H. T. J.; Gabe, E. J.; Enright, G. D.; Armstrong, J. T.; M. Levenson; Cook, L. P.; Hubbard, C. R. *J. Res. Natl. Inst. Stand. Technol.* **2001**, *106*, 1071.
- (15) Smith, J. S.; Desgreniers, S. *J. Synchrotron Radiat.* **2009**, *16* (1), 83.
- (16) CrysAlisPro 1.171.38.43. **2015**, Rigaku OD.
- (17) Blessing, R. H. *Crystallogr. Rev.* **1987**, *1* (1), 3.
- (18) Farrugia, L. J. *J. Appl. Crystallogr.* **2012**, *45* (4), 849.
- (19) Mighell, A. D. *J. Res. Natl. Inst. Stand. Technol.* **2002**, *107*, 373.
- (20) Mighell, A. D. *Acta Crystallogr. Sect. B* **2003**, *59* (2), 300.
- (21) Sheldrick, G. M. *Acta Crystallogr. Sect. A* **2008**, *64* (1), 112.
- (22) Sheldrick, G. M. *Acta Crystallogr. Sect. C* **2015**, *71* (1), 3.
- (23) Kissel, L.; Pratt, R. H. *Acta Crystallogr. Sect. A* **1990**, *46* (3), 170.
- (24) Henke, B. L.; Gullikson, E. M.; Davis, J. C. *At. Data Nucl. Data Tables* **1993**, *54* (2), 181.
- (25) Grosse-Kunstleve, R. W.; Sauter, N. K.; Moriarty, N. W.; Adams, P. D. *J. Appl. Crystallogr.* **2002**, *35* (1), 126.
- (26) Dolomanov, O. V.; Bourhis, L. J.; Gildea, R. J.; Howard, J. A. K.; Puschmann, H. *J. Appl. Crystallogr.* **2009**, *42* (2), 339.
- (27) Thorn, A.; Dittrich, B.; Sheldrick, G. M. *Acta Crystallogr. Sect. A* **2012**, *68* (4), 448.
- (28) Spackman, M. A.; Jayatilaka, D. *CrystEngComm* **2009**, *11* (1), 19.
- (29) Turner, M. J.; McKinnon, J. J.; Wolff, S. K.; Grimwood, D. J.; Spackman, P. R.; Jayatilaka, D.; Spackman, M. A. *CrystalExplorer17* **2017**, University of Western Australia.
- (30) McKinnon, J. J.; Jayatilaka, D.; Spackman, M. A. *Chem Commun* **2007**, No. 37, 3814.
- (31) Vinet, P.; Ferrante, J.; Smith, J. R.; Rose, J. H. *J. Phys. C Solid State Phys.* **1986**, *19* (20), L467.
- (32) Vinet, P.; Ferrante, J.; Rose, J. H.; Smith, J. R. *J. Geophys. Res. Solid Earth* **1987**, *92* (B9), 9319.
- (33) Angel, R. J.; Gonzalez-Platas, J.; Alvaro, M. Z. *Für Krist. - Cryst. Mater.* **2014**, *229*, 405.
- (34) Gonzalez-Platas, J.; Alvaro, M.; Nestola, F.; Angel, R. J. *J. Appl. Crystallogr.* **2016**, *49* (4), 1377.
- (35) Stewart, R. F. *Acta Crystallogr. A* **1976**, *32* (4), 565.
- (36) Hansen, N. K.; Coppens, P. *Acta Crystallogr. Sect. A* **1978**, *34* (6), 909.
- (37) Volkov, A.; Macchi, P.; Farrugia, L. J.; Gatti, C.; Mallinson, P.; Richter, R.; Koritsanszky, T. *XD2006 (version 5.42) A computer program for multipole refinement, topological analysis of charge densities, and evaluation of intermolecular energies from experimental or theoretical structure factors.*; 2006.
- (38) Johnson, C. K.; Levy, H. A. *International Tables for X-ray Crystallography Vol. IV*; Birmingham: Kynoch Press, 1974.

- (39) Frisch, M. J.; Trucks, G. W.; Schlegel, H. B.; Scuseria, G. E.; Robb, M. A.; Cheeseman, J. R.; Scalmani, G.; Barone, V.; Mennucci, B.; Petersson, G. A.; Nakatsuji, H.; Caricato, M.; Li, X.; Hratchian, H. P.; Izmaylov, A. F.; Bloino, J.; Zheng, G.; Sonnenberg, J. L.; Hada, M.; Ehara, M.; Toyota, K.; Fukuda, R.; Hasegawa, J.; Ishida, M.; Nakajima, T.; Honda, Y.; Kitao, O.; Nakai, H.; Vreven, T.; Montgomery, J.; Peralta, J. E.; Ogliaro, F.; Bearpark, M.; Heyd, J. J.; Brothers, E.; Kudin, K. N.; Staroverov, V. N.; Kobayashi, R.; Normand, J.; Raghavachari, K.; Rendell, A.; Burant, J. C.; Iyengar, S. S.; Tomasi, J.; Cossi, M.; Rega, N.; Millam, J. M.; Klene, M.; Knox, J. E.; Cross, J. B.; Bakken, V.; Adamo, C.; Jaramillo, J.; Gomperts, R.; Stratmann, R. E.; Yazyev, O.; Austin, A. J.; Cammi, R.; Pomelli, C.; Ochterski, J. W.; Martin, R. L.; Morokuma, K.; Zakrzewski, V. G.; Voth, G. A.; Salvador, P.; Dannenberg, J. J.; Dapprich, S.; Daniels, A. D.; Farkas, Ö.; Foresman, J. B.; Ortiz, J. V.; Cioslowski, J.; Fox, D. J. *Gaussian09 Revision B.01*; Gaussian, Inc.: Wallingford CT, 2009.
- (40) Roy, L. E.; Hay, P. J.; Martin, R. L. *J. Chem. Theory Comput.* **2008**, *4* (7), 1029.
- (41) Volkov, A.; Koritsanszky, T.; Chodkiewicz, M.; King, H. F. *J. Comput. Chem.* **2009**, *30* (9), 1379.
- (42) Batke, K.; Eickerling, G. *J. Phys. Chem. A* **2013**, *117* (45), 11566.

12.4 Supporting Information – Chapter 7: High-Melting, Elastic Polypropylene**High-Melting, Elastic Polypropylene: A One-Pot, One-Catalyst Strategy toward Propylene-Based Thermoplastic Elastomers**

Martin R. Machat<sup>†</sup>, Dominik Lanzinger<sup>†</sup>, Markus Drees<sup>†</sup>, Philipp J. Altmann<sup>§</sup>, Eberhardt Herdtweck<sup>§</sup>, and Bernhard Rieger<sup>\*†</sup>

<sup>†</sup>Wacker-Lehrstuhl für Makromolekulare Chemie, Catalysis Research Center, Technische Universität München, Lichtenbergstraße 4, 85748 Garching bei München, Germany

<sup>‡</sup>Chair of Inorganic and Metal-Organic Chemistry, Catalysis Research Center, Technische Universität München, Ernst-Otto-Fischer Straße 1, 85748 Garching bei München, Germany

<sup>§</sup>Catalysis Research Center, Technische Universität München, Ernst-Otto-Fischer Straße 1, 85748 Garching bei München, Germany

Supporting Information Placeholder

## Table of contents:

1. Synthesis – Procedures .....	2
2. Synthesis – <sup>1</sup> H and <sup>13</sup> C { <sup>1</sup> H} spectra.....	5
3. Tacticity determination <i>via</i> <sup>13</sup> C { <sup>1</sup> H} NMR spectroscopy.....	13
4. Olefinic end group analysis <i>via</i> <sup>1</sup> H NMR spectroscopy.....	23
5. Single crystal XRD (SC-XRD) data .....	32
6. DFT-calculations.....	41
7. References.....	44

## 1. Synthesis – Procedures

5,6-Cyclopenta-2-phenyl-1-indanone (1: R<sup>1</sup> = C<sub>6</sub>H<sub>5</sub>, R<sup>2</sup> = -(CH<sub>2</sub>)<sub>3</sub>-)

262 mL (2.14 mol, 9.19 eq.) indane and 520 mL Eaton's reagent (7.7 wt% phosphorous pentoxide solution in methanesulfonic acid) were stirred at 55 °C and a solution of 34.5 g (233 mmol, 1.00 eq.) atropic acid in 420 mL (3.43 mol, 14.7 eq.) indane was added dropwise. After stirring for additional 4 h at 55 °C the reaction mixture was poured into iced water (800 mL), phases were separated and the aqueous phase was extracted with diethyl ether (3×300 mL). The combined organic phases were washed with a saturated K<sub>2</sub>CO<sub>3</sub>-solution (3×400 mL), water (400 mL) and brine (400 mL), dried over MgSO<sub>4</sub> and all volatiles are removed under reduced pressure. After recrystallization in cyclohexane and methanol 11.5 g (20%) of **1** are obtained as colorless crystals. Anal. Calcd for C<sub>18</sub>H<sub>16</sub>O: C, 87.06; H, 6.49. Found: C, 87.34; H, 6.13. <sup>1</sup>H NMR (300 MHz, CDCl<sub>3</sub>, 298 K): δ (ppm) = 7.63 (s, 1H, H-Ar), 7.36-7.15 (m, 6H, H-Ar), 3.90 (dd, <sup>3</sup>J = 8.2, 3.8 Hz, 1H, -CH(CH<sub>3</sub>)-), 3.62 (dd, <sup>2</sup>J = 17.3 Hz, <sup>3</sup>J = 8.2 Hz, 1H, -CH<sub>2</sub>-), 3.19 (dd, <sup>2</sup>J = 17.3 Hz, <sup>3</sup>J = 3.8 Hz, 1H, -CH<sub>2</sub>-), 3.03-2.90 (m, 4H, -CH<sub>2</sub>-CH<sub>2</sub>-CH<sub>2</sub>-), 2.21-2.09 (m, 2H, -CH<sub>2</sub>-CH<sub>2</sub>-CH<sub>2</sub>-). <sup>13</sup>C {<sup>1</sup>H} NMR (75 MHz, CDCl<sub>3</sub>, 298 K): δ (ppm) = 205.8, 153.6, 153.1, 144.8, 140.3, 135.2, 128.9, 127.9, 127.0, 122.0, 119.9, 54.0, 35.8, 33.3, 32.2, 25.9.

5,6-Cyclopenta-2-phenyl-1-indene (2: R<sup>1</sup> = C<sub>6</sub>H<sub>5</sub>, R<sup>2</sup> = -(CH<sub>2</sub>)<sub>3</sub>-)

1.26 g (33.2 mmol, 0.75 eq.) LiAlH<sub>4</sub> were suspended in 50 mL THF at -78 °C, a solution of 11.0 g (44.3 mmol, 1.00 eq.) **1** in 160 mL THF was added dropwise and the reaction mixture was allowed to thaw overnight. Iced water (100 mL) and 3.0 M HCl-solution (95 mL) were added, phases were separated and the aqueous phase was extracted with diethyl ether (3×100 mL). The combined organic phases were washed with water (3×200 mL) and brine (200 mL), dried over MgSO<sub>4</sub> and all volatiles are removed under reduced pressure. The crude product was dissolved in 200 mL toluene, 0.27 g (1.55 mmol, 0.03 eq.) *p*-toluenesulfonic acid was added and the reaction mixture was refluxed in a Dean-Stark apparatus for 2 h. A 1.0 M NaOH-solution (60 mL) was added, phases were separated, the aqueous phase was extracted with dichloromethane (3×70 mL) and the combined organic phases were washed with brine (150 mL), dried over MgSO<sub>4</sub> and all volatiles were removed under reduced pressure. After recrystallization in cyclohexane 7.50 g (73%) of **2** as slightly brownish crystalline solid were obtained. Anal. Calcd for C<sub>18</sub>H<sub>18</sub>: C, 93.06; H, 4.94. Found: C, 91.05; H, 6.97. <sup>1</sup>H NMR (300 MHz, CDCl<sub>3</sub>, 298 K): δ (ppm) = 7.67-7.60 (m, 2H, H-Ar), 7.42-7.33 (m, 3H, H-Ar), 7.30-7.19 (m, 3H, H-Ar, -CH=), 3.75 (s, 2H, -CH<sub>2</sub>-), 2.95 (t, <sup>3</sup>J = 7.4 Hz, 4H, -CH<sub>2</sub>-CH<sub>2</sub>-CH<sub>2</sub>-), 2.12 (p, <sup>3</sup>J = 7.4 Hz, 2H, -CH<sub>2</sub>-CH<sub>2</sub>-CH<sub>2</sub>-). <sup>13</sup>C {<sup>1</sup>H} NMR (75 MHz, CDCl<sub>3</sub>, 298 K): δ (ppm) = 145.5, 143.8, 142.6, 141.6, 141.2, 136.3, 128.6, 127.2, 126.6, 125.4, 119.9, 116.9, 38.4, 32.8, 32.7, 25.9.

1-(9-Fluorenyl)-2-(5,6-cyclopenta-2-phenyl-1-indenyl)ethane (3: R<sup>1</sup> = C<sub>6</sub>H<sub>5</sub>, R<sup>2</sup> = -(CH<sub>2</sub>)<sub>3</sub>-, R<sup>3</sup> = H)

5.57 g (24.0 mmol, 1.00 eq.) of **2** were dissolved in 550 mL THF, cooled down to -78 °C and 19.2 mL (48.0 mmol, 2.00 eq.) 2.5 M *n*-BuLi-solution in hexane were added dropwise. After stirring the reaction mixture for 2 h at room temperature all volatiles were removed under reduced pressure and the residue was washed with hexane (2×50 mL). The residue was again dissolved in 280 mL THF and a solution of 6.56 g (24.0 mmol, 1.00 eq.) 1-Bromo-2-(9-fluorenyl)ethane in 110 mL THF was added dropwise. After stirring the reaction mixture overnight it was poured into a saturated NH<sub>4</sub>Cl-solution (200 mL), phases were separated and the aqueous phase was extracted with a THF/diethyl ether mixture (1/1; 2×80 mL). The combined organic phases are washed with water (200 mL), brine (200 mL), dried over MgSO<sub>4</sub> and all volatiles are removed under reduced pressure. After recrystallization in cyclohexane 4.90 g (48%) of **3** as slightly brownish

crystalline solid were obtained. Anal. Calcd for  $C_{33}H_{28}$ : C, 93.35; H, 6.65. Found: C, 90.20; H, 6.46.  $^1H$  NMR (400 MHz,  $CDCl_3$ , 298 K):  $\delta$  (ppm) = 7.81-7.77 (m, 2H, H-Ar), 7.63-7.59 (m, 2H, H-Ar), 7.45-7.37 (m, 4H, H-Ar), 7.35-7.31 (m, 5H, H-Ar), 7.29-7.22 (m, 1H, H-Ar), 7.10 (s, 1H, H-Ar), 4.18 (t,  $^3J = 5.0$  Hz, 1H, 9-H-Flu), 3.65 (s, 2H,  $-CH_2-$ ), 2.97 (dt,  $^3J = 10.2$ , 7.4 Hz, 4H,  $-CH_2-CH_2-CH_2-$ ), 2.55-2.47 (m, 2H,  $-CH_2-CH_2-$ ), 2.42-2.34 (m, 2H,  $-CH_2-CH_2-$ ), 2.14 (p,  $^3J = 7.4$  Hz, 2H,  $-CH_2-CH_2-CH_2-$ ).  $^{13}C$   $\{^1H\}$  NMR (100 MHz,  $CDCl_3$ , 298 K):  $\delta$  (ppm) = 146.8, 145.2, 142.4, 141.6, 141.3, 141.2, 139.7, 139.1, 137.7, 128.4, 127.9, 127.2, 127.1, 126.6, 124.4, 120.1, 119.8, 115.3, 47.6, 40.7, 33.0, 32.9, 31.4, 26.1, 21.6.

Rac-[1-(9- $\eta^5$ -fluorenyl)-2-(5,6-cyclopenta-2-phenyl-1- $\eta^5$ -indenyl)ethane]hafnium dichloride (IV:  $R^1 = C_6H_5$ ,  $R^2 = -(CH_2)_3-$ ,  $R^3 = H$ )

1.69 g (4.00 mmol, 1.00 eq.) of **3** were dissolved in a toluene/1,4-dioxane mixture (9/1; 60 mL) and 3.58 mL (8.01 mmol, 2.00 eq.) of 2.24 M *n*-BuLi solution in hexane were added dropwise at  $-78$  °C. After 10 min the cooling was removed and the reaction mixture was stirred for another 2 h at room temperature. After cooling the solution again to  $-78$  °C, 1.28 g (4.00 mmol, 1.00 eq.)  $HfCl_4$  were added and the reaction mixture is slowly warmed to room temperature overnight leading to a yellow suspension. The solid is allowed to deposit. The suspension is filtered, and the solvent of the filtrate is removed under reduced pressure. The obtained residue is extracted with dichloromethane (20 mL), the solvent is again reduced *in vacuo* and the residual solid is recrystallized in toluene to yield 140 mg (5%) of **IV** as a crystalline yellow powder. **IV** was found to co-crystallize with 0.5 eq. toluene. Anal. Calcd for  $C_{33}H_{26}Cl_2Hf \times 0.5 C_7H_8$ : C, 61.06; H, 4.21. Found: C, 61.39; H, 4.24.  $^1H$  NMR (500 MHz,  $CD_2Cl_2$ , 298 K):  $\delta$  (ppm) = 7.86-7.67 (m, 5H, H-Ar), 7.53-7.29 (m, 6H, H-Ar), 7.25-7.08 (m, 2H, H-Ar), 6.85-6.76 (m, 1H, H-Ar), 6.41 (s, 1H,  $-CH=$ ) 6.28 (d,  $^3J = 8.6$  Hz, 1H, H-Ar), 4.49 (ddd,  $J = 15.1$ , 10.5, 8.0 Hz, 1H,  $-CH_2-$ ), 4.30 (ddd,  $J = 15.1$ , 7.2, 4.0 Hz, 1H,  $-CH_2-$ ), 4.22-4.08 (m, 2H,  $-CH_2-$ ), 3.01-2.71 (m, 4H,  $-CH_2-CH_2-CH_2-$ ), 2.05-1.87 (m, 2H,  $-CH_2-CH_2-CH_2-$ ).  $^{13}C$   $\{^1H\}$  NMR (125 MHz,  $CD_2Cl_2$ , 298 K):  $\delta$  (ppm) = 146.0, 145.1, 134.3, 129.5, 129.1, 128.7, 128.6, 128.2, 128.1, 126.9, 126.8, 126.2, 126.0, 125.4, 125.3, 124.9, 124.7, 123.6, 123.0, 122.4, 119.1, 116.9, 115.5, 108.2, 99.6, 32.8, 32.6, 28.6, 28.4, 26.8.

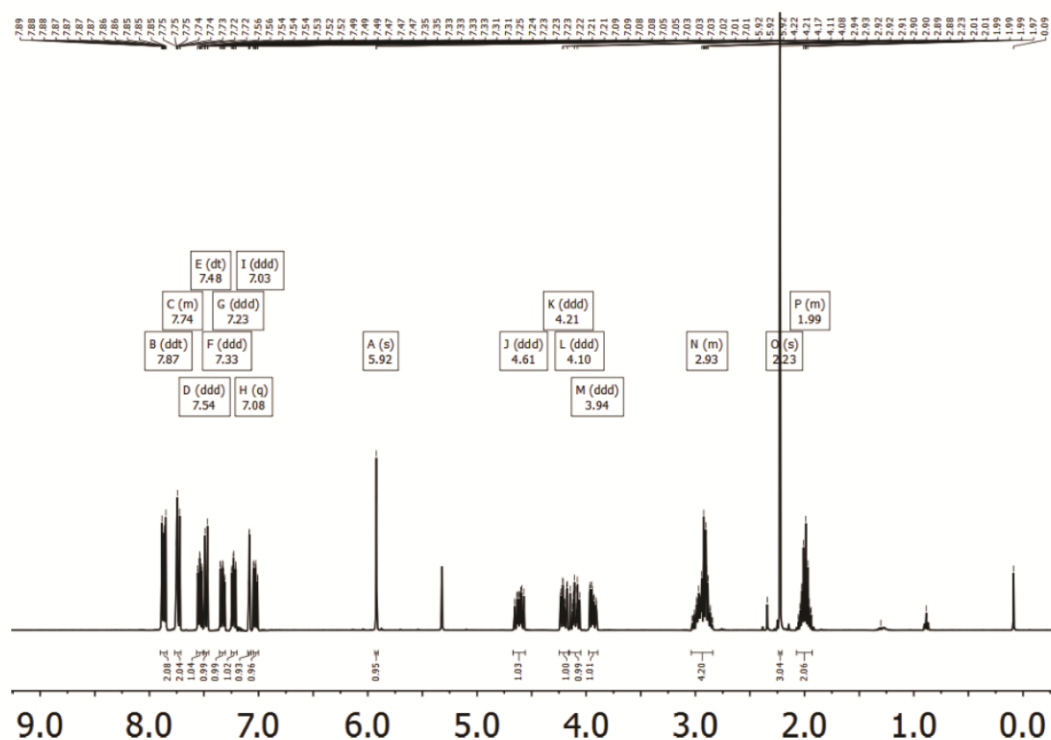
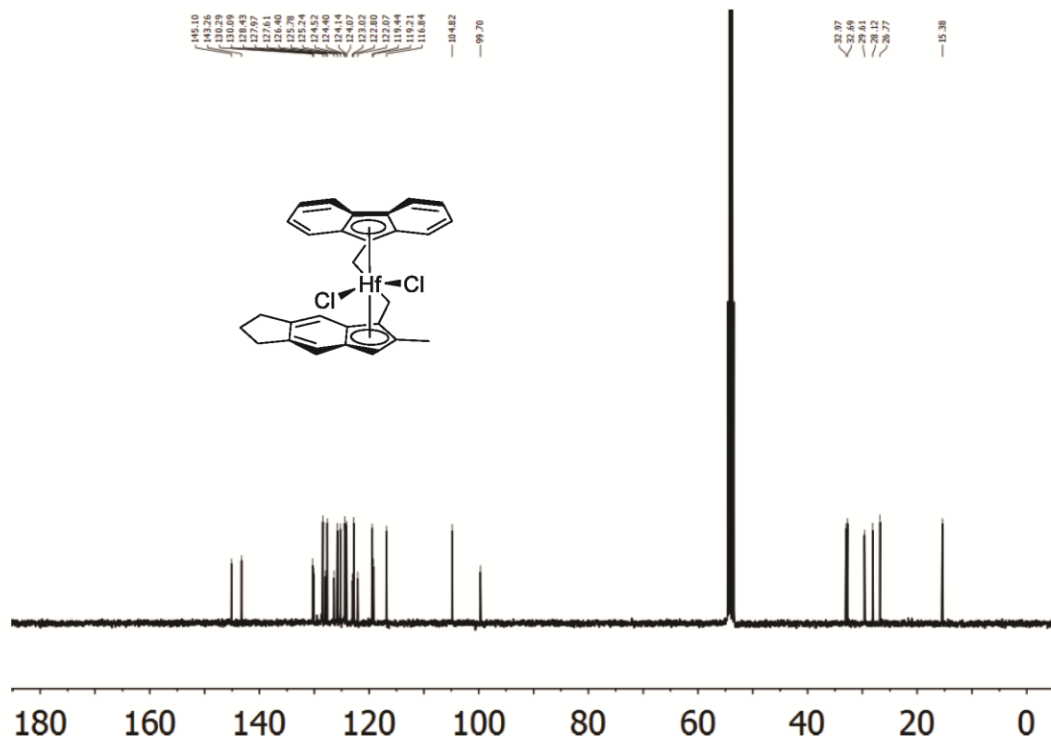
1-Phenyl-1-(9-fluorenyl)-2-(5,6-cyclopenta-2-methyl-1-indenyl)ethane (4:  $R^1 = CH_3$ ,  $R^2 = -(CH_2)_3-$ ,  $R^3 = C_6H_5$ )

7.13 g (41.9 mmol, 1.20 eq.) of 5,6-Cyclopenta-2-methyl-1-indene were dissolved in a toluene/1,4-dioxane mixture (1/1; 200 mL) and 17.5 mL (41.9 mmol, 1.20 eq.) 2.4 M *n*-BuLi solution in hexane were added dropwise at 0 °C. After stirring the reaction mixture for 2h 14.6 g (34.9 mmol, 1.00 eq.) 2-Phenyl-2-(9-fluorenyl)ethyltrifluoromethanesulfonate in 1,4-dioxane (100 mL) were added dropwise at room temperature and the reaction was stirred overnight. All volatiles are removed *in vacuo*, diethyl ether (400 mL) and saturated  $NH_4Cl$ -solution (200 mL) were added, phases were separated and the aqueous phase was extracted with diethyl ether (2x150 mL). All combined organic phases were washed with brine (250 mL), dried over  $MgSO_4$  and all volatiles were removed under reduced pressure. The crude product was purified *via* column chromatography (toluene/hexane 2/7;  $R_f = 0.3$ ) and recrystallized in a dichloromethane/methanol mixture to yield 5.55 g (36%) of **4** as white powder. Anal. Calcd for  $C_{34}H_{30}$ : C, 93.11; H, 6.89. Found: C, 92.62; H, 6.91.  $^1H$  NMR (300 MHz,  $CD_2Cl_2$ , 298 K):  $\delta$  (ppm) = 7.68-7.54 (m, 3H, H-Ar), 7.41-7.19 (m, 5H, H-Ar), 7.16-7.07 (m, 4H, H-Ar), 7.07-6.99 (m, 3H, H-Ar), 6.34 (p,  $J = 1.5$  Hz, 1H,  $-CH=$ ), 4.23 (d,  $J = 4.4$  Hz, 1H, 9-H-Flu), 3.90 (dt,  $J = 11.6$ , 3.9 Hz, 1H,  $-CH(C_6H_5)-$ ), 2.98 (dd,  $J = 9.6$ , 3.3 Hz, 1H, 1-H-Ind), 2.84 (td,  $J = 7.5$ , 6.5, 3.2 Hz, 4H,  $-CH_2-CH_2-CH_2-$ ), 2.62 (ddd,  $J = 13.6$ , 11.6, 3.5 Hz, 1H,  $-CH_2-$ ), 2.06 (qd,  $J = 7.5$ , 1.3 Hz, 2H,  $-CH_2-CH_2-CH_2-$ ), 1.98 (d,  $J = 1.5$  Hz, 3H,  $-CH_3$ ), 1.63 (ddd,  $J = 13.6$ , 9.6, 3.5 Hz, 2H,  $-CH_2-$ ).  $^{13}C$   $\{^1H\}$  NMR (75 MHz,  $CD_2Cl_2$ , 298 K):  $\delta$  (ppm) = 149.1, 146.5, 146.0, 145.9, 143.7, 142.7, 142.1, 141.8,

141.8, 140.0, 129.5, 128.2, 127.7, 127.5, 127.0, 127.0, 126.9, 126.7, 125.9, 125.8, 120.2, 120.2, 120.0, 116.2, 50.0, 47.4, 33.7, 33.2, 33.2, 26.4, 15.6.

Rac-[1-phenyl-1-(9- $\eta^5$ -fluorenyl)-2-(5,6-cyclopenta-2-methyl-1- $\eta^5$ -indenyl)ethane]hafnium dichloride (**V**:  $R^1 = \text{CH}_3$ ,  $R^2 = -(\text{CH}_2)_3-$ ,  $R^3 = \text{C}_6\text{H}_5$ )

3.50 g (7.98 mmol, 1.00 eq.) of **4** were dissolved in a toluene/1,4-dioxane mixture (9/1; 100 mL) and 6.65 mL (16.0 mmol, 2.00 eq.) of 2.4 M *n*-BuLi solution in hexane were added dropwise at  $-78^\circ\text{C}$ . After 10 min the cooling was removed and the reaction mixture was stirred for another 2 h at room temperature. After cooling the solution again to  $-78^\circ\text{C}$ , 2.56 g (7.98 mmol, 1.00 eq.)  $\text{HfCl}_4$  were added and the reaction mixture is slowly warmed to room temperature overnight leading to a yellow suspension. The solid is allowed to deposit. The suspension is filtered, extracted with dichloromethane (100 mL) and the solvent of all combined filtrates is removed under reduced pressure. The residue is recrystallized for three times in a toluene/pentane mixture isolating 150 mg (3%) of **V** as intense yellow crystals. **V** contained a 2/1 ( $\mathbf{V}_a/\mathbf{V}_b$ ) mixture of diastereomers ( $\mathbf{V}_a$ : (*R*)-phenyl-(*S*)-indenyl and (*S*)-phenyl-(*R*)-indenyl enantiomers,  $\mathbf{V}_b$ : (*S*)-phenyl-(*S*)-indenyl and (*R*)-phenyl-(*R*)-indenyl enantiomers). Anal. Calcd for  $\text{C}_{34}\text{H}_{28}\text{Cl}_2\text{Hf}$ : C, 59.53; H, 4.11. Found: C, 59.51; H, 4.11.  $^1\text{H}$  NMR (400 MHz,  $\text{CD}_2\text{Cl}_2$ , 298 K):  $\delta$  (ppm) = 7.94-7.71 (m, 11H, H-Ar( $\mathbf{V}_a, \mathbf{V}_b$ )), 7.63-7.43 (m, 5H, H-Ar( $\mathbf{V}_a, \mathbf{V}_b$ )), 7.37-6.96 (m, 29H, H-Ar( $\mathbf{V}_a, \mathbf{V}_b$ )), 6.48 (t,  $^3J = 10.4$  Hz, 1H,  $-\text{CH}(\text{C}_6\text{H}_5)-(\mathbf{V}_b)$ ), 6.25 (s, 2H,  $-\text{CH}=(\mathbf{V}_a)$ ), 6.12 (dd,  $^3J = 12.8$ , 8.2 Hz, 2H,  $-\text{CH}(\text{C}_6\text{H}_5)-(\mathbf{V}_a)$ ), 5.99 (s, 1H,  $-\text{CH}=(\mathbf{V}_b)$ ), 4.71 (dd,  $^2J = 14.5$  Hz,  $^3J = 12.8$  Hz, 2H,  $-\text{CH}_2-(\mathbf{V}_a)$ ), 4.50 (d,  $^3J = 10.4$  Hz, 2H,  $-\text{CH}_2-(\mathbf{V}_b)$ ), 4.43 (dd,  $^2J = 14.5$  Hz,  $^3J = 8.2$  Hz, 2H,  $-\text{CH}_2-(\mathbf{V}_a)$ ), 3.06-2.64 (m, 12H,  $-\text{CH}_2-\text{CH}_2-\text{CH}_2-(\mathbf{V}_a, \mathbf{V}_b)$ ), 2.60 (s, 6H,  $-\text{CH}_3(\mathbf{V}_a)$ ), 2.20 (s, 3H,  $-\text{CH}_3(\mathbf{V}_b)$ ), 2.08-1.83 (m, 6H,  $-\text{CH}_2-\text{CH}_2-\text{CH}_2-(\mathbf{V}_a, \mathbf{V}_b)$ ).  $^{13}\text{C}$   $\{^1\text{H}\}$  NMR (100 MHz,  $\text{CD}_2\text{Cl}_2$ , 298 K):  $\delta$  (ppm) = 145.3, 145.2, 144.5, 144.5, 143.8, 143.2, 131.1, 130.7, 130.5, 129.9, 129.2, 129.1, 129.0, 128.5, 128.1, 127.8, 127.2, 127.2, 127.1, 127.0, 126.7, 126.6, 126.1, 125.7, 125.6, 125.5, 125.2, 125.2, 125.0, 124.9, 124.7, 124.4, 124.3, 124.0, 123.9, 123.7, 123.6, 123.0, 122.8, 121.9, 120.4, 119.8, 118.5, 118.0, 116.6, 114.5, 113.9, 110.7, 105.1, 102.2, 101.8, 46.3, 45.7, 33.1, 32.8, 32.7, 32.7, 32.6, 32.6, 26.8, 26.7, 15.6, 15.6.

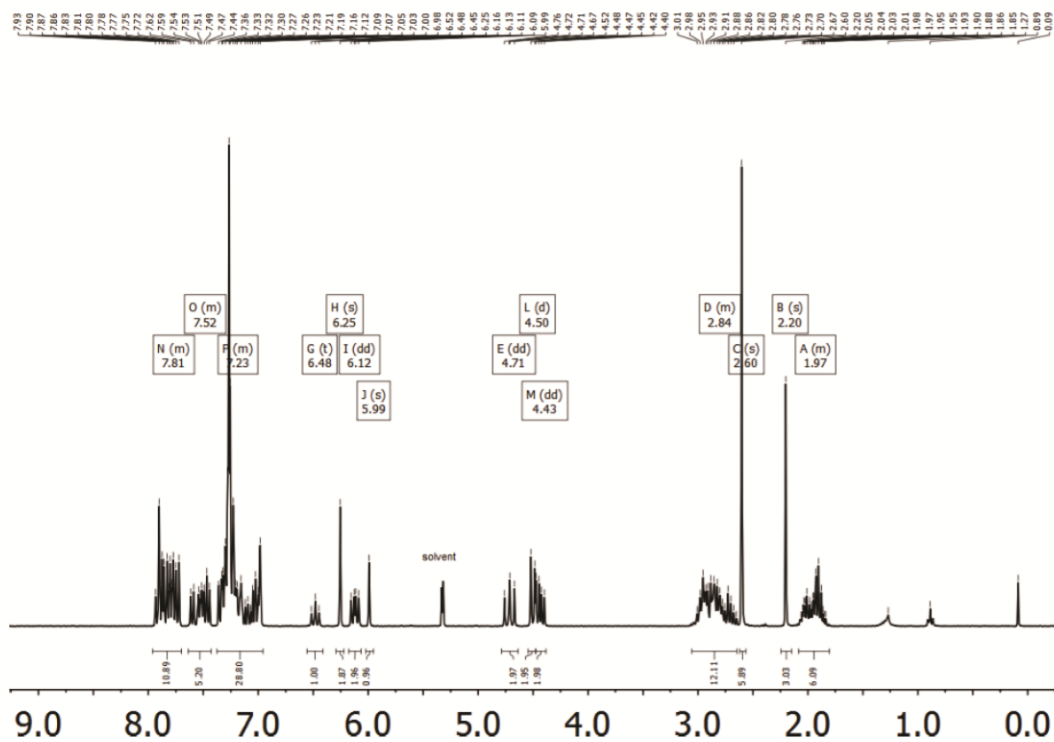
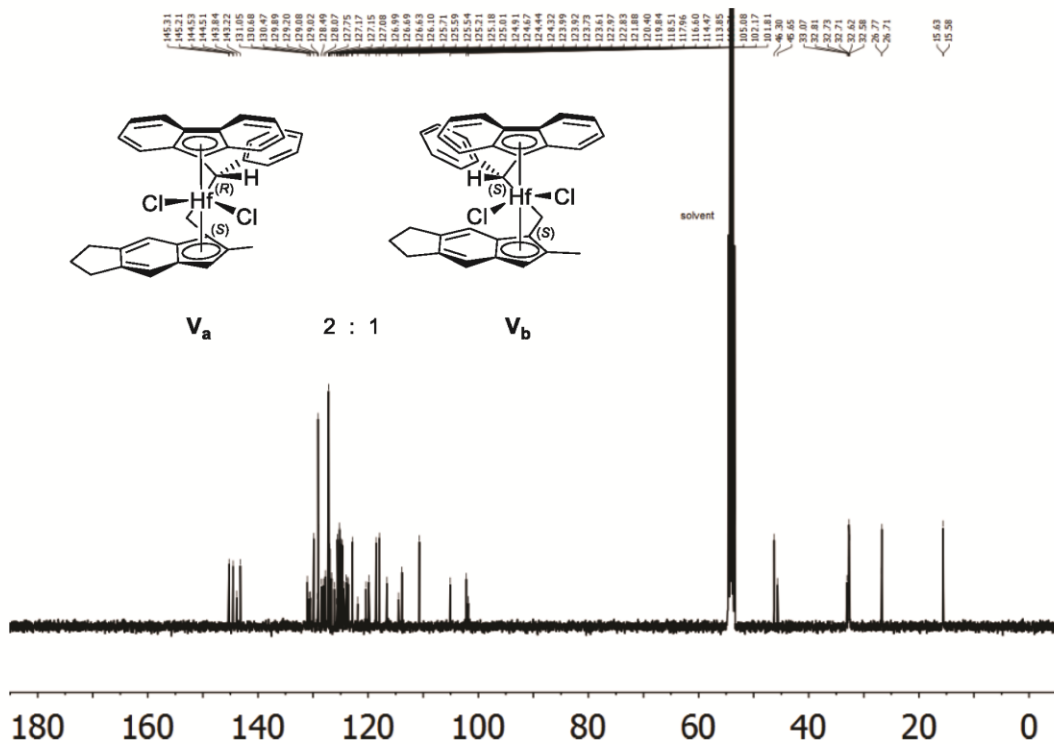
2. Synthesis –  $^1\text{H}$  and  $^{13}\text{C}$   $\{^1\text{H}\}$  spectraFigure S1.  $^1\text{H}$  NMR (400 MHz) of  $\text{I}_{\text{Hf}}$  in  $\text{CD}_2\text{Cl}_2$ . Traces of pentane and grease are visible.Figure S2.  $^{13}\text{C}$   $\{^1\text{H}\}$  NMR (400 MHz) of  $\text{I}_{\text{Hf}}$  in  $\text{CD}_2\text{Cl}_2$ .

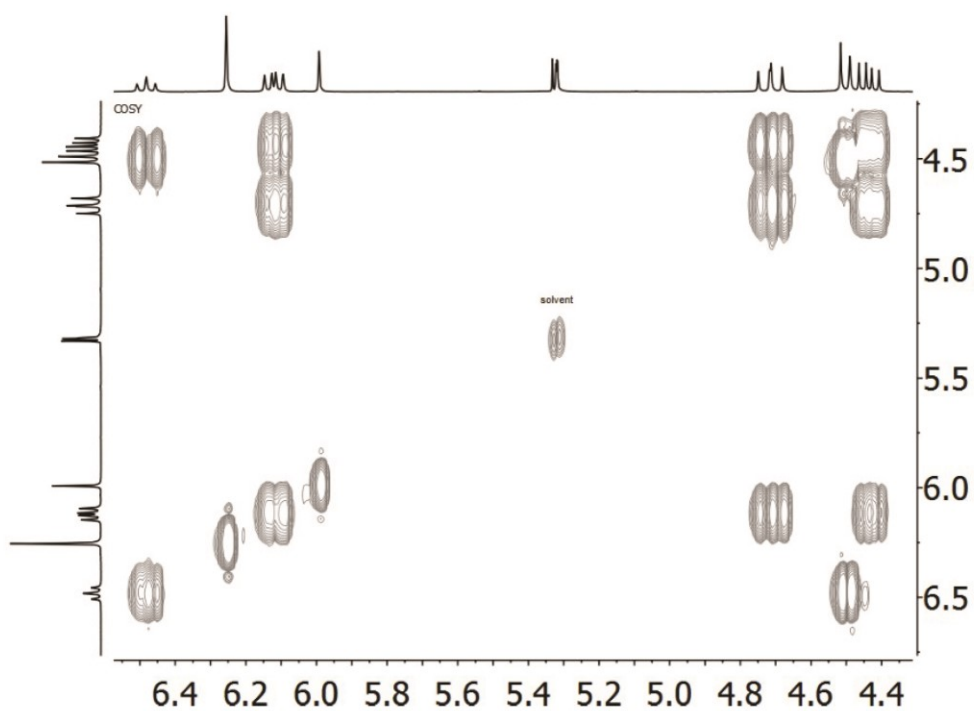
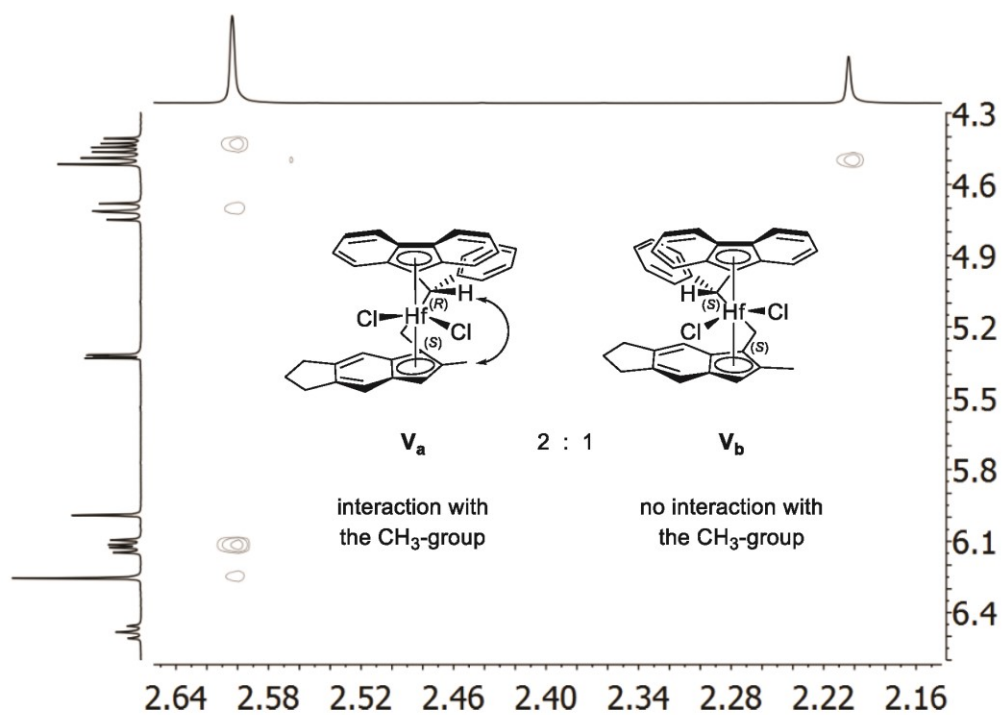


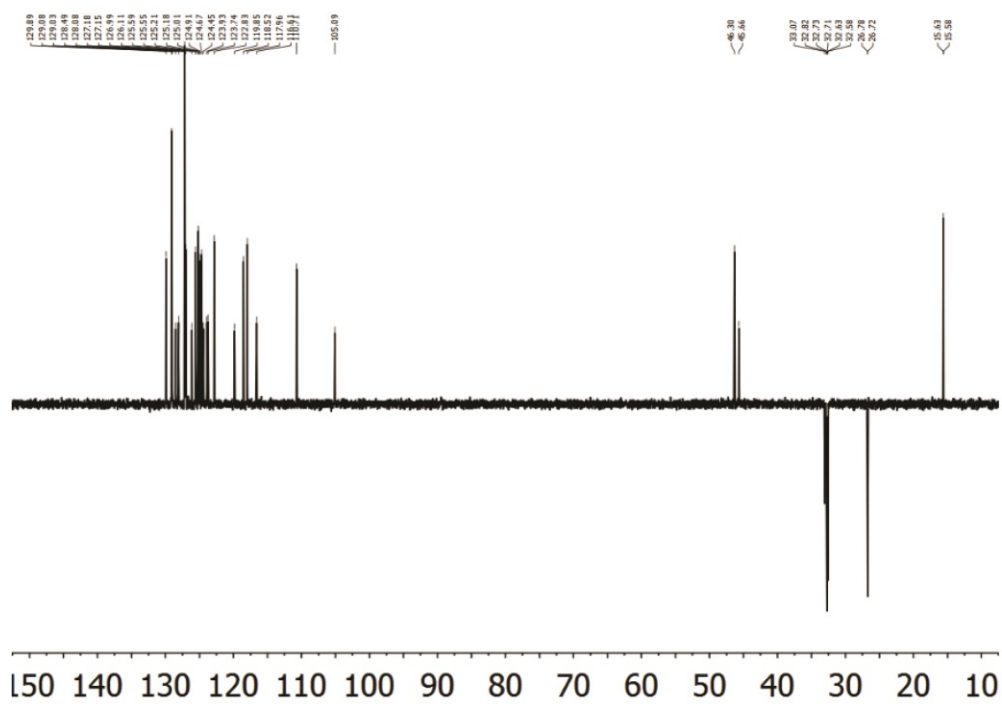
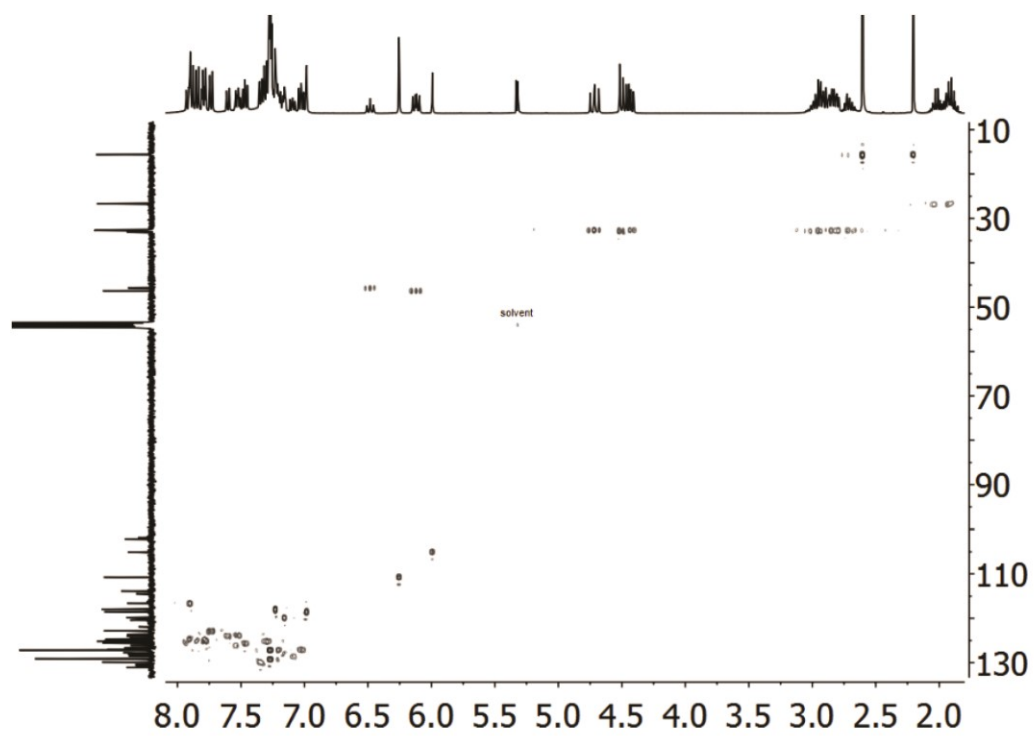






Figure S11.  $^1\text{H}$  NMR (400 MHz) spectrum of **V** in  $\text{CD}_2\text{Cl}_2$ . Traces of pentane and grease are visible.Figure S12.  $^{13}\text{C}$   $\{^1\text{H}\}$  NMR (400 MHz) spectrum of **V** in  $\text{CD}_2\text{Cl}_2$ .

Figure S13. 2D-COSY NMR (400 MHz) spectrum of **V** in CD<sub>2</sub>Cl<sub>2</sub>.Figure S14. 2D-NOESY NMR (500 MHz) spectrum of **V** in CD<sub>2</sub>Cl<sub>2</sub>.

Figure S15. DEPT-135 NMR (400 MHz) spectrum of V in CD<sub>2</sub>Cl<sub>2</sub>.Figure S16. 2D-HSQC NMR (400 MHz) spectrum of V in CD<sub>2</sub>Cl<sub>2</sub>.

3. Tacticity determination via  $^{13}\text{C} \{^1\text{H}\}$  NMR spectroscopy

All  $^{13}\text{C} \{^1\text{H}\}$  NMR measurements were conducted in  $\text{C}_6\text{D}_5\text{Br}$  at  $140^\circ\text{C}$ . All chemical shifts are internally referenced to the methyl signal of the isotactic pentad *mmmm* at 21.85 ppm. The tacticity distribution was quantified via integration of the methyl region between 22.0 – 19.7 ppm. The relative content of isotactic *mmmm* pentad is reported as mole fraction (in percentage) with respect to the sum of all steric pentads.

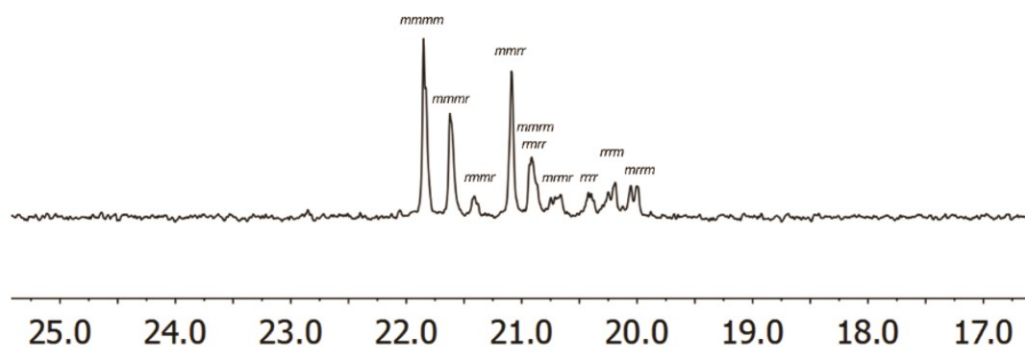


Figure S17. Exemplary pentad assignment<sup>[S1]</sup> of table 4, entry 31 in the  $^{13}\text{C} \{^1\text{H}\}$  NMR (300 MHz) spectrum ( $\text{C}_6\text{D}_5\text{Br}$ ,  $140^\circ\text{C}$ ).

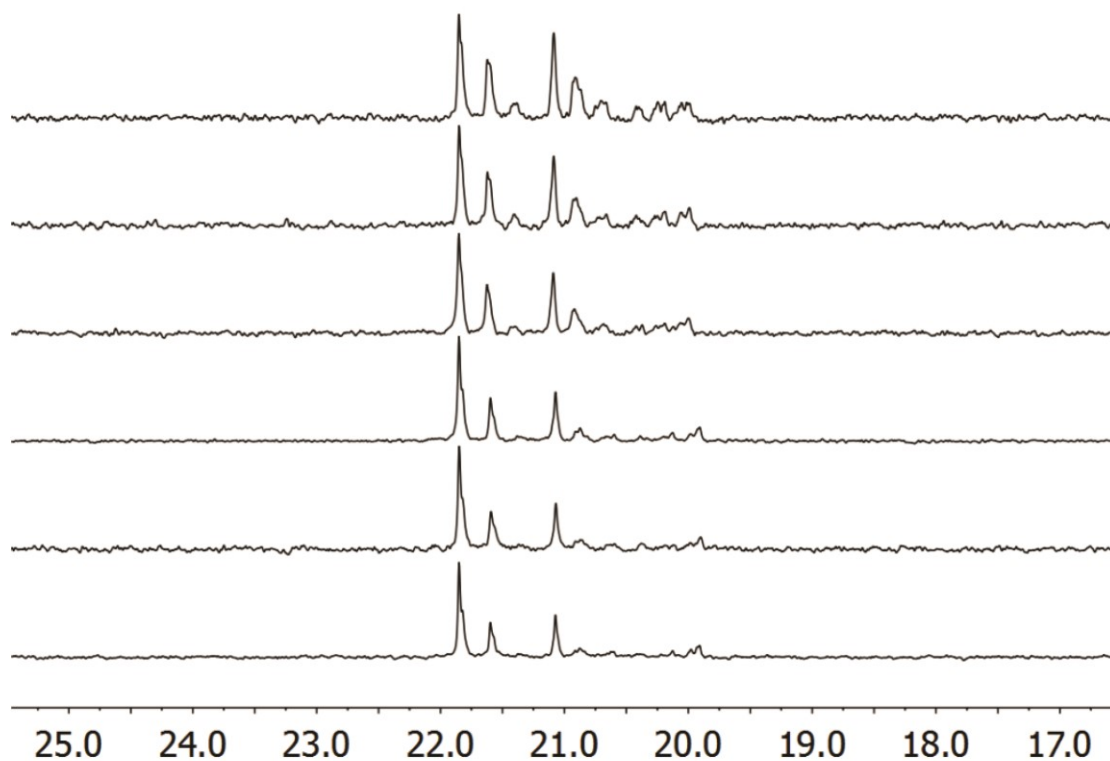


Figure S18. Pentad distribution of table 4, entry 1-3, 7-9 ( $I_{\text{Hf}}$ ,  $T_{\text{p}}$ :  $0_{\text{top}} - 90_{\text{bottom}}^\circ\text{C}$ ) in the  $^{13}\text{C} \{^1\text{H}\}$  NMR (300 MHz) spectrum ( $\text{C}_6\text{D}_5\text{Br}$ ,  $140^\circ\text{C}$ ).

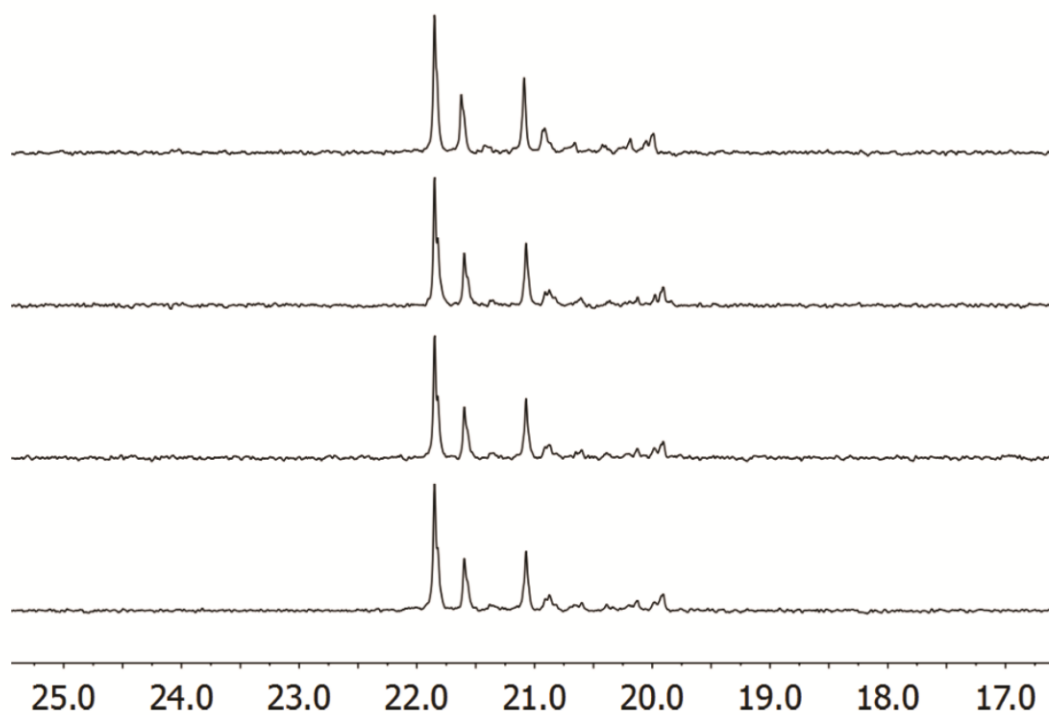


Figure S19. Pentad distribution of table 4, entry 4-7 ( $I_{\text{H}}$ , [propene]: 0.50<sub>top</sub> – 2.14<sub>bottom</sub> mol/L) in the  $^{13}\text{C}$   $\{^1\text{H}\}$  NMR (300 MHz) spectrum ( $\text{C}_6\text{D}_5\text{Br}$ , 140 °C).

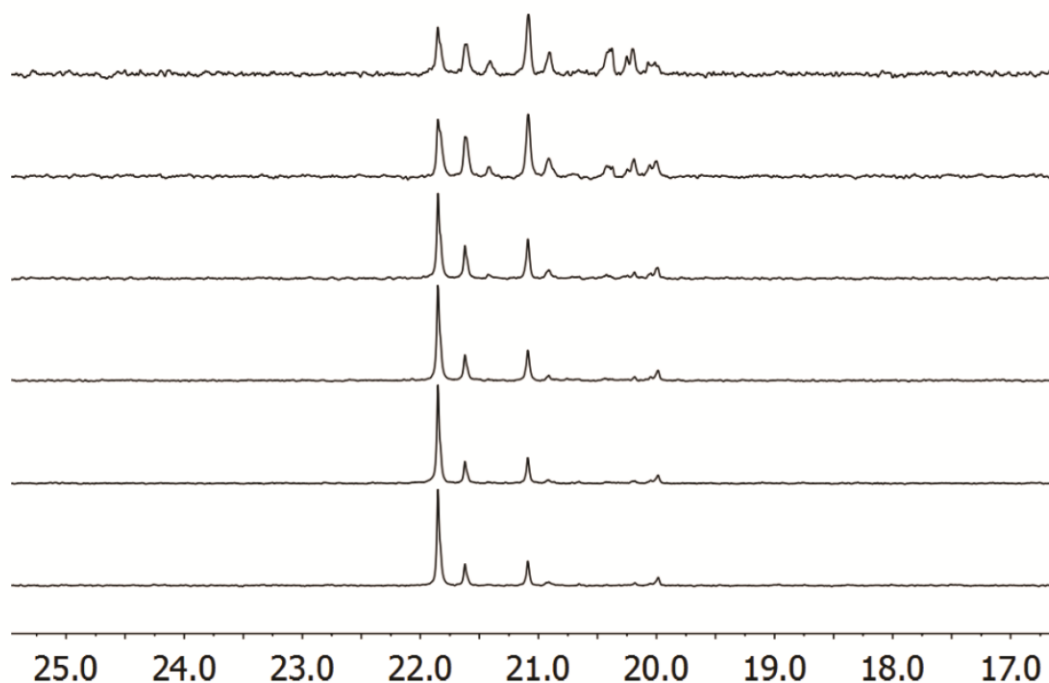


Figure S20. Pentad distribution of table 4, entry 10-12, 16-18 ( $I_{\text{Zr}}$ ,  $T_{\text{p}}$ : 0<sub>top</sub> – 90<sub>bottom</sub> °C) in the  $^{13}\text{C}$   $\{^1\text{H}\}$  NMR (300 MHz) spectrum ( $\text{C}_6\text{D}_5\text{Br}$ , 140 °C).

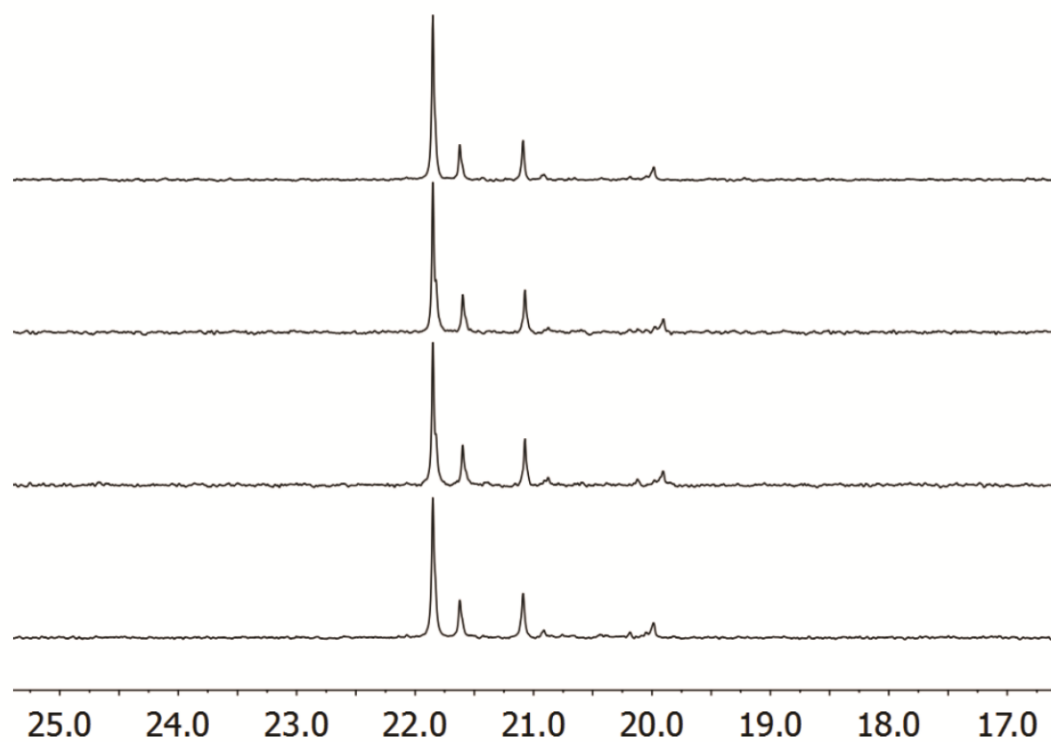


Figure S21. Pentad distribution of table 4, entry 13-16 ( $I_{zr}$ , [propene]:  $0.50_{\text{top}} - 2.14_{\text{bottom}}$  mol/L) in the  $^{13}\text{C} \{^1\text{H}\}$  NMR (300 MHz) spectrum ( $\text{C}_6\text{D}_5\text{Br}$ ,  $140^\circ\text{C}$ ).

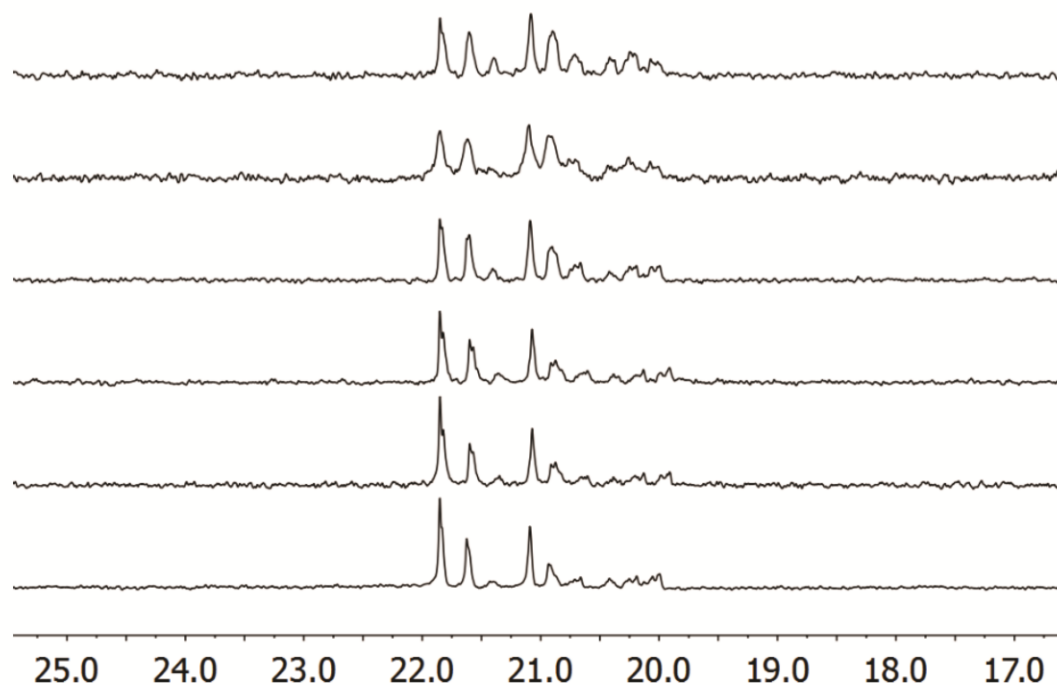


Figure S22. Pentad distribution of table 4, entry 19-21, 25-27 (**II**,  $T_p$ :  $0_{\text{top}} - 90_{\text{bottom}}$   $^\circ\text{C}$ ) in the  $^{13}\text{C} \{^1\text{H}\}$  NMR (300 MHz) spectrum ( $\text{C}_6\text{D}_5\text{Br}$ ,  $140^\circ\text{C}$ ).

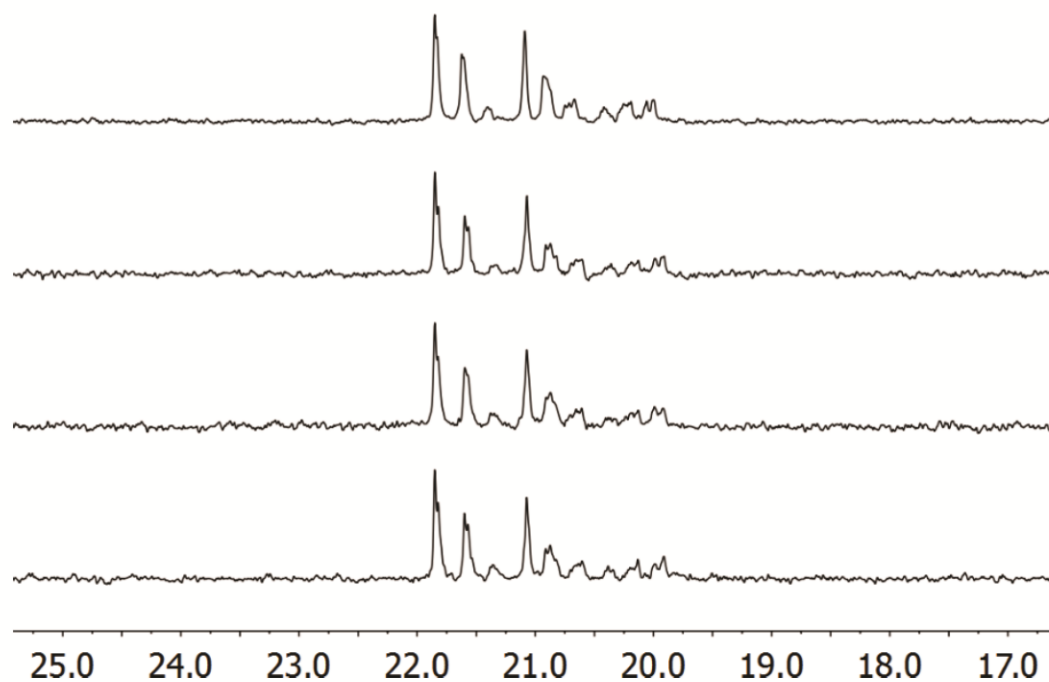


Figure S23. Pentad distribution of table 4, entry 22-25 (**II**, [propene]: 0.50<sub>top</sub> – 2.14<sub>bottom</sub> mol/L) in the  $^{13}\text{C} \{^1\text{H}\}$  NMR (300 MHz) spectrum ( $\text{C}_6\text{D}_5\text{Br}$ , 140 °C).

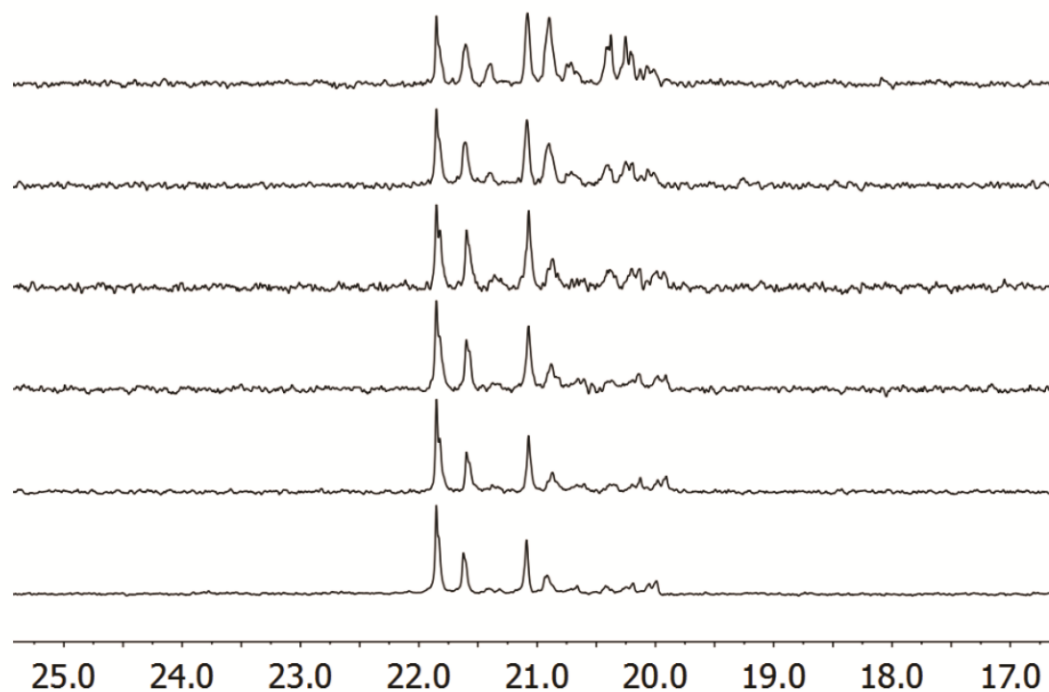


Figure S24. Pentad distribution of table 4, entry 28-30, 34-36 (**III**,  $T_p$ : 0<sub>top</sub> – 90<sub>bottom</sub> °C) in the  $^{13}\text{C} \{^1\text{H}\}$  NMR (300 MHz) spectrum at ( $\text{C}_6\text{D}_5\text{Br}$ , 140 °C).

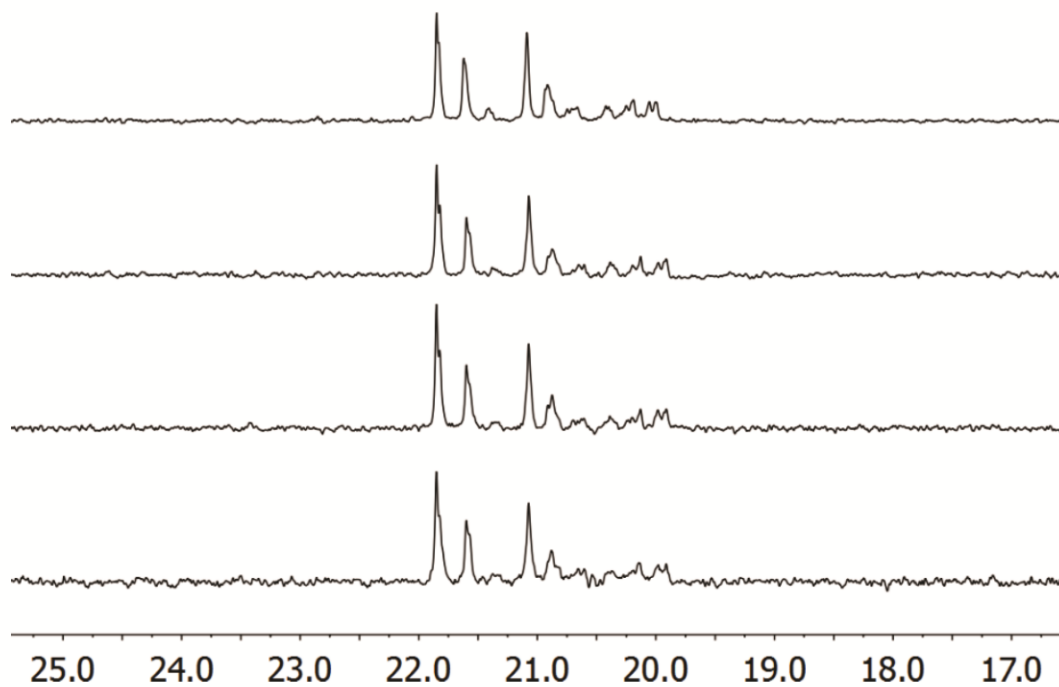


Figure S25. Pentad distribution of table 4, entry 31-34 (**III**, [propene]: 0.50<sub>top</sub> – 2.14<sub>bottom</sub> mol/L) in the  $^{13}\text{C} \{^1\text{H}\}$  NMR (300 MHz) spectrum ( $\text{C}_6\text{D}_5\text{Br}$ , 140 °C).

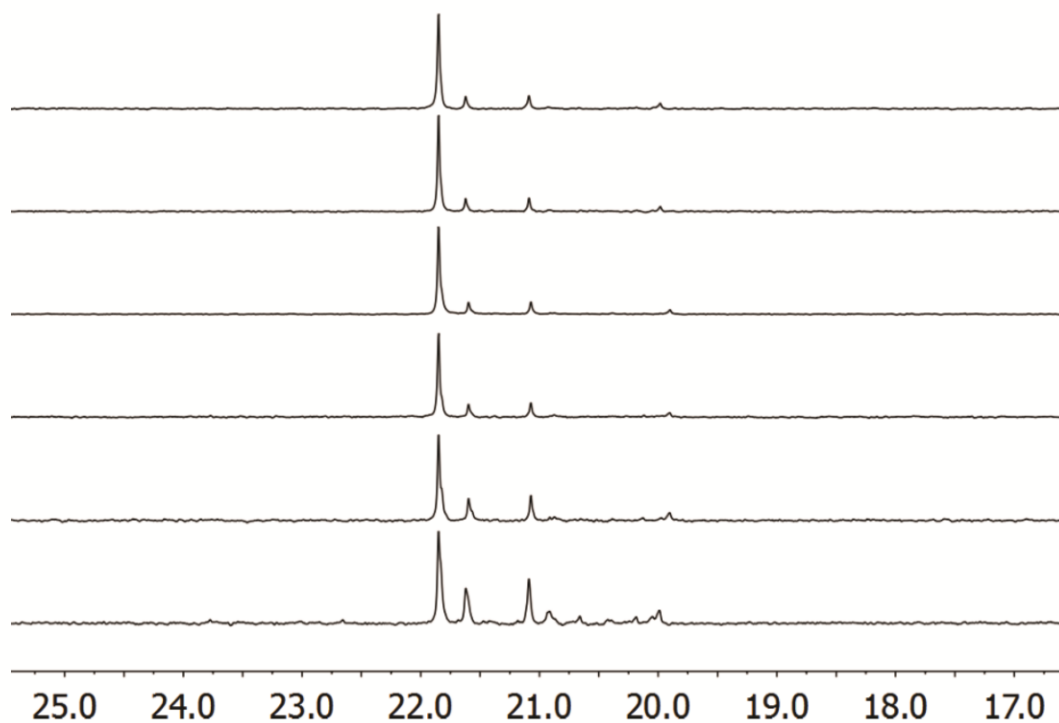


Figure S26. Pentad distribution of table 4, entry 37-39, 43-45 (**IV**,  $T_P$ : 0<sub>top</sub> – 90<sub>bottom</sub> °C) in the  $^{13}\text{C} \{^1\text{H}\}$  NMR (300 MHz) spectrum ( $\text{C}_6\text{D}_5\text{Br}$ , 140 °C).

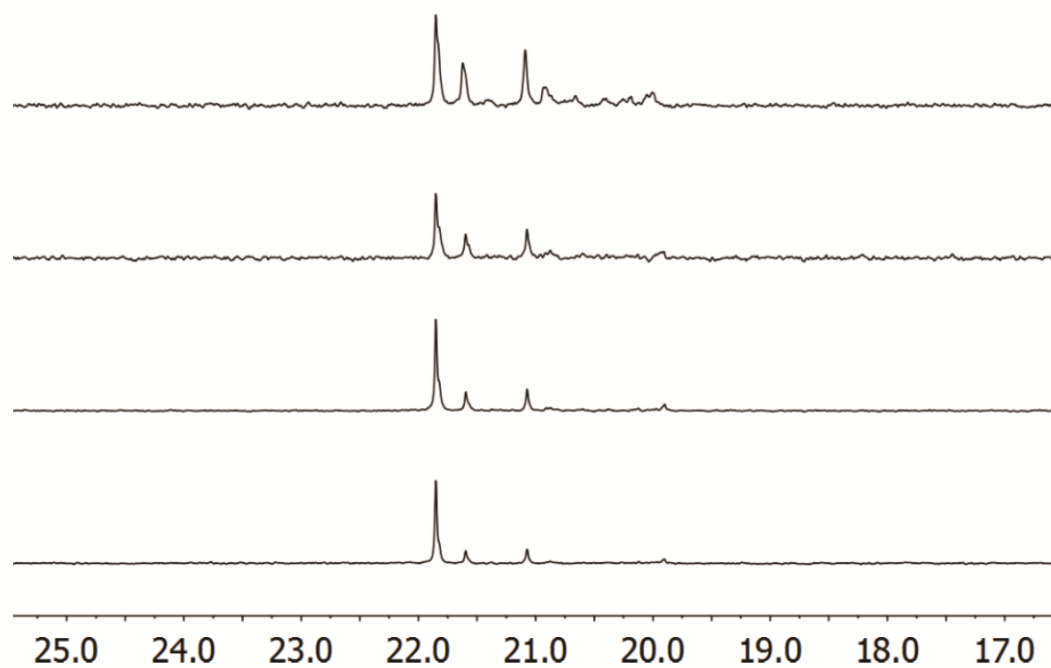


Figure S27. Pentad distribution of table 4, entry 40-43 (**IV**, [propene]: 0.50<sub>top</sub> – 2.14<sub>bottom</sub> mol/L) in the  $^{13}\text{C} \{^1\text{H}\}$  NMR (300 MHz) spectrum at ( $\text{C}_6\text{D}_5\text{Br}$ , 140 °C).

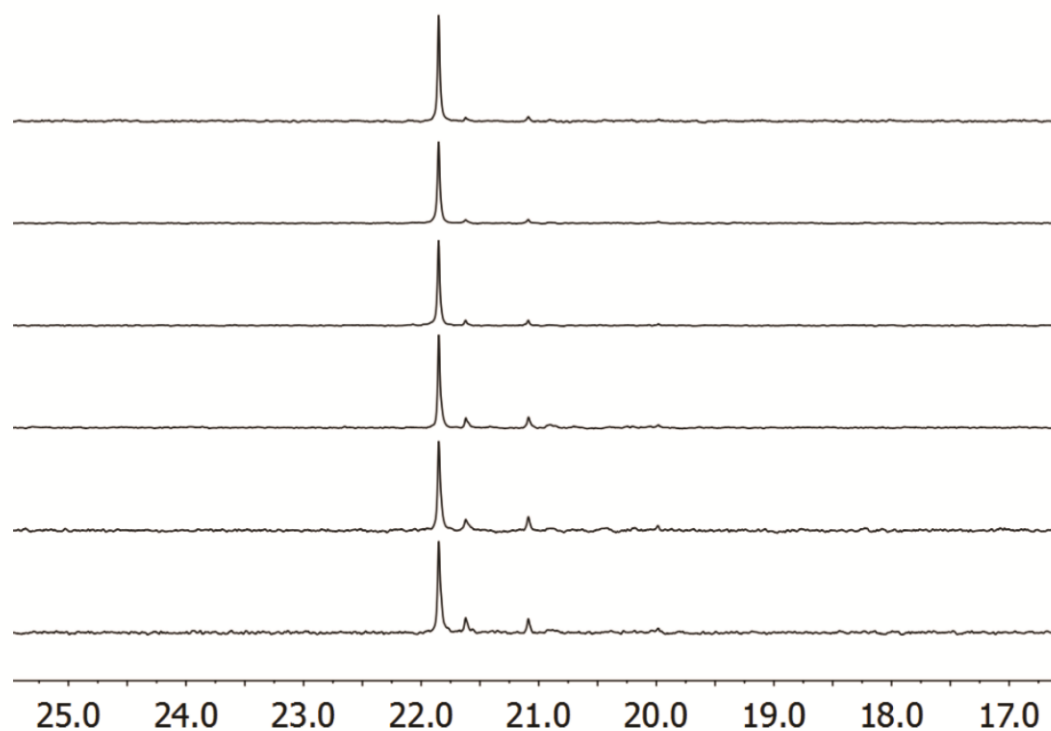


Figure S28. Pentad distribution of table 4, entry 46-48, 52-54 ( $\mathbf{V}_a$   $T_p$ : 0<sub>top</sub> – 90<sub>bottom</sub> °C) in the  $^{13}\text{C} \{^1\text{H}\}$  NMR (300 MHz) spectrum ( $\text{C}_6\text{D}_5\text{Br}$ , 140 °C).

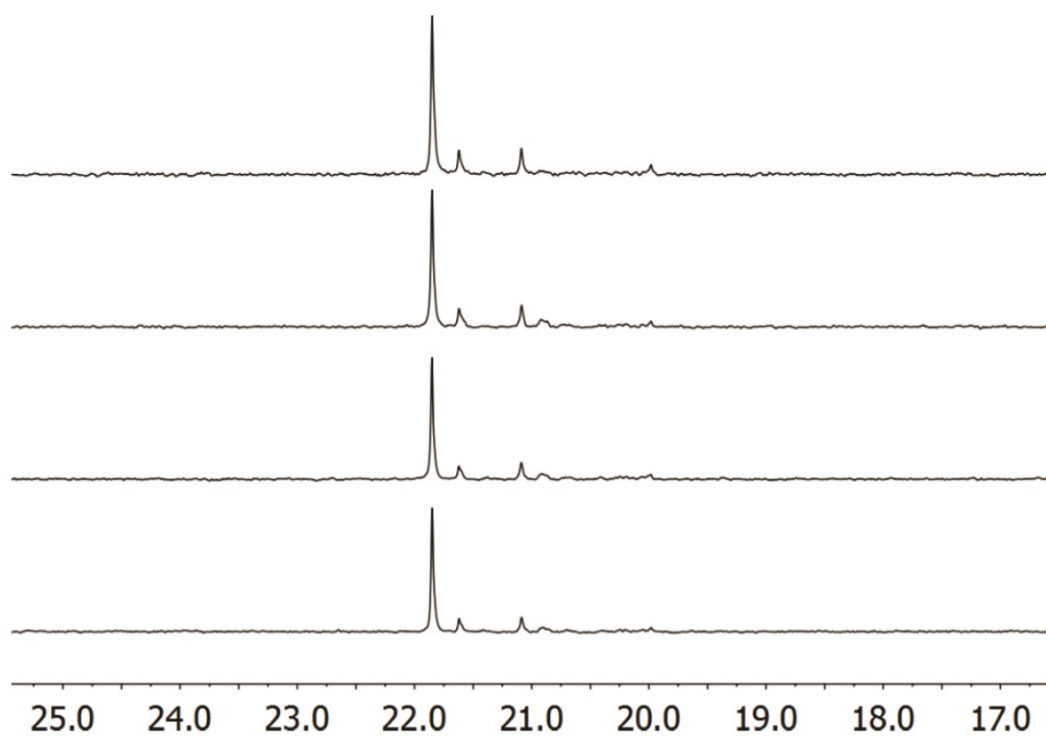


Figure S29. Pentad distribution of table 4, entry 49-52 ( $V_a$ , [propene]:  $0.50_{\text{top}} - 2.14_{\text{bottom}}$  °mol/L) in the  $^{13}\text{C}$   $\{^1\text{H}\}$  NMR (300 MHz) spectrum ( $\text{C}_6\text{D}_5\text{Br}$ ,  $140^\circ\text{C}$ ).

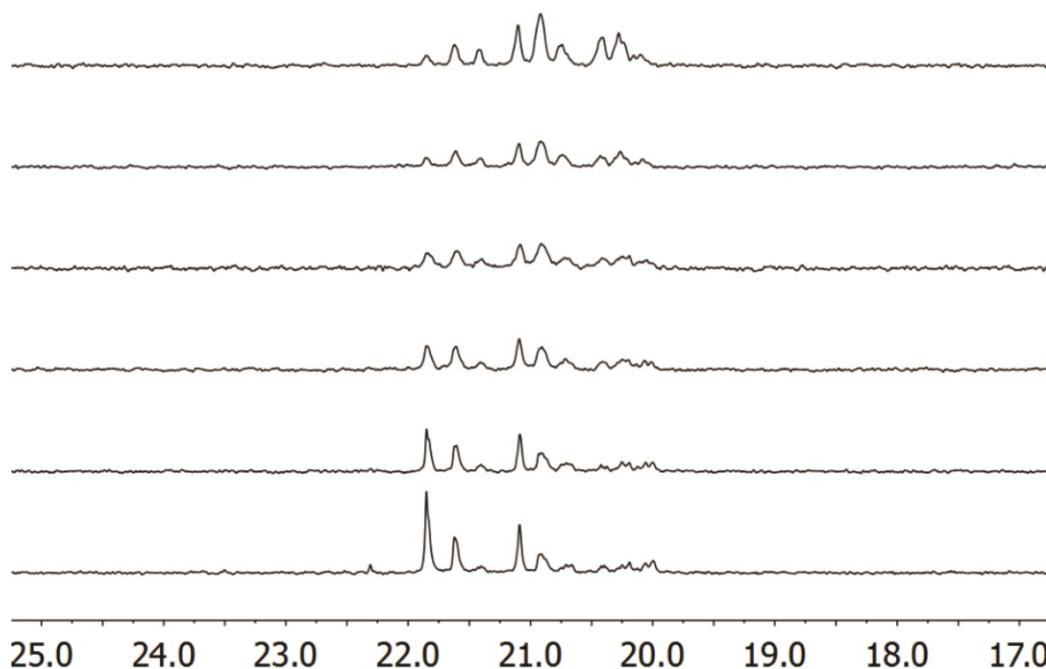


Figure S30. Pentad distribution of table 4, entry 55-57, 61-63 ( $V_b$ ,  $T_p$ :  $0_{\text{top}} - 90_{\text{bottom}}$  °C) in the  $^{13}\text{C}$   $\{^1\text{H}\}$  NMR (300 MHz) spectrum ( $\text{C}_6\text{D}_5\text{Br}$ ,  $140^\circ\text{C}$ ).

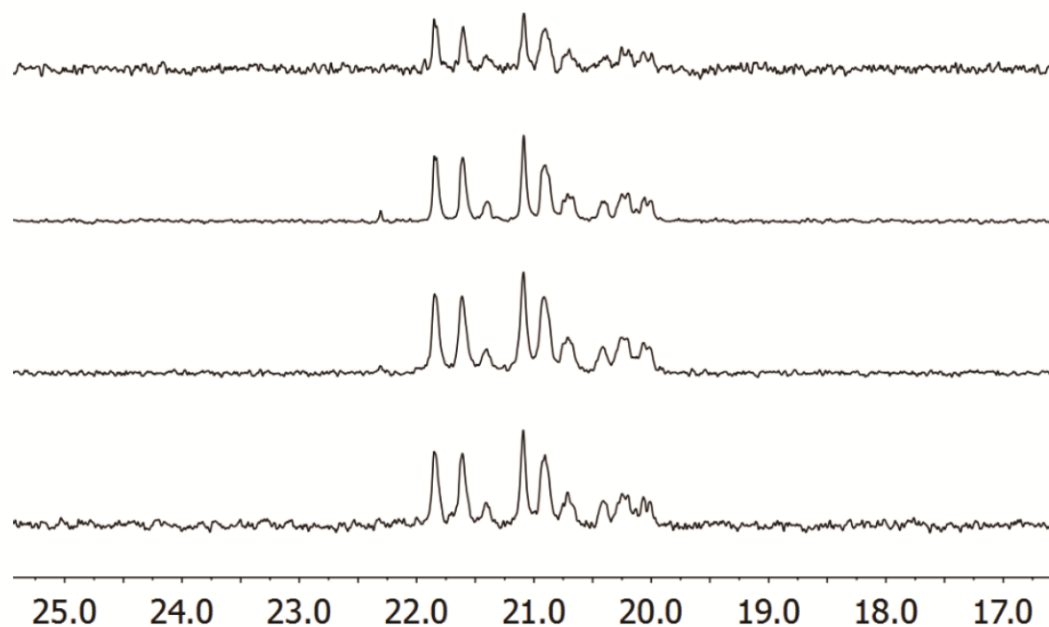


Figure S31. Pentad distribution of table 4, entry 58-61 ( $V_b$ , [propene]:  $0.50_{\text{top}} - 2.14_{\text{bottom}}$  °mol/L) in the  $^{13}\text{C} \{^1\text{H}\}$  NMR (300 MHz) spectrum ( $\text{C}_6\text{D}_5\text{Br}$ , 140 °C).

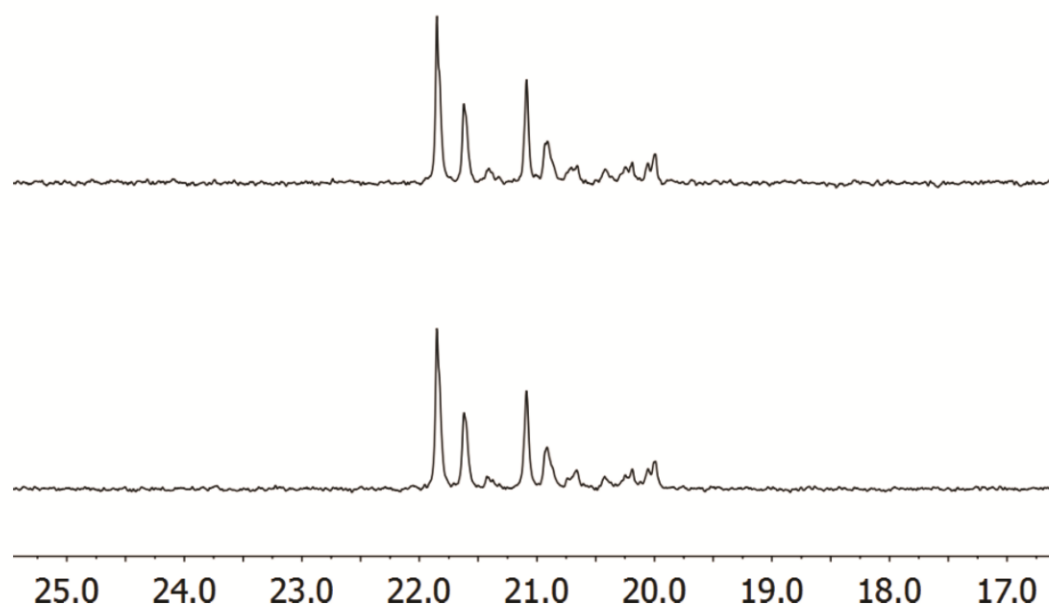


Figure S32. Pentad distribution of table 5, entry 1-2 ( $I_{\text{H}}$ ,  $T_p$ :  $-40_{\text{top}}, -20_{\text{bottom}}$  °C) in the  $^{13}\text{C} \{^1\text{H}\}$  NMR (300 MHz) spectrum ( $\text{C}_6\text{D}_5\text{Br}$ , 140 °C).

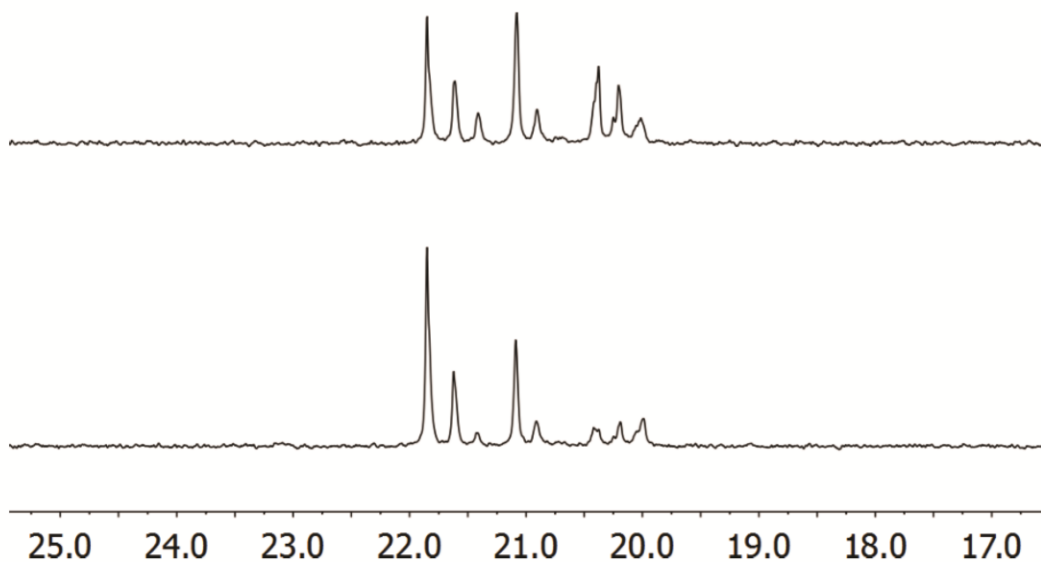


Figure S33. Pentad distribution of table 5, entry 7-8 ( $\mathbf{I}_{Zr}$ ,  $T_p$ :  $-40_{\text{top}}$ ,  $-20_{\text{bottom}}$  °C) in the  $^{13}\text{C}$   $\{^1\text{H}\}$  NMR (300 MHz) spectrum ( $\text{C}_6\text{D}_5\text{Br}$ , 140 °C).

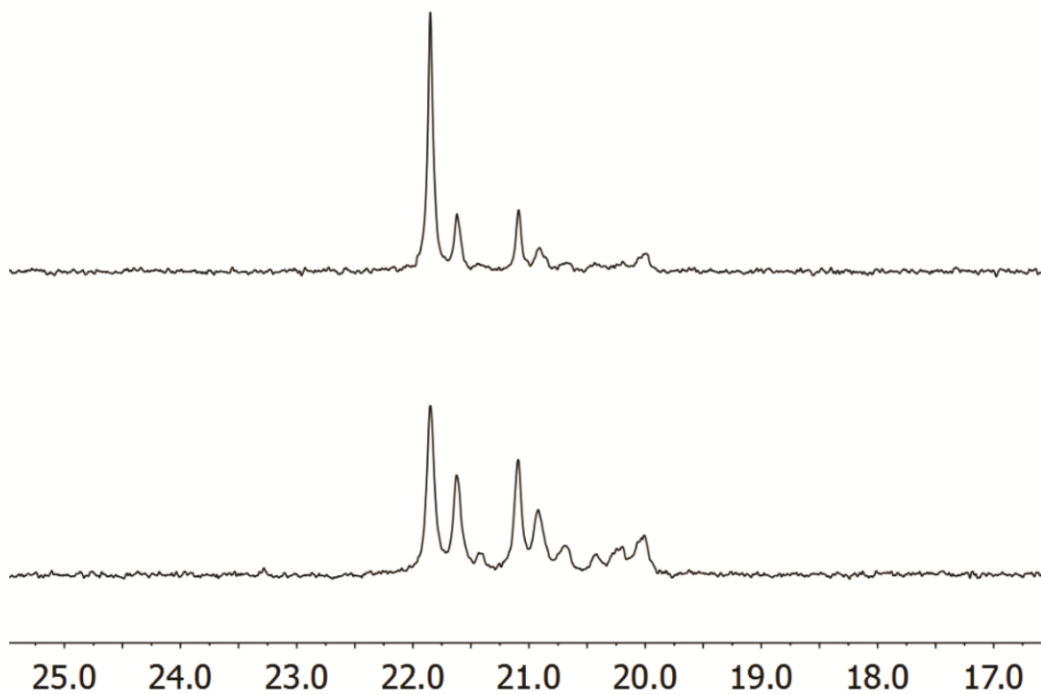


Figure S34. Pentad distribution of table 5, entry 3-4 ( $\mathbf{I}_{Hf}$ , Soxhlet extraction: residue (top), pentane (bottom)) in the  $^{13}\text{C}$   $\{^1\text{H}\}$  NMR (300 MHz) spectrum ( $\text{C}_6\text{D}_5\text{Br}$ , 140 °C).

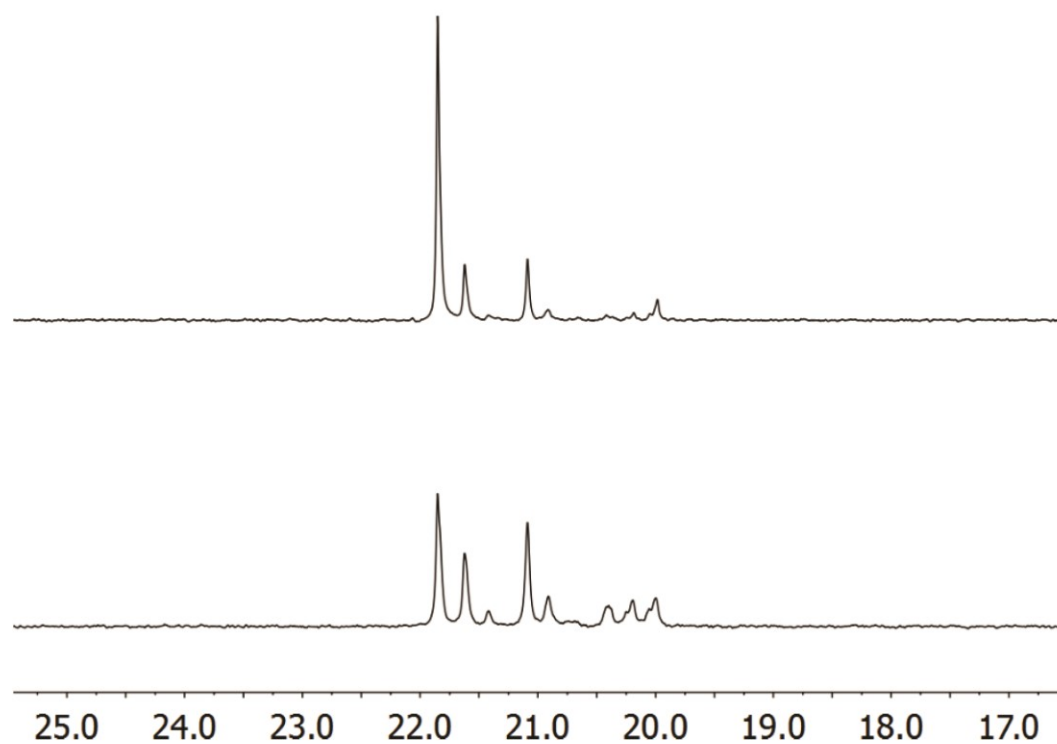


Figure S35. Pentad distribution of table 5, entry 9-10 ( $\mathbf{I}_{zr}$ , Soxhlet extraction: residue (top), pentane (bottom)) in the  $^{13}\text{C}$   $\{^1\text{H}\}$  NMR (300 MHz) spectrum ( $\text{C}_6\text{D}_5\text{Br}$ , 140 °C).



Figure S36. Macroscopic mixture of  $^i$ PP and  $^o$ PP produced with the catalyst mixture  $\mathbf{V}_a/\mathbf{V}_b = 2/1$  at 0 °C (2.14 M) before Soxhlet extraction.

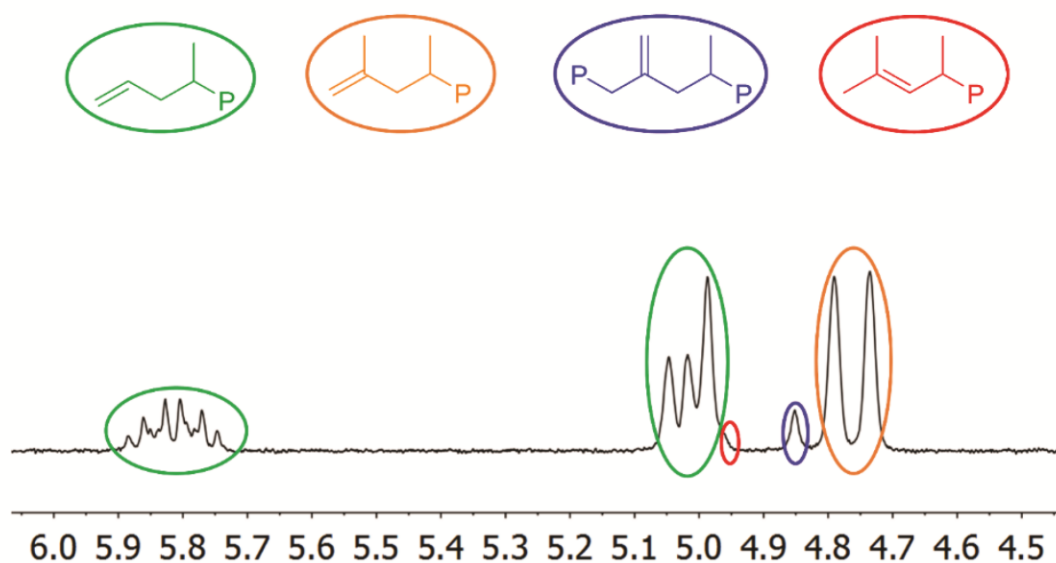
4. Olefinic end group analysis *via*  $^1\text{H}$  NMR spectroscopy

Figure S37. Exemplary olefinic end group assignment of entry S-18 *via*  $^1\text{H}$  NMR spectroscopy ( $\text{C}_6\text{D}_5\text{Br}$ ,  $140^\circ\text{C}$ ).

**Table S1.** Amount of allylic (Figure S32, green), vinylidene (Figure S32, orange) and internal (Figure S32, blue) end groups of the produced polypropylene samples.<sup>a</sup>

entry	catalyst	$T_p^b$	$n^c$	$[\text{C}_3]^d$	allylic [%]	vinylidene [%]	internal [%]
S-4	$\text{I}_{\text{Hf}}$	45	5.0	0.50	92	7	1
S-5	$\text{I}_{\text{Hf}}$	45	2.5	1.01	60	20	20
S-6	$\text{I}_{\text{Hf}}$	45	2.5	1.58	76	15	9
S-7	$\text{I}_{\text{Hf}}$	45	2.5	2.14	80	15	5
S-8	$\text{I}_{\text{Hf}}$	60	2.5	2.14	80	14	6
S-9	$\text{I}_{\text{Hf}}$	75	2.5	2.14	90	9	1
S-13	$\text{I}_{\text{Zr}}$	45	2.5	0.50	59	34	7
S-14	$\text{I}_{\text{Zr}}$	45	2.5	1.01	39	56	5
S-15	$\text{I}_{\text{Zr}}$	45	2.5	1.58	38	56	6
S-16	$\text{I}_{\text{Zr}}$	45	2.5	2.14	33	49	18
S-17	$\text{I}_{\text{Zr}}$	60 <sup>i</sup>	2.5	2.14	43	36	21
S-18	$\text{I}_{\text{Zr}}$	75	1.3	2.14	46	50	4
S-22	$\text{II}$	45	5.0	0.50	87	11	2
S-23	$\text{II}$	45	2.5	1.01	64	20	16
S-24	$\text{II}$	45	2.5	1.58	59	25	16
S-25	$\text{II}$	45	2.5	2.14	47	28	25

Appendix

S-26	<b>II</b>	60	2.5	2.14	78	18	4
S-27	<b>II</b>	75	2.5	2.14	91	8	1
S-31	<b>III</b>	45	5.0	0.50	91	9	0
S-32	<b>III</b>	45	2.5	1.01	90	8	1
S-33	<b>III</b>	45	2.5	1.58	84	15	1
S-34	<b>III</b>	45	2.5	2.14	82	16	2
S-35	<b>III</b>	60	2.5	2.14	81	17	2
S-36	<b>III</b>	75	2.5	2.14	84	14	2
S-40	<b>IV</b>	45	5.0	0.50	95	5	0
S-41	<b>IV</b>	45	2.5	1.01	91	9	0
S-42	<b>IV</b>	45	2.5	1.58	92	8	0
S-43	<b>IV</b>	45	2.5	2.14	90	10	0
S-44	<b>IV</b>	60	2.5	2.14	94	6	0
S-45	<b>IV</b>	75	2.5	2.14	93	7	0
S-49	<b>V<sub>a</sub></b>	45	2.5	0.50	85	3	12
S-50	<b>V<sub>a</sub></b>	45	2.5	1.01	77	2	21
S-51	<b>V<sub>a</sub></b>	45	2.5	1.58	66	8	26
S-52	<b>V<sub>a</sub></b>	45	2.5	2.14	62	8	30
S-53	<b>V<sub>a</sub></b>	60	2.5	2.14	73	13	14
S-54	<b>V<sub>a</sub></b>	75	2.5	2.14	82	9	8
S-58	<b>V<sub>b</sub></b>	45	2.5	0.50	90	9	1
S-59	<b>V<sub>b</sub></b>	45	2.5	1.01	86	11	3
S-60	<b>V<sub>b</sub></b>	45	2.5	1.58	80	16	4
S-61	<b>V<sub>b</sub></b>	45	2.5	2.14	78	16	6
S-62	<b>V<sub>b</sub></b>	60	2.5	2.14	86	12	1
S-63	<b>V<sub>b</sub></b>	75	2.5	2.14	82	17	1

<sup>a</sup> V<sub>toluene</sub>: 300 mL, t<sub>p</sub>: 30 min, scavenger (TIBA): 2.2 mmol, “-“ ≙ “not defined”. <sup>b</sup> T<sub>p</sub> in °C ± 2 °C. <sup>c</sup> In μmol. <sup>d</sup> Concentration of propene [mol/L].

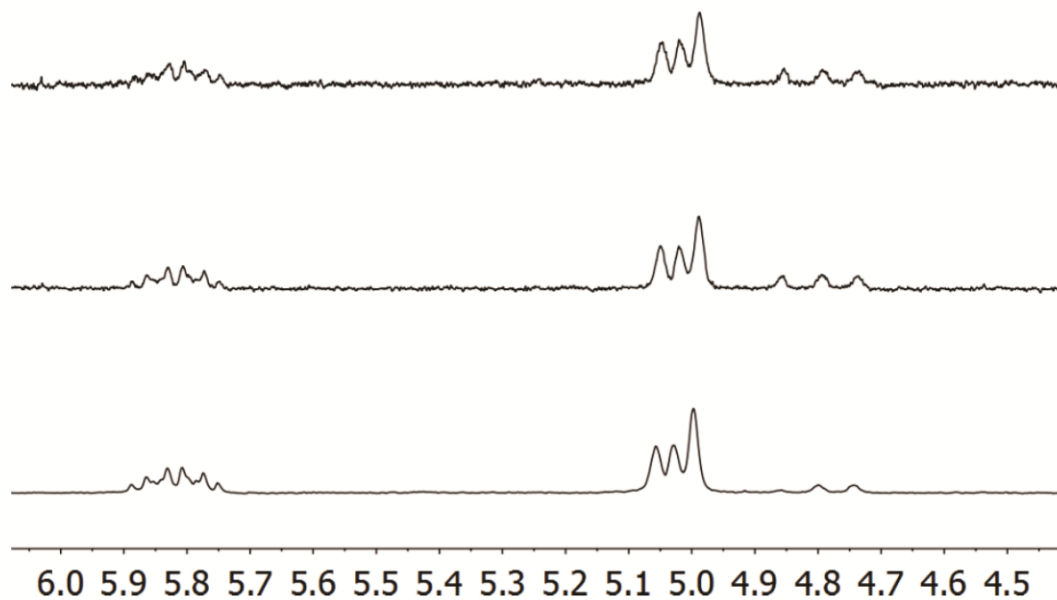


Figure 38. Olefinic end group determination of table 4, entry 7-9 ( $I_{\text{H}}$ ,  $T_p$ :  $45_{\text{top}} - 90_{\text{bottom}}$  °C) via  $^1\text{H}$  NMR spectroscopy ( $\text{C}_6\text{D}_5\text{Br}$ ,  $140^\circ\text{C}$ ).

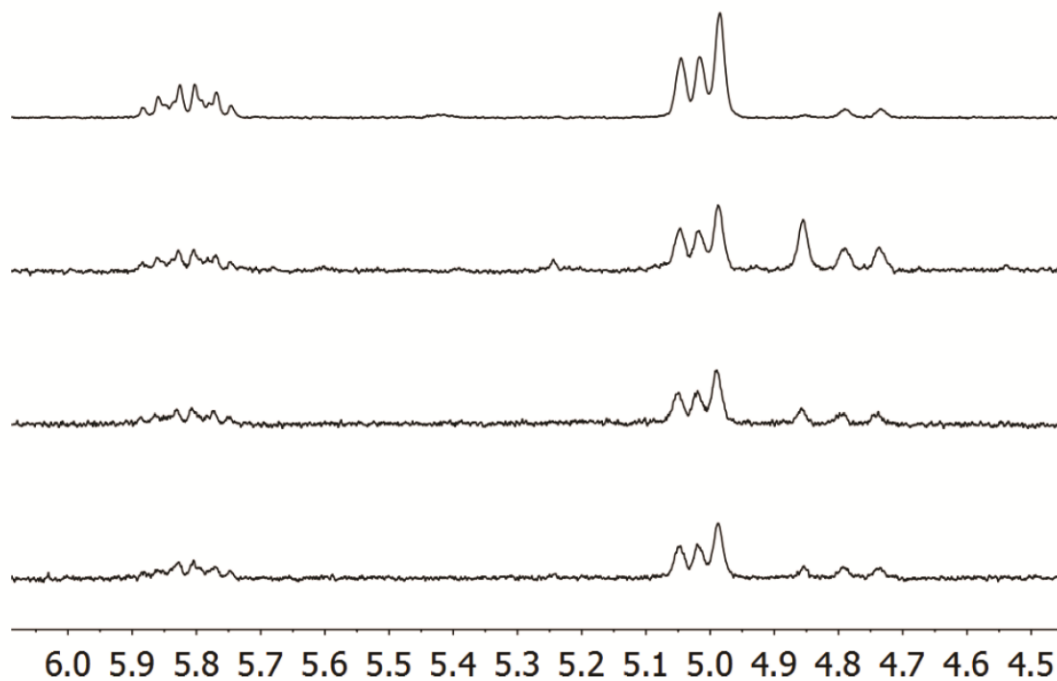


Figure 39. Olefinic end group determination of table 4, entry 4-7 ( $I_{\text{H}}$ ,  $[\text{propene}]$ :  $0.50_{\text{top}} - 2.14_{\text{bottom}}$  mol/L) via  $^1\text{H}$  NMR spectroscopy ( $\text{C}_6\text{D}_5\text{Br}$ ,  $140^\circ\text{C}$ ).

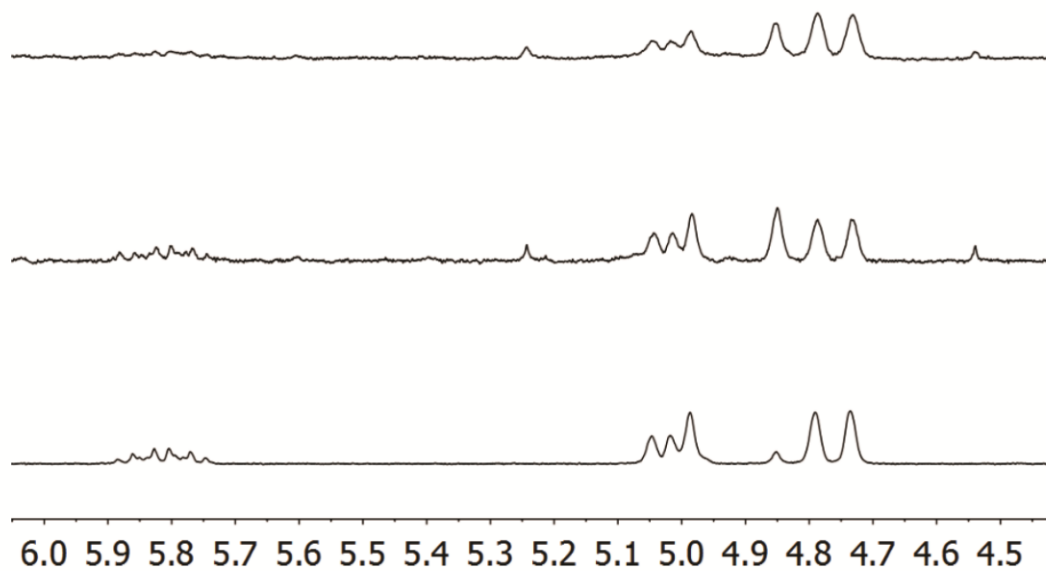


Figure 40. Olefinic end group determination of table 4, entry 16-18 ( $I_{Zr}$ ,  $T_P$ :  $45_{top} - 90_{bottom}$  °C) via  $^1H$  NMR spectroscopy ( $C_6D_5Br$ ,  $140$  °C).

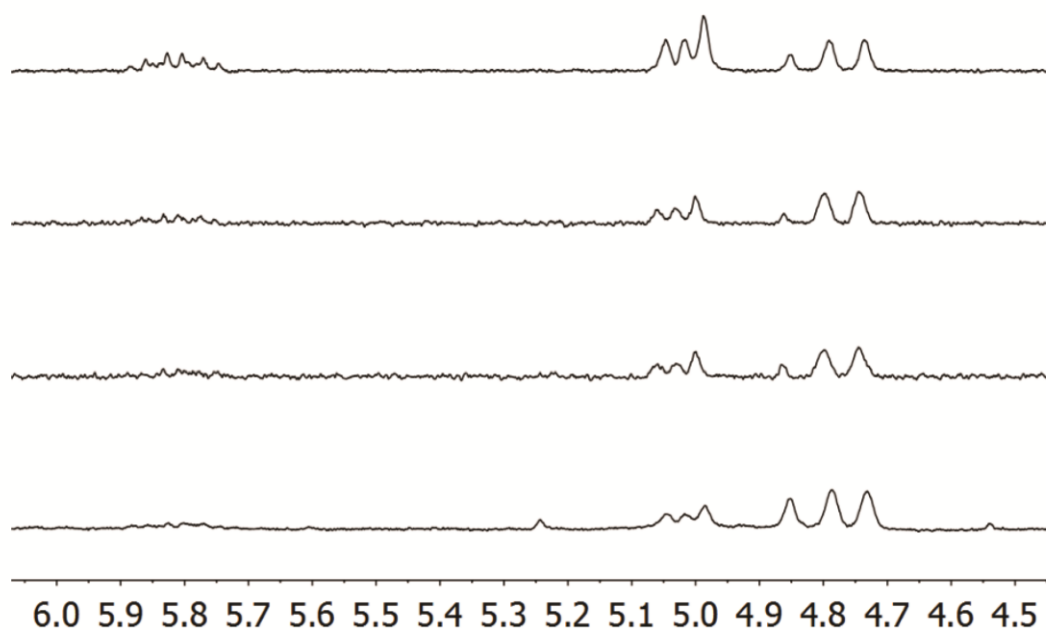


Figure 41. Olefinic end group determination of table 4, entry 13-16 ( $I_{Zr}$ , [propene]:  $0.50_{top} - 2.14_{bottom}$  mol/L) via  $^1H$  NMR spectroscopy ( $C_6D_5Br$ ,  $140$  °C).

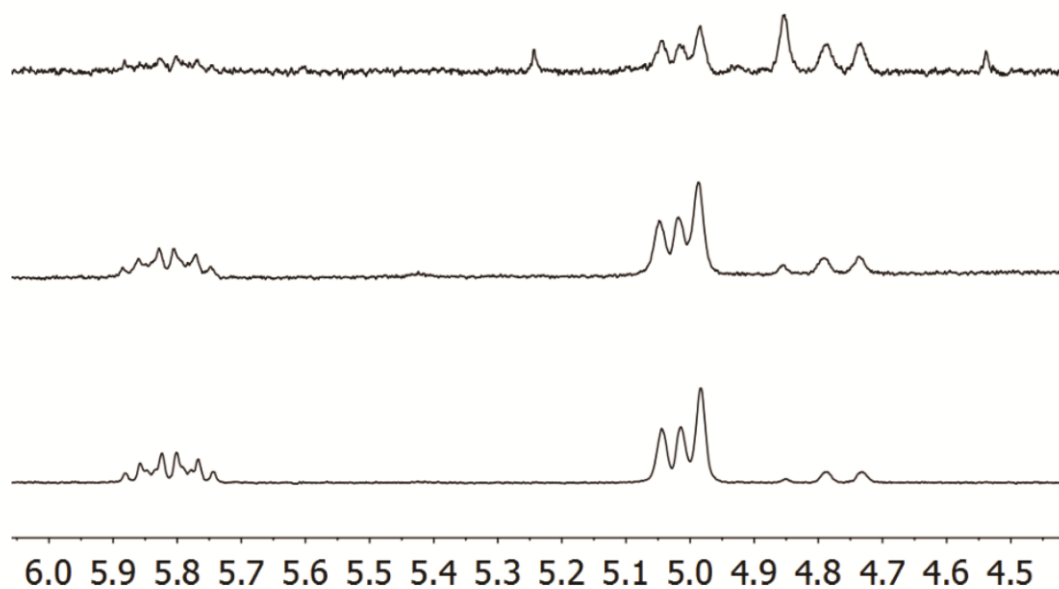


Figure 42. Olefinic end group determination of table 4, entry 25-27 (**II**,  $T_P$ : 45<sub>top</sub> – 90<sub>bottom</sub> °C) via  $^1\text{H}$  NMR spectroscopy ( $\text{C}_6\text{D}_5\text{Br}$ , 140 °C).

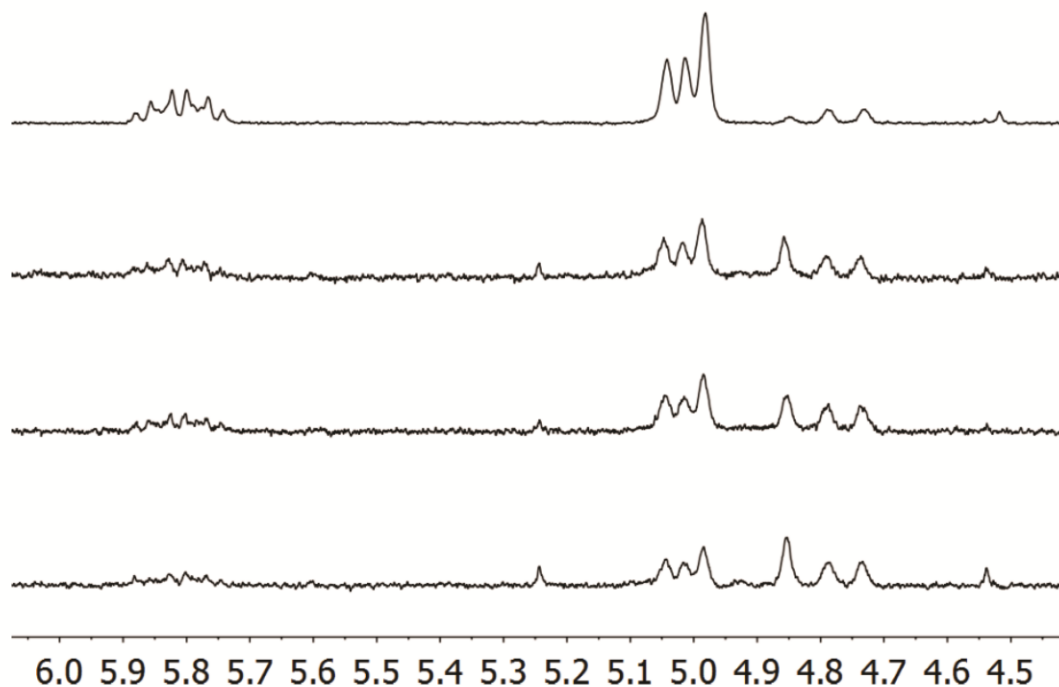


Figure 43. Olefinic end group determination of table 4, entry 22-25 (**II**, [propene]: 0.50<sub>top</sub> – 2.14<sub>bottom</sub> mol/L) via  $^1\text{H}$  NMR spectroscopy ( $\text{C}_6\text{D}_5\text{Br}$ , 140 °C).

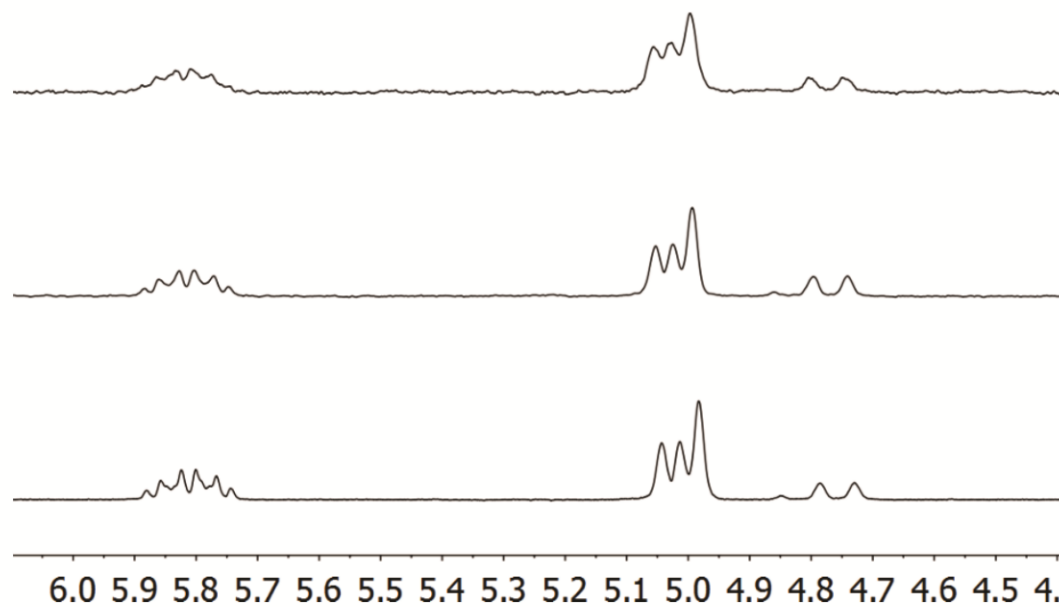


Figure 44. Olefinic end group determination of table 4, entry 34-36 (**III**,  $T_P$ :  $45_{\text{top}} - 90_{\text{bottom}}$  °C) via  $^1\text{H}$  NMR spectroscopy ( $\text{C}_6\text{D}_5\text{Br}$ ,  $140$  °C).

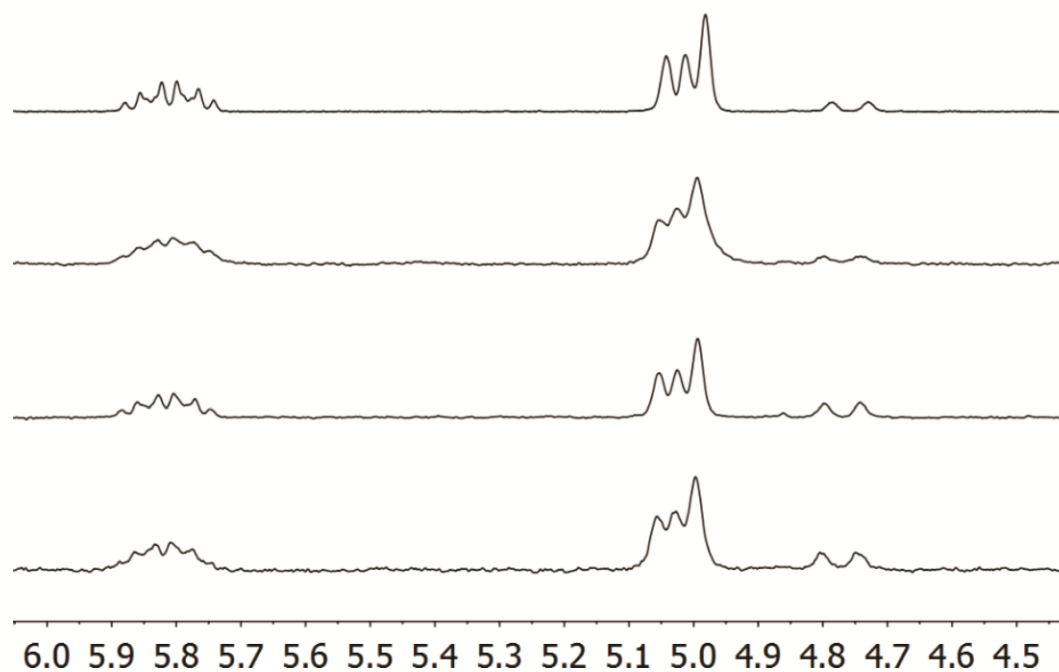


Figure 45. Olefinic end group determination of table 4, entry 31-34 (**III**,  $[\text{propene}]$ :  $0.50_{\text{top}} - 2.14_{\text{bottom}}$  mol/L) via  $^1\text{H}$  NMR spectroscopy ( $\text{C}_6\text{D}_5\text{Br}$ ,  $140$  °C).

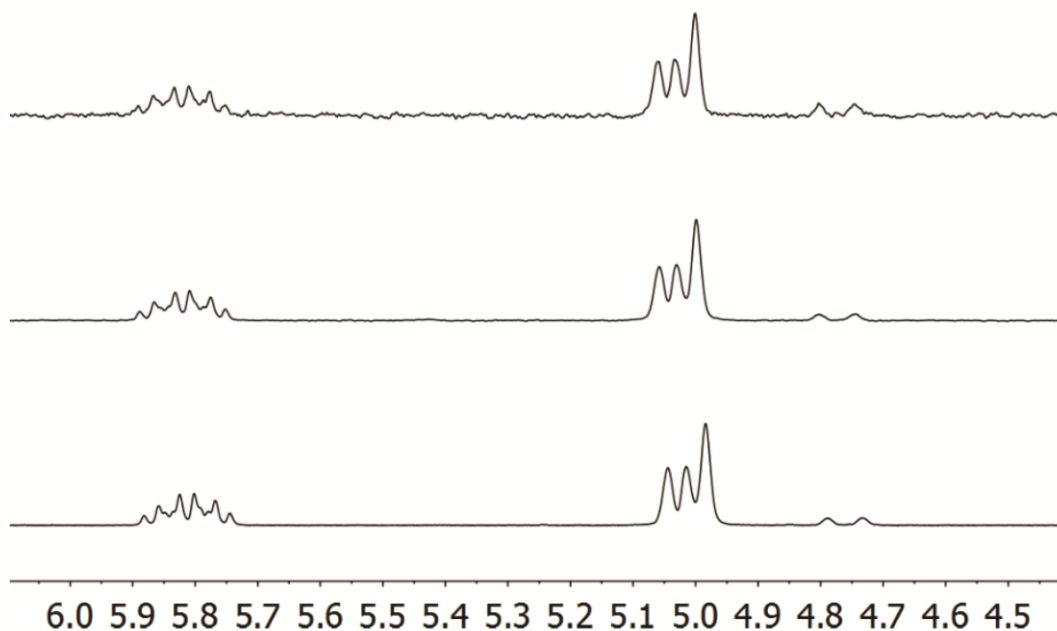


Figure 46. Olefinic end group determination of table 4, entry 43-45 (**IV**,  $T_p$ : 45<sub>top</sub> – 90<sub>bottom</sub> °C) via  $^1\text{H}$  NMR spectroscopy ( $\text{C}_6\text{D}_5\text{Br}$ , 140 °C).

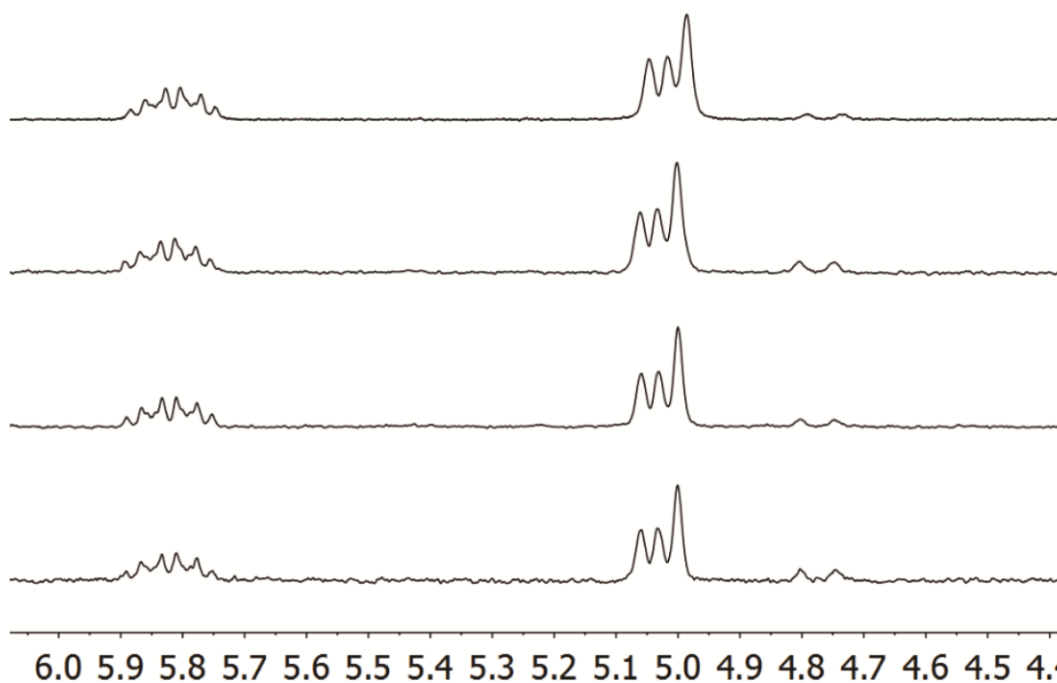


Figure 47. Olefinic end group determination of table 4, entry 40-43 (**IV**, [propene]: 0.50<sub>top</sub> – 2.14<sub>bottom</sub> mol/L) via  $^1\text{H}$  NMR spectroscopy ( $\text{C}_6\text{D}_5\text{Br}$ , 140 °C).

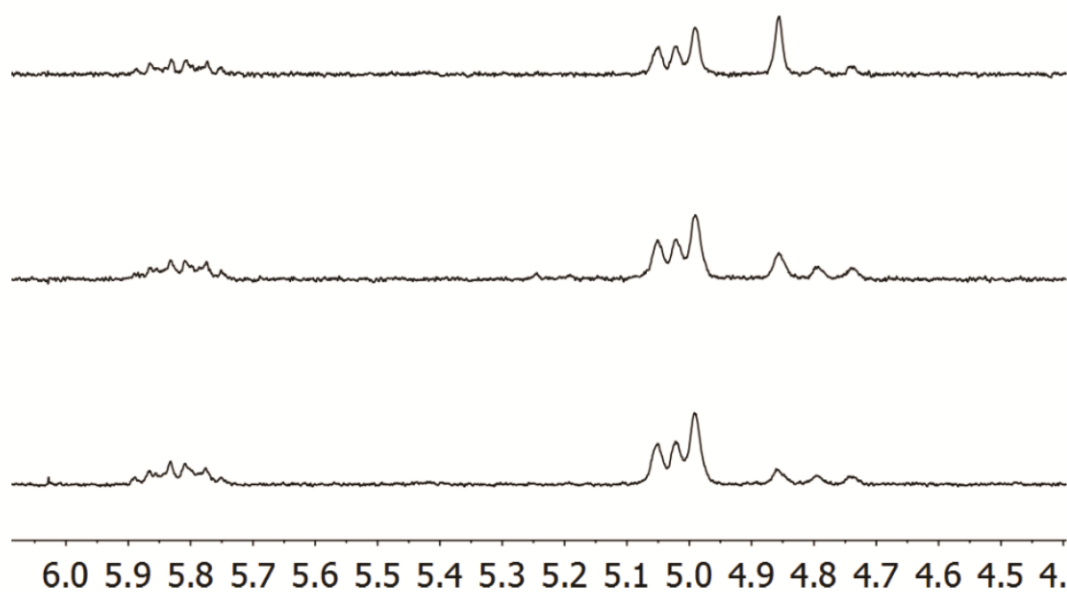


Figure 48. Olefinic end group determination of table 4, entry 52-54 ( $V_a$ ,  $T_P$ : 45<sub>top</sub> – 90<sub>bottom</sub> °C) via  $^1H$  NMR spectroscopy ( $C_6D_5Br$ , 140 °C).

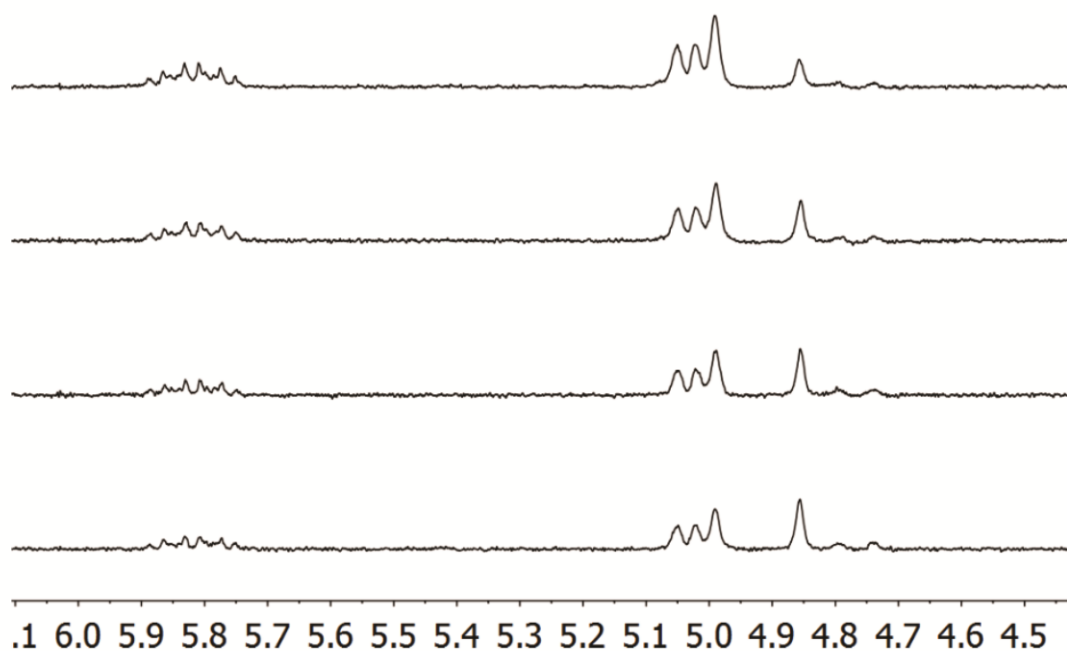


Figure 49. Olefinic end group determination of table 4, entry 49-52 ( $V_a$ , [propene]: 0.50<sub>top</sub> – 2.14<sub>bottom</sub> mol/L) via  $^1H$  NMR spectroscopy ( $C_6D_5Br$ , 140 °C).

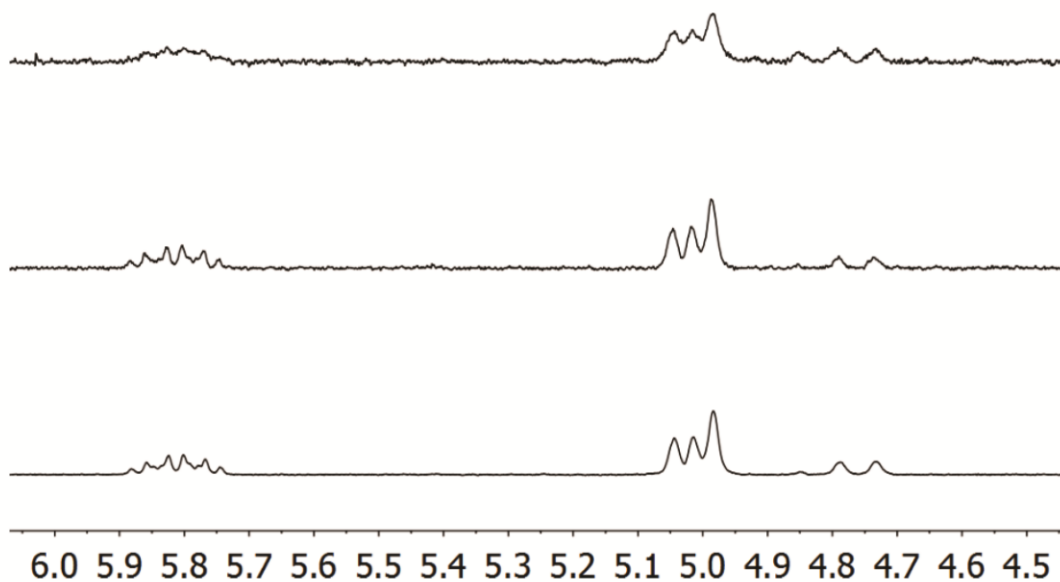


Figure 50. Olefinic end group determination of table 4, entry 61-63 ( $\mathbf{V}_b$ ,  $T_P$ : 45<sub>top</sub> – 90<sub>bottom</sub> °C) via  $^1\text{H}$  NMR spectroscopy ( $\text{C}_6\text{D}_5\text{Br}$ , 140 °C).

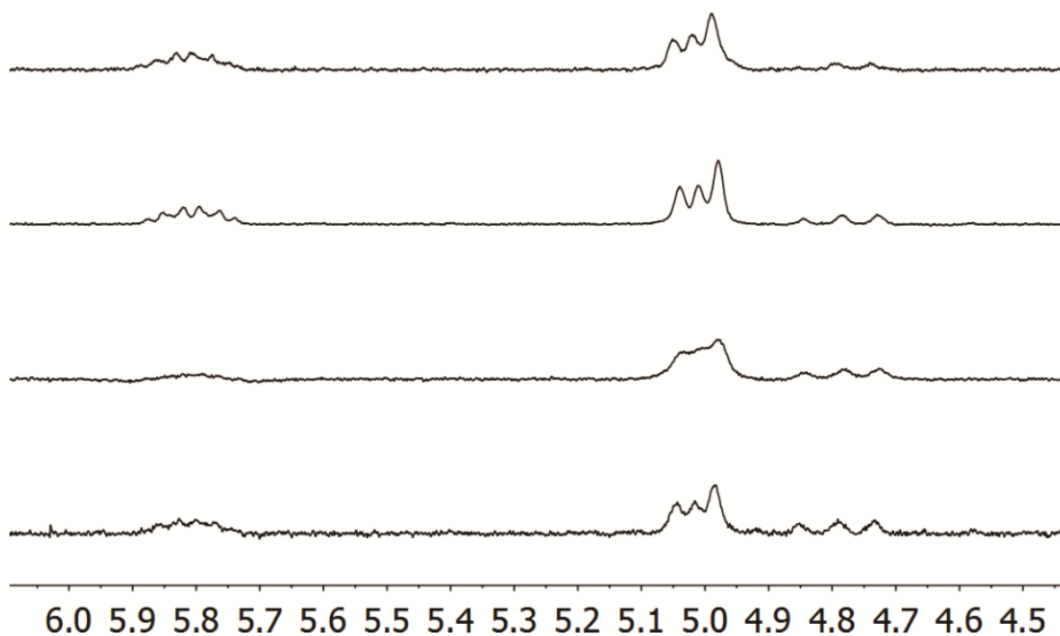


Figure 51. Olefinic end group determination of table 4, entry 58-61 ( $\mathbf{V}_b$ , [propene]: 0.50<sub>top</sub> – 2.14<sub>bottom</sub> mol/L) via  $^1\text{H}$  NMR spectroscopy ( $\text{C}_6\text{D}_5\text{Br}$ , 140 °C).

## 5. Single crystal XRD (SC-XRD) data

The X-ray intensity data of **II** and **V** were collected on an X-ray single crystal diffractometer equipped with a CCD detector (Bruker APEX II,  $\kappa$ -CCD), an fine-focus tube with MoK $\alpha$  radiation ( $\lambda = 0.71073 \text{ \AA}$ ) and a Triumph monochromator by using the APEX II software package.<sup>S2</sup> The X-ray intensity data of **III** were collected on an X-ray single crystal diffractometer equipped with a CMOS detector (Bruker Photon-100), an IMS microsource with MoK $\alpha$  radiation ( $\lambda = 0.71073 \text{ \AA}$ ) and a Helios mirror optic by using the APEX III software package.<sup>S3</sup> The measurements were performed on single crystals coated with perfluorinated ether. The crystals were fixed on the top of a microsampler, transferred to the diffractometer and frozen under a stream of cold nitrogen. A matrix scan was used to determine the initial lattice parameters. Reflections were merged and corrected for Lorenz and polarization effects, scan speed, and background using SAINT.<sup>S4</sup> Absorption corrections, including odd and even ordered spherical harmonics were performed using SADABS.<sup>S4</sup> Space group assignments were based upon systematic absences, E statistics, and successful refinement of the structures. Structures were solved by direct methods with the aid of successive difference Fourier maps, and were refined against all data using the APEX III software in conjunction with SHELXL-2014<sup>S5</sup> and SHELXLE<sup>S6</sup>. Methyl hydrogen atoms were refined as part of rigid rotating groups, with a C–H distance of 0.98  $\text{\AA}$  and  $U_{\text{iso}}(\text{H}) = 1.5 \cdot U_{\text{eq}}(\text{C})$ . Other H atoms were placed in calculated positions and refined using a riding model, with methylene and aromatic C–H distances of 0.99 and 0.95  $\text{\AA}$ , respectively, and  $U_{\text{iso}}(\text{H}) = 1.2 \cdot U_{\text{eq}}(\text{C})$ . Full-matrix least-squares refinements were carried out by minimizing  $\Delta w(F_o^2 - F_c^2)^2$  with SHELXL-97<sup>S7</sup> weighting scheme. Neutral atom scattering factors for all atoms and anomalous dispersion corrections for the non-hydrogen atoms were taken from *International Tables for Crystallography*.<sup>S8</sup>

The X-ray intensity data of **IV** were collected on an X-ray single crystal diffractometer equipped with a CCD detector (Bruker APEX II,  $\kappa$ -CCD) at the window of a fine-focused sealed tube with MoK $\alpha$  radiation ( $\lambda = 0.71073 \text{ \AA}$ ) and a graphite monochromator by using the SMART software package.<sup>S2</sup> The measurement was performed on a single crystal coated with perfluorinated ether. The crystal was fixed on the top of a cactus prickle (*Opuntia ficus-india*) with perfluorinated ether and transferred to the diffractometer. The crystal was frozen under a stream of cold nitrogen. A matrix scan was used to determine the initial lattice parameters. Reflections were merged and corrected for Lorenz and polarization effects, scan speed, and background using SAINT.<sup>S4</sup> Absorption corrections, including odd and even ordered spherical harmonics were performed using SADABS.<sup>S4</sup> Space group assignment was based upon systematic absences, E statistics, and successful refinement of the structure. The structure was solved by direct methods with the aid of successive difference Fourier maps, and were refined against all data using WinGX<sup>S9</sup> based on SIR-92<sup>S10</sup> in conjunction with SHELXL-97<sup>S7</sup>. H atoms were placed in calculated positions and refined using a riding model, with aromatic C–H distances of 0.95  $\text{\AA}$  and methylene C–H distances of 0.99  $\text{\AA}$ , and  $U_{\text{iso}}(\text{H}) = 1.2 \cdot U_{\text{eq}}(\text{C})$ . If not mentioned otherwise, non-hydrogen atoms were refined with anisotropic displacement parameters. Full-matrix least-squares refinements were carried out by minimizing  $\Delta w(F_o^2 - F_c^2)^2$  with SHELXL-97<sup>S7</sup> weighting scheme. Neutral atom scattering factors for all atoms and anomalous dispersion corrections for the non-hydrogen atoms were taken from *International Tables for Crystallography*.<sup>S8</sup>

The image of the crystal structures were generated by PLATON.<sup>S11</sup> CCDC 1578807-1578810 contain the supplementary data for the structures. These data can be obtained free of charge from the Cambridge Crystallographic Data Centre.

## Compound II (CCDC 1578809)

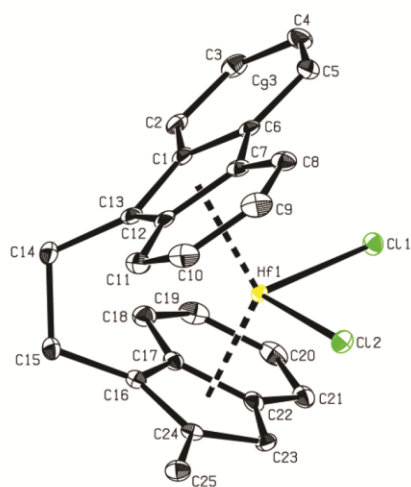


Figure S52. ORTEP style representation of **II** with ellipsoids drawn at 50% probability level. Hydrogen atoms are omitted for clarity.

Table S2: Sample and crystal data for **II**.

Identification code	MacMa26	
Chemical formula	$C_{25}H_{20}Cl_2Hf$	
Formula weight	569.80	
Temperature	100(2) K	
Wavelength	0.71073 Å	
Crystal size	0.053 x 0.095 x 0.617 mm	
Crystal habit	clear yellow fragment	
Crystal system	monoclinic	
Space group	$P2_1/n$	
Unit cell dimensions	a = 9.7645(5) Å	$\alpha = 90^\circ$
	b = 14.7201(7) Å	$\beta = 100.805(2)^\circ$
	c = 13.8849(8) Å	$\gamma = 90^\circ$
Volume	1960.36(18) Å <sup>3</sup>	
Z	4	
Density (calculated)	1.931 g/cm <sup>3</sup>	
Absorption coefficient	5.602 mm <sup>-1</sup>	
F(000)	1104	

Table S3: Data collection and structure refinement for **II**.

<b>Diffractometer</b>	Bruker D8 Kappa Apex II
<b>Radiation source</b>	fine-focus sealed tube, Mo
<b>Theta range for data collection</b>	2.04 to 25.02°
<b>Index ranges</b>	-11<=h<=11, -17<=k<=17, -16<=l<=16
<b>Reflections collected</b>	60935
<b>Independent reflections</b>	3461 [R(int) = 0.0193]
<b>Coverage of independent reflections</b>	100.0%
<b>Absorption correction</b>	multi-scan
<b>Min. and max. transmission</b>	0.5265 and 0.7453
<b>Refinement method</b>	Full-matrix least-squares on F <sup>2</sup>
<b>Refinement program</b>	SHELXL-2014/7 (Sheldrick, 2014)
<b>Function minimized</b>	$\Sigma w(F_o^2 - F_c^2)^2$
<b>Data / restraints / parameters</b>	3461 / 0 / 2545
<b>Goodness-of-fit on F<sup>2</sup></b>	1.177
<b><math>\Delta/\sigma_{\max}</math></b>	0.003
<b>Final R indices</b>	3369 data; I>2 $\sigma$ (I) R1 = 0.0127, wR2 = 0.0260 all data R1 = 0.0134, wR2 = 0.0262
<b>Weighting scheme</b>	$w=1/[\sigma^2(F_o^2)+(0.0041P)^2+3.2548P]$ where $P=(F_o^2+2F_c^2)/3$
<b>Largest diff. peak and hole</b>	0.496 and -0.635 eÅ <sup>-3</sup>
<b>R.M.S. deviation from mean</b>	0.063 eÅ <sup>-3</sup>

## Compound III (CCDC 1578808)

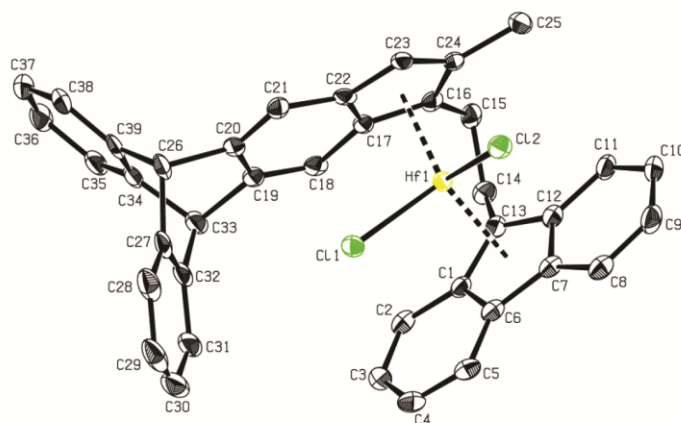


Figure S53. ORTEP style representation of **III** with ellipsoids drawn at 50% probability level. Hydrogen atoms are omitted for clarity.

Table S4: Sample and crystal data for **III**.

Identification code	MacMa27	
Chemical formula	$C_{39}H_{28}Cl_2Hf$	
Formula weight	746.00	
Temperature	100(2) K	
Wavelength	0.71073 Å	
Crystal size	0.137 x 0.182 x 0.472 mm	
Crystal habit	clear yellow fragment	
Crystal system	monoclinic	
Space group	$C2/c$	
Unit cell dimensions	$a = 28.757(5)$ Å	$\alpha = 90^\circ$
	$b = 14.932(3)$ Å	$\beta = 93.341(5)^\circ$
	$c = 15.353(3)$ Å	$\gamma = 90^\circ$
Volume	$6581.2(2)$ Å <sup>3</sup>	
Z	8	
Density (calculated)	$1.506$ g/cm <sup>3</sup>	
Absorption coefficient	$3.358$ mm <sup>-1</sup>	
F(000)	2944	

Table S5: Data collection and structure refinement for **III**.

<b>Diffractometer</b>	Bruker D8 Venture Duo IMS
<b>Radiation source</b>	IMS microsource, Mo
<b>Theta range for data collection</b>	2.53 to 25.03°
<b>Index ranges</b>	-34<=h<=34, -17<=k<=17, -18<=l<=18
<b>Reflections collected</b>	52199
<b>Independent reflections</b>	5826 [R(int) = 0.0193]
<b>Coverage of independent reflections</b>	99.9%
<b>Absorption correction</b>	multi-scan
<b>Min. and max. transmission</b>	0.5923 and 0.7453
<b>Refinement method</b>	Full-matrix least-squares on F <sup>2</sup>
<b>Refinement program</b>	SHELXL-2014/7 (Sheldrick, 2014)
<b>Function minimized</b>	$\Sigma w(F_o^2 - F_c^2)^2$
<b>Data / restraints / parameters</b>	5826 / 0 / 380
<b>Goodness-of-fit on F<sup>2</sup></b>	1.016
$\Delta/\sigma_{\max}$	0.002
<b>Final R indices</b>	4878 data; I>2 $\sigma$ (I) R1 = 0.0282, wR2 = 0.0515 all data R1 = 0.0405, wR2 = 0.0541
<b>Weighting scheme</b>	$w=1/[\sigma^2(F_o^2)+(0.0212P)^2+18.7050P]$ where $P=(F_o^2+2F_c^2)/3$
<b>Largest diff. peak and hole</b>	0.862 and -0.585 eÅ <sup>-3</sup>
<b>R.M.S. deviation from mean</b>	0.095 eÅ <sup>-3</sup>

## Compound IV (CCDC 1580068)

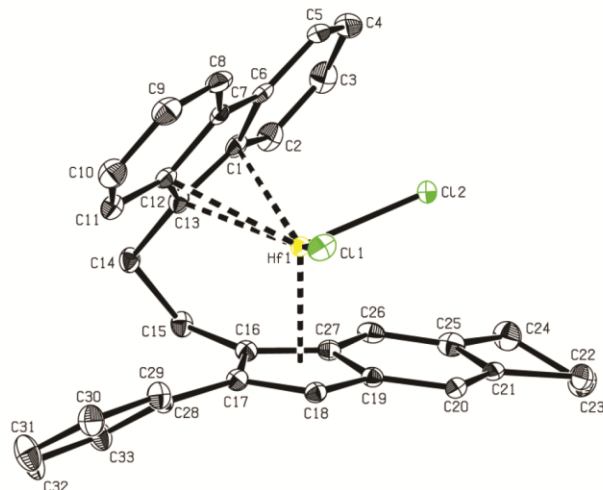


Figure S54. ORTEP style representation of **IV** with ellipsoids drawn at 50% probability level. Hydrogen atoms and co-crystallized solvent molecules are omitted for clarity.

Table S6: Sample and crystal data for **IV**.

<b>Identification code</b>	lana	
<b>Chemical formula</b>	$C_{33}H_{26}Cl_2Hf$	
<b>Formula weight</b>	671.93	
<b>Temperature</b>	123(1) K	
<b>Wavelength</b>	0.71073 Å	
<b>Crystal size</b>	0.36 x 0.38 x 0.53 mm	
<b>Crystal habit</b>	orange prism	
<b>Crystal system</b>	monoclinic	
<b>Space group</b>	$P2_1/n$	
<b>Unit cell dimensions</b>	a = 14.3780(3) Å	$\alpha = 90^\circ$
	b = 14.7549(3) Å	$\beta = 115.4455(8)^\circ$
	c = 14.6714(3) Å	$\gamma = 90^\circ$
<b>Volume</b>	2810.55(10) Å <sup>3</sup>	
<b>Z</b>	4	
<b>Density (calculated)</b>	1.588 g/cm <sup>3</sup>	
<b>Absorption coefficient</b>	3.921 mm <sup>-1</sup>	
<b>F(000)</b>	1320	

Table S7: Data collection and structure refinement for **IV**.

<b>Diffractometer</b>	Bruker D8 Kappa Apex II	
<b>Radiation source</b>	fine-focus sealed tube, Mo	
<b>Theta range for data collection</b>	1.66 to 25.48°	
<b>Index ranges</b>	-17<=h<=17, -17<=k<=17, -17<=l<=17	
<b>Reflections collected</b>	75881	
<b>Independent reflections</b>	5205 [R(int) = 0.0771]	
<b>Coverage of independent reflections</b>	99.6%	
<b>Absorption correction</b>	multi-scan	
<b>Min. and max. transmission</b>	0.5388 and 0.7452	
<b>Refinement method</b>	Full-matrix least-squares on F <sup>2</sup>	
<b>Refinement program</b>	SHELXL-97 (Sheldrick, 1998)	
<b>Function minimized</b>	$\Sigma w(F_o^2 - F_c^2)^2$	
<b>Data / restraints / parameters</b>	5205 / 0 / 325	
<b>Goodness-of-fit on F<sup>2</sup></b>	1.052	
<b><math>\Delta/\sigma_{\max}</math></b>	0.003	
<b>Final R indices</b>	5049 data; I>2 $\sigma$ (I)	R1 = 0.0116, wR2 = 0.0295
	all data	R1 = 0.0121, wR2 = 0.0297
<b>Weighting scheme</b>	$w=1/[\sigma^2(F_o^2)+(0.0120P)^2+2.8847P]$ where $P=(F_o^2+2F_c^2)/3$	
<b>Largest diff. peak and hole</b>	0.31 and -0.27 eÅ <sup>-3</sup>	
<b>R.M.S. deviation from mean</b>	0.053 eÅ <sup>-3</sup>	

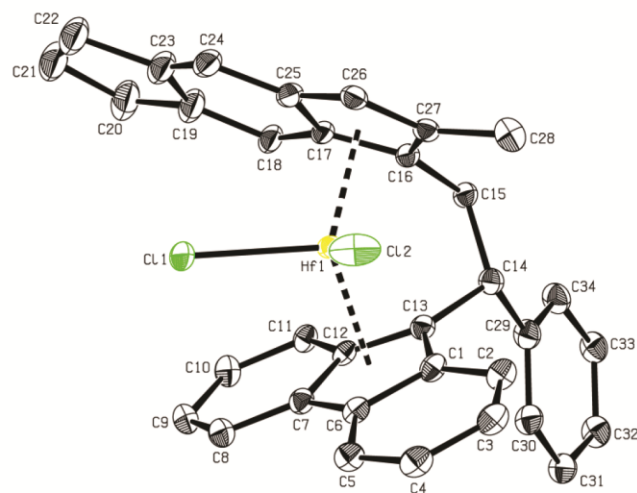
Compound **V** (CCDC 1578810)

Figure S55. ORTEP style representation of **V** with ellipsoids drawn at 50% probability level. Hydrogen atoms are omitted for clarity.

Table S8: Sample and crystal data for **V**.

<b>Identification code</b>	MacMa28	
<b>Chemical formula</b>	$C_{34}H_{28}Cl_2Hf$	
<b>Formula weight</b>	685.95	
<b>Temperature</b>	100(2) K	
<b>Wavelength</b>	0.71073 Å	
<b>Crystal size</b>	0.050 x 0.091 x 0.314 mm	
<b>Crystal habit</b>	clear yellow plate	
<b>Crystal system</b>	orthorhombic	
<b>Space group</b>	<i>Pbca</i>	
<b>Unit cell dimensions</b>	a = 11.582(3) Å	$\alpha = 90^\circ$
	b = 17.782(4) Å	$\beta = 90^\circ$
	c = 25.537(6) Å	$\gamma = 90^\circ$
<b>Volume</b>	5259.(2) Å <sup>3</sup>	
<b>Z</b>	4	
<b>Density (calculated)</b>	1.733 g/cm <sup>3</sup>	
<b>Absorption coefficient</b>	4.193 mm <sup>-1</sup>	
<b>F(000)</b>	2704	

Table S9: Data collection and structure refinement for **V**.

<b>Diffractometer</b>	Bruker D8 Kappa Apex II
<b>Radiation source</b>	fine-focus sealed tube, Mo
<b>Theta range for data collection</b>	2.25 to 25.04°
<b>Index ranges</b>	-13<=h<=13, -21<=k<=21, -29<=l<=29
<b>Reflections collected</b>	135039
<b>Independent reflections</b>	4636 [R(int) = 0.0534]
<b>Coverage of independent reflections</b>	99.6%
<b>Absorption correction</b>	multi-scan
<b>Min. and max. transmission</b>	0.6614 and 0.7453
<b>Refinement method</b>	Full-matrix least-squares on F <sup>2</sup>
<b>Refinement program</b>	SHELXL-2014/7 (Sheldrick, 2014)
<b>Function minimized</b>	$\Sigma w(F_o^2 - F_c^2)^2$
<b>Data / restraints / parameters</b>	4636 / 1312 / 643
<b>Goodness-of-fit on F<sup>2</sup></b>	1.162
<b><math>\Delta/\sigma_{\max}</math></b>	0.002
<b>Final R indices</b>	3372 data; I>2 $\sigma$ (I)    R1 = 0.0418, wR2 = 0.0625 all data                    R1 = 0.0656, wR2 = 0.0694
<b>Weighting scheme</b>	w=1/[ $\sigma^2(F_o^2)+54.0453P$ ] where P=(F <sub>o</sub> <sup>2</sup> +2F <sub>c</sub> <sup>2</sup> )/3
<b>Largest diff. peak and hole</b>	1.003 and -1.031 eÅ <sup>-3</sup>
<b>R.M.S. deviation from mean</b>	0.114 eÅ <sup>-3</sup>

## 6. DFT-calculations

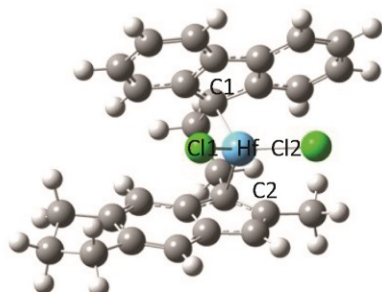
Table S10. Dihedral angles along the ethylene bridge of the bis-chlorinated complexes I–V.<sup>a</sup>

	<i>γ</i> -conformer	<i>π</i> -conformer	Transition state
<b>I<sub>Hf</sub></b>	+38.9°	-34.9°	-2.2°
<b>I<sub>Zr</sub></b>	+39.7°	-35.8°	-2.0°
<b>II</b>	+39.3°	-34.9°	-2.0°
<b>III</b>	+40.3°	-34.9°	-2.7°
<b>IV</b>	+39.7°	-40.6°	-0.3°
<b>V<sub>a</sub></b>	+24.1°	-33.9°	N/A
<b>V<sub>b</sub></b>	+37.7°	-14.3°	N/A

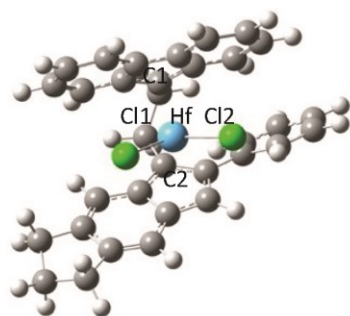
<sup>a</sup>Orientation: fluorenyl–ethylene bridge–indenylTable S11. Dihedral angles along the ethylene bridge of metallocenes I–V in the catalytically active, cationic structure of the type L<sub>2</sub>M(<sup>t</sup>Bu)<sup>+</sup>.<sup>b</sup>

	<i>γ</i> -conformer	<i>π</i> -conformer	Transition state
<b>I<sub>Hf</sub></b>	+36.9°	-35.0°	-2.1°
<b>I<sub>Zr</sub></b>	+37.9°	-36.8°	-0.9°
<b>II</b>	+37.2°	-34.8°	-1.9°
<b>III</b>	+37.1°	-35.1°	-2.5°
<b>IV</b>	+41.2°	-38.3°	-2.1°
<b>V<sub>a</sub></b>	+20.5°	-33.5°	N/A
<b>V<sub>b</sub></b>	+35.0°	-14.5°	N/A

<sup>a</sup>Orientation: fluorenyl–ethylene bridge–indenyl

Comparison between solid state (X-Ray) and calculated structuresFigure S56. Molecular representation of **I<sub>Hf</sub>** (dichloro) – **Y-conformer**.Table S12. Selected bonds and angles of calculated and experimental values of **I<sub>Hf</sub>** (Dichloro) – **Y-conformer**.

	Exp.	Calc.
Hf-Cl1	2.38	2.38
Hf-Cl2	2.40	2.40
Hf-C1	2.41	2.43
Hf-C2	2.47	2.50
Dihedral angle bridge (C1-bridge-C2)	+36.3	+38.9

Figure S57. Molecular representation of **IV** (dichloro) – **II-conformer**.Table S13. Selected bonds and angles of calculated and experimental values of **IV** (dichloro) – **II-conformer**.

	Exp.	Calc.
Hf-Cl1	2.38	2.39
Hf-Cl2	2.42	2.40
Hf-C1	2.41	2.43
Hf-C2	2.48	2.49
Dihedral angle bridge (C1-bridge-C2)	-41.5	-40.6

Detailed **Computational Data (Geometries, Absolute Energies)** of the bischorinated and bismethylated conformers, as well as the transition states of all complexes I–V are available free of charge on the website:

<https://pubs-acsc-org.eaccess.ub.tum.de/doi/abs/10.1021/acs.macromol.7b02679?journalCode=mamobx&quickLinkVolume=51&quickLinkPage=914&selectedTab=citation&volume=51>

## 7. References

- [S1] A., Zambelli; P., Locatelli; G., Bajo; F. A., Bovey, *Macromolecules*, **1975**, 8, 687-689.
- [S2] *APEX suite of crystallographic software, APEX 2, version 2008.4*, Bruker AXS Inc., Madison, Wisconsin, USA (**2008**).
- [S3] *APEX suite of crystallographic software, APEX 3, version 2015.5-2*, Bruker AXS Inc., Madison, Wisconsin, USA (**2015**).
- [S4] SAINT, Version 7.56a and SADABS Version 2008/1, Bruker AXS Inc., Madison, Wisconsin, USA (**2008**).
- [S5] Sheldrick, G. M. "**SHELXL-2014**", University of Göttingen, Göttingen, Germany, (**2014**).
- [S6] Huebschle, C. B.; Sheldrick, G. M.; Dittrich, B. "SHELXLE", *J. Appl. Cryst.* **2011**, 44, 1281.
- [S7] Sheldrick, G. M. "**SHELXL-97**", University of Göttingen, Göttingen, Germany, (**1998**).
- [S8] Wilson, A. J. C. *International Tables for Crystallography*, Vol. C, Tables 6.1.1.4 (pp. 500-502), 4.2.6.8 (pp. 219-222), and 4.2.4.2 (pp. 193-199); Kluwer Academic Publishers: Dordrecht, The Netherlands (**1992**).
- [S9] L. J. Farrugia, *J. Appl. Cryst.* **1999**, 32, 837-838.
- [S10] Altomare, A.; Cascarano, G.; Giacovazzo, C.; Guagliardi, A.; Burla, M. C.; Polidori, G.; Camalli M., *J. Appl. Cryst.* **1994**, 27, 435-436.
- [S11] A. L. Spek, PLATON, A Multipurpose Crystallographic Tool, Utrecht University, Utrecht, The Netherlands, **2010**.

## 12.5 Experimental Information – Chapter 8: Excursus: New Microstructures in Olefin-Based Polymers

**General.** All reactions and handling with air- and moisture-sensitive compounds were performed under an argon atmosphere using standard Schlenk or glovebox techniques. All chemicals, unless otherwise stated, were purchased from Aldrich, Acros, or VWR and used as received. Dry toluene and pentane were purified with an MBraun MB-SPS-800 solvent purification system. Chlorobenzene was dried over molecular sieve (4 Å). Propylene (99.5% by Westfalen AG) was purified by passing it through two columns filled with BASF catalyst (R3-11) and molecular sieves 3–4 Å.

**NMR** ( $^1\text{H}$  and  $^{13}\text{C}$   $\{^1\text{H}\}$ ) measurements were recorded on a Bruker AV400 or AV500C spectrometer at ambient temperature. Chemical shifts  $\delta$  were reported in ppm relative to tetramethylsilane and calibrated to the residual  $^1\text{H}$  or  $^{13}\text{C}$  signal of the deuterated solvent. The NMR spectra of the polymers were measured with an ARX-300 spectrometer at 140 °C with 50–60 mg/mL in bromobenzene- $d_5$ .

**Gel permeation chromatography** was performed with a PL-GPC 220 instrument equipped with  $2 \times$  Olexis  $300 \times 7.5$  mm columns and triple detection using a differential refractive index detector, a PL-BV 400 HT viscometer, and light scattering (Precision Detectors Model 2040;  $15^\circ$ ,  $90^\circ$ ). Measurements were performed at 160 °C using 1,2,4-trichlorobenzene (TCB; 30 mg BHT/L) with a constant flow rate of 1 mL/min and a calibration set with narrow MWD polystyrene (PS) and polyethylene (PE) standards. Samples were prepared by dissolving 0.9–1.1 mg polymer in 1.0 mL stabilized TCB for 10–15 min at 160 °C immediately before each measurement.

**Differential scanning calorimetry** was conducted on a DSC Q2000 instrument. Between 3 and 8 mg of the polymer was sealed into a DSC aluminum pan and heated from 20 °C to 200 °C at a rate of 10 °C/min. After holding the temperature for 2 min, the sample was cooled down to  $-50$  °C at a rate of 10 °C/min and heated up again in the same manner. The reported values are those determined during the second heating cycle. For tempering experiments, the polymer samples were kept at a constant temperature at 10 °C below the melting point for 60 min. The temperature was reduced at a rate of 1 °C/min for an additional 30 min and then cooled down to  $-50$  °C at a rate of 10 °C/min. The polymer was heated up to 200 °C at a rate of 10 °C/min (analyzed exo-down curves) and cooled again to  $-50$  °C at a rate of 10 °C/min.

**Stress–strain measurements** were performed on a ZwickRoell machine with a strain rate of 4 mm/min and analyzed with testXpert II software. Specimen (dog bone shape, 50 mm long, 4 mm wide (smallest distance)) were cut out of a compression molded polymer film produced at 150 °C, 150 bar for one hour.

**Synthesis.** For complex synthesis see Chapter 4 – 7.

**Polymerization (ethylene/propylene copolymers).** All polymerization reactions at 30 °C were performed in a 1.1 L *Büchi* steel autoclave equipped with a paddle agitator, temperature sensor, and a heating/cooling jacket attached to a cryo-/thermostat unit (Thermo Scientific HAAKE DynaMax). The Ar pressure for all manipulations was set to 1.3 bar. Prior to polymerization the autoclave was equipped with 300 mL of dry toluene and 2.0 mL of 1.1 M TIBA solution in toluene and heated up to 90 °C. After maintaining the temperature for 15 min the scrubbing solution was released. For the polymerization, the autoclave was charged with 280 mL of dry toluene and 2.0 mL of 1.1 M TIBA solution in toluene. The metallocene complex (1.0 eq.) was dissolved in 10 mL toluene and preactivated with 200 eq. of TIBA at 60 °C for 1 h. After the desired temperature (30 °C) was adjusted, the alkylated metallocene solution was transferred into the autoclave and was pressurized (4.0 bar) with the ethylene/propylene mixture (the monomer feed was premixed by a master (propylene) – slave (ethylene) system). When the system was equilibrated and stable, the polymerization was started by adding 5.0 eq. of  $[\text{Ph}_3\text{C}][\text{B}(\text{C}_6\text{F}_5)_4]$  dissolved in 10 mL of toluene to the autoclave using a pressure burette ( $p_{\text{pol}} + 1.0$  bar). The olefin consumption was monitored using a gas flow meter (Bronkhorst F-111C-HA-33P). Temperature, pressure, time, and total olefin consumption were recorded as well. The polymerization reaction was quenched with 2.0 mL of methanol and the reaction mixture was poured into 1.0 L of acidified methanol. The precipitated polymer was removed from the autoclave and all the combined polymer was washed and dried at 70 °C *in vacuo* overnight.

**Polymerization (chain shuttling).** All polymerization reactions at 0 or 30 °C were performed in a 1.1 L *Büchi* steel autoclave equipped with a paddle agitator, temperature sensor, and a heating/cooling jacket attached to a cryo-/thermostat unit (Thermo Scientific HAAKE DynaMax). The Ar pressure for all manipulations was set to 1.3 bar. Prior to polymerization the autoclave was equipped with 300 mL of dry toluene and 2.0 mL of 1.1 M TIBA solution in toluene and heated up to 90 °C. After maintaining the temperature for 15 min the scrubbing solution was released. For the polymerization, the autoclave was charged with 260 mL of dry toluene and 2.0 mL of 1.1 M TIBA solution in toluene. Both metallocene complexes (the

amounts of the complexes are adjusted according to a productivity ratio in the homopolymerization of  $(P(C_1-M):P(C_2-M) = 2:1)$  were dissolved separately in 10 mL toluene and preactivated with 200 eq. (referring to the amount of each complex) of TIBA at 60 °C for 1 h (For  $C_2-Ti$  the *in situ* alkylation was eliminated by using a bismethylated precursor). After the desired temperature was adjusted, both alkylated metallocene solutions and the chain transfer agent ( $ZnEt_2$ , 100 or 200 eq. referring to  $C_2-M$ ) were transferred into the autoclave and the setup was pressurized with propylene. When the system was equilibrated and stable, the polymerization was started by adding 5.0 eq. (referring to the amount of each complex) of  $[Ph_3C][B(C_6F_5)_4]$  dissolved in 20 mL of toluene to the autoclave using a pressure burette ( $p_{pol} + 1.0$  bar). The propylene consumption was monitored using a gas flow meter (Bronkhorst F-111C-HA-33P). Temperature, pressure, time, and total propylene consumption were recorded as well. The polymerization reaction was quenched with 2.0 mL of methanol and the reaction mixture was poured into 1.0 L of acidified methanol. The precipitated polymer was removed from the autoclave and all the combined polymer was washed and dried at 70 °C *in vacuo* overnight. The obtained  $^aPP/iPP$  polymer blend was separated by Soxhlet extraction with methanol, *n*-pentane, *n*-hexane and *n*-heptane (each solvent for 24 h).

## 12.6 Licences for Copyrighted Content

## Chapter 4 – Manuscript Title: Ultrarigid Indenyl-based Hafnocene Complexes for the Highly Isolelective Polymerization of Propylene: Tunable Polymerization Performance Adopting Various Sterically Demanding 4-Aryl Substituents

The screenshot shows the ACS Publications website interface. At the top, there are navigation links for 'Log In', 'Register', and 'Cart'. The main header features the ACS Publications logo and navigation options for 'ACS Journals', 'ACS eBooks', and 'C&EN Global Enterprise'. A search bar is prominently displayed with options for 'Search', 'Citation', 'Subject', and 'Advanced Search'. Below the search bar, the journal title 'ORGANOMETALLICS' is shown in large, bold letters. The article title is displayed in a large font, followed by the authors' names: Martin R. Machat<sup>†</sup>, Dominik Lanzinger<sup>‡</sup>, Alexander Pöthig<sup>§</sup>, and Bernhard Rieger<sup>\*†</sup>. The article is identified as an 'Article' and includes a 'Table of Contents' link. On the right side, there are social media sharing icons and an 'Article Options' section with links for 'ACS ActiveView PDF', 'PDF (2039 KB)', 'PDF w/ Links (358 KB)', 'Full Text HTML', 'Abstract', 'Supporting Info', 'Figures', 'References', and 'Citing Articles'. At the bottom of the article page, there is a note about ACS Editors' Choice and a link to the full article.

[Click here if you have difficulty reading this email >>](#)

Dear Martin,

Your permission requested is granted and there is no fee for this reuse. In your planned reuse, you must cite the ACS article as the source, add this direct link <https://pubs.acs.org/doi/abs/10.1021/acs.organomet.6b00814>, and include a notice to readers that further permissions related to the material excerpted should be directed to the ACS.

“ACS Editors' Choice: This is an open access article published under an ACS AuthorChoice License, which permits copying and redistribution of the article or any adaptations for non-commercial purposes.”

## Chapter 5 – Manuscript Title: Titanocenes in Olefin Polymerization: Sustainable Catalyst System or an Extinct Species?



RightsLink®

Home

Create Account

Help



**Title:** Titanocenes in Olefin Polymerization: Sustainable Catalyst System or an Extinct Species?  
**Author:** Martin R. Machat, Christian Jandl, Bernhard Rieger  
**Publication:** Organometallics  
**Publisher:** American Chemical Society  
**Date:** Apr 1, 2017  
Copyright © 2017, American Chemical Society

LOGIN

If you're a [copyright.com](#) user, you can login to RightsLink using your copyright.com credentials. Already a [RightsLink](#) user or want to [learn more?](#)

### PERMISSION/LICENSE IS GRANTED FOR YOUR ORDER AT NO CHARGE

This type of permission/license, instead of the standard Terms & Conditions, is sent to you because no fee is being charged for your order. Please note the following:

- Permission is granted for your request in both print and electronic formats, and translations.
- If figures and/or tables were requested, they may be adapted or used in part.
- Please print this page for your records and send a copy of it to your publisher/graduate school.
- Appropriate credit for the requested material should be given as follows: "Reprinted (adapted) with permission from (COMPLETE REFERENCE CITATION). Copyright (YEAR) American Chemical Society." Insert appropriate information in place of the capitalized words.
- One-time permission is granted only for the use specified in your request. No additional uses are granted (such as derivative works or other editions). For any other uses, please submit a new request.

BACK

CLOSE WINDOW

Copyright © 2018 [Copyright Clearance Center, Inc.](#) All Rights Reserved. [Privacy statement](#). [Terms and Conditions](#). Comments? We would like to hear from you. E-mail us at [customer@copyright.com](mailto:customer@copyright.com)

## Chapter 7 – Manuscript Title: High-Melting, Elastic Polypropylene: A One-Pot, One-Catalyst Strategy toward Propylene-Based Thermoplastic Elastomers



RightsLink®

[Home](#)[Create Account](#)[Help](#)

**Title:** High-Melting, Elastic Polypropylene: A One-Pot, One-Catalyst Strategy toward Propylene-Based Thermoplastic Elastomers

**Author:** Martin R. Machat, Dominik Lanzinger, Markus Drees, et al

**Publication:** Macromolecules

**Publisher:** American Chemical Society

**Date:** Feb 1, 2018

Copyright © 2018, American Chemical Society

[LOGIN](#)

If you're a [copyright.com user](#), you can login to RightsLink using your copyright.com credentials.

Already a [RightsLink user](#) or want to [learn more?](#)

### PERMISSION/LICENSE IS GRANTED FOR YOUR ORDER AT NO CHARGE

This type of permission/license, instead of the standard Terms & Conditions, is sent to you because no fee is being charged for your order. Please note the following:

- Permission is granted for your request in both print and electronic formats, and translations.
- If figures and/or tables were requested, they may be adapted or used in part.
- Please print this page for your records and send a copy of it to your publisher/graduate school.
- Appropriate credit for the requested material should be given as follows: "Reprinted (adapted) with permission from (COMPLETE REFERENCE CITATION). Copyright (YEAR) American Chemical Society." Insert appropriate information in place of the capitalized words.
- One-time permission is granted only for the use specified in your request. No additional uses are granted (such as derivative works or other editions). For any other uses, please submit a new request.

[BACK](#)[CLOSE WINDOW](#)

Copyright © 2018 [Copyright Clearance Center, Inc.](#) All Rights Reserved. [Privacy statement](#). [Terms and Conditions](#). Comments? We would like to hear from you. E-mail us at [customercare@copyright.com](mailto:customercare@copyright.com)